# SELECTIVE FLOCCULATION OF PYRITE AND/OR SILICA IN THE PRESENCE OF COAL

R. Venkatadri, R. Markuszewski, and T. D. Wheelock
Iowa State Mining and Minerals Resources Research Institute
and Chemical Engineering Department
Iowa State University
Ames, Iowa 50011
and
Arden B. Walters
Florida Power & Light Company
Juno Beach, Florida 33408

## Abstract

Two cationic surfactants, Arquad T-50 and Duomac T, were investigated as possible selective flocculants or coagulants for iron pyrite or silica particles in the presence of particles of eastern bituminous coal. Although these surfactants were adsorbed by all three materials, they were found to promote the flocculation of pyrite and silica much more than the flocculation of coal when the solid materials were flocculated separately. In subsequent selective flocculation tests involving binary mixtures of the solid components, a good separation of coal and silica was achieved with Duomac T by agitating the flocculating suspension for a prolonged time. However, the separation of coal and pyrite proved more elusive. While some separation was achieved with Arquad T-50 because pyrite was flocculated more extensively than coal, the separation was marginal at best.

## Introduction

There is an increasing need for industry to clean ultrafine-size coal, and one of the more promising methods for cleaning such coal is selective flocculation of either the organic material or the mineral matter (1). The principles and various applications of selective flocculation have been reviewed extensively (1-3). Much of the earlier work on this method as well as some of the recent work (4,5) has been based on the use of very long-chain, water-soluble organic polymers which act as bridging flocculants. Examples of such flocculants are polyacrylamide and polyethylene oxide polymers having a molecular weight of $10^6$ or more. Recently some success has been achieved with completely hydrophobic, water-insoluble polymers which have a greater affinity for the organic portion of coal than have the water-soluble polymers (6-8). Another class of reagents, which may act as selective flocculants or coagulants, is comprised of ionic surfactants of much lower molecular weight than the polymeric flocculants. When the surfactants are adsorbed, they produce a hydrophobic coating on the coal or mineral particles (2). If the treated particles are brought into very close contact, they can stick together because of hydrophobic interaction. However, since this interaction involves very short-range forces, the effect of longer-range electrostatic repulsive forces may need to be minimized. Achieving rapid flocculation or coagulation of hydrophobic particles smaller than 10 μm in size may require the application of very high shear rates; hence, the term "shear flocculation" has been used to describe such a method (9).

In the work described below an attempt was made to selectively flocculate iron pyrite or silica in the presence of an eastern high volatile bituminous coal by employing a cationic surfactant. Pyrite and silica are two of the most common mineral impurities in coal and their removal has been difficult to achieve when they are finely disseminated. Of the two commercial surfactants selected for this study, Arquad T-50 is an alkyltrimethylammonium chloride in which the alkyl group is derived from tallow, and Duomac T is N-tallow derivative of 1,3-propanediamine diacetate. These surfactants were selected because long-chain amines are widely used as selective flotation collectors for quartz and silicate minerals due to their ability to render these materials hydrophobic (10-12). Unfortunately various amines

are also known to be adsorbed by coal, and some have been used as coal flocculants or coagulants (13-16). Therefore, it remained to be seen whether the chosen surfactants would be selective.

In order to see if the flocculants are adsorbed by the different materials, the zeta potential of coal, pyrite, and silica was measured in both the presence and absence of the surfactants. Flocculation tests were conducted with the materials individually using various surfactant concentrations and pH levels. Based on the flocculation characteristics of the individual materials, promising conditions for the selective flocculation of pyrite or silica in the presence of coal were selected and tested.

## Experimental

### Materials

Materials used in coagulation and flocculation experiments included a specially selected high volatile bituminous coal, iron pyrite, and silica. The coal sample was from the No. 2 gas seam in Raleigh County, West Virginia, and on a dry basis it had a fixed carbon content of 65%, volatile matter content of 33%, ash content of 2-3%, a total sulfur content of 1.0-1.5%, and a pyritic sulfur content of 0.2-0.3%. The coal appeared to be highly hydrophobic and was difficult to wet or disperse in water.

Floated silica powder was obtained from Fisher Scientific Company, and iron pyrite which originated in Huanzala, Peru, was obtained from Ward's Natural Science Establishment. X-ray diffraction analysis showed the silica to be pure quartz with no detectable impurities, and it showed the pyrite to be over 99.5% pure with only traces of silica, calcite, and alumina.

Coarse lumps of coal or pyrite were crushed and then ground. A ball mill containing stainless steel balls was used to grind the pyrite in a dry state. The ground pyrite was analyzed with a Leeds and Northrup Microtrac particle size analyzer which showed that 90% of the material was smaller than 16.6 µm. The coal and silica were ground separately with a high speed impact mill, and the products which passed through a screen with 38 µm openings were used for flocculation.

Arquad T-50 and Duomac T Diacetate were supplied by Armak Chemicals and used as cationic flocculants. Arquad T-50 is a quaternary ammonium compound with the formula $RN(CH_3)_3Cl$ in which R represents alkyl groups of 14 to 18 carbon atoms derived from tallow. Duomac T is an acetic acid salt of an aliphatic diamine and has the formula $RNH(CH_2)_3NH_2\cdot(HOOCCH_3)_2$ in which R represents alkyl groups of 12 to 18 carbon atoms also derived from tallow. The typical molecular weight of Arquad T-50 is 340 and that of Duomac T is 480. Deionized water having a resistivity of 18 megohm-cm was used in the experimental work; it was prepared by passing steam condensate through a Barnstead NANOpure II deionization system. The pH of the particle suspensions was adjusted by adding either reagent grade ammonium hydroxide or hydrochloric acid.

### Methods

A cylindrical Plexiglas vessel having an inside diameter of 6 cm and height of 10 cm was used for coagulation and flocculation tests. The volume of the vessel was 250 ml, and the vessel was fitted with four vertical baffles which projected 0.7 cm into the vessel. An agitator with a variable-speed drive motor and a two-blade impeller having a diameter of 2.8 cm was used for stirring the contents of the vessel.

Flocculation tests were conducted by first dispersing either 1.0 or 2.0 g of material in 200 ml of water. If a single component was to be flocculated, 1.0 g was

used whereas if a two-component mixture was to be flocculated, 2.0 g were used. The slurry was stirred at 1700 rpm for 30 s to obtain a uniform suspension. The pH of the suspension was adjusted with either ammonium hydroxide or hydrochloric acid, and then the particles were redispersed by stirring at 1700 rpm for an additional 10 s. While stirring was continued at 1700 rpm, a dilute solution of the organic flocculant was added rapidly, whereupon the agitator speed was immediately reduced to 300 rpm and stirring was continued for 60 s. After stirring was stopped and the suspension had settled for 60 s, the clear supernatant liquid was decanted, and the remaining solids were recovered by filtration, dried, and weighed to determine the recovery or mass yield of flocculated material.

After treating a two-component mixture by the above procedure, the recovered solids were analyzed to determine the mass recovery of each component. For a coal/pyrite mixture this involved determining the total sulfur content of the flocculated product by means of a Fisher Sulfur Analyzer, and using a sulfur material balance to estimate the distribution of coal and pyrite in the product. For a coal/silica mixture, the ash content of the product was determined and used to estimate the distribution of coal and silica in the product.

For measuring the zeta potential of particles, a concentrated suspension was prepared first by mixing 1 g of material with 50 ml of 0.01 M potassium nitrate and stirring for 1 hr. Twenty drops of the concentrated suspension were subsequently diluted to 100 ml with 0.01 M potassium nitrate. The pH of the suspension was adjusted with either ammonium hydroxide or hydrochloric acid, and the suspension was stirred vigorously for 10 min. If the zeta potential of the material in the presence of a surfactant was to be determined, the requisite amount of surfactant was added and stirring was continued for 1 min. The suspension was allowed to sit overnight without stirring. The particles were resuspended by placing the mixture in an ultrasonic bath and then 20 readings of the zeta potential were made with a Zeta-Meter, system 3.0. The readings were averaged to obtain the reported value. Also the pH of the remaining suspension was redetermined and reported.

The surface of silica was characterized by measuring the induction time or time required for attachment of one or more particles of silica to a small gas bubble when brought into contact. The apparatus and procedure described by Yordan and Yoon (17) were used for this purpose. A short induction time is indicative of a hydrophobic surface, whereas a longer induction time is indicative of a hydrophilic surface.

## Results and Discussion

### Electrokinetic Properties

The measured zeta potentials of different materials in 0.01 M potassium nitrate are shown as a function of pH in Figure 1. For the bituminous coal the variation in zeta potential with pH was similar in general to that observed for other coals (18-21), and this variation has been attributed to the adsorption of positively charged hydronium ions at low pH and negatively charged hydroxyl ions at high pH (18). The nature of the zeta potential curve for pyrite suggests that the surface of the pyrite was oxidized, since similar curves were reported for oxidized pyrite by others (19,21). The zeta potential curve for unoxidized pyrite was reported to be monotonic with a single isoelectric point between pH 2 and 4. The zeta potential curve for silica was similar to that reported for quartz by Pugh (22).

When the zeta potential of the different materials was determined in a solution containing 20 ppm Arquad T-50, the results shown in Figure 2 were obtained. The large positive values of the zeta potential for coal and silica indicate that surfactant cations were adsorbed strongly by these materials over the pH range from 2 to 10. While results for pyrite were not as dramatic, they still confirm adsorption of the surfactant at both high and low pH where the zeta potential was

reversed because of adsorption. In the pH range from 3 to 10, the zeta potential of pyrite may not have been as high as that of the other materials because of competition for adsorption sites by potassium ions. Since sodium ions are known to be adsorbed by pyrite (23), it is anticipated that potassium ions would be adsorbed as well.

The results in Figure 3 indicate that Duomac T was also adsorbed strongly by the various materials over a wide pH range. The decline in zeta potential of the materials between pH 8 and 10 was probably due to a reduction in the dissociation of the diamine. The dissociation of amines is known to decrease between pH 8 and 10 whereas the dissociation of quaternary ammonium compounds remains high over the entire pH range. This would explain why the zeta potential of the materials declined at high pH in the presence of Duomac T but not in the presence of Arquad T-50.

The zeta potential of silica was found to be greatly affected by the concentration of Duomac T in the suspending medium (see Figure 4). The measurements were made at the natural pH of the suspension and showed that the zeta potential increased markedly as the concentration of Duomac T increased. These results again reflect adsorption of surfactant cations.

Flocculation of Individual Materials

The results of flocculating silica suspensions with different concentrations of Duomac T are presented in Figure 4. The recovery or yield of flocculated product increased with increasing concentrations of Duomac T until a concentration of 3 ppm was employed. At this point the silica recovery was 87% and further increases in flocculant concentration had little effect on the recovery. Interestingly, the zeta potential data for silica in Figure 4 show that silica was close to its isoelectric point when suspended in 3 ppm Duomac T. The correspondence between silica recovery and zeta potential for Duomac T concentrations up to 3 ppm suggest that a charge neutralization mechanism may have accounted for the type of flocculation which took place. On the other hand, when Duomac T concentrations of 20 ppm or more were applied, the zeta potential of silica was so high that electrostatic repulsion would create a formidable barrier to flocculation or coagulation. Nevertheless, a high recovery of silica was achieved which apparently was due to the hydrophobic coating imparted by the surfactant. The hydrophobicity of the treated silica was verified by measuring the induction time of both the treated and untreated material. Thus, the induction time of silica in water was 27.7 ms whereas in 20 ppm Duomac T it was 1.3 ms. This decrease in induction time indicates a large increase in hydrophobicity (17).

The hydrodynamics of the flocculation system may have been such that shear flocculation prevailed, since an increase in agitation time after the surfactant was added produced an increase in silica recovery. Thus with 0.5 ppm Duomac T the recovery increased from 54% for 1 min of agitation to 83% for 5 min of agitation and remained the same for up to 20 min of agitation. This type of behavior is not observed with electrolytic coagulation or polymeric flocculation where the flocs break up with prolonged agitation (9).

The effect of Duomac T concentration on silica recovery is further illustrated by the results presented in Figure 5 which show that the recovery decreased when the concentration was raised above 100 ppm. The same diagram also indicates the effect of Duomac T concentration on the recovery of pyrite and coal when these materials were treated separately at the natural pH of their respective suspensions. The maximum recovery of pyrite was achieved with a surfactant concentration of 20 ppm. Since the recovery of coal never exceeded 10%, little or no flocculation or coagulation of this material took place over the surfactant concentration range of 5 to 80 ppm. The results with coal suggest that adsorption of the surfactant cations may have reduced the hydrophobicity of the coal. This could have occurred if the

hydrophobic tails of the adsorbed cations were directed towards the surface and the hydrophilic head groups were directed away from the surface.

The effect of pH on the recovery of the different materials with 20 ppm Duomac T is shown in Figure 6. Again the materials were treated separately. While the recovery of silica remained high over the entire pH range, the recovery of pyrite was exceptionally large only between pH 4.5 and pH 10 and coal recovery peaked at pH 8-9. The maximum coal recovery was only 53% compared to a maximum recovery of about 90% for the other materials. The results indicated that it might be possible to selectively flocculate either silica or pyrite in the presence of the coal within the pH range from 2 to 6.

Flocculation results achieved when the different materials were flocculated individually with various concentrations of Arquad T-50 are presented in Figure 7. The maximum recovery of silica was obtained with 10-20 ppm Arquad T-50 and the maximum recovery of pyrite with 80 ppm at the natural pH of the suspension. The coal did not appear to be flocculated at any concentration of the surfactant within the range from 10 to 150 ppm.

The effect of pH on the recovery of the materials with 80 ppm Arquad T-50 is indicated by Figure 8. The recovery of silica and pyrite was high above pH 5, and while the recovery of coal never exceeded 25%, the best coal recovery was observed above pH 8. The results indicated that it might be possible to selectively flocculate either silica or pyrite in the presence of coal at pH 5-6.

Flocculation of Binary Mixtures

Mixtures of coal and either pyrite or silica were flocculated using conditions which would favor the selective flocculation of the inorganic material based on the preceding work. In some cases the coal constituted 90% of the mixture by weight whereas in other cases it constituted 50%. The mass recovery or yield of each component which was recovered in the settled material is given in Table 1. The separation efficiency as defined below is also indicated for each test.

$$\text{Separation Eff. (\%)} = \text{Mineral Recovery (\%)} - \text{Coal Recovery (\%)}$$

Although the percentage recovery of pyrite or silica was generally greater than the percentage recovery of coal, the difference in recovery was small so that the separation efficiency was low. The largest separation efficiency for a mixture of pyrite and coal was 26-27% which was achieved with 80 ppm Arquad T-50 at pH 4.6. Also, the highest separation efficiency for a mixture of silica and coal was only 9.7% which was obtained with 10 ppm Arquad T-50 at pH 4.9. Generally the recovery of one component of a binary mixture went hand in hand with the recovery of the other component, suggesting that the two materials underwent a process of mutual coagulation. Furthermore, in the case of silica/coal mixtures it appeared that the overall recovery was controlled by the relative amount of silica present. Thus, when a mixture containing 10% silica was flocculated, the recovery of either silica or coal was only 25-30%, whereas the recovery of each of these was generally over 80% when the initial mixture contained 50% silica. It is unlikely that electrostatic interaction would cause mutual coagulation of the particles since all of the solid components where charged positively in the presence of the cationic surfactants. On the other hand, the coal particles may have been physically entrapped in the pyrite or silica flocs (2). Also, the different solids may have been held together by hydrophobic association.

An interesting result was achieved when the time of agitation was extended after adding Duomac T to a suspension of silica and coal. As the data in Table 2 indicate, the recovery of silica increased while the recovery of coal decreased. Consequently by agitating the suspension for 20 min it was possible to obtain a separation efficiency of over 84%. However, when the same procedure was applied to

Table 1. Results of flocculating binary mixtures of particles with cationic surfactants

| Particle mixture | | Slurry | Surfactant | | Recovery, % | | Sepn. |
|---|---|---|---|---|---|---|---|
| Materials | Ratio | pH | Type | ppm | Mineral | Coal | Eff., % |
| pyrite/coal | 10/90 | 4.5 | Duomac | 20 | 76.0 | 64.9 | 11.1 |
| pyrite/coal | 50/50 | 4.5 | Duomac | 20 | 87.1 | 78.9 | 8.2 |
| pyrite/coal | 10/90 | 5.4 | Arquad | 10 | 53.0 | 36.3 | 16.7 |
| pyrite/coal | 10/90 | 4.6 | Arquad | 80 | 49.7 | 23.4 | 26.3 |
| pyrite/coal | 50/50 | 4.6 | Arquad | 80 | 54.9 | 28.1 | 26.8 |
| pyrite/coal | 50/50 | 6.0 | Arquad | 10 | 82.8 | 73.2 | 9.6 |
| pyrite/coal | 50/50 | 9.4 | Arquad | 10 | 82.0 | 78.0 | 4.0 |
| silica/coal | 10/90 | 4.5 | Duomac | 20 | 31.5 | 32.0 | -0.5 |
| silica/coal | 10/90 | 1.5 | Duomac | 20 | 25.1 | 29.3 | -4.2 |
| silica/coal | 50/50 | 1.5 | Duomac | 20 | 83.8 | 87.6 | -4.8 |
| silica/coal | 50/50 | 4.9 | Arquad | 10 | 88.3 | 78.6 | 9.7 |
| silica/coal | 50/50 | 9.6 | Arquad | 10 | 76.0 | 72.8 | 3.2 |
| silica/coal | 50/50 | 6.0 | Arquad | 80 | 86.3 | 81.5 | 4.8 |
| silica/coal | 10/90 | 6.0 | Arquad | 80 | 29.6 | 25.5 | 4.1 |

Table 2. Results of flocculating binary mixtures of particles at pH 4-5 with 20 ppm Duomac T

| Particle mixture | | Agitation | Recovery, % | | Sepn. |
|---|---|---|---|---|---|
| Materials | Ratio | time, min. | Mineral | Coal | Eff., % |
| silica/coal | 50/50 | 1 | 80.0 | 79.1 | 0.9 |
| silica/coal | 50/50 | 5 | 98.8 | 45.2 | 53.6 |
| silica/coal | 50/50 | 20 | 95.7 | 11.3 | 84.4 |
| pyrite/coal | 50/50 | 1 | 87.1 | 78.9 | 8.2 |
| pyrite/coal | 50/50 | 5 | 92.0 | 82.0 | 10.0 |
| pyrite/coal | 50/50 | 20 | 80.2 | 75.7 | 4.5 |

a suspension of pyrite and coal, no benefit was realized. Apparently the interaction between coal and silica particles was weaker than that between coal and pyrite particles. Further work is needed to explain these divergent results and to see whether the method can be extended to the separation of clay or shale and coal.

## Conclusions

Two cationic surfactants, Arquad T-50 and Duomac T, were found to strongly promote the flocculation or coagulation of iron pyrite and silica particles while showing only a moderate tendency to promote the flocculation of an eastern bituminous coal. Selective flocculation tests showed that it is possible to achieve a good separation of coal and silica with Duomac T providing the particle suspension is agitated for a prolonged time after introducing the surfactant. However, an

extended treatment time did not benefit the separation of coal and pyrite, and the separation of these materials proved more elusive.

By observing the effect on the zeta potential it was shown that the surfactants were adsorbed by all three solid materials. Adsorption of Duomac T by silica greatly increased the hydrophobicity of this solid as indicated by a corresponding decrease in measured induction time. While charge neutralization could account for coagulation of silica in the presence of small concentrations of Duomac T, it is likely that in the presence of high concentrations hydrophobic interaction between particles plays a leading role in flocculation. The increased silica recovery achieved by prolonging the time of agitation is indicative of shear flocculation of hydrophobic particles. Further research is needed to account for the interaction between coal and silica or between coal and pyrite in the presence of the surfactants.

## Acknowledgments

This work was performed for the Iowa State Mining and Mineral Resources Research Institute through funds provided by the Florida Power and Light Company. The laboratory assistance of Mr. D. A. Clark is gratefully acknowledged.

## Literature Cited

1. S. V. Krishnan, "Selective Flocculation of Fine Coal", in: Fine Coal Processing, S. K. Mishra and R. R. Klimpel (eds.), Noyes Publications, Park Ridge, New Jersey, 1987, pp. 160-178.

2. J. A. Kitchener, "Flocculation in Mineral Processing", in: The Scientific Basis of Flocculation, K. J. Ives (ed.), Sijthoff & Noordhoff, Aphen aan den Rijn, The Netherlands, 1978, pp. 283-328.

3. Shaning Yu and Y. A. Attia, "Review of Selective Flocculation in Mineral Separations", in: Flocculation in Biotechnology and Separation Systems, Y. A. Attia (ed.), Elsevier, Amsterdam, 1987, pp. 601-637.

4. L. Spencer and G. F. Brookes, "Polyacrylamides and Selective Flocculation of Coal/Shale Mixtures", Coal Preparation, 4, 133-159 (1987).

5. G. Barbery and P. Dauphin, "Selective Flocculation of Coal Fines", in: Flocculation in Biotechnology and Separation Systems, Y. A. Attia (ed.), Elsevier, Amsterdam, 1987, pp. 535-546.

6. Y. A. Attia, "Cleaning and Desulfurization of Coal Suspensions by Selective Flocculation", in: Processing and Utilization of High Sulfur Coals, Y. A. Attia (ed.), Elsevier, Amsterdam, 1985, pp. 267-285.

7. Y. A. Attia, Shaning Yu, and S. Vecci, "Selective Flocculation Cleaning of Upper Freeport Coal with a Totally Hydrophobic Polymeric Flocculant", in: Flocculation in Biotechnology and Separation Systems, Y. A. Attia (ed.), Elsvier, Amsterdam, 1987, pp. 547-564.

8. L. Spencer, S. Thompson, and G. F. Brookes, "Hydrophobic Polymers in Coal Preparation", Proceedings of International Symposium on Innovative Plant and Processes for Minerals Engineering, Doncaster, UK, March 31-April 2, 1987, (The Minerals Engineering Society), pp. 173-193.

9. L. J. Warren, "Shear Flocculation", Chemtech, 11, 180-185 (1981).

10. J. Leja, Surface Chemistry of Froth Flotation, Plenum Press, New York, 1982.

11. R. W. Smith and S. Akhtar, "Cationic Flotation of Oxides and Silicates", in: Flotation, A. M. Gaudin Memorial Volume, Vol. 1, M. C. Fuerstenau (ed.), AIME, New York, 1976, pp. 87-116.

12. A. Bleier, E. D. Goddard, and R. D. Kulkarni, "The Structural Effects of Amine Collectors on the Flotation of Quartz", in: Flotation, A. M. Gaudin Memorial Volume, Vol. 1, M. C. Fuerstenau (ed.), AIME, New York, 1976, pp. 117-147.

13. P. J. Bethel and G. F. Brookes, "Reversibility of Long-chain Alkyl Amine Adsorption at the Coal Surface", Transactions of the Institution of Mining and Metallurgy, Sec. C, 86, C164-C165 (1977).

14. N. J. Miles, "Amines and their Applicability to Coal Flotation", Ph.D. Thesis, University of Nottingham, Nottingham, England, 1983.

15. G. F. Brookes and P. J. Bethel, "Zeta Potential, Contact Angle and the Use of Amines in the Chemical Dewatering of Froth-Floated Coal", Powder Technology, 40, 207-214 (1984).

16. J. R. Field, "Some Development Associated with Flocculants during the Last Decade", Coal Preparation, 4, 79-107 (1987).

17. J. L. Yordan and R. H. Yoon, "Induction Time Measurements for the Quartz-amine Flotation System", Preprint No. 86-105 for SME Annual Meeting, New Orleans, LA, March 2-6, 1986.

18. J. A. L. Campbell and S. C. Sun, "Bituminous Coal Electrokinetics", Transactions of the Society of Mining Engineers of AIME, 247, 111-122 (1970).

19. W. W. Wen and S. C. Sun, "An Electrokinetic Study on the Oil Flotation of Oxidized Coal", Separation Science and Technology, 16, 1491-1521 (1981).

20. D. W. Fuerstenau, J. M. Rosenbaum, and J. Laskowski, "Effect of Surface Functional Groups on the Flotation of Coal", Colloids and Surfaces, 8, 153-173 (1983).

21. S. Kelebek, T. Salman, and G. W. Smith, "An Electrokinetic Study of Three Coals", Canadian Metallurgical Quarterly, 21(2), 205-209 (1982).

22. R. J. Pugh, "Selective Coagulation in Quartz-Hematite and Quartz-Rutile Suspensions", Colloid & Polymer Science, 252, 400-406 (1974).

23. A. M. Gaudin and W. D. Charles, "Adsorption of Calcium and Sodium on Pyrite", Transactions AIME, 196, 195-200 (1953).

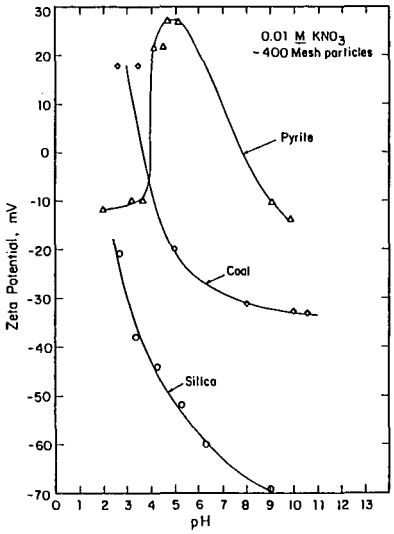


Figure 1. Zeta potential of coal, pyrite, and silica.

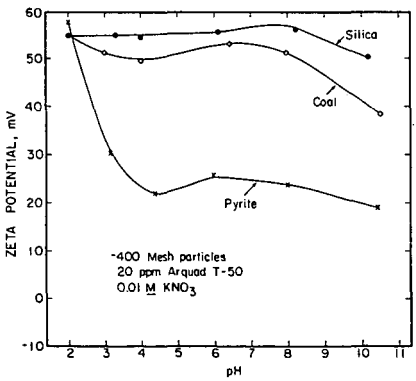


Figure 2. Zeta potential of different materials in the presence of Arquad T-50.

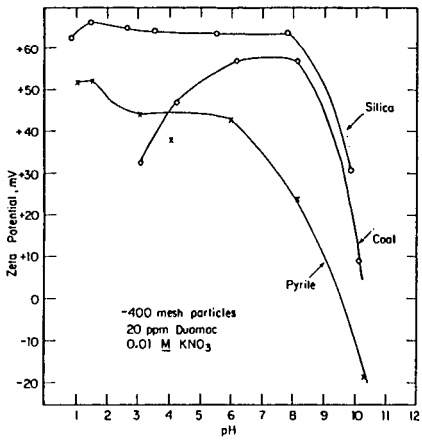


Figure 3. Zeta potential of different materials in the presence of Duomac T.

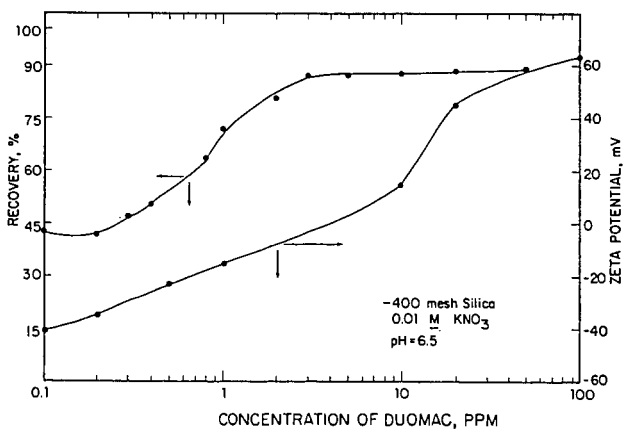


Figure 4. Effect of Duomac T concentration on the zeta potential and recovery of silica.

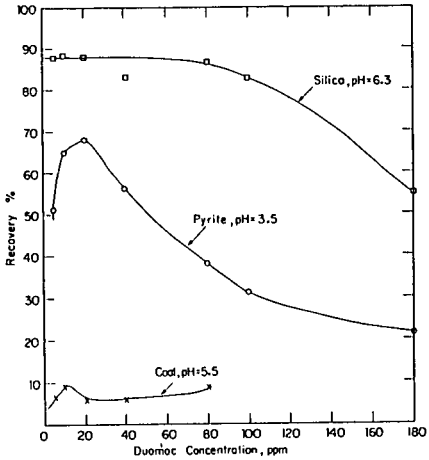


Figure 5. Effect of Duomac T concentration on the flocculation recovery.

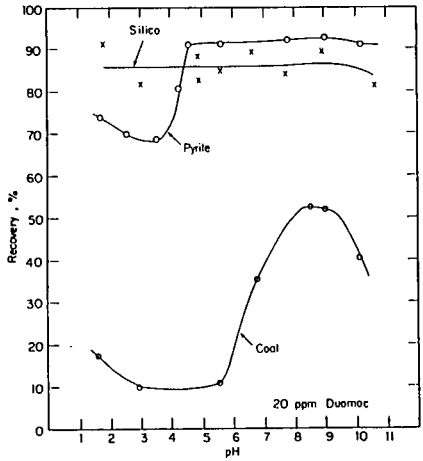


Figure 6. Effect of pH on the recovery of different materials with Duomac T.

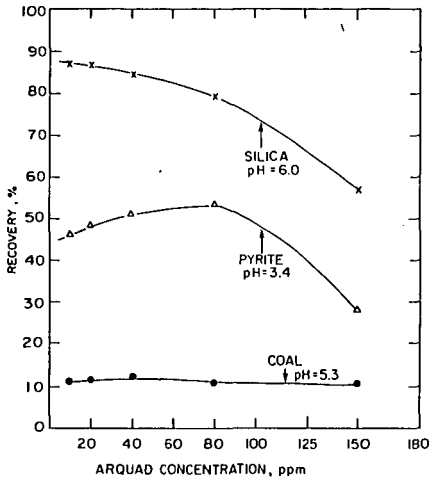


Figure 7. Effect of Arquad T-50 concentration on the flocculation recovery.

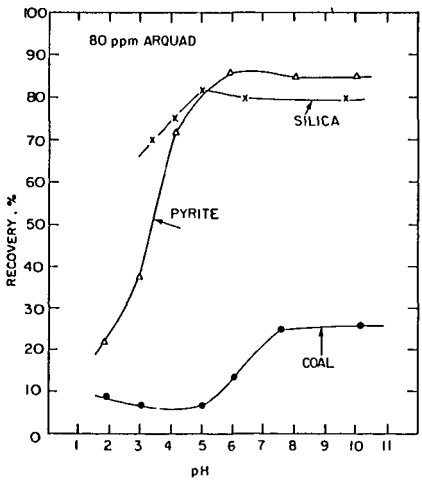


Figure 8. Effect of pH on the recovery of different materials with Arquad T-50.

# The Effects of Advanced Physical Coal Cleaning on Mineral Matter and Ash Composition and its Relationship to Boiler Slagging and Fouling Potential

P. J. DeMaris, R. B. Read, and L. R. Camp

Illinois State Geological Survey
615 East Peabody Drive
Champaign, IL 61820

## INTRODUCTION

Recent progress in cleaning medium to high-sulfur coals from the Illinois Basin by advanced flotation methods (Read et al., 1987a) has led to the need to evaluate changes in the ash fusion temperatures of deep cleaned coal. Because the alumina- and silica-rich clay minerals and coarse pyrite are more easily removed during coal cleaning than finely disseminated pyrite, it is believed that deeply cleaned coal products may have lower ash fusion temperatures because of altered composition of the remaining ash.

To investigate this question a suite of six coals, cleaned to various degrees, were analyzed for ash chemistry (ASTM method on 750°C Ash), ash fusion temperatures, petrographic variation and mineralogic composition. The samples include the two major mined seams in the Illinois Basin, the Herrin (No. 6) and Springfield (No. 5) Coal Members, as well as the widely used Pittsburgh seam. In this abbreviated paper results for ash chemistry and ash fusion analysis are reported and evaluated.

The coals tested contain a variety of minerals. For a run-of-mine (ROM) or channel sample the typical mineral suite listed in decreasing abundance order is: various clay minerals (kaolinite, illite and expandables), pyrite/marcasite, quartz, calcite and other minerals.

As these coals are cleaned certain components are more easily removed, such as the free clay and quartz (largely from floor and roof materials) and coarse pyrite/marcasite and calcite from the coal seam. While some of the mineral matter can be liberated with minimum crushing and removed by gravity separation without significant Btu loss, the finely dispersed (framboidal) pyrite requires extensive grinding to achieve significant liberation levels (Read et al., 1987B)

Ash minerals remaining in the flotation concentrates are predominantly clay, quartz, and pyrite/marcasite, with only traces of calcite remaining. Ash values for the six samples examined at various stages of cleaning are shown in Table 1. Particle size for the wet tabling step was 6M x 0. The table concentrate was ground to 80% passing 400M for the flotation step. Grinding time was 5 minutes in a stirred ball mill; mean particle size fell between 15 and 20 $\mu$m based on particle size analysis. Flotation was not optimized for ash rejection, but was maintained at acceptable (>75%) Btu recoveries.

## ASH FUSION TEMPERATURES AND ANALYSIS

Coal cleaning causes significant changes in ash fusion temperature (Table 1). Taking first the changes from the ROM sample to the tabled samples, most temperatures under reducing condition stayed the same or dropped slightly (most less than 50°C) with the largest changes in the initial deformation temperature (IDT) and lesser changes through the fluid temperature (FT). Exceptions to this were the Herrin-SC1 where the IDT dropped 75°, and the Herrin-SW where the FT dropped 75°.

From the ROM sample to tabled sample most temperatures under oxidizing conditions changed only slightly, dropping by less than 50°F; largest changes generally occurred in the FT (Table 1). Exceptions to this are the Springfield-SE sample where the FT increased 60°F and the Herrin-SW samples where the FT increased 115°F.

Examination of the changes between ROM samples and the flotation concentrates points to a wider variation. In general, the reducing temperature increased for the Springfield-SE, but decreased for the three Herrin samples. The Herrin sample with the largest drop (210°F) was the Herrin-SC2. Changes between ROM and flotation concentrate samples in a reducing environment varied considerably; for the Springfield-SE from +45°F to +95°F, for the Herrin-SC1 sample little change (+35°F to -30°F), and for Herrin-SC2 and Herrin-SW significant drops (-65°F to -205°F and +30°F to -180°F, respectively).

For the two samples received as preparation plant products (Herrin-SC3 and Pittsburgh) the flotation concentrate generally had low to moderate increases in ash fusion temperature. Under reducing conditions the Herrin-SC3 increased from +130°F for the IDT to +80°F for the FT. Similarly, the Pittsburgh coal increased 60°F for the IDT and +35°F for the FT. Under oxidizing conditions the IDT for the Herrin-SC3 was increased 210°F while the FT went up only 30°F. The Pittsburgh sample under oxidizing conditions was hardly changed; the IDT was decreased by 5°F and the FT increased 50°F.

No consistent patterns in the changes of ash fusion temperatures emerged from this data, and it was anticipated that chemistry of the ash would also be needed to gain understanding of the variations. Using the work of Winegartner and Rhodes (1975) as a model, statistical correlation analysis for 16 cases was peformed. Significant correlations between a set of variables including various oxide abundance data and derived ratios (See Table 3 for equations) and various ash fusion temperatures and temperature ranges, significant at the 99% confidence level, are reported in Table 2.

For the prediction of reducing ash fusion temperature (reducing), factors involving CaO and base % plus indices involving $SiO_2$ and $Al_2O_3$ values had high correlation coefficients (Table 2; Table 3). Best predictors for the initial deformation temperature were FeO*CaO ($r = -.91$) and the R-250 ratio ($r = .90$). Best predictors of the softening temperature were the slagging factor ($r = -.88$) and FeO*CaO ($r = -.78$). Likewise, the best predictors of the hemispherical temperature were the slagging factor ($r = -.91$) and FeO*CaO ($r = -.81$). The fluid temperature was best predicted by the slagging factor ($r = -.91$) and CaO ($r = -.81$). The temperature spread between IT and FT in reducing conditions was less strongly correlated with these variables; the highest correlation ($r = -.84$) was with FeO*$Al_2O_3$. In general, the slagging factor was the strongest single variable, and it has an inverse relationship with the ash fusion temperature. The second strongest variable for prediction of these ash fusion temperatures is FeO*CaO and it also varies in inverse relationship with the temperature.

The prediction of ash fusion temperature under oxidizing conditions is not as clear cut as those found for the reducing temperatures. The correlation coefficients are generally lower, indicating less precise matches of variation. Best predictors of initial deformation temp. were the base/acid ratio and % base, both inversely correlated ( $r = -.72$). Best predictors of the softening temperature are the slagging factor ($r = -.75$) and the base/acid ratio ($r = -.68$). The hemispherical temperature was best predicted by the slagging factor ($r = -.78$) and the $Al_2O_3$ value ($r = .70$). The fluid temperature was best predicted by the slagging factor ($r = -.80$) and the FeO*CaO value ($r = -.68$). The temperature spread between IT and FT in oxidizing conditions is not well predicted by any of the variables; signifi-

cant but weak positive correlations exist only with the fouling factor (r = .60) and the MgO value (r =.57).

## Discussion and Conclusions

In comparing these correlation coefficients to the discussion of coefficients reported in Winegartner and Rhodes (1975) for their eastern data set (which was dominated by Herrin Coal samples) many similarities exist. CaO, % base and the base/acid ratio generally had strong negative correlations with both the reducing and oxidizing ash fusion temperatures in the two studies. The dolomite ratio had a strong correlation (-.72) in our study only with the reducing temperature spread, not with both reducing and oxidizing temperatures as they found.

Winegartner and Rhodes (1975) expected to find FeO well correlated with ash fusion temperature, but were disappointed. In contrast, in our data set FeO*CaO had strong negative correlations with both reducing and oxidizing temperatures, and FeO was also correlated with the initial deformation temperature under reducing conditions. In our data set $Al_2O_3$ was positively correlated with the ST, HT and FT but not with the RT (Table 2).

Silica ratio values for these 16 samples varied between .76 and .89 and this suggests that high viscosity slags (400 poise) would be produced by this ash (Gibbs and Hill, Inc. 1978). In 4 of 6 cases the flotation concentrates had lower silica ratios than parent feeds, suggesting higher slag viscosities would result. Base/acid ratios for these coals all fell in the 0.13 to 0.28 range, making these coals suitable for dry-bottom furnaces, but unsuitable for slag-tap furnaces.

Analysis of this data set is continuing. We have presented only empirical data on a limited set of coals; broadening of the sample set and running actual combustion tests on selected samples would be most useful.

## Bibliography

Gibbs and Hill, Inc., 1978. Coal Preparation for Combustion and Conversion. EPRI Final Report AF-791 Electric Power Research Institute

Harvey et al., 1983. Mineral Matter and Trace Elements in the Herrin and Spring-Field Coal, Illinois Basin Coal Field. ISGS Contract/Grant Report 1983-4. 162 pp.

Read et al., 1987A Advanced Physical Fine Coal Cleaning: Developments in Pyritic Sulfur and Ash Reduction of Illinois Coal by ISGS Aggregate Flotation in "Processing and Utilization of High Sulfur Coals II". Y. P. Chugh and R. D. Caudle, Eds., pp. 83-93.

Read et al., 1987B The ISGS Aggregate Flotation Fine Coal Cleaning Process, Part A: Development, Characterization and Testing. Final Technical Report to Illinois Coal Development Board, 58 pp.

Winegartner, E. C. and B. T. Rhodes 1975. "An Empirical Study of the Relation of Chemical Properties to Ash Fusion Temperatures". ASME Journal of Engineering for Power . v 97. pp. 395-404.

Table 1. Changes in Ash Fusion Temperatures as a Function of Progressive Ash Reduction

| Coal | Condition* | Reducing (°F)** | | | | Oxidizing (°F)** | | | | 750°C Ash |
|---|---|---|---|---|---|---|---|---|---|---|
| | | IDT | ST | HT | FT | IDT | ST | HT | FT | (wt.%) |
| Springfield-SE | ROM | 1985 | 2095 | 2205 | 2330 | 2325 | 2395 | 2455 | 2515 | 30.8 |
| | Tabled | 1970 | 2150 | 2250 | 2350 | 2295 | 2385 | 2485 | 2575 | 12.0 |
| | AF Conc | 2040 | 2245 | 2360 | 2475 | 2370 | 2455 | 2525 | 2610 | 7.3 |
| Herrin-SC1 | ROM | 2325 | 2445 | 2565 | 2690 | 2475 | 2565 | 2660 | 2700+ | 27.7 |
| | Tabled | 2250 | 2390 | 2520 | 2655 | 2480 | 2550 | 2620 | 2670 | 10.4 |
| | AF Conc | 2230 | 2420 | 2520 | 2620 | 2510 | 2575 | 2630 | 2700+ | 5.4 |
| Herrin-SC2 | ROM | 2220 | 2335 | 2440 | 2555 | 2340 | 2510 | 2590 | 2665 | 25.5 |
| | Tabled | 2210 | 2330 | 2440 | 2550 | 2365 | 2465 | 2560 | 2665 | 8.7 |
| | AF Conc | 2010 | 2210 | 2330 | 2550 | 2135 | 2365 | 2490 | 2600 | 2.5 |
| Herrin-SC3 | PPP | 2040 | 2220 | 2350 | 2480 | 2305 | 2450 | 2530 | 2615 | 5.5 |
| | AF Conc. | 2170 | 2365 | 2460 | 2560 | 2515 | 2555 | 2605 | 2645 | 4.8 |
| Herrin-SW | ROM | 2020 | 2165 | 2305 | 2470 | 2285 | 2355 | 2425 | 2515 | 38.6 |
| | Tabled | 2045 | 2140 | 2270 | 2395 | 2285 | 2370 | 2460 | 2630 | 17.0 |
| | AF Conc | 1970 | 2125 | 2260 | 2395 | 2105 | 2345 | 2445 | 2545 | 6.4 |
| Pittsburgh | PPP | 2015 | 2345 | 2445 | 2550 | 2490 | 2550 | 2610 | 2650 | 6.5 |
| | AF Conc | 2075 | 2375 | 2480 | 2585 | 2485 | 2560 | 2615 | 2700+ | 3.8 |

* ROM = run of mine; PPP = prep. plant product; AF conc = Aggregate Flotation concentrate
** IDT = intial deformation temp; ST = softening temp.; HT = hemispherical temp.; FT = fluid temp.

Table 2 Correlation matrix of most significant coefficients

| Ash Variables | Reducing Temp. (°F) IDT | ST | HT | FT | Temp. Spread | Oxidizing Temp. (°F) IDT | ST | HT | FT | Temp. Sread |
|---|---|---|---|---|---|---|---|---|---|---|
| $SiO_2$ | | | | | -.73 | | | | | |
| $Al_2O_3$ | | .67 | .65 | .67 | | | .67 | .70 | .68 | |
| FeO | -.73 | | | | .74 | | | | | |
| CaO | | -.76 | -.79 | -.81 | | | -.66 | -.66 | -.67 | |
| MgO | | | | | | -.60 | | | | .57 |
| $K_2O$ | | | | | | | | | | |
| $Na_2O$ | | | | | | | | | | |
| $TiO_2$ | | | | | | | | | | |
| FeO*$SiO_2$ | -.78 | | | | .68 | | | | | |
| FeO*$Al_2O_3$ | | | | | .84 | -.61 | | | | |
| FeO*CaO | -.91 | -.78 | -.81 | -.79 | | -.72 | -.65 | -.67 | -.68 | |
| % Base | -.87 | -.75 | -.76 | -.68 | | -.72 | -.67 | -.67 | -.64 | |
| Base/Acid | -.86 | -.74 | -.76 | -.67 | | .57 | -.68 | -.67 | -.64 | |
| Silica ratio | .86 | .61 | .64 | .58 | | | | | | |
| Dolomite r. | | | | | -.72 | | | | | |
| R-250 ratio | .90 | .67 | .70 | .66 | | .59 | | .58 | | |
| B & W - SF | -.75 | -.88 | -.91 | -.91 | | -.62 | -.75 | -.78 | -.80 | |
| B & W - FF | | | | | | .58 | | | | .60 |

* Spread is FT minus IT in °F.

Table 3 Equations for indices*

| | | | |
|---|---|---|---|
| 1. | $FeO*SiO_2$ | = | $(FeO)(SiO_2)$ |
| 2. | $FeO*Al_2O_3$ | = | $(FeO)(Al_2O_3)$ |
| 3. | $FeO*CaO$ | = | $(FeO)(CaO)$ |
| 4. | % base | = | Sum of FeO, CaO, MgO, $K_2O$ and $Na_2O$ |
| 5. | Base/acid ratio | = | $\frac{\%\ Base}{100 - \%\ Base}$ |
| 6. | Silica value | = | $\frac{SiO_2}{SiO_2 + FeO + CaO + MgO}$ |
| 7. | Dolomite ratio | = | $\frac{CaO + MgO}{FeO + CaO + MgO + K_2O + Na_2O}$ |
| 8. | R-250 value | = | $\frac{SiO_2 + Al_2O_3}{SiO_2 + Al_2O_3 + FeO + CaO}$ |
| 9. | Babcock-Wilcox Slagging Factor | = | $\frac{Na_2O + K_2O + Fe_2O_3 + CaO + MgO}{SiO_2 + Al_2O_3 + TiO_2} \times TS\%$ |
| 10. | Babcock-Wilcox Fouling Factor | = | $\frac{Na_2O + K_2O + Fe_2O_3 + CaO + MgO}{SiO_2 + Al_2O_3 + TiO_2} \times Na_2O$ |

* oxides are expressed as mole percent with iron as FeO, normalized to $SO_3$ - free basis

# BEHAVIOR OF ASH-FORMING MINERAL MATTER IN COAL DURING CHEMICAL CLEANING WITH MOLTEN CAUSTIC

S. M. Kaushik, G. A. Norton, and R. Markuszewski

Ames Laboratory, Iowa State University, Ames, Iowa 50011

## ABSTRACT

Coal-derived mineral matter, obtained by low-temperature ashing of Kentucky No. 11 coal, as well as mineral-grade samples of quartz, illite, kaolinite, and pyrite, were treated with various ratios of molten caustic (NaOH, KOH, and 1:1 NaOH-KOH mixtures) at 370°C for 1-2 hours to study the nature of reaction products obtained under the conditions of chemical cleaning of coal by the molten caustic leaching (MCL) process. Under these conditions, most of the reactions of minerals with caustic were very rapid, being complete in less than 10 minutes. The reaction products were characterized by x-ray diffraction, thermogravimetric analysis, atomic absorption spectrophotometry, and chemical analysis. The nature of these products was related to the stoichiometry of the reaction and was useful in explaining the process chemistry and in developing regeneration schemes for the spent caustic.

## INTRODUCTION

The reaction of pyrite and coal with molten caustic has been studied first by Masciantonio (1) and then by Meyers and Hart (2) as a potential basis for the chemical cleaning of coal. It became rapidly obvious that molten caustic leaching (MCL) is of unparallelled effectiveness for removing sulfur and ash-forming minerals from coal, leading to the development of the Gravimelt Process by TRW (3-7). The process has been shown to be especially effective for the removal of organic sulfur (7-9).

However, to make this process economical, spent caustic will have to be regenerated for recycling. And to propose and test reactions for the regeneration of caustic, the nature of the reaction products anticipated in the spent caustic needs to be known. Thus, it is important to study the reactions of ash-forming minerals, present in coal, with molten caustic under conditions similar to those of the MCL process. We have undertaken such a study using quartz, kaolinite, illite, and pyrite as the major minerals found in coal and testing coal-derived mineral matter in the form of a low temperature ash.

## EXPERIMENTAL

### Materials

Quartz (St. Peters sand); kaolinite ($Al_2Si_2O_5(OH)_4$) from Twiggs Company, Georgia; illite ($KAl_2[Si_3AlO_{10}(OH)_2]$, 85% pure, from Ward's Natural Science Establishment, Inc.; and pyrite, both mineral-grade and coal-derived, were used in this study. The low temperature ash (LTA) of a Kentucky No. 11 coal was prepared by using standard procedures. Reagent-grade NaOH and KOH were powdered for easy mixing. Because of

its higher moisture content, the KOH was dried by heating above 410°C for several hours. The powdered NaOH and heated KOH contained 3% and 7% moisture, respectively, as determined by titrimetric assay or TGA.

Procedures and Analyses

Experiments were performed by mixing 1.5 g of quartz with powdered NaOH, KOH, or a 1:1 NaOH + KOH mixture using caustic-to-quartz mole ratios of 2:1, 4:1, 6:1, and 8:1. Similarly, 2 to 3 g each of kaolinite and illite were mixed with appropriate amounts of the above caustics to obtain caustic-to-clay mole ratios of 5:1, 10:1, 15:1, and 20:1. The mixtures of caustic and minerals were heated in an Inconel crucible at 370°C for 2 hours under a slow purge of helium. The reaction products were removed from the crucible while hot and then transferred to a glove box for cooling. The reaction mixture was powdered in an inert atmosphere of a glove box, and the powders were analyzed by x-ray diffraction (XRD) with a Picker x-ray diffractometer using Mo $K_\alpha$ radiation. All the time, the samples were protected from moisture during the analysis by purging the sample holder with nitrogen.

Products from the reaction of quartz with 1:1 NaOH + KOH were also washed with methanol to remove excess caustic. The residues were then dissolved in water and analyzed for Na and K by ion chromatography (IC). These data were used to calculate the $Na_2SiO_3$ and $K_2SiO_3$ mole fractions in the reaction products as a function of caustic-to-quartz mole ratio in the original mixture.

In addition, the reactions of quartz, kaolinite, illite, pyrite, and the low temperature coal ash with NaOH, KOH, or 1:1 NaOH + KOH mixtures were studied by thermogravimetric analysis (TGA) using a DuPont 951 Thermogravimetric Analyzer. The samples were prepared by mixing the appropriate amount of caustic with mineral matter or coal ash to achieve the desired caustic-to-mineral mole ratio (6:1 for quartz, 20:1 for kaolinite and illite, 10:1 for pyrite, and 2:1 for the LTA). For a typical TGA experiment, 30-50 mg of the sample mixture (mineral plus caustic) was transferred to the TGA pan and heated continuously, or isothermally at 370°C, under a nitrogen purge (50 mL/min.). The reaction products were subsequently washed with methanol or water, and the washed products were analyzed by chemical methods and by XRD.

## RESULTS AND DISCUSSION

Reactions of Caustic with Quartz

An x-ray diffraction pattern of the reaction product obtained by heating a 2:1 NaOH-to-quartz mixture at 370°C for 2 hours is shown in Figure 1. The main product has been identified as sodium metasilicate ($Na_2SiO_3$). A small amount of unreacted quartz was also present. At higher NaOH-to-quartz ratios, the reaction product was mostly sodium orthosilicate, $Na_4SiO_4$ (a representative XRD pattern of this product is shown in Figure 2). Also, unreacted NaOH was present at the higher NaOH-to-quartz mole ratios. The reactions can be described by the following equations:

$$SiO_2 + 2\ NaOH \xrightarrow{370°C} Na_2SiO_3 + H_2O\uparrow \qquad \text{(Eq. 1)}$$

$$SiO_2 + 6\ NaOH \xrightarrow{370°C} Na_4SiO_4 + 2\ NaOH + 2\ H_2O\uparrow \qquad \text{(Eq. 2)}$$

where 2 or 4 moles of NaOH react with 1 mole of quartz to form $Na_2SiO_3$ or $Na_4SiO_4$, respectively, and water is also one of the products. The products are consistent with the equilibrium diagram of the $Na_2O$ - $SiO_2$ system which shows the formation of $Na_2SiO_3$ and $Na_4SiO_4$ with a richer $Na_2O$ content in the reaction mixture (10). Although Kautz et al. (11) have found $Na_4SiO_4$ and $Na_6Si_2O_7$ as products in the NaOH - $Na_2SiO_3$ - $SiO_2$ reaction system, the absence of $Na_6Si_2O_7$ in our study is probably due to our lower temperature.

When KOH was used as the caustic, potassium metasilicate, $K_2SiO_3$, was the main reaction product at all KOH-to-quartz mole ratios. A representative XRD pattern of the reaction product obtained at the 6:1 KOH-to-quartz ratio is shown in Figure 3. This reaction can be shown by the following equation, in which only 2 moles of KOH are used for each mole of quartz to result in $K_2SiO_3$, water, and unreacted KOH:

$$SiO_2 + 6\ KOH \xrightarrow{370°C} K_2SiO_3 + 4\ KOH + H_2O\uparrow \qquad \text{(Eq. 3)}$$

The other potential product, potassium orthosilicate ($K_4SiO_4$), was not found. It is also not listed in the powder diffraction file.

When the 1:1 NaOH + KOH mixture was employed in the reactions with quartz, the products were a mixture of only $Na_2SiO_3$ and $K_2SiO_3$. Surprisingly, no $Na_4SiO_4$ was found in the reaction products when both NaOH and KOH were present, even at higher caustic-to-quartz ratios. Thus, 2 moles of the mixed caustic were always used up in the reaction for each mole of quartz.

From the IC results for Na and K, obtained during the analysis of the reaction products from treating quartz with various amounts of the 1:1 NaOH + KOH mixtures, the relative amounts of $Na_2SiO_3$ and $K_2SiO_3$ were calculated. The data for Na and K, converted to $Na_2SiO_3$ and $K_2SiO_3$, respectively, are shown in Figure 4 as a function of the amount of caustic. As can be seen, the ratio of $Na_2SiO_3$ to $K_2SiO_3$ increased with increasing caustic-to-quartz mole ratio, indicating that under these conditions quartz forms preferentially $Na_2SiO_3$. This unforeseen result has implications for chemical coal cleaning by MCL, since the spent caustic will be enriched in KOH, thus requiring less makeup KOH to maintain the 1:1 NaOH-KOH ratio in the mixed caustic used for leaching.

Reactions of Caustic with Clays

The clay minerals kaolinite and illite reacted with molten NaOH to form $NaAlO_2$ and $Na_2SiO_3$ at all NaOH-to-clay mineral ratios, i.e., 5:1, 10:1, 15:1, and 20:1. A representative XRD pattern of the NaOH-kaolinite reaction product at the 20:1 ratio is presented in Figure 5. Unreacted kaolinite, or illite, was observed in the product when reaction mixture contained 5:1 NaOH-to-clay ratio, and unreacted NaOH was found at 15:1 and 20:1 NaOH-to-clay ratios.

The reactions of excess NaOH with kaolinite and with illite can be shown by equations 4 and 5, respectively:

$$Al_2Si_2O_5(OH)_4 + 20\ NaOH \xrightarrow{370°C} 2\ NaAlO_2 + 2\ Na_2SiO_3 + 14\ NaOH + 5\ H_2O\uparrow \quad \text{(Eq. 4)}$$

$$KAl_2[Si_3AlO_{10}(OH)_2] + 20\ NaOH \xrightarrow{370°C} 3\ NaAlO_2 + 3\ Na_2SiO_3 + 11\ NaOH + 5\ H_2O \quad \text{(Eq. 5)}$$

Similarly, kaolinite and illite reacted with molten KOH to form the analogous products $KAlO_2$ and $K_2SiO_3$ at all caustic-to-clay ratios. A representative XRD pattern of the products of the KOH-illite reaction at a 20:1 KOH-to-clay ratio is shown in Figure 6.

Reactions of Caustic with Pyrite and LTA

The reaction of pyrite with molten NaOH has been studied by Chiotti and Markuszewski (12). They have proposed equation 6 under reducing and equation 7 under non-reducing conditions:

$$2\ FeS_2 + 11\ NaOH + 1/2\ C \longrightarrow 4\ Na_2S + 2\ NaFeO_2 + 1/2\ Na_2CO_3 + 5\ 1/2\ H_2O \quad \text{(Eq. 6)}$$

$$FeS_2 + 5\ NaOH \longrightarrow 1\ 5/6\ Na_2S + 1/6\ Na_2SO_3 + 2\ 1/2\ H_2O \quad \text{(Eq. 7)}$$

In both cases, $Na_2S$ and $NaFeO_2$ were the main reaction products, and approximately 5 moles of NaOH were used for the reaction with 1 mole of pyrite.

The mineral matter in the low temperature ash (LTA) of coal is composed mostly of quartz, pyrite, and clay minerals. Therefore, the anticipated products from molten caustic reaction with low temperature ash are $Na_2SiO_3$, $NaAlO_2$, $Na_2S$, and $NaFeO_2$, and the analogous potassium salts $K_2SiO_3$, $KAlO_2$, $K_2S$, and $KFeO_2$. No XRD patterns were obtained, however, since the amount of LTA sample was too small.

TGA Studies

The mineral-caustic reactions were also studied by TGA. For the reaction of quartz with caustic, the TGA in Figure 7 shows an incipient reaction at about 240°C, a more vigorous reaction at 310°C, and completion at 340°C. The TGA curves for the caustic reactions with other minerals were comparable. The isothermal plot (wt. % vs. time) at 370°C indicated that the reaction at this temperature was very fast and was completed in less than 10 minutes. The amount of weight loss, due to water evolved in this reaction, also supports the formation of $Na_4SiO_4$ and $K_2SiO_3$ as the main products of reactions with NaOH and with KOH, respectively, at 6:1 caustic-to-quartz ratios.

Figure 7 shows the isothermal TGA plots of the reactions of NaOH with low temperature ash (Kentucky No. 11 coal) and with mineral-grade pyrite. Both reactions were also very fast and were completed within 10 minutes.

Similarly, the clay minerals kaolinite and illite and a coal-derived pyrite reacted very fast with molten NaOH. Again, the reactions were completed in less than 10 minutes. Comparable results were obtained using KOH and the 1:1 NaOH + KOH mixture as the caustic.

## CONCLUSIONS

This study shows that coal mineral matter can react with fused or molten caustic at 370°C in a much shorter time of heating than that commonly used in the MCL process for chemical cleaning of coal. The reaction products are mostly $Na_2SiO_3$, $NaAlO_2$, $Na_2S$ and $NaFeO_2$ plus the analogous potassium compounds when a 1:1 NaOH + KOH mixture is employed as the molten caustic. It is, therefore, possible to calculate the amount of caustic that will be used up in reactions with mineral matter in a particular coal.

These reaction products are water-soluble, but they can form insoluble complex aluminosilicates when present together. Such insoluble aluminosilicates are expected to form during the countercurrent washing with water, and they will probably stay with the coal and the sodium carbonate (13). Fortunately, these are soluble in acid (aqueous $H_2SO_4$ or HCl) and, therefore, can be removed during the subsequent acid-washing step. Soluble silicates could then be removed from the waste streams by liming to form the insoluble calcium silicate.

## ACKNOWLEDGMENTS

Ames Laboratory is operated for the U. S. Department of Energy by Iowa State University under Contract No. W-7405-ENG-82. This work was supported by the Assistant Secretary for Fossil Energy through the Pittsburgh Energy Technology Center. We gratefully acknowledge some experimental assistance from John Finn and helpful discussions with Dr. Premo Chiotti, Dr. Colin Chriswell, and Dr. Kenneth Windom.

## LITERATURE CITED

1. P. X. Masciantonio, "The Effect of Molten Caustic on Pyritic Sulphur in Bituminous Coal," Fuel 44, 269-275 (1975).

2. R. A. Meyers and W. D. Hart, "Chemical Removal of Organic Sulfur from Coal," presented at the Amer. Chem. Soc. Meeting, Houston, TX, March 23-28, 1980.

3. TRW Energy Development Group, "Gravimelt Process Development," Final Report No. DOE/PC/42295-T7, June 1983.

4. B. Maijgren and W. Hubner, "Coal Cleaning by Molten Caustics," Proc. International Conf. on Coal Science, 1983, pp. 256-259.

5. R. A. Meyers, "Gravimelt Process Applications and Economics, Proc. 1st Annual Pittsburgh Coal Conf., 1984, pp. 381-384.

6. R. Markuszewski, D. R. Mroch, G. A. Norton, and W. E. Straszheim, "Coal Desulfurization and Demineralization by Molten Caustic Mixtures," in Fossil Fuels Utilization: Environmental Concerns, R. Markuszewski and B. D. Blaustein, eds., Am. Chem. Soc., Washington, D. C., 1986, pp. 42-50.

7. R. A. Meyers, W. D. Hart, J. F. Jones, L. C. McClanathan, J. L. Anastasi, and E. M. Barrish, "Gravimelt Process Modular Circuit Test Results," Proc. 3rd Annual Pittsburgh Coal Conf., 1986, pp. 115-129.

8. G. A. Norton, D. R. Mroch, C. D. Chriswell, and R. Markuszewski, "Chemical Cleaning of Coals with High Organic Sulfur Using Fused Caustic," in Processing and Utilization of High Sulfur Coals - II, Y. P. Chugh and R. D. Caudle, eds., Elsevier, 1987, pp. 213-223.

9. M. A. Nowak, B. R. Utz, D. J. Fauth, and S. Friedman, "Fused Salt Reactions of Organosulfur Compounds," Am. Chem. Soc. Div. Fuel Chem. Preprints, 32(4), 46-52 (1987).

10. F. C. Kracek, "The System Sodium Oxide-Silica," J. Phys. Chem. 34, 1583-1598 (1930).

11. K. Von Kautz, G. Muller, and W. Schneider, "Determination of the Cell Constants and Space Groups of Sodium Orthosilicate ($Na_4SiO_4$) and Sodium Pyrosilicate ($Na_6Si_2O_7$) and Investigation of their Regions of Stability by Using a High-Temperature Camera," Glastechn. Ber., 43, 377-381 (1970).

12. P. Chiotti and R. Markuszewski, "Reaction of Pyrite with Fused NaOH," Ind. Eng. Chem. Process Des. Dev., 24, 1137-1140 (1985).

13. N. D. Shah, C. D. Chriswell, and R. Markuszewski, "Separation by Countercurrent Washing of Coal-Caustic Mixtures During Chemical Cleaning of Coal," submitted to Separation Science and Technology, 1988.

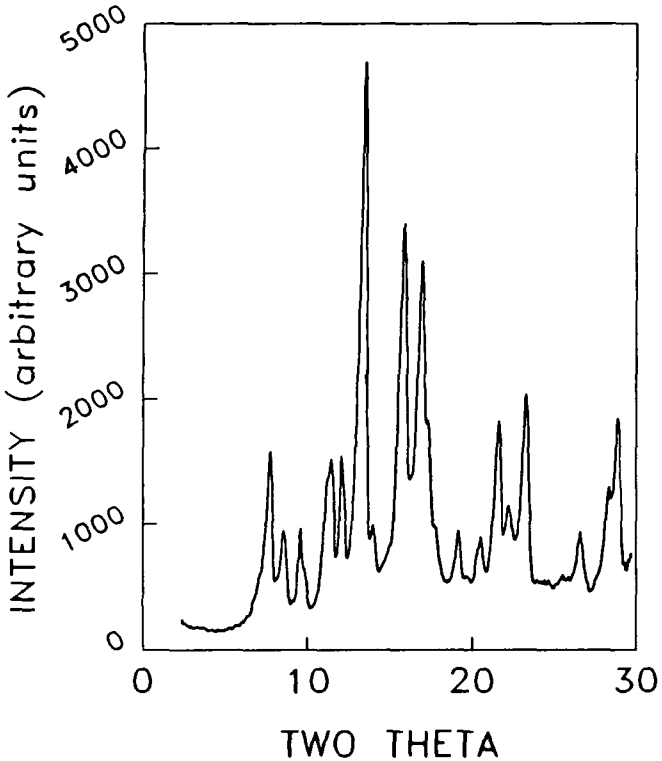


Figure 1. Typical XRD pattern for products from the reaction of $SiO_2$ with NaOH.

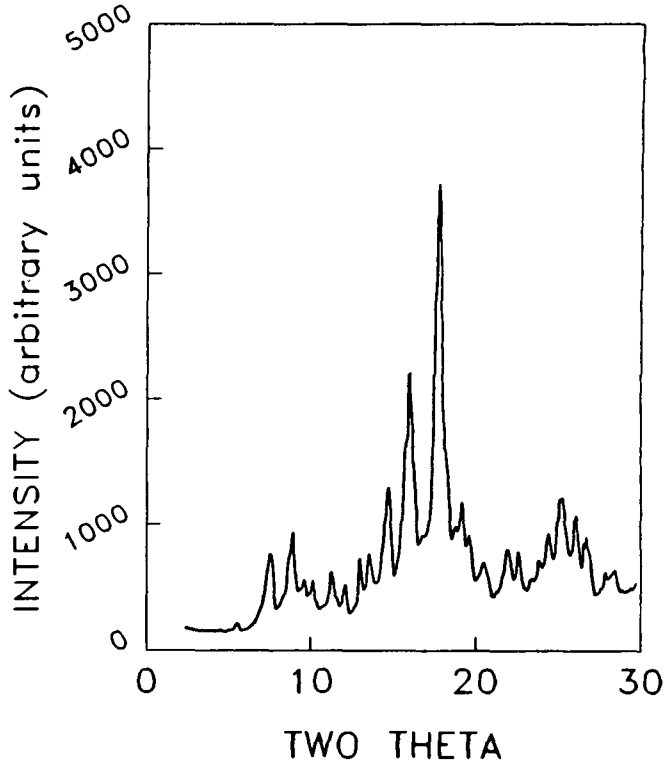


Figure 2. Typical XRD pattern for products from the reaction of $SiO_2$ with excess NaOH.

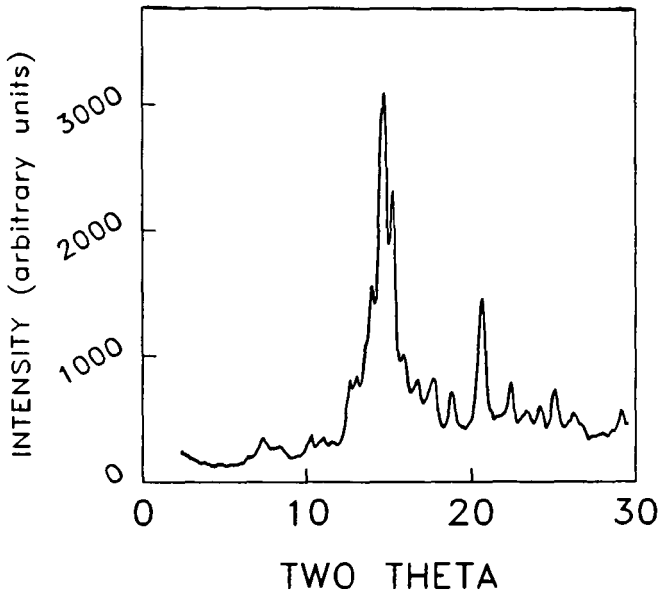


Figure 3. Typical XRD pattern for products from the reaction of $SiO_2$ with excess KOH.

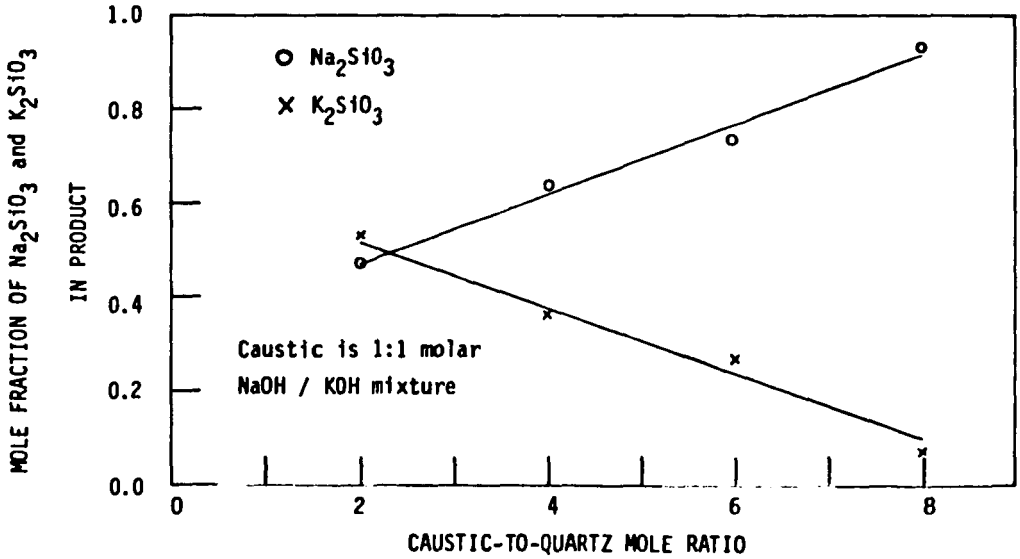


Figure 4. Mole fraction of $Na_2SiO_3$ and $K_2SiO_3$ in the product from the reaction of caustic with quartz.

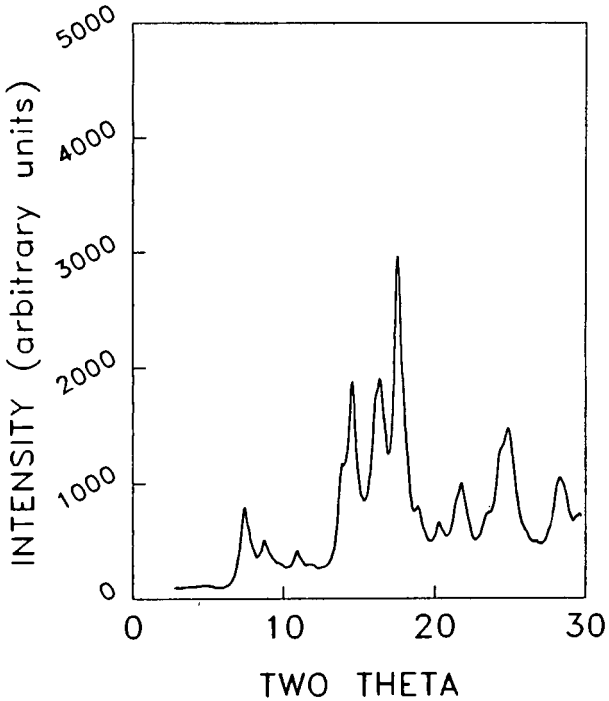


Figure 5. Typical XRD pattern for products from the reaction of kaolinite with excess NaOH.

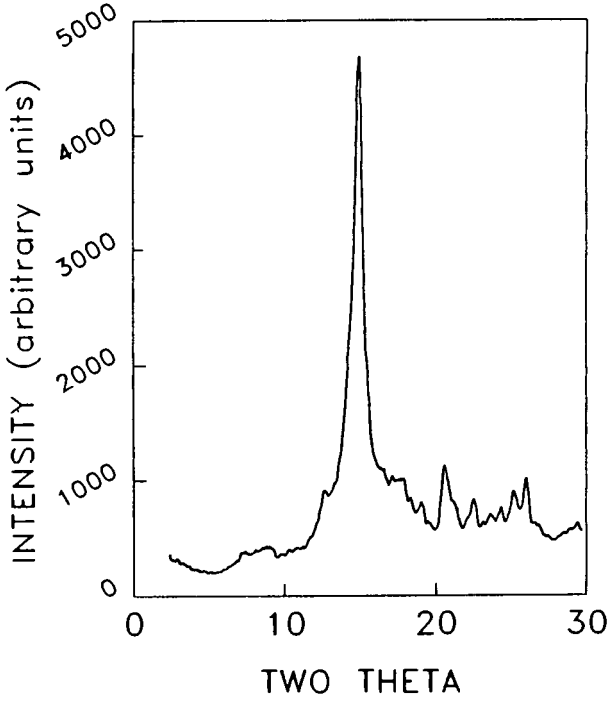


Figure 6. Typical XRD pattern for products from the reaction of illite with excess KOH.

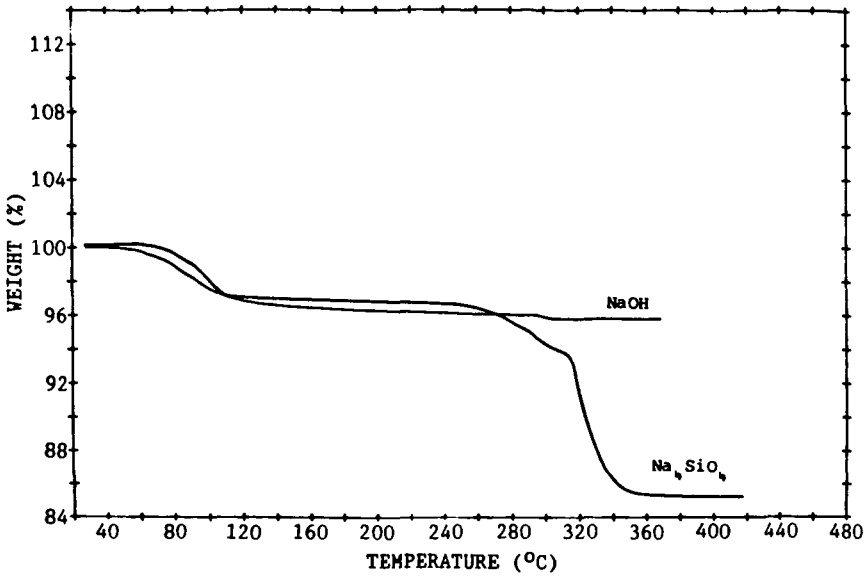


Figure 7. TGA results for the reaction of quartz with NaOH.

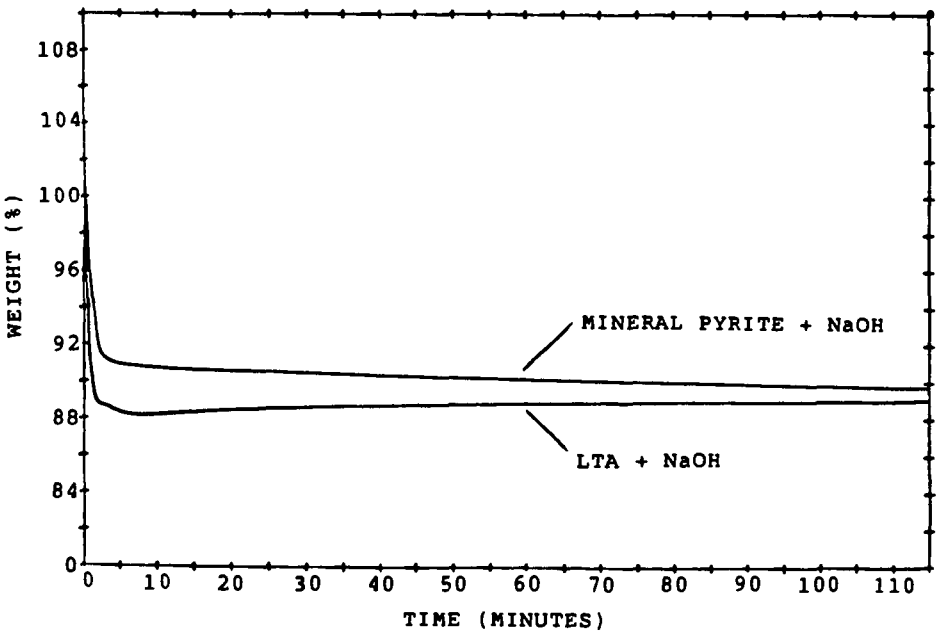


Figure 8. Isothermal TGA curves for the reaction of NaOH with mineral-grade pyrite and a low-temperature coal ash.

# THERMODYNAMIC AND RHEOLOGICAL MODELING OF COAL ASH BEHAVIOR

Harold H. Schobert and Bong-Jin Jung
Fuel Science Program
Department of Materials Science and Engineering
The Pennsylvania State University
University Park, PA 16802

## INTRODUCTION

This paper describes some recent results attained in modelling the behavior of coal ash and slags derived from it. This work is part of a larger effort which seeks to develop a unified model of ash behavior in combustion or gasification systems. A detailed description of the modelling effort has recently been published (1). Briefly, the focus of the model is on the effects of increasing temperature on coal ash and the recognition that ash will undergo a series of transformations which are specified by the composition and temperature of the ash but which may be independent of the configuration of the processing hardware in which the coal is being consumed.

The feature common to all combustion and gasification systems is that the inorganic components of the coal are exposed to temperatures high enough to induce chemical reactions, phase changes, or both. At low temperatures, dehydration reactions and thermally induced structural rearrangements occur, and are particularly important for clays. In low-rank coals, decarboxylation of the coal structure liberates alkali and alkaline earth cations for reaction elsewhere, such as substitution into the clays (2). At higher temperatures carbonate decomposition can occur.

As the temperature continues to increase, a point is eventually reached at which one or more of the low-melting components of the ash will melt. The formation of a liquid phase often marks the onset of troublesome ash behavior, such as clinkering on grates, agglomeration in fluidized beds, and deposition on steam tubes. In each of these instances, the liquid phase acts as a glue to bond solid particles together. The sintering is governed by the Frenkel equation, which relates the interparticle bonding to the viscosity and surface tension of the liquid phase (3).

At a given temperature, the viscosity and surface tension of the liquid phase will be determined by the liquid composition. However, in cases of partial melting (or of a liquid phase remaining after partial crystallization of a melt) it is unlikely that the composition of the liquid phase is the same as the bulk composition as customarily determined by analysis of the ash produced by the standard ASTM ashing procedures. Consequently, before one can apply a model to calculate the viscosity or surface tension, it is first necessary to determine the actual composition of the liquid.

Our approach to calculating liquid phase composition is the thermodynamic model SOLGASMIX (4,5,6). This program is based on minimization of the free energy of the system. An iterative calculation determines the mole fractions of the components which give the minimum Gibbs free energy, consistent with mass balance constraints. In recent work at Penn State, SOLGASMIX has been used with some success to determine the effects of composition on the growth of strength in slag deposits from pulverized coal firing of low-rank coals (7,8).

Numerous models for calculating viscosity as a function of composition are available in the literature. On the other hand, the surface tension of liquids derived from coal ash has been studied very little. Consequently, our recent work has focused on viscosity. The variety of viscosity models available, and the conflicting results occasionally obtained from them, has led us to develop a master program which incorporates six of the major viscosity models and which calculates the viscosity of a given liquid by all six models. This allows us to make an immediate comparison of the calculated results with the experimental data, and will be of assistance in assessing the applicability of the various viscosity models in our overall program.

## PROCEDURE

The objective of the present work was to test the combined SOLGASMIX - viscosity program against available experimental data. The material chosen for the test was Martin Lake (Texas) lignite, for which good slag viscosity data and x-ray fluorescence and diffraction analyses of the solidified slag were available. The experimental data derived from an earlier viscosity project, of which the methods and results have already been published (9,10).

The current version of SOLGASMIX used for this work is written in FORTRAN and is running on the Penn State IBM mainframe computer. The viscosity model program is written in FORTRAN and is also running on the mainframe. The input data for SOLGASMIX was the composition determined by x-ray fluorescence analysis of the ash produced by the ASTM ashing procedure. The liquid phase composition was calculated at 25°C intervals in the range 1200 - 1700°C. At each temperature interval, the calculated liquid phase composition was then used as the input data for the viscosity model.

## RESULTS AND DISCUSSION

### Viscosity

The viscosity was calculated using the six-model program described above. The results for this lignite showed that the best accuracy (agreement between calculated and experimental viscosities) was obtained from the $S^2$ viscosity model of Hoy et al. (11). These results are summarized in Table 1.

TABLE 1. Comparison of calculated and experimental viscosity data ($S^2$ model (11); viscosity units are poises)

| Temp. °C | Calcd. | Exptl. |
|---|---|---|
| 1350 | 321 | 220 |
| 1375 | 203 | 160 |
| 1400 | 131 | 110 |
| 1425 | 89 | 77 |
| 1450 | 64 | 55 |
| 1475 | 50 | 38* |

*Extrapolated; experimental data end at 1471°.

When comparing the calculated and experimental results shown in Table 1, it should be borne in mind that these results were obtained with absolutely no a priori assumptions about what the composition of the liquid "should be." The liquid phase composition used as input data for the viscosity model was obtained directly from the minimization of the free energy of a system having the composition of the lignite ash.

As is the case with virtually all viscosity calculation models, the work we have done so far does not provide a prediction of the temperature of critical viscosity, $T_{cv}$, nor of the viscosity vs. temperature behavior in the non-Newtonian flow region below $T_{cv}$. However, it would seem that the ability to calculate the amount and composition of the liquid and solid phases afforded by SOLGASMIX may provide the key to development of a means for calculating both of these important slag properties. Efforts to develop $T_{cv}$ and non-Newtonian viscosity predictions are planned for the future.

Liquid composition

The predicted liquid phase composition changes slightly with temperature, over the range 1350 - 1475°C for which we compared calculated and experimental viscosity data. Nevertheless, the agreement between the SOLGASMIX predictions and the x-ray fluorescence analysis of the solidified slag after a viscosity test are remarkably good, as shown in Table 2, which is given on the next page. The normal SOLGASMIX calculation determines mole fractions of elements and various compounds; however, since the x-ray analysis data are customarily reported as weight percents of the oxides, we have converted the SOLGASMIX output to the same basis for ease of comparison. (In addition, this conversion is necessary to use the SOLGASMIX results as input data for several of the viscosity calculation models.)

Although the reporting of analytical results as oxides and the use of such results as input data for viscosity models are traditions of long standing, in fact a list of oxides does not by itself convey much information about the molecular species actually present in the melt. It is extremely unlikely that very

TABLE 2. Comparison of predicted and determined compositions of Martin Lake lignite ash slag. (Data in weight percent.)

| Component | Calcd. 1350° | Calcd. 1475° | Exptl. |
|---|---|---|---|
| $SiO_2$ | 50.9 | 48.5 | 48.3 |
| $Al_2O_3$ | 15.9 | 15.0 | 14.9 |
| $Fe_2O_3$ | 7.1 | 11.9 | 11.8 |
| $TiO_2$ | 1.0 | 1.0 | 1.0 |
| $P_2O_5$ | 0.0 | 0.0 | 0.0 |
| CaO | 11.7 | 10.6 | 10.5 |
| MgO | 3.6 | 3.5 | 3.5 |
| $Na_2O$ | 1.0 | 0.9 | 0.9 |
| $K_2O$ | 0.5 | 1.1 | 1.1 |
| $SO_3$ | 8.3 | 7.5 | 7.5 |

reactive oxide donors such as the alkali and alkaline earth oxides would coexist in a melt, as oxides, with oxide acceptors such as silica or alumina. In fact, the species in the melt are most likely aluminosilicate polymers (12,13). Therefore a real test of the SOLGASMIX predictions is a comparison of the liquid phase molecular species with those found by analysis.

Information on the species in the melt was obtained by x-ray diffraction analysis of the solidified slag after a viscosity test. There are of course limitations to this method, most notably the potential for changes to occur as the melt is cooled, the presence of amorphous phases not detected by diffraction analysis, and the presence of materials in quantities below the detection limits of the equipment. Furthermore, x-ray diffraction analysis is not quantitative. These limitations notwithstanding, the comparison of x-ray diffraction results with SOLGASMIX predictions, shown in Table 3, is encouraging.

TABLE 3. Comparison of predicted (SOLGASMIX) and observed (x-ray diffraction) species in liquid phase of Martin Lake lignite ash.

| Predicted (a) | Observed | |
|---|---|---|
| $CaAl_2Si_2O_8$ | $CaAl_2Si_2O_8$ | (c) |
| $SiO_2$ | $SiO_2$ | (b) |
| $MgSiO_3$ | $MgSiO_3$ | (c) |
| $CaSO_4$ | $CaSO_4$ | (b) |
| FeO | $Fe_2O_3$ | (c) |
| $Fe_3O_4$ | | |

Notes: (a) Species predicted by SOLGASMIX are listed in decreasing order of abundance; (b) identified as a "major" phase by XRD; (c) identified as a "minor" phase by XRD.

Regarding these results, it should be noted that the calcium aluminum silicate observed by x-ray diffraction was reported as "plagioclase" (14). The term plagioclase refers to a series of

general formula (Ca,Na)(Al,Si)$AlSi_2O_8$ of which the compound listed, $CaAl_2Si_2O_8$ (anorthite), is an end member (15,16). We are not yet certain of the reason for the discrepancy between the predicted and observed iron-containing species.

At the present stage of development of the model, SOLGASMIX itself is not without difficulties. Problems have been encountered in obtaining convergence in the SOLGASMIX calculations for some systems. In particular, the calculations seem extremely sensitive to the amounts of CaO and $SO_3$ in the ash composition used as input data.

In the context of the development of the unified model of ash behavior, the work reported here indicates that, at least for some ashes, it is possible to obtain useful predictions of the liquid phase composition and viscosity over a range of temperatures using only the initial ash composition as the necessary data. Much work remains to be done. As mentioned, a problem exists with the convergence of the SOLGASMIX calculation for some compositions. The prediction of $T_{cv}$ and the viscosity - temperature curve in the non-Newtonian region remains a target for future investigations. The measurement of surface tension of ash-derived liquids and the development of a method for calculating surface tension vs. temperature from composition are research areas that are woefully under-explored. When these hurdles have all been crossed, there still remains the task of synthesizing the overall model from these components. Of course, any model at any stage of development needs continual testing against available experimental data.

ACKNOWLEDGEMENTS

This research has been supported by the Department of the Interior's Mineral Institutes program administered by the Bureau of Mines under allotment grant number G1164142. In particular, the support of the Pennsylvania Mining and Mineral Research Institute is hereby acknowledged. The authors are also pleased to acknowledge the financial support provided by The Pennsylvania State University Research Initiation Grant Program.

LITERATURE CITED

1. Schobert, H. H.; Conn, R. E.; Jung, B-J. Proc. 4th Annual Pittsburgh Coal Conf. 1987, 423.

2. Falcone, S. K.; Schobert, H. H. In "Mineral Matter and Ash in Coal"; Vorres, K. S., Ed.; American Chemical Society: Washington, 1986; Chapter 9.

3. Frenkel, J. J. J. Physics USSR 1945, 9, 385.

4. Eriksson, G. Acta Chem. Scand. 1971, 25, 7.

5. Eriksson, G. Chem. Script. 1975, 8, 100.

6. Eriksson, G.; Rosen, E. Chem. Script. 1973, 4, 193.

7. Benson, S. A. Ph.D. Dissertation, The Pennsylvania State University, University Park, PA, 1986.

8. Austin, L. G.; Benson, S. A.; Schobert, H. H.; Tangsathitkulchai, M. U.S. DOE Report 1987, No. DOE/FE-70770.

9. Streeter, R. C.; Diehl, E. K.; Schobert, H. H. In "Chemistry of Low-Rank Coals"; Schobert, H. H., Ed.; American Chemical Society: Washington, 1984; Chapter 12.

10. Schobert, H. H.; Streeter, R. C.; Diehl, E. K. Fuel 1985, 64, 1611.

11. Hoy, H. R.; Roberts, A. G.; Wilkins, D. M. Inst. Gas Engineers Pubn. 1964, No. 672.

12. Vorres, K. S. ACS Div. Fuel Chem. Preprints 1977, 22(4), 118.

13. Schobert, H. H. ACS Div. Fuel Chem. Preprints 1977, 22(4), 143.

14. Rindt, D. K. Grand Forks Energy Technology Center, personal communication, 1981.

15. Bowen, N. L. "The Evolution of the Igneous Rocks"; Dover Publications: New York, 1956; p. 45 ff.

16. Berry, L. G.; Mason, B. "Mineralogy"; W. H. Freeman: San Francisco, 1959; Chapter 15.

# FORMATION AND GROWTH OF COAL ASH AGGLOMERATES

R. H. Carty, D. M. Mason, S. D. Kline, and S. P. Babu

Institute of Gas Technology
3424 South State Street
Chicago, Illinois 60616

## BACKGROUND

The behavior of the mineral matter of coal and its reaction product, ash, is of concern in gasification processes because it governs deposition on gasifier and downstream surfaces as well as agglomeration in ash-agglomerating gasifiers. In general, fluidized-bed coal gasifiers operate under backmixed conditions. Consequently, the gasifier solids drain stream could carry with it some unconverted carbon. In contrast, in the KRW and U-GAS processes, the high-velocity jet in the gasifier effectively agglomerates the ash, thereby facilitating its selective removal from the fluidized-bed, and thus achieving carbon conversion in excess of 98%.

The minerals in high-sulfur bituminous coal are predominantly pyrite, quartz, and clay minerals. The reactions of most importance in the formation of ash agglomerates are 1) the oxidation of the ferrous sulfide produced by the decomposition of the pyrite and 2) the subsequent or simultaneous reaction of the resulting iron oxide with the clay minerals and quartz to produce relatively low-melting iron aluminosilicates that form the matrix material for the ash agglomerates. For the ash-agglomerating fluidized-bed gasifier, the iron oxidation and iron aluminosilicate formation occur in the jet region of the reactor due to its oxidizing atmosphere and elevated temperature.

In a fluidized-bed gasifier, the char particles that contain mineral matter may be divided into two groups. One group contains a combination of clays and quartz (the acids) and pyrite or other fluxing agents such as CaO, MgO, $Na_2O$, and $K_2O$ (the bases) that will form a low-melting aluminosilicate agglomerate as the carbon in the particle is gasified. The second group of particles contain either a single type of mineral matter or very small amounts of pyrite or the other fluxing agents and lead to the formation of "free ash" that does not melt as the char is gasified. Agglomerate growth occurs both by combination of the smaller molten agglomerates and by capture of the free ash by the molten agglomerates. Therefore, the tendency of a coal to form ash agglomerates should be dependent on both the distribution of the mineral matter as well as its average composition.

Coal Mineral Matter: The overall aim of the IGT ash chemistry studies is to predict the behavior of the coal ash in a fluidized-bed gasifier on the basis of a minimum analysis of the characteristics of the feed coal mineral matter and the operating conditions of the gasifier. In this study the objective was to correlate the composition and distribution of the mineral matter for five eastern and two western coals to the behavior of their ash in a laboratory gasifier. The choice of the eastern coals was limited to washed products to concentrate on the initial phases of ash reactions — those of the ash brought into juxtaposition for reaction by the gasification of the carbon of individual particles.

Coals were sought whose ash composition would reflect the full range of the most important variable for agglomeration, the average concentration of pyrite relative to the siliceous minerals. The concentration of calcium minerals — typically calcite — is probably next most important variable. Accordingly, we selected four U.S. bituminous coals covering a wide range of iron oxide and only

small amounts of calcium oxide in the ash. An Illinois No. 6 Seam coal with high calcium oxide and low iron oxide, a western bituminous (York Seam), and a subbituminous coal (Rosebud Seam) were also selected for testing.

The mineral matter in each coal was characterized by: determination of the concentration of major and minor oxides in the ash; Mossbauer analyses to measure the concentration by type of the iron compounds present; and mineralogical analyses by computer-assisted scanning electron microscopy (SEM).[1,2] Typically, in the eastern bituminous coals, iron is present as pyrite and its oxidation products, namely sulfates. In the York coal, the iron is mainly present in chamosite and in siderite.

**MINERAL MATTER DISTRIBUTION**

For this study, a method of characterizing the distribution of the mineral matter of coal was developed. Of interest here is a practical method of determining how much of the ash of the coal yield slag of viscosity low enough for agglomeration as the char of single particles becomes completely gasified. Most important are the iron and calcium oxide contents of the ash in relation to silica plus alumina. For this investigation, the ash compositions of 32 single particles of the coals were determined chemically. Particles from the -10+12 mesh fraction of the coal were taken for analysis; this size furnishes enough ash for the chemical analysis and is about the average size, by weight, of the coal feed to a pilot plant or commercial fluidized-bed gasifier. Particle weight, ash content, and iron oxide and calcium oxide in the ash were determined. Also, the concentration of basic constituents (BC) was estimated for each particle. The estimation, which included a correction for sulfate in the particle ash, was deemed to be satisfactory on particle ashes containing less than about 20% CaO.

The agreement, or lack thereof, of the average calcium oxide and iron oxide contents of the ash of the particles with those found by the conventional analyses (Table 1) was significant in the behavior of the mineral matter in agglomeration. For example, although the average iron oxide in the ash of the 32 particles of Kentucky No. 9 coal agrees well with the conventional analysis, less than half as much calcium oxide was present in the -10+12 mesh particles as in the conventional analysis. Evidence indicates that the missing calcium oxide occurs as calcite in the cleat of the coal, along which fracture occurs in crushing, and that loss of the calcite by attrition from coal particles occurs in crushing and sieving, resulting in its concentration in the finer sieve fractions. The presence of plates of calcite, about 10 μm thick, in the cleat fractures of the Kentucky No. 9 coal was found by macroscopic examination of LTA-etched coal sections oriented perpendicular to the bedding.[1]

A loss of almost 90% of the calcium oxide from the -10+12 mesh particles is evident with the Indiana VI and Illinois No. 6 coals. No loss, or only a marginal one, is evident from the Pittsburgh No. 8 or Kentucky No. 13 coals. Nor did it occur with the subbituminous B Rosebud coal, in which the calcium occurs dispersed in the organic matter, partly as carboxylate and (probably) partly as calcite from decomposition of calcium carboxylates. However, about 90% of the average amount of iron oxide is abaent from the -10+12 mesh particles of this coal because of a similar occurrence of pyrite in the cleat.[3,4]

The distributions in particles larger and smaller than the -10+12 mesh also should be considered. In general, the distribution is expected to become wider (greater deviation from the average) as particle size decreases, and, for example, the number of particles with a single layer, whether attrital coal or vitrain, increases. The opposite may be true of larger particles, but not if the size of

particles is less than that of the predominant width of the layers. The appearance of the ashes of individual -4+5 mesh particles of the Kentucky No. 9 coal suggested that the distribution of iron in these particles does not differ much from that of the -10+12 mesh particles.[1]

At present, it is estimated that, in the absence of more than about 2 weight percent of calcium oxide, single-particle ash with iron oxide contents of between 15 and 80 weight percent may form a low-melting agglomerate after carbon burn-off without the need for combination with the ash of a different particle. A summary of the distribution of iron oxide in the ash of the -10+12 mesh particles is presented in Table 2 for the eastern bituminous coals, together with the bulk average iron oxide content. Ash of Kentucky No. 9 coal, from the same mine as that used here, agglomerated without difficulty in U-GAS pilot-plant tests with bed temperatures at about 1870°F and substantially higher temperatures in the jet. The particle analyses of this coal show 44% of the ash to have 0 to 15 weight percent $Fe_2O_3$ and 53% to have 15 to 80 weight percent $Fe_2O_3$. Although the ash of the Pittsburgh No. 8 coal has an average $Fe_2O_3$ content of 31.7 weight percent, much higher than that of the ash of the Kentucky No. 9; its fraction of ash in the 15 to 80 weight percent $Fe_2O_3$ range is much lower, only 12%. This indicates that the ash of the Pittsburgh coal should agglomerate more slowly. The same is true of the Indiana VI coal, whose ash has overall sufficient iron, 15.7 weight percent $Fe_2O_3$, for agglomeration, although very little falls in the 15% to 80% range. The Kentucky No. 13 and Illinois No. 6 coals probably have insufficient iron for agglomeration of their ash, but if so, the ash content of the bed in a gasifier can be allowed to rise to such an extent that almost all of the carbon is gasified.

**EXPERIMENTAL**

In the batch gasification tests used in this work, chars rather than coals were used to prevent caking of the coal particles. The preparation of the chars for the gasification tests is described in detail elsewhere.[2] The preparation of char from each coal was identical except for a sample of the Kentucky No. 9 coal that was prepared as a test of the effect of uniformity of distribution of the coal mineral matter on ash agglomeration. This sample of coal was first ground to -200 mesh to more uniformly distribute the coal mineral matter, and then it was devolatilized. During devolatilization, the coal agglomerated to form a bulk sample of char. This char was then ground and sized similar to the other char samples used in the agglomeration tests.

For the ash agglomeration tests of these coals, a previously constructed 2-inch-diameter fluidized-bed gasifier with a center jet configuration was used. A fluidizing gas of nitrogen and steam was introduced through a perforated metal disk at the bottom of the reactor and air was fed through the center jet to produce a hot region within the fluidized-bed where the temperature may be as much as 200° to 300°F higher than the temperature of the bed. Each test used a charge to the reactor of 100 g of coal char. The testing was standardized at a steam-to-oxygen molar ratio of 2:1, a bed temperature of 1950°F, and a superficial gas velocity of between 1.3 and 2.0 ft/s.

Before preparation of aliquots of the residues of the gasification tests, any clinker obtained was crushed to pass an 8-mesh sieve and was mixed with other residue. One portion of the residue was riffled and used for estimation of agglomerate content. This portion was ashed at 900° to 1100°F in a muffle furnace for at least 20 hours to remove carbon and achieve better visibility of the mineral matter. The temperature of ashing is high enough to burn off the carbon but low enough to avoid further reactions of the mineral matter, other than oxidation of the ferrous sulfide. The agglomerates, free ash, and pieces of clinker that are

isolated by the combustion of the carbon in the reactor residue were then sieved and each sieve fraction examined visually under a low-power microscope to estimate the amount of agglomerates.

A point-count analysis was also performed on the residues. Fractions of the ash coarser than 325 mesh were combined for this purpose, mounted in epoxy resin containing a yellow pigment, and polished. Removal of most of the material resulting from ashing of the char, consisting of fine grains, was essential to facilitate the point-count. Particles containing any matrix material, identified by occurrence of vesicles and usually by low reflectance, were counted as agglomerates; all others were counted as free ash, which was then augmented by the addition of the -325 mesh fraction. For the present purposes, the point-count was taken to be proportional to weight percent. Other details of the procedure are reported elsewhere.[2]

**RESULTS AND DISCUSSION**

A summary of results obtained for the agglomerate content of the ashed residues is presented in Table 3; this table includes agglomerate contents of ash from completely gasified char, calculated on the assumption that the quantity of this ash is proportional to the carbon conversion. In Table 3, excellent agreement is shown between agglomerate contents of the ash by inspection of sieve fractions and by point-count for tests on the Kentucky No. 9, Pittsburgh No. 8, and Illinois No. 6 chars in which no clinkers were produced, and also in tests on the fine-ground Kentucky No. 9, Indiana VI, and Illinois No. 6 in which clinkers were produced.

A comparison of agglomerate contents of ash from completely gasified chars for the tests on the Pittsburgh No. 8 and Illinois No. 6 chars, with and without clinkering, indicates that clinkering increases the agglomerate content. The average percent of agglomerate content obtained without clinkering is 65% to 71% of the agglomerate content obtained with clinkering; depending on the inclusion or not of the low value for agglomerates found by examination of sieve fractions in the test on the Pittsburgh No. 8 char in which clinkering occurred. With application of the correction, the "best" estimate of agglomerates obtained from the fine-ground Kentucky No. 9 is 60% to 66%, and from the Indiana VI is 61% to 67%.

An important step in the agglomeration of ash is the reaction of iron compounds with siliceous ones to form iron aluminosilicates. In a U-GAS pilot-plant test, conversion amounted to as much as 82% of the total iron, according to a Mossbauer analysis of the ash discharge. In the gasification tests reported under the previous program in which a central jet was not used, only a minor amount of iron aluminosilicate was formed.[4,5] With the addition of a central jet tube through which the oxygen is introduced, the tests on bituminous coal chars reported here show formation of iron aluminosilicate mostly in the range of 50% to 80% of the iron, as shown by the Mossbauer analyses.[1]

In the present series, the low conversion of iron to aluminosilicate in the Rosebud char can be attributed to the occurrence of pyrite both in the cleat and as large particles. Both of these factors can be expected to make conversion of iron to aluminosilicate less likely.

For the eastern coals, the best estimate of the agglomerate content of ashed residues in Table 3 gives an overall indication of their initial agglomeration potentials. It is noteworthy that these agglomerate amounts from completely gasified char range from only 38% to 66%, whereas the iron oxide of the ash of these coals ranges from 8% to 32%. An explanation is that the agglomerates from the coals with low iron oxide (the Kentucky No. 13 and the Illinois No. 6) in comparison to

the Kentucky No. 9, contain a substantially greater proportion of clay-derived material engulfed in or attached to the iron aluminosilicate matrix material.

It is also noteworthy that the agglomerate content of the ashed residue from the fine-ground Kentucky No. 9 coal was greater than that of the residues from the usual preparation. In the usual preparation, 1/4-in. top size coal was devolatilized and the resulting char was crushed to pass an 8-mesh sieve, whereas for the fine-ground tests the same coal was ground to pass a 200-mesh sieve before charring. The particle-by-particle distribution of iron in the char made by the usual preparation is probably well-represented by the data of Table 2, according to which 53% of the ash had from 15% to 80% $Fe_2O_3$. The expected effect of the fine grinding is to cluster the iron content of the ash of the particles of char more closely around the average 20% of $Fe_2O_3$ in the ash of this coal (Table 2). The test results indicate that this distribution is better for agglomeration than that of the original Kentucky No. 9 coal. These results and those on the Kentucky No. 13 coal indicate that ash containing as little as 10% $Fe_2O_3$ contributes to agglomeration. However, the resulting iron aluminosilicate may have a higher iron content because reaction with the siliceous minerals is incomplete.

The agglomerate content of the ashed residue from the Pittsburgh No. 8 char was only equal to that of the Kentucky No. 9, in spite of the substantially higher average iron oxide content of its ash — 31.7 versus 19.9 weight percent. This is attributed to the isolation from siliceous minerals of much of its pyrite, as shown by the iron oxide distribution where only 12 weight percent of the ash had between 15% and 80% $Fe_2O_3$; the effect is substantiated by a detailed point count analysis of the residue from Run 1744-30, in which no clinker was formed and in which 40% of the unagglomerated ash was in the form of iron oxide.

Three residues were analyzed by computer-assisted SEM to investigate the effect of large amounts of calcium oxide in the ash: the low calcium Kentucky No. 9 for reference; the Illinois No. 6, a high-calcium eastern bituminous; and the Rosebud, a western subbituminous with about the same amount of iron oxide and calcium oxide in the ash as the Illinois No. 6. In the residues of the gasification tests, the ratio of weight of iron-containing silicate compounds to that of other iron compounds (oxide and sulfide) is roughly equal (10:1) for the Kentucky No. 9 and Illinois No. 6 tests, and is significantly lower (about 6:1) for the Rosebud char test. This trend agrees with the Mossbauer results, which were attributed to the large size of pyrite particles and its occurrence in the cleat of the Rosebud coal. The opposite is true of the calcium; all of it in the Rosebud char has reacted to form silicates, whereas a substantial part of the calcium in the Illinois No. 6 char has not reacted, as shown by a weight ratio of about 3:1 of calcium silicates to other calcium compounds. The ratio of calcium reacted with silica to unreacted calcium would be even lower. Here again, a mineral in the cleat — calcite of the Illinois No. 6 coal — has reacted with siliceous minerals to a lesser extent than the well-distributed calcium — calcite and carboxylate — of the Rosebud coal.

The analyses for agglomerates in the residues from the Rosebud char show poor agreement, for which no explanation is apparent; no clinker was formed in either of two tests. According to the SEM analysis, the calcium oxide did react to form silicates and aluminosilicates, which should yield slag of about the same viscosity as a slag that would result if the calcium oxide had been iron oxide. As noted previously, the pyrite in this coal has been reported to occur in relatively large grains and, at the 30 mesh level of crushing, to be unattached to coal. Hence, the small amount of iron in the ash (7.0 weight percent $Fe_2O_3$) may also be less reactive than usual, similar to part of the iron in the Pittsburgh No. 8 coal.

Iron and calcium oxides in the York coal were each slightly higher than in the Rosebud, but the iron is mostly in a clay mineral and thus probably evenly distributed among all the siliceous minerals; as a result, the formation of iron calcium aluminosilicates of higher than average iron and calcium content would be much less favorable than when the iron is present as a discrete phase, as in the other coals.

In summary, the following conclusions have been made based on these results:

- A particle-by-particle method of chemical analysis can be used to determine the distribution and association of minerals in the coal feed to fluidized-bed gasifiers.

- With few exceptions, in gasification tests in which oxygen was introduced through a central jet and the fluidized bed was maintained at 1950°F, a major part of the iron was converted to iron aluminosilicates irrespective of a wide range of iron content from 10 to 32 weight percent $Fe_2O_3$ in the ash.

- Consistently low conversion of iron to aluminosilicate in the case of the subbituminous Rosebud char can be attributed to the large size of the pyrite and its occurrence in the cleat of this coal. A greater fraction of the calcium of the Rosebud coal, in which the calcium is uniformly distributed, was converted to silicates than was that of the Illinois No. 6 coal, most of which occurs in the cleat. Analyses also confirmed that a greater fraction of the iron of the Kentucky No. 9 and Illinois No. 6 coals was converted to silicates than was that of the Rosebud, most of which occurs in the cleat. This shows that calcite and pyrite that occur in the cleat and separate as free ash during grinding are less likely to form ash agglomerates.

- The results of the gasification tests performed in this study indicate that in individual coal particles $Fe_2O_3$ concentrations between 15 and 80 weight percent of the ash promote the formation of ash agglomerates, whereas ash outside this range tends to form free ash rather than agglomerates.

- In the gasification of coals of low-iron-content ash, significant formation of ash agglomerates can occur by the joining of unmelted mineral matter with relatively small amounts of the iron aluminosilicate matrix material.

- Characterization of the composition and distribution of the coal ash using the techniques developed in this study could be of assistance in setting the operating conditions of fluidized-bed, ash-agglomerating gasifiers.

**ACKNOWLEDGEMENT**

The funds for this research were provided by the Morgantown Energy Technology Center, United States Department of Energy under Contract No.: DE-AC21-84MC21313

**REFERENCES**

1. Mason, D. M. and Chao, S. S., "Determination of the Distribution of Ash, Pyrite and Basic Constituents in Coal Particles," Am. Chem. Soc. Div. Fuel Chem. Prepr. 32 (4), 203-13 (1987) Aug.-Sept.

2. Carty R. H., Mason, D. M. and Babu, S. P., Reaction Kinetics and Physical Mechanisms of Ash Agglomeration. Washington, D.C., U.S. Department of Energy, DOE/MC/21313 (To be published).

3. Kuhn, J. K., Fiene, F. and Harvey, R., "Geochemical Evaluation and Characterization of a Pittsburgh No. 8 and a Rosebud Seam Coal," Report METC/CR-78/8, 1978.

4. Chadwick, R. A., Rice, R. C., Bennett, C. M. and Woodriff, R. A., "Sulfur and Trace Elements in the Rosebud and McKay Coal Seams, Colstrip Field, Montana," Mont. Geol. Soc. Ann. Field Conf. Guide, 22, 167-75 (1975)

5. Mason, D. M., Carty, R. H., Babu, S. P., Ghate, M. R. and Lai, H. Y., "Mineral Matter Behavior in High Carbon Conversion Coal Gasifiers." Paper presented at the 1985 International Conference on Coal Science, Sydney, Australia, October 28-November 1, 1985; published in Proceedings: 1985 International Conference on Coal Science.

Table 1. SUMMARY OF AVERAGES OF SINGLE-PARTICLE ANALYSES

| | Ash (Moist Basis) | | $Fe_2O_3$ in Ash | | CaO in Ash | |
|---|---|---|---|---|---|---|
| | Avg. of Particles (Range) | Bulk Avg. | Avg. of Particles (Range) | Bulk Avg. | Avg. of Particles (Range) | Bulk Avg. |
| | wt % | | | | | |
| Kentucky No. 9 | 6.3 (0.4-32.8) | 7.6 | 22.3 (3.3-98.1) | 19.9 | 1.10 (0.41-19.2) | 2.29 |
| Pittsburgh No. 8 | 10.9 (1.0-42.1) | 7.5 | 34.2 (0.7-91.0) | 31.7 | 1.14 (0.25-28.2) | 0.90 |
| Kentucky No. 13 | 8.2 (0.3-21.2) | 7.3 | 8.6 (0.8-52.8) | 8.1 | 0.69 (0.17-11.5) | 0.90 |
| Illinois No. 6 | 10.3 (1.1-32.5) | 11.9 | 12.1 (1.8-91.7) | 10.7 | 0.83 (0.21-14.0) | 8.34 |
| Indiana VI | 16.4 (0.6-56.6) | 13.4 | 6.9 (2.0-81.7) | 15.7 | 0.36 (0.10-20.3) | 2.48 |
| Rosebud | 10.3 (2.1-45.8) | 11.3 | 0.55 (0.1-6.14) | 7.0 | 9.4 (1.95-45.3) | 7.2 |

Table 2. SUMMARY OF DISTRIBUTION OF $Fe_2O_3$ IN -10+12 MESH PARTICLES OF EASTERN BITUMINOUS COALS

| Coal | $Fe_2O_3$ Content Bulk Avg. | $Fe_2O_3$ Content Particle Avg. | Distribution of $Fe_2O_3$ Concentration in All Particle Ashes: 0-15% $Fe_2O_3$ | 15-80% $Fe_2O_3$ | 80-100% $Fe_2O_3$ |
|---|---|---|---|---|---|
| | wt% | | % of all particle ashes | | |
| Kentucky No. 9 | 19.9 | 22.3 | 44 | 53 | 3 |
| Pittsburgh No. 8 | 31.7 | 34.2 | 59 | 12 | 29 |
| Kentucky No. 13 | 8.1 | 8.6 | 89 | 11 | 0 |
| Illinois No. 6 | 10.7 | 12.1 | 82 | 16 | 2 |
| Indiana VI | 15.7 | 6.9 | 91 | 9 | 0 |

Table 3. SUMMARY OF AGGLOMERATE CONTENT OF ASHED RESIDUES FROM 2-INCH-ID GASIFICATION TESTS BY POINT-COUNT AND SIEVE ANALYSIS

| Coal | Basic Constituents, wt % | Dolomite Ratio | Test No. | Carbon Conversion, wt % | Clinker Formed | Agglomerate Content of Ashed Residue, wt %: In Total Ash: By Point-Count | In Total Ash: On Sieve Fractions | In Ash From Completely Gasified Char: By Point-Count | In Ash From Completely Gasified Char: On Sieve Fractions | Best Estimate |
|---|---|---|---|---|---|---|---|---|---|---|
| Kentucky No. 9 | 26 | 12 | 1744-06 | 63 | None | 36 | 35 | 57 | 56 | 57 |
| | | | 1744-07 | 73 | Small amt. | -- | 46 | -- | 63 | |
| Kentucky No. 9 Fine-Ground | 26 | 12 | 1744-14 | 83 | 1.2 g | 76 | 77 | 92 | 93 | 60-66[a] |
| Pittsburgh No. 8 | 35 | 4 | 1744-08 | 74 | 1.35 g | 62 | 48 | 84 | 65 | 57 |
| | | | 1744-30 | 51 | None | 26 | 29 | 56 | 57 | |
| Kentucky No. 13 | 13 | 16 | 1744-12 | 78 | 2.8 | 36[b] | 19 | 53[b] | 24 | ~38[a,b] |
| | | | 1744-15 | 46 | 1.2 | 33[b] | 24 | 61[b] | 45 | |
| Illinois No. 6 | 24 | 41 | 1744-17 | 61 | Yes | 38 | 40 | 62 | 65 | 41 |
| | | | 1744-20 | 55 | None | 22 | 23 | 39 | 42 | |
| Indiana VI | 24 | 16 | 1744-21 | 53 | 3.4 g | 55 | 50 | 100 | 94 | 61-67[a] |
| York | 23 | 50 | 1744-23 | 64 | None | 22 | 8 | 34 | 13 | ~23 |
| | | | 1744-29 | 64 | None | -- | 14 | -- | 22 | |
| Rosebud | 19 | 57 | 1744-26 | 75 | None | -- | 40 | -- | 53 | -- |
| | | | 1744-27 | 67 | None | 23 | 10 | 31 | 15 | |

[a]Corrected for the effect of clinkering as shown by the tests on the Pittsburgh No. 8 and Illinois No. 6 coals.

[b] Includes much clay with small amounts of attached iron aluminosilicate.

rhcpsp-ta

**Relation of Slag Viscosity and Surface Tension to Sintering Potential**

S.Falcone Miller* and D.P. Kalmanovitch**

*The Pennsylvania State University
Department of Material Sciences, Fuel Science
University Park, PA 16802

**University of North Dakota Energy and Mineral Research Center
Box 8213, University Station
Grand Forks, ND 58202

The purpose of this paper is to discuss the relative effect of viscosity and surface tension on sintering potential or agglomeration in coal utilization systems. Of specific interest is the effect of composition and atmosphere on viscosity and surface tension.

## BACKGROUND

Sintering is the process by which individual particles or ash particles and slag bind together to form a compact mass. The mechanisms by which sintering occurs are: viscous flow, vapor condensation, diffusion, and surface tension (1,2). Raask (3) has shown that, for coal utilization systems, the major mechanism is that of viscous flow with a reactive liquid phase. The extent of sintering, given by the square of the radius of the contact area ($x^2$) for a given time, t, is defined by the Frenkel model (3):

$$x^2 = \frac{3\gamma rt}{2\eta} \qquad (1)$$

where r is the initial particle radius, $\gamma$ is the surface tension of the liquid phase, and $\eta$ is the viscosity of the liquid phase. According to the Frenkel model, the extent of sintering is inversely proportional to the viscosity of the liquid phase and proportional to the surface tension. It is known that viscosity and surface tension are dependent on composition and atmosphere. Figure 1 (after Raask) shows the variation of surface tension , viscosity, and the rate of sintering with respect to temperature.

It must be noted that the Frenkel model is based on studies in which particles are in intimate contact with one another prior to heating. Sintering then occurs, in the case of ash species, with the formation of a liquid phase on the particle surface. In coal utilization systems, the particles are not in intimate contact with one another but are in constant relative motion. Therefore, the process of sintering or agglomeration only begins when particles collide and adhere to each other or to a slag layer. During initial contact the surface tension of the respective surfaces can play a rate-limiting role as it affects the adhesion of ash particles. The lower the surface tension of the liquid phase on the particle surface the greater the degree of adhesion and sintering resulting in either a fairly strong or large agglomerate. If the surface tension of the molten phase is sufficiently high initial adhesion may be limited. This would also be the case for particles with low viscosity liquid phases. If two particles collide, each having liquid phases of relatively high viscosity and low surface tension, initial adhesion can occur which could lead to some degree of agglomeration. However, the extent of sintering would be limited resulting in a relatively weak agglomerate (4).

To account for the non-static condition of ash particles relative to one another a modification of the Frenkel model is used (4):

$$x^2 = f\left[\frac{1}{\gamma}, t_1, r, \frac{1}{\eta}\right] \frac{3\gamma t_2\, 4}{2\eta} \qquad (2)$$

where $t_1$ refers to the contact time and $t_2$ refers to time after the initial contact. The function term indicates that as the probability and extent of initial adhesion approaches zero (high surface tension) then the degree of sintering will approach zero. However, after $t_1$, the degree of sintering will follow the Frenkel model

(Equation 1). In the probability function surface tension is inversely related to rate, whereas, in the Frenkel model the rate is proportional to the surface tension. The reason for this is that at initial contact the higher the surface tension the less the liquid "wets" the adjacent surface. After the formation of a "neck" or liquid bridge between particles (after $t_1$) surface tension pulls the liquid material from the convex surface to the concave surface at the region of the neck. With increasing surface tension the force with which adhesion of the particles occurs increases. So the case is made that surface tension does initially affect the critical adhesion of particles in the agglomeration process. However, after adhesion, the rate of sintering is governed by the viscosity of the molten phases present on the particle surface.

## EXPERIMENTAL

Ash samples used in both viscosity and surface tension determinations were produced from coal samples pulverized to -60 mesh and then ashed for three hours at 1000°C. Each sample was ashed in an oxidizing atmosphere and a reducing atmosphere of 8% hydrogen in nitrogen. The ash samples were then analyzed by X-ray fluorescence to determine bulk chemical composition.

A Haake RV-2 Rotovisco (rotating bob viscometer) unit was used for viscosity determinations. Each sample was heated to 1450°C and soaked for several to ensure complete melting. A cool down cycle was then initiated with readings taken every 10°C. The sample was equilibrated for 20 to 30 minutes at each temperature when viscosity measurements were made.

To determine surface tension a sessile drop method was used. A sample of ash was pressed into a pellet, weighed, and centered on a plaque of relatively nonreactive vitreous carbon. During heating a slag bead is formed upon melting of the ash pellet. The bead shape is determined by the surface tension forces between the liquid, gas, and solid phases. Therefore, the sessile drop technique requires geometric definition of the bead at any one temperature. The pellet image was photographed at 1000°C and 1200°C and then at 5°C intervals until the ash pellet was completely melted or a temperature of 1400°C was reached.

The computer method used to calculate surface tension was proposed by Maze and Burnet (5,6). The advantage of this technique is that a series of measurements from photographs are used to define the bead shape to calculate surface tension rather than relying on one measurement, as in the case of contact angle, thereby reducing measurement error. For a more detailed discussion of this technique refer to Miller (4) or Maze and Burnet (5,6).

## RESULTS AND DISCUSSION

### Relation of Viscosity to Atmosphere and Composition

Work conducted at the Bituminous Coal Research National Laboratory and the University of North Dakota Energy and Mineral Research Center (UNDEMRC) has shown that there are differences in slag behavior in oxidizing, reducing, and inert atmospheres (4). The results show that slag viscosity is decreased under reducing conditions and increases under oxidizing conditions as in the case of the Baukol-Noonan coal slag in Figure 2.

In general, ash melts can be classified as silicate melts. The compositional components can be described as follows: glass formers ($SiO_2$ and $P_2O_5$), modifiers (CaO, MgO, $Na_2O$, and $K_2O$), and amphoterics ($Al_2O_3$ and $Fe_2O_3$). Glass formers tend to enhance polymerization of the melt while modifiers tend to disrupt polymerization. The amphoterics can act either as glass formers or modifiers (4). For high-silica slags the important factor in determining viscosity is the ratio of $SiO_2$ to modifiers. Large amounts of network formers (silica) result in a higher degree of polymerization, a rapid rate of nucleation and crystallization. This behavior produces liquid phases having higher viscosities resulting in a decreased potential for sintering.

The viscosity behavior of low-silica slags is governed by the ratio of CaO to modifiers or alkalies. Alkalies tend to inhibit silica polymerization by weakening the bonds between silica tetrahedra. Alkalies, as modifiers, also increase the rate of crystal growth by reducing viscosity thereby permitting more rapid diffusion of ions to the crystal front. Such liquid phases of low viscosity present during the ash phase would increase the potential of sintering.

Viscosity tests where additions of calcium and sodium were made to intermediate to high-silica slags show a decrease in the viscosity at all temperatures. The result of decreasing viscosity of a liquid phase is to enhance the rate of sintering or potential for agglomeration of ash particles producing a liquid phase of high alkali composition.

Effect of Atmosphere on Surface Tension

Results from three different coal slag surface tension tests conducted under oxidizing and reducing atmospheres are illustrated in Figure 3. Each point is labeled to identify the coal slag and the atmosphere under which the test was performed: Gascoyne Red (GRR, GRO), Gascoyne Blue (GBR, GBO) and Beulah (BSR, BSO) where "O" refers to oxidizing and "R" refers to reducing conditions. The oxidizing and reducing tests for each slag are connected with a straight line. In general, the surface tension of a slag is greater in a reducing atmosphere versus an oxidizing atmosphere. In addition, the temperature at which the ash pellet becomes completely liquid is higher in oxidizing atmospheres than in reducing atmospheres. Assuming a constant composition, viscosity decreases under reducing environments while surface tension increases. Given these facts the potential for sintering is enhanced in reducing versus oxidizing environments.

Relation of Surface Tension to Composition and Viscosity and Its Effect on Sintering

As previously discussed, surface tension and viscosity are important in governing the rate of sintering and the tendency of particles to agglomerate. Both surface tension and viscosity decrease with temperature while the rate of sintering increases (Figure 1). However, the rate of sintering shows an inverse relationship with viscosity and direct relationship with surface tension (Equation 2). Therefore, it is necessary to determine how viscosity and surface tension change relative to one another with changes in temperature and composition.

A series of fifteen low-rank coal slags were studied as to viscosity, surface tension, and bulk composition as shown in Table 1. Of particular interest is the relationship of silica and sodium oxide to surface tension because of their prevalence in coals, agglomerates, and ash deposits, and their effect on viscosity. While fouling tendency may not be considered to be a rigorous measure of sintering it has some merit in this study. The adhesion and sintering of ash particles in a fouling deposit is produced under dynamic conditions where the relative motion of ash particles occurs along with impaction. As discussed earlier, the process of sintering begins when particles collide and adhere to each other. Therefore the initial adhesion of particles is an important step in initiating sintering. In a standard sintering test, the ash particles are packed and heated in a static conditions where no consideration of relative motion or impaction of ash particles occurs. Ashes which tend to agglomerate are designated with an "-H" or "-M" for high or moderate agglomerating tendency, respectively. Ashes which displayed a low tendency to foul or agglomerate are designated with an "-L". The classification is qualitative and determined by pilot-scale combustion and deposition results.

In general, slags having higher silica content tend to have higher surface tension while slags high in sodium content have lower surface tensions. Figure 4 is a plot of the ratio of the mole fraction of $SiO_2$ to $Na_2O$ as a function of surface tension. There is a separation between those ashes which have a lower tendency to agglomerate and those ashes which tend to agglomerate. This data along with viscosity data suggests that increased silica oxide content increases both surface tension and viscosity. An increase in sodium oxide content decreases both viscosity and surface tension. Figure 4 shows those coals characterized as low agglomerating ashes having increased silica content and higher surface tensions. Conversely, coals with increased sodium content have lower surface tension but have increased fouling and agglomerating tendency. These results seem to be contrary to the relations in Equation 1. Therefore the effect on sintering due to compositional variations must be due to the relative change in surface tension and viscosity with composition.

To determine the relationship of surface tension and viscosity as it varies with composition it was decided to use a combination of experimental surface tension data with calculated viscosity values. The following assumptions were made in the Frenkel model:

- The particle radius (r) and time ($t_2$) were assumed to be constant. Therefore $x^2$ is proportional to $\gamma\eta$.
- A modified version of the Urbain equation developed by Kalmanovitch (7) was used to calculate the viscosity of the molten phases at the temperature at which each surface tension measurement was taken. The equation used was based on its successful application in predicting viscosities in previous studies (4).

In Figure 5 a plot of the calculated viscosities versus surface tension reveals some separation of low- and high-fouling coals. In general, the ratio of surface tension to viscosity is related to sintering potential (Equation 2). Those ashes observed to have low agglomerating behavior have low surface tension to viscosity ratios. Those ashes which tend to exhibit agglomeration have larger surface tension to viscosity ratios.

## CONCLUDING REMARKS

The discussion here suggests the following relationships:

- Slag viscosity decreases while surface tension increases under a reducing atmosphere. The net result is increased sintering potential of an ash in a reducing versus oxidizing environment
- An increased silicon dioxide content increases the viscosity of a slag at a greater rate than the surface tension of the slag. The net result is reduced sintering.
- An increased sodium oxide content (possibly total alkali content) decreases the viscosity of a slag at a greater rate than the slag surface tension. The net result is an increase in sintering.
- Those ashes which tend not to sinter or agglomerate form molten phases which have higher viscosities relative to their surface tension at a given temperature and those ashes which tend to agglomerate form molten phases which have lower viscosities relative to their surface tension at a given temperature.

## REFERENCES


1. Kuczynski, G.C. 1949. J. Metals, 169.
2. Kuczynski, G.C. 1977. J. Science Sintering, 243.
3. Raask, Erich. 1985. Mineral Impurities in Coal Combustion. Hemisphere Pub. Corp., Washington, 484pp.
4. Miller, S.F. 1987. Ash and Slag Characterization Final Technical Report (1986-1987), University of North Dakota Energy and Mineral Research Center to the U.S. Department of Energy, Cooperative Agreement No. DE-FC21-85MC10637, 53pp.
5. Maze, C. and G. Burnet. 1969. Surface Science, 13, 451.
6. Maze, C. and G. Burnet. 1971. Surface Science, 24, 335.
7. Kalmanovitch, D.P. and M. Frank. 1988. Engineering Foundation Conference on Mineral Matter and Ash in Coal, Santa Barbara, February 1988.


## ACKNOWLEDGEMENTS


This work is funded under DOE Cooperative Agreement No. DE-FC21-85MC10637 at the University of North Dakota Energy and Mineral Research Center (UNDEMRC). The authors wish to thank Dr. Steve Benson, Research Supervisor, Combustion Studies, UNDEMRC Combustion and Environmental Research Institute for his comments and Julie Weinmann for conducting surface tension tests.

**Table 1. Chemical Composition of Sample Coal Slags (Analysis by X-Ray Fluorescence)**

| Coal | ID | Oxide Weight Percent | | | | | | | | | |
|---|---|---|---|---|---|---|---|---|---|---|---|
| | | $SiO_2$ | $Al_2O_3$ | $Fe_2O_3$ | $TiO_2$ | $P_2O_5$ | CaO | MgO | $Na_2O$ | $K_2O$ | $SO_3$ |
| Beulah High Sodium | BH | 16.4 | 12.7 | 12.9 | 1.3 | 1.7 | 27.0 | 8.6 | 19.4 | 0.0 | 0.0 |
| Beulah Low Sodium | BL | 24.3 | 16.4 | 21.2 | 1.1 | 1.2 | 21.2 | 10.1 | 4.0 | 0.3 | 0.0 |
| Gascoyne Blue | GB | 28.8 | 16.5 | 5.3 | 0.0 | 0.0 | 22.5 | 10.7 | 8.9 | 0.5 | 0.0 |
| Gascoyne Red | GR | 37.0 | 12.5 | 9.6 | 0.0 | 0.0 | 27.0 | 9.9 | 3.5 | 0.6 | 0.0 |
| Indianhead | IH | 33.8 | 20.9 | 10.0 | 0.9 | 0.3 | 20.2 | 4.9 | 2.8 | 0.9 | 5.2 |
| Indianhead | IHO | 36.0 | 22.1 | 2.8 | 1.2 | 0.1 | 24.0 | 5.8 | 1.9 | 0.9 | 5.2 |
| Martin Lake | ML | 32.9 | 17.2 | 7.5 | 1.7 | 0.0 | 25.8 | 6.2 | 4.5 | 0.4 | 3.8 |
| Martin Lake | MLO | 33.3 | 19.0 | 10.4 | 1.2 | 0.0 | 24.9 | 5.9 | 1.5 | 0.4 | 3.3 |
| Pittsburgh 8 | P8 | 46.0 | 21.8 | 20.3 | 1.2 | 0.3 | 5.4 | 1.1 | 0.0 | 2.4 | 1.5 |
| Pittsburgh 8 | P8O | 49.4 | 20.6 | 17.8 | 1.3 | 0.2 | 5.1 | 1.1 | 0.0 | 2.7 | 1.7 |
| Rosebud McKay | RM | 41.3 | 24.3 | 6.4 | 1.5 | 0.8 | 18.2 | 6.7 | 0.8 | 0.0 | 0.0 |
| Velva | VE | 23.6 | 11.4 | 7.9 | 0.9 | 0.4 | 35.9 | 9.8 | 1.6 | 0.2 | 8.4 |
| Velva | VEO | 24.7 | 22.8 | 7.4 | 0.7 | 1.1 | 20.2 | 5.1 | 3.2 | 0.6 | 14.3 |
| Wyodak | WY | 46.8 | 23.4 | 3.3 | 1.6 | 0.5 | 15.0 | 3.4 | 1.0 | 0.4 | 4.5 |
| Wyodak | WYO | 41.2 | 20.0 | 4.6 | 2.0 | 0.8 | 24.1 | 5.3 | 1.0 | 0.5 | 0.5 |

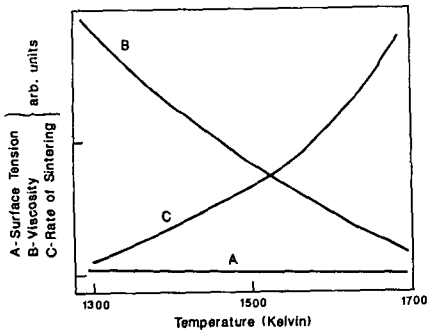


$$x^2 = \frac{3r\gamma t}{2\eta}$$

where x = radius of the interface assumed to be circular
r = radius of the spherical particles
$\gamma$ = surface tension
t = time
$\eta$ = viscosity

**Figure 1. Relation of Surface Tension and Viscosity to Sintering as a Function of Temperature**

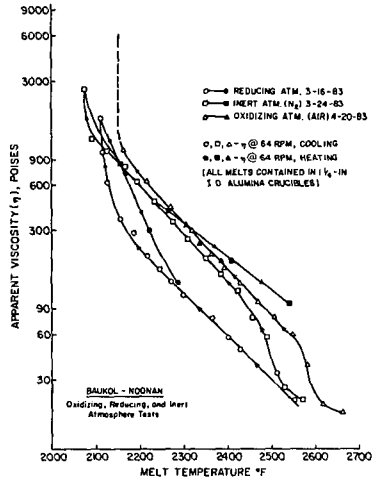


**Figure 2. Effect of Atmosphere on Boukol-Noonan Slag Viscosity**

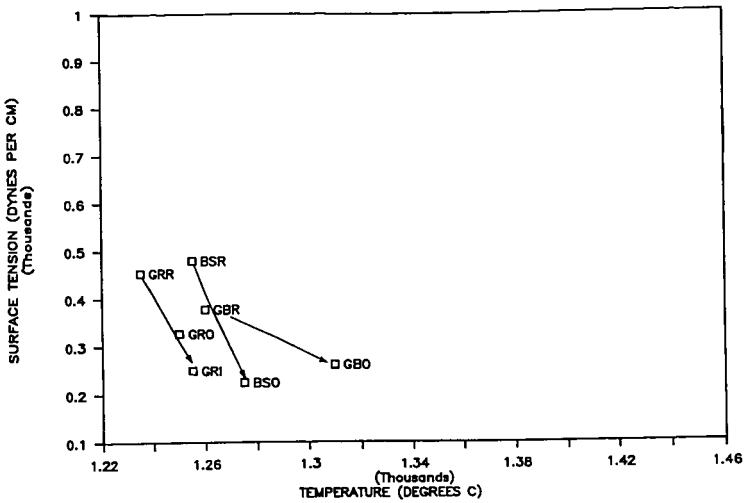


**Figure 3. Effect of Atmosphere on Slag Surface Tension**

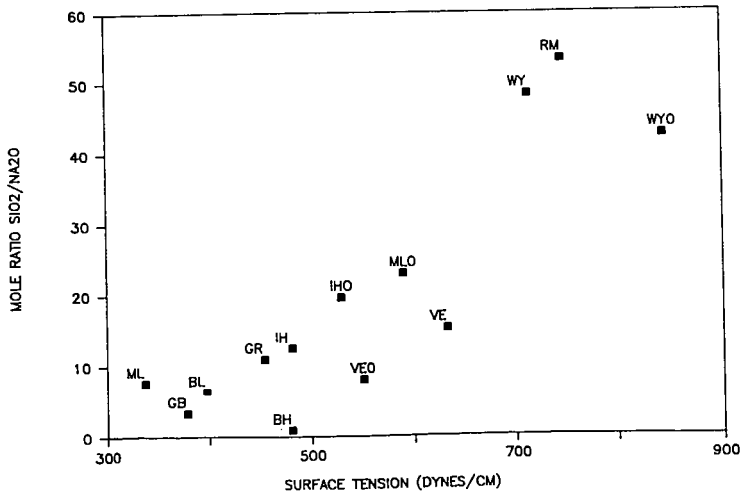


**Figure 4. Coal Slag Surface Tension Versus Mole Ratio $SiO_2/Na_2O$.**

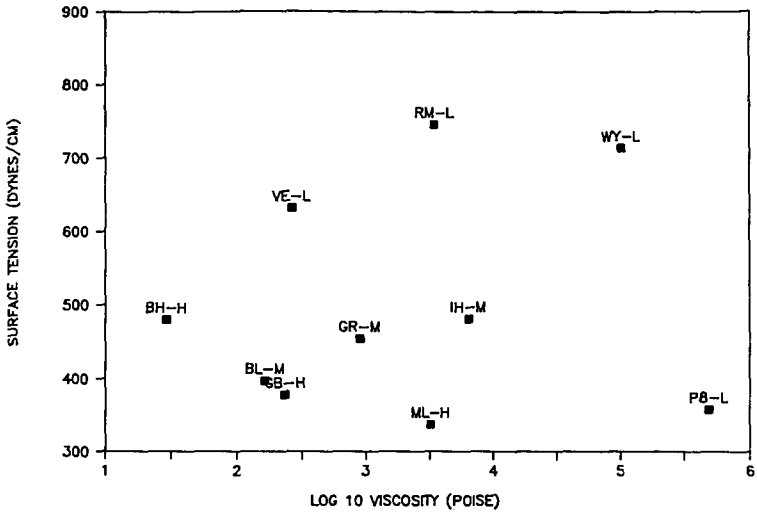


**Figure 5. Calculated Viscosity (Log 10 η) Versus Measured Surface Tension**

# Crystallization in Coal Ash Slags and Its Effect on Slag Strength

Steven A. Benson* and Leonard G. Austin

The Pennsylvania State University
108 Steidle Building
University Park, PA

## INTRODUCTION

An understanding of the crystallization behavior of coal ash melts can provide insight into slag flow behavior and the development of ash deposit strength. Past studies have shown that both the strength and crystallization behavior of coal ash pellets during sintering experiment varies dramatically from one coal to another (1). Tangsathitkulchai (1) showed that the development of strength for selected bituminous ash pellets increased to a maximum and then decreased with increasing temperature. The decrease in strength was attributed to a high degree of crystallization. The formation of the crystals was thought to change the physical properties of the pellet, thereby lowering the strength. Tangsathitkulchai found that lower ranked coal ashes exhibited a quite different behavior. These ashes exhibited a high degree of crystallization at lower temperatures and the strength appeared to increase with the degree of crystallization. In addition, no maximum in strength with temperature was found.

Kalmanovitch (2) has shown the crystallization of specific components from coal ash melts changes the composition of the residual liquid phase. Therefore, the residual liquid phase in the deposit is more ilkely to be responsible for the sintering of the ash components. This may explain the differences in ash behavior noted by Tangsathitkulchai. Kalmanovitch was able to estimate the slagging propensities of coal ashes based on the nature of the residual liquid phases as a result of crystallization of the primary components.

The formation of tenacious deposits during the combustion of western U.S. coals has been correlated with the formation of crystalline alkali and alkaline earth aluminosilicates (3,4,5). It was suggested by these investigators that the key in understanding the depositional processes related to these coals is to determine the mechanism of formation of these phases.

In this paper, low-rank coals from the U.S. were combusted and deposits were formed in a laboratory scale laminar flow tube furnace. This system has been used to evaluate the fundamentals of coal ash deposition relative to utility boilers (6,7,8,9,10). In this test a thin ray of pulverized coal is burned in a tube furnace heated to simulate the temperature history of a utility boiler. To form a deposit, the fly ash is accelerated through a simple ceramic nozzle to a velocity similar to that in a boiler. The resultant fly ash is then impacted on an oxidized steel substrate held at a controlled temperature similar to that of a boiler steel surface. A coal feed rate of about one-third of a gram per minute is sufficient to

* Presently at the University of North Dakota Energy & Mineral Research Center, Box 8213, University Station, Grand Forks, ND 58202

build a deposit within 30 minutes. The resulting deposits were examined to determine rate of growth, strength, and microstructural features.

The results presented in this paper are for deposits formed from selected western U.S. coals under simulated slagging conditions. The deposits were characterized in detail using x-ray diffraction and scanning electron microscopy and electron microprobe analysis (SEM-EDS) to determine the distribution of crystalline and amorphous phases. The distribution of these phases are compared to the strength of the deposits formed.

## EQUIPMENT AND PROCEDURES

The test apparatus is shown in detail in Figure 1. The main furnace tube of 99.8 % fused alumina (6.35 cm internal diameter and 90 cm long) has a maximum heated length of 50 cm. The tube is heated by three tangentially-fired natural gas-air burners and the temperature is controlled by adjusting the air-to-fuel ratio. The injector and secondary air preheat section is located at the top of the furnace. The secondary air is preheated to approximately 900$^{o}$C before entering the main furnace which was at 1500$^{o}$C for these tests. In addition, the preheat/injector system is equipped with a flow straightener which evenly distributes the secondary air across the muffle tube cross-section. Depending upon the coal, the total air flow is between 3-4 L/min with a coal feed rate of 0.25-0.40 g/min. Estimated particle residence times within the furnace are between 1 and 2 seconds. At the exit of the furnace the gas stream and fly ash are accelerated by a ceramic nozzle to approximately 4 m/sec prior to impingement on a boiler steel substrate held at a controlled temperature as shown in Figure 2. The gas temperature at the ceramic nozzle was approximately 1260$^{o}$C. The temperature of the boiler steel substrate was held at 500$^{o}$C.

A device was developed to measure the strength of deposits after they were removed from the test furnace. It consists of two primary components as shown in Figure 3, a miniature horizontal translator and a miniature pressure transducer. The output of the transducer is read from a strain and transducer indicator and has maximum value of 5.5 MPa (750 psi). The strength of ash deposits was determined by compressing them between the end of a steel rod and a stationary aluminum block. The deposits from the tube furnace are quite small (approximately 20 mm high and 5 mm in diameter) and strength measurements can be made at 3 mm intervals.

The deposits were examined to determine the variations in crystalline and amorphous phases. Bulk deposits were sectioned and ground for x-ray diffraction analysis to identify the crystalline phases. Deposits were also mounted in epoxy, allowed to harden, cross-sectioned, and polished for scanning electron microscopic examination. Both secondary and backscattered electron imaging were used to examine the morphology of the deposit cross-sections. Quantitative elemental analysis of specific regions within the deposits were performed with an energy dispersive x-ray detector.

## RESULTS AND DISCUSSION

The coals combusted included two lignites from the Gascoyne mine of North Dakota and a subbituminous from the Wyodak mine of Wyoming. The analysis of these coals are summarized in Table 1.

The deposits formed from these coals were lightly sintered near the base of the deposit at the deposit substrate interface. As the deposit grew in the direction of the oncoming gas stream more sintering and fusing occurred as a result of higher temperatures. In some instances the tops of the deposits appeared to have been molten.

The compressive strength of the deposits were measured from the base to the top of the deposit. Figure 4 illustrates the deposit strength versus height measured for the ash deposits produced from the three coals. The Gascoyne Blue deposit exhibited the greatest strength lower in the deposit as compared to the others. The Gascoyne White and the Wyodak deposits had very similar strengths but were weaker than the Gascoyne Blue.

The crystalline phases common to these deposits and their chemistries are listed in Table 2. The crystalline phases identified in the deposit sections are summarized in Table 3. The distribution of phases are listed in order of decreasing abundance based on the intensity of the x-ray peaks. The abundance designation is only an estimate.

The crystalline phases identified in the top portions of the Gascoyne Blue and Wyodak deposits consist mainly of complex alkali and alkaline earth aluminosilicates such as melilite and pyroxene. The top portion of the Gascoyne White deposit contained mostly amorphous material or glass. This may be due to the lower relative calcium content found in the ash of this coal. The calcium will act as a network modifier that can break up the glass network and aid in crystallization. In general, the base layer of the deposits, closest to the cooled steel substrate, contain lower quantities of the crystalline alkali and alkaline earth elements. The crystalline phases present in the base layers consist mostly of simple oxides such as quartz, lime, periclase and hematite. The silicates and aluminosilicates are in an amorphous form. The distribution of crystalline phases found in the base layer is similar to those found in fly ash.

SEM-EDS analysis was used to examine the microstructure of polished deposit cross-sections. Backscatterd electron imaging was used to distinguish between the crystalline and glassy phases. Analysis of points and areas were performed to determine the composition of the glass and crystalline phases in the melts.

Figure 5 is a backscattered electron image of a region near the top of the Gascoyne White deposit. The important features of the figure to note are the following: the deposit contains abundant glass material with small crystals growing within the glassy matrix, numerous partially reacted quartz grains, and that the crystals appear to nucleate from regions that appear bright. These bright regions contain high levels of iron as shown by the analysis of point 1 in Table 4. Point 2 has slightly lower iron content. These crystals are probably melilite based on their morphology and the x-ray diffraction analysis. The region that appears to be glass is quite homogeneous. A typical analysis of this region is point 3 in Table 4. The glass phase is very rich in sodium as compared to the crystalline phases.

SEM-EDS examination of the Gascoyne Blue deposit cross-section indicated more crystalline phases than glass material near the top. Figure 6 is a backscattered electron image of a selected area. The area is highly crystalline consisting mostly of melilite and some pyroxene crystalline phases. The materials surrounding the crystals appear to be the glass phase. The crystals found in this deposit were about twice the size of those found in the Gascoyne White deposit. Point analyses

were performed on the crystals and glass material shown in Table 5 by analysis 1 and 2, respectively. As can be seen by the analysis sodium was found to be concentrated in the glass and not in the crystals.

Figure 7 is a backscattered electron image of region near the top of the Wyodak deposit polished cross-section. The deposit appears to very dense and crystalline. There are several types of crystalline phases present in the deposit. The darker crystals have lower concentrations of iron and calcium. These may be plagioclase crystals. The brighter crystals observed are probably melilite. The crystal growth was very dense and a good analysis of the glass phase was difficult. The composition of these crystals are listed in Table 6. This coal was very low in sodium content, but formed a strong highly-crystalline ash deposit. Besides the low-sodium content, the only difference between the Wyodak and Gascoyne coals is the Si/Al molar ratio. The high strength exhibited by this deposit may be due to the interaction of calcium with the aluminosilicates to form a low melting-point phase.

The characteristics of the residual liquid phase after crystallization of the primary phases may influence the strength of these deposits. This is evident by the high concentrations of sodium in the glass or amorphous phase. Sodium containing phases have been identified as one of the primary causes of ash deposition in utility boilers firing Western coals (5). The sodium in the amorphous phase probably decreases its viscosity allowing continued sintering after crystallization has taken place.

## SUMMARY AND CONCLUSIONS

The melting and sintering of deposited ash material rich in alkali and alkaline earth elements results in the formation of highly crystalline deposits. The crystalline phases identified include melilite, plagioclase, and pyroxene.

The crystallization of components appears to be most pronounced when the ash is rich in sodium and calcium. Detailed characterization of deposit cross-sections indicates a partitioning of elements between the crystalline and glass phases. In both deposits from the Gascoyne lignite sodium was found to be concentrated in the glass phase.

The deposit formed from the Wyodak coal was highly crystalline and developed a high strength. This coal did not contain very high sodium content. The only other difference between this coal and the lignites is the Si/Al molar ratio. The available calcium in the ash may have interacted with the aluminosilicate to form a low-melting point phase that allowed sintering to take place.

The residual liquid phase after crystallization may be responsible for the development of deposit strength, and deposit growth. Therefore, the relative amounts of glass and crystalline phases formed in deposits are important parameters that affect deposit strength and growth.

## REFERENCES

1. Tangsathikulchai, M., "Studies of the Initiation, Growth and Sintering in the Formation of Utility Boiler Deposits," Ph.D. Thesis, The Pennsylvania State University, 1986.

2. Kalmanovitch, D.P., "Reactions in Coal Ash Melts," Ph.D. Thesis, Imperial College University of London, 1983.

3. Sondreal, E.A., Tufte, P.H., and Beckering, W., "Ash Fouling in the Combustion of Low-Rank Western U.S. Coals," Combustion Science and Technology, 16, 95, 1977.

4. Rindt, D.K., Selle, S.J., and Beckering, W., "Investigations of Ash Fouling Mechanisms for Western Coals using Microscopic and x-ray Diffraction Techniques," ASME, Paper No. 79-WA/CD-5, 1979.

5. Rindt, D.K., Jones, M.L., and Schobert, H.H., "Investigations of the Mechanism of Ash Fouling in Low-Rank Coal Combustion," in Fouling and Slagging from Mineral Impurities in Combustion Gases, R.W. Bryers, Ed., p17-36, 1983.

6. Abbott, M.F., and Austin, L.G., "A Study of Slag Deposit Initiation in a Drop Tube Type Furnace," in Mineral Matter and Ash in Coal, K.S. Vorres, Ed., ACS Symposium Series, No. 301, American Chemical Society, Washington, D.C., p325-352, 1986.

7. Tangsathitkulchai, M. and Austin, L.G., "Studies of Boiler Slag Deposit Formation Using a Laboratory Furnace: Part 1. Preliminary Results," ASME Paper No. 85-JPGC-Pwr-45, 1985.

8. Benson, S.A., Tangsathitkulchai, M. and Austin, L.G., "Studies of Ash Deposit Formation Using A Laboratory Furnace," Second Annual Pittsburgh Coal Conference, 689-694, 1985.

9. Austin, L.G., Benson, S.A., and Schobert, H.H., "Description of the Growth of Slag Deposits in an Accelerated Laboratory Test," Sixth International Coal Liquids and Alternative Fuels Technology Workshop, Halifax, Nova Scotia, September 1986.

10. Conn, R.E., Benson, S.A., and Austin, L.G., "Laboratory Coal Ash Slagging and Fouling Studies at Simulated Utility Boiler Conditions," ASME Paper No. 87-JPGC-FACT-6, 1987.

Table 1. Coal and ash analysis (all data on a dry basis except for the moisture determination).

| | Gascoyne White | Gascoyne Blue | Wyodak |
|---|---|---|---|
| Proximate, wt % | | | |
| Moisture | 30.0 | 24.6 | 30.4 |
| Volatile Matter | 41.6 | 47.5 | 43.8 |
| Fixed Carbon | 41.3 | 42.3 | 47.7 |
| Ash | 17.2 | 10.2 | 8.3 |
| Ultimate, wt % | | | |
| Carbon | 57.0 | 63.1 | 67.4 |
| Hydrogen | 3.8 | 4.2 | 4.8 |
| Nitrogen | 0.9 | 1.0 | 1.0 |
| Oxygen (diff.) | 19.7 | 20.1 | 17.8 |
| Sulfur | 1.3 | 1.2 | 0.7 |
| Calorific Value (BTU/lb) | 9649 | 10484 | 11818 |
| Ash Composition, wt % as equivalent oxide | | | |
| $SiO_2$ | 49.9 | 22.5 | 23.8 |
| $Al_2O_3$ | 12.0 | 9.7 | 14.8 |
| $Fe_2O_3$ | 3.0 | 5.0 | 6.6 |
| $TiO_2$ | 1.4 | 5.0 | 1.2 |
| $P_2O_5$ | 0.8 | 0.7 | 1.5 |
| CaO | 12.4 | 24.3 | 22.8 |
| MgO | 4.1 | 8.2 | 5.9 |
| $Na_2O$ | 3.5 | 6.9 | 0.7 |
| $K_2O$ | 0.8 | 0.1 | 0.3 |
| $SO_3$ | 12.2 | 21.9 | 22.4 |
| Si/Al Molar Ratio | 3.5 | 2.0 | 1.4 |

Table 2. Chemistry of crystalline phases identified by x-ray diffraction.

| Phase | Chemistry |
|---|---|
| Melilite (solid solution series) | |
| Gehlenite | $Ca_2Al_2SiO_7$ |
| Soda melilite | $NaCaAlSi_2O_7$ |
| Akermanite | $Ca_2MgSi_2O_7$ |
| Pyroxene (solid solution series) | |
| Augite | $(Ca,Na)(Mg,Fe,Al)(Si,Al)_2O_6$ |
| Diopside | $CaMgSi_2O_6$ |
| Plagioclase (solid solution series) | |
| Albite | $NaAlSi_3O_8$ |
| Anorthite | $CaAl_2Si_2O_8$ |
| Spinel | $Fe_3O_4$ - $MgFe_2O_4$ |
| Hematite | $Fe_2O_3$ |
| Lime | $CaO$ |
| Periclase | $MgO$ |
| Quartz | $SiO_2$ |
| Anhydrite | $CaSO_4$ |

Table 3. Crystalline phases identified in the deposits using x-ray diffraction (phases listed in order of decreasing abundance).

| Deposit location | Gascoyne White | Gascoyne Blue | Wyodak |
|---|---|---|---|
| Top half | major:<br>quartz<br>amorphous | major:<br>melilite<br>minor:<br>pyroxene<br>trace:<br>quartz | major:<br>melilite<br>quartz<br>trace:<br>plag*<br>pyroxene<br>spinel<br>hematite<br>periclase |
| Lower half | major:<br>quartz<br>melilite<br>pyroxene<br>minor:<br>spinel | major:<br>melilite<br>quartz<br>minor:<br>periclase<br>hematite<br>pyroxene | major:<br>melilite<br>quartz<br>trace:<br>$Ca_3Al_2O_6$<br>periclase<br>lime |
| Base | major:<br>quartz<br>minor:<br>melilite<br>periclase<br>hematite | major:<br>periclase<br>hematite<br>lime<br>minor:<br>melilite<br>quartz<br>amorphous | major:<br>lime<br>periclase<br>quartz<br>minor:<br>$Ca_3Al_2O_6$<br>trace:<br>anhydrite<br>melilite |

* plag -- plagioclase (anorthite).

Table 4 EDS analyses of selected points located in Figure 5. (Wt. % as equivalent oxide)

| Oxide | 1 | 2 | 3 (Glass) |
|---|---|---|---|
| $SiO_2$ | 23.9 | 26.9 | 59.7 |
| $Al_2O_3$ | 10.5 | 13.5 | 10.2 |
| $Fe_2O_3$ | 44.6 | 34.5 | 0.9 |
| $TiO_2$ | 0.6 | 2.6 | 3.1 |
| $P_2O_5$ | 0.0 | 0.0 | 0.0 |
| CaO | 12.6 | 13.9 | 16.4 |
| MgO | 6.5 | 6.0 | 2.5 |
| $Na_2O$ | 0.9 | 1.1 | 5.3 |
| $K_2O$ | 0.1 | 0.1 | 0.5 |
| $SO_3$ | 0.2 | 0.3 | 0.2 |
| Si/Al molar ratio | 1.9 | 1.7 | 5.0 |

Table 5 EDS analyses of selected points in Figure 6. (Wt. % as equivalent oxide)

| Oxide | 1 (Crystal) | 2 (Glass) |
|---|---|---|
| $SiO_2$ | 47.5 | 54.3 |
| $Al_2O_3$ | 9.8 | 13.0 |
| $Fe_2O_3$ | 8.9 | 3.7 |
| $TiO_2$ | 1.0 | 0.5 |
| $P_2O_5$ | 0.0 | 0.0 |
| CaO | 25.4 | 21.4 |
| MgO | 6.1 | 0.9 |
| $Na_2O$ | 0.8 | 5.2 |
| $K_2O$ | 0.3 | 0.1 |
| $SO_3$ | 0.1 | 0.0 |
| Si/Al molar ratio | 4.1 | 3.6 |

Table 6 EDS analyses of selected points in Figure 7.
(Wt. % as equivalent oxide)

| Oxide | Bright Crystals | Darker Crystals |
|---|---|---|
| $SiO_2$ | 41.8 | 50.8 |
| $Al_2O_3$ | 17.2 | 27.5 |
| $Fe_2O_3$ | 7.8 | 1.4 |
| $TiO_2$ | 2.0 | 0.0 |
| $P_2O_5$ | 1.4 | 0.0 |
| CaO | 24.9 | 18.6 |
| MgO | 4.1 | 0.4 |
| $Na_2O$ | 0.4 | 0.6 |
| $K_2O$ | 0.1 | 0.2 |
| $SO_3$ | 0.3 | 0.2 |
| BaO | 0.0 | 0.4 |
| Si/Al molar ratio | 2.1 | 1.6 |

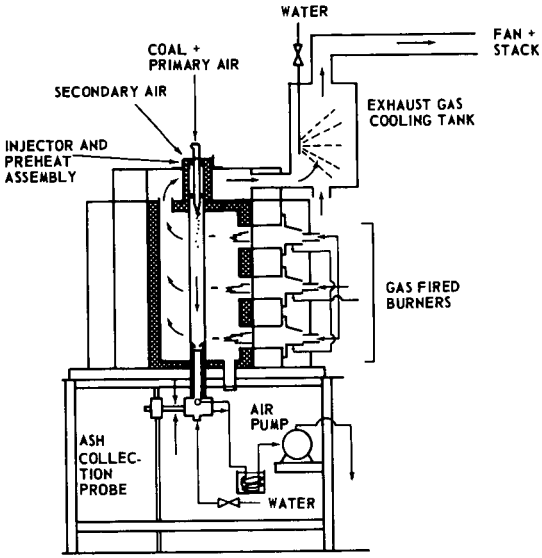


Figure 1. Laminar flow tube furnace system.

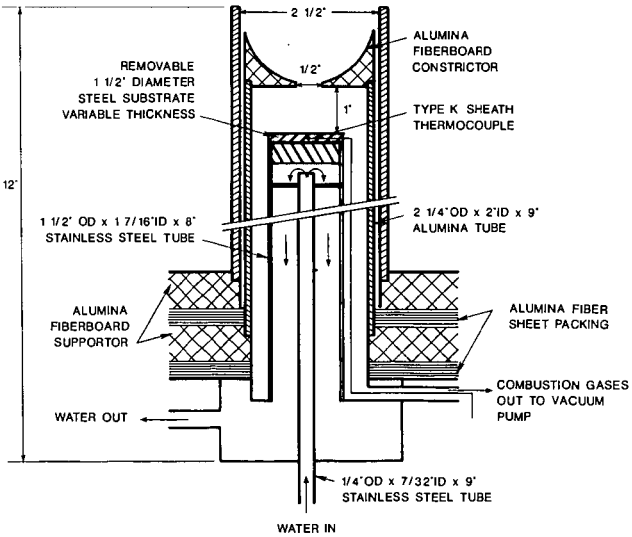


Figure 2. Base of main furnace containing the ceramic nozzle (constrictor) and ash deposition probe.

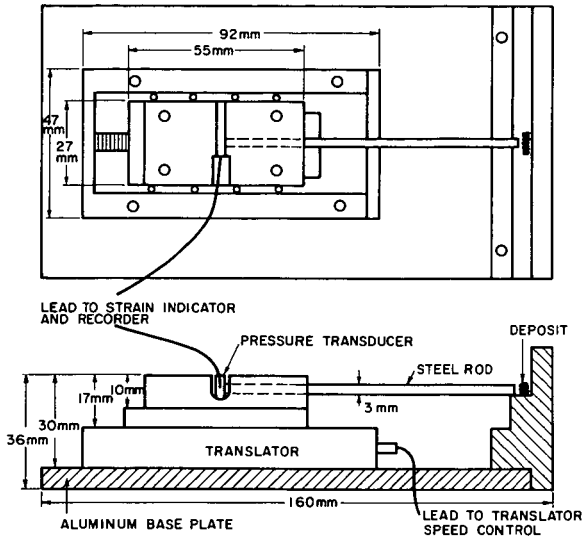


Figure 3. Deposit strength measuring device.

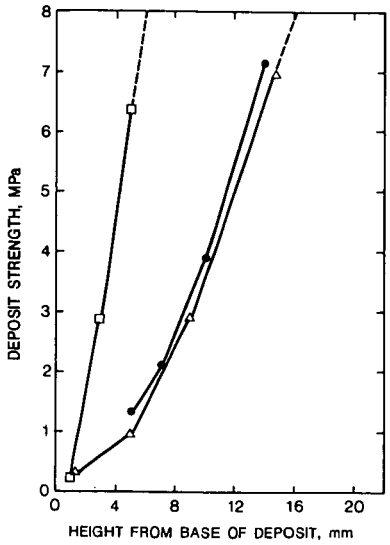


Figure 4. Deposit strength versus height for deposits formed in the laboratory scale furnace ( □ Gascoyne Blue, △ Gascoyne white, and ● Wyodak).

Figure 5. Backscatter electron image of a polished section of Gascoyne White lignite deposit at 8.1 mm from the base of the deposit.

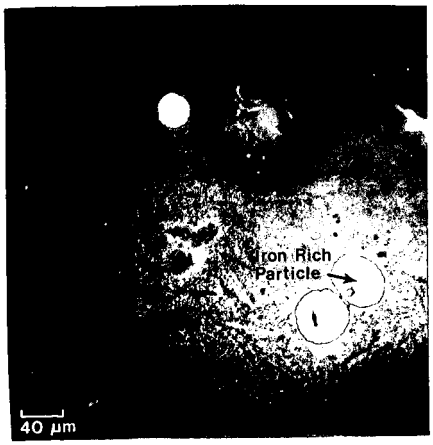


Figure 6. Backscatter electron image of a polished section of a Gascoyne Blue lignite deposit at 14 mm from the base.

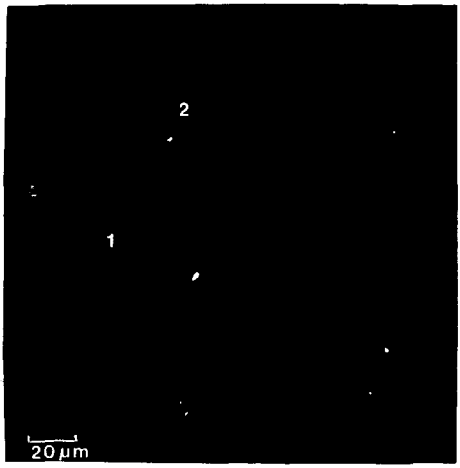


Figure 7. Backscatter electron image of polished sections of subbituminous coal deposits. A) Rosebud, B) Wyodak.

# EVALUATION OF COAL-MINERAL ASSOCIATION AND COAL CLEANABILITY BY USING SEM-BASED AUTOMATED IMAGE ANALYSIS

W. E. Straszheim, K. A. Younkin, R. Markuszewski and F. J. Smit[1]

Ames Laboratory, Iowa State University, Ames, Iowa 50011 and
[1]AMAX Research and Development Center, Golden, Colorado, 80403

## ABSTRACT

A technique employing SEM-based automated image analysis (AIA) has been developed for assessing the association of mineral particles with coal, and thus the cleanability of that coal, when the characteristics of the separation process are known. Data resulting from AIA include the mineral distribution by particle size, mineral phase, and extent of association with coal. This AIA technique was applied to samples of -325 mesh (-44 μm) coal from the Indiana No. 3, Upper Freeport, and Sunnyside (UT) seams. The coals were subjected to cleaning by float-sink separations at 1.3, 1.4, 1.6, and 1.9 specific gravity and by froth flotation. For the three coals, the float-sink procedure at a given specific gravity produced different amounts of clean coal, but with similar ash content. Froth flotation removed much less ash, yielding a product ash content of ~8% for the Upper Freeport coal, regardless of recovery, while reducing the ash content to less than 5% for the other two coals. The AIA results documented significantly more association of minerals with the Upper Freeport coal, which thus led to the poor ash reduction.

## INTRODUCTION

The task of removing mineral matter from coal is greatly aided by a thorough characterization of the distribution and/or association of mineral and coal particles. Conventional characterization, based on laboratory float-sink and froth flotation tests at different sizes and conditions, is cumbersome and does not generally lead to any clear understanding of coal-mineral matter associations.

SEM-based automated image analysis (AIA) has unique capabilities for analyzing mineral particles in-situ for the important characteristics of size, phase, and association with the coal matrix. These AIA techniques have previously been applied to the determination of mineral matter size and phase distributions in coal (1-3) and are now being extended to the measurement of association. This work describes our application of AIA to characterize the association of minerals with coal and to correlate the AIA results with those of conventional tests such as float-sink separation and froth flotation.

## EXPERIMENTAL

### Coals

The characteristics of the three coals used in this study are presented in Table 1. The coals had been precleaned and ground to pass a 325 mesh screen. Since the conventional analyses give values for ash, whereas AIA provides results in terms of mineral matter, low temperature ash values were also obtained for easier comparison with AIA measurements.

Table 1. Characteristics of the three coals used (results are expressed as % of dry coal)

| | Indiana No.3 | Upper Freeport | Sunnyside |
|---|---|---|---|
| Proximate Analysis | | | |
| Ash | 7.35 | 9.88 | 5.19 |
| Volatile Matter | 40.67 | 26.02 | 38.54 |
| Fixed Carbon | 51.98 | 64.10 | 56.19 |
| Forms of Sulfur | | | |
| Total | 4.26 | 1.56 | 0.61 |
| Pyrite | 2.23 | 0.95 | 0.05 |
| Sulfate | 0.07 | 0.01 | 0.00 |
| Low Temperature Ash | 10.5 | 12.5 | 6.1 |

Cleaning tests at AMAX

The coals were subjected to float-sink separations at the specific gravities (sp. gr.) of 1.3, 1.4, 1.6, and 1.9, and samples from each incremental sp. gr. range were weighed and analyzed. Another set of samples was subjected to froth flotation in an automated Denver batch cell, using 28 ppm MIBC and 0.54-1.92 ml kerosene per kg of coal. Froth was collected after 1.5, 3, 6, 12, and 24 minutes, and the remaining unfloatable material (tailings) was also collected for analysis.

SEM-based image analyses at Ames Lab

Samples of coal were embedded in carnauba wax, and a cross section was prepared for analysis as described previously (4). The AIA system included a JEOL JSM-U3 electron microscope, a Tracor-Northern TN-2000 energy-dispersive x-ray analyzer, and a LeMont Scientific DB-10 image analyzer. Samples were examined at magnifications of 300-400 diameters using an accelerating voltage of 25 kV and a beam current of 1-2 nA.

Software from LeMont Scientific was used to distinguish coal and mineral features from the background and from each other based on the brightness of their backscattered electron signal. Area and perimeter were measured for each feature, along with the fraction of perimeter in contact with each of the adjoining phases. Mineral particles were identified from the relative intensities of the characteristic x-ray emissions. X-rays were collected for 4 seconds per particle at a nominal rate of 500 counts per second. Data for contiguous features (i.e., with shared boundaries between coal and mineral matter) were grouped together so that the characteristics of the composite features could be determined.

## RESULTS AND DISCUSSION

Conventional cleaning studies

The results of the float-sink separations are presented in Table 2. Data are presented for both the incremental fractions and for the cumulative fraction lighter than the indicated specific gravity. Plots of recovery and cumulative ash content are shown in Figure 1.

Table 2. Float-sink results for three coals (results are expressed as % of dry coal)

| Sp. Gr. | | Incremental | | | Cumulative | | |
|---|---|---|---|---|---|---|---|
| Sink | Float | Weight | Ash | S(tot) | Weight | Ash | S(tot) |
| | | | Indiana No. 3 Coal | | | | |
| | 1.30 | 24.0 | 1.09 | 2.31 | 24.0 | 1.09 | 2.31 |
| 1.30 | 1.40 | 64.5 | 3.23 | 2.45 | 88.5 | 2.65 | 2.41 |
| 1.40 | 1.60 | 4.7 | 15.86 | 4.52 | 93.2 | 3.32 | 2.52 |
| 1.60 | 1.90 | 1.5 | 29.14 | 7.34 | 94.7 | 3.72 | 2.59 |
| 1.90 | | 5.3 | 64.32 | 32.47 | 100.0 | 6.95 | 4.18 |
| | | | Upper Freeport Coal | | | | |
| | 1.30 | 7.1 | 0.98 | 0.71 | 7.1 | 0.98 | 0.71 |
| 1.30 | 1.40 | 70.1 | 2.60 | 0.75 | 77.2 | 2.45 | 0.75 |
| 1.40 | 1.60 | 12.9 | 12.21 | 1.03 | 90.1 | 3.85 | 0.79 |
| 1.60 | 1.90 | 3.8 | 31.77 | 1.49 | 93.9 | 4.98 | 0.82 |
| 1.90 | | 6.1 | 70.94 | 10.78 | 100.00 | 8.99 | 1.42 |
| | | | Sunnyside Coal | | | | |
| | 1.30 | 23.6 | 0.57 | 0.57 | 23.6 | 0.57 | 0.57 |
| 1.30 | 1.40 | 67.1 | 1.66 | 0.57 | 90.7 | 1.38 | 0.57 |
| 1.40 | 1.60 | 5.4 | 13.82 | 0.54 | 96.1 | 2.07 | 0.57 |
| 1.60 | 1.90 | 0.8 | 38.26 | 0.48 | 96.9 | 2.37 | 0.57 |
| 1.90 | | 3.1 | 81.10 | 0.67 | 100.0 | 4.85 | 0.57 |

As expected, the ash contents were relatively similar for the three coals for the same incremental specific gravity fraction. However, since the weight distribution among the fractions varied between the coals, the ash content of the cumulative fractions also varied somewhat between the coals.

The curves in Figure 1 indicate that the recoveries were similar for the Indiana No. 3 and Sunnyside coals. This suggests comparable coal-mineral association for these coals, provided that their mineralogical properties are similar. The recovery was notably lower for the Upper Freeport coal. Much more sample was found in the 1.4-1.9 specific gravity range (as seen from Table 2). This resulted in a higher ash content for the 1.6 and 1.9 sp. gr. float product.

Results of the froth flotation tests are shown in Table 3 and Figure 2. The recovery curves for all three coals flattened out after about 6 minutes collection time. The Upper Freeport coal appears to have been more responsive to the froth flotation, showing more recovery at shorter times. However, this reflects more the hydrophobicity of the coal than the degree of association of the mineral matter with the coal.

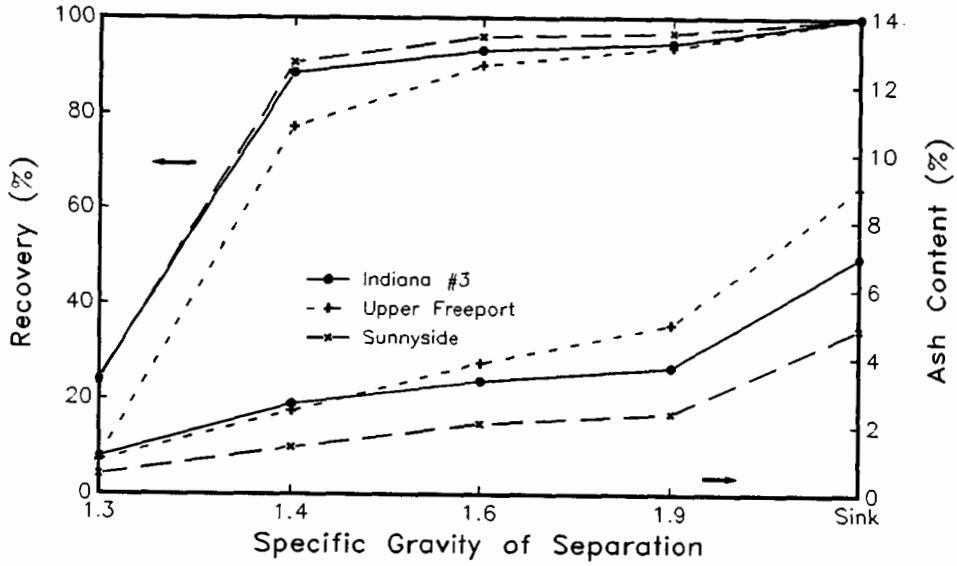


Figure 1. Recovery and ash content as a function of the specific gravity of float-sink separations

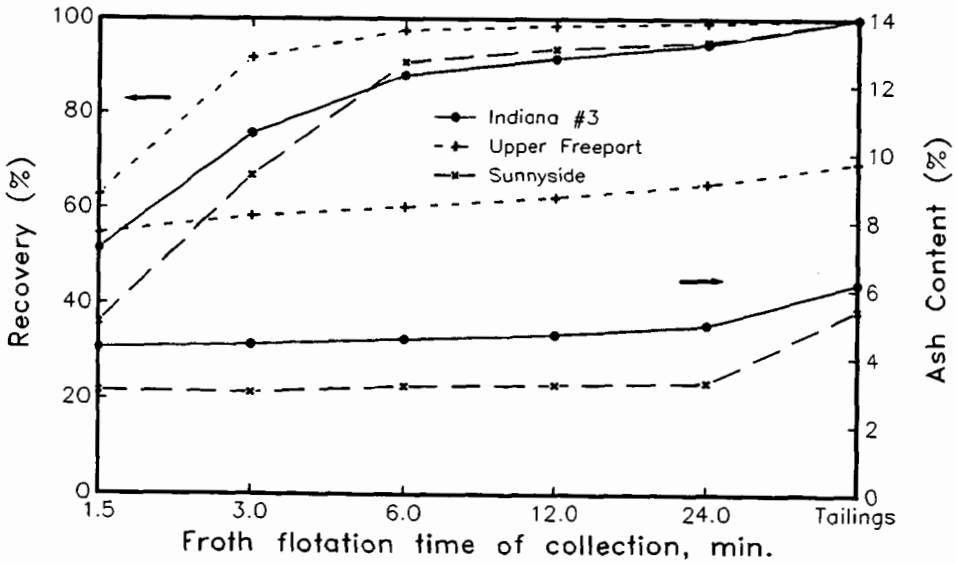


Figure 2. Recovery and ash content as a function of flotation time

Table 3. Froth flotation results for all three coals using 28 ppm MIBC and differing ml of kerosene per kg of coal (results are expressed as % of dry coal)

| Flotation Time, Total Minutes | Incremental Float Product | | | Cumulative Float Product | | |
|---|---|---|---|---|---|---|
| | Weight | Ash | S(tot) | Weight | Ash | S(tot) |
| Indiana No. 3 coal(using 1.92 ml kerosene) | | | | | | |
| 1.5 | 51.5 | 4.30 | 3.34 | 51.5 | 4.30 | 3.34 |
| 3.0 | 24.2 | 4.58 | 3.26 | 75.7 | 4.39 | 3.31 |
| 6.0 | 12.3 | 5.53 | 3.49 | 88.0 | 4.55 | 3.34 |
| 12.0 | 3.6 | 8.27 | 4.04 | 91.6 | 4.69 | 3.37 |
| 24.0 | 3.0 | 13.23 | 5.06 | 94.6 | 4.97 | 3.42 |
| Tailings | 5.4 | 27.62 | 8.78 | 100.0 | 6.19 | 3.71 |
| Upper Freeport coal (using 0.54 ml kerosene) | | | | | | |
| 1.5 | 62.8 | 7.66 | 1.36 | 62.8 | 7.66 | 1.36 |
| 3.0 | 28.9 | 9.29 | 1.53 | 91.7 | 8.17 | 1.41 |
| 6.0 | 5.9 | 12.59 | 1.83 | 97.6 | 8.44 | 1.44 |
| 12.0 | 1.0 | 36.25 | 4.27 | 98.6 | 8.73 | 1.47 |
| 24.0 | 0.6 | 77.86 | 8.46 | 99.2 | 9.12 | 1.51 |
| Tailings | 0.8 | 85.65 | 9.17 | 100.0 | 9.74 | 1.57 |
| Sunnyside coal (using 0.55 ml kerosene) | | | | | | |
| 1.5 | 36.0 | 3.03 | 0.56 | 36.0 | 3.03 | 0.56 |
| 3.0 | 30.9 | 2.95 | 0.58 | 66.9 | 2.99 | 0.57 |
| 6.0 | 23.9 | 3.67 | 0.57 | 90.8 | 3.17 | 0.57 |
| 12.0 | 2.8 | 4.59 | 0.59 | 93.6 | 3.21 | 0.57 |
| 24.0 | 1.5 | 7.37 | 0.58 | 95.1 | 3.28 | 0.57 |
| Tailings | 4.9 | 46.93 | 0.63 | 100.0 | 5.41 | 0.57 |

From Figures 1 and 2, it is also evident that much less ash reduction was achieved by froth flotation than by float-sink separation for all three coals. Since froth flotation is a surface-sensitive process, small amounts of coal attached to mineral particles can result in these mineral particles being carried along to the froth. This effect appears to be especially significant for the Upper Freeport coal, for which minimal ash reduction was observed, apparently due to its great hydrophobicity. Examination of ash content of the incremental fractions in Table 3 indicates that after 6 minutes, the ash content of the incrementally recovered material rises dramatically, nullifying the small amount of ash reduction achieved previously. For the Upper Freeport coal, practically all of the mineral matter could float if given enough time. For the Indiana No. 3 and Sunnyside coals, on the other hand, some mineral matter simply would not float at all.

AIA results compared to float-sink results

The association results for the three coals, included in Table 4, show the incremental and cumulative percent distributions of coal, mineral matter, and coal+mineral matter as a function of the amount of mineral matter apparent in the particle cross sections. The cumulative distribution relates how much of the original sample (i.e., coal plus mineral matter) could be recovered by collecting particles of a certain mineral matter content.

The mineral matter content in a particle, listed in column 1 of Table 4, can be translated to a specific gravity estimate, assuming a coal density of 1.30 and an average mineral density of 2.60. Thus, a specific gravity of 1.3 corresponds to 0% mineral matter, 1.4 to 20%, 1.6 to 40%, 1.9 to 60%, and a specific gravity of more than 1.9 corresponds to 100%. In this manner, the distributions of Table 4 may be correlated with float-sink results. Such AIA results are plotted in Figure 3, and they can be used for comparison with the float-sink separation results in Figure 1.

Several parallel trends may be noted between the AIA and float-sink results in Figures 3 and 1, respectively. The recovery curves for the three coals generally appear in the same order in both figures. The recovery of the Sunnyside coal is greater than that of the other two coals, and the Indiana No. 3 coal generally shows higher recovery than the Upper Freeport coal for separations at specific gravities greater than 1.4. Likewise, the ash (or mineral) content curve for the Sunnyside coal is consistently below those of the other two coals. Unfortunately, the influence of stereological effects on the AIA results prevents a completely quantitative comparison of the AIA and float-sink results.

However, because the same qualitative trends appear in both figures, AIA results can be more useful since they can be obtained much faster than the float-sink results. During routine operation, sample preparation for AIA requires about 2 hours and the analysis less than 20 hours per sample. At least one sample per day can be analyzed with our equipment, but allowance for sample preparation and data reduction could result in a two-day sample turnaround. Such throughput is better that what can be achieved by testing with float-sink separation followed by ash analysis.

AIA results compared to froth flotation results

It is more difficult to relate the AIA results to froth flotation results. No comparable set of curves can be produced using the AIA results as they appear in Table 4. However, some useful information can still be obtained. The AIA results in Table 4 do show more association of minerals with the Upper Freeport coal. The plots in Figure 4 show the distribution of coal and mineral matter for the mixed (i.e., coal plus mineral matter) particles of the three coals taken from Table 4; free coal has been excluded. It can now be seen graphically that the Upper Freeport coal contains more mineral matter in this type of particle. In fact, the average mineral content of the mixed particles (i.e., the associated coal-mineral fraction) of the Upper Freeport coal is 45%, compared to only 26% and 29% for the Indiana No. 3 and Sunnyside coals, respectively.

However, even with these coal-mineral association insights, the previously stated tendency for the Upper Freeport coal to respond more to froth flotation than the other two coals appears to be the determining factor in the poor mineral removal for this coal. Apparently, the mineral matter in the Upper Freeport coal can float, even with very little coal associated with it. However, this issue cannot be answered by AIA alone and requires further study by other analytical techniques.

Table 4. Distributions (in %, dry basis) of coal and mineral matter for all three coals, as a function of particle mineral matter (MM) content

| MM Content | Incremental Coal | Incremental MM | Incremental Total | Cumulative Coal | Cumulative MM | Cumulative Total | % MM in Cumulative Total |
|---|---|---|---|---|---|---|---|
| **Indiana No. 3 coal** | | | | | | | |
| 0 | 61.61 | 0.00 | 61.61 | 61.61 | 0.00 | 61.61 | 0.00 |
| 0-10 | 14.32 | 0.58 | 14.90 | 75.93 | 0.58 | 76.50 | 0.75 |
| 10-20 | 5.51 | 1.04 | 6.55 | 81.44 | 1.61 | 83.05 | 1.94 |
| 20-30 | 2.86 | 0.96 | 3.82 | 84.30 | 2.57 | 86.88 | 2.96 |
| 30-40 | 2.34 | 1.27 | 3.61 | 86.64 | 3.85 | 90.49 | 4.25 |
| 40-50 | 0.87 | 0.72 | 1.59 | 87.51 | 4.57 | 92.08 | 4.96 |
| 50-60 | 0.96 | 1.17 | 2.13 | 88.47 | 5.73 | 94.21 | 6.09 |
| 60-70 | 0.65 | 1.27 | 1.92 | 89.12 | 7.00 | 96.12 | 7.28 |
| 70-80 | 0.53 | 1.62 | 2.15 | 89.65 | 8.62 | 98.28 | 8.78 |
| 80-90 | 0.20 | 1.14 | 1.34 | 89.85 | 9.77 | 99.62 | 9.80 |
| 90-100 | 0.01 | 0.36 | 0.38 | 89.87 | 10.13 | 100.00 | 10.13 |
| Total | 89.87 | 10.13 | 100.00 | | | | |
| **Upper Freeport coal** | | | | | | | |
| 0 | 73.35 | 0.00 | 73.35 | 73.35 | 0.00 | 73.35 | 0.00 |
| 0-10 | 4.62 | 0.20 | 4.82 | 77.97 | 0.20 | 78.17 | 0.26 |
| 10-20 | 3.32 | 0.57 | 3.88 | 81.28 | 0.77 | 82.06 | 0.94 |
| 20-30 | 1.25 | 0.43 | 1.68 | 82.53 | 1.20 | 83.73 | 1.43 |
| 30-40 | 1.24 | 0.64 | 1.88 | 83.77 | 1.84 | 85.61 | 2.15 |
| 40-50 | 0.95 | 0.75 | 1.70 | 84.72 | 2.59 | 87.32 | 2.97 |
| 50-60 | 1.14 | 1.30 | 2.44 | 85.86 | 3.89 | 89.75 | 4.34 |
| 60-70 | 0.94 | 1.79 | 2.73 | 86.81 | 5.68 | 92.48 | 6.14 |
| 70-80 | 0.31 | 0.88 | 1.19 | 87.11 | 6.56 | 93.68 | 7.01 |
| 80-90 | 0.67 | 3.83 | 4.50 | 87.78 | 10.39 | 98.17 | 10.59 |
| 90-100 | 0.11 | 1.71 | 1.82 | 87.89 | 12.11 | 100.00 | 12.11 |
| Total | 87.89 | 12.11 | 100.00 | | | | |
| **Sunnyside coal** | | | | | | | |
| 0 | 84.28 | 0.00 | 84.28 | 84.28 | 0.00 | 84.28 | 0.00 |
| 0-10 | 6.06 | 0.32 | 6.38 | 90.34 | 0.32 | 90.66 | 0.35 |
| 10-20 | 1.88 | 0.31 | 2.19 | 92.22 | 0.63 | 92.85 | 0.68 |
| 20-30 | 0.86 | 0.27 | 1.13 | 93.08 | 0.90 | 93.97 | 0.95 |
| 30-40 | 0.66 | 0.37 | 1.04 | 93.74 | 1.27 | 95.01 | 1.34 |
| 40-50 | 0.85 | 0.71 | 1.56 | 94.59 | 1.98 | 96.57 | 2.05 |
| 50-60 | 0.27 | 0.32 | 0.59 | 94.86 | 2.30 | 97.16 | 2.37 |
| 60-70 | 0.25 | 0.46 | 0.71 | 95.11 | 2.77 | 97.88 | 2.83 |
| 70-80 | 0.25 | 0.74 | 0.99 | 95.36 | 3.51 | 98.87 | 3.55 |
| 80-90 | 0.10 | 0.55 | 0.65 | 95.46 | 4.06 | 99.52 | 4.08 |
| 90-100 | 0.04 | 0.44 | 0.48 | 95.49 | 4.51 | 100.00 | 4.51 |
| Total | 95.49 | 4.51 | 100.00 | | | | |

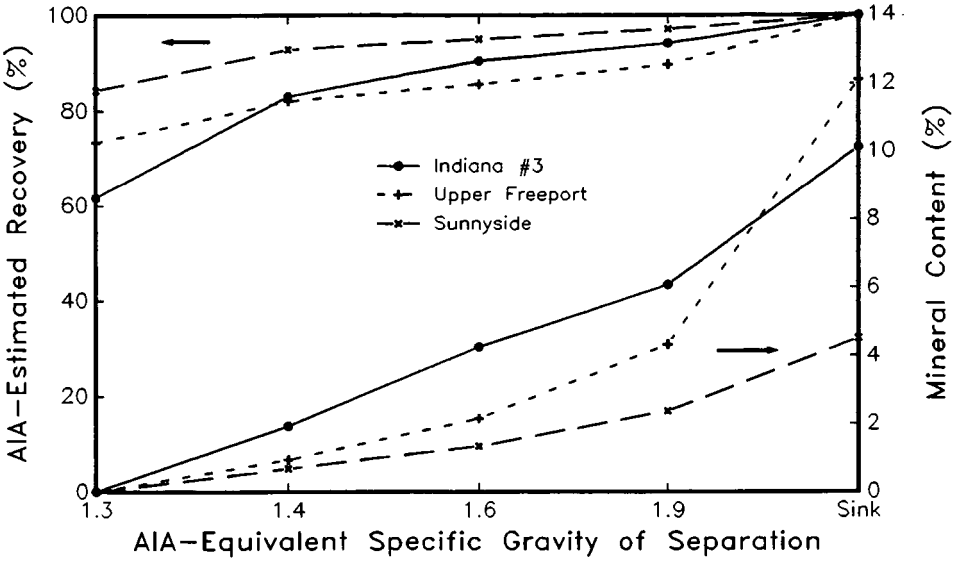


Figure 3. AIA-estimated recovery and mineral content as a function of AIA-equivalent specific gravity

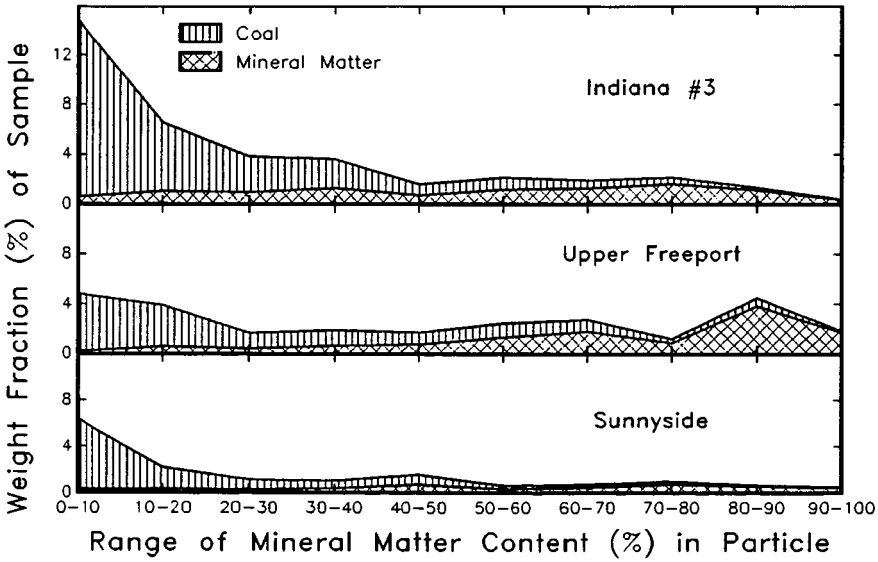


Figure 4. Distribution of coal and mineral matter as a function of weight fraction of mineral matter in the particles

## CONCLUSIONS

Automated image analysis was used to determine the association of mineral features with coal, and the results were expressed in a format that provided insight into the float-sink response of the sample. Qualitatively similar trends were observed for the conventional float-sink and the AIA results; however, quantitative comparisons are currently limited by stereological effects on the AIA results.

The AIA results, as developed and presented in this work, provide less direct insight into the froth flotation behavior. However, there did appear to be a correlation between the large amount of mineral matter in the mixed particles of the associated coal and mineral fraction measured by AIA and the poor ash rejection from the Upper Freeport coal during froth flotation. Work is continuing on other AIA reporting formats which could be more directly related to froth flotation.

AIA results can be obtained considerably quicker than results from either of the conventional cleaning tests. This suggests that AIA may be useful in monitoring the character of feed to a preparation plant, particularly since AIA is able to detect differences in the association of coal and mineral matter particles.

## ACKNOWLEDGEMENT

Ames Laboratory is operated for the U. S. Department of Energy by Iowa State University under Contract No. W-7405-Eng-82. The work at Ames was supported by the Assistant Secretary for Fossil Energy through the Pittsburgh Energy Technology Center and by a grant from AMAX through the Iowa State Mining and Mineral Resources Research Institute. The work at AMAX was supported by DOE Contract No. DE-AC22-84PC72007.

## LITERATURE CITED

1) W.E. Straszheim, J.G. Yousling, K.A. Younkin, and R. Markuszewski, "Mineralogical Characterization of Lower Rank Coals by SEM-based Automated Image Analysis and Energy-Dispersive X-ray Spectrometry", Fuel, in press, 1988.

2) W.E. Straszheim, K.A. Younkin, and R. Markuszewski, "Determination of Pyrite Association with Coal Particles by Automated Image Analysis", Processing and Utilization of High Sulfur Coals-II, Y.P. Chugh and R.D. Caudle, eds., Elsevier, New York, 1987, pp. 41-48.

3) W. E. Straszheim, J. G. Yousling, and R. Markuszewski, "Analysis of Ash-Forming Mineral Matter in Raw and Supercleaned Coals by Automated Image Analysis-Scanning Electron Microscopy", in Mineral Matter and Ash in Coal (ACS Symp. Series No. 301), K. S. Vorres, ed., Am. Chem. Soc., Washington, D. C., 1986, pp. 449-461.

4) W.E. Straszheim, K.A. Younkin, R.T. Greer, and R. Markuszewski, "Mounting Materials for SEM-based Automated Image Analysis of Coals", submitted to Scanning Microscopy, 1988.

# COMPARISON OF COMBUSTION DEPOSITS FROM BITUMINOUS COALS AND A LIGNITE

F. E. Huggins[1], G. P. Huffman[2],

Departments of Geological Sciences[1] and Chemical Engineering[2],
University of Kentucky,
Lexington, KY 40506

and A. A. Levasseur

Kreisinger Development Laboratory,
Combustion Engineering, Inc.,
P.O. Box 500,
Windsor, CT 06095

## INTRODUCTION

Deposits generated during combustion of pulverized coals are determined to a large extent by the type, relative amounts, size, and association of the different inorganic species present in the coal. In this investigation, we examine and compare the inorganic constituents in various samples of two bituminous coals and of a Texas lignite and the deposits generated from these coals in the same test furnace. Whereas the principal basic mineral in the bituminous coals is pyrite, which is found in these coals in relatively coarse particle form, the principal component in the lignite is carboxyl-bound calcium, which is highly dispersed throughout the lignite macerals. These situations can be considered to represent different ends of the spectrum with respect to the size and distribution of the major basic component of the inorganic species.

The mineral matter of the coals was characterized using a combination of computer-controlled SEM (CCSEM) and Mössbauer spectroscopic methods. Similar techniques were used to examine deposits.

## EXPERIMENTAL

(a) Samples:

The Illinois #6 coal was obtained as a combustion product (Il#6-Base) and as a cleaned metallurgical product (Il#6 - Met). The other two coals, a Kentucky #9 coal and a Texas Lignite, were subjected to cleaning at the EPRI Coal Cleaning Test Facility, near Homer City, PA. A medium-cleaned product (Ky#9 - MCln) and a deep-cleaned product (Ky#9 - DCln) were prepared from the original Kentucky #9 coal (Ky#9-Raw) and a cleaned product (TexL - Cln) was prepared from the original lignite (TexL - Raw). Pulverized coal samples were prepared from the original coals and the cleaned products. These coals were then burnt in the Fireside Performance Test Facility (FPTF) at Combustion Engineering and a variety of deposit samples were collected, including in-flame solids, superheater deposits and waterwall deposits.

(b) Techniques:

The combination of Mössbauer spectroscopy and CCSEM for the determination of coal mineralogies has been described in detail elsewhere (1). Basically, the CCSEM technique determines quantitatively the types, relative amounts, and size distributions of the major discrete minerals in the coal, whereas Mössbauer spectroscopy provides more detailed complementary information regarding the iron-bearing minerals, in particular pyrite. For lignites, however, the CCSEM method does not determine the carboxyl-bound inorganics dispersed in the lignite macerals. These components were semi-quantitatively

estimated from a comparison of the discrete mineralogy and the overall inorganic composition as revealed by wide area energy dispersive X-ray scans or the chemical analysis of the high-temperature ash.

For samples generated in the FPTF, Mössbauer spectroscopy was used to document the behavior of iron in the various deposits and optical and electron microscopic techniques were used to examine the microstructure and mineralogy in polished sections of the deposit mounted in epoxy. Much reliance was placed on elemental X-ray and backscattered electron intensity mapping techniques in the CCSEM to document element distributions and associations.

Some exploratory extended X-ray absorption fine-structure (EXAFS) spectroscopy measurements were made at the calcium K-edge to investigate the form of occurrence of Ca in the Texas lignite and Illinois #6 coal and in deposits generated from the coals. These measurements will be discussed in detail elsewhere and will merely be mentioned here in passing where information from the EXAFS technique corroborates or supplements data from the other techniques.

## RESULTS

### (a) Coal Mineralogies:

The mineralogies of the various coal samples are summarized in Table 1. The samples from the Illinois #6 and Kentucky #9 bituminous coals exhibit somewhat similar mineralogies: pyrite, along with its oxidation products, is the principal basic mineral, although both raw coals also contain significant amounts of calcium minerals: gypsum in Kentucky #9, calcite in Illinois #6. However, the combination of quartz and clay minerals dominates the mineralogies. The Texas lignite discrete mineralogy is dominated by quartz; pyrite and other basic minerals are very minor components. Cleaning does effect some differences in mineralogy: both bituminous coals become relatively poorer in pyrite with cleaning. However, for the Kentucky #9 coals, the decrease in pyrite is compensated by an increase in magnetite, which was introduced into the cleaned coals from the heavy media used for cleaning. This contamination is best revealed by the Mössbauer data and spectrum (Fig. 1). The discrete mineralogy of the Texas lignite is little affected by cleaning; however, the ratio of the discrete mineral matter to the dispersed maceral inorganics changes from approximately 2:1 to less than 1:1 based on changes in the overall energy-dispersive X-ray composition. The major dispersed inorganic elements were calcium and sulfur. EXAFS spectroscopy confirmed that calcium was present as carboxyl-bound Ca in macerals, based on the similarity of the Ca EXAFS spectrum to previously published data on Ca in lignites (2).

Some data are presented on mineral size distributions in Table 2. As can be seen from Table 2 and more clearly for the Kentucky #9 coals shown plotted on a wt% coal basis in Fig. 2, cleaning has the effect of preferentially removing the coarser mineral matter (>20μm). Hence, specific minerals with a coarser size distribution are removed more completely than those with size distributions biased to smaller size ranges. It is clear that the relative size distributions explains why pyrite and not quartz is removed by the cleaning of the Kentucky #9 coal. Although less dramatic, there is also a significant reduction in the coarse quartz content of the Texas lignite upon cleaning; however, there is little change in the discrete mineralogy (Table 1), implying that all minerals are, on average, similarly affected.

It should be noted, however, that cleaning reduces the basic mineral content of the bituminous coals, but increases the proportion of basic inorganics for the Texas lignite.

TABLE 1a: COAL MINERALOGIES BY CCSEM+

| | Kentucky #9 | | | Illinois #6 | | Texas Lignite | |
|---|---|---|---|---|---|---|---|
| Mineral | Raw | MCln | DCln | Base | Met. | Raw | Cln |
| Quartz | 14 | 16 | 24 | 17 | 20 | 47 | 36 |
| Kaolinite | 2 | 4 | 5 | 8 | 9 | 3 | 12 |
| Illite | 3 | 6 | 9 | 10 | 17 | 3 | 3 |
| Misc. Sil. | 22 | 26 | 21 | 28 | 31 | 34 | 28 |
| Pyrite | 29 | 19 | 16 | 22 | 11 | 3 | 9 |
| Gypsum | 8 | 3 | 3 | 2 | 2 | -- | -- |
| Fe sulfate | 2 | 5 | 4 | 1 | 2 | -- | -- |
| Misc. Sulf. | 5 | 3 | 3 | 2 | 2 | -- | -- |
| Fe-rich | 1 | 6 | 6 | <1 | 2 | 1 | 2 |
| Ca-rich | -- | -- | -- | 8 | <1 | 2 | 1 |
| Misc., mixed | 14 | 12 | 9 | 2 | 4 | 6 | 8 |

+Data expressed as percentage of mineral matter

TABLE 1b: MÖSSBAUER DATA ON DISTRIBUTION OF IRON

| | Kentucky #9 | | | Illinois #6 | | Texas Lignite | |
|---|---|---|---|---|---|---|---|
| %Fe in | Raw | MCln | DCln | Base | Met. | Raw | Cln |
| Pyrite | 65 | 60 | 48 | 87 | 84 | 71* | 67* |
| Clay | 3 | 4 | 3 | -- | 5 | -- | -- |
| Szomolnokite | 1 | -- | -- | 7 | -- | 14 | 8 |
| Jarosite | 32 | 26 | 33 | 5 | 11 | 15* | 25* |
| Magnetite | -- | 11 | 16 | -- | -- | -- | -- |
| Wt% Pyr. S | 1.30 | 0.81 | 0.34 | 1.05 | 0.48 | 0.32 | 0.17 |

*Absorptions are broad; may include minor FeOOH

(b) Deposits:

(i) In-flame Solids: The samples of in-flame solids collected from in or near the flame region during the burning of the bituminous coals consisted, for the most part, of very loose aggregates of fly-ash cenospheres. Compositions of the individual cenospheres as revealed by EDX spectra and CCSEM mapping were highly variable reflecting the different associations of minerals in the coal particles. As might be expected, the fly ash particles were smaller and more uniform in size for the cleaned coals compared to the raw coals. Occasionally, these aggregates had nuclei of more highly agglomerated material or of large pieces of incompletely burnt char. Iron in all the samples was distributed among glass (both ferric and ferrous components), magnetite, and minor hematite. No iron sulfide or crystalline iron silicate phase could be discerned from the Mössbauer spectra. Typically over 50% of the iron was present in glass and the cleaned lignite had the most Fe in this form, up to 90%. Extensive reaction between silicates and pyrite must occur very rapidly in the initial combustion process in the flame.

TABLE 2: MINERAL SIZE DISTRIBUTION DATA FOR COALS

| Coal | Size Distribution Data - All Minerals | | | | | |
|---|---|---|---|---|---|---|
| | <2.5μm | 2.5-5μm | 5-10μm | 10-20μm | 20-40μm | >40μm |
| Ky#9 - Raw | 20 | 14 | 21 | 25 | 14 | 7 |
| - MCln | 27 | 21 | 23 | 16 | 11 | 1 |
| - DCln | 27 | 29 | 26 | 12 | 4 | 2 |
| Il#6 - Base | 21 | 16 | 19 | 21 | 11 | 12 |
| - Met. | 30 | 17 | 22 | 17 | 6 | 7 |
| TexL - Raw | 21 | 7 | 13 | 14 | 21 | 23 |
| - Cln | 21 | 15 | 20 | 16 | 13 | 16 |

| Coal | Size Distribution Data - Pyrite | | | | | |
|---|---|---|---|---|---|---|
| | <2.5μm | 2.5-5μm | 5-10μm | 10-20μm | 20-40μm | >40μm |
| Ky#9 - Raw | 9 | 6 | 25 | 22 | 21 | 17 |
| - MCln | 10 | 15 | 24 | 21 | 30 | 0 |
| - DCln | 14 | 16 | 35 | 26 | 9 | 0 |
| Il#6 - Base | 9 | 6 | 18 | 31 | 20 | 16 |
| - Met. | 16 | 11 | 29 | 27 | 14 | 4 |
| TexL - Raw | -- | -- | -- | -- | -- | -- |
| - Cln | -- | -- | -- | -- | -- | -- |

| Coal | Size Distribution Data - Quartz | | | | | |
|---|---|---|---|---|---|---|
| | <2.5μm | 2.5-5μm | 5-10μm | 10-20μm | 20-40μm | >40μm |
| Ky#9 - Raw | 15 | 22 | 33 | 24 | 4 | 3 |
| - MCln | 22 | 25 | 38 | 13 | 2 | 0 |
| - DCln | 17 | 31 | 36 | 8 | 2 | 6 |
| Il#6 - Base | 13 | 22 | 38 | 16 | 3 | 8 |
| - Met. | 21 | 18 | 24 | 13 | 1 | 24 |
| TexL - Raw | 10 | 5 | 10 | 13 | 31 | 31 |
| - Cln | 16 | 16 | 20 | 19 | 17 | 12 |

<u>(ii)a Superheater Deposits - Initial:</u> The initial superheater deposits from the bituminous coals are composed of largely undeformed silica and aluminosilicate cenospheres, less regular spherical particles rich in Fe and Si or Ca and S, and highly deformed Fe-rich particles. The latter particles often appear to be molded around the more rigid spheres, probably as a result of collision, and to be the "glue" that cements the deposit together. The interparticle contacts are quite sharp, indicating that little, if any, chemical reaction has taken place. Mössbauer data indicate a significant enrichment in iron by more than 50% for this type of deposit (Fig. 3), which also reinforces the importance of the iron particulate matter in the

cohesion of the deposit. In contrast to the in-flame solid samples, only 5-15% of the iron is present in glass, with the other 85-95% in the form of iron oxides, predominantly hematite.

Mössbauer data for the lignite superheater deposits, however, show no such enrichment in iron and less than 20% of the iron is present in magnetic oxides. For these deposits, iron does not appear to play a similar role to that in the bituminous coals. In this case the "glue" material may be calcium sulfate as this phase was shown by EXAFS spectroscopy to be very abundant in the initial deposit.

(ii)b Superheater Deposits - Outer: The structure of the outer superheater deposit is derived from the initial superheater structure by partial fusion and blending of the different fly-ash particulate matter. Many larger Fe-rich and Si-rich particles, however, persist unassimilated in the matrix so that the aluminosilicate particles become important at this stage as the major bonding phase. Partial fusion of these particles coupled with incorporation of all potassium and calcium phases and an appreciable fraction of the iron particles into this partial melt creates an extensive continuous framework. When frozen, these deposits were extremely tough and resistant to fracture because of this structure. For the bituminous deposits, Mössbauer data indicate that there is only a very minor enrichment of iron in these deposits compared to the in-flame solids and that there is a significantly higher percentage of iron in glass compared to the initial deposit.

The lignite outer superheater deposits varied from lightly sintered fly-ash to highly agglomerated amber-brown vitreous material. Fly-ash relicts, mostly large quartz particles and a few Fe-rich cenospheres, persist in less agglomerated areas and diminish in abundance with increasing agglomeration. The matrix is rich in calcium, aluminum and silicon and appears to have formed by reaction between Ca-rich and aluminosilicate particles. The matrix is quite highly crystallized with melilite ($Ca_2(Al,Mg,Fe,Si)_2SiO_7$) and anorthite ($CaAl_2Si_2O_8$) being the most common phases. Melilite tended to occur in the less agglomerated areas whereas anorthite was found in the more highly agglomerated areas.

(iii) Waterwall Deposits: An initial and outer waterwall deposit was collected for each coal. The initial deposit consisted of thin deposit whereas the outer deposit was considerably thicker and often collected in large masses. Mössbauer data showed some differences between the initial and outer deposits in that the initial deposits always contained more iron as oxides (except for the lignite), had a higher $Fe^{3+}/Fe^{2+}$ ratio for the glass, and had less Al substituted for Fe in hematite, based on the magnetic hyperfine splitting parameter for this phase. However, there was little difference in the amount of iron between corresponding samples of waterwall deposit (Fig. 3).

The microstructure of the outer waterwall deposits from the bituminous coals varies significantly from the wallside to the fireside. At the immediate wallside is a thin layer that resembles the outer superheater deposit in that considerable fly-ash structure is present in a partially fused matrix. This layer is typically discontinuous towards the wall and offers a somewhat tenuous connection between the wall and the main body of the waterwall deposit. The continuous part of the deposit nearest the wallside exhibits a similar structure. Upon moving away from the wall, the relict Si-rich cenospheres are quickly assimilated into the matrix whereas the Fe-rich cenospheres fragment as the iron oxide equilibrates with the matrix. Upon moving further into the middle of the deposit, the Fe-rich fragments become increasingly angular and are eventually superseded by well crystallized, often skeletal, crystals of iron oxides. At the same time the glassy matrix becomes more

uniform in composition and appearance. On moving closer to the fireside, the iron oxides become less frequent and mullite laths begin to appear. At the immediate fireside, mullite occurs along with glass and the iron oxides occur as extremely fine scale dendrites. This latter phase probably developed upon cooling and was not present at temperature.

Similar microstructural changes are seen for the outer waterwall deposits from the lignite, but with different phases. In the adhesive layer, the fly-ash material is very calcium rich and contains appreciable sulfur and some Fe-rich particles. Large relict quartz particles are found near the wall and these appear to be only very slowly assimilated into the matrix. The matrix structure near the wall is fine-grained and chaotic, but coarsens considerably towards the center of the deposit as melilite crystallizes. Upon moving further towards the fireside, fewer quartz relicts are observed and the melilite crystallization is replaced by anorthite. In addition, crystallization of some minor phases such as calcium ferrites occurs in the outer waterwall samples.

For the raw Texas lignite sample, relict quartz was significantly more abundant than for the cleaned lignite sample. Furthermore, it appeared that the quartz was not so easily incorporated into the matrix of the raw lignite waterwall deposits. Occasionally, it was noted that a mantle of immiscible liquid was formed around the quartz particles that hindered the assimilation of this mineral into the Ca-rich matrix.

## CONCLUSIONS

Despite significant differences in chemical composition, the microstructures of the lignite and bituminous deposits were quite similar and it would be difficult to identify a particular deposit as coming from a given coal in the absence of compositional information. However, this implies that similar structures can be brought about by quite different chemical interactions. In particular, the role of iron oxides in the initial formation of the superheater deposits and possibly also for the waterwall deposits from the bituminous coals is not evident for the lignite deposits. For these latter deposits, calcium sulfate may play a similar critical role, but this remains to be demonstrated. Partial fusion of the aluminosilicates accompanied by assimilation of basic cations into the matrix appears to be the principal cementing mechanism of both types of deposit, once they are established. As the deposits thicken and are subject to higher temperatures, the melts become more homogeneous and their mineralogy and behavior are largely governed by phase equilibria considerations.

In both types of deposits, relict Fe-rich and quartz fly-ash particles resist assimilation into the aluminosilicate matrix. In the case of the bituminous deposits, the abundance of iron oxide is such that it is either the liquidus phase or close to it. Hence, the aluminosilicate melts, except at very high temperatures, are effectively saturated with iron. In the case of the lignite deposits, quartz particles are generally quite large and assimilation in the melt is probably retarded because of sluggish reaction kinetics and also perhaps liquid immiscibility. This effectively makes the melt more basic than it should be and enables the crystallization of basic phases such as melilite. However, as quartz is absorbed into the melt and the composition becomes more acidic, anorthite takes over as the major crystallizing phase, as would be predicted from the $CaO-Al_2O_3-SiO_2$ phase equilibria diagram.

**ACKNOWLEDGEMENTS**

This work was supported by the Electric Power Research Institute by means of a contract to Combustion Engineering, Inc.

**REFERENCES**

(1) F.E. Huggins, G.P. Huffman, and R.J. Lee, in: Coal and Coal Products: Analytical Characterization Techniques, ACS Symposium Series 205 239-258, (1982).
(2) G.P. Huffman, and F.E. Huggins, in: Chemistry of Low-Rank Coals, ACS Symposium Series 264 158-174, (1984).

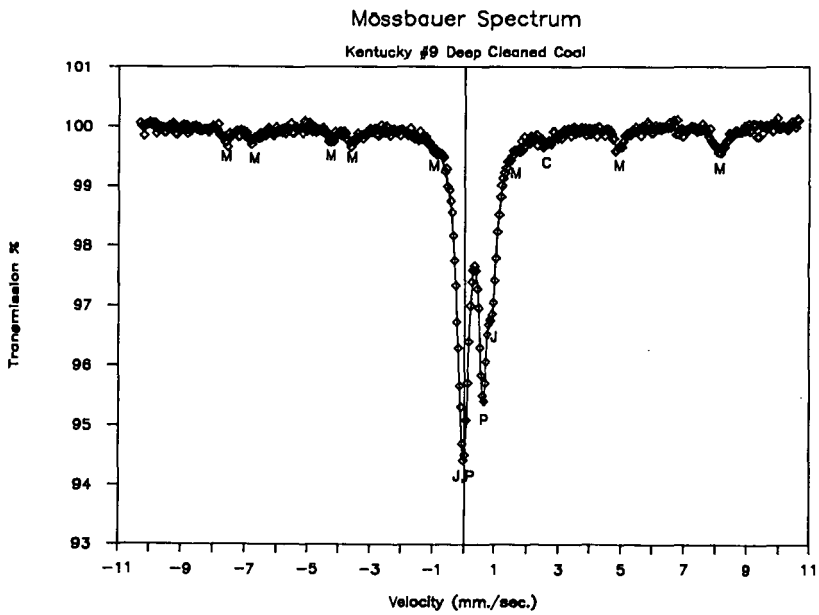


Figure 1: Mössbauer spectrum of the deep-cleaned Kentucky #9 coal showing the contamination by magnetite (M) from heavy-media cleaning. Other iron-bearing minerals present in the spectrum are pyrite (P), jarosite, (J) and ferrous-bearing clay (C).

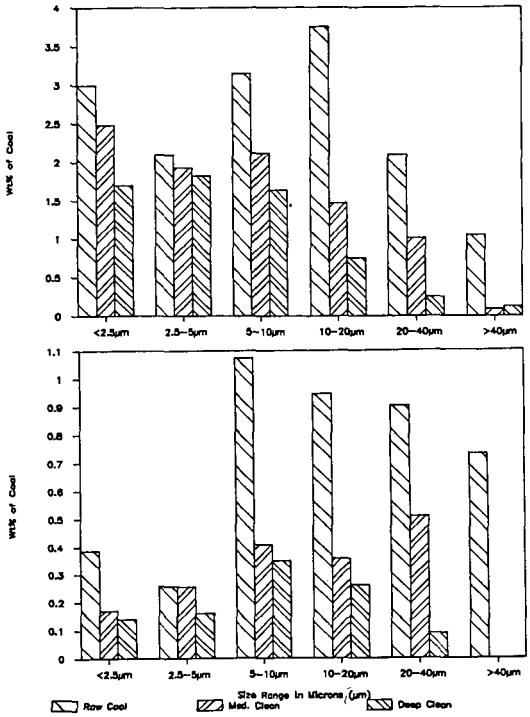


Figure 2: Size distribution data for all minerals (upper) and pyrite (lower) in Kentucky #9 coals. Data are expressed as wt% of the coal.

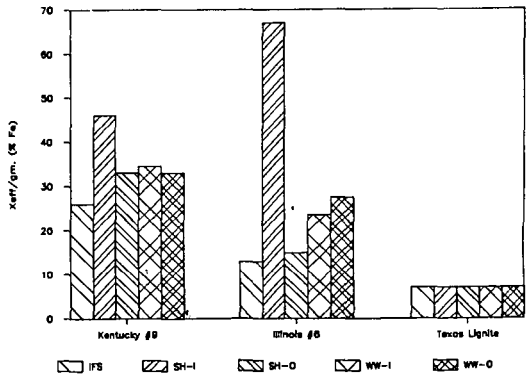


Figure 3: Histogram showing the significant enrichment in iron (based on the Mössbauer effective thickness parameter, $X_{eff}/gm$) for the initial superheater deposits from the raw bituminous coals and the lack of iron segregation exhibited by the lignite.
Key: IFS - in-flame solids; SH-I - initial superheater; SH-O - outer superheater; WW-I - initial waterwall; WW-O - outer waterwall.

# PHYSICAL AND CHEMICAL TRANSFORMATIONS DURING PULVERIZED COAL COMBUSTION -- OPTICAL SYSTEMS FOR MEASUREMENTS

D. K. Ottesen and D. R. Hardesty
Sandia National Laboratories
Combustion Research Facility
Livermore, CA 94550

L. J. Radziemski
Physics Department
New Mexico State University
Las Cruces, NM 88003

## INTRODUCTION

One of the most difficult problems in developing diagnostic methods for coal combustion research is that of determining the composition of entrained coal, char, and mineral matter particles in the combustion zone. We have employed two laser-based techniques for the simultaneous measurement of the size, velocity, and elemental composition of particles in combustion flows. Laser spark spectroscopy [1,2], also called laser induced breakdown spectroscopy (LIBS) [3], is used to determine the elemental composition of coal particles. Sizing measurements are done using two-color laser light scattering [4].

Laser spark spectroscopy is a variation of conventional emission spectroscopy which uses a focused pulsed laser beam to generate an optical breakdown, commonly called a laser spark or a laser induced plasma. The origin and uses of this technique are well summarized [5]. Many of its properties are similar to those of conventional arc or spark plasmas as discussed in standard texts on spectrochemistry [6]. As with conventional techniques, the laser spark allows simultaneous multi-element detection. An important advantage is the ability to obtain information in hostile environments, in situ, where electrodes cannot be introduced.

Two principal applications for this technique are proposed. The first is the simultaneous measurement of size, velocity, and composition of single particles and is primarily an analytical research tool for coal combustion studies. The second is the measurement of bulk properties before, during, and after combustion by coaddition of hundreds or thousands of individual spectra. This can be envisioned as an on-line monitor in an operating combustor. Our experiments have elucidated the advantages and difficulties which will be encountered in these applications.

## INSTRUMENTATION

The apparatus was arranged so that sizing and spectroscopic information could be obtained simultaneously. A general apparatus diagram for all experiments is shown in a top view in Figure 1. Measurement of particle size and velocity using a two-color colinear beam has been more fully described elsewhere [4].

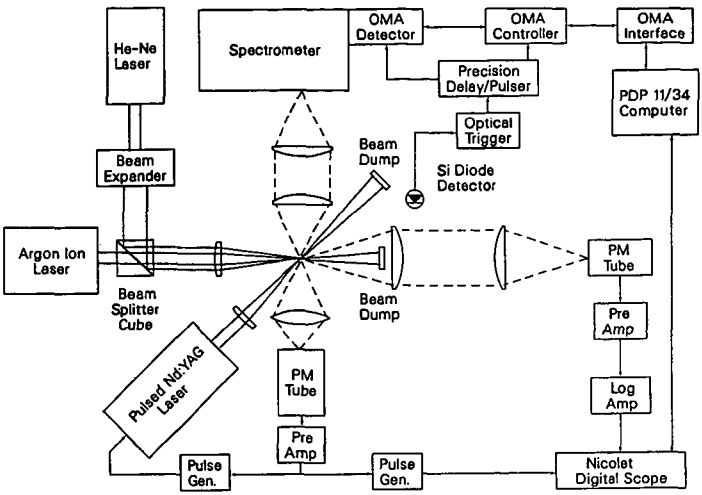


Figure 1. Top view of laser sizing and spark spectroscopy system.

## Light Scattering Instrumentation

The two-color scattering technique permits an accurate estimate of particle size and velocity. Beams from He-Ne and Ar-ion lasers were combined using a beam splitter cube. Scattered light from particles passing vertically through the common focal volume was viewed with two photomultiplier tubes: one in the near-forward direction, and the other at 90 degrees to the laser beam axis. Particle scattering signals were used to fire a pulsed Nd:YAG laser, creating a high temperature laser spark from the particle.

This technique can be very satisfactorily calibrated to measure particle size by using regularly shaped particles and orifices. Particle velocity was calculated from a knowledge of the Ar-ion laser beam waist diameter and the transit time of a particle determined from the 1/e points in the measured near-forward scattered light intensity.

## Laser Spark Instrumentation

Spectra were generated from the plasma formed by the focused Nd:YAG laser beam (Quanta Ray DCR-2, Q-switched, oscillator only). Laser energy was a nominal 110 mJ per pulse at 5320 Å. Important parameters for the acquisition of spectra were timing, optical alignment, and temporal resolution. The irradiance at the focus of the Nd:YAG laser beam was adjusted to ensure breakdown would occur only in the presence of a particle in the focal volume. This eliminated spurious data from a triggered breakdown of the entrainment gases.

The operation of the Nd:YAG laser Q-switch introduced a 250 μs delay between the arrival of the trigger pulse and firing of the laser. Because the particles under investigation were moving, the optimum focal volume for the Nd:YAG

laser beam was displaced from that of the sizing laser beams. The mean particle velocity could be maintained at a fairly constant value (± 10%) in the range of 1 - 5 m/s. We found that with proper experimental alignment of the three beams, about 90% of the particles which triggered the Nd:YAG laser actually formed a plasma due to laser induced breakdown.

Light from a laser spark was imaged on a silicon diode detector to generate a trigger pulse which initiated collection of the spectrum (Figure 1). The laser spark was imaged on the entrance slit of the spectrometer (Spex Model 1870) with a nominal 20 μm slit width and a gated, intensified diode array (PAR Model 1420). The emission spectrum was then digitized and stored on hard disc for subsequent analysis.

Previous investigators [2,7] have shown that time resolution is essential for analytical uses of laser plasmas. For times less than 1 μs following laser induced breakdown the emission spectrum was dominated by continua and lines due to ionized species. Time delays of at least 2 μs were necessary to discriminate against the continuum and to restrict the observed species to neutral and singly ionized atoms. Molecular spectra were observed but were due to recombination of atoms in the plasma, not from molecules originally in the sample. Integration times depended primarily on the intensity of lines observed in a given spectral region, and ranged from 1 to 10 μs for this study.

### Particle entrainment system and reactor

Samples investigated were of two forms, liquid droplets or solids of various composition. Liquid droplets of pure substances or solutions were produced using a vibrating orifice generator and were dropped through the optical focal region under ambient conditions. They were used primarily to calibrate the scattering signal.

The entrainment of solid particles into a stream of purified dry nitrogen was done with a particle feeder. The fluidized solid particles were introduced along the vertical centerline of a circular premixed burner through a central tube. This was aligned below the intersection of the three laser beams as shown in Figure 1. The combustion region of the burner was 50 mm in diameter and was surrounded by a co-flow region for flow regulation and to prevent mixing with the laboratory atmosphere.

A flat flame above the burner surface produced a hot, vertically flowing column of gases into which the particulates were entrained. By varying the amounts of the fuel, oxidizer and diluent gases, one could control the combustion temperature and residual oxygen partial pressure in the hot environment. Methane and oxygen were used in this study, with nitrogen added as a diluent. Gas flows were controlled with mass flowmeters. Temperatures 50 mm above the burner surface measured with a Pt-Rh thermocouple in the absence of particles were on the order of 1500° C.

## CALIBRATION

### Calibration of the sizing apparatus

Calibration of the particle sizing apparatus was done by the measurement of near-forward scattering intensities of uniform liquid droplets and precision

pinholes. Once the calibration scale was established, the daily measurement of scattering intensity from a single reference pinhole was used to establish a current working curve. This is more fully described elsewhere [4].

Calibration of and factors affecting the spectroscopic signal

To be useful, the observed emission intensities had to be related to relative and absolute elemental compositions. There were several variables with which to deal: (1) incident laser power, (2) particle size, (3) particle composition and associated matrix effects, (4) location of the particle in the laser focal volume, (5) amount of the particle material removed and ionized, (6) plasma temperature and possible self-absorption, (7) image location on the spectrometer entrance slit, and (8) the lack of "standard reference materials" for coals on a particle-by-particle basis.

It was first necessary to establish the level of reproducibility of the emission signal for well-characterized, monodispersed, homogenous samples. The use of pure solid particles was not found to be particularly valuable for this purpose. Analytical lines for most metallic species found in coal were strongly self-absorbed in laser spark emissions from target particles consisting of the pure oxides or simple salts.

Calibration experiments were undertaken using homogenous solid particles composed of an ion exchange resin, Amberlite, loaded with calcium at 10 wt %. A typical spark emission spectrum is shown in Figure 2. A small magnesium impurity was present in the ion-exchange material, and additional lines due to Mg I and Mg II were also observed in this spectrum.

These multiple line spectra (and others discussed below) were fit by a non-linear least squares computer program using Lorentzian line shapes and reference intensities from the NBS collections [8,9]. The calculated reference intensities for each species were multiplied by a coefficient to fit the experimental data. Because the reference intensities were determined for standard concentrations [8,9], the ratio of the coefficients for different elements should be closely related to the relative elemental concentrations.

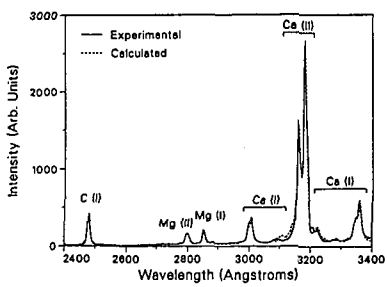


Figure 2. Laser spark spectrum of a single ion-exchange resin particle.

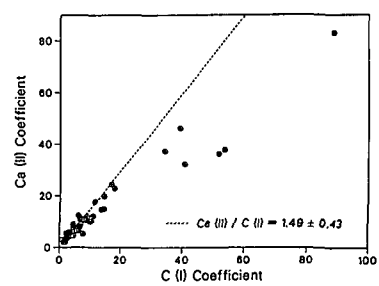


Figure 3. Least-squares fitting coefficients for Ca II and C I in 80 spark spectra.

About 80 particles were analyzed for the various C, Ca, and Mg transitions. Ratios of metal/carbon coefficients were calculated in order to assess the reproducibility of emission intensities on a shot-to-shot basis. The intensities for Ca II and C I (Figure 3) are clearly correlated and show an initial linear relationship. Points corresponding to higher counts show a gradual saturation. Within the linear regime the scatter may be due to particle heterogeneity and shot-to-shot variations of the excitation within the plasma. The latter can be caused by variations in the coupling of the energy into the plasma, or the size or morphology of the particle. Even so, the existence of a linear regime is evidence of significant shot-to-shot reproducibility.

Previous studies [10] have shown that matrix effects exist for different atomic species included in a solid material using laser spark spectroscopy. This is typical of conventional emission spectroscopy techniques also. For a given matrix composition of a bulk phase the most volatile atomic species were preferentially removed in the high temperature plasma, and the observed elemental composition of the ionized material was found to differ from the bulk composition accordingly. We might also expect such effects in our study.

Measurements on solid particles will always have to contend with incomplete vaporization. Calculations based on the heat of vaporization of carbon indicated that the coupling of 1% of the available incident laser energy into a solid particle would completely vaporize particles no larger than 10 μm in diameter. For incomplete vaporization, particle heterogeneity could be a serious problem. However, it appears impractical to use a laser with sufficient energy to vaporize large particles.

Coupling of the laser energy into the target particle is complicated by the complexities of hitting a moving particle with a pulsed laser beam at a stationary focal point. Careful control of particle feeding conditions and laminar flow of the gases above the reactor surface helped to minimize variations in particle velocity. Light scattering data indicated an axial velocity distribution of ± 10% about a mean velocity of 2 m/s for pulverized coal particles. For a Q-switch delay of 250 μs, this would yield an axial variation of ± 50 μm in particle position. This is quite large compared to the calculated beam waist of 100 μm for our Nd:YAG laser, and is probably the dominant experimental variable for the coupling of incident laser light with the plasma.

## RESULTS

Pulverized coal particles were entrained in the reactor system and spark emission spectra were collected with and without sizing data for single particles under different conditions. Three bituminous coals were studied: an Illinois #6, a Pittsburgh #8, and a Kentucky #11 coal. All had high temperature ash contents of 13 to 14% with varying amounts of inorganic constituents. Particles were size classified and the 63-75 μm diameter fraction for the first two coals, and the 30-50 μm diameter fraction for the third coal, were used here.

### Qualitative Results

Extensive spectra were taken from 1900 to 7700 Å to assign emission lines and determine sensitivity to trace components. Representative spectra of single particles for the same coal sample are shown in Figures 4a and 4b. Two of the

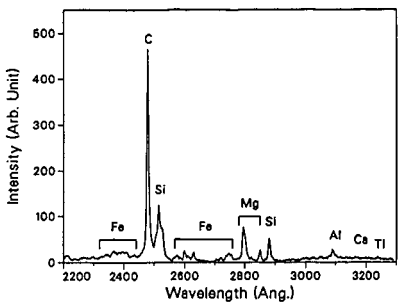


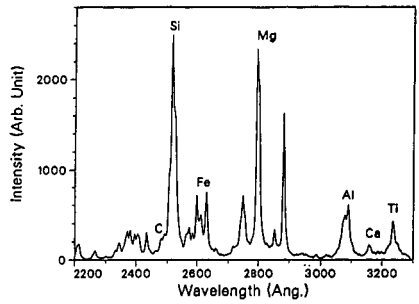


Figures 4a - 4b. Representative laser spark spectra of single coal particles.

most useful aspects of laser spark spectroscopy in the study of coal combustion are seen: the sensitivity to inorganic constituents in the organic material, and the capability for simultaneous multi-element detection.

The following elements were identified in these survey spectra at room temperature: C, H, O, N, Li, Na, K, Mg, Ca, Sr, Ba, Al, Si, Ti, Mn and Fe. Major species were silicon, aluminum, calcium, magnesium, iron, sodium, potassium and titanium. The rest were trace constituents. All the identifications were made from spectra of individual particles.

We also searched for sulfur and phosphorous lines. The array-spectrometeter system was not sensitive at the sulfur resonance lines (1800-1900 Å), and phosphorous was simply not seen. Other trace metallic elements at lower concentrations, such as chromium and vanadium (with average bulk concentrations of 3-30 ppm), were not detected with our current instrumentation. Sensitivity to these elements may be improved by coaddition of many single particle shots. An ultimate detection limit for most metallic species in single coal particles is likely to be below 100 ppm. Molecular species originally in the coal are dissociated by the plasma and not observed. Recombination of hot atoms gave rise to strong CN bands, however, which obscured the regions from 3750- 3900 Å and 4150-4220 Å. No other excited molecular or radical spectra were observed.

Experiments were also performed at combustion temperatures. While the residence time was quite short, the coal particles had ignited and were undergoing vigorous devolitalization at this point. Data of high quality, similar to Figures 4a and 4b, were collected in situ without significant degradation in the signal/noise ratio for ambient conditions.

Semi-quantitative results

The absolute mass sensitivity of the technique may be illustrated by considering the spectrum in Figure 5. Sizing data indicated that this particle was of 29.5 µm diameter. Based on a density of 1.5 g/cc for coal, this yielded a total particle mass of 20 ng. We assumed a plasma temperature of 1 eV (11,600 K) and calculated relative intensities for transitions of C and Fe. With an average carbon content of 83% (dry basis), the observed relative intensities

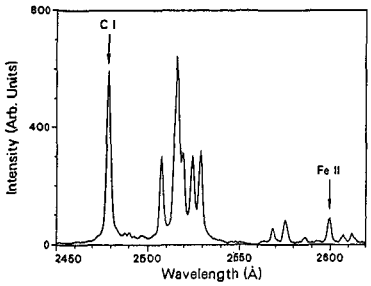


Figure 5. Laser spark spectrum of a single, 20 ng coal particle showing detection of 700 fg of iron.

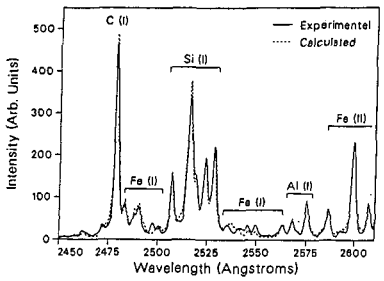


Figure 6. Comparison of experimental and calculated spectra for a single coal particle.

corresponded to detected quantities of 0.7 pg of iron. The actual absolute amount of material in the plasma was probably less due to incomplete vaporization of the particle during the excitation process.

Since coal is a very heterogeneous material, one expects a large variation in emission intensity for the observed constituents on a particle-by-particle basis. A convenient and systematic way of studying these variations is to examine the relative intensity for two elements for a large number of particles. If this is done over a narrow spectral bandwidth, then the optical system response will be reasonably constant and the observed intensity ratios can be semi-quantitatively related to reference intensities [8,9] for a given average plasma temperature.

For particles at ambient temperature and those examined after short residence times at combustion temperatures, we observed the spectral region from 2400 to 2650 Å and chose the ubiquitous C I transition at 2478 Å as the reference line. This region also contained several transitions due to Si I, Al I, Fe I and Fe II. Even though carbon is a major species, the C I line at 2478 Å is not likely to saturate since the lower level of the transition is at 2.68 eV.

In our first attempt at quantitative analysis, we obtained spectra from eighty particles of Kentucky #11 coal entrained at room temperature in nitrogen. Synthetic spectra were computed rapidly and produced a good fit to each individual spectrum as illustrated in Figure 6. Deviations between calculated and observed intensities for several Fe I and II transitions were probably due to a difference in plasma temperatures for our experiment and the reference intensity data. The least-squares analysis yielded fitting coefficients which we related to the relative concentration of the element.

Matrix effects also will alter these relative elemental line intensities with respect to the reference data [8,9]. While these variations may be most directly accounted for by calibration with suitable homogeneous reference particles, difficulties in making such standards may necessitate their evaluation

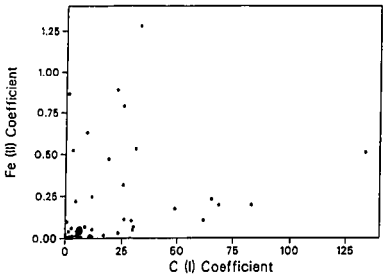


Figure 7. Relative amounts of Fe and C for 80 single coal particles.

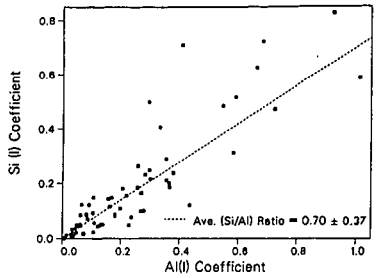


Figure 8. Relative amounts of Si and Al for 80 single coal particles.

through a detailed statistical comparison of bulk chemical analyses with a large number of laser spark spectra.

A plot of C I and Fe II fitting coefficients obtained from these spectra is shown in Figure 7 and illustrates the heterogeneity of the coal particles. Particles rich in iron show a random distribution of points with high Fe II coefficients, and are attributed to inclusions of iron-bearing minerals (predominantly pyrite). On the other hand, a second population of points is seen near the x-axis with low values of Fe II coefficients. These appear to be highly correlated with carbon content, and may be due to iron distributed homogeneously throughout the organic matrix. Scanning electron microscopy results on a sample of this coal substantiated that these two distinct iron populations exist [11].

A second example of relative elemental composition is shown in Figure 8 for silicon and aluminum from the same set of 80 spectra. These two elements appear to be correlated and present in comparable amounts. Some of the considerable scatter in the data is due to variations in plasma temperature; however, a much larger effect is that the various clay minerals containing aluminum and silicon may differ significantly in relative elemental composition. Further, another source of silicon in the coal is quartz, which would be completely uncorrelated with the silicon and aluminum present in clays.

In contrast to these two examples, sodium is often quite evenly distributed in bituminous coals, and this is illustrated in Figure 9 for 50 particles of the Kentucky #11 sample. This plot is of experimental intensities for the doublet at 5890 and 5896 Å, and these values have not been normalized against other transitions. The data illustrate the very uniform distribution of sodium in this coal despite differences in plasma conditions mentioned above.

## DISCUSSION

Our results demonstrate the potential for laser spark spectroscopy as an in situ analytical technique for particulate composition in ambient and high

temperature environments. An obvious next step is the quantitation of emission intensities. This can take two directions: correlation with available bulk analyses through coaddition of many single particle analyses, and development of appropriate standard materials.

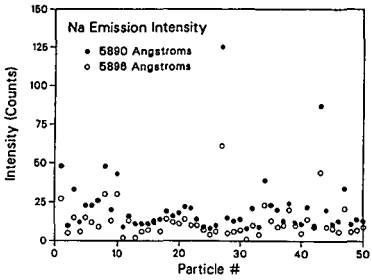


Figure 9. Distribution of sodium in spark spectra of 50 coal particles.

In the present study, the sizing capability was often not employed because sized particles were used. In general, however, simulataneous sizing and spectral analysis will allow an approximate mass analysis on each particle. The addition of hundreds to thousands of these could begin to emulate the bulk analysis. The study of coals with significantly differing composition could verify the sensitivity of the technique, and the likely result would be a semi-quantitative in situ analysis capability.

Experiments with uniform ion exchange resin particles have demonstrated that reproducible results can be obtained with well characterized particles. The difficulty in acquiring adequate calibration standards for quantitative analysis lies not only in their preparation, but also in the certification of their homogeneity on a particle-by-particle basis. A possible approach might be the doping of porous char particles with a given elemental species. The issue of emission intensity dependence on the amount of particle vaporized during excitation may be studied using reference particles with varying levels of incident laser energy.

Another important aspect of particle inhomogeneity is the evolving character of surface composition during combustion, since significant quantities of mineral species may coalesce on the particle surface. Incomplete vaporization of the solid during excitation would yield intensities not representative of the entire particle, and calculated compositions would be biased as a result.

The increase in mineral composition relative to the organic matrix during the combustion process would be expected to show an increasing amount of self-absorption and, finally, line reversal for the strongest transitions. This potential problem may be mitigated in the analysis of post-combustion material since ash particles are smaller than the initial pulverized fuel particles, and might be quantitatively vaporized by the incident pulsed laser beam.

## CONCLUSIONS

The experiments described above have demonstrated that qualitative analysis can be performed on single particles, in situ, in hostile environments. The practical level of signal reproducibility has been measured, and the first indication of semi-quantitative results has been established. Problem areas have been identified. Some can be overcome while others will limit the applicability of the technique.

The studies will continue with emphasis on establishing the semi-quantitative capability of the combined techniques for well characterized coals, and for new homegeneous standard materials. The experiment will be integrated with a laboratory bench-scale combustor, and the capability to discern changes in coal composition during burning will be investigated by spectral analysis as a function of coal type, combustion residence time, and gas phase chemistry.

## ACKNOWLEDGEMENTS

This work was supported by the U. S. Department of Energy, Office of Fossil Energy, Advanced Research and Technology Development Program, Morgantown Energy and Technology Center. We acknowledge the technical assistance of Bill Kent who assembled and maintained the experimental apparatus, and Don Nissen who kindly provided the SEM analyses.

## REFERENCES

1. R. W. Schmieder, "Techniques and Applications of Laser Spark Spectroscopy," Sandia Natl. Laboratories Report, SAND83-8618, Mar., 1983.
2. D. K. Ottesen, "In Situ Real-Time Analysis of Particulates Using Laser Spark Spectroscopy," Proc. Int. Conf. on Coal Science, ed. J. A. Moulijn, Elsevier, NY, p. 777 (1987).
3. L. J. Radziemski and T. R. Loree, J. Plasma Chem. Plasma Proc. 1, 281 (1981).
4. J. C. F. Wang and K. R. Hencken, Applied Opt. 25, 653 (1986).
5. D. A. Cremers and L. J. Radziemski, "Laser Plasmas for Chemical Analysis," Ch. 5 in Laser Spectroscopy and Its Applications, eds. L. J. Radziemski, R. W. Solarz, and J. A. Paisner, Marcel Dekker, NY (1987).
6. J. Mika and T. Torok, Analytical Emission Spectroscopy, Butterworth, London (1974).
7. L. J. Radziemski, T. R. Loree, D. A. Cremers, and N. M. Hoffman, Anal. Chem. 55, 1246 (1983).
8. W. F. Meggers, C. H. Corliss and B. D. Scribner, "Tables of Spectral-Line Intensities, Part I," Natl. Bur. of Stds., NBS-MN-145, May, 1975.
9. W. L. Wiese and G. A. Martin, "Wavelengths and Transition Probabilities for Atoms and Atomic Ions," Natl. Bur. of Stds., NSRDS-NBS 68, Dec., 1980.
10. E. Cerrai, and R. Trucco, Energia Nucleare 15, 581 (1968).
11. D. Nissen, Sandia Natl. Laboratories, private communication, Aug., 1987.

# A NEW MODEL FOR PREDICTING THE FOULING DEPOSIT WEIGHT OF COAL

J.D. Yeakel

Exxon Production Research Co.
P.O. Box 2189, Houston, TX 77001

R.B. Finkelman

U.S. Geological Survey, MS 956
Reston, VA 22092

## INTRODUCTION

One of the major problems associated with coal combustion is the buildup of sintered ash deposits in the convective passes of boilers. These deposits, referred to as fouling deposits, can drastically reduce heat transfer, cause erosion by channelizing gas flow, and contribute to the corrosion of exposed metal surfaces. Downtime for cleaning fouled commercial boilers can be a multi-million- dollar expense (1).

Utility boilers generally are designed to burn coal that falls within a specific fouling behavior range. Therefore, to minimize the deleterious effects of boiler fouling and to maximize boiler efficiency, it is necessary to anticipate or assess the fouling characteristics of a coal prior to combustion.

This paper introduces a new method for predicting fouling deposit weights by using commonly available coal quality data.

We have developed a modified concept of the coal quality characteristics that influence fouling. This concept evolved from a review of the literature and from the statistical analysis of results from 44 combustion tests.

## COAL-FOULING-ASSESSMENT INDICES

Several fouling indices based on ash chemistry have been proposed (2). Most are applicable to coal with eastern, or bituminous, ash.* These indices have met with mixed success. Wall et al. (3) state that "there may be very severe limitations to the applicability of 'fouling indices' based on elemental analysis or even on fusion observations...." Moreover, Wall et al. (3, p. 8) note that at a conference on combustion "a number of speakers stated that fouling indices they had used appeared applicable only to coal from a particular field."

*For technological purposes, coals in which the sum of the calcium oxide and magnesium oxide content is greater than the ferric oxide content are characterized as having "eastern" or "bituminous" ash. The relationship is reversed for coals characterized as having "western" or "lignitic" ash.

One reason for the lack of success in applying the fouling indices is that fouling deposits are formed from a complex series of physical and chemical interactions involving several chemical constituents in the coal. The fouling indices, however, focus on only a few of these constituents and put major emphasis on the sodium content.

## METHODS

The data used in this study were supplied by the University of North Dakota Energy Research Center (UNDERC) in Grand Forks, North Dakota. The UNDERC supplied the results from over 200 combustion tests conducted in a pilot-scale test combustor. In addition to the combustion test results, the UNDERC also provided complete characterization of the coal samples tested, and the combustion conditions maintained during the course of each test. Coal characterization included proximate, ultimate, and ash composition information. Table 1 shows the coal composition values and combustion test results used as variables in our study.

We selected a set of 44 samples from the raw data provided by UNDERC. This data set served as the basis for developing the model for fouling deposit prediction. The development data set 1) is representative of the UNDERC data set containing data on lignites and subbituminous coals predominantly from the Northern Great Plains Coal Province, 2) contains at least one observation from each mine or locality represented in the UNDERC file, 3) has no sample duplication, 4) is taken from samples that exhibit a wide range of compositions and fouling behaviors, and 5) had similar combustion test conditions.

Our goal was to use the development data set to model fouling deposit weight in grams per million Btu by using coal quality parameters as independent variables. Coal feed rates and total coal burned in a test could vary from test to test, depending upon the calorific value of the coal. Therefore, conversion of deposit weights to a weight per million Btu basis puts the fouling tendency on a unit energy input basis, a basis frequently used by boiler operators for other purposes such as evaluating sulfur emissions.

The first step in data analysis was to determine if the natural frequency distributions of the variables in the development data set approximate a normal frequency distribution. In all statistical analyses, we assumed the variables to be approximately normally distributed. Therefore, the variables that, in their original form, were not normally distributed were mathematically transformed to yield frequency distributions that approximated normal distribution. The transform functions (Table 1) for each variable were used in all subsequent analysis.

The second step in our study was to conduct bivariate analyses, i.e., calculation and interpretation of correlation coefficients (r-squared values). This analysis determined which variables most closely correlate with fouling deposit weight.

The third and principal step in our analysis was to employ multiple regression analysis to develop a model. We used the STEPWISE, RSQUARE, and REG procedures in SAS (4) to develop and evaluate possible models. All of these

procedures are linear least-squares methods for establishing empirical relationships between one or more independent variables and some response variable. In our case, the independent variables, or regressor variables, are transformed coal-quality parameters. The response variable is the log function of the fouling deposit weight in grams of deposit per million Btu fired.

Models were evaluated on the basis of the improvement in r-squared values, the decrease in the residual sum of squares, the significance of parameter estimates for each variable, and the linkage between fouling behavior and each variable being considered. Statistical significance alone was not enough to include a variable in the model. The final model selected was one that maximized the fit of the predicted values to the actual fouling deposit weight values; thus, maximizing the r-squared value and minimizing the sum of squared residuals.

Finally, we tested the model. For this purpose, we selected a second set of observations from the raw UNDERC data set. This set had the same characteristics as the development data set but contained only 15 samples and had no observations in common with the original data set. We tested the model by calculating a predicted fouling deposit weight using the model and then by comparing the calculated deposit weight with the actual deposit weight.

## RESULTS

### Bivariate Analysis

In the process of calculating the correlation coefficients for the variables in the development data set we discovered that several coal compositional parameters have significant correlation with fouling deposit weight (Table 2). The amount of ash, total sulfur, titania ($TiO_2$), potash ($K_2O$), silicon (Si), sodium (Na), aluminum (Al), and the alkali ratio are significantly related to fouling deposit weight. However, even though the correlations are significant at the 1-percent confidence level, the correlation coefficients are not very high indicating that no one variable is principally responsible for variation in fouling deposit weight. The relationship between fouling and coal composition is too complex to explain with just one variable. This relation is illustrated by means of a few scatter plot diagrams, one showing sodium versus deposit weight (Fig. 1) and the other showing ash yield versus deposit weight (Fig. 2).

Sodium, at present, is the most widely used predictor of fouling tendency; yet, Figure 1 demonstrates that low sodium oxide content in a coal does not guarantee low fouling or that high sodium oxide content equates with severe fouling. Obviously, fouling behavior is dependent upon something other than, or in addition to, the sodium oxide content of coal.

Figure 2 shows the dry ash yield of a coal plotted against the coal's fouling deposit weight. The relationship here is more linear than the one observed for $Na_2O$, therefore, as ash yield increases so too should fouling deposit weight. This may be thought of as the boiler tubes being exposed to more potential fouling material per unit energy generated. However, the

significant scatter in the relationship of ash yield and deposit weight would preclude the use of only ash as a predictor.

Both sodium (5) and ash yield have been shown to enhance fouling behavior (6). If we plot sodium, ash, and deposit weight on a three-dimensional diagram (Figure 3) we can see the relative influence of the two variables on deposit weight.

Figure 3 indicates that low sodium, low ash coals are low fouling coals. High fouling coals are having with moderate to low amounts of sodium but high ash yields. Deposit weights are more variable when ash yields are low to moderate and sodium values are moderate to high.

The use of ash and sodium together as predictors of fouling may be more reliable than the use of sodium alone, however, we had reliable predictions only in end member situations (low sodium, very high ash). One or two coal composition variables cannot adequately explain or predict fouling behavior. Consequently, we used multiple regression analysis to develop a model to explain the variation of fouling deposit weight values in the development data set.

## THE REGRESSION MODEL.

The regression model we found that best fits the fouling deposit weights in the development data set is given in equation 1. The variables incorporated into the model and their basis are listed in Table 3. The model calculates the logarithm of the fouling deposit weight in terms of grams of deposit per million Btu fired and it incorporates $TiO_2$, total sulfur, ash yield, Ca/S, and a factor called the alkali ratio. This latter term is calculated by using calcium, magnesium, sodium, and potassium oxide values and the ash yield. The fouling prediction equation is:

$$\log_{10}(\mathbf{FDW}) = 1.21 + 0.45\ (\log_{10}Ti) + 1.46\ (\log_{10}S) + 0.38\ (\log_{10}\mathbf{ASH}) + 1.14\ (\log_{10}Ca/S) + 0.63\ (\log_{10}\mathbf{ALK}) \qquad (1)$$

Where: **FDW** = Fouling Deposit Weight (grams/million Btu)
Ti = Titanium Dioxide % (sulfate-free ash)
S = Sulfur % (dry coal)
**ASH** = Ash Yield % (dry coal)
Ca/S = Calcium/Sulfur (both % wt. of dry coal)

$$**\mathbf{ALK} = \frac{\text{Ash \% (dry} * (Na_2O + .659K_2O)}{CaO + MgO} \qquad \textbf{(alkali ratio)}$$

** $Na_2O$, $K_2O$, CaO, and MgO are all on a % of sulfate-free ash basis.

To use the model, the coal quality information required is: ash yield (percent dry coal), sulfur (percent dry coal), and titanium, sodium, calcium, potassium, and magnesium oxides (percent sulfate-free ash). The calcium-sulfur ratio and the alkali ratio are then calculated. Then the logarithm of each parameter in Table 3 is calculated and inserted in equation 1. The result of the calculation is the base 10 logarithm of the fouling deposit weight. This can then be converted directly to grams deposit per million Btu, the predicted fouling deposit weight.

In Figure 4, predicted and observed deposit weight values are plotted. The proximity of the points to the parity line indicates that the model and actual data are in good agreement. Also, the r-squared value, 0.84, is high and significant and indicates that a significant amount of the variability in actual fouling deposit weight is explained or accounted for by the model. The sum of the squared residuals is 1.35. This value is low relative to those obtained for other potential models that we tested. In addition, all of the variables included in the model, except the calcium-sulfur ratio, correlate with fouling deposit weight.

## TESTING THE MODEL

Our test of the regression model using the smaller test data set shows that the model works well. The actual versus predicted fouling deposit weights for the test samples are plotted in Figure 5. As with the development data set, points are clustered along the parity line. However, for the test data, the r-squared value is lower than that calculated for the development data because the range in values in the test data set is more limited and there are fewer observations.

We recognize that the model is subject to error. The plots are on a logarithmic scale thus small deviations from the parity line could result in errors of several 10's of grams per million Btu. However, a comparison of Figures 4 and 5 with Figure 1 shows that our model is superior to sodium oxide as a predictor of fouling deposit weight.

The error associated with any individual prediction is approximately 20-30 percent of the calculated fouling deposit weight. This figure is based on the range of differences between actual and predicted values for all the observations in both the development and test data sets. We found that 90 percent of the differences were <57 grams per million Btu, 75 percent of the differences were <28 grams per million Btu, and 50 percent of the differences were less than 15 grams per million Btu. Also, the largest errors occurred in samples that had very high actual fouling deposit weights. Large errors in this range are acceptable because, once deposit weights exceed 150 grams per million, a severe fouling problem exists and actual deposit weights are relatively unimportant. Accuracy is required, however, in the lower range of values, below 150 grams per million Btu. Our data indicate that equation 1 can be used to estimate fouling deposit weight to within 15-30 grams per million Btu, or less, an acceptable margin of error.

## DISCUSSION

We believe that that fouling behavior of low-rank coal is predictable but that predictions will not be reliable when based on information from only one or two quality variables. Fouling is a complex phenomenon that involves a complex process (combustion) acting on a complex material (the coal). Therefore, predicting the fouling behavior of any coal will to depend on a variety of coal components, their relative amounts, their mode of occurrence, and on furnace conditions.

A variety of components in the coal interact with one another during combustion to form or retard the formation of fouling deposits. These components include the total ash yield of the coal; sulfur content; and the amount of sodium, calcium, magnesium, potassium, and perhaps silica. The ash content, particularly the more siliceous minerals, forms the bulk or aggregate of the fouling deposits. Calcium, sulfur, sodium, etc., interact to influence how much and what types of materials will bind this siliceous/ash aggregate together and to the boiler tubes. Coal that has a low ash yield exhibits low fouling behavior. Coal that has a high ash yield exhibits extreme fouling behavior but only if there is sufficient adhesive material to amalgamate the deposit. Consequently, diluting high-sodium coal with ash material (roof rock for instance) may be inadvisable if ash yields are already very low. The aggregate or bulk phase of the fouling deposit is accounted for in our model by ash, by ash as part of the alkali ratio, and also by the $TiO_2$ factor, which we believe is indicative of the detrital component of the coal ash.

The binding, or hardening, of the deposits is, in our opinion, the least understood and probably the most complex aspect of the fouling deposit formation. In our view of fouling deposit formation, the sodium and potassium ions released by coal combustion compete with the calcium and magnesium ions for sulfur. There is evidence that potassium and sodium sulfates are present in fouling deposits or play a role in their formation (7). The picture is less clear for calcium and magnesium sulfates. However, in our opinion the calcium and magnesium sulfates do not participate as a binding phase in fouling deposit formation, but may,however, be incorporated into the deposit as inert material.

The sulfur, Ca/S, and alkali ratio factors in equation 1 all relate to this binding phase of the fouling deposit. The sulfur content is obviously important, for, without sulfur, no binding phase could be present. The calcium-sulfur ratio is a measure of how much sulfur will be bound by calcium and is, thus, not available to binding by sodium. The alkali ratio is a measure of the quantity of alkali elements that have been positively linked to deposit formation (sodium and potassium [8, 9]) relative to the elements that may have a negative impact on deposit formation (calcium and magnesium).

Finally, we be stress that the model proposed in equation 1 is based principally on the degree of fit between the modeled data and the actual data, moderated by our perception of how various components in coal may behave during the formation of fouling deposits. The model is redundant because ash yield is represented in two places and the binding phase of the fouling deposits is represented by three terms. Two factors cause this redundancy. First, the mode of occurrence of the elements in the model affects the reactivity of the elements, in fouling deposit formation. Our model does not take mode of occurrence into account. Second, the development and test data sets are heavily biased towards moderate fouling coals. Only a few examples of coal that had extreme fouling behavior were available for inclusion in the data set. Inclusion of more low and high fouling coal samples in the data set might clarify the situation and result in a less redundant and more theoretically sound model. However, given the data currently available, this model does a good job of accurately predicting fouling behavior and it is clearly an improvement over the conventional (sodium) index currently in use.

## CONCLUSIONS

1. We have developed a new model for predicting the fouling behavior of low rank coal. The model is based on commonly available coal quality data.

2. The proposed model has the potential to provide accurate quantitative estimates of fouling deposit weight per million Btu.

3. This model is more accurate in predicting fouling behavior than the sodium index.

4. Actual combustion tests of unknown coals need to be conducted to fully test the utility of this model.

5. The fouling potential of a coal cannot be adequately evaluated by using one or two compositional variables. A multivariate approach is more apt to yield reliable evaluations of fouling behavior.

## REFERENCES


1. Honea, F.I., Montgomery, G.G., and Jones, M.L., 1982, Recent research on ash fouling in combustion of low rank coals, in W.R. Kube, E.A. Sondreal, and D.M. White, comps., Technology and use of lignites, Vol. 1, Proceedings, Eleventh Biennial Lignite Symposium: Grand Forks Energy Technology Center IC-82/1, p. 504-545.

2. Vaninetti, G.E., and Busch, C.F., 1982, Mineral analysis of ash data--a utility perspective: Coal Quality, Spring, p. 22-31.

3. Wall, R.F., and others, 1980, Pulverized coal-firing--the effects of mineral matter: Energy Work (UK), Vol. 70, p. 7-8.

4. SAS, 1985, SAS Users Guide: Statistics, version 5: SAS Institute Inc., Box 8000, Cary, NC 27511.

5. Reid, W.T., 1981, Coal ash--its effect on combustion systems, in M.A. Elliott, ed., Chemistry of coal utilization, 2nd Suppl. Vol.: New York, John Wiley, p. 1389-1445.

6. Tufte, P.H., and Beckering, W., 1975, A proposed mechanism for ash fouling burning Northern Great Plains lignite: Jour. Eng. Power, Vol. 97A, p. 407-412.

7. Tufte, P.H., Grohnovd, G.H., Sondreal, E.A., and Selle, S.J., 1976, Ash fouling potential of western subbituminous coals as determined in a pilot plant test furnace: Proceedings, American Power Conference, Chicago, IL.

8. Hurley, J.P., Miller, B.G., Jones, M.L., Finkelman, R.B. and Yeakel, J.D., 1985, Correlation of coal characteristics and fouling tendencies of various coals from the Gascoyne mine: Thirteenth Biennial Lignite Symposium: Technology and Utilization of Low Rank Coals; M.L. Jones, editor, DOE/METC/86/6036, p. 76-85.

9. Attig, R.C., and Duzy, A.F., 1969, Coal ash deposition studies and application to boiler design: Proceedings of the American Power Conference, Vol. 31., p. 290-300.

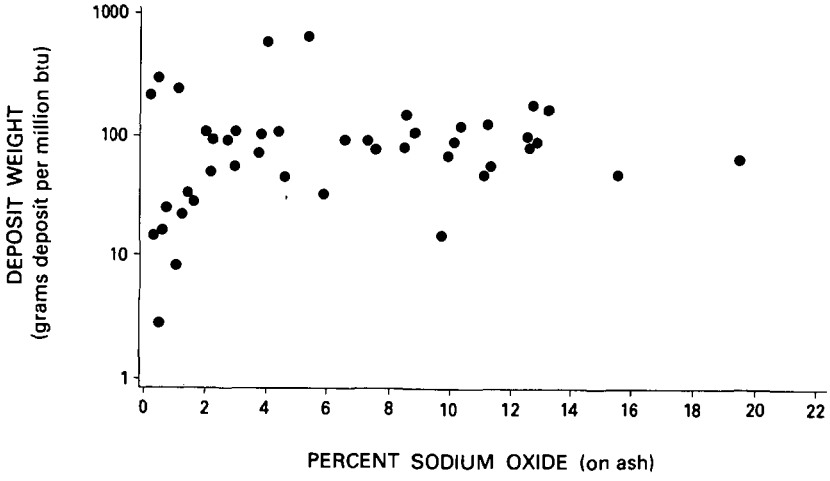


Figure 1.--Relation of sodium content to Fouling Deposit Weight.

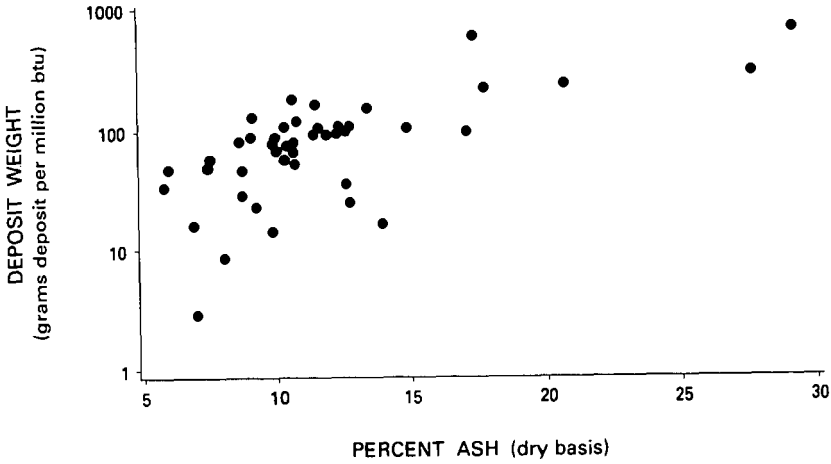


Figure 2.--Relation of coal ash yield to Fouling Deposit Weight.

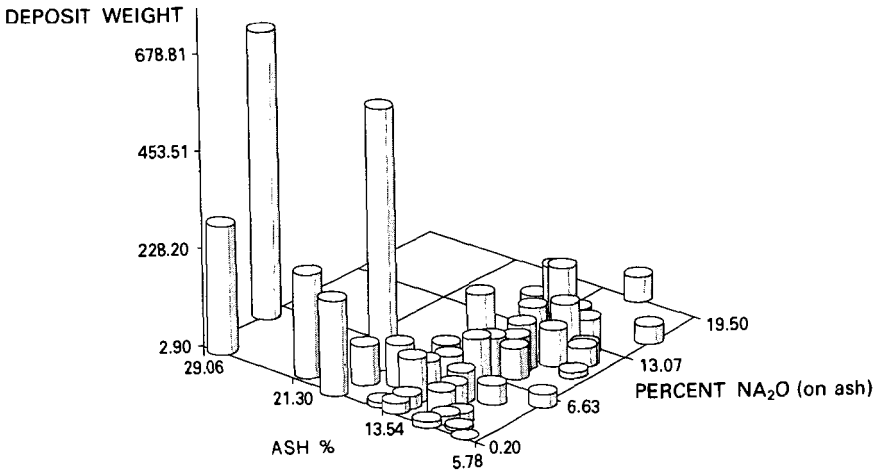


Figure 3.--Relation of ash and sodium contents to Fouling Deposit Weight.

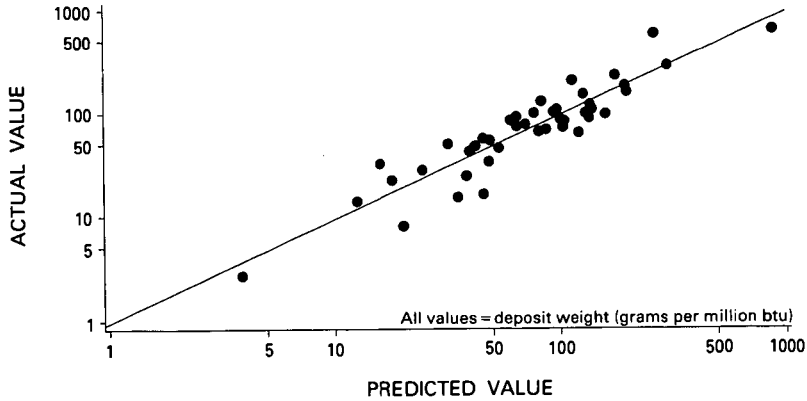


Figure 4.--Log/log plot of actual versus predicted Fouling Deposit Weight using our multivariate model (development data).

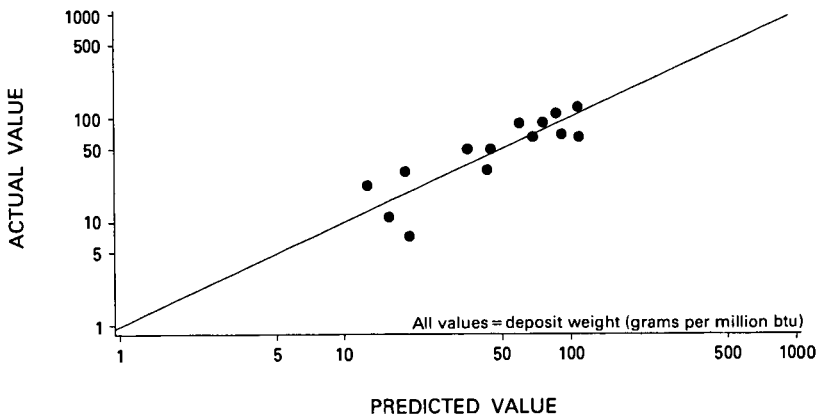


Figure 5.--Log/log plot of actual versus predicted Fouling Deposit Weight using our multivariate model (test data).

Table 1.--List of variables included in multivariate statistical analysis

| Variable | Mean | Range | Transform* Function |
|---|---|---|---|
| Ash (dry) | 11.73 | 5.78 - 29.06 | Log(10) |
| Btu (dry) | 10634 | 8400 - 12110 | - |
| Carbon (daf=dry ash-free) | 71.89 | 68.81 - 77.94 | - |
| Hydrogen (daf) | 4.75 | 2.78 - 5.73 | Square |
| Nitrogen (daf) | 1.16 | 0.99 - 1.86 | - |
| Oxygen (daf) | 20.68 | 15.73 - 24.49 | - |
| Volatile Matter (daf) | 48.25 | 42.41 - 55.13 | - |
| Sulfur (dry) | 1.29 | 0.29 - 4.13 | Log(10) |
| $SiO_2$ (sulfate-free ash) | 32.75 | 15.20 - 61.50 | - |
| $Al_2O_3$ (sulfate-free ash) | 15.02 | 8.50 - 22.90 | - |
| $TiO_2$ (sulfate-free ash) | 0.68 | 0.20 - 1.70 | Log(10) |
| $Fe_2O_3$ (sulfate-free ash) | 11.62 | 1.80 - 24.50 | - |
| CaO (sulfate-free ash) | 25.45 | 6.00 - 45.70 | - |
| MgO (sulfate-free ash) | 7.06 | 0 - 13.00 | - |
| $K_2O$ (sulfate-free ash) | 0.61 | .10 - 2.50 | Log(10) |
| $Na_2O$ (sulfate-free ash) | 6.26 | .20 - 19.5 | Sq. Root |
| Silicon (dry coal) | 1.64 | .43 - 7.71 | Log(10) |
| Aluminum (dry coal) | 0.78 | .27 - 2.78 | Log(10) |
| Sodium (dry coal) | 0.39 | .02 - 1.34 | Sq. Root |
| Calcium (dry coal) | 1.59 | .27 - 2.70 | - |
| $SiO_2/Al_2O_3$ | 2.25 | 1.11 - 5.02 | Log(10) |
| Ca/S (dry coal) | 1.83 | .27 - 9.26 | Log(10) |
| Base-Acid Ratio | 1.21 | .22 - 3.15 | - |
| Alkali Ratio | 2.75 | .14 - 23.48 | Log(10) |
| Deposit Weight (gm/$10^6$ Btu) | 112.7 | 2.90 -678.81 | Log(10) |

*Function applied to those variables whose natural frequency distribution did not approximate a normal distribution. Transformed values do approximate a normal distribution.

All values except deposit weight, Btu, and ratios are percentages on basis shown.

Table 2.--Coal quality variables that significantly correlate with fouling deposit weight (g/million Btu)

| Variable | Correlation Coefficient |
|---|---|
| Ash (percent wt. of dry coal) | 0.67 |
| Sulfur (percent wt. of dry coal) | 0.49 |
| Btu/lb (dry coal) | -0.61 |
| $TiO_2$ (percent wt. of sulfate-free ash) | 0.39 |
| $K_2O$ (percent wt. of sulfate-free ash) | 0.36 |
| Volatile Matter (daf) | 0.52 |
| Si (percent wt. of dry coal) | 0.43 |
| Na (percent wt. of dry coal) | 0.49 |
| Al (percent wt. of dry coal) | 0.44 |
| Alkali Ratio | 0.65 |
| $Na_2O$ (percent wt. of sulfate-free ash) | NS* |

*NS = not siginficant

Table 3.--List of coal quality variables used in prediction of fouling deposit weight (g/million Btu)

| Quality Parameter | Basis |
|---|---|
| Titanium Oxide ($TiO_2$) | percent wt. of sulfate-free ash |
| Ash Yield | percent wt. of dry coal |
| Total Sulfur | percent wt. of dry coal |
| Calcium Oxide (CaO) | percent wt. of sulfate-free ash |
| Sodium Oxide ($Na_2O$) | percent wt. of sulfate-free ash |
| Potassium Oxide ($K_2O$) | percent wt. of sulfate-free ash |
| Magnesium Oxide (MgO) | percent wt. of sulfate-free ash |

# A GRANULATION/SINTERING METHOD FOR THE CODISPOSAL OF SOLID RESIDUES FROM COAL CONVERSION PROCESSES

G. Burnet, A. J. Gokhale, and R. F. Meisinger

Ames Laboratory, U.S.D.O.E. and Department of Chemical Engineering
Iowa State University, Ames, IA 50011

## ABSTRACT

A stabilization process for coal cleaning and coal combustion-related wastes has been developed that uses the energy derived from the fuel contained in the coal cleaning waste. The wastes are pulverized, when necessary, formed into granules in a rotary pan agglomerator, and then fired to a sintering temperature. The resulting readily disposable product consists of rock-hard granules that are highly resistant to environmental degradation. The green (nondried and nonfired) granules satisfy durability tests that measure the capability to be handled and stored. The sintered granules meet requirements of the standard ASTM and EP leaching tests and a freeze-thaw cycle test. The strength of the sintered granules compares favorably with the strength of natural aggregates. The process has been applied to coal cleaning refuse alone and to refuse/fly ash and refuse/FGD sludge mixtures.

## INTRODUCTION

Disposal of coal cleaning and of coal combustion wastes looms as a significant problem for many coal producers and utilities. This has stimulated research on environmentally acceptable alternatives to current disposal practices. About 35% of the nearly 700 million tons of coal consumed by utilities each year receives some cleaning before it is burned (1). Most of the cleaning is performed on eastern and midwestern bituminous coals, resulting in an annual production of coal cleaning wastes in excess of 100 million tons (2). The waste piles are a source of severe air, stream, and ground water pollution (3).

Other environmentally troublesome solid wastes result from coal combustion and are proving to be even more difficult to deal with. For every three tons of coal cleaning refuse, about one ton of ash and one ton of flue gas desulfurization (FGD) solids result from combustion of the clean coal produced. Besides contributing to pollution, the waste disposal sites required mar the landscape and consume large amounts of land area.

The principle combustion-related solid waste today is fly ash from the burning of pulverized coal. In spite of vigorous research and marketing efforts, uses have been found for only about one-fifth of nearly 50 million tons of fly ash produced each year (4). Disposal is the only practical option available today for wet or dry FGD wastes. More than 150 U.S. utility installations generating wet scrubber sludge are operating, under construction or planned, with a total capacity of over 70,000 MWe (5). About 25 million tons (dry basis) of sludge or 50 million tons of wet vacuum filter cake are now generated annually and, as new systems come online, this amount will increase significantly.

A potentially beneficial approach to the disposal of the above wastes could be pretreatment in the form of stabilization or fixation. The research work reported herein deals with development of a stabilization by sintering process for the above wastes that uses the energy derived from fuel contained in the coal cleaning refuse itself. The process calls for pulverizing the wastes when necessary, forming them into granules in a rotary pan agglomerator, and then firing

the granules to a sintering temperature. The resulting, readily disposable product consists of rock-hard granules that are highly resistant to environmental degradation. A flowsheet for the process is shown in Figure 1.

Stabilization results are reported for coal cleaning refuse alone and for refuse/fly ash and refuse/sludge mixtures. The amount of carbon in the granules is critical to their behavior during combustion/sintering. Other investigators (6,7) have found that a carbon content of 5-10%$_w$ is sufficient to achieve the desired level of sintering. If the carbon content is too high, the granules overheat upon combustion of the fuel present and soften, forming a slag. Blending fly ash or FGD sludge with the refuse provides the necessary reduction in carbon content per unit weight of granules and an effective means for disposing of these wastes.

## DESCRIPTION OF WASTES USED

Analyses of the coal cleaning and coal combustion wastes used are given in Table 1. The coal cleaning refuse was collected at the Peabody Coal Company River King coal preparation plant in Freeburg, Illinois. The waste was derived from Illinois No.6 coal which is high volatile C, bituminous, medium heating value (24,400 kJ/kg; 10,500 Btu/lb, as received) and medium sulfur (4.5%$_w$). The coal is cleaned of unwanted clay, pyrite, and other impurities by jigging at a rate of up to 800 tons/hr. The major minerals present in the raw refuse are illite, kaolinite, quartz, calcite, and iron pyrite.

Table 1. Analyses of Coal Cleaning and Coal Combustion Wastes

| Item | Weight Percent or Value | | |
|---|---|---|---|
| | Cleaning Refuse[a] | Fly Ash[b] | FGD Sludge[b] |
| Constituent | | | |
| $Al_2O_3$ | 15.1% | 19.8% | 3.4% |
| CaO | 5.7% | 24.9% | 33.7% |
| $SiO_2$ | 43.8% | 34.4% | 15.6% |
| $Fe_2O_3$ | 13.5% | 5.1% | 6.1% |
| MgO | n.a.[c] | 4.0% | 0.6% |
| $Na_2O$ | n.a. | 2.1% | 0.2% |
| $K_2O$ | n.a. | 0.3% | n.a. |
| $TiO_2$ | n.a. | 1.5% | n.a. |
| $P_2O_5$ | n.a. | 1.8% | n.a. |
| C | 13.9% | n.a. | n.a. |
| S (inorganic) | 6.0% | n.a. | n.a. |
| S (total) | 7.3% | 0.7% | 5.4% |
| $H_2O$ | 4.5% | - | - |
| LOI | 24.3% | 0.2% | n.a. |
| Value | | | |
| Heating value (gross) | 6055 kJ/kg (2610 Btu/lb) | | |

[a] Air dried from an as-received moisture content of 20%$_w$.
[b] Reported on a dry basis. The sludge contained 26.5%$_w$ total C reported as $CO_2$.
[c] n.a. denotes not analyzed for.

The as-received refuse contained lumps as large as 8 cm in diameter and had to be ground to a size suitable for granule formation. The refuse was ground using two passes through a Holmes hammer mill equipped first with a screen with 3/16 in. circular holes and then a screen with 1/16 in. circular holes. The weighted average diameter of the product was about 330 microns; 95%$_w$ was retained on a 325 mesh screen.

The fly ash used was obtained from the Ottumwa power station of Iowa Southern Utilities in Ottumwa, Iowa and was from combustion of a subbituminous coal mined near Gillette, Wyoming. The particle size of the ash was such that about 20%$_w$ was retained on a 325 mesh screen. The FGD sludge came from the LaCygne station of the Kansas City Power and Light Company near Kansas City, Missouri. The plant was burning Missouri subbituminous coal and using a wet limestone scrubber that produced a non-oxidized sludge. The limestone was ground to about 70 microns prior to slurrying and the crystals of sulfur-containing compounds formed ranged from 5-200 microns. The S was present 78%$_w$ as $CaSO_3 \cdot \frac{1}{2}H_2O$ and 22%$_w$ as $CaSO_4 \cdot 2H_2O$; 78%$_w$ of the Ca was present as $CaCO_3$.

## PREPARATION OF GREEN GRANULES

Granules as formed in the pan agglomerator are referred to as green granules. The parameters controlling green granule formation are the particle size of the wastes, amount of water added as a binder, residence time of the granules in the agglomerator (feed rate), and the angle of inclination and rpm of the agglomerator.

The pan agglomerator (Agglomiser, 36 cm pan, 1/8 hp, Mars Mineral Corp.) was equipped with a vibratory feeder (Syntron, Model FTOC, FMC Corp.). The water to serve as the binding agent was added using an automatic spray system or a manually operated spray bottle. The refuse/ash and refuse/sludge mixtures were prepared by blending the solids in a ball mill before they were added to the agglomerator.

A batch method of operation for small scale testing was developed that gave granules of predictable and reproducible properties. Depending upon the conditions used, each run lasted for 30-80 minutes and consumed about 1500 grams of feed. Granules were removed from the pan during the run as they reached the desired product size of about 12 mm diameter.

Large quantities of green granules (10-12 kg) were subsequently prepared for sintering and testing for resistance to leaching and freeze-thaw degradation. The pan agglomerator was operated continuously at a set of conditions previously determined from the small-scale batch tests.

The green granules formed had to be sufficiently durable to withstand the vibration, attrition, compression, and similar forces that would be encountered in a commercial sintering facility. Durability was measured using the ASTM B440-49 Drop Shatter Test (modified) and a drops-to-fracture test (8). Satisfactory granules would show 95%$_w$ intact or better for the drop shatter test and 15 drops or better for the drops-to-fracture test.

In determining the optimum conditions for green granule formation, the total moisture content in the pan was varied from 15-22%$_w$, the pan angle from 45-55°, and the feedrate from 15-60 g/min. Lower moisture contents resulted in poor particle adhesion and granules that developed breakage planes easily. Higher moisture contents resulted in caking in the pan.

Steeper pan angles resulted in greater granule compaction but a reduced residence time. A pan speed of 19 rpm was found to provide the rolling and cascading action required to promote continuous granule growth. The best granules were obtained at lower feed rates where uniform granule growth occurred and the longer residence time resulted in greater granule compaction.

The best refuse only granules as determined by durability testing were obtained in the 18-20%$_w$ moisture range using a pan angle of 45°. Refuse/fly ash granules showed lower durability and required less moisture as the ash content was increased. Very satisfactory granules containing 25%$_w$ ash were obtained at feed rates of 15-30 g/min, a pan angle of 50°, and a moisture content of 17-18%$_w$, wet basis.

Granule durability for refuse/sludge mixtures decreased as the sludge content increased. Depending upon the amount of sludge present, the optimum moisture content varied from 15-22%$_w$. The best results were obtained with a pan angle of 50° and a feedrate of about 50 g/min.

The amount of refuse in a refuse/ash mixture was determined by carrying out a standard loss on ignition (LOI) test. The ash present had already been ignited when it was formed in the furnace so that the total LOI could be attributed to the refuse present. The amount of sludge in a mixture was determined by analyzing for Ca by xray fluorescence. Knowing the ratio of Ca in the sludge to that in the refuse, it was then possible to calculate the composition of the blend.

## COMBUSTION/SINTERING OF THE GREEN GRANULES

To cause sintering to occur, the granules were heated in the presence of air causing the coal in the refuse to burn, thus raising the temperature of the granules to the desired sintering temperature. The green granules used had been produced using the conditions previously found to give optimum granule durability.

The effect on sintered granule properties of different time-temperature treatments was determined using small scale boat tests carried out using an electrically heated laboratory tube furnace (I.D. 3.4 cm). Five to ten granules that had been previously dried in a 100°C oven were placed in an alumina boat which was then inserted into the tube furnace preheated to the test temperature. A carefully measured flow of air (10 L/min at 1 atm. and 20°C) was then introduced into one end of the furnace tube.

Granules were sintered at temperatures ranging from 900-1200°C for 1 hour to approximate the conditions in a traveling grate furnace. The amount of sintering that had taken place was determined by subjecting the cooled sintered granules to an unconfined compressive strength test using an Instron machine. The best of the small scale test results determined the operating conditions for the production of environmental test quantities of sintered granules in a large tube furnace.

Figure 2 gives the force-at-fracture for the sintered refuse only granules as a function of sintering temperature. The granules sintered at 1200°C were very weak due to early slagging on the surface and incomplete sintering inside. Insufficient sintering overall took place at temperatures below about 1075°C. The strongest granules were produced at about 1100°C.

Similar small scale sintering tests were conducted on granules made from refuse/fly ash and from refuse/sludge mixtures. The highest force at fracture (105 lb) for refuse/subbituminous coal fly ash was obtained for a 3:1 refuse/ash mixture sintered at 1000°C. Refuse/sludge mixtures in a ratio of 4:1 gave satis-

factory strength (85-90 lb) at 1050°C and at 1075°C. At 1100°C, granules of both mixtures developed a vitreous melt or slag on the surface that resulted in an undersintered core and low granule strength.

The large-scale boat tests were carried out using a large horizontal, electrically heated tube furnace and a boat (4 cm x 4 cm x 15 cm) custom made from a ceramic brick. The walls of the boat were about 8 mm thick and contained frequent holes about 6 mm in diameter to allow for passage of air and combustion gases. The boat could accommodate up to 180 g of granules.

Using the best of the conditions from the small-scale boat tests, dried green granules were placed in the large boat and introduced into the furnace which had been preheated to 600°C. The flow of combustion air was then started and the furnace temperature controls reset to 1050°C for the duration of the run. A thermocouple placed in the bed of granules indicated that the bed would reach 1050°C in about 45 minutes and a peak temperature of about 1100°C after about 60 minutes. Total residence times of 90 minutes and 120 minutes were investigated.

The individual sintered granules from the large boat tests were either red-brown or black-brown in about a 1:1 ratio. The black-brown granules were found towards the bottom of the bed where the temperature was the highest and the supply of oxygen was limited. These conditions would be similar to those encountered in the granule bed in a traveling grate furnace. The black-brown granules were significantly stronger with the strength influenced by residence time. The black color is thought to result from the presence of $Fe_3O_4$ and of hersynite, $FeAl_2O_4$, a spinel group that would add to granule strength. The red-brown granules were found at the top of the bed where oxygen was readily available and $Fe_2O_3$ would form.

For a total residence time of 90 minutes, the refuse only black-brown granules gave a force at fracture of about 120 lb, the 3:1 refuse/subbituminous coal fly ash granules 100 lb, and the 4:1 refuse sludge granules 150 lb. The compounds in the sludge facilitate sintering and increase strength.

## EVALUATION OF SINTERED GRANULES

In order to be environmentally disposable, the sintered granules must be very strong, able to resist cycles of freezing and thawing, and essentially non-leachable. The latter two characteristics were measured using a standard freeze-thaw resistance test (9), shake Extraction with Water Test, ASTM D3987-81 (10), and EP Toxicity Test (11).

The concentrations of elements in the leachates from the refuse/sludge granules as determined by mass spectroscopy along with the permissible levels established by RCRA regulations (12) are given in Table 2. The results for all elements are well below the current RCRA standards. Similar satisfactory results were obtained for leachates from the sintered refuse only and refuse/fly ash granules.

The results from the freeze-thaw cycle tests were most encouraging for all three types of sintered granules. The weight loss by degradation was less than $0.5\%_w$. Natural aggregate such as crushed rock will commonly show a degradation in the range of $5\text{-}10\%_w$ (13). None of the sintered granules should offer a problem when disposed of where leaching and/or freezing weather occur.

Table 2. Leachate analysis of sintered refuse/FGD sludge granules

| Element | RCRA** | Concentration of metals in leachate, ppm (mg/L)* | | | | | | | |
|---|---|---|---|---|---|---|---|---|---|
| | | 10% FGD | | 20% FGD | | 30% FGD | | Green Granules | |
| | | ASTM | EP | ASTM | EP | ASTM | EP | ASTM | EP |
| Al | - | .68 | 5.33 | .51 | 3.74 | .54 | 7.72 | - | .55 |
| As | 5 | - | - | - | .03 | - | .07 | - | - |
| Ba | 100 | .16 | .05 | .22 | .05 | .16 | .08 | - | .09 |
| Cd | 1 | - | - | - | - | - | - | .024 | .109 |
| Ca | - | 587 | 303 | 558 | 287 | 626 | 545 | 533 | 2131 |
| Cr | 5 | - | - | - | - | .05 | - | - | - |
| Fe | - | - | 4 | - | 1.5 | - | 2.3 | - | .1 |
| Pb | 5 | - | - | .005 | - | - | - | - | - |
| Hg | .02 | .0065 | .0041 | .0071 | .0007 | .0048 | .0031 | .008 | .0096 |
| Se | 1 | .007 | .009 | - | - | .015 | - | .34 | .072 |
| Si | - | 10 | 23 | 8 | 18 | 9 | 42 | 5 | 4 |
| Ag | 5 | - | - | - | - | - | - | - | - |

* Concentrations not shown were below detection limits.
** RCRA (EPA) limits are 100 times drinking water standards.

## EVOLUTION OF SULFUR DURING SINTERING

Combustion/sintering of the green granules results in release of about three-fourths of the S present as $SO_2$ in the off gases. A microreactor system illustrated in Figures 3 and 4 has been built to obtain a more fundamental understanding of S evolution and the reactions taking place.

The microreactor is made of stainless steel and is equipped with a combustion air distributor and a removable mount for a single granule. This arrangement ensures uniform contact between the combustion air and the granule, and control of the sintering taking place. By analysis of the off gases and the granule, the effects of sintering conditions and of granule composition, diameter, and particle size on the pattern of S evolution can be determined.

Preliminary tests have shown that a surge of $SO_2$ consisting of about two-thirds of the S present in the granules is released in about the first one-third of the combustion process. The $SO_2$ concentration in the off gases during this time would be expected to be relatively high because of the limited amount of combustion air required and the recycle of combustion air from windboxes to hoods along the traveling grate furnace. A $SO_2$ content of 3-5%$_v$ appears to be readily attainable. If it proves to be unattractive to thus process all of the off gases, the more dilute fraction could be recycled to the power station FGD system. Recovery of S from the off gases as S or $H_2SO_4$ would serve the dual purpose of controlling S emissions and generating a valuable byproduct. Sulfur recovery from waste gas streams is a well proven and well established technology (14).

## CONCLUSIONS

The combustion/sintering of granules of coal cleaning refuse or of refuse mixed with fly ash or FGD sludge has been shown to yield a strong and highly vitrified product. Durable green granules were prepared in a pan agglomerator using

water as the binder. A laboratory, bench scale procedure was developed to approximate the combustion/sintering that occurs in a commercial traveling grate furnace. Most of the energy required for the sintering can be derived from the fuel inherently present in the refuse. All three types of sintered granules were found to be environmentally compatible as measured using standard ASTM and EP leaching tests and a freeze-thaw cycle test. The byproduct recovery of S from the combustion/sintering off gases looks promising based on laboratory microreactor studies.

## ACKNOWLEDGEMENTS

Ames Laboratory is operated for the U.S. Department of Energy by Iowa State University under Contract No. W-7405-Eng-82. This work was supported by the Assistant Secretary for Fossil Energy through the Morgantown Energy Technology Center.

## REFERENCES

1. Shepard, M., EPRI Journal, 14-21, Nov. (1985).
2. Lemon, A.W., G.L. Robinson, S.E. Rogers and P. Van Voris, Environmental Assessment of Coal Cleaning Processes, NTIS EPA-600/7-28-024 (1982).
3. Nriagu, J.O. (Editor), Sulfur in the Environment, Part II: Ecological Impacts, John Wiley and Sons, New York, 316 (1978).
4. American Coal Ash Association, Washington, DC, Ash Production and Ash Utilization-1985 (1986).
5. Gutschick, K.A., Lime for Environmental Uses, STP 931, ASTM, Philadelphia, PA, 52-53 (1985).
6. Gutt, W., P.J. Nixon, R.J. Collins and R. Bollinghaus, Precast Concrete (3), 120-127 (1980).
7. Ball, D.F., J. Dartnell, J. Davison, A. Grieve and R. Wild, Agglomeration of Iron Ores, American Elsevier, New York, 250, 314-319 (1973).
8. Burnet, G. and A.J. Gokhale, Processing and Utilization of High Sulfur Coals II, Y.P. Chugh and R.D. Caudle (Editors), Elsevier Science Publishing Company, New York, 431-443 (1987).
9. Annual Book of ASTM Standards, D3987-81, ASTM, Philadelphia, PA (1977).
10. Federal Register, 43, No. 243, 58956-57, December 18 (1978).
11. Dolar-Mantuani, L., Handbook of Concrete Aggregates, Noyes Publications, Park Ridge, NJ, 216-218 (1983).
12. Federal Register, 45, No. 98, 33122, May 19 (1980).
13. Hockett, P., Personal communication, Iowa Dept. of Transportation, Ames, IA, November (1986).
14. Ford, P.G., Modern Power Systems, 7, No. 6, 37-43 (1987).

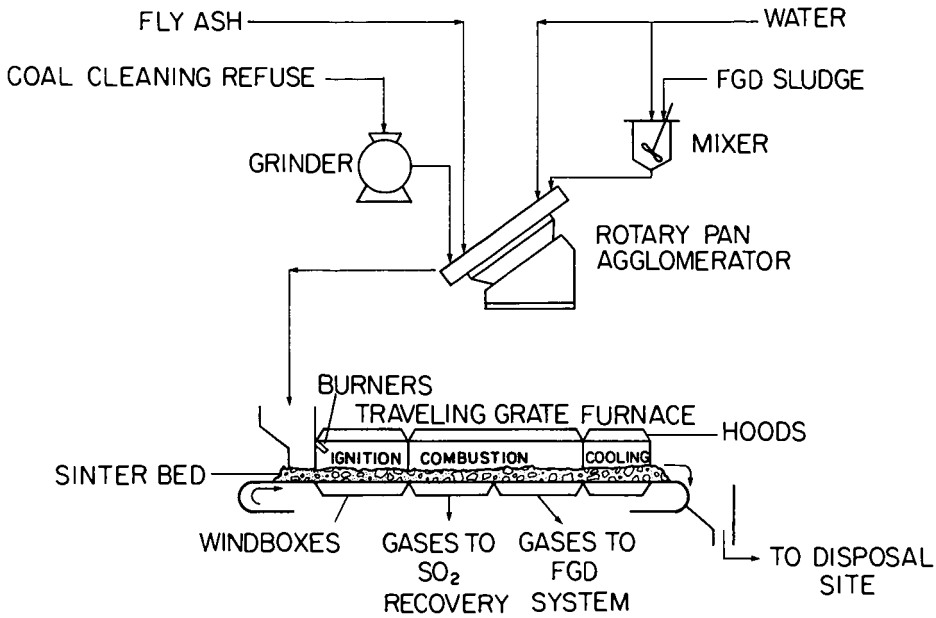


Fig. 1 Schematic flowsheet for the granulation/sintering waste stabilization process.

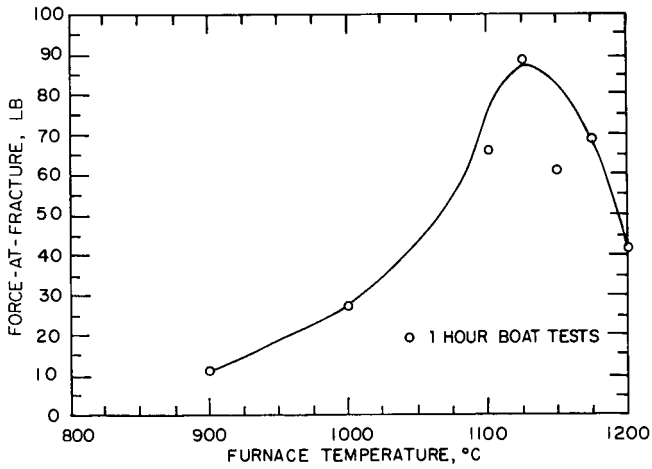


Fig. 2 Force-at-fracture for sintered refuse only granules as a function of small-tube furnace temperature.

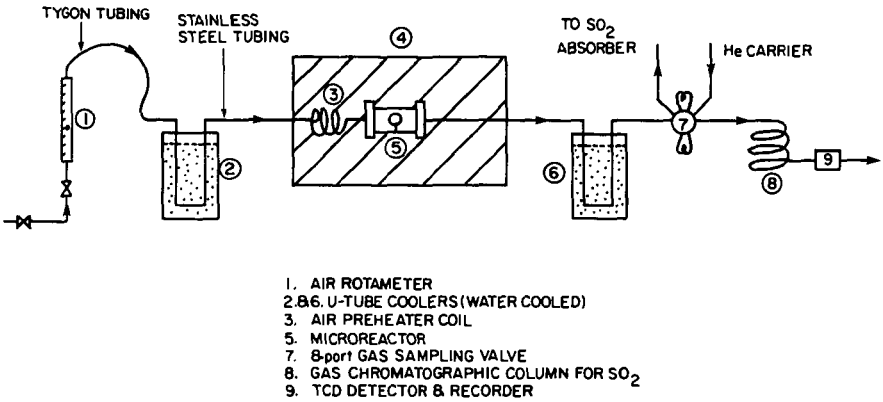


Fig. 3 Schematic flowsheet for the system to measure $SO_2$ evolution.

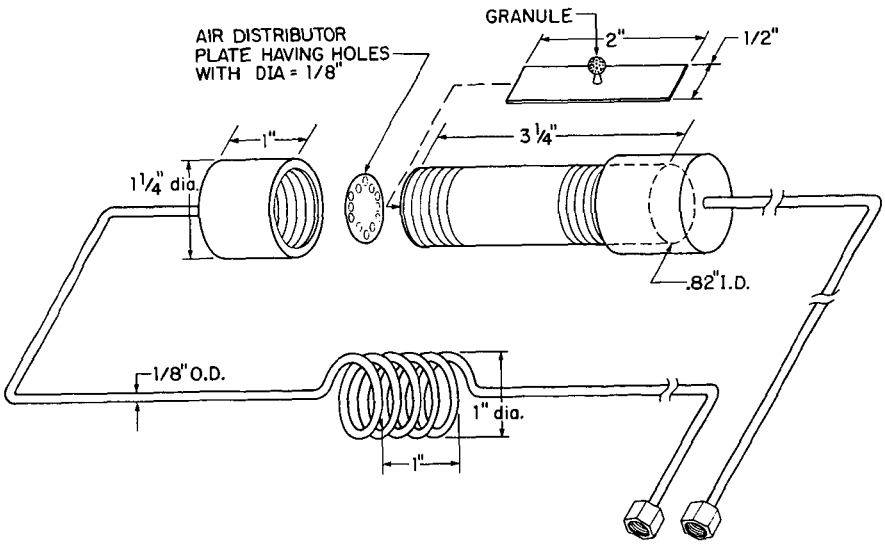


Fig. 4 Microreactor for the combustion/sintering of single granules.

# APPLICATION OF FIRST-ORDER SINGLE-REACTION MODEL FOR COAL DEVOLATILIZATION OVER A WIDE RANGE OF HEATING RATES

G.H. Ko, D.M. Sanchez, W.A. Peters, and J.B. Howard

Department of Chemical Engineering and Energy Laboratory
Massachusetts Institute of Technology, Cambridge, MA, 02139

## INTRODUCTION

The first-order single-reaction model offers a simple but effective mathematical description of coal devolatilization. Under conditions where the effects of physical transport processes and secondary reactions are relatively small but not negligible, the model approximates the complex chemical decomposition and any transport effects by a single global first-order decomposition reaction occurring uniformly throughout the particle. In more complete devolatilization descriptions that explicitly include mass transfer, the model represents only the chemical decomposition.

The model is most useful in applications where minimizing computational effort is important such as in large combustion or gasification models that fully describe fluid mechanics, heat and mass transport, and reaction kinetics; and in comprehensive devolatilization models that explicitly include the complex decomposition and secondary reaction chemistry, and multicomponent mass transfer in a gaseous or liquid phase environment. However, the model has a major weakness in that a different set of rate parameters is required at different heating rates. Thus, for a given set of rate parameters, the applicability of the model is confined to a narrow range of heating rates.

This paper presents a novel method to extend the applicability of the first-order single-reaction model over a wide range of heating rates. The two rate parameters in the model, a pre-exponential factor and activation energy, are derived in the form of heating rate dependent functions. The total weight loss data from devolatilization of a Montana lignite over heating rates from ≈0.1 to $10^4$ C/s were used to illustrate the derivation procedure, and to test the reliability of this method.

## EXPERIMENTAL DATA

The devolatilization weight loss data used in this work were obtained using the thermogravimetric analyzer at low heating rates (0.67-2.67 C/s) (1), and the electrical screen-heater reactor at high heating rates (650-$10^4$ C/s) (2). In both reactors, small samples ( <20 mg) of a Montana lignite in the particle size range 50 to 100 μm were used, with reactor conditions of 1 atm pressure and 1000 C maximum temperature.

The maximum volatiles yield, $V^*$, indicated by the upper asymptotic limit of the time-resolved yield curve, is one of the input parameters in the first-order single-reaction model. For a Montana lignite, $V^*$ can be assumed to be independent of heating rate since the experimentally observed $V^*$ is reported to be constant at ≈40 wt% (as-received) between the heating rates of 0.1 and $10^4$ C/s (1,2,3). For higher rank coals, e.g., softening HVB coals, this assumption is still valid, but only over a narrower heating rate range. Suuberg et al.(3) observed a constant $V^*$ of 47 wt% (as-received) between the heating rates of 350 and 15,000 C/s for a Pittsburgh Seam HVB coal under 1 atm, whereas Serio(4), and

Weimer and Ngan(5) reported a much lower $V^*$ of 30 to 37 wt% (as-received) between 0.05 and 0.2 C/s for the same type of coal.

## MODEL DESCRIPTION

The rate of volatiles evolution in the first-order single- reaction model is represented as,

$$dV/dt = k_{os} \exp(-E_s/RT)\ (V^* - V) \qquad (1)$$

where V is the cumulative amount of volatiles evolved up to time t, $V \rightarrow V^*$ at large t, and the subscript s denotes single-reaction. The global rate parameters, $k_{os}$ and $E_s$, are heating rate specific, and thus a given set is only applicable over a narrow range of heating rates. This limitation restricts the use of the model over the confined heating rate range in which the rate parameters are valid.

Integrating Eq.(1), using the approximation of Agrawal and Sivasubramanian (6), under a constant heating rate, m, up to temperature, T, yields

$$\ln\ [(V^*-V)/V^*] = \frac{-k_{os}RT^2}{mE_s} \left[ \frac{1-2(RT/E_s)}{1-5(RT/E_s)^2} \right] \exp(-E_s/RT) \qquad (2)$$

The above equation was found to be the most accurate integral approximation among different methods reported in the literature (7,8,9). The approximation deviates < ±1% from Simpson's 1/3 numerical method for the ranges of $E_s$ and T typically encountered in coal devolatilization ($E_s$> ≈10 kcal/mole and T< ≈1000 C).

Another commonly used global devolatilization model, the multiple independent parallel reaction (MIPR) model was used (next section) to represent the experimental weight loss data from different heating rates. With just one set of rate parameters, the MIPR model successfully describes volatiles evolution data with heating rates that span several orders of magnitude (2,5,10,11), but it has a drawback in that it requires more computational effort. The rate of volatiles evolution in the MIPR model is expressed as the sum of the contributions from multiple first-order independent parallel reactions,

$$dV/dt = \sum k_{oi} \exp(-E_i/RT)\ (V_i^*-V_i) \qquad (3)$$

where i denotes one reaction. The same pre-exponential factor is used for all reactions, i.e., $k_{oi} = k_o$, and the activation energies are described by a Gaussian distribution with mean $E_o$ and standard deviation $\sigma$. Thus,

$$f(E) = [\sigma(2\pi)^{1/2}]^{-1} \exp[-(E-E_o)^2/2\sigma^2] \qquad (4)$$

where $f(E) = V_i^*/V^*$ for a large number of reactions and $V^*$ is the sum of the $V_i^*$ for all i. Integration of Eq.(3) for any temperature history yields

$$(V^*-V)/V^* = \int_o^\infty \exp[-k_o \int_o^t \exp(-E/RT)dt]\ f(E)dE \qquad (5)$$

## DERIVATION OF HEATING RATE DEPENDENT KINETIC PARAMETERS

To extend the use of the model over a wider heating rate range, we seeked to relate $E_s$ and $k_{os}$ to the heating rate, m, in the form of

$$E_s = f(m) \tag{6}$$

$$k_{os} = g(m) \tag{7}$$

where f and g represent mathematical functions derived below.

The combined weight loss data of Ciuryla et al.(1) and Anthony et al.(2) were fitted using the MIPR model. Table 1 gives the best-fitted parameter values from fitting the combined data set, as well as those obtained by Ciuryla et al.(1) and Anthony et al.(2) using only their own data. The two groups of investigators(1,2) have shown that this model has an excellent capability to fit the data over a wide range of heating rates with just one set of parameter values.

An arrhenius plot (Fig.1) was then produced using the rate of total volatiles evolution predicted by the MIPR model at heating rates 0.1, 1, 10, $10^2$, $10^3$, and $10^4$ C/s [Eq.s (3) and (5), Table 1(c)]. The lines in the figure are sufficiently straight to assume a first-order single-reaction behavior for each of the heating rates. Table 2 gives the values of $E_s$ and $k_{os}$ computed from Fig.1, which respectively represent the slope and the y-intercept of the lines in the figure.

Plotting individually the values of $k_{os}$ and $E_s$ versus $[3+\log_{10}(m)]$ from Table 2 produced the following relationship:

$$\log_{10}k_{os} = -3.16514 + 0.941867(3+\log_{10}m) \tag{8}$$

$$E_s = 5909.411 + 182.7911(3+\log_{10}m) + 66.80278(3+\log_{10}m)^2 \tag{9}$$

The correlation coefficient exceeded 0.999 in both cases, assuring that the rate parameters computed from the above equations closely agree with those obtained from Fig.1.

## RESULTS AND DISCUSSION

Figure 2 shows that the predicted weight loss behavior by the first-order single-reaction model [Eq.s (2), (8) and (9)] agree well with the data represented by the predictions from the MIPR model [Eq.s (3) and (5), Table 1]. Thus, with the heating rate dependent kinetic parameters derived in this study, the single-reaction model can successfully be applied over a wide range of heating rates. Furthermore, the use of the integral approximation of Agrawal and Sivasubramanian(6) allows the volatiles evolution rate equation [Eq.(1)] to be expressed in an analytical form, which considerably reduces the computational effort.

The empirical coefficients in Eq.s (8) and (9) are specific for the data from which they were best-fitted. However, since a given data set can accurately be described by a set of MIPR model parameters, a more general form of Eq.s (8) and (9) may respectively be represented as functions $\psi$ and $\phi$

$$\psi(E_s, E_o, \sigma, k_o, m, T) = 0 \tag{10}$$

$$\phi(k_{os}, E_o, \sigma, k_o, m, T) = 0 \tag{11}$$

$V^*$ also varies for different data, but it has no effect on the rate parameters of either models. Equating $[(dV/dt)/(V^*-V)]/\ln[(V^*-V)/V^*]$ from Eq.s (1) and (2) to that from Eq.s (3) and (5) yields the function $\psi$ in the form of

$$E_s^2 + (QRT^2/m)E_s - [5(RT)^2+2QR^2T^3/m] = 0 \qquad (12)$$

where Q is $[(dV/dt)/(V^*-V)]/\ln[(V^*-V)/V^*]$ obtained from Eq.s (3) and (5), and is a function of only $E_o$, $\sigma$ $k_o$, m and T. Having obtained $E_s$ from Eq. (12), rearranging Eq. (1) yields the function $\phi$

$$k_{os} - [(dV/dt)/(V^*-V)] \exp(E_s/RT) = 0 \qquad (13)$$

where $[(dV/dt)/(V^*-V)]$ is obtained from Eq.s (3) and (5). Although rigorous, the above equations are too complex to readily observe the effect of changing $E_o$, $\sigma$, or $k_o$ on $E_s$ and $k_{os}$. Also, for the same reason, it is difficult to detect any relationship between Eq.s (8) and (12), and Eq.s (9) and (13).

Although qualitative, Table 3 provides a useful means to predict the effect of a new data set on $E_s$ and $k_{os}$. For a given heating rate, the new time-resolved rate (or yield) curve is characterized by Tmax and Tsig, where Tmax represents the temperature at which the maximum rate occurs, and Tsig the temperature spread of the curve. The temperature spread is arbitrarily defined as the range of temperatures in which the yield is between two fixed values [e.g., Ko et al. (11) used 15.87 and 84.13% of the final yield]. Some examples will illustrate how to use the table. E.g., 1: for a fixed heating rate, the new data have higher Tsig, but no change in Tmax. Table 3 shows that the newly fitted $k_{os}$ must be lower to match the increased Tsig, and the new $E_s$ must also be lower to off-set the increase in Tmax caused by the lower $k_{os}$. E.g., 2: again for a fixed heating rate, the new data have higher Tmax, but no change in Tsig. The table shows that the newly fitted $E_s$ has to be higher to match the increased Tmax, and the new $k_{os}$ is unchanged. Table 3 can also be used to relate qualitatively $E_o$, $\sigma$, and $k_o$ to $E_s$ and $k_{os}$. For example, the reason why the fitted $E_s$ and $k_{os}$ for the same data are generally smaller than the $E_o$ and $k_o$ ,respectively, is that a finite $\sigma$ requires $k_{os}$ to be smaller than $k_o$ to produce to same Tsig. Since lowering $k_{os}$ increases Tmax, $E_s$ must also be smaller to off-set the increased Tmax.

The correlation procedure developed here can easily be applied to describe the evolution of total volatiles of other coals, and individual product species. A new set of $E_o$, $\sigma$, $k_o$ and $V^*$, best-fitted using the MIPR model, can be used to represent the new data set. Despite the lack of rigorous proof, the form of the Eq.s (8) and (9) are expected to remain the same, only the coefficients need to be re-fitted using the newly computed values of $E_s$ and $k_{os}$ at different heating rates.

## CONCLUSIONS

This work has demonstrated that the first-order single-reaction model can successfully be applied over a wide range of heating rates using the heating rate dependent kinetic parameters [Eq.s (8) and (9)].

The use of the integral approximation method of Agrawal and Sivasubramanian(6), provides an accurate analytical solution of the single-reaction model rate equation [Eq.(1)] for the ranges of $E_s$ and T typically encountered in coal devolatilization.

The heating rate dependent kinetic parameters combined with this integral approximation are expected to be useful in applications where minimal computational effort is desired.

## ACKNOWLEDGEMENTS

The authors are grateful to the U.S. Department of Energy, Morgantown Energy Technology Center, for financial support of this work under Contract No. DE-RA21-85MC-22049. A 1967 Science and Engineering Scholarship to GHK from the Natural Sciences and Engineering Council of Canada is also appreciated.

## REFERENCES

1. Ciuryla, V.T., Weimer, R.F., Bivans, D.A., and Motika, S.A.: *Fuel*, 58, 748 (1979).

2. Anthony, D.B., Howard, J.B., Hottel, H.C,. and Meissner, H.P.: *Fifteenth Symposium (International) on Combustion*, 1303, The Combustion Institute, Pittsburgh, 1974.

3. Suuberg, E.M., Peters, W.A., and Howard, J.B.: *Seventeenth Symposium (International) on Combustion*, 117, The Combustion Institute, Pittsburgh, 1979.

4. Serio, M.A., *Secondary Reactions of Tar in Coal Pyrolysis*, Ph.D. Thesis, Dept. of Chemical Engineering, M.I.T., Cambridge, Mass., 1984.

5. Weimer, R.F., and Ngan, D.Y.: *Am. Chem. Soc. Div. Fuel Chem. Preprints*, 24 (3), 129 (1979).

6. Agrawal, R.K., and Sivasubramanian, M.S.: *AIChE J.*, 33, 1212 (1987).

7. Coates, A.W., and Redfern, J.P.: *Nature*, 201, 68 (1964).

8. Gorbachev, V.M.: *J. Thermal Anal.*, 11, 125 (1977).

9. Li, C.H.: *AIChE J.*, 31, 1036 (1985).

10. Sprouse, K.M., and Schuman, M.D.: *Combustion and Flame*, 43, 265 (1981).

11. Ko, G.H., Peters, W.A., and Howard, J.B.: submitted for publication in *Energy and Fuel* (1987).

Table 1 : Best-Fitted Global Rate Parameters for the Multiple Independent Parallel Reaction Model Using Total Weight Loss Data from Montana Lignite.

| | (a) | | (b) | (c) | |
|---|---|---|---|---|---|
| Fitted By: | Ciuryla et al.(1) | | Anthony et al.(2) | This Study | |
| Data Source: | Ciuryla et al.(1) | | Anthony et al.(2) | Ciuryla et al.(1)<br>Anthony et al.(2) | |
| Heating Rate: (C/s) | 0.67 | 2.67 | $650\text{-}10^4$ | $0.67\text{-}10^4$ | |
| Cooling Rate: (C/s) | -[c] | -[c] | ≈200 | ≈200 | |
| Log(ko/$s^{-1}$) | 13.22[b] | 13.22[b] | 13.22[b] | 13.22[b] | 8.91[a] |
| Eo, kcal/mole | 54.3 | 53.3 | 56.3 | 56.8 | 38.6 |
| $\sigma$, kcal/mole | 1.32 | 1.21 | 1.09 | 1.16 | 0.706 |
| $V^*$, wt% as received | 41.1 | 41.2 | 40.6 | 41.0 | 40.0 |

[a] Allowed to vary. This set of parameters was used to produce Fig.1.
[b] This parameter was fixed.
[c] Continuous heating until all reactions are completed.

Table 2 : Computed $E_s$ and $k_{os}$ from the Arrhenius Plot in Fig. 1.

| Heating Rate[a] C/s | Pre-Exponential Factor(kos) $s^{-1}$ | Activation Energy(Es) cal/mole |
|---|---|---|
| 0.1 | 0.05076 | 6528 |
| 1 | 0.4578 | 7078 |
| 10 | 4.089 | 7718 |
| $10^2$ | 36.19 | 8489 |
| $10^3$ | 309.2 | 9385 |
| $10^4$ | 2582.0 | 10480 |

[a] Continuous heating until all reactions are completed.

Table 3 : The Effect of Changing Tmax and Tsig on the Global Rate Parameters of the First-Order Single-Reaction Model ($E_s$ and $k_{os}$) and of the Multiple Independent Parallel Reaction Model ($E_o$, $\sigma$ and $k_o$).

| The Effect of Increasing(↑) the parameter X on : | $T_{max}$ | $T_{sig}$ |
|---|---|---|
| Parameter X | | |
| $E_s$, $E_o$ | ↑ | -[a] |
| $k_{os}$, $k_o$ | ↓ | ↓ |
| $\sigma$ | - | ↑ |

[a] No change.

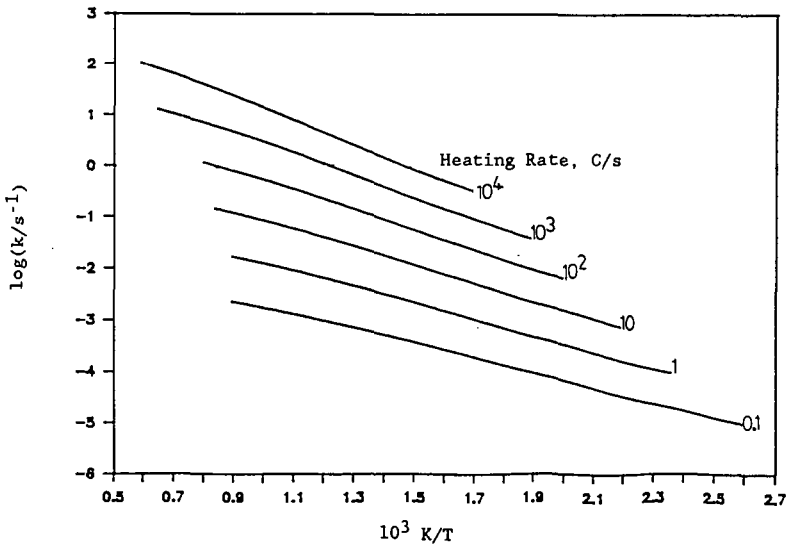


Figure 1 : Arrhenius Plot for Total Volatiles Evolution of Montana Lignite Described by the MIPR Model [Eq.(3) and (5), Table 1(c)]. The lines represent the rates computed between 1 to 99% of total volatiles yield.

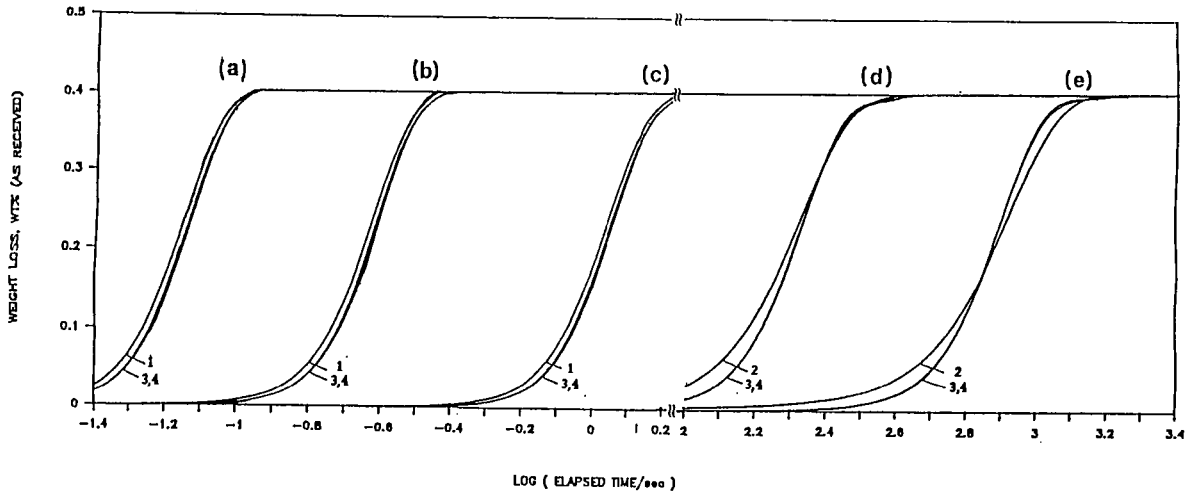


Figure 2 : Comparison of Predicted Total Volatiles Yield from the First-Order Single-Reaction Model [Eq.s (2), (8) and (9)] and from the MIPR Model [Eq.(5) and Table 1].

Heating, cooling rates in C/s (a) $10^4$, 200; (b) 3000,200; (c) 650,200; (d) 2.67 continuous heating to Tmax; (e) 0.67 continuous heating to Tmax(< ≈1000 C).

The curves represent model, source of kinetic parameters 1. MIPR, Anthony et al.(1974); 2. MIPR, Ciuryla et al.(1979); 3 MIPR, this study; 4. First-Order Single-Reaction, heating rate dependent kinetic parameters derived in this study. The kinetic parameter values for the curves 1,2 and 3 are given in Table 1, and those for the curve 4 can be computed from Eq.s (8) and (9). For non-continuous heating cases [curve sets (a), (b) and (c)], let m be the equivalent heating rate equal to $m_H m_C/(m_H+m_C)$ where $m_H$ and $m_C$ are heating and cooling rates respectively.

# NUMERICAL MODELING OF DIRECT SORBENT INJECTION FOR $SO_2$ REMOVAL

J. J. Lee

The University of Tennessee Space Institute, Tullahoma, Tennessee, 37388

Abstract

A modeling study of steady, turbulent, reactive multi-phase flow in a duct injection flue gas desulfurization (FGD) system is reported in this paper. The stream-function/vorticity method was used in finite difference form. The $\kappa$-$\varepsilon$ model was used for turbulence closure. A simple integrated formulation was employed to compute the behavior of sorbent droplets injected into the flue gas stream. The sorbent may be injected either as slurry or solution into a hot flue gas, or a dry sorbent may be injected into a cooled and humidified flue gas. A comprehensive heat and mass transfer model was developed to simulate the evaporation of the sorbent droplets and the absorption/reaction of $SO_2$ in the sorbent droplets. Dissolution kinetics of lime particles within a slurry droplet was also included in this model to determine the overall $SO_2$ removal rate. Numerical calculations and comparisons with available experimental data were made and are discussed.

## 1. Introduction

In the United States, the emission of sulfur oxides has attracted much attention. The dispersion of sulfur oxides arising from combustion of fossil fuels has a dramatic impact on the environment. Removal of sulfur oxides from flue gases is very important in air pollution control. A sorbent in-duct injection system is proposed as a method for flue gas desulfurization. Chemically the system is similar to a spray dryer or dry scrubber.

In the sorbent in-duct injection system, a chemically reactive sorbent, usually lime or hydrated lime or dolomite, is injected into a highly turbulent flue gas containing sulfur dioxide. The sorbent may be injected as slurry or solution into the hot (typically 275 to 350$^0$ F) flue gas, or a dry sorbent may be injected into a cooled and humidified flue gas (typically 160 to 180$^0$ F). Processes that occur in the duct include the evaporation of water from slurry or solution spray with resulting cooling and humidification of the gas; sorption of sulfur dioxide into the water of the slurry or solution droplet; dissolution of the slaked lime into the water; reaction of the sulfur dioxide with the lime or dolomite; and some as-yet less understood effects, such as, the reaction of sulfur dioxide with "dry" sorbent after evaporation of slurry or injection of dry sorbent following humidification of the gas.

The Energy Conversion Research and Development Programs of the University of Tennessee Space Institute (UTSI) is presently involved in research of of direct sorbent injection for combined $SO_2/NO_x$ removal under Department of Energy Pittsburgh Energy Technology Center contract[1]. Experiments are being conducted in the Direct Sorbent Injection Facility (DSIF). The objective of testing in this facility is to confirm the feasibility of a direct sorbent injection FGD system to control emissions of sulfur dioxide and nitrogen oxide from a fossil fuel plant. An extensive literature search also has been conducted at UTSI to collect and collate associated spray chemical reaction models.[3] As a prelude to the development of an in-duct sorbent injection FGD system for commercial application by 1992, this literature search was carried out by UTSI at the request of Brookhaven National Laboratory and Department of Energy, Pittsburgh Energy Technology Center. The overall objective of the study was to assist the above organizations in ascertaining the state-of-the-art of computational methods applicable to the in-duct sorbent injection FGD system. This effort included analysis of existing analytical models, identifying salient features and shortcomings, and determining the ability of these models to be extended to adequately design and scale-up sorbent injection systems.

From the above studies, it is found that there is an extremely large gap between the needs of the design engineer in practice and the understanding and proposed research tasks of the academic researcher who desires to make a contribution on the FGD modeling front. Literature which describes numerical models for the sorbent injection FGD process is limited. Numerical models for predicting chemical reaction in multi-phase turbulent flow occurring in in-duct sorbent injection systems rest on two foundations: mathematical models of physical processes (turbulence, evaporation, absorption, reaction, and multi-phase effects) and computer codes for solving the appropriate level of sophistication of the resulting nonlinear governing differential equations.

Attempts to calculate the detailed performance of the FGD processes have only been undertaken during the last few years. Prior to 1986, the best computations available were based on overall global calculations[4-9]. The details of the interaction processes between the flue gas and the reacting, evaporating particle/droplet were not quantitative. Modeling of turbulent, reactive multi-phase flow in a spray dryer FGD processes is still in a state of development. Recent reviews of this subject for the FGD systems are given in reference materials.[1,3,5,8,10,11] It has been determined that no model currently exists that will completely and accurately model the complex flow field and chemical reactions that take place in the sorbent injection system. However, models are available for portions

of the overall process. The available models that have been reviewed at UTSI are summarized in reference 3.

One objective of the FGD research at UTSI is to develop a numerical modeling for predicting steady, turbulent, reactive multi-phase flow in a spray dryer FGD system. In the $SO_2/NO_x$ removal process development, a modeling technique using an adaptation of the LEE-2 computer program[2] has been employed at UTSI to simulate operation of the experimental program in order to delineate data that has been collected and to provide a route which leads to the accomplishment of design objectives. These efforts have included analyses directed at achieving an adequate model of the gas/particle dynamics and heat/mass transfer with or without chemical reaction for evaluation of experiments.

## 2. FGD Modeling Efforts

This section summarizes the numerical models which characterize the complex gas/particle flow field features for the direct sobent injection in the FGD system. This work was undertaken to aid in evaluation of experimental performance of the DSIF test train. Its objectives were to provide a means by which the flowfields and the $SO_2$ removal process that develop within the FGD system could be viewed and qualified. Background on the model development and case studies that were performed using this numerical code in its original form are contained in the published works of Lee[2,12-14] For this present study, the model was refined to make it more amenable to the FGD duct. These refinements included a recasting of the governing flow equations to incorporate the effects of multi-phase flow behavior. A detail description of the model used is much to involved for any indepth discussion herein. However, a general overview of the model highlighting some of its techniques and salient features is briefly presented in following paragraphs.

The numerical model provides a solution to the elliptical, fully turbulent form of flowfield conservation equations in either a two-dimensional Cartesian or an axisymmetric coordinate system. The gas dynamic model which utilizes a stream function/vorticity formulation to the Navier-Stokes equations for compressible, turbulent flows forms the basis for the modeling. This approach provides a powerful means of analyzing recirculating flows wherein explicit dependency of the flow upon pressure is eliminated. Recovery of both the pressure and the velocity distributions throughout the flow is accomplished once the stream function and vorticity are defined from solution. The model utilizes the standard high Reynolds number form of the $\kappa$-$\varepsilon$ model for turbulence closure.[15] The model employs the law-of-the-wall and its related techniques to address near wall phenomena. This hypothesis allows realistic predictions of both wall shear losses and convective heat/mass transfer rates.

To solve the flow field equations in a non-equal spacing grid system a chain-rule technique is used to transform the physical spray-dryer plane into a rectangular computational plane. The governing equations and boundary conditions are rewritten in terms of computational plane coordinates and solved using finite-difference approximations. In order to extend the finite-difference equations beyond second order accuracy, a "decay function"[16] is introduced. This technique assures stability in numerical manipulation of the equations at interior grid points of computational field. Solution of the finite-difference equations together with prescribed boundary conditions is achieved by an iterative, point by point, successive under/over relaxation Gauss-Seidel scheme.

The equations needed to model the particle or droplet trajectories are the differential equations of motion[13]. The particle trajectories are computed by integrating these equations, gravitational force, gas viscosity and gas velocity are assumed constant over the time of integration. The spray model involves mass, momentum and energy transfer processes which through their mutual coupling define the local state of the flow. This coupling can be either unilateral or bilateral, in other words, it can be assumed that the effects on the gas flow of the spray embedded within it are negligible, or, the effects of the presence of particles on the gas phase can be accounted for. The unilaterally coupled spray trajectory model is a useful first approximation to the overall behavior of a spray within a complex aerodynamic flow field. This technique becomes more exact as the spray becomes more dilute. Therefore, unilateral coupling is assumed for the spray trajectory model for the initial investigation. In order to employ this assumption, particle trajectories are computed by the equations of motion given the gas phase flow field for a variety of assumed initial particle sizes, velocities, and spray angles.

A heat and mass transfer model, SPRAYMOD, of $SO_2$ removal in a spray-dryer FGD system developed by Damle[5] was employed to simulate the evaporation of the sorbent droplets and the absorption/reaction of $SO_2$ in the sorbent droplets. The code of SPRAYMOD was written in BASIC. This code was translated to FORTRAN for incorporation into LEE-2. The model is based on the assumption that the spray dryer could be simulated using a plug or backmixed flow model. Under this assuption, the effect of relative velocity between the flue gas and droplet is ignored. If the relative velocity is zero, the evaporation is the same as in a still-air condition. However, the initial velocity of the droplet at the exit of the nozzle is much higher than the surrounding flow. The effects of relative velocity on the simultaneous heat transfer from gas phase to the droplet, and mass transfer from the droplet to the gas phase have been considered during the constant rate of drying period. The particle/droplet trajectories of various droplet sizes and sorbent particle diameters superimposed in the two-dimensional turbulent flow stream have also been taken into account.

## 3. Results and Discussions

The numerical results performed in modeling of the DSIF are presented and discussed. A uniform gas velocity profile (Figure 1) adjusted in magnitude to satisfy mass conservation was used at the entrance to the test duct. Shown in Figure 2 is a 16" ID, 18' long cylindrical duct. Flue gas at 305° F enters from the left with a velocity of 10 m/s. The water particles at 110°F with a uniform velocity of 36 m/s enters from the left through a single water spray nozzle producing a 35° cone. The trajectories of the evaporating and reacting particles were calculated once the gas flowfield was obtained from solution. Figure 2 shows the trajectories of particles 25 $\mu m$ in diameter superimposed in the gas flow stream. The shape of the particle trajectory is directly influenced by the magnitude and relationship between the drag forces and the buoyancy forces. A comparison to experimental data[1] obtained from the DSIF is shown in Figures 3 and 4. Therein it can be seen that the two-dimensional model for predicting this turbulent, two-phase flow is in near agreement with the laboratory experiments.

Figures 5-11 show the predicted $SO_2$ removal efficiency for both sorbent solution (sodium carbonate) and slurry (hydrated lime) cases. The results were computed subject to variety of sorbent particle diameters, dry sorbent reaction rate coefficients, inlet droplet diameters, inlet droplet temperature, inlet gas temperature, approach to saturation, and $Ca/S$ stoichometric ratio. The specifications for the spray dryer chosen as a reference case was based on the input conditions of DSIF SL00103A[17]. These are as follows: inlet gas temperature of 722 R, inlet gas velocity of 30 ft/sec, inlet droplet temperature of 600 R, inlet droplet diameter of 40 micron, inlet droplet velocity of 250 ft/sec, inlet $SO_2$ of 1171 PPM, a molecular weight of sorbent $(Ca(OH)_2)$ of 74 lb/mole, sorbent density of 137 lbm/ft$^3$, sorbent particle diameter of 4 micron, dry sorbent reaction rate coefficient of $1.0\times10^7$, mole fraction of water in inlet gas of 9.3 , approach to saturation of 29° C, and $Ca/S$ stoichiometric ratio of 1.86. The discussion of these figures are given as following:

Effect of Inlet Sorbent Particle Size. Figure 5 shows that $SO_2$ removal efficiency decreases with increasing inlet sorbent particle diameter for the sorbent slurry. Smaller sorbent particles provide a larger cumulative surface area for reaction and would, thus, enhance the $SO_2$ removal efficiency. On the other hand, since the sorbent solution are highly soluble, the $SO_2$ removal efficiency is expected to be higher than that of sorbent slurry case. The sorbent solution case is shown not to be a function of inlet sorbent particle size.

Effect of Inlet Droplet Size. Figure 6 shows that $SO_2$ removal efficiency slightly decreases for the sorbent solution and slightly increases for the sorbent slurry with increasing inlet droplet diameter.

Effect of Dry Sorbent Reaction Rate Coefficient. The reaction rate coefficient depends on the diffusivity of $SO_2$ in the solid material, the particle size, and the moisture content of the particle/droplet.[9] The ability of the chemical reaction model to predict observed efficiency is highly dependent on the user's choice of a reaction rate coefficient. Figure 7 shows the correspondence between the reaction rate coefficient and $SO_2$ removal efficiency for the set of operating conditions. This figure indicates that the reaction rate coefficient does not affect the efficiency until the coefficient exceeds a value of $10^6$ cm$^3$/gmole.s. In the present study, a value of $10^7$ was assumed until further information becomes available.

Effect of Inlet Droplet Temperature. Figure 8 shows that $SO_2$ removal efficiency decreases very slightly with increasing inlet droplet temperature for both solution and slurry cases.

Effect of Inlet Gas Temperature. Several conclusions have been reported regarding the effect of inlet gas temperature on $SO_2$ removal efficiency. The experimental results performed by Apple and Kelly[18] indicate that $SO_2$ removal efficiency increases with increasing inlet gas temperature. However, Buell[4] concluded from his experimental tests that the inlet gas temperature has a negligible effect. The numerical results performed by Damle, et al.[9] and Ma, et al.[10] indicate that $SO_2$ removal efficiency increases slightly with increasing inlet gas temperature. Figure 9 shows that $SO_2$ removal efficiency increases for the sorbent solution and decreases for the sorbent slurry with increasing inlet gas temperature. This implies that the effect of inlet gas temperature on $SO_2$ removal efficiency depends upon the form of sorbent.

Effect of Approach to Saturation. Approach to saturation is defined as the difference between flue gas exit temperature and dew point. Once the gas exit temperature and dew point are defined from the solution based on the process stream material and energy balance, the approach to saturation temperature can be computed. This is an important process parameter. Numerical results indicate that $SO_2$ removal efficiency decreases with increasing approach saturation temperature[6,9] as illustrated in Figure 10. This is due to the decrease in total droplet area resulting from the decreased volume of spray during the drying period and the decrease in core volume of equilibrium water held by the solid after the drying period ends.

Effect of Inlet $Ca/S$ Stoichiometric Ratio. Stoichiometric ratio is defined as the moles of $Ca(OH)_2$ fed to the system per mole of $SO_2$. This parameter is thought to be the most important factor influencing the FGD system performance. The overall $SO_2$ removal efficiency increases successively with increasing inlet $Ca/S$ ratio.[4,6,9,19] Figure 11 demonstrates this for both sorbent solution and slurry cases. This is due mainly to the decrease in liquid-phase resistance to $SO_2$ mass transfer during the drying period.

Finally, a comparison to DSIF experimental $SO_2$ removal data for this calculation is given in Figure 12. The

model predicted the $SO_2$ removal efficiency with a tendency to under-predict at the upstream of the spray dryer. Since no good correlations are available to estimate the liquid-phase resistance in the droplet to the mass transfer[5] the difference between predicted and measured efficiencies was anticipated.

## 4. Conclusions

The numerical results presented above predict several significant phenomena in the FGD system. Although it is the author's opinion that a full understanding of these phenomena is far from being achieved, it is hoped that these results will aid in advancing the future research efforts. Major highlights and conclusions of the present study are:

1. A general two-dimensional computational procedure was developed to model steady, turbulent, reactive, multi-phase flow in a spray dryer FGD system. A chemical modeling program, SPRAYMOD, was successfully incorporated into a general fluid modeling program, LEE-2.

2. The effects of relative velocity on the simultaneous heat transfer from gas phase to the droplet, and the mass transfer from the droplet to the gas phase were considered during the constant rate of drying period. The particle/droplet trajectories superimposed in the two-dimensional turbulent flow stream were also taken into account.

3. Comparison with one set of the DSIF data shows good agreement between model predicted and observed particle velocity distributions.

4. Parametric studies reviewed herein have brought to light some of the gross effects of inlet-gas specifications and operating parameters on the duct injection FGD performance. The numerical results show that inlet $Ca/S$ stoichiometric ratio remains the single most important aspect of the duct injection on its performance. However, other variables which showed appreciable influence included the dry sorbent reaction rate coefficient and the form of sorbent. This study provided a considerable insight for duct injection FGD performance optimization and scale-up.

5. To correct the tendency to under-predict the $SO_2$ removal efficiency at the upstream of the duct injection would require modeling of the wet particle stage.

6. A three-dimensional numerical model for a duct injection FGD system will be pursued as a future effort to compute the gas flow field, the droplet or sorbent particle dynamics, and the evaporation and chemical reactions simultaneously. The droplet/particle size distribution, agglomeration of particles, and wall deposition should also be considered in the model.

## Acknowledgement

The author would like to thank Mr. T. E. Dowdy and Dr. J. M. Henry for providing valuable suggestions on the chemical model. The author would also like to thank Professor J. T. Lineberry for his assistance with this work. This work was sponsored by the U. S. Department of Energy under Contract DOE/PETC-DE-AC22-85PC81008.

## References

1. Dowdy, T. E., et al., "Direct Sorbent Injection for Combined $SO_2/NO_x$ Removal," Annual Technical Progress Report, DOE Contract No. DE-AC22-85PC81008, August 1985 - July 1986.
2. Lee, J. J., "Theoretical Studies of Recirculating Duct Flows for the UTSI MHD Combustor and Diffuser Designs," Ph.D. Dissertation, The University of Tennessee, Knoxville, December 1983.
3. Sheth, A. C., et al., "Review of Fluid Dynamics Math Models for In-Duct Sorbent Injection FGD Systems," Process Sciences Division, Department of Applied Science, Brookhaven National Laboratory and United States Department of Energy, Pittsburgh Energy Technology Center, November 1987.
4. Parsons, E. L., et al., "$SO_2$ Removal by Dry FGD," Proceedings of Sixth Symposium on Flue Gas Desulfurization, Houston, Texas, EPA-600-/9-81-0196, Vol. 2, April 1981.
5. Damle, A. S., "Modeling of $SO_2$ Removal in Spray-dryer Flue-gas Desulfurization System," EPA/600/7-85/038, December 1985.
6. Harriott, P and Kinzey, M., "Modeling the Gas and Liquid Phase Resistances in the Dry Scrubbing Process for $SO_2$ Removal," Third Annual Pittsburgh Coal Confereuce, Pittsburgh, PA, September 1986.
7. Maibodi, M., "Simulation of Spray Dryer Absorber for Removal of $SO_2$ from Flue Gases," M. S. Thesis, University of Tennessee, Knoxville, March 1986.
8. Pearson, T. E., "Mathematical Model for the Removal of Sulfur-Dioxide in a Pilot Scale Spray Dryer," M. S. Thesis, Univeristy of Tennessee, Knoxville, March 1984.
9. Damle, A. S. and Sparks, L. E., "Modeling of $SO_2$ Removal in Spray Dryer Flue Gas Desulfurization System," 1986 AIChE Spring National Meeting, New Orleans, LA, April 1986.
10. Ma, H. K, Huang, H. S., and Chiu, H. H., "Turbulent Group Reaction Model of a Spray Dryer Scrubber," Accepted for Publication in the International Journal of Energy Systems.

11. O'Rourke, P. J., Wadt, W. R., "Two-Dimensional, Two-Phase Numerical Model for Spray Dryers," NTIS, PC A06/MF A01, Order No. DE82021847, July 1982.
12. Lee, J. J., Lineberry, J. T., and Wu, Y. C. L., "MHD Diffuser Studies," 23rd SEAM, Paper Ref. No. 22, Somerset, PA, June 1985.
13. Lee, J. J. and Lineberry, J. T., "Theoretical Studies of CFFF Radiant Furnace," AIAA-87-0385, AIAA 25th Aerospace Sciences Meeting, Reno, Nevada, January 1987.
14. Lee, J. J. and Schulz, R. J., "Numerical Studies of Recirculating Ducted Flows," Journal of Propulsion and Power, Vol. 3, No. 4, July-August 1987.
15. Launder, B. E. and Spalding, D. B., "The Numerical Computation of Turbulent Flows," Computer Methods in Applied Mechanics and Engineering, Vol. 3, pp 269-289, 1974.
16. Chien, J. C., "A General Finite-Difference Formulation with Application to Navier-Stokes Equations," Computers and Fluids, Vol. 5, pp 15-31, 1977.
17. Dowdy, T. E., et al., "Direct Sorbent Injection for Combined $SO_2/NO_x$ Removal," Quarterly Technical Progress Report, DOE Contract No. DE-AC22-85PC81008, January-March 1987.
18. Apple, C. and Kelly, M. E., "Mechanisms of Dry $SO_2$ Control Processes," Radian Corporation's Report, 1983.
19. Partridge, G. P., et al., "A Mathematical Model for $SO_2$ Removal in a Spray Dryer Absorber," 1987 AIChE Spring National Meeting, Houston, Texas, March 1987.

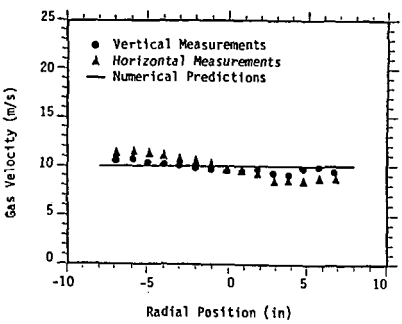


Figure 1. Gas Velocity Profile at Inlet to Test Section

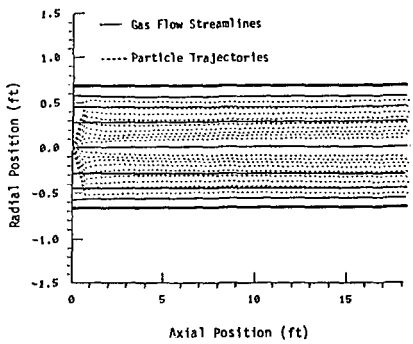


Figure 2. Particle Trajectories of 25$\mu m$ in Diameter Superimposed in the Gas Flow Stream

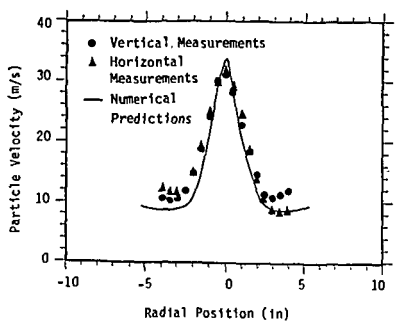


Figure 3. Particle Velocity Distributions, 18" Downstream of Spray Nozzle

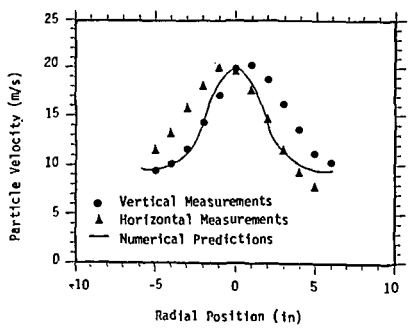


Figure 4. Particle Velocity Distributions, 36" Downstream of Spray Nozzle

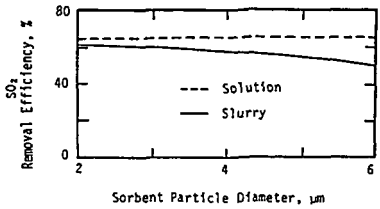


Figure 5. Effect of Inlet Sorbent Particle Size

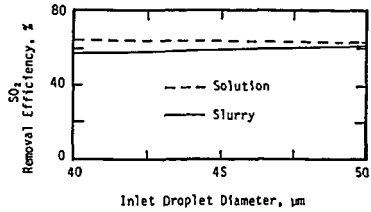


Figure 6. Effect of Inlet Droplet Size

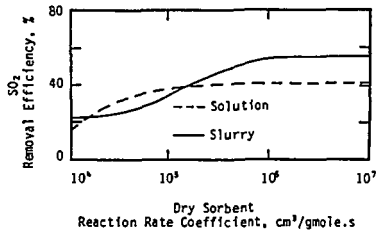


Figure 7. Effect of Dry Sorbent Reaction Rate Coefficient

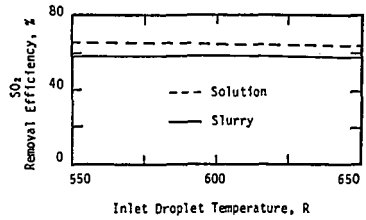


Figure 8. Effect of Inlet Droplet Temperature

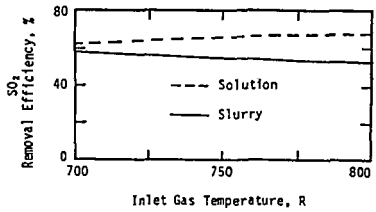


Figure 9. Effect of Inlet Gas Temperature

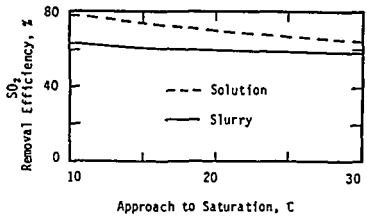


Figure 10. Effect of Approach to Saturation Temperature

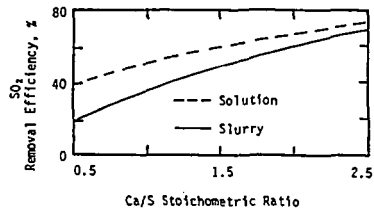


Figure 11. Effect of Inlet $Ca/S$ Stoichiometric Ratio

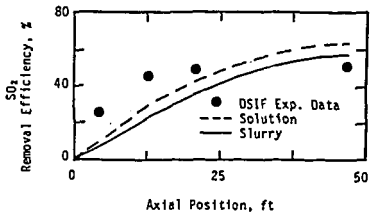


Figure 12. Calculated vs. Experimental $SO_2$ Removal Efficiency

# A MECHANISTIC MODEL FOR AXISYMMETRIC CAVITY GROWTH DURING UNDERGROUND COAL GASIFICATION

Jerald A. Britten and Charles B. Thorsness

Lawrence Livermore National Laboratory, P.O. Box 808, L-367, Livermore, California 94550

Underground coal gasification (UCG) is a process in which coal energy is recovered without mining by artificially enhancing gas permeability in a section of a coal seam, igniting the coal remotely, partially combusting and gasifying coal by means of injected oxygen-steam-air mixtures, and collecting the product gas for cleanup and processing for a variety of end uses. The technology has been the subject of active field, laboratory and modeling research in the U.S. and Europe for more than 15 years, and during this time significant advances have been made and the process is nearing commercialization.

The size of the cavity formed during UCG impacts directly the economic and environmental factors crucial to its success. Lateral dimensions influence resource recovery by determining the spacing between modules, and ultimate overall dimensions dictate the hydrological and subsidence response of the overburden. Field experiments of UCG are expensive, and unless the cavity can be excavated after the experiment, cavity geometry can only be approximately inferred from post-burn coring, thermowell responses, electromagnetic and seismic mapping data and material balance calculations. In 1986, normal coal mining operations at the site of an UCG field test performed in 1983 near Centralia, Washington, the Partial Seam CRIP or PSC test (1), offered a unique opportunity to excavate a cavity of near-commercial scale. This excavation (2,3) provided data on ultimate cavity shape and characteristics which have profoundly aided our understanding of the UCG process. However, the data provide only indirect information as to cavity growth dynamics, and it is clear that a reliable mechanistic model for UCG cavity evolution and gas production would be extremely useful for site characterization and process simulation. Previous cavity growth models (e.g. (4-7)) are of limited use since they rely on one or more of the following: arbitrary assumptions regarding oxidant flow distribution in the cavity, oversimplification of some crucial phenomena at the expense of detailed modeling of others, or boundary conditions on upward or outward cavity growth, either arbitrarily chosen or fitted to field data, which decouple growth rates from heat and mass balance constraints. Also, until now detailed data for full-scale cavity dimensions were not available to compare with model results.

The model described in this paper applies to flat-seam UCG of subbituminous or lower rank coals in which the oxidant injection point remains low in the coal seam, and has progressed, we feel, to the point where it has become a useful tool with predictive ability for these conditions. It is based on a few key assumptions which are difficult to verify fully at the scale of interest, but which seem to be justified by model comparisons with field data. The global cavity growth model integrates results of interacting submodels describing water influx from the coal aquifer, dispersion of injected reactants in a rubble bed at the cavity bottom, thermal degradation and chemical attack of rubble-covered coal sidewalls, and recession of cavity surfaces enclosing a void space in the upper cavity, caused by radiation-driven spalling and gasification. Also, a submodel which calculates the growth of an outflow channel through which hot product gas flows to the production wellhead, is included for cases in which a horizontal uncased production borehole is utilized. The global model is of course highly idealized in the interest of tractability, and all apparent geometrical and physicochemical symmetries have been exploited to simplify the problem, but it retains sufficient physics to describe very well leading order UCG process

dynamics.

A mathematical description of the model and its many submodels would require far too many pages than allotted. The following sections describe briefly in words the submodels and their integration into the global cavity growth simulator, present comparisons of model results with results of two field experiments, and finish with a prediction of cavity characteristics for a proposed field test. Complete details of the model and its many parts can be found in (8-15).

## MODEL FORMULATION

The model envisions upward and outward growth of a cavity with origin at the point of injection of gaseous reactants. Figure 1 shows typical cavity cross-sections at varying stages of development. The cavity itself consists of up to four zones of differing properties: an ash rubble pile at the bottom of the cavity, left by reacted coal; a rock rubble or slag pile which can exist on top of the ash rubble once the cavity has grown to incorporate overburden rock; and a void space at the top of the cavity through which radiative heat transfer from hot rubble surfaces drives reaction and/or rubblization of exposed coal and rock surfaces. Also, geometrical considerations based on surface area distribution of the coal-void interface and the location of the oxygen source, reinforced by early modeling results and observations of the aforementioned excavated cavity, suggest that a pile of pyrolyzed char rubble can accumulate around the edge of the cavity and is therefore modeled. Densities of the rubble in the various regions are specified and assumed constant. Dynamics of flow, heat and mass transfer, and chemical reaction in and across these zones and in the surrounding coal seam are described by the following submodels, and results incorporated into the global cavity growth simulator. Reaction chemistry is simplified by lumping $CO_2 + H_2O$ and $H_2 + CO$ into singlr gasification reactant and product species, respectively, with suitably defined heats of formation (15). This simplification is justified by the similar sthoichiometric and kinetic behavior of the individual species in the reactions of importance. By use of the assumption of equilibrium of the water-gas shift reaction at the calculated product gas trmperature and a carbon balance, detailed gas compositions can be calculated from model results. The model does not treat tar evolution or its secondary reactions.

Water Influx Submodel Water influx to a UCG reactor plays a major role in determining process efficiency. Water can enter the reactor through drying of overburden rock, gravity drainage, depressurization of the coal aquifer, and reflux of condensate from escaped product gas if gas losses to the formation occur. Although some water in the UCG reactor is essential as a gasification agent, often far more than desired enters the reactor, and the energy necessary to vaporize and heat it to the product gas temperature is essentially lost.

The water influx submodel used in the global simulation, described in detail in (8), calculates flow of free water through the (assumed) homogeneous aquifer of the coal seam by gravity drainage, which occurs independent of the reactor pressure, and depressurization of the coal seam, which occurs when the reactor is operated below the hydrostatic pressure. The model assumes that strata above and below the coal seam are impermeable. (Water from overburden drying is accounted for naturally in the roof recession submodel.) Reactor geometry in thr influx submodel is idealized as a cylinder extending the full height of the seam representing the cavity, and a noninteracting slot of variable width representing a horizontal outflow channel. Cylinder and slot volumes are specified by demanding equality with cavity and outflow channel volumes at each time step. We assume that gas displacing the water in the coal strata is of sufficiently high mobility that only the flow equations for the water-filled region need be considered. Also, capillary pressure effects are assumed negligible. These assumptions imply that the gas pressure on all

water/gas interfaces are equal. The two-dimensional (radial and axial) flow problem for gravity drainage is reduced to a one-dimensional problem by use of the so-called Dupuit approximation (16) which considers Darcy flow only in the radial direction based on a radial gradient in piezometric head. This system has been solved numerically using a finite difference scheme to discretize the differential equation in the space dimension and integrating the resulting system of ODE's in time using a standard solver. In (8) it is shown that, except for very early times, the Dupuit approximation gives flowrate values in very close agreement with those calculated by solution of the full two-dimensional solution, for both stationary and uniformly expanding cylinder walls. Depressurization is included in this formulation by matching the drainage solution valid in the cone of depression with the solution for unsteady potential flow in the fully saturated far field aquifer, at the boundary where both solutions are valid.

In coupling the water influx submodel to the global cavity growth solution, the model equations are solved for a fixed geometry over a time interval equal to the time step of the full problem. At the start of each time step a new grid system is established with its inner boundary on outer edge of the cavity or outflow channel. Values of hydraulic head are obtained through interpolation of the previous solution. Drainage and depressurization water is assumed to enter the at the ash-rubble covered sidewall in the lower cavity. Values for parameters characterizing water influx, with the exception of flow porosity, can be obtained from standard well hydrology testing. One additional parameter, an initial pumping time, has been introduced to make allowance for the time during which the wells are pressurized or pumped down before initiating the UCG burn.

Injection Gas Flow Submodel At any instant flow through the ash rubble is quasi-steady, since the evolution of its geometry is over a much longer time scale than the flow residence time. The flow distribution is described by the compressible form of Darcy's law in the axisymmetric volume of the ash rubble pile (see Figure 1), with a source term at the origin, and an impermeable cavity floor. We assume a region of high permeability exists at the ash pile-coal sidewall boundary, since it is here that void space is being created by removal of carbon and volatiles from the coal. This assumption is critical to the success of the model. We also assume that the char rubble overlying the outer edges of the ash rubble is highly permeable. This is justified by observations of rubble characteristics of the excavated UCG cavity (3). These assumptions imply that the sides and top of the ash rubble are at the same sink pressure while the cavity remains in the coal seam. Once rock rubble enters the cavity, a resistance to upward flow through the central ash pile is added, proportional to the height of the rock rubble and the permeability ratio of rock to ash rubble. The system is solved by a finite difference method. A vertical half-plane with origin at the center of the axisymmetric rubble pile is mapped onto a grid rectangular in r and z coordinates, which is normalized at each time step to maximize the number of nodes lying inside the rubble pile. Permeability values at nodes lying on or outside the rubble pile are set very large, effectively tying the edge of the pile to the sink pressure $P_s$. The difference equations for the pressure at each node, linear in $P^2$, are solved iteratively using successive overrelaxation. The solution for the previous time step is used as the initial guess for the next step. Calculated fluxes at boundary nodes are smoothed with a polynomial fit for each of the interfaces adjacent to the coal sidewall, void and char bed. The integrated flow out of the entire boundary is normalized with the injection flow to remove errors introduced by the smoothing, and average flowrates to each of the three zones are computed.

Wall Recession Submodel The wall region is defined as the cavity boundary extending downward to the cavity floor from point d in Figure 1A. We assume the existence of a thin, highly permeable, char-filled zone between the ash and the solid coal wall. Here oxygen entering from the ash side

combusts char, supplying heat to drive gasification reactions, vaporize and heat influxed water and dry, pyrolyze and degrade fresh coal to char rubble. The net effect of this rubblization, which involves relaxation of thermal and drying induced (shrinking) stresses coupled with overburden stresses at the solid wall, is to propagate this permeable reaction zone into the coal. We describe this failure mechanism in terms of a convective heat transfer rate from hot gas at temperature $T_w$ to the coal wall at a specified failure temperature $T_f$, with the heat flux balanced by that required to dry and heat coal to temperature $T_w$ at the rate of the sidewall recession. Also, settling of char and/or ash from above and upward flow of product gas is considered to occur in this layer. Solution of the fully-coupled two-dimensional heat and material flow problem described here is far beyond the scope of a module to be used in a global UCG simulation. A major simplification is the division of the wall into several discrete elements in the axial direction, and the assumption that the temperature is constant within a given segment. This temperature is presumed to be given by the formula for the effective extinction temperature of the steam/char reaction in a packed bed (12,13), subject to the constraints of energy and mass balances and the convective heat transfer conditions at the cold coal wall. This temperature is primarily a function of the Arrhenius kinetic parameters of the steam-char reaction and the local flux of the product gas in the layer. This formulation allows the computation of recession velocities and char conversion rates for each segment.

Void/Rubble Zone Submodel This submodel describes the interaction of the coal, overburden and rubble pile surfaces enclosing the void region at the top of the developing cavity. Competent coal or rock surfaces here are exposed to high temperatures, and thermally induced and lithostatic stresses interact in a fashion not completely understood to cause spalling (small scale failure) of material on the order of centimeters to occur. A one-dimensional transient model (14,15) has been developed to describe drying, pyrolysis, gasification and spalling of coal (or rock) exposed to a constant high temperature radiative heat source. Spalling behavior is empirically characterized by a failure length $\ell_f$ and a failure temperature $T_f$, in such a way that when the temperature a distance $\ell_f$ from the surface exceeds $T_f$, an element of this size is removed from the surface and the process repeated. Values of $\ell_f$ and $T_f$ are obtained from analysis of one-dimensional transient heating experiments on overburden cores (17) when available, or appropriate values are chosen and regarded as model parameters. This model is used to calculate mean recession rates and related quantities, averaged over a series of spalls, as functions of the mean surface temperature. Heat transfer to the curved roof surface can be considered one-dimensional, since the thermal penetration depth is always much smaller than the local radius of curvature. The void space is assumed to be well-mixed.

The roof surface is divided into several conic sections. Oxygen exiting the top of the ash pile combusts with char which spalls onto this surface while the cavity is in the coal, and combusts product gas at the surface of the rock rubble when it is present, creating a hot surface which radiates to the other surfaces. Radiative exchange equations are written for the surfaces enclosing the void, in which the temperature of the roof surfaces determines their recession rates, and material and energy balances are solved (9,15) subject to two constraints, as discussed in a later section. While the cavity is in the coal seam, it is demanded that no char accumulate on the central surface of the ash rubble; all char arriving here must be reacted by combustion and gasification. When overburden rock is present, complete combustion of oxygen with product gas ($H_2 + CO$) at this surface is demanded. The char pile at the outer cavity edge is considered a one-dimensional packed bed modeled as in (13) in which oxygen and steam entering from below react with char, and the product gas exits into the void. Reaction chemistry is simplified in this region by considering $H_2 + CO$ as one chemical species, and $CO_2 + H_2O$ as another, as described

in (15), with suitably defined reaction enthalpies.

Outflow Channel Model This model describes growth of an outflow channel, originally an open horizontal borehole in the coal seam, by thermally-induced rubblization of the coal as described above, driven by convective heat transfer from the hot product gas. Heat transfer is modeled in a semi-empirical fashion with constants fitted to the PSC excavation data (12). This channel is considered physically removed from the cavity such that no geometrical interaction occurs to break the symmetry of the cavity. Channel volumes calculated, and measured in the field, typically amount to about 10% of the main cavity volume.

Global Cavity Growth Module An initial cavity is defined as a series of line segments connecting points along one-half of a cavity cross section looking from the side. Initial cavities are defined as cylinders with unit height/diameter ratio and specified total, char and ash rubble volumes. (Parametric studies have shown that initial cavity configuration has a very small effect on late-time cavity characteristics.) This geometrical data is passed to the submodels which calculate temperatures, recession rates and chemical reaction rates for the various surface segments. The control segment then advances cavity segments over a time step, tentatively computes new cavity boundaries and rubble amounts. A unique cavity shape is calculated differently depending on whether the cavity interacts with overburden rock. When the cavity is contained in the coal, this shape is determined by noting that the amount of char which falls into the inner ash pile surface determines the upward growth of this surface, the temperature distribution in the enclosure and the amount of char remaining in the rubble bed. In other words, there is only one solution for the amount of char deposited on the ash-void interface, for which the location of point a in figure 1A simultaneously satisfies both char and ash material balances. When the cavity grows to encompass overburden rock, the ash pile ceases to grow upward and thus point b in Figure 1B is determined solely by the ash material balance. In this case the location of point a is fixed by simultaneous satisfaction of char and rock rubble material balances. Provision is made during late stages of cavity development for complete coverage of char by rock rubble, and also for the eventual depletion of the char rubble, by adjustment of point c in Figure 1D. The control algorithm also periodically performs various smoothing and point equalization operations on the calculated results. These are necessary since adjacent cavity points moving at significantly different velocities could cross paths if no intervention occurred, leading to highly irregular, multiply-connected cavity shapes numerically and physically unrealistic. Cavity volumes are computed before and after each smoothing operation and the errors incurred as a result of smoothing are recorded. For all cases considered, the cumulative smoothing error is about 3-6% of the total cavity volume. Time steps are constrained such that no point on the cavity surface can advance farther than a specified fraction of its distance from the cavity origin.

The present version of the code developed for this simulation requires relatively little memory and uses about 5 seconds per time step early on when an iteration on the void radiative exchange equations is required, decreasing to less than a second per time step for the latter stages of the calculation. Total cpu time on a Cray 1 computer needed for a 15 day simulation is about 3 minutes.

## RESULTS AND COMPARISON WITH FIELD DATA

Partial Seam CRIP Field Test The parameter with the largest effect on model results is the ratio of permeability between the rock and ash rubble piles. This parameter controls the split of injected oxidant flow between the sidewalls and the void region once overburden is exposed, which occurs relatively early in the life of the burn. Generally, oxidant which is forced to the cavity sidewalls

comes in intimate contact with coal, producing high quality gas, while oxidant passing into the void partially combusts product gas, heating overburden rock which represents an energy loss. A lower rock rubble permeability thus diverts more oxidant flow to the sidewalls, resulting in a wider, shorter ultimate cavity and enhanced energy recovery. This permeability ratio is very difficult to quantify. From observations of ash and rock rubble during the excavation of the PSC site (3) it was concluded that the rock rubble was probably somewhat less permeable than the ash, since much of it had fused, leaving an irregular network of fissures to conduct the gas, while the ash rubble clinker appeared relatively more porous. The effect of this permeability ratio is seen in Figure 2, which shows the molar ratio of produced hydrogen and carbon monoxide to injected oxygen, and excellent measure of process efficiency. Results using physical and process parameters given in Table 1A, corresponding to the PSC test conditions and with permeability ratios spanning three orders of magnitude, are here compared with test data. It is clearly seen that $\kappa_R/\kappa_A = 1$ gives the best agreement. This result, and the observation that past field tests also exhibited gradual declines in product gas quality, instead of consistent high values or precipitous declines when overburden was encountered, suggest that this ratio is of O(1) and we therefore specify a value of unity for all subsequent calculations.

The model calculation for $\kappa_R/\kappa_A = 1$ resulted in a final cavity shape which is compared in Figure 3 with that mapped during the excavation. The actual cavity was slightly asymmetric with respect to the injection point, but the agreement is quite good; both in sweep and the narrowing of the cavity midsection. This latter phenomenon occurs because this area of the cavity is covered for most of the burn with insulating char rubble, and is not exposed to direct oxidant attack as below, or high-efficiency radiative heat transfer as above. The simulation predicts total coal volume gasified to be 675 $m^3$. Analysis of the field data (1) suggest that about 700 $m^3$ of coal was gasified during the part of the test in which this cavity was formed. While the upper part of the actual cavity was destroyed by mining operations and cavity shape in the overburden cannot be directly compared, but the good agreement in produced gas quality shown in Figure 2 suggests that the simulation calculated reasonably the volume of overburden affected.

Rocky Mountain I Field Test The recently completed Rocky Mountain I (RMI) UCG field test provides another opportunity to test model results with a system in which oxidant injection remained low in the coal seam. Flow and pressure schedules used during the test and parameter values taken from a number of literature sources characterizing the Hanna coal, given in Table 1B, were used as inputs in the simulation. Day zero is defined as the beginning of forward gasification with steam and oxygen, and the initial cavity volume is specified by carbon removed during air gasification which occurred for about 3 days prior. Figure 4 compares model results of $(H_2 + CO)/O_2$ for these conditions with the test data. The agreement is striking. Figure 5 compares calculated cavity volumes with that calculated for the actual cavity by a material balance which assumes no char accumulation in the underground system. Also on this figure the product gas temperature is compared. Volumes agree quite well early but diverge by about 15% for later stages of the 40 day burn of the first cavity. Also, the predicted product gas temperature is somewhat higher than actual, though the slight upward trend with time is well-represented. The actual cavity shape is not reliably known, so no direct comparisons can be made. Qualitatively, the computed cavity shape is similar to that calculated for the PSC simulation, since this is largely determined by the proximate analysis of the coal, which is similar for these two coals.

Two weaknesses of the model are its neglect of the hydrogasification reaction ($2H_2 + C \rightarrow CH_4$) and its neglect of tar evolution and secondary tar reactions. The former may account for the discrepancy in $CH_4$ production between model and data (7% -vs- 11% respectively, on a dry gas

basis). This reaction is endothermic and thus its inclusion in the model would serve to reduce product gas temperature. Tar cracking could produce a considerable amount of $H_2$ and $CO$, since tar amounts to as much as 15% by weight of the original coal (20). This could explain the equivalent $H_2 + CO$ production rates between model and data, when the model predicts up to 15% more coal was affected. One must keep in mind in interpreting this test data, however, that it is raw data; known errors have not yet been removed.

Proposed Brazilian UCG Field Test As part of the Lawrence Livermore Laboratory effort to provide technical support for a UCG feasability study in Brazil, cosponsored by the DOE, a simulation was performed using all available data concerning the coal and overburden at the proposed test site, near Porto Alegre in southern Brazil. This simulation provided estimates for sweep width and coal recovery used in planning link numbers and spacing for the two year demonstration test plan. Coal and overburden physical data specific to the site, as well as operating parameters are given in Table 1C. Rubble pile densities were adjusted from values measured at the PSC excavation based on the density differences in the original materials, and other necessary data unavailable for this site, such as coal and rock failure criteria, were taken as the same as for the PSC simulation. This test is of great interest because the characteristics of the coal, very dry, very impermeable and of a high ash content, represent conditions felt to be ideal for flat seam UCG.

Figure 6 shows the cavity shape produced by the simulation at approximately 11.5 days. The high ash content of this coal results in a larger volume of the cavity filled by ash rubble compared with coals previously studied. Thus, a larger fraction of the cavity surface is covered by rubble. The void region of the cavity is relatively small, such that the efficient radiative heat transfer mechanism dominant in the void is focused largely at the topmost part of the cavity, which gets quite hot and recedes rapidly. These factors combine to form a cavity wide at the bottom with a chimney-type upper end. The simulation was terminated when the void space became filled with bulked rubble, a situation that cannot be treated by the present model. The behavior of the system would not be expected to change substantially in the short term once the cavity is completely filled, however. The bed of pyrolyzed, unreacted char which persists in simulations of other UCG systems studied, disappears early on in this system. The volume of coal and rock affected by the cavity predicted by the simulation is 454 and 220 $M^3$, respectively. The results suggest that gas production efficiencies at sites such as this are expected to be quite good, but very hot product gas temperatures may be experienced.

## CONCLUSIONS

A model for cavity growth and gas production during UCG, based on the assumption of cylindrical cavity symmetry and applicable for gasification of shrinking coals when injection low in the coal seam can be maintained, has been developed. The model is highly idealized, but treats includes all important factors impacting cavity growth such as water influx, porous media flow, heterogeneous and homogeneous chemical reactions, radiative and convective heat transfer, and rock mechanics. Model predictions have been shown to agree very well with available field data, and while detailed produced gas compositions cannot be estimated, it is felt quite adequate to describe in a semiquantitative fashion cavity evolution, energy recovery, aquifer response, and effects of process parameter changes, and therefore is a useful tool for UCG site characterization and module optimization.

**Acknowledgement** This work was performed under the auspices of the U.S. Department of Energy by Lawrence Livermore National Laboratory under contract number W-7405-Eng-48.

## REFERENCES


1. Cena, R.J., Hill, R. W. and Thorsness, C. B., (1988) 'The Partial Seam CRIP Underground Coal Gasification Test' Lawrence Livermore National Lab. UCRL rept. (in press)
2. Oliver, R.L., (1987) 'Results of the Controlled Excavation of the TONO I UCG Cavity, Centralia, Washington' Proc. 13th UCG Symp. (in press)
3. Cena, R.J., Britten, J.A. and Thorsness, C.B., (1987) (Proc. UCG Symp. (in press) Lawrence Livermore Nat'l Lab. preprint no. 97245
4. Chang, H.L., Himmelblau, D.M. and Edgar, T.F (1984) Proc 10th UCG Symp. U.S. DOE rept. DOE/METC/85-5 460-476.
5. Thorsness, C.B and Cena, R.J., (1983) Proc. 9th UCG Symp. U.S. DOE rept. DOE/METC/84-7 246-281
6. Kunselman, L.V., Faucett, D.W and Mones, C.G., (1983) Proc. 9th UCG Symp., U.S. DOE rept. DOE/METC/84-7 182-195
7. Riggs, J.B. and Edgar, T.L., (1983), in **Underground Coal Gasification, the State of the Art**, W.B. Krantz and R.D. Gunn, eds. AIChE Symp. Ser. **226** 108-120
8. Thorsness, C.B. and Grens, E.A., (1987) Proc. 13th UCG Symp., (in press) Lawrence Livermore Nat'l Lab. preprint no. 97203
9. Thorsness, C.B. and Britten, J.A., (1986) Proc. 12th UCG Symp. DOE/FE/60922-H1 239-251
10. Grens, E.A. and Thorsness. C.B., (1985) Proc. 10th UGC Symp. DOE/METC-85-7 448-461
11. Grens, E.A. and Thorsness. C.B., (1986) Proc. 11th UGC Symp. DOE/METC-85/6208 413-423
12. Britten, J.A. and Thorsness, C.B., (1987) Proc. 13th UCG Symp., (in press) Lawrence Livermore Nat'l Lab. preprint no. 96461
13. Britten, J.A. (1988) 'Extinction Phenomena in Countercurrent Packed Bed Coal Gasifiers: A Simple Model for Gas Production and Char Conversion Rates'*Ind. Eng. Chem. Research* (in press)
14. Britten, J.A. (1986) *Int. J. Heat Mass Transfer* **29** 965-978
15. Britten, J.A. and Thorsness, C.B., (1985) Proc. 11th UCG Symp. DOE/METC-85/6208, 365-380
16. Bear, J. (1972) **Dynamics of Fluids in Porous Media** American Elsevier Publishing, New York, ch. 8
17. Tantekin, S.B. (1986), M.S. Thesis, University of Colorado
18. Kotowsky, M.D. and Gunn, R.D., (1976) Laramie Energy Research Center rept LERC/RI-76/4
19. Mason, J.M., Oliver, R.L., Schrieber, J.D., Moody, C., Smith, P., and Healy, M.J., (1987) Western Research Institute Rept. 86-062
20. Hill, R.W. and Thorsness, C.B., (1987) Lawrence Livermore National Lab. rept. UCID 20951

**Table I.** Physical and process parameters used in the simulations.

A. Partial Seam CRIP

coal specific gravity 1.39, 17% water, 21% ash, 28% fixed carbon
rock specific gravity 2.10, 12% water
coal failure temperature (K) 700 (roof) 850 (sidewalls)
rock failure temperature (K) 700 (roof) 850 (sidewalls)**
coal roof failure length (cm) 1; rock roof failure length (cm) 2
rubble specific gravities; ash 1.0, rock 1.3, char 0.8
permeabilities (mD); ash rubble 10000, rock rubble 10000, native coal 30
hydrostatic head (kPa)* 630, pumpdown time (days) 10
seam height 6 (m), initial cavity height & radius (m) 1.0 & 0.5
nominal gas flow (mol/s) 30, steam/oxygen ratio 2/1, ramp time (days) 5
injection temperature (K) 400, cavity pressure (kPa) 430
References: (1), (3), (8)

B. Rocky Mountain I

coal specific gravity 1.39, 9% water, 27% ash, 32% fixed carbon
rock specific gravity 2.10, 10% water
coal failure temperature (K) 700 (roof) 700 (sidewalls)
rock failure temperature (K) 660 (roof) 660 (sidewalls)
coal roof failure length (cm) 1; rock roof failure length (cm) 1.7
rubble specific gravities; ash 1.0, rock 1.3, char 0.8
permeabilities (mD); ash rubble 10000, rock rubble 10000, native coal 140
hydrostatic head (kPa) 990, pumpdown time (days) 12
seam height 7.6 (m), initial cavity height & radius (m) 3.6 & 1.8
gas flow schedule from actual data, injection temperature (K) 400
cavity pressure schedule from actual data
References: (17), (18), (19)

C. Brazil Test

coal specific gravity 1.78, 8% water, 46% ash, 28% fixed carbon
rock specific gravity 2.42, 4% water
coal failure temperature (K) 700 (roof) 850 (sidewalls)
rock failure temperature (K) 700 (roof) 850 (sidewalls)
coal roof failure length (cm) 1; rock roof failure length (cm) 2
rubble specific gravities; ash 1.1, rock 1.5, char 0.9
permeabilities (mD); ash rubble 10000, rock rubble 10000, native coal 0
seam height 3.7 (m), initial cavity height & radius (m) 1.0 & 0.5
nominal gas flow (mol/s) 30, steam/oxygen ratio 2/1, ramp time (days) 5
injection temperature (K) 400, cavity pressure (kPa) 1500
Reference: (20)

* measured from bottom of coal seam
** best fit to excavated outflow channel volume

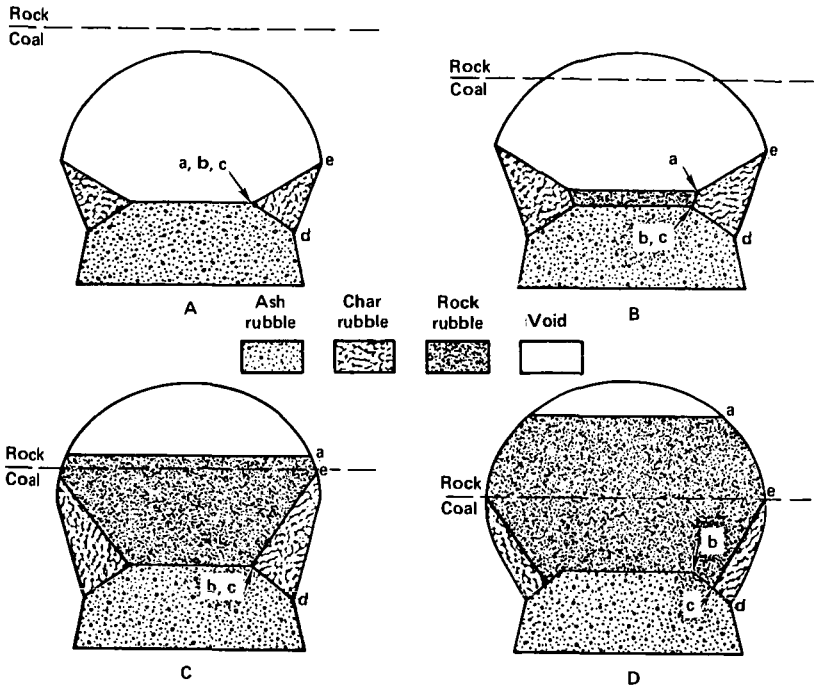


**Figure 1** Generic cavity shapes constructed by the model.

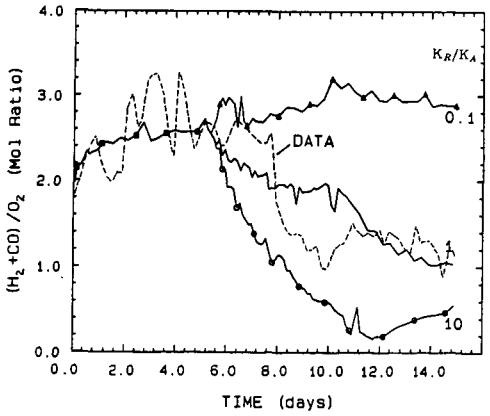


**Figure 2** Effect of rock-to-ash rubble permeability ratio on the ratio of $H_2 + CO$ produced to $O_2$ injected. Conditions of Table 1A. Field data from PSC field test shown as dashed line

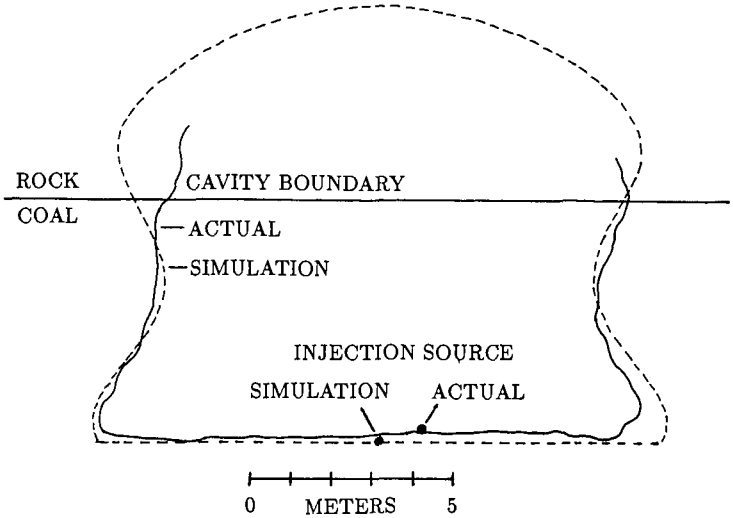


**Figure 3** Comparison of actual and calculated cavity shapes in the plane perpendicular to the injection borehole at the injection point of the PSC CRIP cavity. Simulation used parameter values of Table 1A

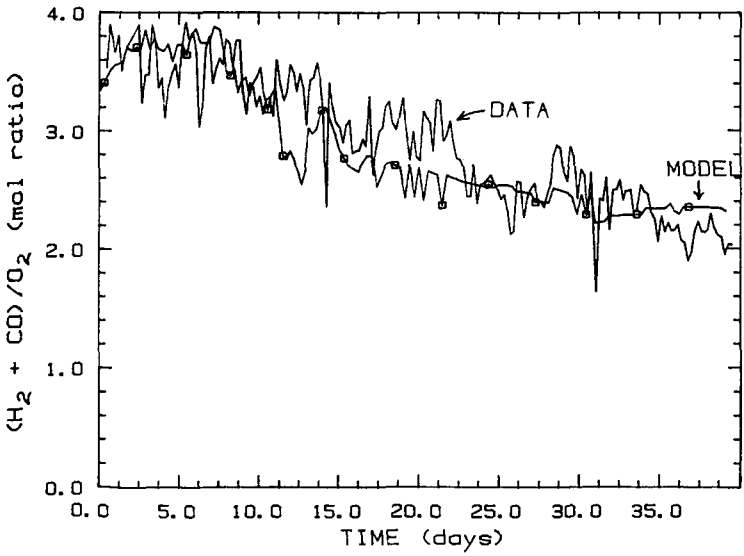


**Figure 4** Ratio of $H_2 + CO$ produced to oxygen injected calculated for the simulation of the RMI field test compared with actual data. Conditions of Table 1B.

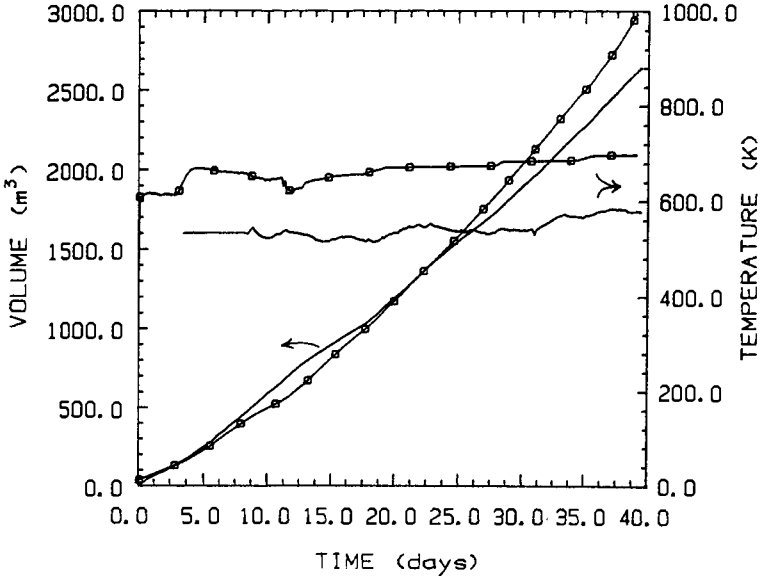


**Figure 5** Cavity volumes and product gas temperature calculated by the model (marked lines), compared with material balance and temperature data from RMI CRIP side cavity.

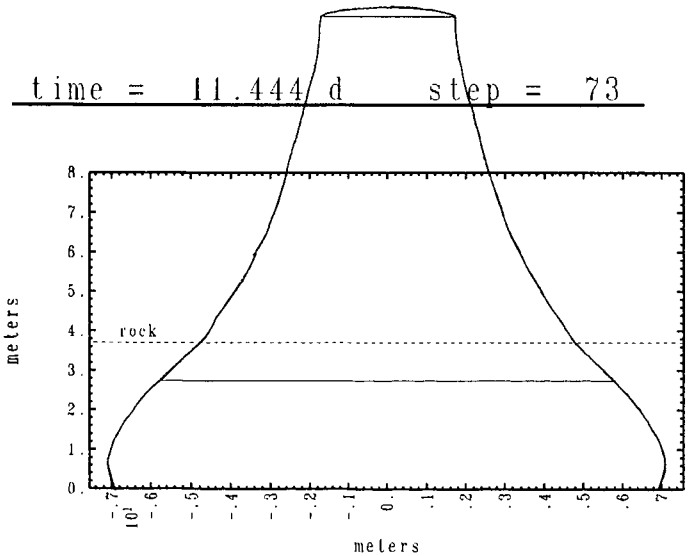


**Figure 6** Cavity profile calculated at 11 days for simulation of the proposed UCG field test in Brazil. Simulation used parameter values given in Table IC.

# MODELING OF A HIGH-TEMPERATURE DIRECT COAL GASIFICATION PROCESS IN A TWO-STREAM REACTOR

K. Hanjalić and M. Sijerčić

University of Sarajevo-Energoinvest, Sarajevo, Yugoslavia

C. T. Crowe and S. Wojcicki

Washington State University, Pullman WA, 99164-2920

## ABSTRACT

A new scheme for direct gasification of pulverized coal has been analyzed by a mathematical model. Gasification occurs in the annular region of a cylindrical reactor during the cocurrent flow of a steam/coal mixture, with combustion products in the reactor core region serving as an internal heat source. The model incorporates the two equation model for turbulence, mass exchange between phases due to chemical reactions and radiative heat transfer. Detailed calculations are carried out to assess the feasibility of the scheme.

## INTRODUCTION

The basic concept for a two-stream gasifier for pulverized coal has been described in earlier publications (see reference 1). The basic configuration is shown in figure 1. Steam and coal are introduced on the periphery of the reactor while air and coal are injected as the core flow. It is assumed that the gasification will occur in the annular region of the cylindrical reactor during the cocurrent flow of a coal/steam mixture with hot combustion products in the reactor core region, the latter serving as the heat source. In this manner, the scheme capitalizes on two well known gasification concepts: direct supply of heat from internal combustion and hydrodynamic separation of gasification products from the combustion gases. The product gases, acceptably clean, are ducted away at the end of the reactor through an annular slot while the combustion gases from the core region are utilized for heat recovery in the system.

A global analysis of the system shows that the scheme is feasible provided that:

a) sufficient radiative heat transfer occurs between the two streams in cocurrent flow to ensure the completion of the gasification process and,
b) proper fluid dynamic conditions are achieved to avoid intensive mixing of the two streams in the reactor.

An experimental investigation of the process and the conditions which satisfy these requirements would require costly and extensive experimentation. We have chosen to develop a computer model as the first phase of a research program aimed at establishing the potential feasibility of the scheme and elucidating the important parameters in system design. If the scheme appears feasible, the results of the numerical model will be used to complement design of the experimental rig.

## MATHEMATICAL MODEL

The mathematical model of the gasification process entails solving the appropriate conservation equations for the gas and particle phases, as well as a number of auxiliary equations which describe various phenomena and interactions in the process. The model is based on the following assumptions:

- the process is adiabatic.
- the flow and temperature fields are axisymmetric.
- chemical reactions are first order reactions.
- thermal radiation is monochromatic and scattering due to the particles is isotropic.

The gas phase is described by a system of time-averaged conservation equations for momentum, mixture enthalpy and concentrations of chemical species. In addition the equation set contains conservation equations for the kinetic energy and dissipation rate of turbulence following the well known $k-\epsilon$ model (2). The general form for the conservation equations is

$$\frac{\partial}{\partial x}(\rho U \phi) + \frac{1}{r}\frac{\partial}{\partial r}(r\rho V \phi) = \frac{\partial}{\partial x}(\Gamma_\phi \frac{\partial \phi}{\partial x}) + \frac{1}{r}\frac{\partial}{\partial r}(r\Gamma_\phi \frac{\partial \phi}{\partial r}) + S \qquad 1)$$

where U and V are the axial and radial velocity components and the dependent variable $\phi$ represents the density, velocity components, turbulence parameters, enthalpy and concentration of chemical species. The chemical composition of the gases is assumed to be nitrogen, oxygen, carbon dioxide, water vapor and gasification products (carbon monoxide and hydrogen). The transfer function $\Gamma_\phi$ represents such quantities as effective viscosity, thermal conductivity and diffusion coefficients. The source term S incorporates such phenomena as production or depletion of chemical species due to chemical reaction and the mass, momentum and energy sources provided by the particle phase. The definition of these terms will not be included in the interest of brevity.

In order to evaluate thermal radiation exchange, the number density of the particles is needed. Equation 1 is utilized with the transfer function being the effective diffusion coefficient, as taken from Melville and Bray (3), and the source term being zero. The influence of the particulate phase on the effective viscosity of the gas is also modeled with a corrective factor based on the local mass concentration of the particles.

The thermal radiation is simulated with the "six-flux" model (4) with the assumption that the gas radiation is a volume phenomena and the particle radiation is a surface phenomena. It is also assumed that the radiation scattering by the particles is isotropic. Two diffusion-type equations are solved for the radiative heat flux in the axial and radial directions.

The particle velocities and temperatures are obtained by integrating the momentum and energy equations along trajectories for single particles. The effect of particle dispersion due to turbulence is accounted for by adding a "diffusive" velocity to the particle motion which is proportional to the concentration gradient and the effective diffusion coefficient (5). The particle energy equation relates the change in thermal energy of the particle to the convective and radiative heat transfer as well as the energy associated with the change of phase.

To simplify the gasification model, the coal is regarded as char. The mass rate of change of the coal particle is given by

$$\frac{dm_p}{dt} = \dot{r}_c + \dot{r}_g \qquad 2)$$

where $\dot{r}_c$ is the reaction rate for combustion and $\dot{r}_g$ for gasification. It is assumed that chemical kinetic and diffusion processes occur in parallel so the reaction rates are given by

$$\dot{r}_g = \mathcal{M}_p A_p \rho X_{H_2O} \Big/ \left[\mathcal{M}_{H_2O}\left(\frac{1}{K_g} + \frac{d_p}{ShD}\right)\right] \qquad 3a)$$

$$\dot{r}_c = 1.5\mathcal{M}_p A_p \rho X_{O_2} \Big/ \left[\mathcal{M}_{O_2}\left(\frac{1}{K_c} + \frac{d_p}{ShD}\right)\right] \qquad 3b)$$

where $\rho$ is the gas density, $A_p$ is the particle cross-sectional area, $X_{O_2}$ and $X_{H_2O}$ are the mass fractions of oxygen and water vapor, $\mathcal{M}$ is the moelcular weight, $Sh$ is the Sherwood number and $d_p$ is the particle diameter. The chemical recation rates are given in the form of Arrhenius expressions with coeffcients determined experimentally for Yugoslav coals (6); namely,

$$K_g = 1.2 \times 10^6 exp(-\frac{23077}{T}) \qquad 4a)$$

$$K_c = 5.6 \times 10^4 exp(-\frac{15035}{T}) \qquad 4b)$$

It must be mentioned that these coefficients can vary by an order of magnitude or more depending on the literature source.

The phase coupling in the model is accomplished using the PSI cell scheme (7). Particles are released from a discrete number of radial locations to simulate an initially uniform particle number density. The number flow rate along each trajectory is constant. The change in particle mass, momentum and energy are recorded as each trajectory traverses a computational cell and these become the source terms in the gas-phase flow equations. The energy source term also includes the radiative heat transfer from the particles.

The boundary conditions for the gas phase follow the standard formulations used in conjunction with the $k - \epsilon$ turbulence model (2). The gradient for the concentration of the chemical species is set equal to zero at the wall. Also the incident radiation at the wall is set equal to the wall radiation.

## MODEL PREDICTIONS

The verification of the computational model has been partially achieved through its application to simple flow fields for which data are available. Reasonably good agreement between model predictions and experimental results has been achieved for turbulent flows in a circular pipe (8) and a "cold" model of the gasification reactor (9). Verification of the model under realistic conditions for the reactor has yet to be established.

The model was applied to reactor geometry for which the lip separating the two streams was set at a radius ratio of 0.8. The initial velocity of the inner core flow was 6.4 m/s while a velocity of 3.87 m/s was selected for the annular flow. The initial temperature of the inner flow was 1300 K and that of the outer flow was 900 K.

The development of the axial velocity profile at progressive distances downstream is shown in figure 2. There is a rapid mixing initially and momentum diffuses into the low speed outer annular flow to increase the velocity. The temperature of the core stream increases rapidly with the combustion of the coal and there is a consequent acceleration of the flow to satisfy mass flow continuity because of the decreased gas density. Then radiative heat transfer to the outer stream cools down the core flow and heats the outer flow giving rise to velocity changes in each stream (decelerating the core flow and accelerating the annular flow) which drive them both toward velocity equilibrium.

The radial profiles for the gasification products, $H_2$ and $CO$, at progressive downstream locations are shown in figure 3. One notes that the gasification products remain basically in the outer region of the reactor and could be separated by an annular slot shown schematically in figure 1. This prediction supports the feasibility of the concept.

The fraction of coal consumed in the gasification process is shown in figure 4. One notes that 60% of the coal at the outside of the reactor has been gasified at approximately five reactor radii from the inlet. Of course, the rate of coal consumption will depend strongly on the gasification rate for specific coals.

The predicted isotherms are shown in figure 5. One notes a very rapid temperature change at the reactor inlet due to combustion of the coal and the subsequent decrease in temperature as the heat is radiated from the hot core to the annular flow. The gas composition at three duct diameters downstream from the inlet is shown in figure 6. One notes, as also shown in figure 3, that the gasification products remain in the peripheral region while the combustion products are concentrated in the core. As shown in the figure, if the slot for the removal of the gasification products were located at a radius ratio of 0.7, the recovery would be primarily $CO$ and $H_2$ with some $CO_2$ and water vapor. The relative fractions of chemical species in the slot would be

$$CO + H_2 = 0.54$$

$$CO_2 = 0.16$$

$$H_2O = 0.05$$

$$N_2 = 0.25$$

Of course, the fraction of gasification products to combustion products can be increased by increasing the radius ratio of the slot. However the yield of the gasification products would be reduced. The optimum design remains to be established.

## CONCLUSION

Based on the predictions of the mathematical model, the proposed gasification concept appears feasible. The scheme is attractive because of the direct contact heat exchange and the separation of combustion and gasification products. The ultimate assessment of the scheme will only be possible through well-designed pilot plant tests in which the operational conditions and configurations are changed to achieve an optimum design. The numerical model developed here will be a useful tool to complement the design and operational adjustments of an actual system.

## ACKNOWLEDGEMENTS

The authors acknowledge the support of Dr. Soliman of the International Programs Office of the US Department of Energy.

## REFERENCES

1. Hanjalić, K., Sijerčić, M, Crowe, C.T.and Wojcicki, S. (1985) Analysis of a Two-Stream Coal Gasification System, Spring Meeting, The Combustion Institute, San Antonio, TX.

2. Launder, B.E. and Spalding, B.D. (1972) *Mathematical Models of Turbulence*, Academic Press, London.

3. Melville, W.K. and Bray, K.N.C. (1979) The Two Phase Turbulent Jet, *Int. Jnl. Heat and Mass Trans.*, **22**, 279.

4. Chu, C-M and Churchill, S.W. (1955) Numerical Solution of Problems in Multiple Scattering of Electromagnetic Radiation, *Jnl. Phys. Chem.* 59, 855.

5. Smoot, L.D. and Pratt, D.T. (ed.) (1979) *Pulverized Coal Combustion and Gasification*, Plenun Press, New York.

6. Karč, H. (1986) Isledovanie gazifikaciji i szigania burogo uglja "Zenica", *Politechnika Wroclawska.*

7. Crowe, C.T., Sharma, M.P. and Stock, D.E. (1977) The Particle-Source-in-Cell (PSI-Cell) Model for Gas-Droplet Flows, *Jnl. of Fluids Engr.* **99**, 2, 325.

8. Laws, E.M., Lim, E.H. and Livesey, J.L. (1974) Turbulent Pipe Flows in Development and Decay, 2nd Symposium on Turbulent Shear Flows, London

9. Krajišnik, S., Žerajić, D. and Sijerčić, M. (1982) Eksperimentalno izucavanje procesa strujanja u reaktoru za direktnu gasifikaciju uglja, *Energoinvest -ITEN.*

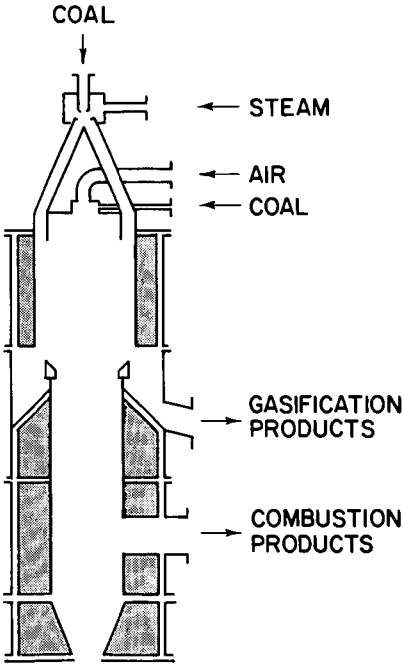


Figure 1. Schematic Diagram of Gasification Reactor.

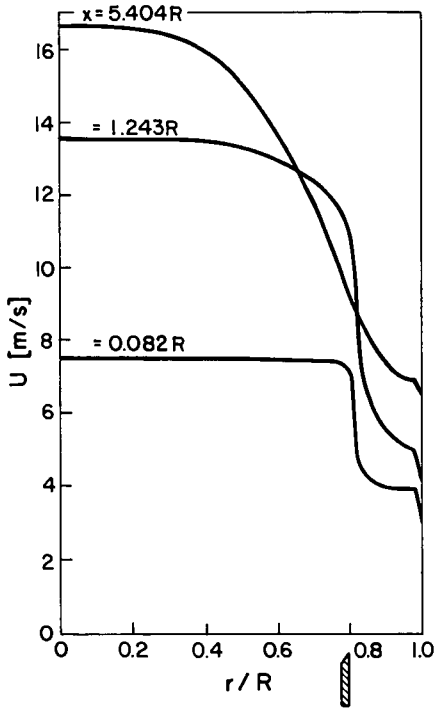


Figure 2. Development of axial velocity profile along reactor.

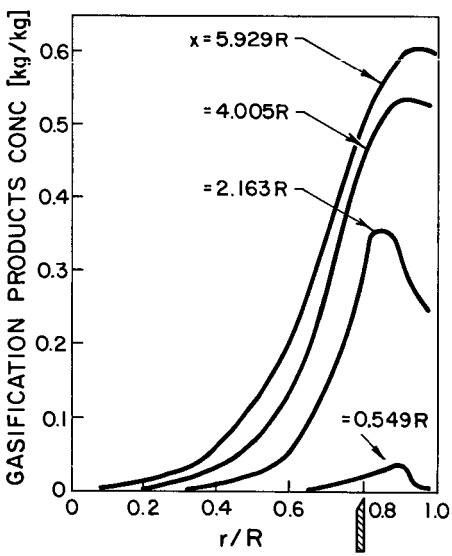


Figure 3. Development of concentration profiles for gasification products along reactor.

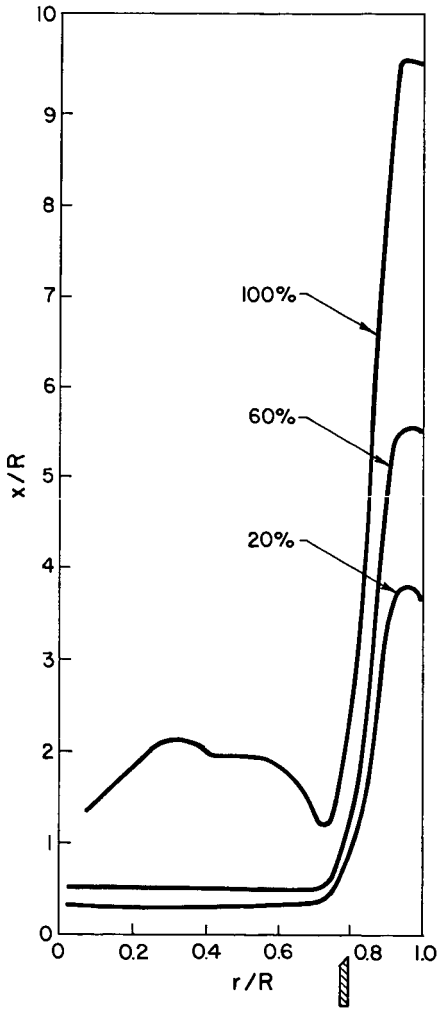


Figure 4. Fraction of coal particle consumption along reactor.

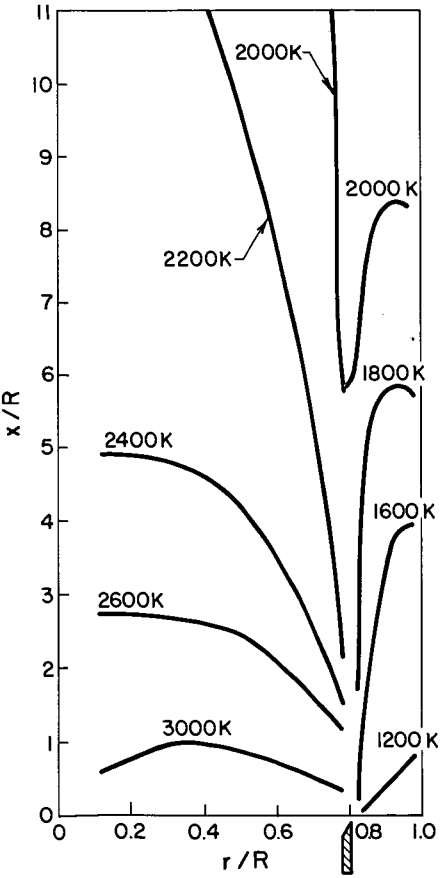


Figure 5. Isothermal profiles in reactor.

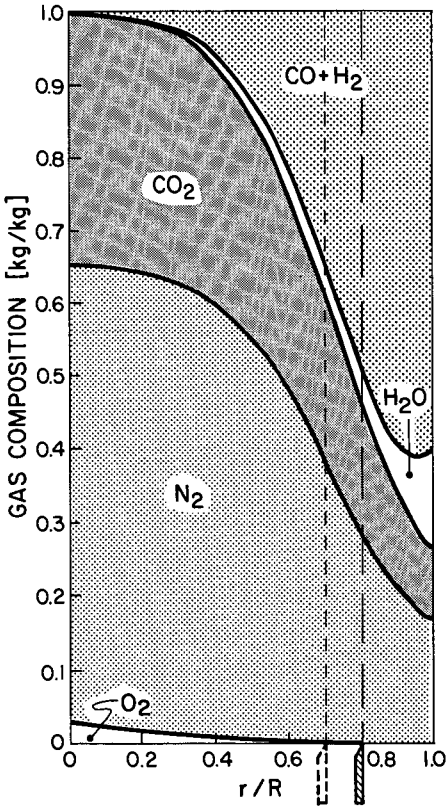


Figure 6. Radial gas phase composition at three duct diameters from inlet.

# PERFORMANCE SIMULATION OF FLUIDIZED-BED COAL COMBUSTORS

Ravi R. Chandran and Denny D. Sutherland

The Babcock & Wilcox Company, R&D Division, Alliance, Ohio 44601

## ABSTRACT

*A code, referred to as FBCSIM, is being developed to predict large-scale atmospheric fluidized-bed combustor (AFBC) performance with fundamental fuel data from bench-scale test units as input. This work is carried out as a part of AFBC fuels characterization program sponsored by the Electric Power Research Institute (EPRI). The code accounts for the physics of fluidization, which is unit specific, and the chemistry of combustion, which is fuel specific. The code includes a 3-D model and modules on bed hydrodynamics, chemical kinetics, solid distribution, and transport phenomena. The model for in-bed combustion incorporates a two-region particle mixing formulation. The code for in-bed combustion has been validated for different AFBC unit sizes (0.1, 2, and 20 MW) and different coals (two bituminous and a lignite). Sensitivity analyses have been carried out to identify the controlling variables and guide experimental work. Computer simulations have also been performed to delineate system response to operational parameters.*

## INTRODUCTION

Test results from small-scale to pilot plant AFBC units have proven the viability of fluidized-bed combustion technology for large-scale applications. However, commercialization of this technology has been slow due in part to concerns regarding scale-up for unit size and fuel type. To overcome this hurdle, Babcock & Wilcox (B&W) under the sponsorship of EPRI has developed an AFBC fuels characterization method (1)(2). The approach involves the generation of fundamental fuel data using inexpensive bench-scale tests and the development of a mathematical model or performance code to link bench-scale results to large-scale operation. The objectives are to 1) facilitate the optimal design of commercial-size AFBC units, and 2) quantify the fuel flexibility of existing AFBC designs. For a review of the models reported in the literature along with the rationale for the present model, the reader is referred to an earlier publication (3).

## FORMULATION

The performance code (FBCSIM) under development for bubbling-bed combustion comprises a model and four modules, and has been set up in this fashion so that it is easily adaptable to circulating as well as pressurized FBC. The first module evaluates hydrodynamics, which is unit specific. It accounts for fluidization regime, gas flow, bubble dynamics, and solids mixing characteristics. The second module deals with chemical kinetics (devolatilization, char combustion, and sorbent sulfation), which is influenced by coal and sorbent properties. The third module accounts for solids distribution in bed and above bed due to swelling, fragmentation, attrition, elutriation, and entrainment. The fourth module deals with transport phenomena such as interphase heat and mass transfer. For a given coal and specified operating conditions, the code seeks to predict overall combustion and sulfur capture efficiencies and combustion split and sulfur capture split between in-bed and freeboard. The first goal of this code development was to model in-bed combustion for the underbed-feed mode of operation. Additional goals are to model freeboard combustion, overbed-feed mode, and sulfur capture. The in-bed combustion model is described here.

### Model for In-Bed Combustion

The in-bed combustion model currently addresses underbed feed with zero recycle. Future modifications will account for recycle. Figure 1 shows an idealization of the combustion sequence, and Figure 2 shows the corresponding conceptual model. The figures depict a unit cell defined as the bed cross section served by one feedpoint. Primary air enters the bed through a distributor plate, while coal particles of a broad size distribution (typically 6.35 mm x 0, or 1/4 inch x 0) and transport air enter through the feedpoint. Based on a review of the pertinent physical and chemical time scales, it is suggested that these coal particles entering the bed be classified in a binary fashion for modeling volatile release and heterogeneous combustion. Material below the maximum elutriable size for the given operating conditions is termed "fines" and the larger size fraction is denoted as "coarse". For example, at typical AFBC operating conditions, the fines would correspond to material passing through 30 sieve (590 microns).

The solids injected through the feedpoint flow up through the bed and diffuse laterally. The fines are considered to be in plug flow. They heat up, devolatilize, and burn while convecting axially and dispersing radially until they reach the bed surface and elutriate. The coarse particles also heat up and devolatilize as they mix above the feedpoint. If the coal contains a significant proportion of volatiles, a volatile-rich zone above the feedpoint could result. The volatiles released would rise as a plume and burn in a gaseous diffusion flame with the surrounding oxygen. Whether this plume closes within the bed or not would depend on the coal's ratio of volatile to fixed carbon, feedpoint spacing, and the bed operating conditions. Some coarse particles could fragment during devolatilization if their size exceeds the critical stable size for fragmentation. The coarse char particles mix in the bed, generate flakes and fines due to combustion-enhanced mechanical attrition (CEMA), and combust in the oxidizing zone outside the plume until they reach the elutriable size. The flakes and fines resulting from CEMA are subject to the competing processes of combustion in the bed and elutriation to the freeboard. Therefore, feedpoint spacing has different implications for different coal ranks with regard to in-bed combustion. For low volatile coals or other solid fuels, the wider the feedpoint spacing, the lower the combustion of fines in the feed due to high concentration of fuel and low concentration of oxygen above the feedpoint. For high volatile coals, the occurrence of a volatile-rich plume additionally could diminish in-bed combustion. A video of the bed surface taken recently during 0.1 MW AFBC operation supports the conceptual model discussed above.

To model in-bed combustion, it is necessary to properly account for the combustion of volatiles, devolatilized fines in the feed, and coarse char particles. These three components burn in a coupled fashion and the degree of combustion is governed by fluidization physics and fuel chemistry. The underlying physical and chemical processes are complex and not fully understood. Therefore, some simplifying assumptions have been introduced (3). Consequently, combustion is visualized to occur in two regions. The first region is where the physical processes of convection and dispersion of coal particles are important. This region lies directly above the feedpoint and provides the setting for coal particle heat up, volatile release, volatile combustion, and the combustion of fines in the feed. Although swelling and fragmentation could occur in this region, they do not involve an oxidation step and need not be considered here. The second region includes the whole unit cell, where the coarse char particles are uniformly distributed and undergo heterogeneous combustion in the oxidizing zone outside the plume. The unit cell coordinate geometry for the 3-D formulation is shown in Figure 3.

Considerable attrition occurs in underbed feed systems (1)(2). A distributed fracture model along with an experimentally determined coal-specific attrition parameter are used to estimate the coal particle size distribution $F_i(d_i)$ entering the bed.

<u>Region I</u>. The formulation here corresponds to an adaptation of the model of Bywater (4). Five conservation equations are used to designate the problem. These are for the concentration of i) volatiles remaining in the coarse coal particles ($C_{vc}$), ii) volatiles remaining in the fines ($C_{vf}$), iii) solid combustibles in the devolatilized fines ($C_{cf}$), iv) gaseous volatiles ($C_g$), and v) oxygen ($C_o$). The gaseous volatiles are assumed to combust according to the stoichiometric reaction,

$$[\nu \text{ kg}] \text{ volatiles} + [1 \text{ kg}] \text{ oxygen} \rightarrow [(\nu+1) \text{ kg}] \text{ products.} \qquad 1)$$

Also the fast reaction or large Damkohler limit is presumed to apply. The hetergeneous combustion of devolatilized fines is considered to follow the reaction,

$$[\nu' \text{ kg}] \text{ combustible} + [1 \text{ kg}] \text{ oxygen} \rightarrow [(\nu'+1) \text{ kg}] \text{ products.} \qquad 2)$$

The reaction order in oxygen is taken to be 0.6 based on the work of Daw (5). Finally, the classical treatment of Burke and Schumann (6) is applied to the combustion of gaseous volatiles. This facilitates the description of a new variable,

$$C_{go} = C_g - \nu C_o, \qquad 3)$$

and reduces the number of variables (and equations) by one.

The mass balance equations are normalized by defining the following variables:

$$x^* = \frac{x}{x_b},\ y^* = \frac{y}{y_b},\ z^* = \frac{z}{H'},\ x_f^* = \frac{x_f}{x_b},\ x_o^* = \frac{x_o}{x_b},\ y_f^* = \frac{y_f}{y_b},\ y_o^* = \frac{y_o}{y_b},$$

$$C_{vc}^* = \frac{C_{vc}}{C_{vci}},\ C_{vf}^* = \frac{C_{vf}}{C_{vfi}},\ C_{cf}^* = \frac{C_{cf}}{C_{cfi}},\ C_{go}^* = \frac{C_{go}}{\nu C_{oi}},$$

where subscript i denotes the parameter value at feedpoint or distributor, $x_b$ and $y_b$ are the length and width of the unit cell, and H' is the bed plus splash zone height.

The governing equations in dimensionless form are:

$$\frac{\partial C_{vc}^*}{\partial z^*} = \alpha_x \frac{\partial^2 C_{vc}^*}{\partial x^{*2}} + \alpha_y \frac{\partial^2 C_{vc}^*}{\partial y^{*2}} - k_{vc}^* C_{vc}^* J_c, \tag{4}$$

$$\frac{\partial C_{vf}^*}{\partial z^*} = \beta_x \frac{\partial^2 C_{vf}^*}{\partial x^{*2}} + \beta_y \frac{\partial^2 C_{vf}^*}{\partial y^{*2}} - k_{vf}^* C_{vf}^* J_f, \tag{5}$$

$$\frac{\partial C_{cf}^*}{\partial z^*} = \beta_x \frac{\partial^2 C_{cf}^*}{\partial x^{*2}} + \beta_y \frac{\partial^2 C_{cf}^*}{\partial y^{*2}} - k_{cf}^* C_{cf}^* (-C_{go}^*)^{0.6} LI, \text{ and} \tag{6}$$

$$\frac{\partial C_{go}^*}{\partial z^*} = \eta_x \frac{\partial^2 C_{go}^*}{\partial x^{*2}} + \eta_y \frac{\partial^2 C_{go}^*}{\partial y^{*2}} + \frac{k_{cf}^* C_{cf}^* (-C_{go}^*)^{0.6} LI \psi \nu R_{fi}}{\nu} + k_{vc}^* C_{vc}^* J_c \phi + k_{vf}^* C_{vf}^* J_f \psi - k_{oc}^* C_{go}^* I, \tag{7}$$

where

$$J_c = \begin{cases} 0 & \text{if } (z^* H'/u_{sc} - \tau_c) \le o \\ 1 & \text{if } (z^* H'/u_{sc} - \tau_c) > o \end{cases} \qquad J_f = \begin{cases} 0 & \text{if } (z^* H'/u_{sf} - \tau_f) \le o \\ 1 & \text{if } (z^* H'/u_{sf} - \tau_f) > o \end{cases}$$

$$L = \begin{cases} o & \text{if } C_{vf}^* > o \\ 1 & \text{if } C_{vf}^* = o, \end{cases} \qquad I = \begin{cases} o & \text{if } C_{go}^* \ge o \\ 1 & \text{if } C_{go}^* < o \end{cases}$$

Subject to the boundary conditions:

$$\text{at } z^* = o: \left.\begin{matrix} C_{vc}^*(x^*, y^*, o) \\ C_{vf}^*(x^*, y^*, o) \\ C_{cf}^*(x^*, y^*, o) \end{matrix}\right\} = \begin{cases} 1 & \text{for } x_f^* - \frac{x_o^*}{2} \le x^* \le x_f^* + \frac{x_o^*}{2},\ y_f^* - \frac{y_o^*}{2} \le y^* \le y_f^* + \frac{y_o^*}{2} \\ 0 & \text{for } o \le x^* < x_f^* - \frac{x_o^*}{2},\ x_f^* + \frac{x_o^*}{2} < x^* \le 1, \\ & o \le y^* < y_f^* - \frac{y_o^*}{2},\ y_f^* + \frac{y_o^*}{2} < y^* \le 1 \end{cases}$$

$$C_{go}^*(x^*, y^*, o) = -1 \text{ for } 0 < x^* \le 1,\ o < y^* \le 1$$

$$\text{for } z^* > 1: \quad \frac{\partial C^*_{vc}}{\partial x^*}, \frac{\partial C^*_{vf}}{\partial x^*}, \frac{\partial C^*_{cf}}{\partial x^*}, \frac{\partial C^*_{go}}{\partial x^*} = o \text{ at } x^* = o, 1$$

$$\frac{\partial C^*_{vc}}{\partial y^*}, \frac{\partial C^*_{vf}}{\partial y^*}, \frac{\partial C^*_{cf}}{\partial y^*}, \frac{\partial C^*_{go}}{\partial y^*} = o \text{ at } y^* = o, 1$$

$\alpha$, $\beta$ and $\eta$ are dimensionless dispersion coefficients, $k^*_{vc}$ and $k^*_{vf}$ are normalized devolatilization rate constants, $k^*_{cf}$ is a non-dimensional rate constant for oxidation of combustibles in devolatilized fines, $\phi$ and $\psi$ are dimensionless solid to gas flux transfer parameters, $R_{fi}$ is the ratio of $C_{cfi}$ and $C_{vfi}$ at the feedpoint, and $k^*_{oc}$ is a normalized reaction rate constant for the depletion of oxygen in the bed due to coarse char particle combustion.

The parameter J accounts for the effect of finite heating rate and the consequent delay in the onset of volatile evolution. It activates the volatile generation term when the particles have convected a distance that corresponds to the heatup time $\tau$. L and I are off/on switching parameters for the heterogeneous combustion of devolatilized fines and coarse char particles respectively. Equations 6 and 7 are coupled through the fines heterogeneous combustion term and hence need be solved simultaneously. Finally, the last term in equation 7 requires a trial and error procedure to match the coarse char particle combustion occurring in Region II.

<u>Region II</u>. The objective here is to determine the rates of oxygen consumption and elutriation due to the heterogeneous combustion of coarse char particles. This can be accomplished by carrying out solids population balances of the type proposed by Levenspiel, et al. (7)(8).

The flow rates pertaining to the different steps of the combustion sequence are shown in Figure 4. Sorbent and ash particles are assumed to be inert for this analysis. Coarse coal particles represented by (n-m) cut sizes undergo devolatilization. The inflow rate of cut i with mean diameter $\bar{d}_i$ is denoted as $F_i(\bar{d}_i)$. To simplify the analysis, swelling is decoupled from devolatilization. A differential mass balance for the devolatilization step yields:

$$F_w(\bar{d}_i) = (1 - v_i)\, F_i(\bar{d}_i) \text{ for } i = m+1, m+2, \ldots, n, \qquad 8)$$

where $v_i$ is the gaseous volatile yield fraction for the ith cut.

Size as well as density change during swelling. Therefore, a number balance rather than a mass balance is indicated. The number flow rate before swelling is related to the mass flow rate according to:

$$N_w(\bar{d}_i) = F_w(\bar{d}_i) \,/\, (\rho_{wi}\, \pi \bar{d}_i^3/6) \qquad 9)$$

with $\rho_{wi} = \rho_{coal}(1 - v_i)$ and $\rho_{coal}$ is coal density.

From a steady state number balance, the number flow rate after swelling is:

$$N_f(\bar{d}_i) = N_w(\bar{d}_{i-1})(SI_{i-1}-1)\, \frac{\bar{d}_{i-1}}{\bar{d}_i - \bar{d}_{i-1}} + N_w(\bar{d}_i) \left[1 - (SI_i - 1)\, \frac{\bar{d}_i}{\bar{d}_{i+1} - \bar{d}_i}\right] \qquad 10)$$

$$\text{for } i = m+1, m+2, \ldots, n,$$

with $N_w(\bar{d}_m) = 0$. $SI_i$ is the swelling index for the ith cut size.

The corresponding mass flow rate is:

$$F_f(\bar{d}_i) = N_f(\bar{d}_i)\, \rho_{fi}(\pi \bar{d}_i^3/6) \text{ for } i = m+1, m+2, \ldots, n, \qquad 11)$$

where $\rho_{fi} = \rho_{wi} / SI_i^3$.

For typical underbed feed sizes (6.35 mm x 0, or 1/4 inch x 0, experimental data indicates fragmentation to be negligible, therefore,

$$F_c(\bar{d}_i) = F_f(\bar{d}_i) \text{ for } i = m+1, m+2, \ldots, n, \tag{12}$$

and

$$\rho_{ci} = \rho_{fi}.$$

The model for char combustion would depend upon coal properties and is likely to correspond to either shrinking size or shrinking core kinetics. Bench-scale experimental data suggest that a shrinking particle model would be a reasonable approximation for bituminous coals. A solids population balance carried out with the modification suggested by Overturf and Kayihan (9) for discrete cut sizes gives:

$$W_c(\bar{d}_i) = \frac{[F_c(\bar{d}_i) - F_{bd}(\bar{d}_i)]\ \Delta d_i + W_c(\bar{d}_{i+1})\ S_c(\bar{d}_{i+1})\ \Delta d_i/\Delta d_{i+1}}{S_c(\bar{d}_i) + E_c(\bar{d}_i)\ \Delta d_i + 3S_c(\bar{d}_i)\ \Delta d_i/\bar{d}_i} \tag{13}$$

$$\text{for } i = n, n-1, \ldots, (m+1), m,$$

with $W_c(\bar{d}_{n+1}) = 0$ and $F_c(\bar{d}_m) = 0$. $W_c(\bar{d}_i)$ is weight of char particles of size $\bar{d}_i$ in bed and $\Delta d_i$ is size interval for ith cut. Tests in the 1- x 1- foot (1 x 1) and 6- x 6- foot (6 x 6) AFBC units at B&W indicate that the char content of the bed drain solids is very small, therefore,

$$F_{bd}(\bar{d}_i) = 0 \text{ for } i = n, n-1, \ldots, (m+1), m. \tag{14}$$

$E_c(\bar{d}_i)$ denotes entrainment rate constant of char particles of size $\bar{d}_i$ from the bed surface. The overall shrinkage rate $S_c(\bar{d}_i)$ is expressed as the sum of the shrinkage rates due to combustion and attrition (10)(11):

$$S_c(\bar{d}_i) = S_{cc}(\bar{d}_i) + S_{ca}(\bar{d}_i). \tag{15}$$

Attrition rate here corresponds to the flakes and fines generated in the CEMA tests. The shrinkage rate for char combustion according to a first order reaction is:

$$S_{cc}(\bar{d}_i) = -\left.\frac{d\bar{d}_i}{dt}\right|_{cc} = \frac{2\ \bar{C}_{ob}}{\rho_{ci}\ f_{cci}\left[\frac{1}{\lambda_i R_{mc}} + \frac{1}{R_{cc}}\right]} \tag{16}$$

where $\bar{C}_{ob}$ is the mean oxygen concentration in the bed, $f_{cci}$ is the weight fraction of equivalent carbon in char, $R_{mc}$ is the external mass transfer coefficient, and $R_{cc}$ is the chemical rate coefficient for char combustion. $\lambda_i$ is a parameter that depends on stoichiometry and has a value between 3/8 for $C + O_2 \rightarrow CO_2$ reaction at the char surface and 3/4 for $C + 1/2\ O_2 \rightarrow CO$ reaction.

The shrinkage rate due to attrition $S_{ca}(\bar{d}_i)$ is:

$$S_{ca}(\bar{d}_i) = k_{ca}(u_o - u_{mf})/(3\ f_{cci}), \tag{17}$$

where $k_{ca}$ is CEMA rate constant for carbon, $u_o$ is superficial gas velocity, and $u_{mf}$ is the superficial gas velocity at minimum fluidization.

The flakes and fines generated due to CEMA seem to follow the Rosin-Rammler distribution. If $q_{ij}$ and $q_{nj}$ are the weight fraction of flakes and fines of size $\bar{d}_j$, and $f_{fl}$ is the proportion of flakes in the attrited material, then the weight of char particles of size $\bar{d}_j$ by mass balance is:

$$W_c(\bar{d}_j) = \frac{\sum_{i=m}^{n} W_c(\bar{d}_i) S_{ca}(\bar{d}_i)\,[q_{1j} f_{f1} + q_{nj}(1-f_{f1})]\,\frac{\Delta d_j}{\Delta d_i} + W_c(\bar{d}_{j+1}) S_{cc}(\bar{d}_{j+1}) \frac{\Delta d_j}{\Delta d_{j+1}}}{S_{cc}(\bar{d}_j) + E_c(\bar{d}_j)\Delta d_j + 3\, S_{cc}(\bar{d}_j)\,\Delta d_j / \bar{d}_j} \qquad 18)$$

$$\text{for } j = m-1,\ m-2,\ \ldots,\ 1.$$

The shrinkage rate $S_{cc}$ depends upon $\bar{C}_{ob}$, the mean oxygen concentration in the bed which is not known a priori. So the procedure is to start with a guess value of $\bar{C}_{ob}$ and iterate in conjunction with Region I model until convergence. The flow chart for the computer code is given in Figure 5. Subroutines are listed within quotation marks. "FSATT" accounts for feed system attrition, "HYDRO" for bed hydrodynamics, "SOLDIS" for solids distribution, and "CHEMK" for chemical kinetics. "TRANSP" provides interphase heat and mass transfer coefficients and "TEMP" evaluates burning char particle temperature by energy balance. The code is written in FORTRAN and makes use of ACM Algorithm #565, PDETWO/PSETM/GEARB, for solving partial differential equations. Run times for in-bed performance simulations typically range from 2-6 CPU minutes on a DEC VAX 11/785.

To conserve space, the ensuing discussion will be qualitative and will not include equations. From the bed char weight distributions determined above, the rate of oxygen consumption due to char combustion ($w_{occII}$), char elutriation rate from the bed and the conversion of char in the bed ($X_c$) are evaluated. It is assumed that any volatiles remaining in the coarse coal particles when they reach the bed surface (based on the solution of Equation 4) are released uniformly in the bed. The oxygen consumption rate due to this component is added to $w_{occII}$ to calculate the overall rate of oxygen consumption in Region II ($w_{ocII}$).

By integrating the bed-surface concentrations computed in Region I, the fraction of the volatiles released in-bed from the fines ($X_{vf}$), the conversion of gaseous volatiles in-bed ($X_v$), and the conversion in the bed of combustibles in devolatilized fines ($X_{cf}$) are determined. Also, the oxygen consumption rate in Region I ($w_{ocI}$) is calculated by mass balance. The parameter $k^*_{oc}$ is adjusted until $w_{oc}$ values converge. Then the iteration for $\bar{C}_{ob}$ is performed until convergence. From the converged values for $X_v$, $X_{cf}$, and $X_c$, the total in-bed carbon conversion ($X_{tic}$) and in turn the in-bed combustion efficiency ($E_{ibc}$) are computed.

Typical parameters for which the performance code requires input and their origin are indicated in Table 1.

## VALIDATION

The objective is to validate the performance code for different AFBC unit sizes and fuel types. The code predictions for in-bed combustion of Kentucky No. 9 coal are compared with experimental data from 1 x 1 [B&W], 6 x 6 [EPRI/B&W], and 20 $MW_e$ [TVA/EPRI] AFBC units in Figure 6. The data correspond to a gas residence time of about 0.5 second based on superficial velocity. Good agreement is observed. The in-bed combustion efficiency tends to decrease with an increase in feedpoint spacing but does not exhibit a smooth variation. The relatively high value obtained in the case of the 1 x 1 unit is due to lower gas velocity and lesser feed system attrition.

Figure 7 presents the results for Texas lignite. The square symbol stands for experimentally determined in-bed combustion efficiency and the solid line represents the code predictions. Experimental values of the overall combustion efficiency are also plotted for comparison. Predicted in-bed combustion and experimental overall combustion efficiency curves diverge with an increase in superficial gas velocity. This implies increased freeboard combustion at higher gas velocities. This is to be expected in view of the greater freeboard solids loading caused by CEMA, elutriation, and carry over of fines in the feed. Additional comparisons for Kentucky No. 9 and Pittsburgh No. 8 bituminous coals have been presented in a previous paper (3).

## SENSITIVITY ANALYSIS

An analysis for sensitivity over the range of parameter uncertainty is desirable to further evaluate the code, identify the controlling parameters, and guide experimental work. The parameters which have significant impact on code predictions are anticipated to differ with AFBC unit size, design, and coal type. Therefore, a number of test analyses are required to generalize the results. Based on initial studies, the sensitivity of different parameters for burning Kentucky No. 9 coal in two different AFBC units (1 x 1/0.1 MW and 18 x 12/ 20 $MW_e$) are given in Table 2. Volatile conversion in-bed is typically complete (~100%) in the 1 x 1 AFBC unit and there-

fore its performance is primarily sensitive to char conversion parameters. VYULT impacts char fraction and hence is important. Due to the large feedpoint spacing in the 20 $MW_e$ pilot plant, the parameter COFDO assumes a lead role. It is difficult to combust fines in a short residence time and consequently DHOP exerts a considerable influence on performance of both units.

## SIMULATION

The response of the 20 $MW_e$ pilot plant to changes in the fines content of the feed and feed system attrition coefficient are shown in Figure 8. COFATT of 11.0 corresponds to the extent of attrition that occurs in the current design. Clearly, it is beneficial to control the amount of fines in the feed and reduce feed system attrition. Results of additional simulations pertaining to the operation of the unit will be presented in another paper (12).

## CONCLUSIONS

A phenomenological code for predicting in-bed combustion performance of AFBC units has been developed and validated. It provides a measure of required in-bed heat transfer surface allocation. Work is in progress to develop a freeboard combustion model. Future goals are to incorporate the effect of recycle and model overbed-feed mode and sulfur capture. The code is being tested and refined constantly based on new information and data. Upon completion, FBCSIM will become a versatile tool for performance simulation and design of fluidized-bed coal combustors.

## ACKNOWLEDGMENT

This work was performed with the support of EPRI. We are thankful to N. Soltys and L. A. Oberjohn of B&W for their help in conducting the sensitivity analysis.

## REFERENCES

1. Chandran, R.R., Duqum, J.N., Perna, M.A., Jafari, H.C., Rowley, D.R., Petrill, E.M., and Hansen, W.A., "A New Method for AFBC Fuels Characterization", 1987 International Conference on Fluidized Bed Combustion, The American society of Mechanical Engineers, p. 292, 1987.

2. Chandran, R.R., Duqum, J.N., and Modrak, T.M., "Coal Classification for Fluidized Bed Combustion", International Symposium on Coal Combustion, Beijing, China, Sept. 1987 (to be published by Hemisphere Publ. Corp.)

3. Chandran, R.R., Duqum, J.N., and Petrill, E.M., "A Performance Code for AFBC Scaleup - Part I: In-Bed Combustion", 1987 International Conference on Fluidized Bed Combustion, The American Society of Mechanical Engineers, p. 300, 1987.

4. Bywater, R.J., "The Effects of Devolatilization Kinetics on the Injector Region of Fluidized Beds," 6th International Conference on FBC, Atlanta, GA, Conf. 800428, Vol. III, p. 1092, 1980.

5. Daw, C.S., "Tubular Flow Reactor Experiment - Task 13", Oak Ridge National Laboratory, Oak Ridge, TN, July 1985.

6. Burke, S.P. and Schumann, T.W.E., Ind. Eng. Chem., Vol 20, p. 998, 1928.

7. Levenspiel, O., Kunii, D., and Fitzgerald, T., Powder Technology, Vol. 2, p. 87, 1968/69.

8. Kunii, D. and Levenspiel, O., Fluidization Engineering, John Wiley & sons, Inc., New York, NY, 1969.

9. Overturf, B.W. and Kayihan, F., "Computations for Discrete Cut Particle Size Distributions in a Fluidized Bed Reactor", Powder Technology, Vol 23, p. 143, 1979.

10. D'Amore, M., Donsi, G., and Massimilla, L., "Bed Carbon Loading and Particle Size Distribution in Fluidized Combustion of Fuels of Various Reactivity," 6th International Conference on FBC, Atlanta, GA, Conf-800428, Vol. I, p. 675, 1980.

11. Beer, J.M., Massimilla, L., and Sarofim, A.F., Inst. Energy Symposium Series 4: Fluidized Combustion, Systems and Applications, p. IV.5.1, 1980.

12. Divilio, R. J., Towers, T.A., and Chandran, R.R., "Applications of FBCBAL and B&W Combustion Model to the EPRI AFBC Demonstration Programs", 1988 EPRI Seminar, Palo Alto, CA, May 3-5, 1988 (to be presented).

**TABLE 1. PERFORMANCE CODE INPUT DATA**

| Model Input Parameter | Description | Source |
|---|---|---|
| Unit cell cross section<br>Feedpoint location<br>Bed temperature<br>Coal feed rate<br>Bed height<br>Transport air<br>Primary air<br>Bed material density<br>Bed weight<br>Freeboard cross section<br>Bed material size distribution<br>Coal size distribution at the hopper | Operating conditions | Validation test conditions or design specifications |
| Coal composition<br>Coal density<br>Higher heating value | Coal properties | ASTM procedures |
| Coal attrition parameters | FSATT subroutine | Feed System attrition tests |
| Gas dispersion coefficient<br>Solids velocity<br>Solids dispersion coefficient<br>Entrainment rate coefficient | Hydrodynamics module | Literature |
| Coal particle heatup time<br>Volatile yield<br>Devolatilization rate constant<br>Volatile composition<br>Char fraction<br>Char reactivity<br>Char composition | Chemical kinetics module | Fixed bed reactor |
| Swelling index<br>Fragmentation index | Chemical kinetics module | Bench-scale AFBC unit |
| CEMA rate constant<br>Weight fraction of flakes | Solids distribution module | Bench-scale AFBC unit |

## TABLE 2. SENSITIVITY ANALYSIS

| Parameter | Type | Description | Sensitivity | |
|---|---|---|---|---|
| | | | 1 x 1 B&W | 20 $MW_e$ TVA |
| DBED | Operational | Bed material mean size | Negl | Negl |
| DHOP | Operational | Coal feed size distribution | High | High |
| COFATT | Unit/Fuel | Feed system attrition coeff | Medium | High |
| ATTEXP | Unit/Fuel | Feed system attrition exponent | Medium | High |
| COFUSC | Hydrodynamic | Coarse particle velocity coeff | Medium | Medium |
| COFDSC | " | Coarse particle dispersion coeff | Low | Medium |
| COFDO | " | Gas dispersion coeff | Low | High |
| COFUSF | " | Fines velocity coeff | Low | Low |
| COFDSF | " | Fines dispersion coeff | Low | Low |
| COFUOE | " | Entrainment rate coeff | High | Medium |
| FRFLAK | Fuel | Weight fraction of CEMA flakes | Negl | Low |
| KCAN | " | CEMA rate constant | Low | Low |
| COFTAU | " | Coal particle heat-up time coeff | Negl | Medium |
| VYULT | " | Ultimate volatile yield | High | Low |
| COFFVY | " | Volatile yield coeff | Negl | Negl |
| COFKV | " | Devolatilization rate coeff | Low | Medium |
| KVEXP | " | Devolatilization rate exponent | Low | Low |
| SIULT | " | Swelling index upper limit | Low | Low |
| COFRCC/ RCCACT | " | Char reactivity (Pre-exponential factor/activation energy) | High | High |
| $E_{ibc}$ Range (%) | | | 68 - 91 | 63 - 85 |

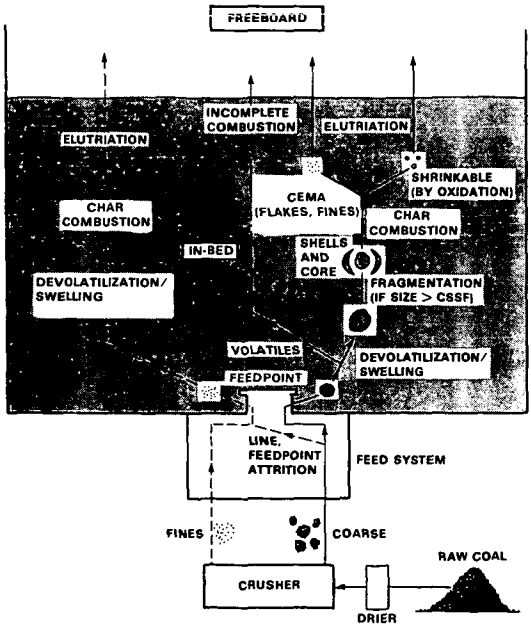


**Figure 1. Coal combustion sequence for underbed feed.**

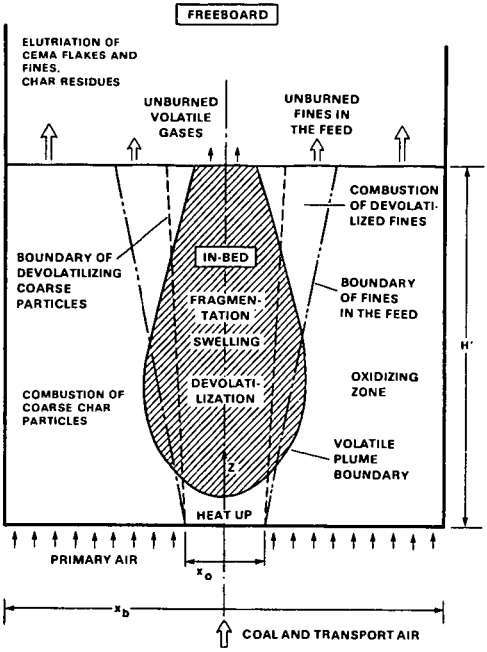


**Figure 2. Conceptual model of in-bed combustion.**

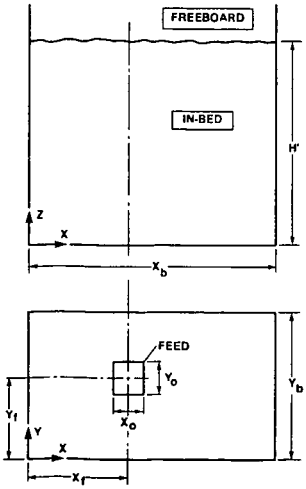


**Figure 3. Unit cell coordinate geometry.**

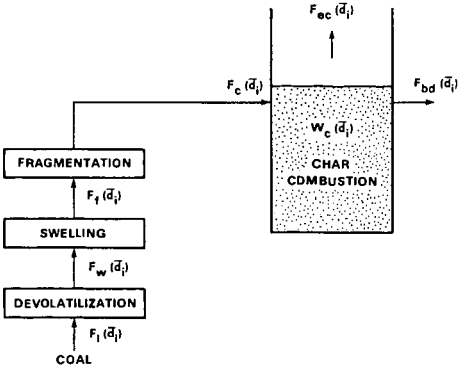


**Figure 4. Flow rates pertaining to different steps of the combustion sequence – Region II model.**

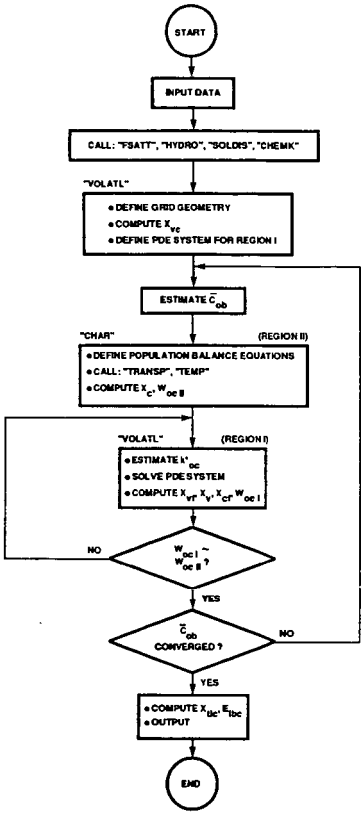


**Figure 5. Performance code flowchart.**

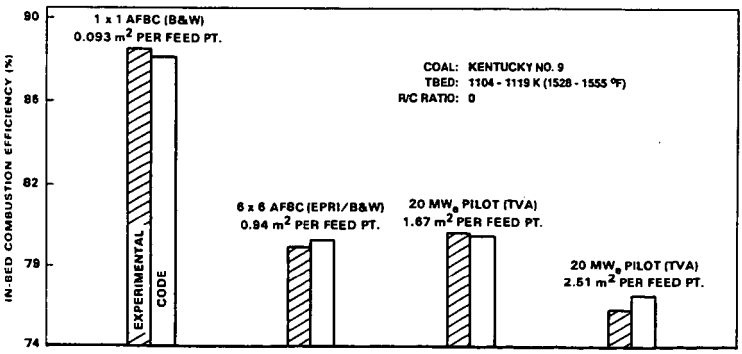


**Figure 6. Comparison of performance code predictions with experimental data.**

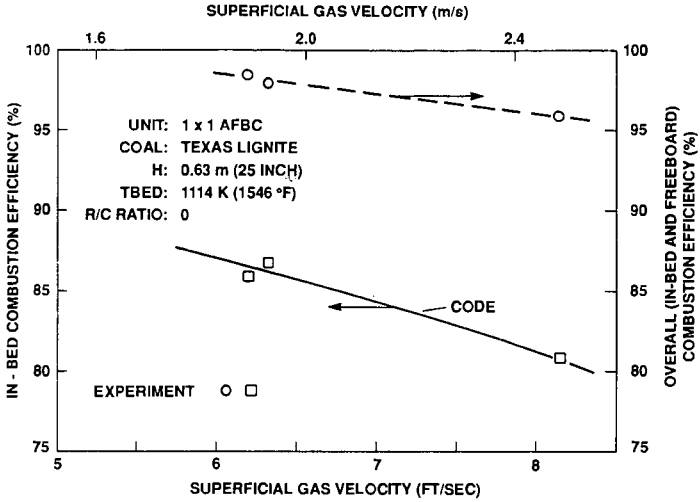


**Figure 7. Comparison of code predictions with data.**

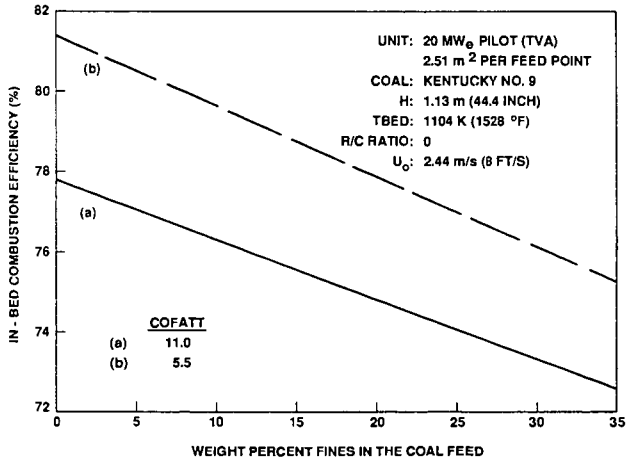


**Figure 8. Simulation for coal hopper particle size distribution.**

# CONTINUOUS KINETIC LUMPING FOR LIGNITE LIQUEFACTION

P. K. Moore and R. G. Anthony

Department of Chemical Engineering
Texas A&M University, College Station, TX 77843

## INTRODUCTION

The need for an alternative energy source to counteract both short-term petroleum supply interruptions and the eventual depletion of petroleum reserves has resulted in an increased interest in the utilization of domestic coal. While coal can be utilized directly for energy applications such as electrical power generation, much of the petroleum demand is based in the liquid fuel and liquid feedstock areas. This potential demand for liquid fuel and feedstock has caused a renewed interest in coal liquefaction technology. However, the development of coal liquefaction technology to an industrially applicable level has been hindered by the lack of a suitable kinetic model. Current kinetic models are based upon simplified analytical techniques in which components are lumped into several solubility or volatility classes. These models must be used cautiously since compounds within the same solubility or volatility class do not necessarily undergo similar reactions. In addition, each kinetic model applies only to the particular coal studied. A critical need exists for a kinetic model based upon the actual chemical reactions occurring and which is applicable to a variety of coals. The development of such a kinetic model is the goal of the coal liquefaction studies at Texas A&M University.

The development of a kinetic model capable of describing a complex, many-component reaction, such as coal liquefaction, requires the investigation of several supporting areas: experimental reactions, analytical method, component lumping, reactor modeling, and parameter estimation. All of these areas depend on each other; hence, the resulting kinetic model is dependent on, and limited by, each area. Any attempt to improve the kinetic model must therefore effect an improvement in one or more of the supporting areas. The coal liquefaction research at Texas A&M University has resulted in significant advances in the areas of analytical technique, component lumping, and reactor modeling, thus providing the foundations for the development of a powerful new kinetic model.

The sections below describe the results which have been achieved and the course of the research now being followed in each of the supportive areas: experimental reactions, analytical method, component lumping, reactor modeling, and parameter estimation. In particular, several of the more significant developments are described and compared to the methods currently being used. These new developments include an improved analytical technique, the SEC–GC–MS method, based upon a combination of size-exclusion chromatography (SEC), gas-chromatography (GC), and mass spectroscopy (MS); an optimum component lumping technique developed by embedding the classical kinetic and equilibrium equations into the vector space of generalized functions; and a reactor model which incorporates an equation-of-state equilibrium calculation to predict the compositions of the reactants in both the liquid and vapor phases.

## EXPERIMENTAL REACTIONS

The commonly used types of coal liquefaction laboratory reactors have been discussed in detail by Shah (1). Continuous-flow reactors were not considered for this study due to the possibility of different residence times existing for each phase, a condition difficult to model, and due also to the difficulty in establishing a steady-state condition for the solid phase. The batch reactors commonly used in laboratory studies thus far are the batch autoclave, the rapid-injection autoclave, and the tubing-bomb microreactor. Of these three, the tubing-bomb microreactor was chosen for this kinetic study due to the reactor's low thermal inertia, good heat and mass transfer characteristics, and the small amount of reactor feed required (2).

The tubing-bomb reactors used at Texas A&M typically consist of a 6 inch long 3/4 inch o.d. stainless steel tube capped on each end. A thermocouple extends into the reactor via a 1/4 inch o.d. thermowell assembly. A 1/8 inch o.d. line to the reactor serves for gas charge and evacuation in addition to providing for pressure measurement during an experimental run. Various tubing-bomb reactors used at Texas A&M and the corresponding experimental procedures are described by Helton (3), Haley (4), Shumbera (5), and Koker (6).

## ANALYTICAL METHOD

The purpose of an analytical method, as applied to kinetic model development, is to provide a measure of the change which has occurred during the experimental reaction. This "measure of change" provided by the analytical method must 1) relate to the kinetic properties of the reaction mixture, so that the fundamental equations governing the chemical reactions may be easily applied, and 2) the properties relating to the uses of the reaction product, so that the resulting kinetic model may be used to optimize product yield and composition. When the reaction mixture is simple, consisting of relatively few components, the analytical technique provides an exact analysis; thus, both Criteria 1 and 2 above are readily satisfied. However, when the reaction mixture is complex, consisting of many components, an exact analysis is often impossible. An approximate analytical technique must then be used, and this approximate technique must attempt to satisfy the above criteria. Therein lies the failing of the approximate analytical techniques commonly used for coal liquefaction studies: solubility analysis and distillation analysis.

Solubility analysis consists of the separation of coal liquefaction products into portions which are soluble in a series of extraction solvents. A commonly used series of solvents consists of hexane, toluene, and tetrahydrofuran. Hexane solubles are designated as "oil," toluene solubles are designated as "asphaltenes," and tetrahydrofuran solubles are designated as "preasphaltenes." All of the material insoluble in tetrahydrofuran is considered to be unreacted coal, char, and ash. The solubility analysis method provides a rough picture of the changes occurring in the reaction mixture, and kinetic models have been developed using the component classes: oil, asphaltenes, preasphaltenes, and unreacted coal. However, the solubility analysis method fails to satisfactorily meet Criteria 1 and 2 mentioned above.

First, each component class, or lump, consists of a broad range of component types. The kinetic behavior of the component lump will, in general, depend in a complicated manner upon the components contained within the lump. Therefore, any information relating to actual molecular mechanism of coal liquefaction, which is formulated in terms of individual molecular types, will be difficult to incorporate into the overall kinetic model, which is formulated in terms of the lumped component classes. Furthermore, coal liquefaction is a multiphase process; the individual components within the reaction mixture are dispersed throughout the solid, liquid, and vapor phases. Since each phase may be expected to exhibit different reaction behavior, the distribution of each component in each phase may significantly affect the kinetic behavior of the reaction mixture. Hence, properties which describe the affinity of each component to a particular phase, such as volatility, should be included in the kinetic model. The solubility analysis method fails to provide such information, since each solubility lump may contain components with a broad range in volatility.

The solubility analysis also fails to satisfy the product criterion; the solubility lumps — oil, asphaltenes, and preasphaltenes — are difficult to relate to the end uses of the product. When the liquefaction products are to be used as chemical feedstock, the engineer is primarily interested in a particular component or group of components. The solubility lumps which contain the desirable group of components may also contain undesirable components. Hence, the liquefaction process cannot be easily optimized for the desired products. When the liquefaction products are to be used as fuel or fuel feedstock, volatility properties of the product become important; however, solubility lumps fail to incorporate such volatility information.

Distillation analysis also fails to satisfy the reaction and product criteria. Distillation

analysis separates the mixture into several volatility classes. However, these volatility classes contain several types of chemical components, with each component type exhibiting different kinetic behavior in the reaction mixture; hence, the volatility lumps, like the solubility lumps, are unable to provide a precise description of the reaction. Furthermore, a product description in terms of volatility lumps fails to provide chemical information about the product, which is often needed when the product is to be used as a chemical feedstock.

The failings of the traditional solubility and distillation analyses led to the development of the SEC–GC–MS analytical method at Texas A&M. In the SEC–GC–MS method, the tetrahydrofuran soluble portion of the liquefaction products is first separated into several fractions (usually 9) using size-exclusion chromatography (SEC) with tetrahydrofuran (THF) as the mobile phase. As shown by Anthony et al. (7), size-exclusion chromatography effects a separation of the mixture based upon molecular size and functionality, with alkanes eluting first, followed by phenols, and then aromatics. Each of the fractions obtained using size-exclusion chromatography is then analyzed using gas chromatography (GC), which effects a separation based upon volatility. A mass spectroscopic (MS) detector can be used with the GC to aid in peak identification. Details of the SEC–GC–MS method have been provided by Anthony et al. (8).

The SEC–GC–MS analytical method provides a distribution of the coal liquid sample with respect to the SEC retention index, which provides a measure of component functionality, and with respect to the GC retention index, which provides a measure of component volatility. This bivariate distribution (Figure 1) provided by the SEC–GC–MS method exhibits several advantages over the univariate distributions provided by the solubility and distillation methods. First, since the SEC–GC–MS method provides a separation of the mixture based on both volatility and component functionality, the bivariate distribution is easily related to both the kinetic properties of the reaction mixture and to the properties relevant to the desired uses of the product. Second, since all components eluting within a particular SEC–GC retention region can be expected to have similar chemical and volatility properties, lumping of neighboring components (components which elute with similar SEC and GC retention times) may be justified. Such lumping may be required when the chromatograms are poorly resolved, or lumping may be desirable to reduce the number of parameters within a kinetic model. Furthermore, all coals can be expected to yield the same types of components upon liquefaction, and these types of components should consistently elute with the same SEC and GC retention time, independent of the coal type being liquefied. This separation of the kinetic model from coal type was not possible with solubility analysis, since solubility lumps derived from different coals do not always contain the same amount of each component, or even the same components.

## CONTINUOUS LUMPING

The SEC–GC–MS analytical method yields an overwhelming amount of information. The method provides not only a good overall description of the mixture compositions, but also often provides detailed concentration information about individual components. However, such detail is often not necessary or desirable. The optimum kinetic model should provide the best possible mixture description using the fewest possible parameters. A kinetic model incorporating a large number of parameters is difficult to use; first, the presence of a large number of parameters makes parameter estimation difficult, and second, the large model becomes difficult to apply in subsequent design situations. Hence, a method was needed whereby the detailed SEC–GC–MS analysis could be parameterized using the fewest possible terms while retaining the bulk of the useful information from the SEC–GC–MS analysis. This parameterization procedure is referred to as "component lumping," or simply as "lumping."

The traditional form of lumping is pseudocomponent lumping, where groups of components are treated as individual components. However, we have developed (9) an alternate method, "continuous-lumping," which is particularly well-suited for calculations involving chromatographic data. Continuous-lumping can be considered a generalization, or reinterpretation, of

the theory of continuous mixtures, as described by Cotterman et al. (10) for thermodynamics and by Aris and Gavalas (11) for reaction kinetics. However, our developments have shown (9) that the continuous mixture hypothesis is not required for the method to be valid.

For continuous-lumping, the individual component properties — concentration, volatility, and reactivity — are considered to be functions of some suitable component index, such as molecular-weight or boiling-point. These component indices, in turn, can then be related to chromatographic retention-times. The classical description of the mixture composition (mole fractions) is then converted to a distribution function (similar to a chromatogram) written in terms of the component index. The classical relationships between the component properties (i.e., equilibrium relations, reaction-rate equations, etc.) are then converted to the functional form. The final step in the continuous-lumped method is the expansion of the functional equations in terms of generalized Fourier series to obtain an approximate set of algebraic equations — the continuous-lumped equations.

The bivariate distribution provided by the SEC–GC–MS analytical method is particularly well suited to the continuous lumping method, since the kinetic and volatility properties of the components vary gradually with the SEC and GC retention indices. In fact, the fundamental parameters of a kinetic model may be considered to be functions of the component indices instead of the usual interpretation, where the kinetic parameters are associated with the set of pseudo-components. Thus, the problem of kinetic model development becomes the determination of a kinetic parameter surface over the SEC–GC component index plane. This approach frees the model from the dependence on a particular choice of a pseudo-component lumping scheme, thus enabling comparison of data from two separate investigations in which different lumping schemes happened to be used. Furthermore, all of the components in a small neighborhood of a particular SEC–GC index pair can be expected to be chemically similar; therefore, a particular component from the neighborhood may be selected for a kinetic study. Such a "model compound" study possesses an advantage over a kinetic study of the complete coal liquid, since a particular kinetic parameter may often be determined with greater precision when the effects of the other kinetic parameters have been removed.

The detailed theory behind the continuous lumping method, as applied to vapor-liquid equilibrium calculations, has been developed by Anthony and Moore (9). The theory is presently being extended and fully developed to include reaction kinetics. The continuous lumping method will be incorporated in a reactor model (described in the next section) which will predict conversion and product distributions for the tubing-bomb reactor.

## REACTOR MODELING AND PARAMETER ESTIMATION

After the products of the experimental liquefaction reactions have been characterized using the SEC–GC–MS analytical method and the continuous lumping method, the resulting parameterized data, which describes the changes that occur during reaction, must be related to the fundamental kinetic model (in general unknown), which governs the changes that occur during reaction. When the assumed form of the kinetic model is simple, the kinetic and reactor model equations may be solved directly to obtain an analytical equation describing the reaction. The fundamental parameters within the kinetic model may then be estimated by fitting the analytical solution to the lumped data using a regression method. However, the assumed kinetic model and the reactor modeling equations often form a complex system, making an exact analytical solution difficult or impossible to obtain. The combined kinetic and reactor model equations, together with an assumed set of parameters, must then be solved using a numerical method to obtain predictions of reaction behavior. The combined kinetic and reactor model can then be incorporated into a parameter estimation routine, such as the Modified Marquart Method used by Tarng (12), in order to obtain optimum estimates of the kinetic parameters. This second approach, the reactor model — parameter estimation method, has been chosen to obtain estimates for the kinetic parameters, since the method is general and may therefore accommodate virtually any assumed form of the kinetic model.

Coal liquefaction is a complicated process involving reactions in and mass transfer between vapor, liquid, and solid phases; any theoretically based kinetic model must therefore account for the fundamentally different reactions and mechanisms in each phase. Heretofore, kinetic models have failed to incorporate this fact; the reaction mixture was treated as if it were one single phase, with any phase equilibrium effects being incorporated into the empirical kinetic model. Such a treatment is unacceptable, however, since different types of industrial reactors exhibit different types of phase equilibrium behavior. The kinetic model must, therefore, be based on the actual compositions in each phase, which must either be measured or predicted.

Measurements of phase compositions in a coal liquefaction reactor are always difficult and, in the case of the tubing-bomb reactor, may be impossible. However, as shown by Anthony et al. (13), an equation-of-state (EOS) vapor-liquid equilibrium calculation is capable of predicting the phase concentrations of key reactants, such as hydrogen, to a sufficient degree of accuracy. Figures 2 and 3 illustrate the prediction of VLE properties for a hydrogen–coal liquid mixture using an equation-of-state. Figure 2 shows an ASTM D–86 of a SRC–II coal liquid fraction. Bubble points for mixtures of this coal liquid with hydrogen were determined experimentally by Chao (14), as shown in Figure 3, where a VLE calculation using an equation-of-state is also shown. Note that the VLE calculation predicts the mole fraction of hydrogen in the liquid phase well. For this reason, plus the difficulty of sampling, an EOS vapor-liquid equilibrium calculation has been chosen to predict phase compositions in the reactor model. The incorporation of an EOS vapor-liquid equilibrium calculation into the reactor model has the disadvantage that the resulting kinetic model will depend on the particular EOS model chosen; however, the inaccuracies due to such a dependence are not likely to exceed the inaccuracies in the assumed form for the kinetic model. Furthermore, the EOS calculation may be used to find the conditions at which the phase compositions yield the optimum reaction behavior; this predictive function of the reactor model would not be easily available if the phase compositions were obtained by measurement. Hence, reactor conditions of particular interest, consisting of temperatures and pressures at which the liquid-phase reactions may be enhanced (such as the near-critical and supercritical regions), may be investigated.

## CONCLUSIONS

The key to an improved coal liquefaction kinetic model is the development of an analytical method capable of separating the reaction products into individual molecular components; The SEC–GC–MS analytical method satisfies this need by providing detailed compositional information, such as the chemical and volatility properties of each component. The tremendous detail provided by the SEC–GC–MS method can then be effectively parameterized using the continuous lumping method, which allows the detailed analytical results to be incorporated into complex kinetic and thermodynamic calculations, such as the equation-of-state VLE calculation described above. Thus, the SEC–GC–MS analytical method and the continuous lumping method, both developed at Texas A&M University, allow the application of advanced theory to the coal liquefaction process.

## ACKNOWLEDGEMENTS

The financial support of the U. S. Department of Energy (Project Number DE–AC18–83FC10601), the Texas A&M University Center for Energy and Mineral Resources, and the Texas A&M Engineering Experiment Station is gratefully acknowledged. The Energy Research Center at the University of North Dakota furnished samples for the study.

REFERENCES


1. Shah, Y. T., *Reaction Engineering in Direct Coal Liquefaction.* Reading, Mass.: Addison Wesley, 1981.

2. Gallakota, S. V., and J. A. Guin, "Comparative Study of Gas-Liquid Mass Transfer Coefficients in Stirred Autoclaves, Tubing Bomb Microreactors, and Bubble Columns," *Ind. Eng. Chem. Process Design and Dev.*, vol. 23, pp. 52–59, 1984.

3. Helton, T. E., "A Solvent Study of the Direct Liquefaction of Big Brown Lignite," Thesis, Texas A&M University, Texas, 1986.

4. Haley, S. K., "A Kinetic Model for the Liquefaction of Texas Lignite," Thesis, Texas A&M University, Texas, 1980.

5. Shumbera, D. A., "Reaction Rate Kinetics for the Non-Catalytic Hydrogenation of Texas Lignite with Tetralin and Hydrogen Gas," Thesis, Texas A&M University, Texas, 1980.

6. Koker, A., "A Study of the Direct Liquefaction of Indian Head Lignite," Thesis, Texas A&M University, Texas, 1985.

7. Anthony, R. G., C. V. Philip, and P. K. Moore, "Kinetic Model Development for Low-Rank Coal Liquefaction," Quarterly Report: Jan. 1, 1986 – March 31, 1986; DOE/FC/10601-11.

8. Anthony, R. G., "Kinetic Model Development for Low-Rank Coal Liquefaction," Quarterly Report: Jan. 1, 1985 – March 31, 1985; DOE/FC/10601-7.

9. Anthony, R. G., and P. K. Moore, "Kinetic Model Development for Low-Rank Coal Liquefaction," Quarterly Report: April 1, 1986 – June 30, 1986; DOE/FC/10601-12.

10. Cotterman, R. L., R. Bender, and J. M. Prausnitz, "Phase Equilibria for Mixtures Containing Very Many Components. Development and Application of Continuous Thermodynamics for Chemical Process Design." *Ind. Eng. Chem. Process Design and Dev.*, vol. 24, pp. 194–203, 1985.

11. Aris, R., and G. R. Gavalas, "Theory of Reactions in Continuous Mixtures," *Phil. Trans. Roy. Soc. London*, vol. A260, pp. 351–393, 1966.

12. Tarng, Y. J., "A Reactor and Kinetic Model for Liquefaction of Lignite in an Upflow Tubular Reactor," Dissertation, Texas A&M University, Texas, 1985.

13. Anthony, R. G., A. Koker, P. K. Moore, Y. Tarng, "Kinetic Model Development for Low-Rank Coal Liquefaction," Quarterly Report: Oct. 1, 1983 – March 31, 1984; DOE/FC/10601-4.

14. Kim, H. Y., T. M. Guo, H. M. Linn, and K. C. Chao, "Equilibrium Vaporization of Coal Liquids," Paper No. 15 *c*, AIChE Annual Meeting, November 1983, Washington, D. C.

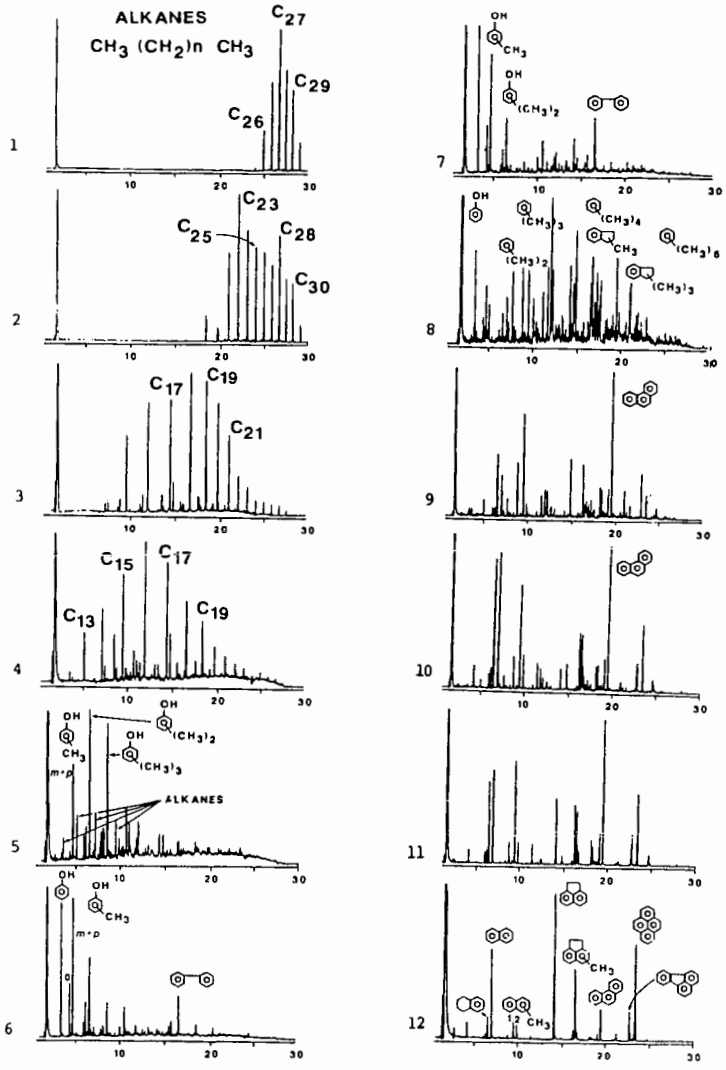


Figure 1 – SEC–GC–MS Material Distribution

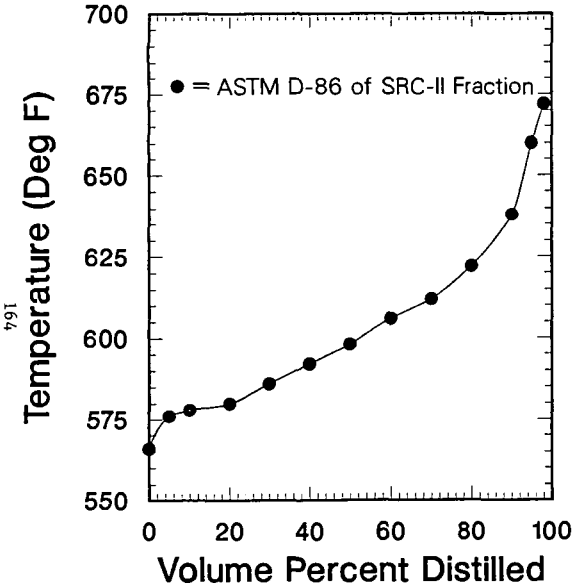


Figure 2 – ASTM D–86 of

SRC–II Coal Liquid Fraction.

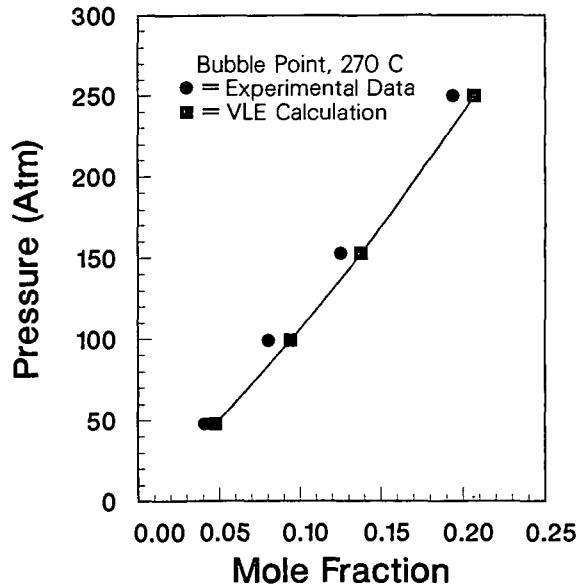


Figure 3 – Bubble Points of

Hydrogen / SRC–II Coal Liquid Mixture

# FUNDAMENTAL MODELLING OF PULVERIZED COAL AND COAL-WATER SLURRY COMBUSTION IN A GAS TURBINE COMBUSTOR

A. Chatwani, A. Turan and F. Hals

Avco Research Laboratory, Inc.
2385 Revere Beach Parkway
Everett, MA 02149

## INTRODUCTION

A large portion of world energy resources is in the form of low grade coal. There is need to utilize these resources in an efficient and environmentally clean way. The specific approach under development by us is direct combustion in a multistage slagging combustor, incorporating control of $NO_x$, $SO_x$, and particulates. While experimental verification provides the ultimate proof of acceptability, there is an increasing realization that the detailed flow field computations of the combustion process can provide much of the necessary understanding and aid in the development process. A number of papers have dealt with the modelling of pulverized coal combustion in burners where flow field is predominantly two-dimensional (1-3). Many elements of this coal combustion model have been developed and validated under those conditions.

Our main interest is in the combustors where three-dimensional effects are of prime importance. An example of such a combustor is shown schematically in Fig. 1. The toroidal vortex combustor is currently under development through a DOE contract to Westinghouse and subcontract to ARL. This subscale, coal-fired, 6 MW combustor will be built and become operational in 1988. The coal fuel is mixed with preheated air, injected through a number of circumferentially-located jets oriented in the radius axis planes. The jets merge at the centerline, forming a vertically directed jet which curves around the combustor dome wall and gives rise to a toroidal shaped vortex. This vortex helps to push the particles radially outward, hit the walls through inertial separation and promote slagging. It also provides a high intensity flow mixing zone to enhance combustion product uniformity, and a primary mechanism for heat feed back to the incoming flow for flame stabilization.

Work describes the essential features of a coal combustion model which is incorporated into a three-dimensional, steady-state, two-phase, turbulent, reactive flow code. The code is a modified and advanced version of INTERN code originally developed at Imperial College which has gone through many stages of development and validation. Swithenbank et al[4-5] have reported spray combustion model results for an experimental can combustor. The code has since then been modified by and made public under a US Army program[6]. A number of code modifications and improvements have been made at ARL. The earlier version of code was written for a small CDC machine which relied on frequent disk/memory transfer and overlay features to carry the computations resulting in loss of computational speed. These limitations have now been removed. For spray applications, the fuel droplet vaporization generates gaseous fuel of uniform composition; hence the earlier formulation relied upon the use of conserved scalar approximation to reduce the number of species equations to be solved. In applications related to coal fuel, coal pyrolysis leads to the formation of at least two different gaseous fuels and a solid fuel of different composition. We have therefore removed the conserved scalar formulation for the sake of generality and easy adaptability to complex fuel situations.

## Pulverized Coal Combustion Model

Combustion of pulverized coal particles is generally assumed to be a two-stage process consisting of devolatilization or pyrolysis of coal and heterogeneous char oxidation and gasification. The model adopted to describe pyrolysis is that of Kobayashi, et al.[7] This model proposes the use of two competing first order reactions to describe particle mass loss during pyrolysis. The process is described as

$$\begin{aligned} DAF &\xrightarrow{k_1} \alpha_1 V_1 + (1 - \alpha_1)\, S_1 \\ DAF &\xrightarrow{k_2} \alpha_2 V_2 + (1 - \alpha_2)\, S_2 \end{aligned} \qquad 1)$$

where $V_1$ and $V_2$ are volatiles of approximate elemental ratio $C_6H_{12}$ and $C_6H_6$, and $S_1$ and $S_2$ are char residuals containing mostly C. Specifically for a dry ash free (daf) coal of the type $CH._8$, these reactions can be expressed as

$$CH._8 \xrightarrow{k_1} \frac{.4}{6}\, C_6H_{12} + .6\ C,$$

and 2)

$$CH._8 \xrightarrow{k_2} \frac{.8}{6}\, C_6H_6 + .2\ C.$$

The rate of disappearance of daf coal is given by

$$-\frac{d}{dt}\, m_{daf} = (k_1 + k_2)\, m_{daf} \qquad 3)$$

where $m_{daf}$ is the mass of dry ash free coal, $k_1$ and $k_2$ are rate constants given by

$$\begin{aligned} k_1 &= 3.7 \times 10^5 \times \exp\,(-\ 8860/T) \\ k_2 &= 1.46 \times 10^{13} \times \exp\,(-\ 3017/T) \end{aligned} \qquad 4)$$

It should be noted that Equation 2 leads to volatiles yield of 0.43 and 0.81 for slow and very rapid heating respectively. It is relatively easy to modify composition of volatiles to fit the experimental data for different coal ranks including their oxygen, nitrogen, and organically bound sulfur content. The devolatilization of coal is assumed to take place without change in the particle radius and leaves behind a lighter porous particle.

## Char Oxidation and Gasification Model

Char gasification may be treated approximately as a three-stage process consisting of (i) diffusion of gaseous species to the surface, (ii) surface reaction, and (iii) diffusion of products to the bulk gas. Any of the processes may be a rate controlling step depending on the gas phase conditions, particle size and temperature, and particle pore structure. The model adopted is an extended version of Field[8] where surface diffusion and chemical reaction are taken into account. Three different surface reactions are included in the model, viz,

$$C + \frac{1}{2} O_2 \xrightarrow{k_3} CO,$$

$$C + CO_2 \xrightarrow{k_4} 2\ CO, \qquad 5)$$

and

$$C + H_2O \xrightarrow{k_5} CO + H_2.$$

For the sake of simplicity, it is assumed that all three reactions proceed independent of each other so that the char consumption rate is sum of individual rates. Rate of $O_2$ diffusion to the surface is given by

$$\frac{d}{dt} m_{O_2} = - k_D\ A_s\ (Y_{O_2}^{\infty} - Y_{O_2}^{s}) \qquad 6)$$

and the rate of $O_2$ consumption at the surface is given by

$$\frac{d}{dt}\ m_{O_2} = - k_r \cdot A_s \cdot Y_{O_2}^{\infty} \qquad 7)$$

Under quasi-steady-state, the two rates from Equations 6 and 7 balance each other and unknown quantity $Y_O$ can be eliminated to give

$$\frac{d}{dt}\ m_{O_2} = - k_{eff} \cdot A_s \cdot Y_{O_2}^{\infty} \qquad 8)$$

where $k_{eff} = k_r k_D/(k_r + k_D)$. The diffusion rate $k_D$ is related to the laminar diffusion coefficient, and the rate constants $k_3$ - $k_5$, taken from Stickler,(9) are given by

$$k_3 = 3.24 \times 10^{10} \times \exp\ (- 14500/T),$$

$$k_4 = 5.75 \times 10^{13} \times \exp\ (- 43200/T), \qquad 9)$$

and

$$k_5 = 6.38 \times 10^{11} \times \exp\ (- 30300/T).$$

Heterogeneous char combustion is assumed to take place at the outer surface resulting in the removal of material from the surface at the constant particle density.

Devolatilization or blowing out of gaseous products hinders the diffusion of gas phase species to the surface. It is assumed that char oxidation does not begin until the devolatilization is complete.

Coal Water Slurry Combustion Model

The presence of water in pulverized coal either as moisture or as a slurry forming medium further complicates the modelling of coal pyrolysis processes. In general, the size distribution of coal slurry droplets is governed by the injector performance, and a typical slurry droplet may consist of many parent coal particles. The slurry droplet may undergo many different processes depending on the history of heating rates to which a particle is

subjected; these may include swelling under simultaneous or sequential vaporization of water and coal gaseous products, shattering of droplet into parent coal particles or even smaller particles, or fusion of porous char and ash particles. The model adopted here is the most simplistic one, which will be replaced by a more realistic model in the future. We assume that water vapor and coal devolatilization occur in a sequential process, with each droplet consisting of a single coal particle and a corresponding mass of water. Hence the spray size distribution is dictated by the original coal particle size distribution assumed. The initial step in the heating of the droplet is to increase particle temperature to the saturation temperature of water. This is followed by the water vaporization at the constant particle temperature until the particle is dry. Once the particle is dried it behaves like a dry coal particle. The sequential vaporization model has been found to be adequate for the case of coal water slurry turbulent diffusion flames.(10)

Gaseous Combustion Model

The original version of INTERN incorporated a two step reaction scheme for which differential transport governing the evolution of the mixture fraction f, mass fraction of unburned fuel $m_{fu}$; and mass fraction of CO, $m_{CO}$, were solved. Concentrations of other reactants including $m_{O2}$ as well as equilibrium combustion products ($M_{CO2}$, $m_{H2O}$, $m_{N2}$, etc.) were obtained via algebraically formulated balance expressions.

To represent the combustion of two different kinds of volatiles and solids typicals of coal combustion, the following global mechanisms are postulated. The volatiles are assumed to combust to yield products CO and $H_2$ in the initial stage.

$$C_6H_6 + 3\ O_2 \xrightarrow{k_6} 6\ CO + 3\ H_2$$

$$C_6H_{12} + 3\ O_2 \xrightarrow{k_7} 6\ CO + 6\ H_2 \qquad 10)$$

The initial breakdown to CO and $H_2$ instead of $CO_2$ and $H_2O$ is chosen to represent the fuel rich combustion situation of interest here. Subsequent oxidation of CO and $H_2$ are given by

$$CO + 1/2\ O_2 \underset{k_{8b}}{\overset{k_{8f}}{\rightleftarrows}} CO_2$$

$$CO + 1/2\ O_2 \underset{k_{9b}}{\overset{k_{9f}}{\rightleftarrows}} H_2O \qquad 11)$$

Empirical rate constants $k_6$ to $k_9$ are required for finite rate kinetics. Reverse rate constants $k_{8b}$ and $k_{9b}$ are calculated from equilibrium considerations. For turbulent flows, the effective reaction rates are calculated from the eddy breakup model(11). In the absence of rate constants, the assumption of fast chemistry is invoked and all rates are limited by the turbulent mixing rates.

## RESULTS AND DISCUSSION

A number of cases were computed for the toroidal vortex combustor geometry of interest. The combustor configuration, and the inlet air flow conditions have been kept constant throughout these computations. The initial conditions are summarized in Table 1. The composition and size distribution of fuel have been varied parametrically to examine its influence on the flow field. The range of variations for the variables are summarized in Table 2. In all the computations reported here, it is assumed that the tip of the coal injector is located at the center of the air jet and in the plane of the combustor wall. Coal particles are assumed to leave the injector at surrounding air velocity, but at room temperature, and the mass flux of carrier gas is assumed negligible compared to the coal mass flux.

The computations were performed on a grid of 37 x 16 x 9 nodes by finite difference algorithm of INTERN code. The iterations were carried out until the absolute sum of mass residuals was below a few percent. A typical set of velocity vector plots is shown in Fig. 2. The results for the injector plane ($k = 5$) show the existence of the jet directed towards the centerline. This jet broadens as it approaches the centerline and changes into a wall directed jet which curves along the walls of the combustor dome and escapes the injector plane by flowing around the initial jet. A circular vortex is seen to exist in the left hand corner of the combustor in each plane.

The typical set of calculated trajectories for the pulverized coal particles are shown in Fig. 3. A total of eight different size groups were selected such that the mass fraction in each size group is uniform. The mass weighted mean diameter for the distribution is 50 μm which roughly corresponds to 80 percent minus 200 mesh. In the computations, the particles are injected at the injector plane and their trajectories are followed until one of the three conditions is met: (i) particle combusts and is converted to an ash particle, at which time it is removed from further consideration, (ii) the particle hits the wall, or (iii) particle exits the combustor.

The fate of the particle hitting the wall depends on the wall boundary conditions. If walls are slagging then a particle is captured by the slag, follow the slag and in the process react through pyrolysis or a char burning mechanism. Since in the present work details of slag wall layer flow are not resolved, two limiting cases of particle wall interaction are considered. In the first case it is assumed that any particle hitting wall is completely lost from further consideration, while in the second case it is assumed that a particle hitting the wall is completely decomposed into gaseous fuel at the constant temperature. The latter process will be approached in the limit of extremely hot and sticky slag of negligible velocity, so that all volatilization will occur in the vicinity of the impact point. Since in most cases of practical interest, the design should ensure maximum burning in suspension, details of wall particle interaction may not be critical to combustion stability and flow field structure. However, wall reaction can contribute extensively to combustion of large coal particles. They ordinarily dominate residence time requirements for pure suspension combustion, and are most effectively combusted via wall reaction, which effectively provides extended residence time. In terms of fuel energy utilization, this mechanism is most attractive under reducing flow conditions.

In the case of dry pulverized coal (Case 1) with a mass mean particle diameter of 50 μm, approximately 81 percent of the fuel is utilized before particles hit the wall. If the fuel is substituted with a coal water mixture containing 30 percent water (Case 2) but otherwise the same size distribution as the dry coal, the fraction of fuel utilized is slightly increased to 86 percent. The slight increase in the fuel utilization may possibly be due

to the increased contribution from the gasification rate. The overall characteristics of the flow are unchanged, and there is a slight decrease in the temperature levels. Particles up to 23 μm are completely converted to ash in less than 34 ms, while larger particles only react partially before hitting the wall. The presence of water in coal alone does not adversely affect the combustion process, and there is slight evidence to suggest a beneficial effect possibly due to increased gasification of the char (see Equation 5).

The combustion process is more strongly dependent on the initial size distribution. Reducing the mass mean size from 50 μm (80 percent minus 200 mesh) to 33 μm (80 percent minus 325 mesh) results in increase of the fraction utilized from 86 percent to 94 percent (Case 3). In many coal water slurry applications, as discussed before, the size distribution of droplets is governed by the injector performance. If it is assumed that the injector produces practically monosized droplets of 33 μm diameter (Case 4), then the fraction of fuel utilized is dramatically reduced to 58 percent. Thus, as is well known, size distribution plays an important role in the combustion process. In the presence of a typical broad size distribution, fine particles release energy to increase the temperature level so that a 33 μm droplet is 70 percent utilized before it hits the wall, while in the presence of monosized droplets, a 33 μm droplet is 56 percent utilized.

If one assumes that a droplet is utilized completely as it hits the wall (Case 5) then by definition fuel is completely converted to gaseous fuel. In all the cases examined here, the combustor is operated fuel rich and utilization of $O_2$ is complete. Even when the fuel is not completely combusted, the combustor outflow is devoid of any oxygen. The volatiles released in the pyrolysis phase are of $C_6H_{12}$ and $C_6H_6$ type, and some uncombusted volatiles (up to 2 percent by weight) are predicted. The presence of uncombusted volatiles may be due to the incomplete turbulent mixing of the volatiles or due to the inadequacy of the model which lacks the kinetic route for the dissociation or sasification of gaseous fuel to CO and $H_2$.

The combustor exit conditions are relatively insensitive to the initial size distribution and composition of fuel. The detailed temperature and species distributions inside the combustor, however, are strongly sensitive to the size distribution. As an example the temperature and CO mass fraction contours in the injector plane are compared in Figs. 4 and 5, respectively.

The ability of the code to compute complex three-dimensional combustor flow fields has been demonstrated. The purpose of the model work was specifically as a design tool for exploration of combustor geometry, sizing, and fuel choices. It was successful and useful in that regard. The model has given reasonable qualitative prediction of the toroidal vortex flow field under cold flow conditions.[12] Also, as the test data become available from the combustor development program, quantitative comparisons will be made and the model revised to improve physical assumptions.

Acknowledgement

This work was performed under the Department of Energy Contract No. DE-AC21-86MC23167 to Westinghouse, Subcontract to ARL under Westinghouse Purchase Order No. 293602.

References

(1) Lockwood, F. C., Rizvi, S.M.A., Lee, G. K. and Whaley, H., Twentieth International Symposium on Combustion, pp 513-522, Combustion Institute, Pittsburgh, 1984.

(2) Truelove, J. S., pp 523-530, ibid.

(3) Smoot, L. D., and Smith, P. J., Coal Combustion and Gasification, Plenum Press, New York, 1985.

(4) Swithenbank, J., Turan, A., Felton, P. G., and Spalding, D. B., AGARD Conference Proceeding No. 275 on Combustor Modelling, 1979.

(5) Turan, A., A Three-Dimensional Mathemetical Model for Gas Turbine Combustors, Ph.D. Thesis, University of Sheffield, 1978.

(6) Bruce, T. W., Mongia, H. C., and Reynolds, R. S. Combustor Design Criteria Validation, Vol. III, USARTL-TR-78-55, AVRAD Com, Fort Eustis, Virginia, March 1979.

(7) Kobayashi, H., Howard, J. B., and Sarofim, A. F., Eighteenth International Symposium on Combustion, p 411, The Combustion Institute, Pittsburgh, 1977.

(8) Field, M. A., Combust Flame, 14 237 (1970).

(9) Stickler, D. B., Becker, F. E., and Ubhayakar, S. K., AIAA Paper No. 79-0298.

(10) Srinivasachar, S., Farmayan, W. F., and Beer, J. M., Second European Conference on Coal Liquid Mixtures, 16-18 Sept., 1985, London.

(11) Magnussen, B.F., and Hertager, B. H., in Sixteenth International Symposium on Combustion, p 719, The Combustion Institute, Pittsburgh, 1977.

(12) Chatwani, A.U., and Turan, A. Submitted to Western States Meeting of the Combustion Institute, Salt Lake City, Utah, March 1988.

TABLE 1

COMBUSTOR CONFIGURATION AND INITIAL CONDITIONS

| | |
|---|---|
| Combustor Diameter | 0.35 m |
| Injector-Dome Length | 0.43 m |
| No. of Injectors | 4 |
| Injection Angle | 60 |
| Air Flow Rate | 0.37 kg/s |
| Air Injection Velocity | 70 m/s |
| Air Injection Temp. | 617 K |
| Air Pressure | 6 atm |

TABLE 2

INITIAL CONDITIONS FOR FUEL COMPOSITION

| | Case 1 | Case 2 | Case 3 | Case 4 | Case 5 |
|---|---|---|---|---|---|
| $\dot{m}_{fuel}$ | 0.051 | 0.073 | 0.073 | 0.073 | 0.073 |
| $\dot{m}_{water}/\dot{m}_{fuel}$ | 0.0 | 0.3 | 0.3 | 0.3 | 0.3 |
| $\dot{m}_{daf}/\dot{m}_{fuel}$ | 0.95 | 0.665 | 0.665 | 0.665 | 0.665 |
| d | 50 μ | 50 μ | 33 μ | 33 μ | 33 μ |
| f(d) | exp ( d/d) | exp ( d/d) | exp ( d/d) | δ (d/d) | δ (d/d) |
| ø | 1.3 | 1.3 | 1.3 | 1.3 | 1.3 |
| Particle/Wall Interaction Model | 1 | 1 | 1 | 1 | 2 |

(1) Particle Capture, no vaporization
(2) Particle Capture, Complete vaporization

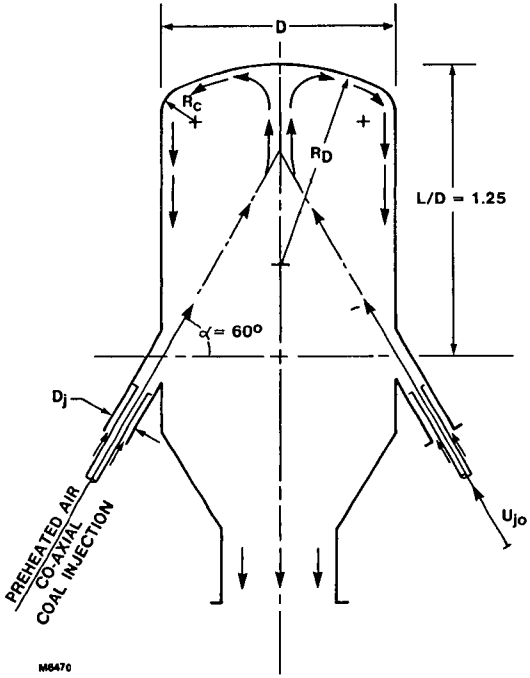


Figure 1 Schematic of Combustor Geometry

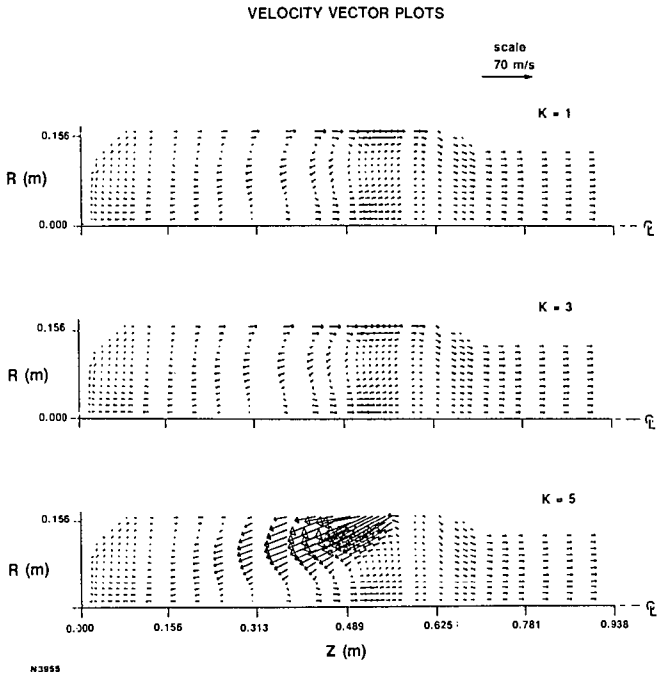


Figure 2 Typical Velocity Vector Plots in r-z Plane

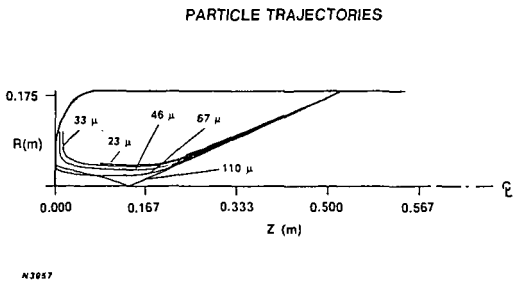


Figure 3 Typical Particle Trajectories in r-z Plane

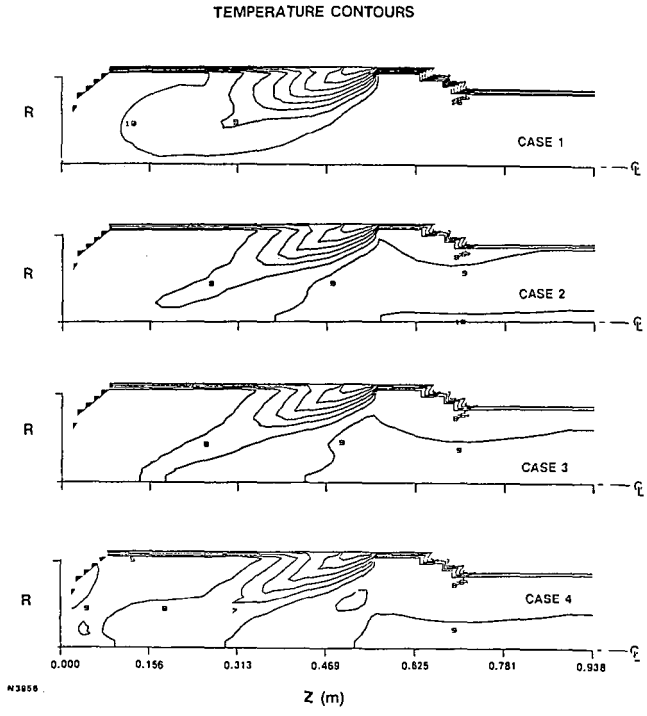


Figure 4 Computed Temperature Contour Plots.
Contour 1 = 300K, Contour 11 = 2800K, increment = 250K

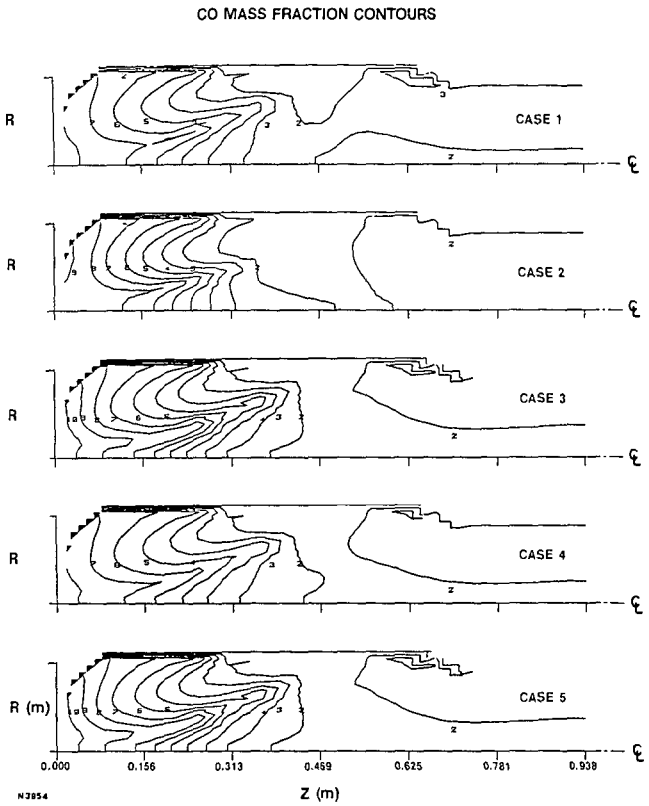


Figure 5 Computed CO Mass Fraction Contour Plots.
Contour 1 = 0, Contour 11 = 0.4, increment = 0.04

# MODELING OF AGGLOMERATION IN A FLUIDIZED BED

A. Rehmat, C. Huang,* R. Carty

Institute of Gas Technology
Chicago, Illinois 60616

H. Hariri, H. Arastoopour

Illinois Institute of Technology
Chicago, Illinois 60616

## ABSTRACT

A fluidized bed containing a central jet was operated with low-temperature melting materials to obtain the rate of agglomeration as well as to measure the temperature distribution within the fluidized bed. The rate of agglomeration was obtained as a function of operating parameters such as temperature and velocity. The agglomeration rate defined, as the rate of change in the number of particles of a particular size, was determined from the particle population balance using the experimental data.

The agglomeration model developed to predict the agglomeration rate constant based on the temperature distribution in the fluidized bed and the rate of entrainment of particles into the jet yielded values for the rate constants similar to the experimental values.

## INTRODUCTION

Fluidized-bed systems have been used in many coal conversion and other chemical processes. The fluidized beds are sometimes operated under agglomerating conditions to maximize coal utilization. The operating conditions in such cases are chosen to prevent the onset of sinters and defluidization (1,2,3,4). Under suitable operating conditions, ash agglomeration provides a very effective means of ash removal from a coal gasifier (5).

A distinguishing feature of an ash-agglomerating coal gasifier is a region where the temperature of the ash particles is high enough to make the surfaces sticky so that when they collide with each other, they adhere to each other to produce agglomerates. The rate of the formation of these agglomerates depends upon several factors such as the oxidant distribution within the bed, the overall fluidization velocity, and the ash properties. The oxidant distribution primarily influence the formation of the localized zone of high temperature within the fluidized bed, whereas the velocity influences the rate of particle collision as well as the particle entrainment within this zone. Based on these factors, a mathematical model for agglomeration has been developed to predict the rate of agglomeration in a fluidized bed containing a central jet. These rates are then compared with those obtained from the actual experiments.

## EXPERIMENTAL APPARATUS AND PROCEDURE

The apparatus consists of a 15.2-cm-ID glass fluidized-bed column, a metal section positioned beneath the glass column for temperature measurement and sampling, a gas distributor, a jet and fluidizing air heating system, temperature controlling and temperature measurement devices, and flow regulation and measurement systems (Figure 1). In the experiment, the jet and the fluidizing air temperatures

*Dr. Huang is currently at Nalco Chemical, Naperville, Illinois.

were varied and the temperature distribution and the agglomeration of the particles in the bed were measured. Polyethylene and polyolefin particles were used as bed material. Two types of gas distributors were used: a flat porous plate with a central jet and a porous cone with a central jet.

The jet gas temperature was adjusted to a value above the melting temperature of the bed material. The fluidizing air (auxiliary air) temperature was generally maintained lower than the softening temperature of the bed material to avoid sinter formation on the distributor.

## EXPERIMENTAL RESULTS

Figure 2 shows the effect of jet temperature on the agglomeration for a flat porous distributor with high-density polyethylene bed material. The measure of agglomeration is the weight percentage of particles greater than 850 μm, which increased linearly with residence time at each temperature level. The percentage of agglomerates also increased linearly with the fluidizing gas and bed temperatures; however, the jet air temperature was found to have the most significant effect on the agglomeration rate.

Another important factor affecting the rate of agglomeration in fluidized beds is the rate of particle entrainment into the high-temperature jet region. The entrainment rate depends on the stress distribution among the particles in the vicinity of the jet region. The direction, magnitude, and component of the stress toward the jet region depends on the cone angle. Figure 3 compares the agglomeration obtained with gas distributors having half-cone angles of 30°, 45°, 60°, and 90° (flat) after 2, 4, 6, and 8 hours of steady-state operation. The agglomeration increased as the cone angle decreased up to 45°. However, when the cone angle was decreased to 30°, the agglomeration was found to be less than that with cone angle of 45°. This implies that, although the steeper inverted cone directed the stress on the particles in the cone section more effectively toward the jet zone, the amount of particles in the cone section decreased resulting in lower entrainment of the particles. Because of this competitive effect, there exists an optimum cone angle for the maximum rate of agglomeration. This half-cone angle is approximately 45°. The optimum angle can be a function of particle-size distribution, shape and surface roughness of the particles, and the jet and the fluidizing air velocities.

The temperature distribution inside the bed was plotted using temperature measurements at more than 50 locations inside the fluidized bed. A typical temperature distribution profile in the area near the porous cone distributor is illustrated in Figure 4. More data concerning other operating conditions are given elsewhere. (6).

## DATA ANALYSIS

In a fluidized bed operated under agglomerating conditions, the rate of agglomeration between particles of two different sizes is proportional to the product of their concentrations. The proportionality constant is called the agglomeration rate constant.

To define the rate of agglomeration, we have adopted a definition that is analogous to the rate of chemical reaction. In a chemical reaction, the rate of reaction is defined in terms of the rate of change in the number of moles of a particular component in the reacting system due to its reaction. In the agglomeration process, what is changed during the process is the particle-size distribution. Therefore, it is appropriate to define the rate of agglomeration of particles of a particular size as the rate of change in the number of particles of that size. Due to the difficulty in measuring the number of particles of a particular size per unit volume of the fluidized bed, it has been found convenient

to express the rate of agglomeration of the particles in terms of its rate of change per unit mass of the bed material.

Since the overall rate of agglomeration is a measure of the rate of change in the number of particles of various sizes, the particle size is defined in a manner that is meaningful and facilitates the numerical computation in the particle population balance. It is assumed that all particles are made up of unit particles of mass $m_o$ and diameter $d_o$. This assumption implies that particle size is discrete and each particle has a mass equal to an integer times the mass of a unit particle. The particle whose mass is I times the mass of a unit particle ($I \times m_o$) is called particle size I. N(I) is defined as the number of particles of size I per unit mass of bed material and is called the mass number density of particles of size I. The rate of agglomeration of particles of size I can be expressed as:

$$R(I) = \frac{dN(I)}{dt} \qquad 1)$$

The value of the rate of agglomeration R(I) is dependent upon operating variables, including the temperature distribution in the bed, velocity, and particle-size distribution.

If we assume the agglomeration process as involving the collision of a single particle of size I and a single particle of size J, then it is reasonable to assume that the generation rate of agglomerates (I + J) forming from particles of size I and particles of size J is proportional to the collision frequency between these particles. As the number of collisions between particles of any two particular sizes is proportional to the product of their mass number densities, the rate of generation of agglomerates of size (I + J) from particles of sizes I and J is:

$$R_{I,J} = K_{I,J} N(I) N(J) \qquad 2)$$

Here, $K_{I,J}$ is the agglomeration rate constant.

Particle Population Balance for Batch Process. In the population balance of the particles of a particular size I, all the possible combinations leading to the formation or consumption of size I particles are to be considered since particles of size I combines with other particles to form agglomerates of larger sizes; on the other hand, smaller particles may stick together and form agglomerates of size I. Using Equation 1, the rate of generation of agglomerates of size I from smaller particles is:

$$\frac{1}{2} \Sigma_{J=1}^{I} K_{I-J,J} N(J) N(I-J)$$

Similarly, the rate of consumption of particles of size I due to agglomeration is:

$$\Sigma_{J=1}^{L} K_{1,J} N(I) N(J)$$

where L is the size of the largest particles that exist in the bed. The population balance for particles of size I in batch process can thus be written as:

$$\frac{\partial N(I)}{\partial t} = \frac{1}{2} \int_1^I K_{I-J,J} N(J) N(I-J) dJ - \int_1^L K_{I,J} N(I) N(J) dJ \qquad 3)$$

Computation of Agglomeration Rate Constant. For the computation of the agglomeration rate constant from the data, it is first expressed in terms of the operating variables and particle sizes. This approach facilitates in solving the rate constant integral equations. The agglomeration rate constant $K_{I,J}$ can be

represented by the product of two functions; the first function, $k_{op}$, is dependent upon the operating conditions, and the other, $k(d_I,d_J)$, is size-dependent, as:

$$K_{I,J} = k_{op}\ k(d_I,d_J) \qquad 4)$$

It is difficult to obtain an expression for $k(d_I,d_J)$ from a theoretical standpoint. Based on the behavior of particles, one restriction that can be imposed on the functional form of $k(d_I,d_J)$ is that it should be symmetric with respect to $d_I$ and $d_J$. The ultimate functional form of $k(d_I,d_J)$ must be determined with the aid of experimental data.

Even with the assumptions of Equation 4, there are still too many possible combinations of $k_{op}$ and $k(d_I,d_J)$ to be tested, and further simplification of the testing procedure is needed. To achieve this, the particle population balance Equation 3, for a specific operating condition, is rearranged as follows:

$$k_{op} = [MN(I)/Mt]/[\frac{1}{2}\ \&_1^I\ k(d_{I-J},d_J)N(J)N(I-J)dJ - \&_1^L\ k(d_I,d_J)N(I)N(J)dJ] \qquad 5)$$

Thus, if the correct functional form of $k(d_I,d_J)$ is used in Equation 5, the calculated $k_{op}$ should have the same value for all of the particle sizes under specific operating conditions. This provides a means to test the functional form of $k(d_I,d_J)$. To find the correct functional form of $k(d_I,d_J)$, several symmetric functions with respect to $d_I$ and $d_J$ were substituted into Equation 5. Our studies showed that the functional form of

$$(d_I^4 + d_J^4)\ (\frac{1}{d_I^3} + \frac{1}{d_J^3})$$

results in a nearly constant value of $k_{op}$ over the whole particle size range at specific operating conditions. Therefore, $K_{I,J}$ can be expressed as:

$$K_{I,J} = k_{op}\ (d_I^4 + d_J^4)\ (\frac{1}{d_I^3} + \frac{1}{d_J^3}) \qquad 6)$$

The experimental data was used to calculate MN(I)/Mt; then the agglomeration rate constant $k_{op}$ was calculated using Equations 5 and 6. These values at different jet temperatures are shown in Table 1.

Table 1. THE CALCULATED VALUES OF $k_{op}$ BY PARTICLE POPULATION BALANCE USING EXPERIMENTAL DATA

| Jet Temp, °C | 144.4 | 143.3 | 142.8 | 142.2 |
|---|---|---|---|---|
| $k_{op}$ | $1.78 \times 10^{-9}$ | $1.20 \times 10^{-9}$ | $0.9 \times 10^{-9}$ | $0.45 \times 10^{-9}$ |

The value of $k_{op}$ increases significantly with a slight increase in jet temperature (Table 1 and Figure 2).

## AGGLOMERATION MODEL

As the hot jet gas stream is fed into the fluidized bed through the nozzle at a temperature substantially higher than the fluidizing gas temperature, a hot jet zone in the central portion of the bed is created. The concentration of solids in the jet zone is much lower than the solids concentration in the bulk of the bed. The solid particles enter the jet zone and exchange heat with the hot jet gas. The temperature of the particles in the jet zone increases; for some particles, this

results in partial melting. Upon the collision of two sticky particles, agglomeration may occur. Whether agglomeration takes place or not depends on several particle characteristics, including the relative velocity of the colliding particles, the thickness of the molten layer, and the viscosity of the molten material.

In the area near the jet, the particles are assumed to travel horizontally as they are entrained into the jet until they reach the jet boundary where particles enter into the jet zone and travel upward and finally exit from the top of the jet.

The entrainment of gas into a free jet has been given by Ricou and Spalding (7) as:

$$\frac{M_g}{M_{go}} = 0.32 \left(\frac{x}{d_n}\right)\left(\frac{\rho_{gi}}{\rho_{go}}\right)^{1/2} \qquad 7)$$

where —

$M_{go}$ = mass flow rate of initial jet gas, kg/h

$M_g$ = mass flow rate of initial and entrained gas, kg/h

$x$ = distance from nozzle exit, m

$d_n$ = nozzle diameter, m

$\rho_{gi}$ = density of entrained gas, kg/m$^3$

$\rho_{go}$ = density of gas exiting nozzle, kg/m$^3$

The presence of particles may affect the entrainment of gas into the jet stream. However, this effect was found to be negligible for the particle-size range (mean particle diameter = 350 μm) used in this study (8). The particles are entrained near the jet by the entrained gas; then they change direction and move upward due to momentum exchange with the jet gas. In this study, the flow of gas entrained to the jet is negligible in comparison with the jet gas flow rate. However, the rate of gas entrainment has been used to estimate the particle entrainment into the jet. As the particles enter into the jet, they travel upward due to the jet gas momentum. The following momentum balance was used to calculate the particle velocity in the jet zone.

$$\varepsilon_p \rho_p v_p \frac{dv_p}{dx} = \frac{3}{4} C_D \frac{\rho_g (v_g - v_p)^2}{g_c d_p} (1 - \varepsilon_p)^{-2.6} - (\rho_p - \rho_g) g \qquad 8)$$

where $x = o$ defines the location where the particles enter the jet zone. $v_p$ and $v_g$ are particle and gas velocities, respectively, $\varepsilon_p$ is the particles void fraction, and $C_D$ is the drag coefficient.

With the assumption that heat transfer to a particle is via heat exchange with its surrounding gas stream, the heat balance on a single particle in the region near and in the jet is expressed as:

$$\frac{\partial T_p}{\partial t} = \alpha \left[\frac{1}{r^2} \frac{\partial}{\partial r} \left(r^2 \frac{\partial T_p}{\partial r}\right)\right] \qquad 9)$$

where $\alpha$ is the particle thermal diffusivity.

$$\text{at } t = 0,\ T_p = T_B \qquad 10)$$

where $T_B$ is the bed temperature

$$\text{at } r = 0, \ \frac{\partial T_p}{\partial r} = 0 \qquad 11)$$

and

$$\text{at } r = R, \ K_S \frac{\partial T_p}{\partial r} = \begin{cases} h(T_v - T_p) & \text{near the jet} \\ h(T_j - T_p) & \text{at the jet zone} \end{cases} \qquad 12)$$

where $K_S$ is the thermal conductivity of particles, $T_j$ is jet temperature, and $T_v$ is the temperature in the region near the jet. (Both temperatures are measured experimentally.) The heat transfer coefficient h is computed using the following expression (9):

$$\frac{hd_p}{k_g} = 2.0 + 0.6 \left(\frac{d_p \rho_g (v_g - v_p)}{\mu_g}\right)^{1/2} \left(\frac{c_p \mu_g}{k_g}\right)^{1/3} \qquad 13)$$

where $k_g$ is the gas thermal conductivity, $v_g$ is the gas stream velocity, $v_p$ is the particle velocity, $d_p$ is the diameter of the particle, $\mu_g$ is gas viscosity, and $c_p$ is the specific heat.

Using the above heat and momentum equations, the temperature of a single particle $T_p$ at any location near and in the jet can be calculated.

If the calculated temperature of the particles, $T_p$, in the jet zone reaches the melting temperature, the outer layer of the particles melt, and the particles may agglomerate upon collision. For each collision, there is only a finite probability of $P^*$ leading to successful agglomeration.

The probability $P^*$ is the fraction of all the collisions, which meet the following agglomeration criteria:

$$\text{Relative Kinetic Energy of Colliding Particles} < \text{Potential for Dissipation of the Kinetic Energy due to Agglomeration} \qquad 14)$$

The relative kinetic energy of two colliding particles may be calculated from their velocities as —

$$\frac{1}{2} \frac{m_1 m_2}{m_1 + m_2} (v_1 - v_2)^2$$

where $m_1$ and $m_2$ are the masses of two particles with velocities $v_1$ and $v_2$, respectively. (See the Appendix.) To calculate the potential of two particles for energy dissipation, the thickness of the molten layer (i.e., the layer with temperature higher than melting point) is denoted as $\delta$ and may be calculated from the temperature distribution inside a particle at any location in the jet. We may write:

$$\text{Potential for Energy Dissipation} = 3\pi\mu_\ell \mid v_1 - v_2 \mid \left(\frac{\delta_1 + \delta_2}{2}\right)^2 \qquad 15)$$

where $\mu_\ell$ is the viscosity of the molten layer and $\delta_1$ and $\delta_2$ are the thicknesses of molten layers on the surface of the two particles. (See the Appendix.) The criterion for agglomeration thus becomes:

$$\frac{1}{2} \frac{m_1 m_2}{m_1 + m_2} \mid v_1 - v_2 \mid < 3\pi\mu_\ell \left(\frac{\delta_1 + \delta_2}{2}\right)^2 \qquad 16)$$

Agglomeration Kinetics. In our agglomeration model, all particles are assumed to be spherical and have the same density. Agglomerates are formed by the collision of a pair of sticky particles. The volume number density n(I), is defined as the number of size I particles per unit volume. The collision frequency between two particles of sizes I and J is proportional to their volume number densities and may be written as:

$$\begin{pmatrix}\text{Frequency of Collision} \\ \text{Between Particle Sizes I and J}\end{pmatrix} = \beta_{I,J} n(I)\ n(J) \qquad 17)$$

where β is the collision frequency constant. The agglomeration rate between size I particles and size J particles is expressed as:

$$R_{I,J} = P^{*} \beta_{I,J} n(I)\ n(J) \qquad 18)$$

The volume number densities n(I) and n(J) may be expressed as:

$$n(I) = E_I\ N(I) \qquad 19)$$

$$n(J) = E_J\ N(J) \qquad 20)$$

where $E_I$ and $E_J$ are the coefficients of entrainment of particle sizes I and J into the jet. It is assumed that the size distribution of particles in the jet dilute phase remains the same as that in the fluidized bed. Therefore, the coefficients of entrainment for all particle sizes into the jet should be equal, as:

$$E_I = E_J = E \qquad 21)$$

The agglomeration rate $R_{I,J}$ may be written as:

$$R_{I,J} = P^{*}\ \beta_{I,J}\ E^{2}\ N(I)N(J) \qquad 22)$$

Comparing Equation 22 with Equation 2, the agglomeration rate constant may be written as:

$$K_{I,J} = P^{*}\ \beta_{I,J}\ E^{2} \qquad 23)$$

As previously mentioned, $K_{I,J}$ can be represented by a multiple of two functions; one dependent on operating conditions and the other on size:

$$K_{I,J} = k_{op}(d_I^4 + d_J^4)\ (\frac{1}{d_I^3} + \frac{1}{d_J^3}) \qquad 24)$$

The value of collision frequency constant β depends on the size of the colliding particles. If β dependency on particle size can be expressed with the same function as that for the agglomeration rate constant,

$$\beta_{I,J} = \beta'\ (d_I^4 + d_J^4)\ (\frac{1}{d_I^3} + \frac{1}{d_J^3}) \qquad 25)$$

and we may then write:

$$k_{op} = P^{*}\ \beta'\ E^{2} \qquad 26)$$

The probability $P^*$ in Equation 26 is the fraction of all the collisions that meet the agglomeration criteria in Equation 14. This probability is calculated by defining $\xi$ as follows:

$$\xi = \begin{cases} 1 & \text{if two particles of size I and J meet the agglomeration criteria} \\ 0 & \text{if two particles of size I and J do not meet the agglomeration criteria} \end{cases}$$

The value of $P^*$ is calculated as the number of collisions for which $\xi = 1$ divided by the total number of collisions.

$\beta' E^2$ depends mainly on the gas and solid flow behavior in the fluidized bed. Our studies indicate that, for the runs with the same jet nozzle diameter and jet air velocity and approximately the same particle-size distribution, $\beta' E^2$ has approximately the same value.

Results and Discussion. The values of $k_{op}$ were calculated for different jet and fluidizing air temperatures at constant jet nozzle diameter, jet and fluidizing air velocities, and feed particle-size distribution using Equation 26 with the value of $\beta' E^2$ set equal to $1.35 \times 10^{-5}$. This value of $\beta' E^2$ was chosen so that the value of $k_{op}$ evaluated from experimental data agreed with that calculated from the model, for the run conducted at the jet air temperature of 144.4°C and fluidizing air temperature of 115.7°C. The values of $k_{op}$ calculated for other jet temperatures are shown in Table 2 which agree well with the values from the experimental data. The predicted values of $k_{op}$ for different fluidizing air temperatures while maintaining constant jet temperature compare reasonably well with the experimental values (Table 3).

Table 2. THE PREDICTED VALUES OF $k_{op}$ AT DIFFERENT JET TEMPERATURES AND A FLUIDIZING AIR TEMPERATURE OF 115.7°C

| Jet Temp, °C | 144.4 | 143.3 | 142.8 | 142.2 |
|---|---|---|---|---|
| $k_{op}$ From Model | $1.78 \times 10^{-9}$ | $1.20 \times 10^{-9}$ | $0.89 \times 10^{-9}$ | $0.63 \times 10^{-9}$ |
| $k_{op}$ From Experiment | $1.78 \times 10^{-9}$ | $1.20 \times 10^{-9}$ | $0.90 \times 10^{-9}$ | $0.45 \times 10^{-9}$ |

Table 3. THE PREDICTED VALUES OF $k_{op}$ AT DIFFERENT FLUIDIZING AIR TEMPERATURES AND A JET TEMPERATURE OF 144.4°C

| Fluidizing Air Temp, °C | 115.7 | 104.6 | 93.5 | 82.3 |
|---|---|---|---|---|
| $k_{op}$ From Model | $1.78 \times 10^{-9}$ | $1.15 \times 10^{-9}$ | $0.68 \times 10^{-9}$ | $0.54 \times 10^{-9}$ |
| $k_{op}$ From Experiment | $1.78 \times 10^{-9}$ | $1.05 \times 10^{-9}$ | $0.84 \times 10^{-9}$ | $0.66 \times 10^{-9}$ |

## REFERENCES


1. Arastoopour, H., Huang, C. S. and Weil, S. A., "Fluidization Behavior of Sticky Particles," Journal of Fine Particle Society (1986).

2. Arastoopour, H., Gu, A. Z. and Weil, S. A., "The Effect of Gas Distributors on the Agglomeration Process in Fluidized Beds," in the Proceedings of the 4th International Symposium on Agglomeration, 443-450, 1985.

3. Arastoopour, H., Weil, S. A., Huang, C. S. and Gu, A. Z., "A Fundamental Study in Support of the Understanding of the Agglomeration of Coal in Coal Gasifiers," in the Proceedings of the 20th Intersociety Energy Conversion Engineering Conference, Vol. 1, 1625-1630, 1985.

4. Gluckman, M. J., Yerushalmi, J. and Squire, A. M., "Defluidization Characteristics of Sticky or Agglomerating Beds," Fluidization Technology, Kearns, D., Ed., 2, 395 (1976).

5. Vora, M. K., Sandstrom, W. A. and Rehmat, A. G., "Ash Agglomeration in the Fluidized Bed." Paper presented at the Sixth National Conference on Energy and the Environment, Pittsburgh, May 21-24, 1979.

6. Hariri, H., Rehmat, A. and Arastoopour, H., "Temperature Distribution in a Fluidized Bed With a Central Jet." Paper presented at the A.I.Ch.E. Annual Meeting, New York, November 15-20, 1987.

7. Ricou, F. P. and Spalding, D. B., "Measurement of Entrainment by Axisymmetrical Turbulent Jets," Journal of Fluid Mechanics 11, 21-32 (1961).

8. Tatterson, D. C., Marker, T. L. and Forgac, J. M., "Particle Effects on Free Jet Entrainment," The Canadian Journal of Chemical Engineering, 65:361-365 (1987).

9. Bird, R. B., Stewart, W. E. and Lightfoot, E. N., Transport Phenomena. New York: John Wiley & Sons, 1960.

## APPENDIX

### Relative Kinetic Energy of Colliding Particles

The compression action between the two collinear-colliding particles will keep on until the relative velocity between these two particles is zero. At this point, the deformation is at the maximum, as is the contact area between the two particles. However, the sum of the kinetic energies of the two particles reaches a minimum. This can be proved using the momentum balances for the collinear-colliding particles. The difference between the sum of the kinetic energies of the two particles before collision and that of the two particles at maximum deformation can be derived using the following assumptions. Assume that the velocities of two particles before collision with mass $m_1$ and $m_2$ are $v_1$ and $v_2$, respectively. ($v_1$ and $v_2$ are collinear.) If the maximum deformation is achieved, these two particles will have the same velocity, v'. The momentum balance may be written as:

$$m_1 v_1 + m_2 v_2 = (m_1 + m_2) v'$$

The difference of the kinetic energies in these two states is:

$$\frac{1}{2} m_1 v_1^2 + \frac{1}{2} m_2 v_2^2 - \frac{1}{2} (m_1 + m_2) v'^2 = \frac{1}{2} m_1 v_1^2$$

$$+ \frac{1}{2} m_2 v_2^2 - \frac{1}{2} (m_1 + m_2) \left(\frac{m_1 v_1 + m_2 v_2}{m_1 + m_2}\right)^2 = \frac{1}{2} \frac{m_1 m_2}{m_1 + m_2} (v_1 - v_2)^2 > 0$$

### Potential For Energy Dissipation in Particles

The potential dissipation capability is associated with the viscous dissipation of molten material on the surfaces of the colliding particles. The molten material is caused to flow relative to the surface mainly by the sudden particle velocity change and the compression action between particles during collision and, to a much

smaller degree, by the action of surface tension. As a first estimate, the flow of the molten layer is approximated by the viscous fluid (the creeping flow) over the spherical particles. Thus, the drag force exerted on the particles is calculated from the following equations (9).

$$F_n = \int_0^{2\pi} \int_0^{\theta} \left(\frac{3}{2} \frac{\mu_\ell v}{R}\right) \cos^2 \theta') R^2 \sin\theta' \, d\theta' \, d\phi = \pi \mu_\ell v R \, (1 - \cos^3 \theta)$$

$$F_t = \int_0^{2\pi} \int_0^{\theta} \left(\frac{3}{2} \frac{\mu_\ell v}{R} \sin^2 \theta'\right) R^2 \sin \theta' d\theta' \, d\phi = \pi \mu_\ell v R \, (2 - 3 \cos \theta + \cos^3 \theta)$$

where $F_n$ and $F_t$ are the summations of the projections of normal and tangential forces exerting on hard-core surface in the direction opposite to the particle flow direction. V is the characteristic velocity of the melted layer relative to the particle hard core. $\mu_\ell$ is the viscosity of the melted material.

$$F_n + F_t = 3\pi \mu_\ell v R \, (1 - \cos \theta) = 3\pi \mu_\ell v R \frac{(\delta_1 + \delta_2)}{2R} = 3\pi \mu_\ell v \left(\frac{\delta_1 + \delta_2}{2}\right)$$

If the thicknesses of the melted layers are $\delta_1$ and $\delta_2$, respectively, the energy dissipated due to viscous flow can be approximated as the product of force exerted on the particle hard core and the relative distance traveled between them.

$$\text{Potential Dissipation Capability} = (F_n + F_t) \times (\delta_1 + \delta_2) = 6\pi\mu_\ell v \left(\frac{\delta_1 + \delta_2}{2}\right)^2$$

It is further assumed that v is equal to the half of the relative velocity $| v_1 - v_2 |$ before particle collision; thus:

$$\text{Potential Dissipation Capability} = 3 \pi \mu_\ell \, | v_1 - v_2 | \left(\frac{\delta_1 + \delta_2}{2}\right)^2$$

ACKNOWLEDGMENT

This work was sponsored by the U.S. Department of Energy under Contract No. DE-AC21-87MC23283.

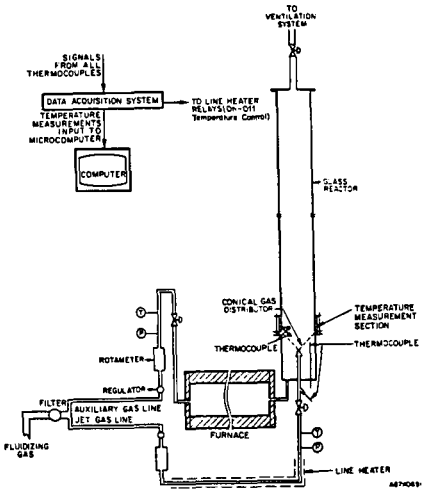


Figure 1. SCHEMATIC DIAGRAM OF THE EXPERIMENTAL SETUP

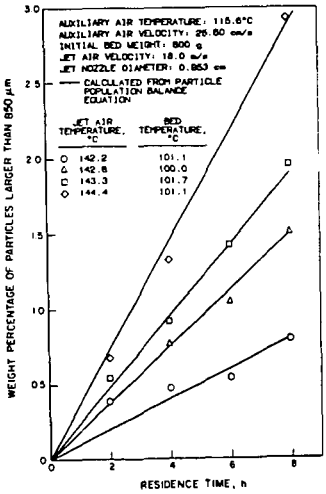


Figure 2. COMPARISON OF WEIGHT PERCENTAGES OF PARTICLES LARGER THAN 850 μm CALCULATED FROM THE PARTICLES' POPULATION BALANCE EQUATION AND EXPERIMENTAL DATA AT FOUR DIFFERENT JET AIR TEMPERATURES

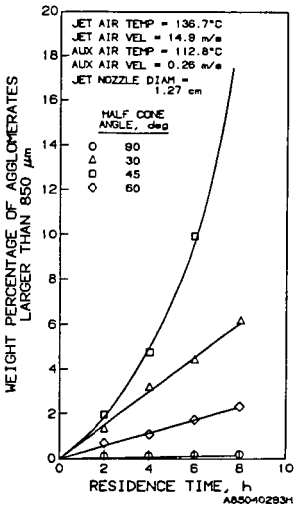


Figure 3. COMPARISON OF WEIGHT PERCENTAGES OF AGGLOMERATES WITH FOUR DIFFERENT CONE ANGLE GAS DISTRIBUTORS

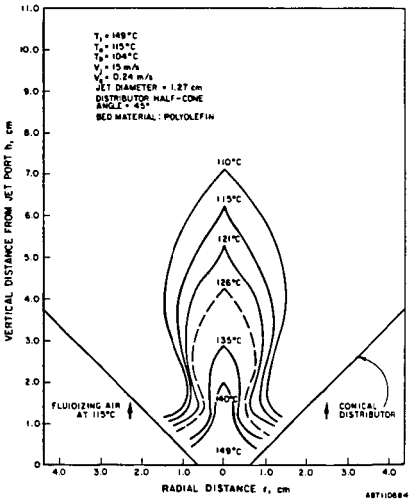


Figure 4. JET ZONE ISOTHERMS IN A FLUIDIZED BED AT A JET AIR TEMPERATURE OF 149°C AND A FLUIDIZING AIR TEMPERATURE OF 115°C

# Numerical Study of Coal Dust Explosions in Spherical Vessels

G. Continillo*

School of Engineering
University of California, Irvine
Irvine, California 92717

The unsteady flame propagation through a coal dust-air suspension in a spherical enclosure is studied by means of a one-dimensional, spherically-symmetric mathematical model. An Eulerian formulation is adopted for the gas phase mass continuity, species and energy balance equations, while a Lagrangian formulation is employed for the mass, energy and momentum balance equations for the particles. The pressure is assumed to be uniform in space (low Mach number) but varies in time. Preliminary calculations have been performed with a very simple coal particle submodel, in which a single-step devolatilization reaction with Arrhenius-type kinetics and quasi-steady heat, mass and momentum transfer to/from the particles is considered. Coal dust-air flame propagation could be predicted on the basis of devolatilization and homogeneous combustion reaction only. The model can represent a useful framework for the development and validation of particle-scale models, to be implemented in more complex coal combustion situations.

## INTRODUCTION

The occurrence of dust explosions can be reconducted to the ability of a dust suspension to be ignited and to sustain a flame front propagating through it. To study the behavior of such systems is a difficult task due to the complex chemical and transport phenomena involved both in accidental explosions and in the controlled combustion of pulverized fuels. A look at the literature on dust explosions reveals substantial disagreement between the experimental results of the various authors, as pointed out by Hertzberg et al. (1). No comprehensive theory is available to explain the phenomenon and arguments are still being made about which is the dominant mechanism. In fact, the flame propagation through a flammable dust cloud can be predicted on the basis of different and even mutually excluding simplified models. For example, Essenhigh and Csaba (2) presented a model of coal dust flame propagation based on the incoming radiating heat from the walls to the particles, neglecting any other form of heat transfer and even the contribution of the combustion reaction. On the other hand, Smoot (3) proposed a coal dust flame model in which the conductive heat transfer is assumed to be the dominant mechanism. However, the experimental situations are still too complicated to be modelled in full detail, thus making quantitative comparison between experiment and theory almost impossible. The ignition and flame propagation in a cold dust suspension requires heat to be transferred from the burning mixture to the neighboring fresh mixture. Mitsui and Tanaka (4) modelled the propagation of a flame in an idealized cloud of particles. The ignition of a particle was assumed to take place at the surface, by etherogeneous combustion, as in Cassel and Liebman (5). Once ignited, an envelope flame was assumed to establish, due to the devolatilization, at a certain somewhat arbitrary distance from the surface and with a certain assigned flame temperature; then the unsteady spherically symmetric heat conduction equation was solved to calculate the temperature in the gas phase surrounding the burning particle. Flame propagation was stated to be possible when the temperature at the location of the adjacent particle reached the ignition temperature before than the envelope flame

* On leave from: Istituto Ricerche sulla Combustione, Consiglio Nazionale delle Ricerche, Naples, Italy

extinguished for the volatile fuel consumption of the first particle. This idealized situation is still amenable of analytical treatment; particle-air relative motion, density and pressure variation, unsteady particle heat up and pyrolysis cannot be introduced without making the analytical solution impossible.

When a numerical solution is considered, the model can be complicated almost unlimitedly. The literature shows that the tendency has been either to refine the model for a single particle, with a very idealized environmental situation (for example Kansa and Perlee (6)) or to study very complicated flow situations like industrial burners, as in the works reviewed by Smoot (7). Both these approaches do not offer a direct contribution to the understanding of the dominant mechanisms of flame propagation in dust explosions, the first because of the poor or non-existing consideration of the particle-gas and particle-particle interactions, the second because of the impossibility of giving a close description of the particle scale phenomena at the same time of describing large scale, complicated flow and heat transfer patterns.

Aim of the present work is to identify a model problem in which the parameters are not too many, and fairly controllable, with a simple geometry and flow field, so that more computational efforts can be devoted to the microscale phenomena. The problem is meant to be still representative of a conceivable practical situation, like the deflagration in a spherical enclosure. The framework is presented in this paper, and preliminary calculations, with the inclusion of a simplified model for the unsteady particle heat-up and pyrolysis, are performed. Some of the results are shown and discussed, and further developments are indicated in the foregoing.

## MATHEMATICAL FORMULATION

Gas Phase Model. The gas phase model is essentially that of Reference (8), in which liquid spray flames were investigated. The following main assumptions are made. The flow is one-dimensional, unsteady, laminar, spherically symmetric. The viscous dissipation rate is negligible and the pressure is constant along the space coordinate (low Mach number), but varies in time due to the confinement in the vessel. The gas mixture is thermally perfect. Binary diffusion coefficients for each pair of species are taken to be equal, thermal mass diffusion is neglected. Mass diffusion and heat conduction are governed by Fick's and Fourier's law, respectively. The diffusion coefficient is assumed to vary with temperature and pressure ($\rho D = \mu_o$ = constant). The Lewis number is unity. Radiative heat transfer is neglected. The combustion chemistry is described by means of a single-step, irreversible reaction of the volatiles with the oxygen; Arrhenius-type kinetics with non-unity exponents for fuel and oxygen concentrations, as proposed by Westbrook and Dryer (9), is included. The equations include coupling terms accounting for mass, momentum and energy exchanges between the two phases.

The dimensional unknown quantities and the variable physical parameters are nondimensionalized with respect to their initial values, except that for the velocity. The following reference quantities are defined: $r_c = R$; $t_c = R^2/D_o$; $u_c = D_o/R$, where r is the space coordinate, R is the radius of the enclosure, t is the time coordinate, $D_o$ is the diffusion coefficient at a reference temperature, u is the gas velocity; furthermore, the nondimensional number density of the (k)th particle group $n_k = n'_k R^3$, the nondimensional heat of combustion $Q = Q'/C_{po}T_o$ and mass production rate for the (i)th species $\dot{w}_i = \dot{w}'_i(R^2/\rho_o D_o)$ are defined, where $\rho_o$ is the gas density evaluated at the initial temperature and pressure, and the following nondimensional equations are derived.

Continuity:

$$\frac{\partial \rho}{\partial t} + \frac{1}{r^2}\frac{\partial}{\partial r}(r^2 \rho u) = \sum_{k=1}^{N} n_k \dot{m}_k \qquad 1)$$

where $\dot{m}_k$ is the mass devolatilization rate of the (k)th particle group, N is the total number of particle groups.

Species:

$$\rho \frac{\partial Y_j}{\partial t} + \rho u \frac{\partial Y_j}{\partial r} - \frac{1}{r^2}\frac{\partial}{\partial r}\left(r^2 \frac{\partial Y_j}{\partial r}\right) = (\delta_{jF} - Y_j) \sum_{k=1}^{N} n_k \dot{m}_k + \dot{w}_j \qquad 2)$$

where $Y_j$ is the (j)th species mass fraction, $\delta$ is the Kroneker delta, and the subscript F stays for "vapor fuel."

Energy:

$$\rho \frac{\partial \phi}{\partial t} + \rho u \frac{\partial \phi}{\partial r} - \frac{1}{r^2}\frac{\partial}{\partial r}\left(r^2 \frac{\partial \phi}{\partial r}\right) = -\frac{\Gamma}{C_p}\left(\frac{C_{pp} T_{po}}{C_{po} T_o} \sum_{k=1}^{N} n_k \dot{q}_k\right) + Q\dot{w}_F \qquad 3)$$

with

$$\phi = T\, p^{\left(\frac{1-\gamma}{\gamma}\right)} = T\, p^{\Gamma}$$

where p is the pressure, $C_p$ is the specific heat at constant pressure, T is the temperature, the subscript p stays for "particle", and $q_k$ is the heat flux coming from one particle belonging to the (k)th group (usually negative), whose expression will be given later.

Ideal gas state equation:

$$p = \rho T \qquad 4)$$

Velocity (integrating Eq. 1 over $r^2 dr$) is given by:

$$u = \frac{1}{\rho r^2} \int_o^r \left( \sum_{k=1}^{N} n_k \dot{m}_k - \frac{\partial \rho}{\partial t}\right) r^2 dr \qquad 5)$$

Pressure (integrating Eq. 1 over $r^2 dr$ between 0 and R) is given by:

$$\left[\int_o^1 \frac{r^2 dr}{T}\right] \frac{dp}{dt} + \left[\frac{\partial}{\partial t}\int_o^1 \frac{r^2 dr}{T}\right] p = \int_o^1 \sum_{k=1}^{N} n_k \dot{m}_k\, r^2 dr \qquad 6)$$

The initial and boundary conditions for the gas phase are:

$$Y_j(r,0) = Y_{jo}\ ;\quad u(r,0) = 0\ ;\quad \phi(r,0) = 1\ ;\quad p(0) = 1 \qquad 7)$$

$$\left.\frac{\partial Y_j}{\partial r}\right|_{r=0} = 0\ ;\quad \left.\frac{\partial Y_j}{\partial r}\right|_{r=1} = 0\ ;\quad \left.\frac{\partial T}{\partial r}\right|_{r=0} = 0\ ;\quad \left.\frac{\partial T}{\partial r}\right|_{r=1} = 0$$

$$u(0,t) = u(1,t) = 0 \qquad 8)$$

Particle Model. In the calculations presented in this paper, the transient behavior of a particle is described by means of an extremely simplified model. The coal particle is represented by a sphere of solid material (ashes and fixed carbon) and volatiles in a specified initial partition. The particle is

considered to remain spherical and conserve its volume. The temperature is considered uniform in the particle and on the particle surface. Following Hubbard et al. (10), the transport processes next to the particle (in the "film") are assumed to be quasi-steady, and the thermophysical properties of the air-fuel vapor mixture are assumed uniform and evaluated at a conveniently averaged value of the temperature in the film. The fuel vapor production rate is assumed to depend on the particle temperature and global composition only. During the particle heat-up, the volatiles are released according to a simple one-step Arrhenius pyrolysis reaction, as in (6). The surface oxidation reaction is not considered, due to the highly transient character of the particle history in this kind of phenomena. This eliminates the need for considering the mass transfer processes in the film: all of the volatiles released by the particle are immediately available in the gas phase. The model accounts for the effects of the convective transport caused by the gas-particle relative motion by means of correction factors to the spherically symmetric stagnant film situation.

The non-dimensional equations for each particle group are:

Volatiles:

$$\frac{dm_v}{dt} = -A_v \exp(-T_v/T_p) m_v \qquad 9)$$

where $m_v$ is the mass of volatiles, $A_v = A'_v R^2/D_o$ is a non dimensional preexponential factor, $T_v$ is a non dimensional activation temperature.

Momentum:

$$\frac{dv}{dt} = \frac{N_1}{8} Re\, C_D\, (u - v) \frac{\rho_\infty}{\rho_p} \qquad 10)$$

with $N_1 = \frac{3}{2} \frac{R^2}{a^2}$ and (11): $C_D = \frac{24}{Re} (1 + \frac{1}{6} Re^{2/3})$ 11)

where v is the particle velocity, Re is the Reynolds number, the subscript $\infty$ stays for "free stream conditions" referring to a particle, a is the radius of the particle.

Energy:

$$\frac{dT_p}{dt} = N_1 \frac{C_p}{C_{pp}} Nu\, (T_\infty - T_p) \frac{\rho_\infty}{\rho_p} \qquad 12)$$

with (12) $$Nu = 2 + 0.6\, Re^{1/2}\, Pr^{1/3} \qquad 13)$$

where Pr is the Prandtl number. The instantaneous position of particle group k is given by

$$\frac{dr_k}{dt} = v_k \qquad 14)$$

The free-stream values of temperature and velocity are those of the gas phase model equations, evaluated at the current particle location. Finally, for the source terms in Eqs. 1, 2, and 3, we have:

$$\dot{m}_k = -\left(\frac{dm_v}{dt}\right)_k \qquad 15)$$

$$\dot{q}_k = \frac{C_{po}}{C_{pp}} \left[3 \frac{\rho_o}{\rho_{po}} \frac{R^2}{a^2} Nu + \beta_v \dot{m}_k C_p\right] (T_{pk} - T) \qquad 16)$$

where $\rho_{po}$ is the initial density of the particle, and $\beta_v = \rho_{vo}/\rho_{po}$ is the initial mass fraction of volatiles in the particles.

For the numerical solution, gas phase and particle calculations are time-split. The source terms provided by the particle calculations for the (n)th time level are used in the (n + 1)th time level of the gas phase calculations, after proper interpolation, and so forth. Explicit finite difference schemes are employed to discretize the PDEs of the gas phase model - except that for the chemical production terms, for which a degree of implicitness is introduced - since they have been proved to be the most effective in such two-phase problems (13). A non-uniform spatial grid is used, with the finest mesh size next to the wall. The time step is dynamically changed in order to describe the evolution of the system according to the current time scale. Due to the coupling of the equations, the calculations are iterated within each time step until the desired level of convergence is achieved. Then the integration in time is continued until desired.

## RESULTS AND DISCUSSION

Ignition is achieved by means of a heat source in the energy equation, in a spherical region for a limited time and an assigned intensity. The model predicts the particle heat-up, the devolatilization and the ignition of the volatiles in the gas phase, and the flame propagates through all the volume. The values of the parameters used for the base case are listed in Table I.

Table I.

Values and Expressions Used for the Most Important Physical Parameters in the Base Case

| | | | |
|---|---|---|---|
| $a$ | $= 2.5\times10^{-5}$ m | $R$ | $= 5\times10^{-2}$ m |
| $A_v$ | $= 1.\times10^{7}$ $s^{-1}$ | $T_o$ | $= 3\times10^{2}$ K |
| $C_p$ | $= 1.01\times10^{3} + 1.95\times10^{-1}$ (T'-300) J/KgK | $T_v$ | $= 15000/\mathcal{R}$ K |
| $m_{vo}/m_{po}$ | $= 0.25$ | $\gamma$ | $= C_p/(C_p - \mathcal{R})$ |
| $p_o$ | $= 1\times10^{5}$ Pa | $\mu_o$ | $= 1.845\times10^{-5}$ Kg/ms |
| $Q$ | $= 4.421\times10^{7}$ J/Kg | $\rho_{po}$ | $= 1.36\times10^{3}$ Kg/m$^3$ |

Figure 1 shows the computed pressure-time patterns for different particle diameters. The predicted final pressure, close to the maximum theoretical adiabatic pressure achievable, is much higher than that found in the experiments. The reasons are that the model does not account for heat losses, nor for the endothermic dissociation in the burned mixture. A slight decrease is observed after the maximum, and this accounts for the cooling effect due to the residual solid particles. During the combustion, the rate of pressure rise is always increasing: this is in agreement with predictions of lumped parameter models and with results of the experiments for the part in which the heat losses are negligible (14). In fact, it has been shown by means of a two-zone, thin flame model (14) that the rate of pressure rise can be expressed as

$$\frac{dp}{dt} = \frac{3\gamma p}{R} \frac{Q_R}{C_v T_u} \left(\frac{r_f}{R}\right)^2 S_u \qquad 17)$$

where $Q_R$ is the heat of reaction per unit mass of gas, $C_v$ is the specific heat at constant volume, $T_u$ is the temperature of the unburned mixture, $r_f$ is the current radial location of the flame, and $S_u$ is a flame speed with respect to the unburned mixture. For Equation 17 all the information connected with the flame structure is included (and hidden) in the parameter $S_u$, like the transport phenomena, the combustion reaction rate, the particle-gas interactions (relative motion, thermal inertia of the condensed phase), the rate of pyrolysis. A distributed-parameters model like that of the present work is capable of resolving the flame structure, therefore it allows for an appreciation of the different behavior of dust suspensions for what all of the parameters in Eq. 17 are equal, except $S_u$. For example, the influence of the particle size is clearly seen in Fig. 1, where finer particles are shown to give rise to faster flame propagation. Figure 2 illustrates the influence of another parameter, namely the oxygen content of the suspending atmosphere; the initial solid concentration is chosen accordingly to be slightly more than stoichiometric, in order to avoid the presence of oxygen in the residual gases together with the residual solid particles, which would require the consideration of the solid-gas surface oxidation reaction, not included in the model at present. The maximum pressure obviously decreases with the content of reactants, since the total amount of heat released by the combustion reaction is lower; the duration of the explosion increases, the system showing a lower overall reactivity, as expected.

Figure 3 represents the spatial profiles of the main variables at successive times for the base case. Each circle represents one particle group, whose particles are distributed on a spherical surface: the abscissa of each one represents the current radial location, while the ordinate corresponds to the particle temperature, in the same scale as that of the gas temperature. The radius of the internal filled circle is proportional to the remaining fraction of volatiles. The ignition zone is rapidly heated to about 1500 K, while the particles remain at a temperature close to the initial. The heat provided by the ignition source is conducted towards the outer region, and to the particles in the ignition region, until they begin to pyrolize. Note that the particles have a tendency to spread out, due to the motion impressed by the expanding gas during the ignition energy supply. This causes a local decrease of the volumetric concentration of dust, but the gas concentration has, of course, become even lower due to thermal expansion, therefore the overall effect is that of the generation of a locally fuel-rich region. When the vapor fuel released is sufficient, individual flames set up at the location of the particles, where the oxygen is seen to be consumed, and peaks in the temperature profiles appear. During the propagation of the flame, it is seen that the vapor fuel is present in the burned region only, meaning that it reacts as soon as it is generated. In fact the gas temperature is much higher than that of the particles when they begin to pyrolyze, up to the point that the combustion reaction is much faster than the pyrolysis, notwithstanding the much higher activation energy and the low concentration of the fuel vapor. Therefore, the limiting stage is the pyrolysis in this case. The relative motion of the two phases generates a deviation from the initially uniform, slightly richer than stoichiometric, equivalence ratio. More precisely, at the beginning the gas velocity is mainly directed towards the wall, and the particles, due to their kinematic inertia, do not follow the gas with the same velocity, thus creating a locally richer mixture in the center. The system is closed, thus a locally lean mixture is being generated in the zones encountered by the flame going towards the wall. When the flame approaches the wall, the gas velocity is mainly directed towards the center, while the particles are still moving towards the wall, and this generates a locally rich mixture next to the wall. As a result of the phenomenon, an uneven residual fuel vapor distribution is found at the end of the propagation.

## CONCLUSIONS

A model problem for ignition and unsteady flame propagation in a coal dust-air suspension has been identified. The simple geometry and flow field allow for

more details to be included in the modelling of the microscale phenomena. The problem can be considered still representative of a practical situation like a deflagration in a spherical enclosure. Results obtained with the inclusion of a simplified model for the unsteady particle heat-up and pyrolysis have been presented and discussed, and qualitative agreement with experimental evidence and simpler theoretical approaches has been found. Coal dust-air flame propagation has been predicted on the basis of devolatilization and homogeneous combustion reaction only, although the range of variation of some parameters is currently limited by the approximations made in the simplified coal particle model. It has been demonstrated that the model can represent a useful framework for the development and validation of much more detailed particle-scale models, to be implemented in more complex coal combustion situations.

Acknowledgments

This work has been partly supported by the Consiglio Nazionale delle Ricerche, Italy, with a NATO-CNR scholarship for exchange visitors granted to the author. Professor William A. Sirignano is gratefully acknowledged for his kind hospitality, support and advice.

## References

1. Hertzberg, M., Cashdollar, K.L., Opferman, J.J., "The Flammability of Coal Dust - Air Mixtures," Bureau of Mines, RI 8360 (1979).

2. Essenhigh, R.H., Csaba, J., Ninth Symp. (Int.) on Combustion, p. 111, The Combustion Institute, Pittsburgh, 1963.

3. Smoot, L.D., Horton, M.D., Prog. Energy Combust. Sci. 3, 235 (1977).

4. Mitsui, R., Tanaka, T., Ind. Chem. Eng. Process Des. Develop. 12, 384 (1973).

5. Cassel, M., Liebman, I., Combust. Flame, 3, 467 (1959).

6. Kansa, E.J., Perlee, H.E.., Combust. Flame 38, 17 (1980).

7. Smoot, L.D., Prog. Energy Combust. Sci 10, 229 (1984).

8. Continillo, G. and Sirignano, W.A., submitted to the Twenty-Second International Symposium on Combustion, Seattle, 1988.

9. Westbrook, C.K., Dryer, F.L., Prog. Energy Combust. Sci. 10, 1 (1984).

10. Hubbard, G.L., Denny, V.E., Mills, A.F., Int. J. Heat Mass Transfer 18, 1003 (1975).

11. Faeth, G.M., Prog. Energy Combust. Sci. 3, 191 (1977).

12. Ranz, W.E., Marshall, W.R., Jr., Chem. Eng. Prog. 48, 141 (1952).

13. Aggarwal, S.K., Fix, G.F., Lee, D.N., Sirignano, W.A., J. Comput. Phys. 35, 229 (1983).

14. Continillo, G., Study on Coal Dust Explosibility in Spherical Vessels, Doctoral Thesis, University of Naples, Naples, Italy, 1987 (in Italian).

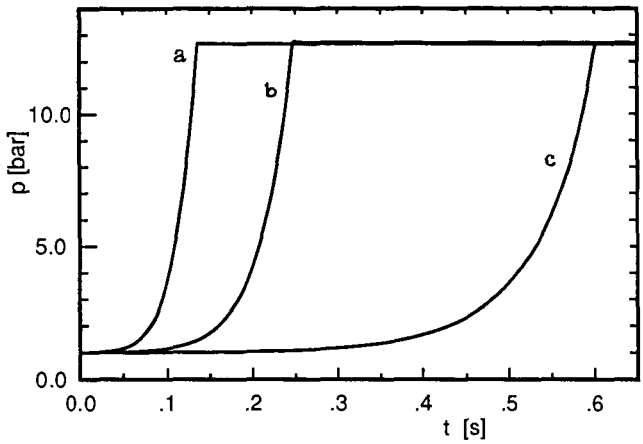


Figure 1. Pressure-time patterns at various particle diameters: a) 30 $\mu$m; b) 50 $\mu$m (base case); c) 100 $\mu$m;

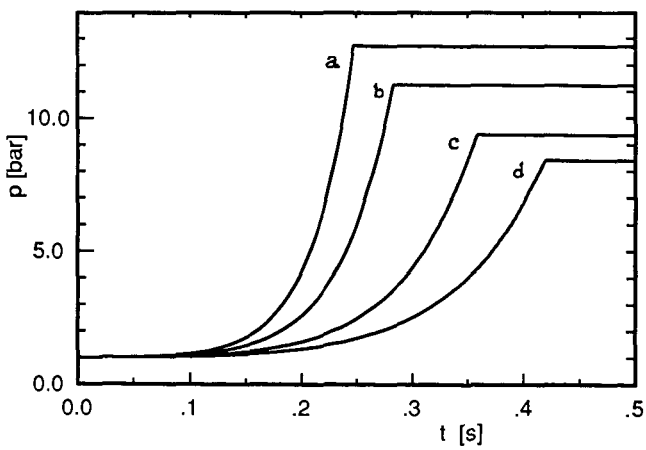


Figure 2. Pressure-time patterns at various oxygen mass fractions in the suspending atmosphere: a) 23.2% (base case); b) 20%; c) 16%, d) 14%

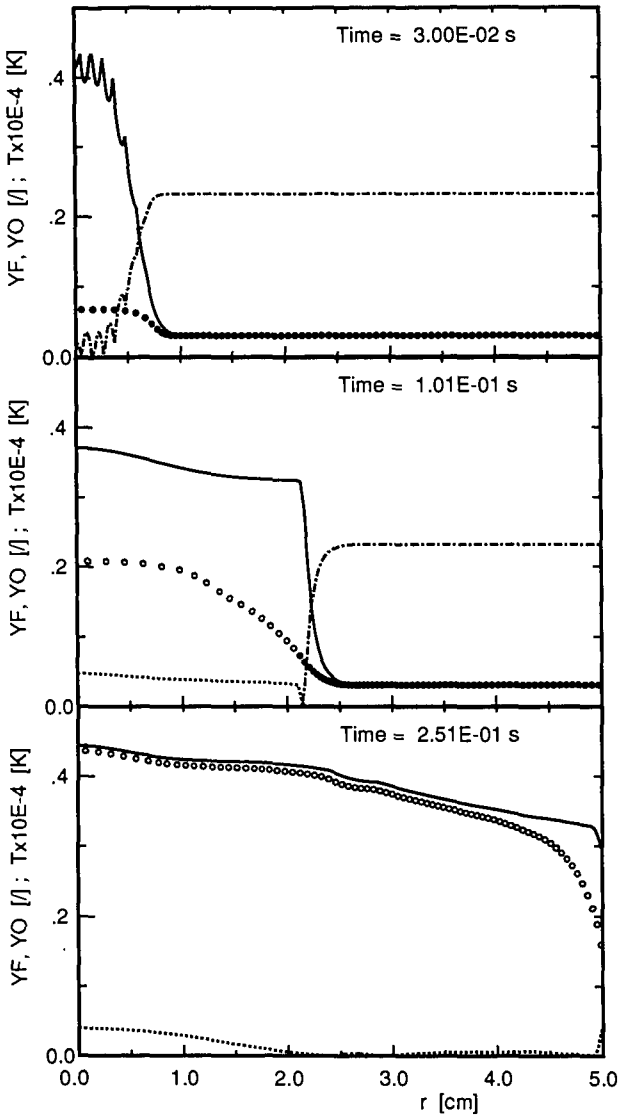


Figure 3. Radial profiles of fuel (YF, dashed) and oxygen (YO, dot and dash) mass fractions, and of temperature (T, solid line) at successive times.

# AN EQUILIBRIUM-THERMODYNAMIC ANALYSIS OF SULFUR RELEASE AND CAPTURE IN A GASIFICATION/COMBUSTION ENVIRONMENT

R. Nagarajan
Department of Mechanical and Aerospace Engineering
West Virginia University, Morgantown, West Virginia 26506-6101

and

M.R. Khan, H.N. Pham, R.J. Anderson, and L.C. Headley
U.S. Department of Energy-Morgantown Energy Technology Center
Morgantown, West Virginia 26507-0880

ABSTRACT

Coal and coal-derived liquids and gases constitute an economically attractive alternative energy source to liquid petroleum fuels. Ongoing research programs at DOE-METC are currently examining the potential of inexpensive production of clean liquid and solid fuels from coal by mild gasification, and of gaseous fuels by countercurrent pressurized fixed-bed gasification. The simultaneous release of gaseous sulfur species ($H_2S$, COS, $SO_2$, $SO_3$) is an inherent environmental limitation to a large-scale practical application of these processes. A computational technique to estimate the release of sulfur from coal and subsequent capture by calcium-based sorbents is presented here, where both processes are assumed to proceed to equilibrium under devolatilization, gasification (reducing), and combustion (oxidizing) conditions. A free-energy minimization computer program (PACKAGE) is used here to simulate local thermochemical equilibria in these reactive atmospheres. Predicted partial pressures of sulfur species are compared with experimental data on sulfur release and sorption, and conclusions are drawn regarding the usefulness and limitations of an equilibrium approach to modeling these processes.

## 1. INTRODUCTION

Coal use for electric power generation has increased in the past decade, and coal use for propulsion is a distinct possibility in the near future; however, the economic conversion of coal to clean fuels still remains a considerable technological challenge. Coal pyrolysis is perhaps the oldest technique for the derivation of hydrocarbon fuels from coal. In all coal conversion and utilization processes (including gasification, combustion, and liquefaction), some form of coal pyrolysis occurs. Gasification is closely related to pyrolysis in that when coal is gasified by reacting it at high temperature with steam and air, pyrolysis is the first stage of the reaction as the coal is heated to reaction temperature. Similarly, pyrolysis occurs at the first stage of combustion and in liquefaction because of the high temperatures employed when solvents are reacted with the coal.

### 1.1 Coal Devolatilization: Current Status of Modeling Efforts

The need to understand devolatilization reaction chemistry is obvious from the above discussion. Khan (1) has described the experimental procedure used to generate coal pyrolysis liquids, gases, and solids in the METC Slow Heating Rate Organic Devolatilization Reactor (SHRODR). This unit simulates, to an extent, the heating rates and residence times of the devolatilization zone of a fixed-bed gasifier. In this 500 ml fixed-bed reactor, 100 grams of coal (particle size -8 by +100 mesh) were heated to 500°C in 40 minutes and maintained at that temperature for 1 hour. Two high-volatile coals, Pittsburgh No. 8 (containing 2 weight percent sulfur) and Illinois No. 6, were tested. A sulfur sorbent, CaO, was added to the coals by direct mixing of the components. Product gases were collected and analyzed using gas chromatographs. Results demonstrated that the presence of lime significantly reduced the yield of $H_2S$. Total gas yield remained almost unchanged, and the yield of ($C_1$-$C_8$) hydrocarbon

gases and hydrogen increased significantly. Greater sulfur capture was seen with smaller CaO particles and at higher pyrolysis temperatures.

Typically, correlation techniques (e.g. [2,3]) are utilized to predict product yield and composition during coal devolatilization. Kinetic schemes proposed to represent the mechanism of coal pyrolysis range from two independent parallel reactions (4) to 42 reactions of 14 different functional groups in coal (5). Scaroni, et al. (6), have presented a compromise based on a hierarchy of bond energies in the coal structure. Serio, et al. (7), have reviewed available models to describe the kinetics of volatile product evolution in coal pyrolysis. All these approaches suffer to varying extents from empiricism. The degree of coal devolatilization depends on several parameters, such as coal type, heating rate, temperature, pressure, residence time at pyrolysis temperature, etc. The extent of sulfur release depends on several additional variables, such as the form of sulfur in the coal (inorganic, organic), sulfur trapped in the pyrolysis liquid, intimacy of contact between CaO and the primary products of devolatilization, etc. Given the uncertainties that unfortunately detract from any effort to describe the kinetics of these individual processes, an alternative systematic yet tractable predictive procedure to assess the products of the basic devolatilization reaction would be of immediate use.

## 1.2 Coal Gasification: Current Status of Modeling Efforts

The attractiveness of such an interim approach is reinforced by the accumulating sulfur-sorption data from the METC fixed-bed gasifier, which still await fundamental analysis. A countercurrent fixed-bed gasifier consists of four overlapping zones ([3]; Figure 1). At the top of the gasifier, the coal is dried and preheated by the exiting hot product gases. In the second zone, the coal is devolatilized and gases and tars are released. In the gasification zone, endothermic reactions occur forming carbon monoxide, carbon dioxide, water, hydrogen, and methane. Combustion of coal and oxygen occurs in the combustion zone, releasing heat to support the gasification reactions. Dry or molten ash will form in this zone depending on the maximum combustion temperature. The effects of pressure, calcium/sulfur ratio, and coal and limestone feedstock on sulfur removal efficiency have been investigated in a series of runs on the METC fixed-bed gasifier. Preliminary results indicate that sulfur capture decreases as pressure increases, and that recycle of regeneration gases to the gasifier may be required to obtain significant sulfur capture at higher pressures.

Several computer models (e.g. [3,8,9,10,11]) have been developed to simulate the chemical and physical processes that occur during steady-state gasification and hot gas cleanup. In these models, typically, carbon outlet flow and outlet gas composition and flow rate are predicted, but sulfur chemistry and the effects of additives are not included in the calculations. In addition, the finite chemical kinetic rate expressions used by these models require a knowledge of the appropriate activation energies and rate constant coefficients for various coal types. To obtain a sufficiently comprehensive reliable data base is thus a Herculean task. This problem can be circumvented to a certain extent by assuming that all chemical reactions proceed to equilibrium, but this would still require that the individual equilibrium rate constants be specified. The free-energy minimization procedure developed by White, et al. (12), is a numerically attractive alternative since it specifies no reaction paths and has been used to perform the equilibrium thermodynamic calculations presented in this report.

## 1.3 Modeling Sulfur-Lime Reaction Kinetics: Uncertain Effect of Pore Structure

The equilibrium approach is also necessitated by the lack (particularly in a fixed-bed environment) of a systematic procedure for the description of the high-pressure sorptive capacity for $SO_2$ (or $H_2S$) removal of a given limestone (or dolomite) starting from basic physical principles and experimental information. The effect of the initial pore structure of the sorbent, structural changes during the calcination

process, accumulation of a surface char layer on the sorbent particles in their transit through the (low-temperature) devolatilization and gasification zones in a gasifier column are among the phenomena that few of the presently available kinetic models incorporate. Ideally, presently available kinetic codes (13,14) should be developed to the point where they can describe these phenomena quantitatively; but in view of the time and effort that would involve, an interim procedure that is insensitive to these microscopic-level details constitutes a feasible alternative.

These considerations have led to the conclusion that a systematic approach to describing sulfur release and sorption processes in coal conversion applications is needed at this stage, even if the approach can only yield (infinite-rate) "limiting" information on sulfur release, sulfur removal, and lime utilization. While the usefulness of the present local thermodynamic equilibrium approach would doubtless be enhanced by interfacing it with the overall material balance for any specific coal conversion application, the advancement of understanding attained with the present preliminary scheme is still considerable. In subsequent sections the fundamentals of the chemical-equilibrium algorithm used here are described, its ability to deal with the complex chemistry of coal conversion product mixtures demonstrated, and its validity evaluated by comparing predicted and measured gas/solid/liquid phase compositions in lime-treated coal process streams.

## 2. THE COMPLEX CHEMICAL EQUILIBRIUM APPROACH: METHODOLOGY

Product gas, liquid, and solid phase compositions are estimated here using an equilibrium-thermodynamic computer program on the premise that the species distribution predicted by a free-energy minimization algorithm is the one likely to prevail. Stinnett, et al. (15), have previously applied the principle of thermodynamic free-energy minimization to fossil fuel gasification processes to predict the effect of operating variables on the composition of the product gas (in the absence of a sulfur sorbent). This approach enables the estimation of the partial-pressure distribution of <u>all</u> sulfur-bearing species in the gas, as well as the mole fractions of the sulfur-containing species in the solid and liquid phases; the analysis is thus not limited to a few user-specified reactions and products. The utility of this method is limited only by the available thermodynamic data base and its assumption of ideal solution phases. Due to the demonstrable efficiency of the PACKAGE computer code (16) in modeling complex phase equilibria in coal conversion gas streams and cleanup devices, the PACKAGE program has been used to perform the equilibrium thermodynamic computations presented here. Input to this program consists of elemental compositions of the reactant streams, relative mass flow rates of the reactant streams (e.g., the fuel/air ratio in a combustion case, [coal+lime]/[air+steam] in a gasification situation), pressures, and temperatures of interest. In the case of coal devolatilization, coal composition, devolatilization temperature, and pressure would constitute the input parameters. Output from the PACKAGE program typically consists of phase fractions and species mole fractions within each phase as a function of temperature. The results of exercising the PACKAGE programs under conditions representative of coal devolatilization, gasification and combustion are presented in the next section.

## 3. THE COMPLEX CHEMICAL EQUILIBRIUM APPROACH: FEASIBILITY

In order to demonstrate the suitability of an equilibrium approach to characterizing coal conversion product streams, illustrative calculations have been performed over a wide range of operating conditions simulating coal devolatilization, gasification, and combustion environments. The parametric studies presented in this section are meant to constitute the operating "envelope" for these systems. The results presented here are mostly qualitative and are intended only to show the feasibility of the approach without reference to quantitative accuracy; the latter aspect will be taken up in the next section.

### 3.1 Devolatilization Products Composition Calculations

The atmospheric pressure devolatilization calculations presented here pertain to slow-heating pyrolysis of Pittsburgh No. 8 coal over a temperature range 600-1200 K. In Figures 2 and 3 the effects of temperature on sulfur release and capture during coal devolatilization are examined. Figure 2 corresponds to untreated coal, whereas Figure 3 displays calculations made for the lime-added case. Under these (fuel-rich) conditions, $H_2S$ is the dominant sulfur-containing vapor species, with the COS concentration being at least an order of magnitude smaller. Both figures show increasing sulfur capture with temperature. Calcium and iron originally in the coal can capture sulfur to a limited extent, forming CaS and FeS, respectively. Sulfur sorption by iron oxide is predicted to be possible at lower temperatures than sorption by CaO, due to the fact that the calcination temperature for $CaCO_3$ is relatively high at atmospheric pressure. Iron and calcium in the coal can recapture close to 30 percent of the released sulfur at temperatures in excess of 900 K. The effect of varying levels of added lime on $H_2S$ mole fraction in the gas phase is shown in Figure 3 on a semi-logarithmic scale. Clearly, under devolatilization conditions, calcium oxide is potentially a very effective sorbent for $H_2S$; indeed, the present equilibrium approach can, at best, indicate the maximum sorption potential of any additive and enable the evaluation of different sorbents on that basis.

### 3.2 Gasification and Combustion Products Composition Calculations

Figures 4-6 represent equilibrium-thermodynamic calculations performed under gasification conditions. These results simulate the products obtained by reacting together varying amounts of coal and moist air at atmospheric pressure, over a temperature range 500-1500 K. The liquid and solid phase fractions in the reaction product mixture are plotted as a function of temperature and coal/air flow rate ratio in Figures 4 and 5, respectively. Sulfur elemental concentration in the product gases is plotted against these variables in Figure 6; no distinction has been made in this representation of gas-phase sulfur between various sulfur-bearing vapor species (such as $H_2S$, $SO_2$, $SO_3$, etc.). With increasing temperature the liquids and solids fractions show a non-monotonic behavior for all fuel/air ratios, while the trend for sulfur elemental concentration is very sensitive to the fuel/air parameter. The condensed phases comprise principally mineral phases at higher temperatures, and sulfates and sulfides at lower temperatures. The program cannot simulate the formation of (thermodynamically unstable) liquid hydrocarbons ("tars"). In the fuel-rich case, (S) in the gas decreases slightly with temperature, as in the case of devolatilization; in the fuel-lean case, $CaSO_4(s)$ will form at temperatures below 700 K, providing a significant "sink" for gas-phase sulfur.

The ability of the PACKAGE program to compute chemical equilibrium compositions under coal combustion conditions has been demonstrated in previous work. In the analysis of ash deposition on coal-fired gas turbine blades, the prediction of condensed liquid ("glue") phase fraction and composition constitutes the first step (17,18). In Figures 7 and 8, respectively, PACKAGE-predicted effects of added calcium on gaseous $SO_2$ and $SO_3$ are presented. For temperatures greater than about 1300 K (depending on the calcium level), added calcium gets bound up in high molecular weight vapor and condensed species (e.g., $CaAl_2Si_2O_8[s]$), and is thus not free to react with all the sulfur present. Unbound calcium is still sufficient, however, to absorb nearly all of the $SO_3$.

In this section, it has been shown that the PACKAGE equilibrium-thermodynamic computer program can estimate the product stream composition in a variety of coal conversion applications. It remains to be seen whether any of these equilibrium predictions has a basis in reality or is strictly of academic value. This concern will be addressed in the remainder of this paper.

## 4. THE COMPLEX CHEMICAL EQUILIBRIUM APPROACH: VALIDITY

### 4.1 Coal Devolatilization Applications

In order to assess the applicability of an equilibrium-thermodynamic procedure to estimate the coal-devolatilization product gas composition, PACKAGE predictions have been compared against in-house SHRODR measurements. Computed and detected molar concentrations of the major vapor species released during atmospheric-pressure slow-heating pyrolysis of Pittsburgh No. 8 coal are presented in Tables 1 and 2. Predicted and observed effects of CaO addition on the composition of devolatilization products are shown in Table 1. Results demonstrate that the presence of CaO during coal devolatilization significantly reduces the yield of $H_2S$. For example, for this Pittsburgh seam high-volatile coal, the $H_2S$ yield was observed to be reduced from 3.7 volume percent to 0.05 volume percent when 21 weight percent of CaO (Ca:S = 6:1) was added to the coal. The equilibrium code overestimates sulfur sorption in the no-lime added case, but otherwise predicts the extent of sulfur capture with reasonable accuracy, especially when smaller lime particles are added. This accuracy is, at first, surprising because the PACKAGE program does a relatively poor job of predicting the partial pressures of the major C-H-O species. The code underestimates gas-phase hydrocarbons ($CH_4$, $C_2H_4$, $C_2H_6$, etc.) by a factor of 2-5 and CO by a factor of 2-5 (at 500°C); it overestimates $CO_2$ by a factor of 1.5-5, $H_2$ by a factor of about 3, and $H_2O$ by an order of magnitude. The code also, in general, underpredicts COS formation.

These gross errors in vapor-phase representation by the PACKAGE computer program would appear to be consequences of an inadequate thermodynamic data base, as well as an inherent failure of the approach itself to model essentially non-equilibrium processes, such as tar cracking. Cracking of tar liquids (phenolic compounds in particular) to lighter products is a primary cause of increased $CH_4$ and hydrocarbon gases ($C_1$-$C_8$) formation (1). The composition of low-temperature (< 700°C) coal tars is very complex and strongly dependent on the conditions at which pyrolysis occurs. Until a comprehensive library of the thermodynamic properties of complex tar liquid mixtures is developed, and utilized along with the equilibrium code, discrepancies between observed and predicted devolatilization product composition are bound to exist. However, the relatively error-free estimation of $H_2S(v)$ concentration in the presence of added lime suggests that the equilibrium approach can serve as a tractable preliminary scheme for the analysis of sulfur chemistry even in the less reactive atmosphere of low-temperature devolatilization.

This tentative conclusion is strengthened by additional comparisons between predicted and observed effects of variations in coal and lime particle size, the devolatilization temperature, and the sulfur sorbent employed. Data obtained with smaller coal particles and smaller CaO particles (< 10 micrometers) reveal improved agreement between predicted and measured sulfur capture (Table 1). This suggests that a better mixture of coal and CaO components (and, hence, greater contact between CaO and devolatilized sulfur products) is possible when the smaller size fraction is utilized. This increased intimacy of contact also implies closer approach to equilibrium; indeed, near-equilibrium sulfur capture may be obtained when hydrated lime is introduced as a "mist" spray. To investigate the influence of pyrolysis temperature on product yield and composition, experiments and computations have been performed at 649°C with and without the presence of calcium compounds. The predicted and observed percentage of sulfur content ($H_2S$ and COS) in the product gases is slightly reduced at 649°C compared to that at 500°C (Table 1). The increased levels of CO and $H_2$ and the reduction in CO at higher temperature are also simulated by the equilibrium code. At both temperatures the influence of CaO addition on sulfur products is seen to be qualitatively similar, as predicted.

The equilibrium model cannot simulate differences in the performance of the same sorbent (e.g., CaO) prepared from different sources (e.g., $CaCO_3$, $Ca[OH]_2$, dolomite,

calcined dolomite, hydrated calcined dolomite), since these differences are caused largely by the varying pore structures of the sorbent. Differentiation of additives generated from various parent compounds and at different treatment conditions necessarily involves kinetic modeling; however, the present equilibrium-rate chemistry model can still be used to compare the maximum reactivity of the CaO additive with that of other low-cost inorganics (e.g., $CaCO_3$, $Fe_2O_3$, MgO, $SiO_2$). These observed and predicted effects on the SHRODR products are listed in Table 2. Adding 35 weight percent $CaCO_3$ (Ca/S of about 6) to the Pittsburgh coal at 500°C is observed to reduce $H_2S$ from 3.7 volume percent to only about 2.3 volume percent, whereas the PACKAGE code predicted a greater reduction. This is perhaps a consequence of previously reported (19) kinetic limitations to the calcination process below 600°C. A 21 weight percent $Fe_2O_3$ significantly reduces the yield of $H_2S$ and COS; this reduction is accompanied by the formation of FeS (troilite, identified by X-ray diffraction). These observed effects of $Fe_2O_3$ addition are also predicted theoretically. SHRODR experiments and simulations were also performed with MgO and $SiO_2$ additives. However, the presence of these inorganics has very little influence on devolatilized product yield and composition, as predicted by the PACKAGE computer program.

## 4.2 Coal Gasification Applications

In view of the long residence times (2-3 hours) associated with fixed-bed gasifiers, the use of an equilibrium approach is well-suited to this environment. Comparisons between PACKAGE predictions and experimental gas-phase sulfur data obtained under gasification conditions in the presence of sorbents are presented in Table 3. The $H_2S$ concentrations reported here were obtained by on-line laboratory analyses of gases generated during a series of METC fixed-bed gasifier runs. Since water was removed from all samples subjected to on-line analyses, results are reported on a dry gas basis; computer predictions are reproduced in Tables 3 and 4 on the same dry basis. The single-temperature, single gas/solid ratio analysis presented here is based upon the hypothesis that sulfur sorption in the gasifier column is controlled by fast chemical reactions that occur in a narrow section of the column, just above the combustion zone (see Figure 1). Further up in the column, calcination of the limestone additive is not thermodynamically feasible, implying severely reduced sulfur uptake by limestone; whereas, below this critical section, the lime is either saturated (due to absorption of recycle sulfur dioxide) or bound up in the form of silicates, aluminosilicates, etc., resulting from ash interactions under oxidizing conditions.

The calculations shown in Table 3 have been performed at a temperature of about 1000 K, and the gas/solids flow rate ratio (approximately 5) consistent with that temperature in the gasifier. The gas/solids ratio represents the distribution of the components of the reactive mixture in the two phases, and the temperature has been chosen on the basis of maximum availability of calcium to react; any temperature in the "temperature window" of 900-1100 K would have served equally well. These attempts to predict the observed sulfur capture by means of a simple equilibrium thermodynamic approach are no more than a prelude to the combined dynamic-thermodynamic-kinetic analysis planned for the future; yet even these preliminary equilibrium calculations show good agreement with experimental measurements for <u>all</u> gas species concentrations, including the hydrocarbons, $CO_2$, CO, $H_2$ (Table 4), as well as $H_2S$ (Table 3). In the case of the C-H-O species, the higher temperatures involved, the relative insignificance of tar-char chemistry, and the close approach to equilibrium of the water-gas shift reaction, apparently bring about a better match between theory and practice.

The PACKAGE code is equally effective in simulating the effect of changes in operating variables on sulfur uptake. At higher pressures (200 psig), calcination is delayed to higher temperatures, occurring further down in the gasifier column. In the absence of excess (recycled) sulfur, lime, once it forms, immediately reacts with the ash mineral constituents and is thus not available to react with the sulfur.

When sulfur is added in the form of a recycle $SO_2$ stream, equilibrium favors the formation of CaS and $CaSO_4$ over calcium silicates and aluminosilicates; this results in increased sulfur capture efficiency and increased sorbent utilization. Thus, in high-pressure runs with no $SO_2$ recycle, $H_2S$ volume percent in the gas is high and insensitive to Ca/S ratio (calculated with respect to the coal), but low and very responsive to the same parameter when some sulfur is fed back in. These predicted trends are consistent with observed gasifier performance. Some observations, such as the difference in effectiveness of the Germany Valley and Lowellville limestones, are beyond the capability of this approach to rationalize, but the present methodology is still of value in evaluating the limits of performance of gasifiers and sorbents.

### 4.3 Coal Combustion Applications

The equilibrium-thermodynamic approach has also been used to analyze the effect on combustion gas-phase sulfur concentration of adding calcium to a coal-water fuel. Conditions used in the calculations simulated those occurring in a recent GE LM500 Turbine Simulator run which indicated high sulfur capture (at the cost of increased deposition). In this experimental study, calcium hydroxide was integrated into coal-water mixtures and injected in a combustion system which simulates the thermodynamic and aerodynamic environment of a gas turbine. Sulfur capture was determined by analysis of extracted gas and solid samples. The PACKAGE computer program predicts 80 percent sulfur capture for calcium-to-sulfur (Ca/S) atomic ratio of 1.5, fuel-to-air ratio of 0.07, 1100°C, and 10 atmospheres. This compares well with the reported GE data of 60-70 percent capture (20) for hydrated sorbents. It is intriguing that even short residence time conditions such as these do not necessarily invalidate equilibrium modeling. Even though sorbent utilization is certainly time-dependent, the assumption of instantaneous reaction is probably not farfetched in the highly reactive, high-temperature combustion environment.

## 5. CONCLUSIONS AND RECOMMENDATIONS

An attempt has been made in this paper to illustrate and justify the use of an equilibrium-thermodynamic approach to modeling the distribution of sulfur species in the product streams of coal conversion processes. It has been demonstrated that equilibrium calculations simulate the qualitative effects of various sulfur sorbents and gas cleanup conditions (temperature, pressure, sorbent-to-sulfur ratio) with good accuracy, especially in reactor configurations that ensure close mixing of the components. The extent to which equilibrium estimates of sulfur capture and sorbent utilization are quantitatively realistic has been evaluated on the basis of comparisons with data obtained under coal devolatilization (in the METC SHRODR), gasification (in the METC fixed-bed gasifier), and combustion (in the GE turbine simulator) conditions. Preliminary indications are that equilibrium composition predictions are in surprisingly good quantitative agreement with measured data for all species included in the extensive thermodynamic data base employed. This tentative conclusion will be verified by repeated comparisons of model predictions with other sulfur-removal data as it becomes available. The unexpected success of the present preliminary computational model for sulfur sorption bodes well for the more comprehensive theoretical analyses planned for the future. The anticipated failure of this simple algorithm to simulate transport and kinetic limitations to the sulfur-lime reaction notwithstanding, the most attractive features of the equilibrium approach remain the elimination of the uncertainties surrounding more detailed gas/solid interfacial kinetic models, and the relative ease and convenience of its application.

## 6. REFERENCES


(1) Khan, M.R., Fuel Sci. Technol. Intl., 5, 185-231, 1987.

(2) Landers, W.S., et al., U.S. Bureau of Mines, Report of Investigation No. 5904, 1961.

(3) Wen, C.Y., Chen H., and Onozaki, M., Final Report, DOE/MC/16474-1390 (DE83009533), January 1982.

(4) Nsakala, N.Y., Essenhigh, R.H., and Walker, Jr., P.L., Combustion Sci. Technol., 16, 153, 1977.

(5) Anthony, D.B., and Howard, J.B., AIChE J., 22, 625, 1976.

(6) Scaroni, A.W., Khan, M.R., Eser, S., and Radovic, L.B., in Ullmann's Encyclopedia of Industrial Chemistry, 5th Edition, Vol. A7, 245-280, 1986.

(7) Serio, M.A., Hamblen, D.G., Markham, J.R., and Solomon, P.R., Energy Fuels J., 1, 138-152, 1987.

(8) Yoon, H., Wei, J., and Denn, M., Electric Power Research Institute Report AF-590, Vol. 1, 1977, Vol. 2, 1978.

(9) Denn, M., Wei, J., Yu, W.-C., and Cwiklinski, R., Final Report prepared for Electric Power Research Institute (EPRI AP-2576), September 1982.

(10) TRW Systems and Energy Group; Report prepared jointly with Morgantown Energy Technology Center, October 1978.

(11) Joseph, B., Bhattacharya, A., Salam, L. and Dudukovic, M.P.; Final Report to U.S. DOE-METC, January 1984.

(12) White, W.B., Johnson, W.M. and Dantzig, G.B.; J. Chem. Phys., 28, 751, 1958.

(13) Simons, G.A., Garman, A.R., and Boni, A.A.; AIChE J., 33, 211-217, 1987.

(14) Sotirchos, S.V., in press, Chem. Eng. Sci., 1987.

(15) Stinnett, S.J., Harrison, D.P., and Pike, R.W., Environ. Sci. Technol., 8, 441-444, 1974.

(16) Yousefian, V., Weinberg, M.H., and Haimes, R., Aerodyne Research, Inc., Report No. ARI-RR-177, 1980.

(17) Ross, J.S., Anderson, R.J., and Nagarajan, R., in press, Energy Fuels J., March 1988.

(18) Nagarajan, R., and Anderson, R.J., to be presented at the Intl. Gas Turb. Aeroeng. Congr. Expo., 33rd, Amsterdam, The Netherlands, June 5-9, 1988.

(19) Franklin, H.D., Ph.D. Thesis, Massachusetts Institute of Technology, 1980.

(20) Slaughter, D., Spiro, C., Lavigne, R., and Kimura, G., to be presented at the EPA/EPRI Comb. FGD and Dry $SO_2$ Control Symp., St. Louis, Missouri, October 25-28, 1988.

## Table 1. Products of Atmospheric-Pressure Slow-Heating Devolatilization of Pittsburgh No. 8 Coal in the SHRODR

| Species | Volume Percent in Gas: No Added Lime, Experimental | No Added Lime, Predicted | + 10 Weight Percent CaO, Experimental | + 10 Weight Percent CaO, Predicted | + 21 Weight Percent CaO, Experimental | + 21 Weight Percent CaO, Predicted |
|---|---|---|---|---|---|---|
| | | | Temperature = 500°C | | | |
| $CH_4$ | 49.80 | 25.36 | — | 30.74 | 53.70 | 39.76 |
| CO | 3.90 | 1.68 | 3.90 | 1.31 | 3.20 | 0.66 |
| COS | 0.39 | 0.0044 | 0.10 | 0.0007 | 0.03 | — |
| $CO_2$ | 5.40 | 7.01 | 1.30 | 4.29 | 0.20 | 1.10 |
| $H_2$ | 11.60 | 33.61 | 12.20 | 38.99 | 13.40 | 42.07 |
| $H_2O$ | 0.25 | 27.32 | — | 23.54 | 0.34 | 13.53 |
| $H_2S$ | 3.70 | 2.68 | 1.0 | 0.61 | 0.05 | 0.004 |
| | (3.20)* | | (0.61)* | | (0)* | |
| | | | Temperature = 649°C | | | |
| $CH_4$ | 49.80 | 8.95 | | | 46.66 | 12.93 |
| CO | 8.60 | 12.80 | | | 3.95 | 5.43 |
| COS | 0.22 | 0.015 | | | 0.02 | — |
| $CO_2$ | 4.20 | 5.17 | | | 0.72 | 0.97 |
| $H_2$ | 20.00 | 61.50 | | | 29.45 | 72.26 |
| $H_2O$ | 0.50 | 12.06 | | | 0.41 | 6.28 |
| $H_2S$ | 3.40 | 2.18 | | | 0.38 | 0.002 |

(* Data with < 10 μm CaO Particles)

T66-0869-1 BP5

## Table 2. Products of Atmospheric-Pressure Slow-Heating Devolatilization of Pittsburgh No. 8 Coal at 500°C in the SHRODR: Effect of Inorganic Additives on Sulfur

| Species | Volume Percent in Gas: + 21 Weight Percent $CaCO_3$, Experimental | + 21 Weight Percent $CaCO_3$, Predicted | + 35 Weight Percent $CaCO_3$, Experimental | + 35 Weight Percent $CaCO_3$, Predicted | + 21 Weight Percent $Fe_2O_3$, Experimental | + 21 Weight Percent $Fe_2O_3$, Predicted |
|---|---|---|---|---|---|---|
| $CH_4$ | 48.90 | 24.60 | 47.90 | 17.48 | 45.90 | 24.81 |
| CO | 3.70 | 1.79 | 4.50 | 2.53 | 2.90 | 1.63 |
| COS | — | — | — | — | — | — |
| $CO_2$ | 6.10 | 8.03 | 7.90 | 15.93 | 8.35 | 9.20 |
| $H_2$ | 10.20 | 33.10 | 9.80 | 27.90 | 16.10 | 33.20 |
| $H_2O$ | — | 26.61 | — | 34.20 | — | 29.5 |
| $H_2S$ | 3.30 | 1.40 | 2.30 | 0.28 | 0.1 | 0.04 |
| | + 21 Weight Percent MgO | | + 21 Weight Percent $SiO_2$ | | | |
| $CH_4$ | 47.70 | 25.33 | 48.90 | 25.33 | | |
| CO | 3.90 | 1.67 | 3.90 | 1.67 | | |
| COS | — | — | — | 0.005 | | |
| $CO_2$ | 7.60 | 8.93 | 5.50 | 6.93 | | |
| $H_2$ | 10.60 | 33.58 | 10.80 | 33.58 | | |
| $H_2O$ | — | 27.16 | — | 27.16 | | |
| $H_2S$ | 3.80 | 3.00 | 3.40 | 3.00 | | |

T88-0869-2 BP5

## Table 3. Effect of Operating Variables on Sulfur Concentraction in the Product (Raw) Gases of the METC Fixed-Bed Gasifier

| Pressure (psig) | Recycle $SO_2$ (lb/h) | Calcium-to-Sulfur Ratio, Ca/S | Volume Percent of $H_2S$ in the Gas: Experimental | Predicted |
|---|---|---|---|---|
| 200 | 0 | Baseline | 0.32 | 0.42 |
| | | 1 | 0.32 | 0.41 |
| | | 2 | 0.30 | 0.40 |
| | | 1* | 0.31 | 0.33 |
| | 60 | 1 | † | 0.67 |
| | | 2 | † | 0.53 |
| | 100 | 1 | † | 1.14 |
| | | 2 | † | 0.93 |
| 100 | 0 | 2 | 0.29 | 0.22 |
| | 70 | 2 | 0.48 | 0.34 |
| | 100 | 2†† | 1.52 | 0.99 |
| | 100 | 2††† | 0.84 | 0.89 |

* Fe:Ca:S = 0.5:1:1
† Data Under Analysis
†† Lowellville Limestone
††† Germeny Valley Limestone

T88-0869-3 BP5

## Table 4. Pittsburgh No. 8 Coal Gasification Product Gas Composition: P = 100 psig, $SO_2$ Recycle = 70 lb/h, Ca/S = 2

| Species | Volume Percent in Gas: Experimental | Predicted |
|---|---|---|
| Ar | 0.57 | 0.53 |
| $CH_4$ | 2.89 | 1.47 |
| CO | 12.47 | 12.47 |
| $CO_2$ | 15.22 | 15.42 |
| $H_2$ | 20.11 | 24.48 |
| $N_2$ | 44.94 | 44.54 |
| $H_2S$ | 0.48 | 0.34 |
| COS | — | 0.005 |
| Total (S) | 0.48 | 0.35 |

T88-0869-4 BP5

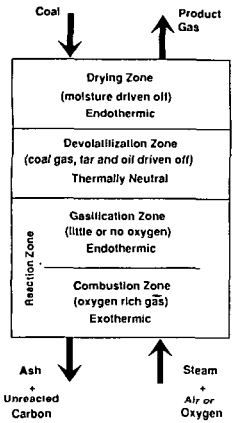


Figure 1. Schematic of Fixed-Bed Gasifier (3)

C89-869-B BP4

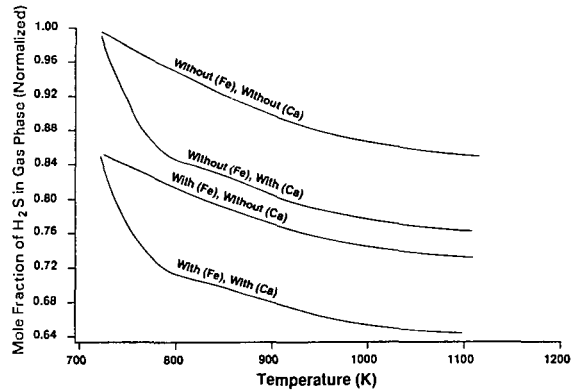


*Figure 2. Effect of Iron and Calcium in Pittsburgh No. 8 Coal on Sulfur in the Atmospheric-Pressure Devolatilization Product Gases*

I88-869-A BP4

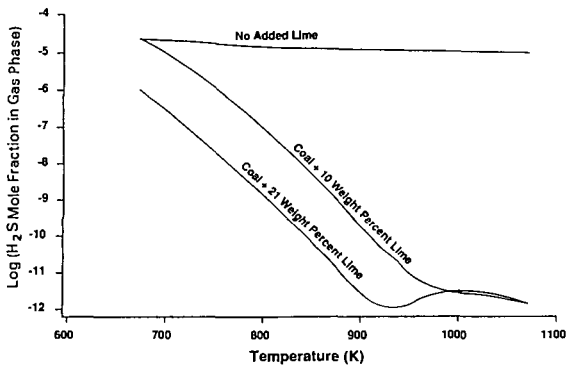


Figure 3. Effect of Added Lime on Gas-Phase Sulfur in Atmospheric-Pressure Devolatilization of Pittsburgh No. 8 Coal

I88-869-B BP4

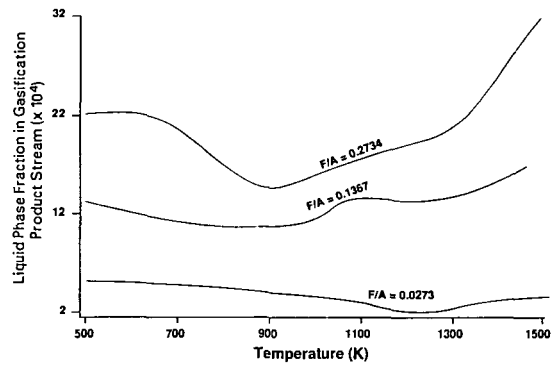


Figure 4. Temperature- and Fuel-to-Air Mass Flow Rate Ratio (F/A) Dependence of Liquids Fraction in the Product Mixture of Atmospheric-Pressure Gasification of Pittsburgh No. 8 Coal

I88-869-C BP4

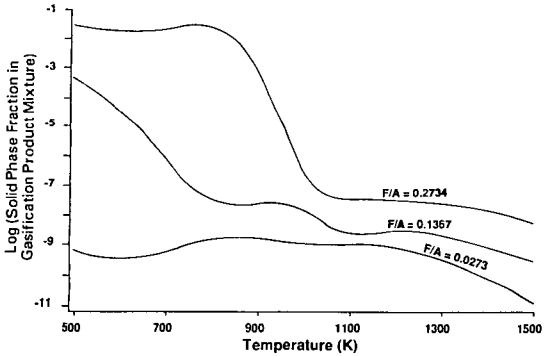


Figure 5. Temperature- and Fuel-to-Air Mass Flow Rate Ratio (F/A) Dependence of Solids Fraction in the Product Mixture of Atmospheric-Pressure Gasification of Pittsburgh No. 8 Coal

188-869-D BP4

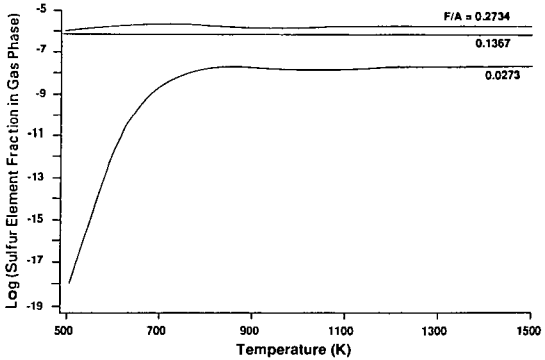


Figure 6. Temperature- and Fuel-to-Air Mass Flow Rate Ratio (F/A) Dependence of Total Sulfur Concentration in the Product Gases of Atmospheric-Pressure Gasification of Pittsburgh No. 8 Coal

188-869-E BP4

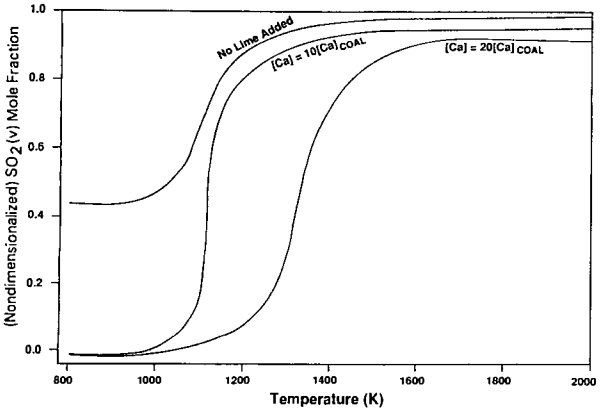


Figure 7. Effect of Temperature and Added Lime on Sulfur Dioxide Concentration in the Product Gases of Atmospheric-Pressure Combustion of Pittsburgh No. 8 Coal

188-535-C BP3

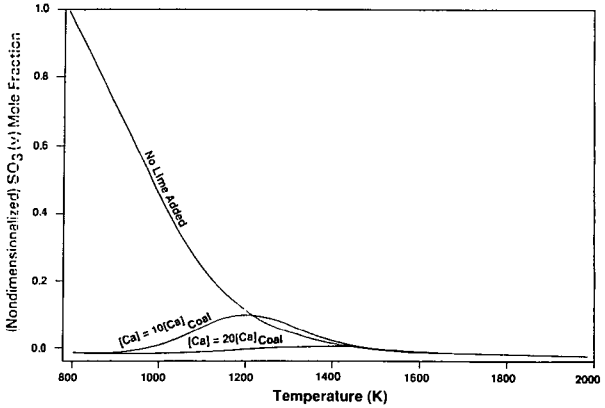


Figure 8. Effect of Temperature and Added Lime on Sulfur Trioxide Concentration in the Product Gases of Atmospheric-Pressure Combustion of Pittsburgh No. 8 Coal

188-535-B BP3

# MODEL OF ASH SIZE DISTRIBUTIONS FROM COAL CHAR OXIDATION

Boyd F. Edwards and Anjan K. Ghosal

Department of Physics, West Virginia University
Morgantown, WV 26506

## 1. Abstract

A flexible model of final ash size distributions resulting from coal char oxidation under varying conditions is presented. To include the important effects of fragmentation during char oxidation, we have modeled three-dimensional char particles as porous spatially random "percolation" clusters on a cubic bond lattice. Random walkers represent oxygen diffusion to the surface of the char particles. A reaction probability $r$ governs whether a random walker reaching the surface will react with a unit mass of char. Thus, values of $r$ from near zero to unity take the model from a chemical-reaction-limited to a diffusion-limited regime. Fragmentation events occur when reactions break the connectivity of the clusters, leading to a distribution of ash particle sizes after burnout. In the chemistry-limited regime, penetration of the random walkers into the pores of the cluster results in major fragmentation events and a correspondingly large number of ash particles. In the diffusion-limited regime, the lack of such penetration results in fewer ash particles with a larger maximum size. Model parameters are related to experimental conditions such as temperature, particle diameter, char porosity, and ash content. Results are compared with experiments.

## 2. Introduction

Coals typically contain about 10% incombustible mineral matter mainly in small separate inclusions in the coal. During combustion these particles can be released into the furnace gases as fly ash and may range from a hundredth of a micron to up to a 100 microns in diameter. These ash particles clog heat transfer equipment, corrode boiler tubes and create environmental hazards. To fully address these problems, it is important to understand the mechanism of ash formation. In this paper, we present a model of coal char oxidation designed to supply this understanding. Our objective is to numerically simulate the effect of coal morphology, burning rate, and initial ash content on the final ash size distribution.

Recent measurements of burning-rate time histories for single char particles in a fluidized bed (1) offer new insights into the dynamics of the combustion process. Of particular interest are successive sharp increases in the burning rate interrupting the overall downward trend. These sharp increases were interpreted as the fragmentation of char particles or subparticles into two or more pieces, and were not observable in previous time-averaged or ensemble-averaged measurements.

Though useful in characterizing various oxidation regimes, standard models of char oxidation deemphasize fragmentation by treating char particles as uniform spheres (2,3), thereby simplifying the problem of oxygen diffusion to the surface. Subsequent models allow for fragmentation effects by treating char particles as random porous shapes. Reyes and Jensen (4,5) modeled char oxidation on a Bethe (tree-like) lattice by randomly removing bonds (unit line segments) from anywhere on the lattice. More realistically, Kerstein and Bug (6) randomly removed an initial fraction of bonds from the Bethe lattice to represent the porosity of the unburned char particle, and randomly removed only surface bonds to simulate oxidation. To account for loop effects (which are absent on the Bethe lattice), Sahimi and Tsotsis (7) studied surface bond removal on a porous three-dimensional site lattice in the chemistry limited regime (Zone I). A Zone III (diffusion-limited) model (8) accounted for the sharp increases in the burning-rate measurements, ascribing them to a higher burning rate per unit surface area of char fragments than their parent char particles. These models demonstrated the utility of modeling char particles as random "percolation" clusters on a three-dimensional cubic lattice.

Models of char oxidation and fragmentation to date neglect ash formation and force all particles into a particular regime (Zone I or Zone III) regardless of size. In contrast, the smallest particles in real combustion systems might be in Zone I (because of their higher surface oxygen concentration) while the larger particles are simultaneously in Zone III (2). The present model incorporates both regimes

along with the intermediate regime (Zone II), as well as incorporating ash formation.

Further measurements on a finely graded Montana lignite (9,10) with mass averaged mineral inclusion size of 2 microns indicate strong dependencies of the final ash size distribution on temperature, initial particle size, and oxygen concentration. In this paper, we directly compare the predictions of the model with these experiments.

## 3. Model

The distribution of ash particle sizes after complete burnout depends on the competition between several mechanisms. Mineral inclusions melt and can coalesce as the surface of the char particle recedes, leading to large ash particles. Small protrusions in the irregular char surface can be liberated as the surface recedes, producing small ash particles. In the chemistry-limited regime, oxygen diffusion and oxidation in the pores can lead to separation of char particles into particles of comparable size, leading to ash particles more evenly distributed in size. Finally, mineral vaporization at the surface and subsequent condensation can lead to very small ash particles (11). Since they solidify from liquid mineral droplets, ash particles are typically spherical or near spherical.

To incorporate the most important mechanisms of ash production into our model in a straightforward way, we employ a representation of char particles on a cubic lattice similar to one used in a previous model (8), except that here we include mineral matter in the representation. The lattice representation employs the site percolation concept; each site on a cubic lattice has probability $p$ = 0.3117 of being "occupied". Groups of adjacent occupied sites are termed site clusters. This value of $p$ is the "percolation threshold" value above which a cluster spanning the cubic site lattice is guaranteed to exist. All unit line segments, or "bonds", within a radius R of occupied sites are designated as solid. The resulting bond cluster represents a porous char particle whose compactness is governed by R. A fraction of the bonds in the cluster are assigned masses of mineral material to simulate mineral inclusions. Note that a bond is a line segment between nearest neighbor sites on a lattice, representing a mass of combustible and mineral material, and does not represent a chemical bond.

Char oxidation is modeled by introducing random walkers representing oxygen. Each time a random walker encounters a solid bond, that is, each time it crosses a solid bond, it has a probability $r$ of reacting with the bond. A reaction is defined as the annihilation of both the walker and the combustible content of the bond. If an encounter does not lead to reaction, the walk continues from the point where it entered the solid. In this way, small values of $r$ lead to many encounters before reaction occurs, allowing walkers to deeply penetrate the pores before reacting. A reaction that breaks the connectedness of a cluster is deemed a fragmentation event. After such an event, the random walkers ignore all solid bonds except those pertaining to a single fragment to simulate physically separated particles produced by fragmentation events, each with a separate supply of oxygen. The fragments are oxidized one at a time in this manner until all have been oxidized. The site lattice oxidation model by Sahimi and Tsosis (7,12) apparently ignores this physical separation. Extension of the model to give the time-dependent char fragment size distribution during oxidation is in progress.

Two limiting behaviors for reallocating the mineral mass of a reacted bond are simulated as follows. Limit I: For strong cohesion between adjacent melted mineral inclusions, the mineral mass of a reacted bond is given to the adjacent solid bond with the largest mineral mass, giving strong coalescence of mineral matter. Limit II: In the opposite case of weak mineral cohesion and relatively strong adhesion between melted mineral inclusions and char material, the mineral mass of a reacted bond is equally divided among its adjacent solid bonds, giving weak coalescence. When the last solid bond of a cluster reacts, its mineral mass is deemed the mass of an ash particle. When all solid bonds have reacted, the ash mass distribution is complete. The corresponding ash size distribution follows from the sphericity of the ash particles. In this way, the model captures the effects on the ash distribution of surface coalescence, liberation of surface protrusions, and pore diffusion during oxidation. Although the model does not account for mineral vaporization (11), the very small submicron ash particles created by this mechanism are negligible in the final mass-weighted size distribution. We assume that the adhesion between melted mineral inclusions of different chemical compositions, if such differences occur in the coal being considered, can be treated as identical to the cohesion of inclusions of the same composition.

The advantage of using a bond lattice rather than a site lattice is the absence of unphysical spurious

multiple fragmention events. Removing a single site from a cubic site lattice can result in up to 6 fragments, whereas removing a single bond from a cubic bond lattice results in no more than two fragments.

The reaction probability $r$ depends on the particle diameter d through the oxygen diffusion rate $K_d$ (see Section 4 below). Thus, it is necessary to define the diameter of a cluster on the cubic bond lattice which can be related to the actual particle diameter d. This "lattice diameter" $d_l$ is defined as the average of the cluster dimensions in the three cartesian directions; $d_l = (x_{max} - x_{min} + y_{max} - y_{min} + z_{max} - z_{min}) / 3$, measured in units of the lattice spacing. The lattice spacing in microns, which remains fixed during the simulation, is determined initially by equating the initial particle diameter d (in microns) to the diameter $d_l$ of the cluster used to simulate it (in lattice spacings). The diameter and the corresponding reaction probability $r$ of a particular particle decrease monotonically from an initial value during oxidation, taking it into the chemistry-limited regime as it decreases in size. Cluster diameters and corresponding reaction probabilities are accordingly updated after each bond reacts.

Random walkers are introduced at random locations on a box with linear dimensions a factor of 1.4 larger than the dimensions of the box of dimensions $x_{max} - x_{min}$, $y_{max} - y_{min}$, and $z_{max} - z_{min}$. Tests to be described elsewhere indicate that this method of introducing random walkers yields probabilities of contacting particular solid bonds that are within 4% of the probabilities obtained by introducing the walkers an infinite distance from the cluster.

## 4. Relation of the reaction probability $r$ to physical quantities

For a first-order reaction, the rate of consumption Q of carbon at the surface of a char particle of diameter d is proportional to the partial pressure $C_s$ of oxygen at the surface through the relation $Q = K_c C_s$, where $K_c = A \exp(-E/RT_s)$ is the chemical reaction rate characterizing the chemisorption process. This oxygen at the surface arrives by diffusion across the relatively stagnant gas film between the bulk gas stream and the solid surface. The corresponding alternative relation $Q = K_d (C_b - C_s)$ involves the oxygen diffusion rate $K_d = B\, T_s^{0.75} / d$ (Refs. 13, 14). Since the bulk oxygen partial pressure $C_b$ is the measurable quantity, a third relation $Q = K\, C_b$ defines the overall reaction rate K, which is simply related to its constituent rates as $K^{-1} = K_d^{-1} + K_c^{-1}$ by combining the three forms for Q. For very small surface temperatures $T_s$, $K = K_c$ and a small oxygen flux to the surface is sufficient to sustain the slow chemical reactions both at the external surface of the solid and deep within its pores (Zone I). At higher temperatures, oxygen is unable to diffuse into the pores fast enough to completely support the faster chemical reactions, but is plentiful at the external surface (Zone II). At yet higher temperatures, $K = K_d$ and oxygen diffusion is unable to completely support the chemical reactions even at the external surface (Zone III).

The foregoing assumes an order of reaction equal to unity. CO is typically the primary oxidation product in char combustion (2), but converts to $CO_2$ a distance from the particle. Experimental evidence that $CO_2$ is the combustion product most relevant to diffusion to and from char particles, and that the order of reaction is consequently close to unity, is given by Field (15) for pulverized chars with $0.05 \text{ atm} < C_b < 0.20 \text{ atm}$, and by Smith (13). Accordingly, we take $A = 8710 \text{ g cm}^{-2}\text{s}^{-1}\text{atm}^{-1}$, $E = 35700$ cal/mole, and $R = 1.986 \text{ cal mole}^{-1} \text{K}^{-1}$ (3), which apparently apply generally, to within the accuracy of our simulations, to coals excluding pyrolitic graphites and anthracites. The value $B = 5.62 \times 10^{-6} \text{ g cm}^{-2}\text{s}^{-1}\text{atm}^{-1}$ based on the external surface area (mass removed per unit external surface area per atmosphere of $O_2$ per unit time) follows from the corresponding mass-based coefficient given by Smith (13), which depends on the diffusivity of $O_2$ in air. More specific values of E, R, and A for various coal types are given by Wall and Gururajan (16).

The reaction probability $r$ of the simulations follows simply from the overall reaction rate K. For $r$ near zero, random walkers encounter the solid many times before reacting with it, allowing the walkers to deeply penetrate pores before reacting, corresponding to chemistry-limited conditions and a slow reaction rate K. For $r$ near unity, an encounter almost always leads to reaction and only the most exposed parts of the cluster are consumed, corresponding to diffusion-limited oxidation and a high reaction rate $K_d$. In this way, the reaction probability is just the overall reaction rate normalized to unity; $r = K/K_d = K_c/(K_c + K_d)$.

## 5. Model tuning

The model is tuned by comparing with data from combustion of a finely graded (38-45 micron diameter with median diameter 39 microns) lightly swelling Montana lignite studied experimentally by Sarofim (9). Their microscopic examination of these particles indicates that the mineral matter is distributed as separate inclusions comprising about 8% of the coal with a maximum weight fraction at a diameter of 2 microns. Lacking detailed information about the small amount of swelling during devolatilization, we simply use the initial coal particle diameter as the diameter relevant to char oxidation. Particle surface temperatures $T_s$ typically exceed bulk gas temperatures $T_b$ by about 200 K (2).

To facilitate careful comparison with the experiments, the mineral masses assigned to bonds in the cluster are chosen to obey the distribution of the mineral inclusions measured in the experiments, which is apparently independent of coal particle size over the relevant range of particle sizes. In particular, the number of required inclusions in each of six bins of width 0.5 microns is determined from Figure 6 of Sarofim (9) based on the overall diameter d of the assumed spherical coal particle, the mineral fraction (8%), and the approximately equal density 3.5 g $cm^{-3}$ of char and mineral matter. The mass of the assumed spherical inclusions in each bin follows from the mean bin diameter. The N mineral inclusions required by the procedure are then randomly assigned to N bonds in the cluster (N = 1749 for d = 39 microns), and the remaining bonds in the cluster are assigned zero mineral mass. Our clusters typically contain from N to 1.1 N bonds. The largest simulated particle diameter was 44 microns.

We use the conditions d = 39 microns and $T_s$ = 2000 K to tune the cluster compactness and the method of mineral matter reallocation during combustion. For unit compactness (R = 1) and for weak mineral cohesion (limit II), we obtain a distribution with a narrow peak in the ash mass fraction per micron at about 2.5 microns compared with a corresponding median diameter of 9 microns for comparable conditions in the experiments [Figure 14 of Ref. (9), $T_b$ = 1830 K]. For higher compactness (R = 2) and for strong mineral cohesion (limit I), the median diameter rises to about 4.4 microns (Figure 1) and the width of the distribution is comparable to that of the experiments. For R = 3 and strong mineral cohesion, we obtain a very broad distribution centered very roughly at 8 microns. To better facilitate the study of the shifts in median diameter with temperature and particle diameter, we henceforth employ the more sharply peaked intermediate compactness R = 2 in the strong mineral cohesion limit. Our choice of compactness may correspond more closely to more porous chars, such as bituminous chars, than to the lignite of the experiments. We believe however that the directions and relative magnitudes of the shifts in the median diameter due to changing temperature and particle diameter should be applicable to a wide range of porosities including the lignite of the experiments, since these shifts arise from different oxidation regimes applied to the same types of particles. Our choice of strong mineral cohesion seems consistent with current understanding of the process of mineral coalescence.

## 6. Predictions and comparisons with experiments

To illustrate the dependence of the ash particle size distribution on temperature, Figure 1 shows our simulated mass-weighted ash size distributions for d = 39 microns at $T_s$ = 1500, 2000, and 2500 K. The data points are the output of the simulations; the solid traces are fifth-order polynomial fits to the data. The cluster used in all three simulations had 1781 bonds including 1749 mineral inclusions. The data show a systematic shift toward larger ash particles with increasing temperature (Figure 1); median diameters deduced from the fits are 3.7, 4.4, and 4.8 microns. A significant decrease in the overall number of ash particles from 171 at $T_s$ = 1500 K to 115 at $T_s$ = 2500 K (Table 1) accompanies the shift toward larger ash particles. Physically, the larger ash particles result from a decrease in pore wall oxidation and a corresponding decrease in fragmentation as the oxidation approaches the diffusion-limited regime with increasing temperature. The experimental data of Sarofim et al. (9) do not show an clear shift toward larger ash particles for increasing temperatures. Even so, for the case of d = 39 microns, the experimental ratio 0.86 between median ash particle diameters at bulk gas temperatures $T_b$ = 1830 K and $T_b$ = 1250 K [deduced from Figure 14 of Ref. (9)] compares well with our ratio 0.84 deduced from the median diameters at the corresponding surface temperatures $T_s$ = 2000 K and $T_s$ =

1500 K. The experimental overall number of ash particles 160 at $T_s = 2000$ K [estimated from data for d = 53-63 and 75-90 microns and bulk temperatures $T_b = 1750$ K, Ref. (10)] is comparable to our value of 121 (Table 1).

To determine the dependence of the ash particle size distribution on initial particle diameter, Figure 2 shows our simulated ash size distributions for d = 34, 39, and 44 microns at $T_s = 2000$ K. The corresponding clusters have 1162 (1152), 1781 (1749), and 2665 (2509) bonds, where parentheses enclose the numbers of bonds assigned mineral inclusions. Over this range of diameters, no clear trend in the ash particle size distribution is discernible (Figure 2). The increase with diameter of the overall number of ash fragments (Table 1) reflects the larger number of mineral inclusions in particles of larger diameter. The initial values of the reaction probability for these particles are 0.58, 0.61, and 0.64, respectively.

## 7. Conclusions

This paper presents, to our knowledge, the first model predicting ash distributions resulting from char oxidation and fragmentation incorporating the three regimes of oxidation. The model yields overall numbers of ash particles and shifts in ash particle distributions which agree with experiments on a Montana lignite. Since the sparse cluster morphologies studied in this paper underestimate the experimental median ash particle size, these morphologies may correspond best to more porous bituminous chars. Over the range of particle diameters studied (34-44 microns), the model predicts no variation in the median ash diameter with initial particle size. Further simulations of denser cluster morphologies and over larger diameter ranges are underway.

Experiments on the process of molten mineral matter reallocation during combustion would be very useful in connection with our ongoing simulations. Additionally, since significant swelling and morphological changes may occur during devolatilization, experiments on combustion of well-characterized chars (including sizes, porosities, and mineral matter distributions) would be useful.

The model provides a flexible and powerful framework in which to study the separate and combined effects of initial mineral content and distribution, coal type and morphology, oxygen concentration, temperature, and particle size on the final ash size distribution. It can used to compare and correlate experimental data, as well as to study parameter sensitivities that are difficult to explore experimentally.

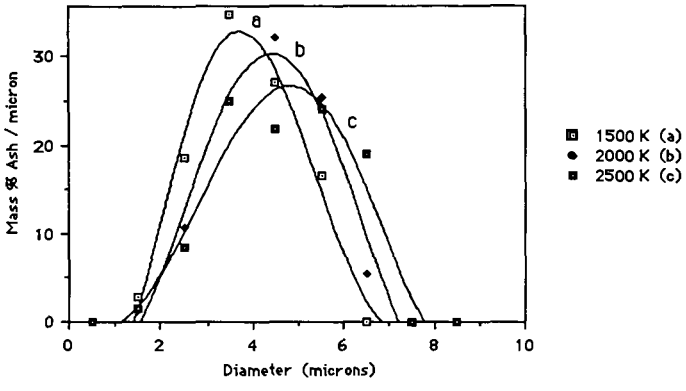


Figure 1. Mass-weighted ash size distribution for simulated coal particle diameter 39 microns and surface temperatures 1500, 2000, and 2500 K.

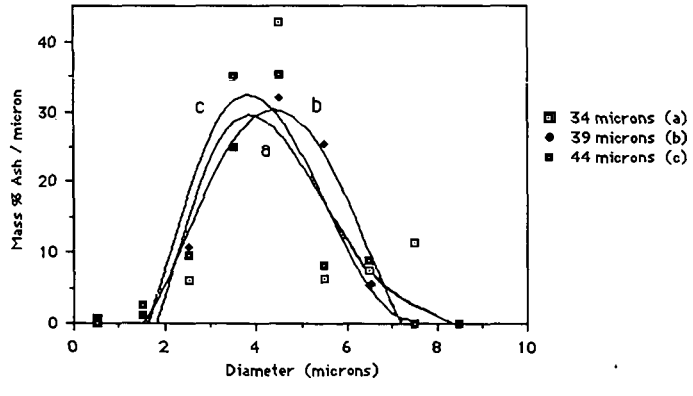


Figure 2. Mass-weighted ash size distribution for simulated coal particle diameters 34, 39, and 44 microns at surface temperature 2000 K.

| | | Ash particle size range (microns) | | | | | | | | | |
|---|---|---|---|---|---|---|---|---|---|---|---|
| d (μm) | $T_s$ (K) | 0-1 | 1-2 | 2-3 | 3-4 | 4-5 | 5-6 | 6-7 | 7-8 | 8-9 | total |
| 39 | 1500 | 25 | 34 | 53 | 39 | 15 | 5 | | | | 171 |
| 39 | 2000 | 24 | 17 | 30 | 26 | 16 | 17 | 1 | | | 121 |
| 39 | 2500 | 27 | 18 | 23 | 26 | 11 | 7 | 3 | | | 115 |
| 34 | 2000 | 12 | 12 | 11 | 17 | 16 | 1 | 1 | 1 | | 71 |
| 44 | 2000 | 45 | 48 | 36 | 54 | 14 | | 2 | | | 216 |

Table 1. Numbers of ash particles of different sizes ranges for simulated coal particles of diameter d and surface temperature $T_s$.

## 8. References


(1) Sundback, C. A., Beer, J. M., and Sarofim, A. F., 1985, Fragmentation Behavior of Single Coal Particles in a Fluidized Bed, *Twentieth Symposium (International) on Combustion.* The Combustion Institute, Pittsburgh, 1495-1504.

(2) Mitchell, R. E. and McLean, W. J., 1982, On the Temperature and Reaction Rate of Burning Pulverized Fuels. *Nineteenth Symposium (International) on Combustion.* The Combustion Institute, Pittsburgh, 1113-1122.

(3) Field, M. A., Gill, D. W., Morgan, B. B., and Hawksley, P. G. W., 1967, *Combustion of Pulverized Coal,* BCURA, Chap. 6 186-195.

(4) Reyes, S. and Jensen, K. F., 1986a, Percolation Concepts in Modelling of Gas-solid Reactions I. Application to Char Gasification in the Kinetic Regime. *Chem. Eng. Sci.* **41**, 333-343.

(5) Reyes, S. and Jensen, K. F., 1986b, Percolation Concepts in Modelling of Gas-solid Reactions I. Application to Char Gasification in the Diffusion Regime. *Chem. Eng. Sci.* **41**, 345-354.

(6) Kerstein, A. R. and Bug, A. L. R., 1986, Scaling Theory of Pore Growth in a Reactive Solid, *Phys. Rev. B* **34**, 1754-1761.

(7) Sahimi, M., and Tsotsis, T. T., 1988, Statistical Modeling of Gas-solid Reaction with Pore Volume Growth: Kinetic Regime. *Chem. Eng. Sci.,* **43**, 113-121.

(8) Kerstein, A. R. and Edwards, B. F., 1986, Percolation Model for Simulation of Char Oxidation and Fragmentation Time-Histories, *Chem. Eng. Sci.*, **42**, 1629-1634.

(9) Sarofim, A. F., Howard, J. B., and Padia, A. S., 1977, The Physical Transformation of the Mineral Matter in Pulverized Coal Under Simulated Combustion Conditions, *Combustion Science & Technology*, **16**, 187-204.

(10)Helble, J. J. and Sarofim, A. F., 1987, Influence of Char Fragmentation on Ash Particle Size Distribution, preprint.

(11)Holve, D. J., 1986, In Situ Measurement of Flyash Formation from Pulverized Coal, *Combustion Science & Technology,* **44**, 269-287.

(12)Sahimi, M., and Tsotsis, T. T., 1987, Dynamic Scaling for the Fragmentation of Reactive Porous Media, *Phys. Rev. Lett.*, **59**, 888-891.

(13)Smith, I.W., 1971, The Kinetics of Combustion of Size Graded Pulverized Fuels in the Temperature Range 1200-2700 K, *Combustion & Flame,* **17**, 304-313.

(14)Walker, P. L., Ruskino, F.,Austin, L. G., 1967, Gas Reactions of Carbon, *Advances in Catalysis*, **11**, 133-221.

(15)Field, M. A., 1970, Measurements of the Effect of Rank on Combustion Rates of Pulverised Coal, *Combustion & Flame,* **14**, 237-248.

(16)Wall, T. F., Gururajan, V. S., 1986, Combustion Kinetics and the Heterogeneous Ignition of Pulverized Coal, *Combustion & Flame,* **66**, 151-157.

# Flowfield Simulations in Industrial Furnace Configurations

Paul A. Gillis and Philip J. Smith

Combustion Computations Laboratory
75 CTB, Brigham Young University
Provo, Utah 84604

## 1 Introduction

A fundamental element of comprehensive pulverized-fuel combustion modelling is the description of the turbulent gaseous flow field within the furnace. As part of a program to develop a three-dimensional coal combustion code, a non-reacting gas flow dynamics model has been developed. This flow model, GAS3D, has been demonstrated in a variety of industrial configurations including corner-fired, cross-fired, and wall-fired furnace geometries. This paper discusses the components and capabilities of the model and presents comparisons between experimental data and model predictions for a wall-fired furnace.

The emphasis of this paper is on evaluating model performance. Experimental data has been obtained from Consolidation Coal Company for a wall-fired furnace. This configuration has been simulated with GAS3D using three different turbulence models. A description of the flow patterns predicted within the furnace are given. Comparisons are made between the predictions and experimental data and between the different turbulence models.

## 2 Solution Method

Steps common to all finite difference numerical techniques are the formulation of the equations, discretization of these equations, and the solution of the resulting coefficient matrices. GAS3D couples the momentum and continuity equations with the SIMPLE algorithm (1), utilizes a first-order hybrid upwind and central differencing scheme, and iteratively solves the difference coefficient matrices by approximating them as tridiagonal systems, which are solved with the Thomas algorithm.

The SIMPLE (Semi-Implicit Method for solving Pressure Linked Equations) algorithm is a technique for solving the equations of motion and continuity in a decoupled fashion. It requires a initial guess of the pressure field which is then updated through the calculation of a pressure correction. This method of solving the pressure field can require hundreds of iterations and alternative numerical techniques are being investigated. These alternatives include solving the equations in a coupled manner, similar to Vanka's BLIMM method (2) and the use of multigrid algorithms (3).

Finite difference coefficient matrices are often very sparse and the direct inversion of these matrices is rarely practical. Due to the first-order differencing of convection terms employed in GAS3D, the matrices formed are heptadiagonal. Each matrix is first approximated as a series of three tridiagonal matrices. These tridiagonal matrices are then solved individually with the Thomas algorithm and the solution procedure is repeated several times to resolve the coupling in the three coordinate directions. This matrix solver was initially observed to account for up to 65% of the overall run time on a CONVEX C-1 computer. Reordering the inner loops of the Thomas algorithm eliminated recursion and allowed for vectorization of the solver. This resulted in a significant reduction in matrix solution($\sim$ 80 %) and overall computational ($\sim$ 40 %) time.

## 3 Model Capabilities

The model allows for simulations to be made in either the Cartesian or polar coordinate system. Initial validation of the model was made through comparisons with the predictions from an extensivity evaluated axisymmetric gas dynamics code (4). A case was first run and documented with the axisymmetric model. This axisymmetric geometry was input and flow was simulated with the three-dimensional model for both coordinate systems. Predictions from the 3-D polar case were indistinguishable from the axisymmetric run. Cartesian predictions were similiarly validated through comparison.

GAS3D has been written in a modular manner to aid understanding and ease modification. The model consists of a main driver and forty-four subroutines, each made up of an average of 134 lines of FORTRAN coding. All boundary conditions are controlled by a single three-dimensional array which specifies each cell (computational node) as being part of an inlet, flow field, or a wall (intrusion). Complex geometries can be easily simulated by input to this geometry array. Thus, a preprocessor can prepare this array for model input. Inlet velocity profiles, including swirling burners, can also be input directly to the code. Inlets and outlets on all six faces of the computational domain are possible through the same array. There is no limitation to the number of inlets or outlets on any one face, nor the number of faces having inlets, outlets, or both. However, if an outlet is located within a recirculation zone, an overall mass balance cannot be adequately closed and the code will not fully converge. The model will also handle structural intrusions at any point in the flow field. Intrusions are needed to model such important features as inlet quarls, ash bins, tube banks, clipped corners, and the furnace nose. Test cases have been successfully converged which included constricted exits, flow around successive baffles, and bluff bodies surrounded on all six sides by the flow field.

## 4 Turbulence Models

The differential equation set employed in the model was derived from the vector forms of the conservation equations for mass and momentum (5). The equations were manipulated into a standard steady-state form to ease differencing. The instantaneous form of the expanded conservation equations were Favre averaged to allow for a computationally feasible length scales:

$$\tilde{\phi} \equiv \frac{\overline{\rho\phi}}{\overline{\rho}} \qquad 1)$$

The Reynold's stresses, $\rho\overline{\acute{u}_i\acute{u}_j}$, where $\acute{u}_i$ is the fluctuating component of velocity in the ith direction, are modelled wtih the Bousinesq hypotheses:

$$-\overline{\acute{u}_i\acute{u}_j} = -\mu_t \nabla \bar{u} \qquad 2)$$

The time averaged differential equations can be manipulated to resemble the instantaneous form of the equations by combining the molecular viscosity, $\mu_l$, with the eddy diffusivity. This differential equation set, for both the Cartesian and cylindrical coordinate systems, is presented in its Favre averaged form in Table 1.

Turbulence closure models have been developed for varying levels of sophistication. The most basic models, such as the constant eddy diffusivity model and Prandtl's mixing length model, contain simplifications which normally restrict their application. The most commonly used turbulence model is the two-equation k-$\epsilon$ model. Its popularity is due in part to the disadvantages of its more sophisticated alternatives, namely, second-order closure models and large-eddy simulations. These alternatives are hindered by the enormous increase in computational resources

needed to either solve the Reynolds stress transport equations in second-order closures or resolve the fine time and spacial scales required for large-eddy simulations.

The simplest turbulence assumption is that of constant eddy diffusivity. Because turbulence is normally generated due to shear forces in the gases, this assumption is rarely true. The a priori determination of an average eddy diffusivity is difficult. A slightly more sophisticated closure scheme is the Prandtl's mixing length model. This model, given by Equation 3, relates the eddy diffusivity to the mean velocity gradient.

$$\mu_t = \rho l_m^2 \left|\nabla \bar{u}\right| \qquad 3)$$

The main drawback with this model is the determination of the mixing length, $l_m$, for complex flows. The value for $l_m$ has been empirically determined for a number of simple jets and flows but a value of $l_m$ for recirculating and three-dimensional flows is difficult to determine.

The k-$\epsilon$ turbulence model was introduced to provide a means of modeling the transport of k, the turbulent kinetic energy, and $\epsilon$, the dissipation of turbulent kinetic energy. Transport equations are devised for both k and $\epsilon$ that include terms to model convection, diffusion, production, and dissipation of these quantities. The differential equations for k and $\epsilon$, including the generation term, G, used in the model are given in Table 1. These equations are solved for each gas phase iteration. After obtaining local values for k and $\epsilon$, the local eddy diffusivity is calculated from the Prandtl-Kolmogorov relationship:

$$\mu_t = \frac{C_\mu \rho k^2}{\epsilon}, C_\mu = 0.09 \qquad 4)$$

GAS3D currently contains options for the use of a constant eddy diffusitivity, the Prandtl's mixing length turbulence model, or the standard k-$\epsilon$ model.

# 5 Reactor Flow Patterns

The pilot scale furnace simulated in this paper is operated by Consolidation Coal Corporation in Liberty, Pennsylvania. The furnace is approximately $\frac{1}{10}$ scale of a full utility boiler and is fired from four swirled burners. The burners are located on a single wall in a diamond configuration and are all swirled in the same direction. The outlet is located above the burners on the east wall. Details about the furnace configuration can be seen in Figures 1 and 2. The furnace geometry is similiar in design to large industrial boilers and contains an ash bin, furnace nose, and several clipped corners. This geometry was modelled with a grid that contained 35 points in the x or depth direction, 45 points in the y or width direction, and 65 points in the z or height direction. Converged results for this 102375 node case were obtained using the three turbulence models described previously. Each turbulence model produced significantly differing results.

The constant eddy diffusivity model produced the simplest flow field. This flow field contained only two large scale vortices. The largest vortex was predominantly visible in the x planes, flowed in the clockwise direction, and extended over the entire length of the reactor. No large recirculation zones were predicted in the z planes, but burner centerline recirculation was present. Figure 1A illustrates flow patterns at a normalized width of 0.5. This figure shows a strong vortex centered below the burners that extends approximately half way up the reactor. The shaded areas in these figures represent reactor walls and the arrows signify velocity vectors constucted from the two components of velocity parrallel to the designated plane. The length and direction of each vector represents predicted velocity for the location specified by the vector tail. In order to reduce congestion, less that one half of the computational nodes are represented with vectors. There are

two sizes of unfilled arrowheads and their ratio along with the scale for the small vectors is given in Figures 1 and 2.

Figure 1B provides the flow field prediction for the center y plane using a mixing length turbulence model. This figure shows a highly viscous type flow, especially in the near-burner region and the absent of major vortices in this plane. The viscous flow is generated because the mixing length model produces high eddy diffusivity values in the high velocity gradient regions around the burners. The x plane predictions show high velocities along the north wall which decrease to near stagnation along the south wall. Strong counter-clockwise swirling vortices are found in all the z planes starting in the ash bin and extending beyond the furnace nose.

The k-$\epsilon$ turbulence model yielded the most complex flow field prediction. Figure 1C reveals numerous swirling patterns in this single plane. Seperate vortices in the ash bin, above the burners, and behind each burner, as well as strong burner centerline recirculations are all predicted. Clockwise swirling vortices are observed in nearly all the z planes. Numerous localized vortices can be found in the predicted x planes. The k-$\epsilon$ turbulence model predicted a central recirculation zone with gases flowing downward in the center of the reactor, but flowing upward near the east,west,north and south walls. Figure 1 illustrates the vast differences in both magnitude and direction of the velocities predicted by the three turbulence models.

# 6 Data Comparisons

Velocity measurements in the Consol furnace were made with a $\frac{1}{4}$ inch pitot tube connected to an electro-manometer. The y component of velocity was not included in these measurements. Experimental velocity data were obtained for 50 points all above the burners. The filled arrowheads in Figures 1 and 2 represent these data points. In Figure 2, all 50 data points are shown with the k-$\epsilon$ predictions. It should be noted in Figure 2 that the data points are for the vertical component of velocity only.

The predictions in Figure 1C agree significantly better than the predictions of Figures 1A or 1C. The agreement between predictions and data in Figures 1A and 1B is poor. For example, the k-$\epsilon$ simulation is the only model that predicted downward flow in the reactor center and higher velocities on east wall than on the west wall. The majority of experimental vectors in Figure 1C agree with the predictions in both direction and magnitude. The obvious exceptions are the center data vectors at a normalized height of 0.58 and 0.70. There are several possible reasons for these decrepancies. The most probable cause is that the central recirculation zone is being overpredicted by the k-$\epsilon$ model. An earlier study on two-dimensional swirling flows faulted the k-$\epsilon$ model with overpredicting the length of recirculation zones (6). The transient nature of turbulence could create difficulties in correcting determining direction and magnitude of gas velocity in a recirculation zone. The steady-state velocity predicted by GAS3D could be difficult to verify in a region where turbulent eddies are constantly passing. More precise inlet conditions could also aid isolated the cause of these decrepancies.

Figures 2 shows predicted flowfields at three different depths: Figure 2A represents a x plane near the burners and east wall; Figure 2B represents a x plane at a normalized depth of 0.5; and Figure 2C is near the west wall. The swirl in the secondary of the burners drives the lower clockwise vortices found in Figures 2A and 2B. A counter clockwise swirling pattern can also be found in outlet in the upper part of Figures 2A and 2B. Although not always exact in magnitude, the k-$\epsilon$ model appears to predict the trends shown by the data. In Figure 2A, the model predicted the change from higher north wall velocities to higher south wall velocities as the gases flowed upward. The two data points in direct directional disagreement with predictions seen in Figure 1C can also be found in Figure 2B. It is probable that if the central recirculation zone length

could be better simulated the agreement in the top data plane (height = 0.70) would improve. The general agreement illustrated in Figures 1C, 2A, 2B, and 2C is reasonable considering the complexity of the flow.

The presence of a fine vortex structure in the k-$\epsilon$ predictions presents some interesting questions. Additional work is needed to determine the dependence of vortex structure on coarseness of the grid. Additional vortex structure could be revealed by converging this case with finer grid sizing. Previous investigators have found that the inlet conditions are vital to correctly simulating turbulent flow. Further investigation is warrented into determining the sensitivity of solutions to such parameters as swirl number and inlet velocity profile.

# 7 Conclusion

A three-dimensional flow model has been developed and validated for simulating complex enclosed flow. The selection of turbulence model has been shown to greatly affects flow predictions. The k-$\epsilon$ model appeared to represent significant predictive improvement over the simpler turbulence models. Although the k-$\epsilon$ model appeared to overpredict the size of some recirculation zones, it yielded predictions in general agreement with experimental data. Further study is warranted to determine the applicabilty of other turbulence models and the effect of grid resolution and inlet conditions on predictions.

# 8 Acknowelgements

We wish to thank Consolidation Coal Corporation for providing the experimental data used in this paper. Additional support for this research was provided by the following organizations: Advanced Fuel Resources, Inc., Babcock and Wilcox, Combustion Engineering, Inc., Consolidation Coal Company, Electric Power Research Institute, Empire State Electric Energy Research Co., Foster Wheeler Development Co., Tennessee Valley Authority, U.S. Department of Energy - METC, U.S. Department of Energy - PETC, and Utah Power and Light Co.

# 9 References

1. Patankar, S.V., Numerical Heat Transfer and Fluid Flow, McGraw-Hill Book Company, New York (1980).
2. Vanka, S.P., "Block-Implicit Multigrid Solution of Navier-Stokes Equations in Primitive Variables," Journal of Computational Physics, Vol. 65, 138-158 (1986).
3. Brandlt, A., Multigrid Techniques: 1984 Guide with Applications to Fluid Dynamics, GMD-Studien Nr. 85, Schloss Birlinghoven, West Germany (1984).
4. Smoot, L.D. and Smith, P.J., Coal Combustion and Gasification, Plenum Press, New York (1985).
5. Bird, R.B., Stewart, W.E., and Lightfoot, E.N., Transport Phenomena, John Wiley & Sons, New York (1960).
6. Sloan, D.G., Smith, P.J., and Smoot, L.D, "Modeling of Swirl in Turbulent Flow Systems," Prog. Energy Combust. Sci., Vol. 12, 163-250 (1986).

## Table 1. Differential Equation Set for GAS3D

### Part A. Cartesian Coordinate System

$$\frac{\partial(\bar{\rho}\tilde{u}\phi)}{\partial x} + \frac{\partial(\bar{\rho}\tilde{v}\phi)}{\partial y} + \frac{\partial(\bar{\rho}\tilde{w}\phi)}{\partial z} - \frac{\partial}{\partial x}\left(\Gamma_\phi \frac{\partial \phi}{\partial x}\right) - \frac{\partial}{\partial y}\left(\Gamma_\phi \frac{\partial \phi}{\partial y}\right) - \frac{\partial}{\partial z}\left(\Gamma_\phi \frac{\partial \phi}{\partial z}\right) = S_\phi$$

| Equation | $\phi$ | $\Gamma_\phi$ | $S_\phi$ |
|---|---|---|---|
| Continuity | 1 | 0 | 0 |
| X Momentum | $\tilde{u}$ | $\mu_e$ | $-\frac{\partial P}{\partial x} + \frac{\partial}{\partial x}\left(\mu_e \frac{\partial \tilde{u}}{\partial x}\right) + \frac{\partial}{\partial y}\left(\mu_e \frac{\partial \tilde{v}}{\partial x}\right) + \frac{\partial}{\partial z}\left(\mu_e \frac{\partial \tilde{w}}{\partial x}\right)$ |
| Y Momentum | $\tilde{v}$ | $\mu_e$ | $-\frac{\partial P}{\partial y} + \frac{\partial}{\partial x}\left(\mu_e \frac{\partial \tilde{u}}{\partial y}\right) + \frac{\partial}{\partial y}\left(\mu_e \frac{\partial \tilde{v}}{\partial y}\right) + \frac{\partial}{\partial z}\left(\mu_e \frac{\partial \tilde{w}}{\partial y}\right)$ |
| Z Momentum | $\tilde{w}$ | $\mu_e$ | $-\frac{\partial P}{\partial z} + \frac{\partial}{\partial x}\left(\mu_e \frac{\partial \tilde{u}}{\partial z}\right) + \frac{\partial}{\partial y}\left(\mu_e \frac{\partial \tilde{v}}{\partial z}\right) + \frac{\partial}{\partial z}\left(\mu_e \frac{\partial \tilde{w}}{\partial z}\right)$ |
| Turbulent Energy | k | $\frac{\mu_e}{\sigma_k}$ | $G - \bar{\rho}\epsilon$ |
| Dissipation Rate | $\epsilon$ | $\frac{\mu_e}{\sigma_\epsilon}$ | $\left(\frac{\epsilon}{k}\right)(c_1 G - c_2 \bar{\rho}\epsilon)$ |

where:

$$G = \mu_e \left\{ 2\left[\left(\frac{\partial \tilde{u}}{\partial x}\right)^2 + \left(\frac{\partial \tilde{v}}{\partial y}\right)^2 + \left(\frac{\partial \tilde{w}}{\partial z}\right)^2\right] + \left(\frac{\partial \tilde{u}}{\partial y} + \frac{\partial \tilde{v}}{\partial x}\right)^2 + \left(\frac{\partial \tilde{u}}{\partial z} + \frac{\partial \tilde{w}}{\partial x}\right)^2 + \left(\frac{\partial \tilde{v}}{\partial z} + \frac{\partial \tilde{w}}{\partial y}\right)^2 \right\}$$

### Part B. Cylindrical Coordinate System

$$r\frac{\partial(\bar{\rho}\tilde{u}\phi)}{\partial x} + \frac{\partial(\bar{\rho}r\tilde{v}\phi)}{\partial r} + \frac{\partial(\bar{\rho}\tilde{w}\phi)}{\partial \theta} - r\frac{\partial}{\partial x}\left(\Gamma_\phi \frac{\partial \phi}{\partial x}\right) - \frac{\partial}{\partial r}\left(r\Gamma_\phi \frac{\partial \phi}{\partial r}\right) - \frac{\partial}{\partial \theta}\left(\frac{\Gamma_\phi}{r}\frac{\partial \phi}{\partial \theta}\right) = S_\phi$$

| Equation | $\phi$ | $\Gamma_\phi$ | $S_\phi$ |
|---|---|---|---|
| Continuity | 1 | 0 | 0 |
| X Momentum | $\tilde{u}$ | $\mu_e$ | $-r\frac{\partial P}{\partial x} + r\frac{\partial}{\partial x}\left(\mu_e \frac{\partial \tilde{u}}{\partial x}\right) + \frac{\partial}{\partial r}\left(\mu_e r \frac{\partial \tilde{v}}{\partial x}\right) + \frac{\partial}{\partial \theta}\left(\mu_e \frac{\partial \tilde{w}}{\partial x}\right)$ |
| R Momentum | $\tilde{v}$ | $\mu_e$ | $-r\frac{\partial P}{\partial r} + r\frac{\partial}{\partial x}\left(\mu_e \frac{\partial \tilde{u}}{\partial r}\right) + \frac{\partial}{\partial r}\left(\mu_e r \frac{\partial \tilde{v}}{\partial r}\right) + \frac{\partial}{\partial \theta}\left(\mu_e \frac{\partial \tilde{w}}{\partial r} - \frac{\tilde{w}}{r}\right) - \frac{2\mu_e}{r}\frac{\partial \tilde{w}}{\partial \theta} - \frac{2\tilde{w}\mu_e}{r} + \bar{\rho}\tilde{w}^2$ |
| $\theta$ Momentum | $\tilde{w}$ | $\mu_e$ | $-\frac{\partial P}{\partial \theta} + r\frac{\partial}{\partial x}\left(\frac{\mu_e}{r}\frac{\partial \tilde{u}}{\partial \theta}\right) + \frac{\partial}{\partial r}\left(\mu_e \frac{\partial \tilde{v}}{\partial \theta} - \mu_e \tilde{w}\right) + \frac{\partial}{\partial \theta}\left[\left(\frac{\mu_e}{r}\right)\left(\frac{\partial \tilde{w}}{\partial \theta} + 2r\frac{\tilde{v}}{\partial r}\right)\right] + \mu_e\left(\frac{\partial \tilde{w}}{\partial r} + \frac{\partial \tilde{v}}{r\partial \theta} - \frac{\tilde{w}}{r}\right) - \bar{\rho}\tilde{v}\tilde{w}$ |
| Turbulent Energy | k | $\frac{\mu_e}{\sigma_k}$ | $r(G - \bar{\rho}\epsilon)$ |
| Dissipation Rate | $\epsilon$ | $\frac{\mu_e}{\sigma_k}$ | $\left(r\frac{\epsilon}{k}\right)(c_1 G - c_2 \bar{\rho}\epsilon)$ |

where:

$$G = \mu_e \left\{ 2\left[\left(\frac{\partial \tilde{u}}{\partial x}\right)^2 + \left(\frac{\partial \tilde{v}}{\partial r}\right)^2 + \left(\frac{\partial \tilde{w}}{r\partial \theta} + \frac{\tilde{v}}{r}\right)^2\right] + \left(\frac{\partial \tilde{u}}{\partial r} + \frac{\partial \tilde{v}}{\partial x}\right)^2 + \left(\frac{\partial \tilde{u}}{r\partial \theta} + \frac{\partial \tilde{w}}{\partial x}\right)^2 + \left(\frac{\partial \tilde{v}}{r\partial \theta} + \frac{\partial \tilde{w}}{\partial r} - \frac{\tilde{w}}{r^2}\right)^2 \right\}$$

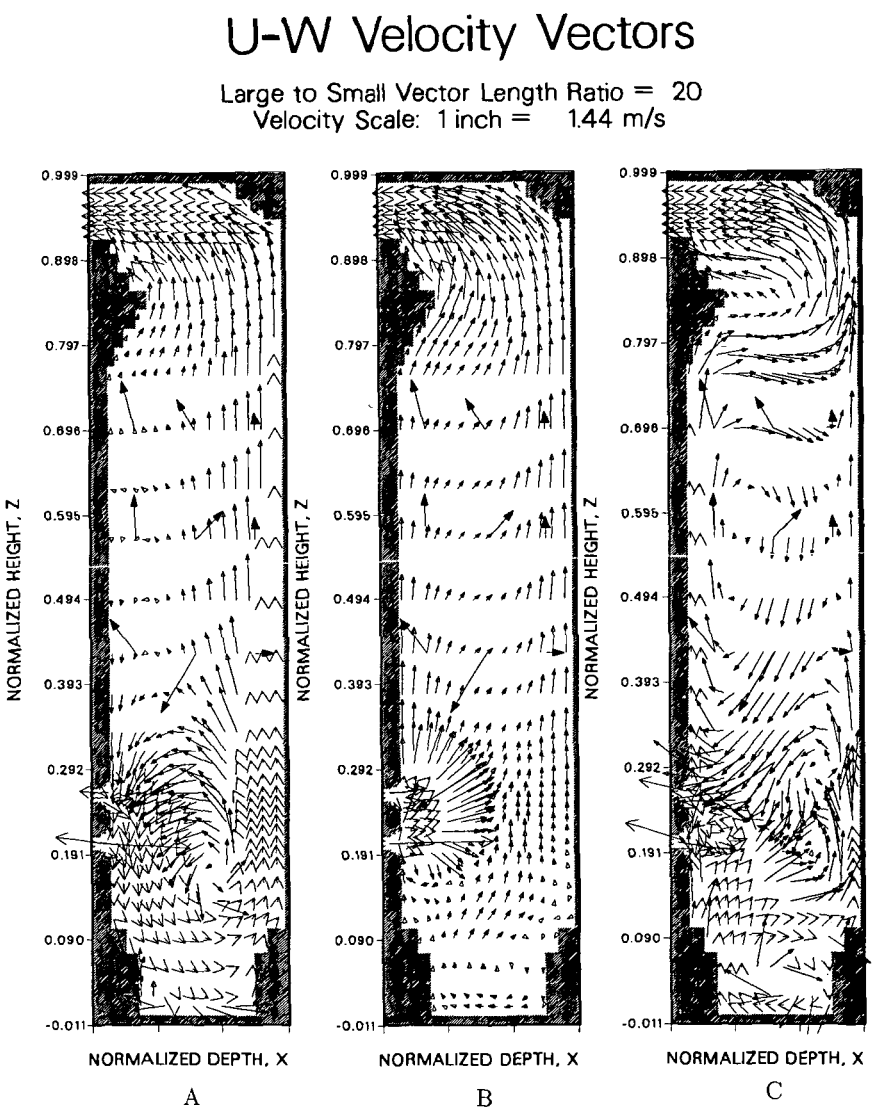


Figure 1. Comparison of velocity predictions and experimental data at a normalized width of 0.5 for the following turbulence models: A, constant eddy diffusivity; B, simple mixing length model; and C, k-$\epsilon$ model.

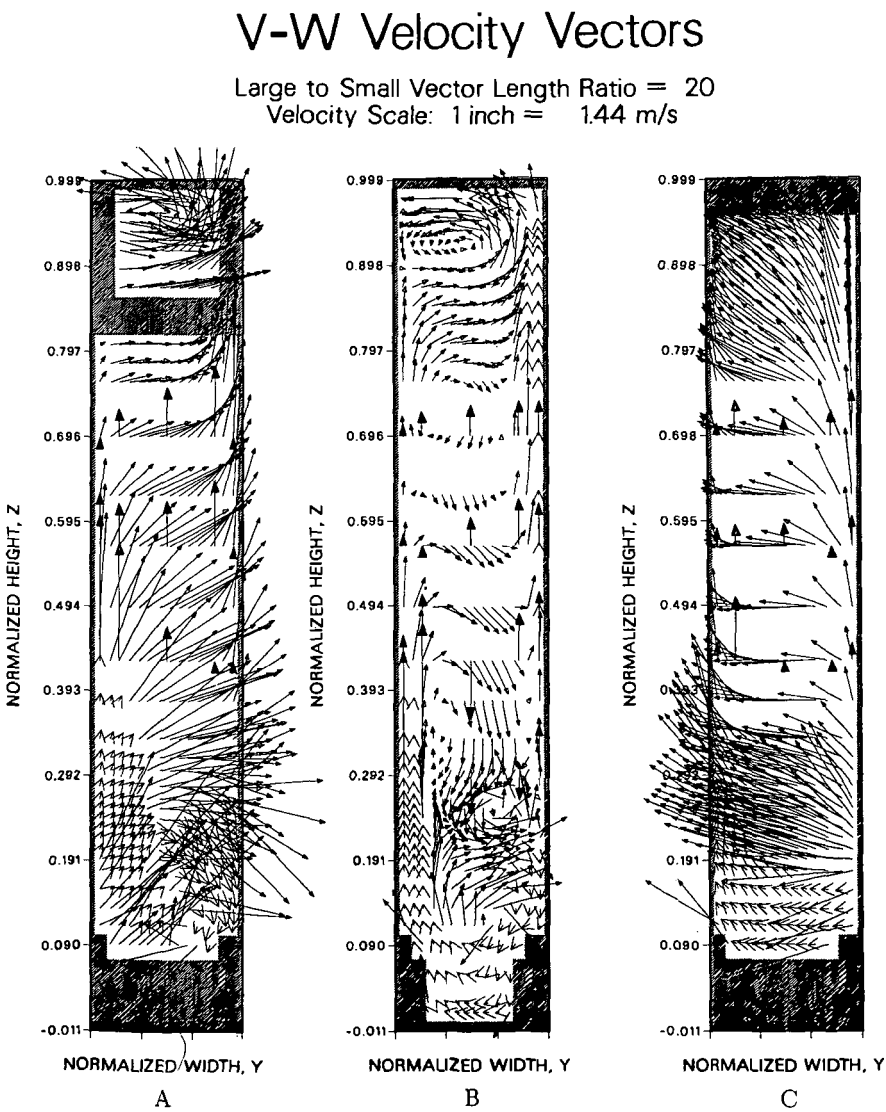


Figure 2. Comparison of velocity predictions and the vertical component of velocity measured in three x planes: A, normalized depth of 0.17; B, normalized depth of 0.50; C, normalized depth of 0.83.

# Correlation Between Refractive Indices and Other Fuel-Related Physical/Chemical Properties of Pyrolysis Liquids Derived From Coal, Oil Shale, and Tar Sand

M. Rashid Khan

U.S. Department of Energy
Morgantown Energy Technology Center
Morgantown, WV 26507-0880

## ABSTRACT

In the literature, characterization techniques based upon the liquid's refractive index are used with petroleum distillates to predict fuel-related properties; however, essentially nothing has been reported on the application of this technique to pyrolysis liquids. Measurements of the refractive indices of the pyrolysis liquids derived from various feedstocks (coal, oil shale, and tar sand) were made and appear to correlate well with the liquids' physical and chemical properties. The refractive indices of the pyrolysis liquids show good correlations with liquid density (correlation coefficient of 0.98), carbon and proton aromaticities (correlation coefficients of 0.88 and 0.91, respectively), and liquid carbon residue (i.e., correlation coefficient of 0.88 with the Conradson carbon residue). The above and other correlations were developed using data from at least 7 to as many as 35 discrete samples. These correlations have been used to develop empirical models. These findings demonstrate the potential of using the liquid's refractive index as a rapid technique to characterize the fuel-related properties of fossil fuel liquids generated by pyrolysis (before they are hydrogenated).

## INTRODUCTION AND OBJECTIVES

The Morgantown Energy Technology Center (METC) results demonstrated that relatively high-quality liquid fuels (low sulfur, high H/C) can be produced by low-temperature devolatilization of coal (1,2). Physical and chemical properties characterization of these liquids has been the focus of several studies during the last few years (1-5).

Correlations based on the data obtained from relatively simple characterization techniques for predicting fuel-related physical and chemical properties of pyrolysis liquids would facilitate the utilization of these liquids in various processing schemes. Properties such as molecular weight and aromaticity of liquids influence their utilization behavior/properties (e.g., viscosity, smoke point). Measurements of molecular weight or aromaticity can be difficult, time consuming, and expensive; can require skilled operators; and are often beyond the resources of most small laboratories.

The correlations between properties of petroleum liquids and their refractive indices are available in the literature (6-8). Sturm et al. (8a), fractionated the pyrolysis liquid generated in a rapid-rate reactor (Coal Oil Energy Development, COED) into various distillate cuts. It was not stated at what condition hydrogenation was effected. The COED liquids were hydrogenated (8b) to remove the heteroatom contents (e.g., sulfur, nitrogen) and to improve their fuel value.

White et al. (6) compared the refractive indices of coal liquefaction products with their chemical properties (e.g., molecular weight). These researchers also reported an excellent review of previous work in this area (6).

In previous studies, it was demonstrated by Khan (9) that the pyrolysis liquids generated from weathered fossil fuel samples (including coal and oil shale) had higher liquid refractive indices than those obtained from unweathered samples.

The objective of this paper is to illustrate the relationship between the refractive indices of pyrolysis liquids and their fuel-related physical (density, Conradson carbon residue) and chemical properties (aromaticity, molecular weight, hydrocarbon type, etc.).

## EXPERIMENTAL SECTION

A fixed-bed reactor (slow heating-rate organic devolatilization reactor, SHRODR) was used to generate pyrolysis liquids at 500°C. More details on this reactor system as well as the experimental procedures used and the reproducibility of data are available (1,2,5). A range of feedstocks (primarily coal, but also oil shale, and tar sand) were devolatilized in this reactor. Coal samples were supplied by the Penn State/DOE coal data bank (10). The origin of shale samples (eastern and western) and the Pittsburgh No. 8 coal has been discussed elsewhere (9). Tar sand samples were procured from the Western Research Institute (WRI).

Sample preservation and avoidance of air oxidation of samples were key considerations to this investigation as reported in previous studies (9,11-14). Availability of fresh (well preserved, not weathered) samples was the criterion used for sample selection. Some coal samples utilized by Given et al. (15) for an investigation on direct liquefaction were selected in this study for comparison. Primarily bituminous coals were used in this study as these are known to yield the highest liquid product during pyrolysis (1,3). All sample preparation and handling were performed in an inert atmosphere.

The refractive index of liquid samples were measured at 20°C by Huffmann Laboratories, Inc., applying ASTM D-1218 methods. The refractive index of 1-bromonaphthalene was measured as a standard before the refractive index of each pyrolysis liquid. The refractive index measurement of 1-bromonaphthalene was within ± 0.0005 units of the reference value (reported by Hoffmann). Conradson carbon residue was determined at Saybolt Lab (Pasadena, Texas) using ASTM D-189. The density measurements were (reproducible within ± 0.0001), also performed at Saybolt at 15.5°C by ASTM D-70.

The aromaticity of the liquids was measured at the University of North Dakota Energy and Minerals Research Center (UNDEMRC) by proton NMR, using the Clutter et al. (16) procedure with a Varian XL200 NMR Spectrometer. $^1$H NMR was used for determination of aromaticities. Molecular weights were calculated based on the NMR data applying the equation used by Clutter et al. (16).

Neutral fractions of pyrolysis liquids were generated chromatographically on activated alumina. A 20-inch x 3/8-inch column was loaded with 25 g of activated alumina (Biorad). A sample of 0.2 g was charged to the column and the neutral fraction was eluted with 50 mL of benzene. The benzene was removed from the sample by rotary evaporation. To ensure that the lower-boiling point components of the sample were not lost during benzene removal, the benzene was not completely removed from the sample. The concentration of the residual benzene was then determined by combined gas chromatography/mass spectrometry (GC/MS) and the final weights of the neutral fractions were adjusted to account for the residual benzene. The polar material was not eluted from the column, but was determined by difference.

The neutral fractions were analyzed using WRI's GC/MS hydrocarbon group type analysis. A Hewlett-Packard Model 5985B GC/MS system was used. The GC column was a 50-meter quartz capillary, coated with methylsilicone, and operated in programmed-temperature modes, which optimized the resolution of components. The method determines the composition of the hydrocarbon group by using selected ions that are

representative of each hydrocarbon group type and relies on the gas chromatographic separation to minimize interferences from fragment ions of other hydrocarbon groups. The results from the analyses are reported as weight percentages of the neutral fractions. The results are provided as weight percentages of the total sample that was charged to the column. The results for the neutral fractions reflect the adjusted weights of the neutral fractions after accounting for the residual benzene. Detailed analysis and distribution of the components identified in various fractions will be presented in a future communication. The distillate cut between 300° and 600°F is of interest because its properties is expected based on literature studies to match the target properties of the high-density fuels (17,18). Liquids were combusted in a thermogravimetric analysis system (TGA) at 100°C/min in air (flowrate of 120 cc/min). In addition TGA distillation of the liquids was performed (heating rate, 5°C/min, He flowrate 50 cc/min). Statistical Analyses System (SAS) Package developed by SAS Institute was used for data analyses. The linear regression analysis available in this package was applied to develop empirical models (19,20).

## RESULTS

A detailed study on the influence of feedstock type on pyrolysis liquid product yield and composition will be presented separately. In addition, comprehensive characterization data for the liquids are the subject of a separate report. Table 1 presents a summary of equations used to predict the properties of pyrolysis liquids.

The hydrogen-to-carbon ratio (H/C) of the pyrolysis liquids is an important fundamental property of liquid fuels that influences various physical (e.g., viscosity, density) and chemical (e.g., molecular weight, aromaticity, etc.) properties. The relationship (negative) between the liquid H/C ratios and the refractive indices of the liquid is presented in Figure 1A (correlation coefficient of 0.90). The following regression model was used for predicting the liquid H/C ratios:

$$[H/C] = 6.876 - 3.50\ n. \qquad 1)$$

The refractive indices (n) of the liquids correlated with the corresponding weight percent (of tar) hydrogen (H) contents (correlation coefficient = -0.83; Figure 1B). A model defined by equation (2),

$$H = 57.264 - 30.5\ n, \qquad 2)$$

was used to predict the hydrogen contents.

Figure 2 shows the correlation between the carbon aromaticities ($C_{aro}$) and the refractive indices (n) for the pyrolysis liquids derived from various fossil fuels. The correlation coefficient between the variables was 0.91. The carbon aromaticity ($C_{aro}$) could be predicted by equation (3) using a linear regression fit:

$$C_{aro} = 3.657\ n - 5.228. \qquad 3)$$

The carbon aromaticity of the same data set could be predicted somewhat better with a two-variable model that includes the liquid H/C atomic ratio:

$$C_{aro} = 2.887\ n - 0.227\ (H/C) - 3.71. \qquad 4)$$

Figure 3 compares the proton aromaticity with the refractive indices of the liquids (correlation coefficient of 0.88). The actual aromaticity data can be predicted based on a single-variable model, defined by

$$H_{aro} = 2.102\ n - 3.103. \qquad 5)$$

TABLE 1

Summary of Predictive Equations for Pyrolysis Liquids

| | Model | $R^2$* | F | P |
|---|---|---|---|---|
| 1. | $(H) = 57.264 - 30.50\ n$ | 0.70 | 65.3 | 0.0001 |
| | $(H/C) = 6.876 - 3.50\ n$ | 0.55 | 35.4 | 0.0001 |
| | n = refractive index<br>H/C = hydrogen-to-carbon ratio of liquids (atomic) | | | |
| 2. | $C_{aro} = 3.657\ n - 5.228$ | 0.82 | 131.9 | 0.0001 |
| | $C_{aro} = 2.887\ n - 0.222\ (H/C) - 3.71$ | 0.86 | 82.5 | 0.0001 |
| | $C_{aro}$ = carbon aromaticity | | | |
| 3. | $H_{aro} = 2.102\ n - 3.103$ | 0.77 | 96.8 | 0.0001 |
| | $H_{aro} = 1.739\ n - 0.105\ (H/C) - 2.39$ | 0.79 | 50.5 | 0.0001 |
| | $H_{aro} = n^{-0.56168} \times (H/C)^{-4.484}$ | 0.97** | 531.5 | 0.0001 |
| | $H_{aro}$ = proton aromaticity | | | |
| 4. | $MW = 4383.2 - 2655\ n$ | 0.70 | 65.3 | 0.0001 |
| | $MW = 1.332\ T_{50} - 1573.28d + 1589.1$ | 0.82 | 9.03 | 0.033 |
| | $MW = 1.348\ T_m - 1249.24d + 1234.6$ | 0.94 | 23.0 | 0.015 |
| | MW = molecular weight<br>$T_{50}$ = temperature of mid-distillation point (TGA)<br>$T_m$ = temperature of mid-distillation point (ASTM D-86) | | | |
| 5. | $d = 1.977\ n - 2.08$ | 0.97 | 155.2 | 0.0001 |
| | d = density, gm/cc | | | |
| 6. | $C_{con} = 37.75\ n - 55.29$ | 0.77 | 16.5 | 0.0097 |
| | $C_{con}$ = Conradson carbon residue | | | |

* $R^2$ measures how much variation in the dependent variable can be accounted for by the model (i.e., independent variable).

** $R^2$ is redefined for the no-intercept case by SAS (20). Note that this is a non-linear equation.

The F-ratio is the ratio produced by dividing the mean square for the model by the mean square of error. It tests how well the model as a whole (after adjusting for the mean) accounts for the behavior of the dependent variable (20).

P defines the "observed level of significance." In statistical terms, the level of significance, $\alpha$, of a test is defined as the probability of rejecting the null hypothesis (i.e., no linear relationship between the dependent and independent variables) given the null hypothesis is true. P gives us the largest value of $\alpha$ that would lead to the acceptance of the null hypothesis.

The predicted model, based on a two-variable model, can be defined by the equation

$$H_{aro} = 1.739\ n - 0.105\ (H/C) - 2.39. \qquad 6)$$

Proton aromaticity could also be predicted based on the following nonlinear model (see also Table 2).

$$H_{aro} = n^{-.56168} \times (H/C)^{-4.484}.$$

The molecular weights (MW) of the pyrolysis liquids (determined using NMR data) could be predicted from the refractive indices. For example, a single-variable model based on the refractive indices of the liquid could be used for this prediction. This model is given by the equation

$$MW = 4383.2 - 2655\ n \qquad 7)$$

A two-variable model based on the liquid density (d) and the mid-distillation point ($T_m$) could also be used for predicting the MW of the pyrolysis liquids (Figure 4):

$$MW = 1.348\ T_m - 1249.24d + 1234.6. \qquad 8)$$

The distillation data were obtained using the ASTM D-86 procedure. A new model, based on the same two-variable model (similar to Equation 8) but the distillation data are obtained from TGA evaporation, can be defined by the equation

$$MW = 1.332\ T_{50} - 1573.28d + 1589.1. \qquad 9)$$

In the above equation, $T_{50}$ stands for the mid-distillation temperature as determined by a TGA. The correlation coefficient between the refractive index and the density (Figure 5) of the liquids was 0.98. A linear regression fit provided the following model:

$$d = 1.977\ n - 2.08. \qquad 10)$$

The correlation coefficient between the refractive indices of various distillation cuts and the corresponding density for the COED syncrudes (reported by Strum et al.[10]) was 0.99, calculated in this study.

The correlation coefficient between the Conradson carbon ($C_{con}$) residue of the mild pyrolysis liquids derived in this study and the refractive indices of the liquids was 0.88 (Figure 6). A single-variable model was defined by the equation

$$C_{con} = 37.75\ n - 55.29 \qquad 11)$$

A liquid combustion parameter (second maximum peak of combustion) measured in a thermogravimetric analyses system (TGA) could be positively correlated somewhat with the refractive indices of the liquids (data not shown).

The significance of this TGA peak is not known. It may be worthwhile to attempt correlations of liquid combustion properties with their refractive indices, keeping previous relationships observed in this study in mind.

Additional correlations between the refractive indices and the pyrolysis liquid characterization data are presented in Figures 7 and 8. Figure 7 shows a relationship between the refractive indices of the whole liquid and the tricyclic saturated compound (so-called "high density fuels") in the 300° to 600°F cut of the neutral fraction of the pyrolysis liquids as determined by a GC/MS technique (the correlation coefficient of the data set was 0.8). The liquid distilled between 300° to 600°F was

of particular interest because this boiling range approximates the range of JP-8, a high-density aviation fuel (17,18,21). The total naphthalenes content in Cut 2 (boiling between 300° and 600°F) of the pyrolysis liquids present in the neutral fraction could be directly correlated with the refractive indices of the whole liquids (Figure 8, correlation coefficient 0.98).

Conradson carbon residue ($C_{con}$) could be correlated with the hydrogen content (correlation coefficient of - 0.92). $C_{con}$ also showed correlations with the carbon and proton aromaticities (correlation coefficients of 0.91 and 0.84, respectively). Thus, the observed correlation between the refractive index and $C_{con}$ is not surprising. The observed relation may reflect the well known fact that aromatic compounds are more susceptible to coke formation during severe heat treatment. Figure 9 compares the cetane index of the hydrogenated (8b) COED liquids distilled at various temperature ranges [data from Strum et al. (8a)] with the corresponding refractive index. A summary of correlations developed in this study are presented in Table 1.

## DISCUSSION

The results of this study demonstrate that the refractive index, used in petroleum literature to correlate fuel properties, is a relevant property to evaluate pyrolysis liquids derived from coal, oil shale, and tar sand. It is demonstrated that the liquids' H/C, density, hydrogen content, molecular weight, and aromaticity correlate with refractive indices of the pyrolysis liquids.

The relationship between the refractive index (n) and density (d) and other properties (e.g., Conradson carbon residue) of the liquids is consistent with our physical understanding of the structural properties of hydrocarbons. Paraffins have the highest hydrogen content and tend to have "fluffy" chain structures with low densities. For pure compounds, the lower the density, the lower the refractive indices. On the other hand, relatively compact cyclic (dense) aromatics are deficient in hydrogen. Cycloparaffins, which are both cyclic and hydrogen saturated, represent the best compromise between density and hydrogen content (21).

The refractive indices of pyrolysis liquids correlate with the liquid H/C ratio (correlation coefficient 0.90) or the hydrogen contents of the liquid (correlation coefficient 0.86). In this study, models have been developed to predict the H/C ratio or hydrogen contents of the liquids based on their refractive indices.

It is not surprising that refractive index correlates well with the liquid aromaticity. An increase in hydrogen content of fuels often lead to a decrease in aromaticity. For example, benzene with H/C = 1 has fa = 1, while $C_6H_{12}$ (cyclohexane) with H/C = 2 has fa = 0. Here, fa is the proton or carbon aromaticity. The correlation coefficients between refractive index and proton, or refractive index and carbon aromaticity were 0.88 and 0.91, respectively. One- and two-variable models were applied to predict the carbon and proton aromaticities of the pyrolysis liquids, based on their refractive indices.

Molecular weights are fundamental properties of liquids. For various classes of pure compounds, refractive indices tend to change rapidly at low molecular weight but less rapidly at higher molecular weight. It appeared that refractive indices of the pure liquids correlated with the negative one-half power of molecular weight (data not shown). In this study, molecular weight could be predicted based on a single (e.g., refractive index, n) or a two-variable model [including density (d) and temperatures of 50 percent evaporation as determined in a TGA ($T_{50}$) or by an ASTM technique (ASTM D-86, $T_m$)].

## SUMMARY AND CONCLUSIONS

It is demonstrated that the refractive indices of pyrolysis liquids derived from coal, oil shale, and tar sand serve as a useful property to evaluate the fuel-related physical/chemical properties of these fuels. The refractive indices of the liquids correlate well with the liquid hydrogen content (weight percent) and the H/C ratio, aromaticity (carbon and proton), molecular weight, density, and Conradson carbon residue. A number of empirical equations have been developed based on these correlations.

## REFERENCES


1. Khan, M. R. Fuel Science and Technology International, 1987, 5(2), 105-231.
2. Khan, M. R. Proceedings. International Conference on Coal Science, 1987. Netherlands, International Energy Agency, IEA.
3. Khan, M. R. "Characterization and Mechanisms of Mild Gasification Processes: Low-Temperature Devolatilization Studies," Proceedings, Fifth Annual Gasifica= tion Contractors' Meeting, June 25-27, Morgantown, WV 26505 (1985).
4. Khan, M. R.; Kurata, T. M. July 1985. The Feasibility of Mild Gasification of Coal: Research Needs. DOE/METC-85/4019. NTIS/DE85013625. 73 pp.
5. Khan, M. R. March 1986. "Production of a High-Quality Liquid Fuel From Coal by Mild Pyrolysis of Coal-Lime Mixtures," DOE/METC-86/4060 (DE86006603).
6. White, C.; Perry, M. B., Schmidt, C. E.; Douglas, L. J. Energy and Fuels,1987, 1, 99-105.
7. Riazi, M. R.; Daubert, T. E. Ind. Eng. Chem. Process Des. Dev. 1980, 19, 289-294.

8a. Sturm, G. P., Jr.; Woodward, P. W.; Vogh, S. A.; Holmes, S. A.; Dooley, J. E. BERC/RI-75/12, November 1975.

8b. Personal Communication with S. Holms, 1988.

9. Khan, M. R. Energy and Fuels, 1987, 1(4), 366-376.
10. Penn State/DOE Coal Data Bank, Office of Coal Research, Penn State University, University Park, Pennsylvania 16802.
11. Khan, M. R. 193rd ACS Petroleum Division Chemistry Preprint 1987, Denver, Colorado, April 1987.
12. Khan, M. R. Proceedings, 19th Oil Shale Symposium, Col. School of Mines, Golden, Colorado, 1986, 139-148.
13. Khan, M. R.; Jenkins, R.G. Fuel, 1985, 64 (2), 189-192.
14. Khan, M. R.; Jenkins, R.G. Fuel, 1985, 64 (11), 1,618-1,622.
15. Given, P. H., et al. Fuel, 1982, 61 (10), 971.
16. Clutter, D. R., et al. Anal. Chem., 1972, 44, 1,395.
17. Korosi, A.; Rubin, J.N. "Hydroprocessing of Light Pyrolysis Fuel Oil for Kerosene Type Jet Fuel," Wright-Patterson Air Force Base, Ohio 45433, February 1980, Technical Report AFWAL TR-83-2048.
18. "High-Density Candidate Hydrocarbon Fuels from Refinery By-Product Streams," Universal Energy Systems, Dayton, Ohio 45432, September 1985, Technical Report (Interim). Contract No. F33615-83-C-2360/585842-83-C-0383, Project No. 745, Task 001, 002.
19. Box, G. E. P. Statistics for Experiments. Wiley and Sons, New York, 1978.
20. SAS User's Guide: Basics, Version 5 Edition, SAS Institute, Box 8000, Cary, North Carolina 27511-8000.
21. Personal Communication with F. Guffy (1987).


3A:1-25-88:vw:5a

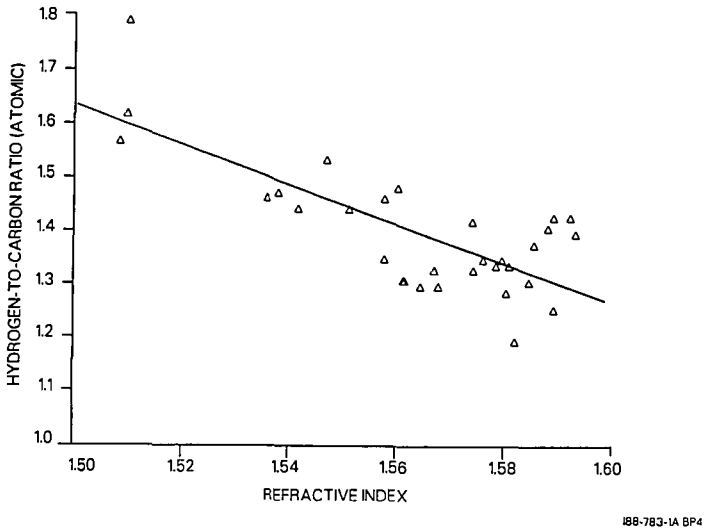


FIGURE 1A. Correlation between the liquid hydrogen-to-carbon ratio and the refractive indices of the liquid.

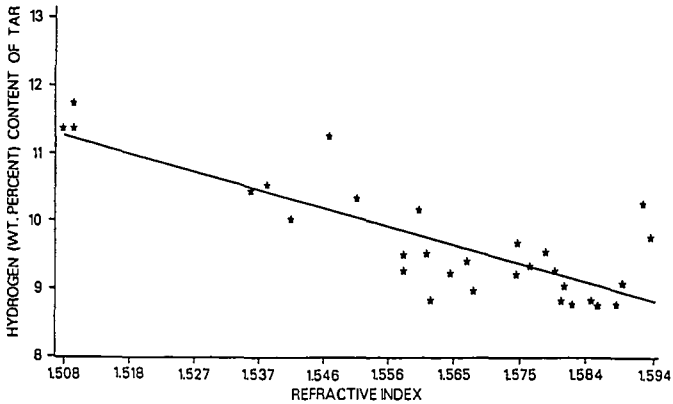


FIGURE 1B. Correlation between the liquid hydrogen content (dry basis) and the refractive indices of the liquid.

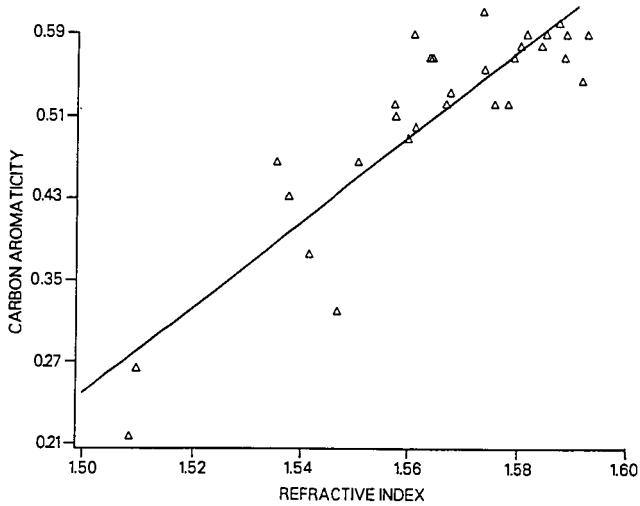


C88-783-2A BP4

FIGURE 2. Correlation between the carbon aromaticity and the refractive indices (correlation coefficient 0.91).

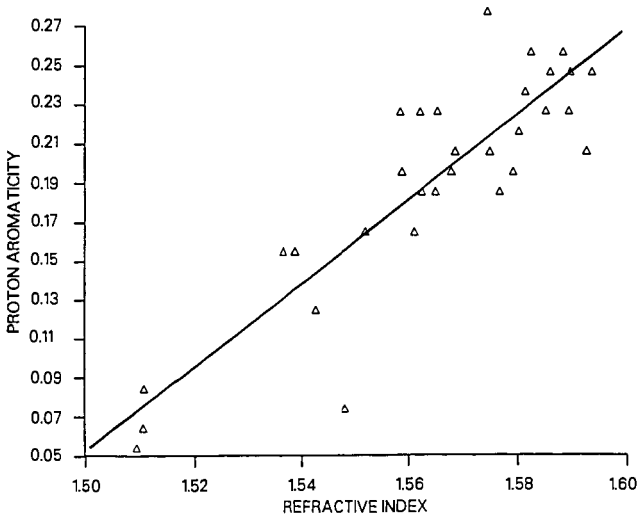


IB8-783-3A BP4

FIGURE 3. Correlation between proton aromaticity and refractive indices (correlation coefficient 0.88).

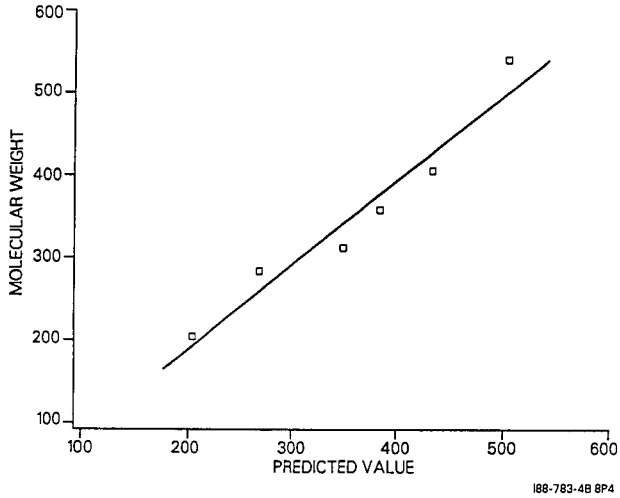


FIGURE 4. Predicted and measured molecular weight based on a two-variable model (including density and mid-distillation point ($T_{50}$). ($R^2$ = 0.93); distillation data obtained by a TGA unit.

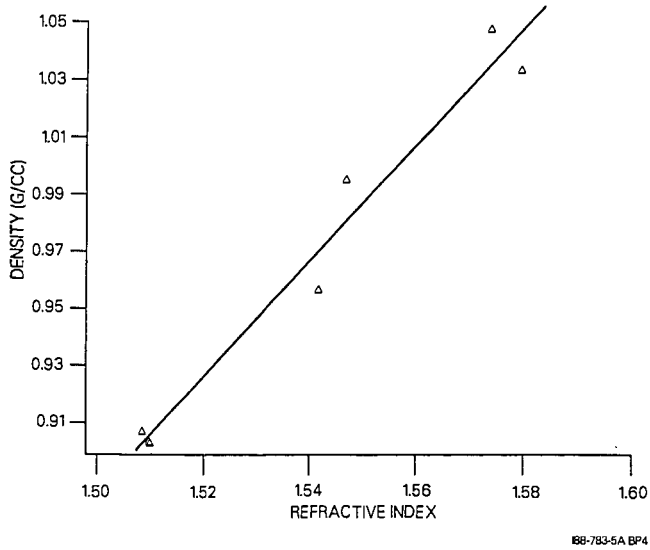


FIGURE 5. The relationship between the density and the refractive indices of the pyrolysis liquids (correlation coefficient 0.98).

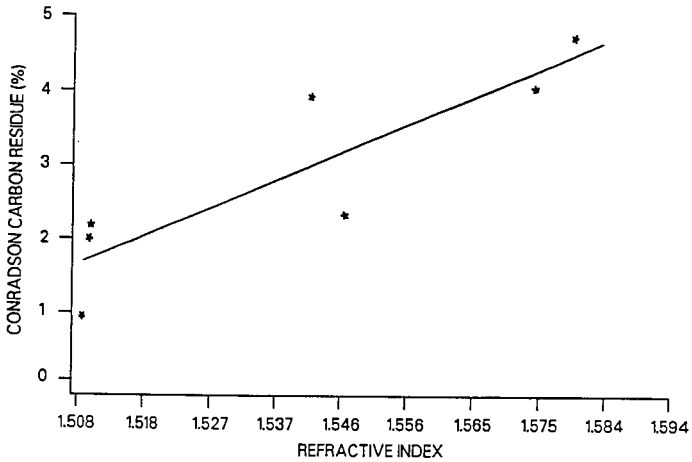


188-783-6A BP4

FIGURE 6. The relationship between the refractive indices and the Conradson carbon residue (correlation coefficient 0.88).

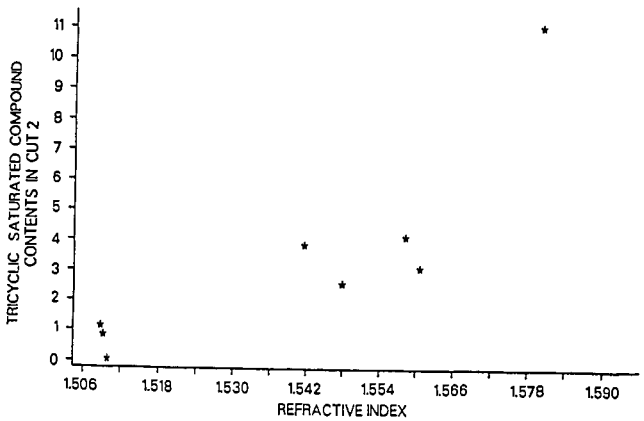


FIGURE 7. Correlation between refractive indices and triaromatic content of the liquids (in Cut 2; i.e., 300° to 600°F fraction of the neutral position of pyrolysis liquids) (correlation coefficient of 0.8).

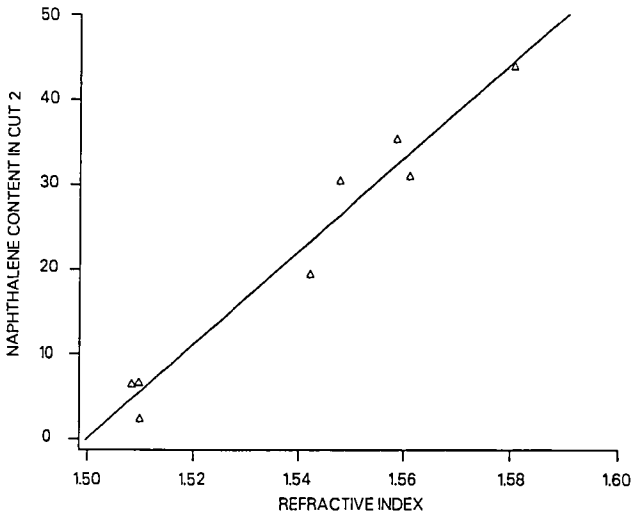


FIGURE 8. Relationship between the total naphthalene contents of the pyrolysis liquids with the refractive indices of the liquids.

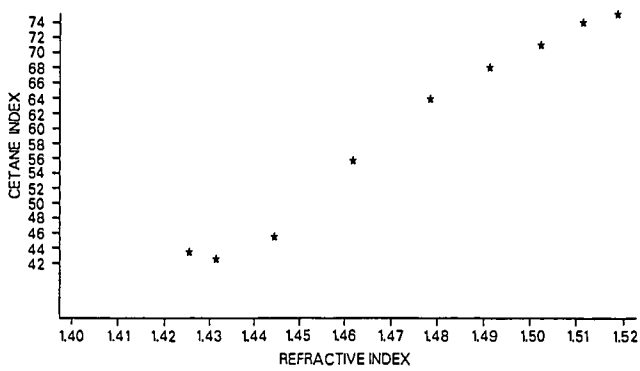


FIGURE 9. Relationship between the Cetane index with the refractive indices for the COED (hydrogenated) syncrude.

# Prediction of the Composition of Coal Tars from the Pyrolysis Mass Spectra of the Parent Coals Using Canonical Correlation Techniques

Tanmoy Chakravarty, Henk L.C. Meuzelaar, Patrick R. Jones

Biomaterials Profiling Center, University of Utah,
Salt Lake City, UT 84102

M. Rashid Khan

Morgantown Energy Technology Center, Morgantown, W. Virginia

## INTRODUCTION

In this study, we show that the mass spectrometric composition of coal tars can be predicted from the pyrolysis mass spectra of their parent coals. Curie-point low voltage electron ionization mass spectrometry (CuPy-EIMS) was performed on nineteen coals and on their respective pyrolysis liquids prepared by means of a fixed bed reactor method described elsewhere (1). Using factor and discriminant analysis techniques, the spectra can be classified and underlying structural variables responsible for the above classification identified. Furthermore, compositional similarities and dissimilarities between the solid samples and their liquids can be brought out using canonical correlation methods (2). Table I lists the samples, their PSOC numbers, geological origin and the rank information. Of the nineteen coal samples, two are of subbituminous rank, three of high volatile B and C bituminous rank and the remainder of high volatile A bituminous rank. Twelve coals are from the Eastern/Appalachian coal province, six are from the Interior province and one is a Western coal from the Northern Great Plains province.

## EXPERIMENTAL

Details of sample preparation and CuPy-EIMS analysis procedures have been described elsewhere (3). Experimental conditions were as follows: Curie-point temperature 610°C; heating rate approx. 100 K/s; total heating time 10s; electron energy 12eV; mass range scanned 20-260 amu; scanning rate 1000 amu $s^{-1}$; total scan time approximately 10s. Each sample was analyzed in triplicate and the spectra recorded and stored by computer (IBM 9000).

### Data Processing

Mass variables with m/z values higher than 90 were selected for multivariate analysis. The reason for this is that the low mass range variables are not suitable for correlating the coals with their tars because of the loss of low molecular weight volatile products in the fixed bed reactor. The remaining data sets consisting of 171 variables were preprocessed, normalized and factor and discriminant analysis performed (4,5). Four discriminant functions were found to be significant, accounting for 55% of the variance in the coal data and 53% variance in the tar data, respectively.

Using four discriminant functions from both the coal and the tar data sets, canonical correlation analysis was done. Two canonical variates were obtained with correlation coefficients >0.9. The two canonical variates for the coal data set accounted for 35% of the total variance; whereas 30% of the total variance was accounted for by the two canonical variates for the tar data set.

Using a "jackknifing" procedure the topology of the canonical variate space was checked. The scores of the "unknown" sample were projected in the canonical variate space and the pyrolysis mass spectra of these unknown samples were then

predicted by calculating a distance weighted average from the spectra of the two nearest neighbors.

## Methods and Procedures

A brief description of the methodology and mathematical rationalization is given below. Factor analysis (6) is an efficient way of reducing a data set (the data is generally preprocessed to form a correlation matrix). The first factor describes the maximum correlated variance in the data set, the second (orthogonal to the first) the maximum of the residual correlated variance, etc.:

$$F_j = a_{1j}z_1 + a_{2j}z_2 + \ldots + a_{mj}z_m \qquad 1)$$

where $F_j$ is factor $j$, with loading $a_{ij}$, which describe the contribution of the variable $z_i$ to the factor.

The scores, i.e., the contributions of the spectra to the factors, are obtained by substituting the intensities of the mass variables in the spectra for $z_i$. The relationship between the data matrix D (size s x m where s is the number of spectra and m is the number of mass variables) and the calculated factor matrix is:

$$D = S \times F \qquad 2)$$

where S is the score matrix (size s x n, n = number of factors) and F (size n x m) contains the factors. The scores in the principal component analysis are calculated in the following way:

$$S = D \times (E \times \Lambda^{-1/2}) \qquad 3)$$

where S contains the standardized scores (mean is zero, standard deviation is 1), and D the standardized data matrix. E is the orthonormal eigenvector for matrix Z = $1/s\ D^T D$, with the eigenvalues given in $\Lambda$.

The standardized data matrix, D, can be reconstructed from the scores using this relation:

$$\begin{aligned} D &= S \times (E \times \Lambda^{-1/2})^{-1} \\ &= S \times (E^{-1} \times \Lambda^{1/2}) \\ &= S \times (E^T \times \Lambda^{1/2}) \\ &= \text{standardized scores} * \text{factor loadings} \qquad 4) \end{aligned}$$

The score of an unknown sample, defined in terms of a standardized data matrix, can be projected using Equation 3. Similarly, the projected unknown score, based on a training data set, can be used to predict a standardized data matrix (in this case of the unknown sample) using Equation 4. The factor loadings, before being used in Equation 4, have to be transformed to the canonical variate space by using the canonical variate matrix.

## RESULTS AND DISCUSSION

The results will be discussed under two separate subheadings; canonical correlation results and prediction results.

### Canonical Correlation Results

Canonical variate scores (CVI vs. CVII) for the two data sets are plotted in Figure 1. The result shows that the data is primarily two-dimensional. The clustering of the samples suggests that the Interior hvb coals (samples #15, 16 and

17, Table I) are more alike in composition than the Eastern hvb coals. The subbit C Upper Block Indiana coal (sample #7) is different from the subbit A coal of the Northern Great Plains (sample #18). The Lower Kittaning coal from West Virginia (hvAb, sample #9) and the Lower Banner Virginia coal (also hvAb, sample #6) do not fall close to the cluster with other hvAb coals. Although the Lower Banner coal has been found to be different from other hvAb coals petrographically, similar data is unavailable for the Lower Kittaning coal.

The clustering pattern of the corresponding tar data set is almost the same as that for the coal data; the scores of the coal and the tar are very close in this two-dimensional canonical variate space. The closer the score of the tar sample to that of the coal, the more alike their spectral patterns are. The average relative deviation between the coal and tar scores is 10% in the direction of CVI and 25% in the direction of CVII (this is related to the uncertainty in the predicted composition). Based on this canonical score plot, it is possible to predict the composition of the coal tars starting from the Py-MS patterns of the coals with the help of Equation 4.

As mentioned before, the prediction is based on the location of the projected score of the unknown sample in the canonical variate space of the coal data set. Two samples were selected for jackknifing tests - one from each marked cluster representing coals of different rank and origin (samples #16 and 2, respectively). Figures 2 and 3 show the score plots for the first two canonical variates with the score of the particular unknown sample projected. The topology of the CVI/CVII space is preserved in both cases (Figures 2 and 3); the projected score of the particular sample falls almost in the same location as if it were a part of the data set.

Prediction Results

Because the projected score of the jackknifed sample lies in the same space as the original data set, we have used a simple technique to predict the mass spectra of the selected samples. For example, the spectrum of sample #16 is derived from the distance weighted averaging of those of samples 15 and 17 (Figure 2). Similarly, the spectrum of sample #2 is derived by weighted averaging of those of samples 4 and 14 (Figure 3).

Since some coal and tar components are not strongly represented in this space the distance weighted averaging method makes the assumption that clustering behavior observed in canonical correlation space is representative of overall clustering tendencies. This assumption can and should be verified by inspection of clustering behavior in multidimensional factor space.

Figure 4a, b, c shows the spectra of the IL #6 coal, that of the corresponding tar, and the predicted tar. Most of the components present in the coal spectrum, Figure 4a, are also seen in the tar spectrum, Figure 4b. For example, the mass peaks at m/z 94, 108, 122 ("phenols"), 110, 124, 138 ("dihydroxybenzenes"); 142, 156, 170, 184, 198 ("naphthalenes"); 168, 182, 196, 210, 224 ("acenaphthenes") and 178, 192, 206 ("phenanthrenes/anthracenes") are all found in both the coal and the tar spectra. The differences between these two spectra should also be noted here. The higher molecular weight masses all have stronger signals in the tar spectrum, and the patterns of the components such as naphthalenes (m/z 142, 156, 170, 184), acenaphthenes (m/z 168, 182, 196) and anthracenes (m/z 178, 192, 206) are different in the tar spectrum. The naphthalene series reaches its maximum at at m/z 156 in the coal spectrum, and at m/z 170 in the tar spectrum; similar shifts in the relative intensity patterns are observed for other components mentioned above. The predicted spectrum, Figure 4c, shows that it preserves the spectral subpatterns of the individual components. Also note that the ratio of the peak heights between

and within separate components in the original tar spectrum (Figure 4b) and the predicted spectrum (Figure 4c) is alike.

Figure 5a, b, c shows the spectra of a typical Eastern hvAb coal from Pennsylvania, of the corresponding tar, and of the predicted tar. In this case the spectral subpatterns of the important components are markedly different between the coal and the tar. Nevertheless, when comparing Figures 5b and 5c the predicted and measured tar patterns show a very high degree of similarity and are distinctly different from the corresponding patterns in Figure 4.

## CONCLUSIONS

The data presented here demonstrate that pyrolysis mass spectrometry in combination with canonical correlation analysis enables modeling and prediction of complex coal conversion processes such as the fixed bed liquefaction method. To the best of our knowledge this represents the first time that the chemical composition of coal-derived liquids has been predicted directly from feed coal characterization data. Moreover, the method is completely general and can be applied to all coal characterization data (whether obtained by conventional or by advanced spectroscopic techniques) and coal conversion processes in which the end products have been carefully characterized.

A shortcoming of the present study is the lack of a sufficiently large number of feed coal/coal tar pairs to allow adequate modeling and prediction of coal conversion behavior for more than two coal clusters. Also, a somewhat simplistic method was used to calculate predicted tar spectra based on a distance weighted average of the two nearest neighbors in a two-dimensional canonical correlation space.

## REFERENCES


1. Khan, M.R., Proc. of Int. Symp. on Coal Science, Coal Science and Technology Series, J.A. Moulijn (ed.), Elsevier, 1987, p. 647.

2. Metcalf, G.S., Windig, W., Hill, G.R., Meuzelaar, H.L.C., Int. J. Coal Geology, 1987, 7, 245-268.

3. Chakravarty, T., Meuzelaar, H.L.C., Report to U.S. Dept. of Energy, July 1987, Contract #DEAP21-87MC05073.

4. Windig, W., Meuzelaar, H.L.C., Anal. Chem., 1984, 56, 2297-2303.

5. Chakravarty, T., Windig, W., Taghizadeh, K., Meuzelaar, H.L.C., Shadle, L.J., Energy & Fuels, 1988 (in press).

6. Malinowski, E.R., Factor Analysis in Chemistry, Academic Press, New York, 1980.


## ACKNOWLEDGEMENTS


The authors wish to acknowledge Ms. Barbara Hoesterey for her assistance in sample preparation and analyses. Helpful discussions with Dr. Willem Windig is also appreciated. This work was supported by the Department of Energy (Contract #DEAP21-87MC05073). This work was sponsored in part by the Advanced Combustion Engineering Research Center. Funds for this Center are received from the National Science Foundation, the State of Utah, 21 industrial participants, and the U.S. Department of Energy. Additional funding was also provided by the Consortium for Fossil Fuel Liquefaction Science.

TABLE I
GEOGRAPHICAL ORIGIN AND RANK INFORMATION OF NINETEEN COAL SAMPLES

| SERIAL # | PSOC # | GEOLOGICAL INFORMATION | RANK INFORMATION |
|---|---|---|---|
| 1 | - | Eastern/Appalachian, OH #6 | hvAb |
| 2 | 1481 | ibid, Upper Clarion | hvAb |
| 3 | - | ibid, Wellmore #8 | hvAb |
| 4 | 375 | ibid, Hazard #9 | hvAb |
| 5 | 267 | ibid, Clintwood | hvAb |
| 6 | 1472 | ibid, Lower Banner | hvAb |
| 7 | - | ibid, Arkwright | hvAb |
| 8 | 1469 | ibid, Mary Lee | hvAb |
| 9 | 123 | ibid, Lower Kittaning | hvAb |
| 10 | 1471 | ibid, Pee Wee | hvAb |
| 11 | 306 | ibid, OH #12 | hvAb |
| 12 | 296 | ibid, OH #5 | hvAb |
| 13 | 1475 | ibid, Elkhorn #3 | hvAb |
| 14 | 275 | ibid, OH #6A | hvAb |
| 15 | 1492 | Interior/Eastern, IL#5 | hvBb |
| 16 | - | ibid, IL#6 | hvCb |
| 17 | 1323 | ibid, IL#6 | hvCb |
| 18 | 181 | ibid, Upper Block | sub. A |
| 19 | 1520 | N. Great Plains/Fort Union, Wyodak | sub. C |

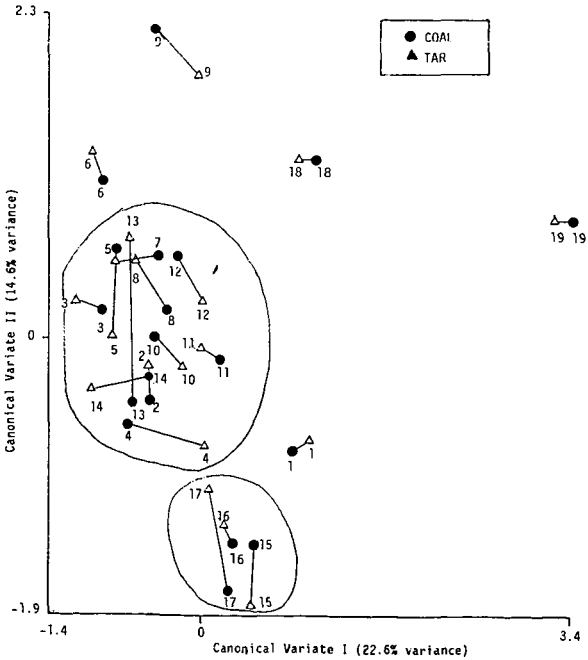


Figure 1. Score plot in the CVI/CVII space for both the coal and the tar samples. Note that only the means of the three scores for each category are plotted.

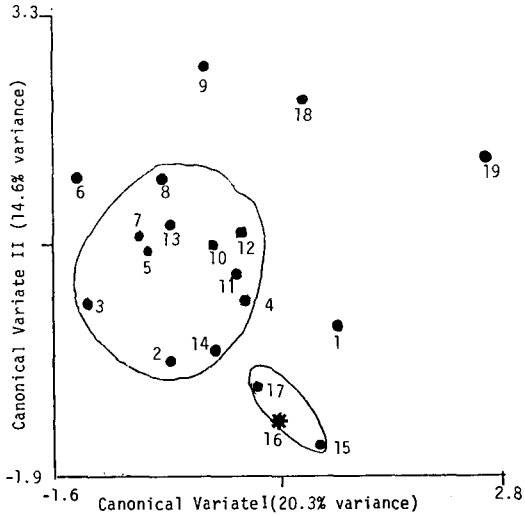


Figure 2. Effect of removing sample #16 from the coal data set on the score plot in the CVI/CVII space. Note the projected score of sample #16 (marked by *).

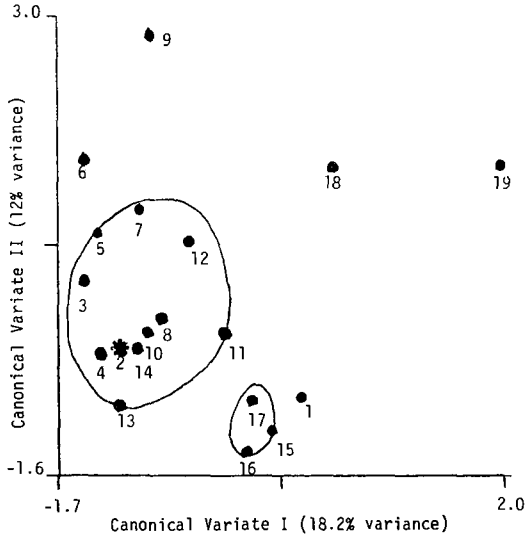


Figure 3. Effect of removing sample #2 from the coal data set on the score plot in the CVI/CVII space. Note the projected score of sample #2 (marked by *).

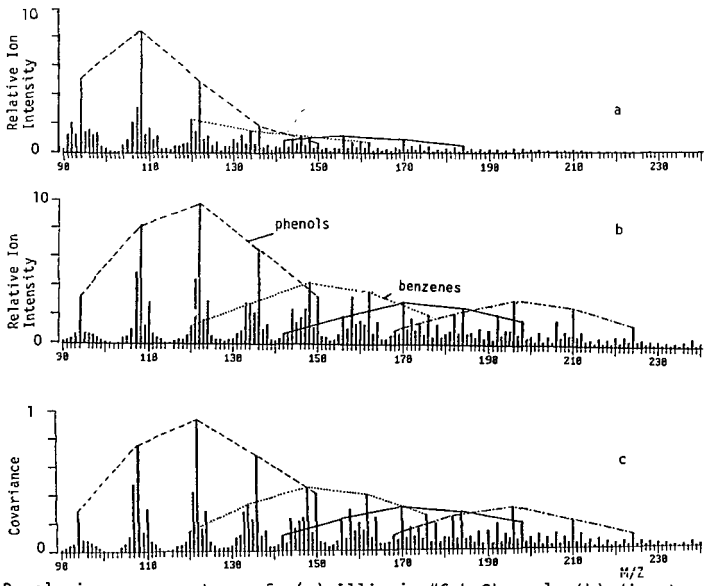


Figure 4. Pyrolysis mass spectrum of: (a) Illinois #6 hvCb coal; (b) direct probe mass spectrum of the corresponding tar, and (c) mathematically predicted spectrum.

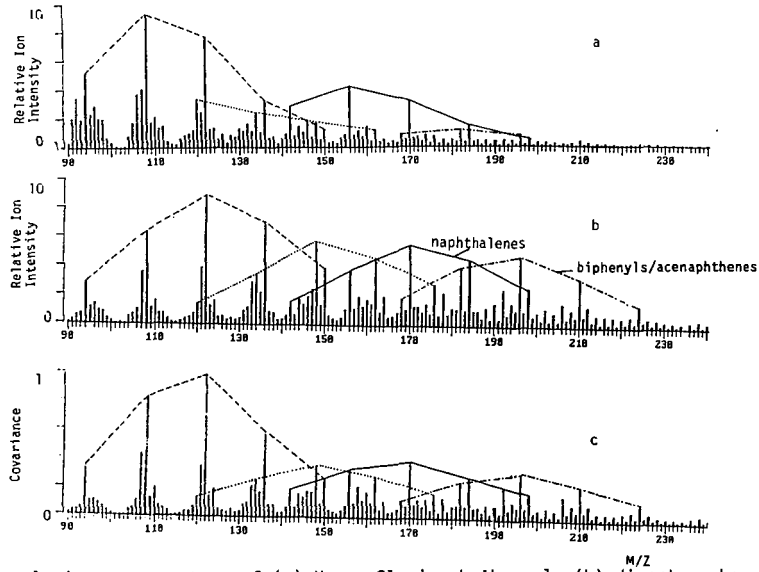


Figure 5. Pyrolysis mass spectrum of:(a) Upper Clarion hvAb coal; (b) direct probe mass spectrum of the corresponding tar, and (c) mathematically predicted spectrum.

# PYROLYSIS OF COMPOUNDS CONTAINING POLYCYCLIC AROMATIC MOIETIES

MINOO JAVANMARDIAN, PATRICK J. SMITH, AND PHILLIP E. SAVAGE

DEPARTMENT OF CHEMICAL ENGINEERING
UNIVERSITY OF MICHIGAN
ANN ARBOR, MI 48109

## INTRODUCTION

Coal is thought to exist in a complex, cross-linked, macromolecular framework in which polycyclic moieties are covalently linked together by aliphatic and heteroatomic bridges (1-3). The condensed aromatic groups can also bear peripheral, non-bridging moieties, including long aliphatic chains (4).

The pyrolysis of numerous compounds mimicking these structural features has provided considerable insight to the thermal reactions of coal. Previous pyrolyses were typically of compounds containing a single aromatic ring, which was intended to mimic the more massive condensed aromatic moieties in coal. It is possible, however, that single-ring compounds might not display the same reaction pathways and kinetics as otherwise identical compounds containing polycyclic aromatic moieties.

One difference between a single aromatic ring and the condensed aromatic moieties in coal is their sizes. This difference suggests that the model-compound-derived free radicals could be considerably more mobile than their coal-derived counterparts. To probe the influence of radical mobility on pyrolysis pathways Poutsma and coworkers (5-7) pyrolyzed coal model compounds immobilized on silica surfaces. They found that surface immobilization can lead to an enhancement of unimolecular pathways relative to bimolecular ones.

In an attempt to gain additional insight into the fundamentals of coal pyrolysis, and particularly the effects of condensed aromatics, we recently initiated experiments with compounds containing polycyclic aromatic moieties, which better represent the aromatic clusters in coal than do single-ring compounds. In this paper, we report on the pyrolysis of two compounds; 2-(3-phenylpropyl)-naphthalene (PPN), and 1-dodecylpyrene (DDP).

## EXPERIMENTAL

PPN and DDP were pyrolyzed at isothermal temperatures between 350 and 425°C for batch holding times between 10 and 180 min.

### Materials.

All chemicals were obtained commercially; 1-Dodecylpyrene (DDP) from Molecular Probes and 2-(3-phenylpropyl)-naphthalene (PPN) from API Standard Reference Materials, and used as received. The nominal purity of each compound was > 99%, and this was confirmed by GC analysis. PPN pyrolyses were accomplished in 1.5 x 100 mm Kimax glass capillary tubes, and DDP pyrolyses were in nominal 3/8" tubing bomb microreactors. The latter reactors were fashioned from a single Swagelok stainless steel port connector and two caps. The glass reactors were not routinely used with DDP because it is a fluffy solid and was difficult to load into the small diameter tubes. However, one experiment was done in a glass reactor to verify the absence of catalysis by the stainless steel surfaces in the tubing bomb microreactor.

### Procedure.

The tubing bomb microreactors were typically loaded with about 10 - 30 mg of DDP and then about 10 mg of biphenyl was added to serve as an internal standard in the chromatographic analyses. All quantities were carefully (± 0.1 mg) weighed. The glass capillary tubes used for PPN pyrolyses were typically charged with 10 $\mu$l of a previously prepared stock solution containing the model compound and the internal standard. The reactors were then sealed and immersed in a preheated, fluidized sand bath. After the desired reaction time had elapsed, the reactors were removed from the sand bath, rapidly cooled to room temperature to quench the reaction, and then opened. Reaction products were extracted in spectrophotometric grade acetone and analyzed by GC and GC-MS. Molar yields were calculated as the number of moles of product divided by the number of moles of reactant initially charged to the reactor.

## RESULTS

The experimental results are presented primarily as the temporal variations of the products' molar yields. Tables I and II provide representative results for PPN and DDP, respectively, at each of the temperatures investigated. Based on the reproducibility of the results we estimate the uncertainty in product molar yields for PPN and DDP to be roughly ± 10% and ± 25%, respectively.

### PPN Pyrolysis.

PPN pyrolysis at 350°C yielded toluene, styrene, 2-methylnaphthalene, and 2-vinylnapththalene as the major products, and at 60 min traces of ethylbenzene and 2-ethylnaphthalene were also detected. GC-MS analysis of the reaction products permitted tentative identification of two additional minor products as 2-isopropylnaphthalene and 1,3-diphenylpropane. The pseudo-first-order rate constant for PPN disappearance was 0.007 $min^{-1}$.

Figure 1, which displays the temporal variation of the major products from PPN pyrolysis at 375°C, shows that the yields of toluene and 2-methylnaphthalene increased steadily throughout the 60 min reaction. The yields of styrene and 2-vinylnaphthalene decreased with holding time. The yields of ethylbenzene and 2-ethylnaphthalene were zero at short times, but they reached 6.2% and 8.5%, respectively at 60 minutes. The pseudo-first-order rate constant for PPN conversion at 375°C was 0.028 $min^{-1}$.

PPN pyrolysis at 400°C proceeded rapidly and was essentially complete at 60 min. Toluene and 2-methylnaphthalene were the major products, but the yields of ethylbenzene and 2-ethylnaphthalene were also substantial. The product alignment at 60 min was toluene (52%), 2-methylnaphthalene (48%), 2-ethylnaphthalene (19%), ethylbenzene (19%), styrene (0.8%), and 2-vinylnaphthalene (< 0.1 %). The pseudo-first-order rate constant was 0.076 $min^{-1}$.

Figure 2 presents the variation of the major products' molar yields with PPN conversion. Toluene and 2-vinylnaphthalene were present in nearly equal yields at low conversions. The yield of toluene increased to roughly 50% at complete conversion, whereas the yield of 2-vinylnaphthalene went through a maximum value (3.6%) and then decreased to 0. The yield of 2-ethylnaphthalene was very low at conversions < 30%, but it increased rapidly at very high conversions. The yield of 2-methylnaphthalene increased steadily with conversion to an ultimate value of nearly 50%. The yield of styrene, like that of 2-vinylnaphthalene, exhibited a maximum value and then decreased to zero. Finally, the yield of ethylbenzene was very low for conversions less than 50%, but it increased to 19% when conversion was nearly complete.

The disappearance of PPN correlated well with first-order kinetics, and the Arrhenius parameters for the pseudo-first-order rate constant were $[\log_{10}A\ (sec^{-1}),\ E^*\ (kcal/mol)] = [10.0, 39.8]$.

### DDP Pyrolysis.

DDP pyrolyses led to pyrene, methylpyrene, dodecane, nonane, and undecene as the major products at short reaction times. Minor products included series of n-alkanes ($C_6$ - $C_{12}$), α-olefins ($C_6$ - $C_{12}$), and alkylpyrenes. GC-MS analysis revealed the presence of a compound tentatively identified as pyrenylpropene. No other pyrenylalkenes were present in yields sufficiently high to be quantified. In addition to the molecular products noted above, an acetone-insoluble char formed as a result of DDP pyrolysis.

The yields of each of the major products from DDP pyrolysis at 375°C increased with batch holding time. The ultimate yields of pyrene, dodecane, nonane, methylpyrene, and undecene were 52%, 28%, 7.0%, 6.7%, and 1.4%, respectively, at 180 min. The yields of several n-alkanes and ethylpyrene increased more rapidly than did the yield of undecene, and these products were more abundant than undecene at the more severe conditions.

The major products from DDP pyrolysis at 400°C and at short times were pyrene, dodecane, methylpyrene, nonane, and undecene. At longer batch holding times the yields of some n-alkanes increased and surpassed the undecene yield, which reached a maximum value of 1.9% at 60 min. The yields of pyrene, dodecane, nonane, and methylpyrene increased with time and achieved ultimate values of 49%, 32%, 9.4%, and 8.3%, respectively at 180 min.

DDP pyrolysis at 425°C was rapid and essentially complete at 45 min. The major products at short reaction times were the same as those observed at the lower temperatures, and Figure 3 displays the temporal variation of their yields. The yields of pyrene, dodecane, nonane, and methylpyrene were relatively time invariant after 60 minutes, and their ultimate values were approximately 49%, 25%, 10%, and 10%, respectively. Undecene, on the other hand, exhibited a maximum yield of 3.1% at 15 min and then its yield decreased to undetectable levels at 120 min.

Figure 4 displays the distribution of alkanes and olefins produced from DDP pyrolysis at 425°C and 17 min. The alkane distribution exhibits a peak at nonane ($C_9$) and a higher one at dodecane ($C_{12}$). The olefinic products were relatively evenly distributed with the exception of the high undecene yield. Note that with the exception of $C_{11}$, alkanes were present in yields higher than the corresponding olefins.

## DISCUSSION

### PPN Pyrolysis.

Figure 2 shows that the product pairs toluene plus 2-vinylnaphthalene and 2-methylnaphthalene plus styrene were present in nearly equal yields at low conversions. This is consistent with the formation of each product pair in a common reaction step. Furthermore, the non-zero initial slopes apparent in the molar yield vs. time curves (i.e., Figure 1) for each of these four products indicates that these are primary reaction products. On the other hand, the initial slopes associated with 2-ethylnaphthalene and ethylbenzene are zero, thus these are secondary products. That the yields of 2-vinylnaphthalene and styrene go through a maximum and then decrease to zero is consistent with their participating in secondary reactions. Toluene and 2-methylnaphthalene were apparently stable at the temperatures studied.

These observations combine to suggest the reaction pathway shown in Figure 5 for PPN pyrolysis. The nearly equal yields of 2-methylnaphthalene and toluene (e.g., both were nearly 50% at essentially complete PPN conversion) indicate that the stoichiometric coefficients $\nu_1$ and $\nu_2$ are both approximately equal to 0.5.

The primary pyrolysis pathway deduced for PPN is essentially the same as that reported for 1,3-diphenylpropane (8-10), the single-ring analogue of PPN. This suggests that, in this instance, substituting a naphthyl for a phenyl moiety does not detectably alter the operative reaction pathways or the reaction mechanism. Note however that this is not true of the reaction rates. The pseudo-first-order rate constants for PPN reported here were 4-10 times as high as pseudo-first-order rate constants determined from data presented by Poutsma and Dyer (8) for the liquid-phase pyrolysis of diphenylpropane. [Note: diphenylpropane pyrolysis was reported to be 3/2 order (8,9) thus the calculated pseudo-first-order rate constants are the product of the intrinsic rate constant and the square root of the concentration. We used the highest reaction rates reported (e.g., for liquid-phase pyrolyses) to calculate pseudo-first-order rate constants for diphenylpropane.]

### DDP Pyrolysis.

Some aspects of DDP pyrolysis are consistent with previous results from the thermal cracking of dodecylbenzene (11,12) and other long-chain n-alkylbenzenes (13,14). Dodecylbenzene pyrolysis (11, 12) was via a free-radical mechanism, and the two pairs of major products, toluene plus undecene and styrene plus decane, arose from $\beta$-scission of a $\gamma$ and an $\alpha$-dodecylbenzene radical, respectively. The minor products comprised complete series of n-alkanes, $\alpha$-olefins, alkylbenzenes, and phenylalkenes. Only traces of benzene were detected.

Elements of similar free-radical reactions appear to be operative in DDP pyrolysis. Methylpyrene and undecene were present in relatively high yields at mild reaction conditions, and these are the expected ultimate products from $\beta$-scission of a $\gamma$-DDP radical. Similarly the product pair nonane plus pyrenylpropene could have been formed via $\beta$-scission of a $\beta$-DDP radical. Finally, as observed in dodecylbenzene pyrolysis, series of alkanes and olefins and some alkylaromatics were produced as minor products from DDP pyrolysis.

Although some aspects of DDP pyrolysis parallel those of its single-ring analogue, there are several interesting differences. The appearance of pyrene and dodecane as the major products from DDP pyrolysis indicates that rupture of the aryl-alkyl C-C bond was facile. This is not expected on the basis of the free-radical reaction mechanism proposed (12) for dodecylbenzene because this C-C bond is the strongest in the

alkyl chain and hence most resistant to cleavage. Furthermore, the alkane distribution for DDP pyrolysis showed a peak at n-nonane, but no such preferential formation of nonane was observed in the pyrolysis of n-alkylbenzenes (11-14).

Finally, pyrene and dodecane together contain more hydrogen than the reactant, DDP. Thus formation of these as major products requires the simultaneous formation of hydrogen-deficient products in relatively high yields. GC analyses revealed no such products, thus we conclude that the experimentally observed, acetone-insoluble char was the source of this hydrogen.

## SUMMARY AND CONCLUSIONS

The pyrolytic pathway for PPN was identical to that of its single-ring analogue, 1,3-diphenylpropane. The apparent first-order kinetics of PPN disappearance were 4-10 times more rapid however. On the other hand, both the pathways and kinetics of DDP pyrolysis differed from those of its single-ring analogue, dodecylbenzene. The major products of DDP pyrolysis, pyrene and dodecane, indicate that bond cleavage occurred predominantly at the ring, whereas the primary pathways in dodecylbenzene pyrolysis involved cleavage of the covalent bonds between the $\alpha$ and $\beta$ carbons and the $\beta$ and $\gamma$ carbons to produce toluene plus undecene and styrene plus decane, respectively. The results of this study demonstrate that the thermal reaction pathways and kinetics of compounds containing condensed aromatic moieties can differ from those of their single-ring analogues.

## ACKNOWLEDGEMENT

This work was supported in part by a grant from the University of Michigan Office of Energy Research.

## LITERATURE CITED

1. Gorbaty, M. L., Ouchi, K., Eds. Coal Structure, ACS Adv. Chem. Ser. No. 192 **1981**.
2. Gorbaty, M. L., Larsen, J. W., Wender, I., Eds. Coal Science, Academic Press, NY **1982**.
3. Meyers, R. A., Ed. Coal Structure, Academic Press, NY **1982**.
4. Nelson, P. F., *Fuel* **1987**, 66, 1264.
5. Buchanan, A. C., Dunstan, T. D. J., Douglas, E. C., Poutsma, M. L. *J. Am. Chem. Soc.* **1986**, 108, 7703.
6. Poutsma. M. L., Douglas, E. C., Leach, J. E. *J. Am. Chem. Soc.* **1984**, 106, 1136.
7. Buchanan, A. C., Biggs, C. A. *ACS Div. Fuel Chem. Prepr.* **1987**, 32, 175.
8. Poutsma, M. L., Dyer, C. W. *J. Org. Chem.* **1982**, 47, 4903.
9. Gilbert, K. E., Gajewski, J. J. *J. Org. Chem.* **1982**, 47, 4899.
10. Sweeting, J. W., Wilshire, J. F. K. *Aust. J. Chem.* **1962**, 15, 89.
11. Blouri, B., Hamdan, F., Herault, D., *Ind. Eng. Chem. Process Des. Dev.* **1985**, 24, 30.
12. Savage, P. E., Klein, M. T., *Ind. Eng. Chem. Research* **1987**, 26, 374.
13. Mushrush, G. W., Hazlett, R. N., *Ind. Eng. Chem. Fundam.* **1984**, 23, 288.
14. Savage, P. E., Klein, M. T., *Ind. Eng. Chem. Research* **1987**, 26, 488.

**TABLE I: Yields (%) of Major Products from PPN Pyrolysis**

| | 350°C | | | 375°C | | | 400°C | | |
|---|---|---|---|---|---|---|---|---|---|
| TIME (min) → | 10 | 31 | 61 | 11 | 30 | 60 | 20 | 30 | 60 |
| Toluene | 2.0 | 5.7 | 10. | 7.8 | 20. | 35. | 39. | 44. | 52. |
| Ethylbenzene | - | - | 0.6 | - | 1.5 | 6.2 | 6.9 | 11. | 19. |
| Styrene | 1.9 | 3.5 | 3.8 | 10. | 6.0 | 4.1 | 7.1 | 4.5 | 0.8 |
| 2-Methylnaphthalene | 2.2 | 6.2 | 11. | 8.2 | 21. | 35. | 39. | 43. | 48. |
| 2-Ethylnaphthalene | - | - | 1.0 | - | 2.4 | 8.5 | 9.7 | 14. | 19. |
| 2-Vinylnaphthalene | 1.8 | 2.1 | 2.1 | 3.5 | 2.9 | 1.5 | 2.8 | 1.2 | - |
| PPN | 88. | 78. | 64. | 77. | 44. | 20. | 15. | 8.4 | 1.1 |

**TABLE II: Yields (%) of Major Products from DDP Pyrolysis**

| | 375°C | | | 400°C | | | 425°C | | |
|---|---|---|---|---|---|---|---|---|---|
| TIME (min) → | 60 | 120 | 180 | 30 | 90 | 180 | 11 | 60 | 120 |
| Hexene | - | - | - | - | - | - | - | 1.3 | 1.5 |
| Hexane | - | - | - | - | 1.5 | 2.6 | - | 4.1 | 8.5 |
| Heptene | - | - | - | - | - | - | - | 1.1 | 1.5 |
| Heptane | - | - | 1.1 | - | 1.3 | 2.2 | - | 3.2 | 5.6 |
| Octene | - | - | - | - | - | - | - | 0.9 | 0.8 |
| Octane | 0.4 | 1.2 | 1.7 | 0.5 | 2.0 | 3.2 | - | 4.0 | 5.9 |
| Nonene | - | - | - | - | - | - | - | 0.7 | 0.6 |
| Nonane | 1.4 | 4.9 | 7.0 | 2.8 | 7.7 | 9.4 | 2.6 | 10. | 13. |
| Decene | - | - | - | - | - | - | - | 0.6 | 0.6 |
| Decane | 0.7 | 1.6 | 2.3 | 1.5 | 3.6 | 4.5 | 2.0 | 5.5 | 6.9 |
| Undecene | 0.8 | 1.2 | 1.4 | 1.8 | 1.2 | - | 2.5 | 1.1 | - |
| Undecane | 0.5 | 2.0 | 3.5 | 0.8 | 4.9 | 6.5 | - | 6.4 | 7.7 |
| Dodecene | - | - | 0.6 | - | 0.6 | - | - | 0.9 | - |
| Dodecane | 4.5 | 19. | 28. | 9.6 | 28. | 32. | 6.9 | 25. | 28. |
| Pyrene | 8.6 | 46. | 52. | 17. | 40. | 49. | 12. | 48. | 50. |
| Methylpyrene | 2.0 | 6.3 | 6.7 | 3.6 | 5.5 | 8.3 | 4.4 | 10. | 10. |
| Ethylpyrene | 0.7 | 2.2 | 2.1 | 1.6 | 1.9 | 1.8 | 2.4 | 2.5 | 1.7 |
| Pyrenylpropene | - | - | - | 2.2 | - | - | 1.9 | - | - |
| DDP | 69. | 68. | 36. | 46. | 4.8 | - | 51. | - | - |

Note: - indicates product yields too low to be determined quantitatively

FIGURE 1: TEMPORAL VARIATION OF PRODUCT YIELDS FROM PPN PYROLYSIS AT 375C

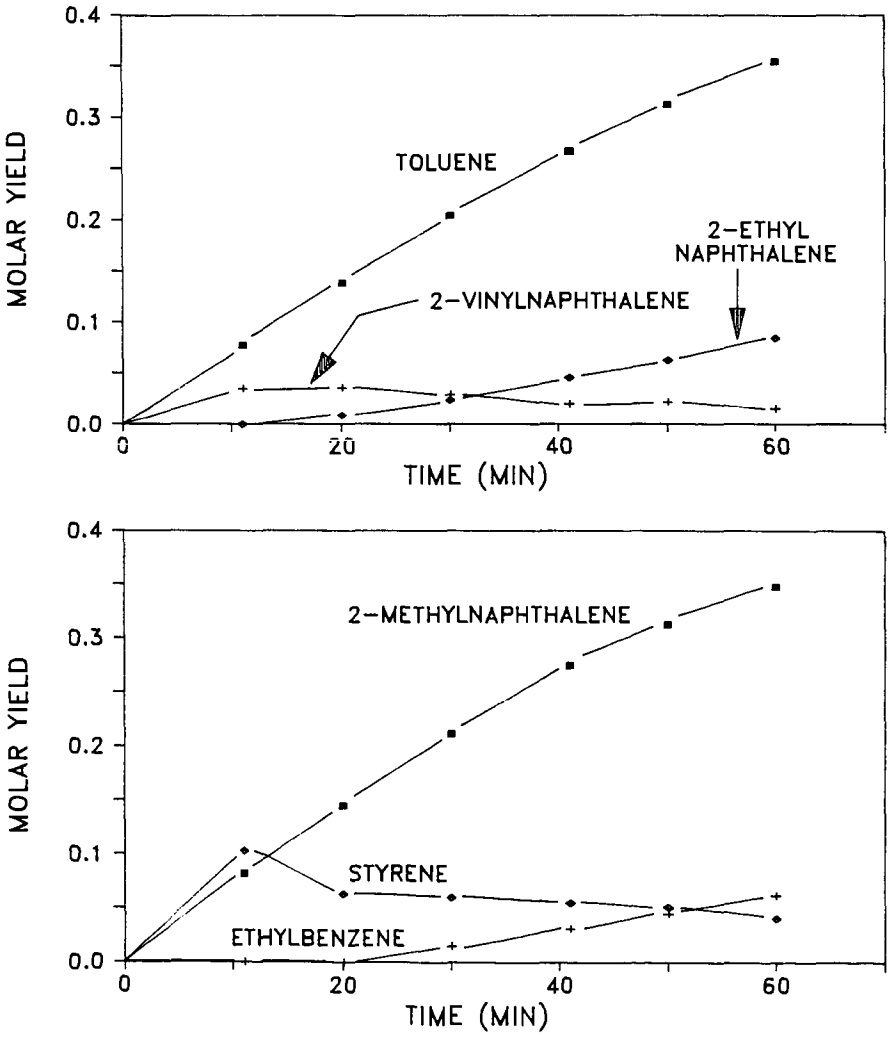

FIGURE 2: VARIATION OF PRODUCT YIELDS WITH PPN CONVERSION

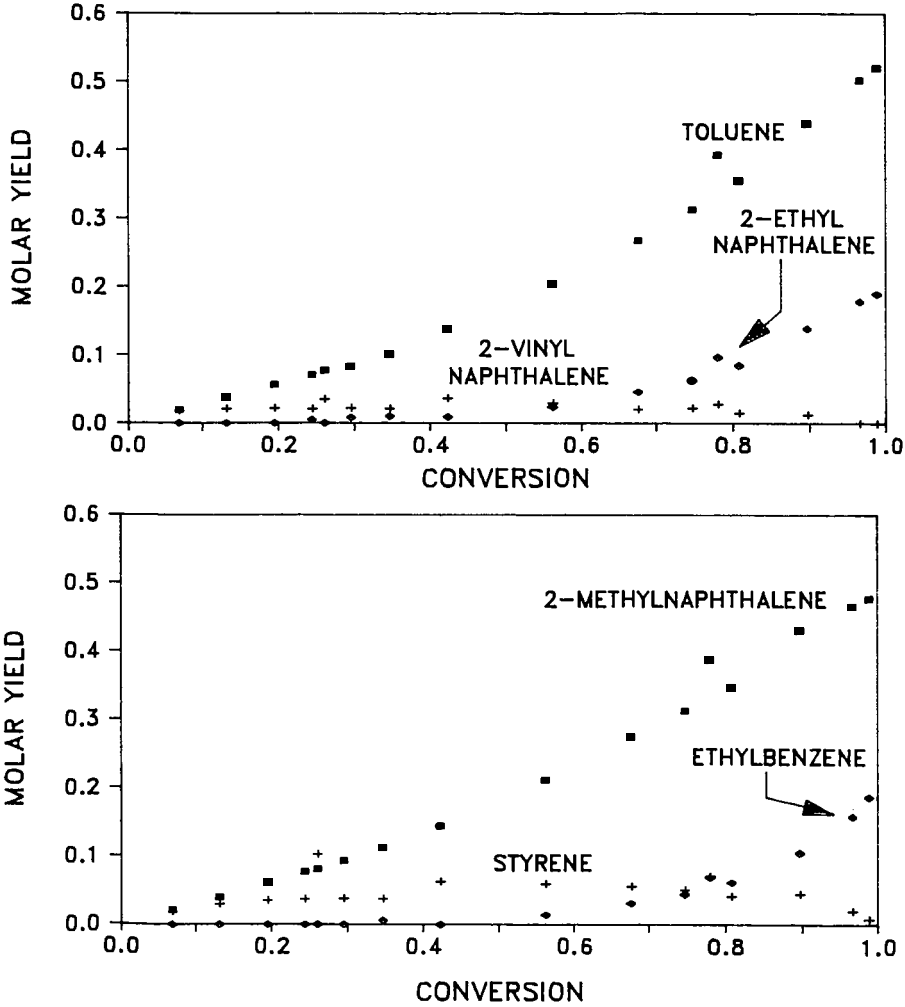

FIGURE 3: TEMPORAL VARIATION OF PRODUCT YIELDS FROM DDP PYROLYSIS AT 425C

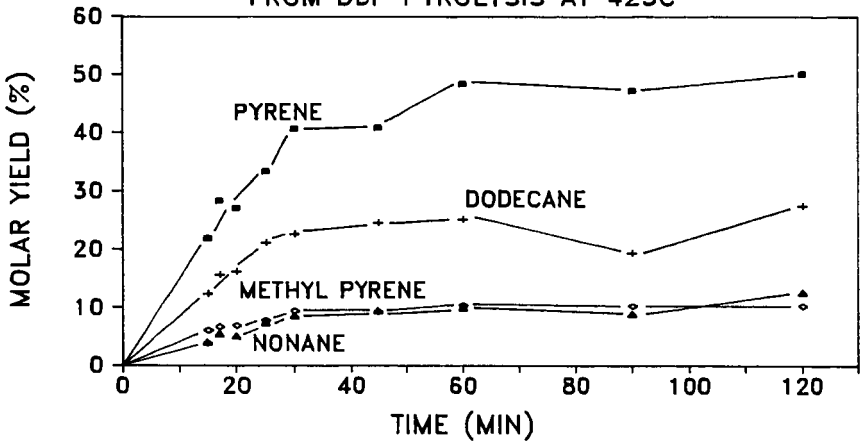


FIGURE 4: VARIATION OF OLEFIN AND ALKANE YIELDS FROM DDP PYROLYSIS (425C, 17 MIN)

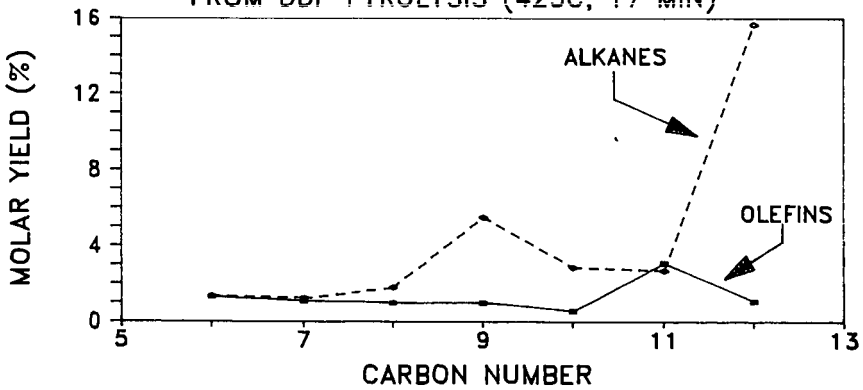


FIGURE 5: PPN PYROLYSIS PATHWAY

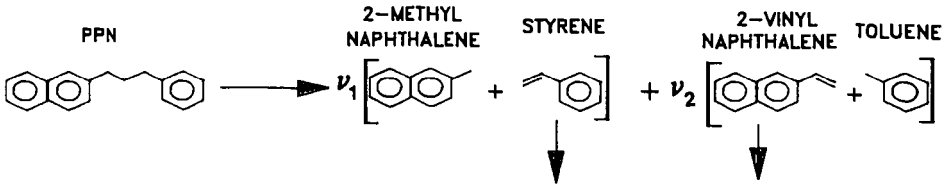

# PYROLYSIS OF A BINARY HYDROCARBON MIXTURE: REACTION MODELING

PHILLIP E. SAVAGE

DEPARTMENT OF CHEMICAL ENGINEERING
UNIVERSITY OF MICHIGAN
ANN ARBOR, MI 48109

## INTRODUCTION

Numerous pyrolyses of coal model compounds (e.g., refs 1-5) have provided substantial insight into the thermal reactions of the moieties they mimicked. The results of experiments with single compounds, however, provide no information about the interactions that can occur between the distinct chemical components in complex reactants such as coal. Because an active center (e.g., free radical) derived from one chemical moiety can react with a second, different moiety, reaction pathways that are important for the pyrolysis of a single model compound might not be equally important for the model-compound-like moiety in a coal macromolecule. Conversely, pathways unobserved in single-component pyrolyses might be operative in coal pyrolysis.

Previous reports of the pyrolysis of binary mixtures of high-molecular-weight compounds, though few (6), demonstrated that reactions between active centers derived from the two different compounds or between an active center from one compound and the second compound itself can affect the reaction rates, product selectivities, and reaction pathways. Zhou and Crynes (7), for example, pyrolyzed isomeric ethylphenols in dodecane and found that ethylphenol inhibited the rate of dodecane cracking and that dodecane accelerated the rate of ethylphenol conversion. They postulated that the interactions between the ethylphenol-derived and dodecane-derived radicals were considerable and were responsible for the differences between the pure compound and copyrolysis results. Allen and Gavalas (8) reported that the rate of decomposition of methylene and ether bridges in coal model compounds was enhanced when the compounds were pyrolyzed in 1,2-dihydronaphthalene (dialin). They suggested that an aromatic displacement reaction with atomic hydrogen (formed from dialin decomposition) was responsible for the accelerated bridge decomposition.

To gain additional insight into the pyrolysis of binary mixtures of high-molecular-weight compounds, a reaction model has been developed to simulate the copyrolysis of tetradecylbenzene (TDB) and dodecylcyclohexane (DDC). These compounds mimic alkylaromatic and alkylnaphthenic moieties in coal and asphaltenes.

## REACTION MODEL

The essential features of the free-radical pyrolysis of both long-chain alkylbenzenes and alkylcyclohexanes can be modeled as three parallel chains coupled via chain transfer steps (9-11). These three chains arise because there are only three types of aliphatic carbons in TDB and in DDC that exhibit unique reactivities. In TDB, hydrogen abstraction at the $\alpha$ carbon leads to a resonance stabilized, secondary benzylic radical whereas abstraction at all other positions produces a less stable secondary alkyl radical. Thus the $\alpha$ carbon possesses unique kinetics in the hydrogen abstraction step. Unique among the non-$\alpha$ radicals in TDB, the $\gamma$ radical leads to a resonance-stabilized, primary benzyl radical upon $\beta$-scission, whereas $\beta$-scission of all other TDB radicals produces a primary alkyl radical. Thus $\beta$-scission of the $\gamma$ radical is the fastest decomposition step. All non-$\alpha$ and non-$\gamma$ positions in TDB share roughly equal reactivities for hydrogen abstraction and $\beta$-scission and therefore collectively constitute the third category.

Similar to the influence of the aromatic ring and the resultant preferential formation of benzylic radicals in TDB, the naphthenic ring in DDC affords preferential formation of tertiary radicals in hydrogen abstraction steps and secondary radicals in $\beta$-scission steps. Hydrogen abstraction at the ring carbon bearing the aliphatic chain, which produces a tertiary DDC radical, is the fastest abstraction step because abstraction

at all other positions yields less stable secondary radicals. $\beta$-scission of the $\beta$-DDC radical, which produces a secondary cyclohexyl radical is the unique decomposition step because all other $\beta$-scission steps lead to primary alkyl radicals. All non-$\beta$ and non-tertiary positions in DDC share roughly equal reactivities for both hydrogen abstraction and $\beta$-scission.

The previously discerned (9-11) elementary reaction steps for neat pyrolysis of TDB and DDC, summarized in Figure 1, include a single initiation step and termination by all possible radical recombinations. R denotes a reactant molecule, and the superscripts A and B refer to TDB and DDC, respectively. Following standard notation, $\mu$ radicals are those that participate in unimolecular propagation steps, and $\beta$ radicals propagate chain reactions via bimolecular steps. Table I provides the chemical identities of the species in Figure 1.

Pyrolysis proceeds via the three parallel chain reactions in the center column of Figure 1 to produce $\beta_1$H plus $Q_1$, $\beta_2$H plus $Q_2$, and $\beta_3$H plus $Q_3$ as the major products. Chain transfer, depicted in the two peripheral columns, can occur via both $\mu$ and $\beta$ radicals. The interaction steps take the form of a free radical derived from one compound abstracting hydrogen from the second compound and additional termination steps involving the recombination of radicals derived from the two different substrates. Note that the copyrolysis mechanism of Figure 1 depicts only the primary reactions.

## KINETICS DEVELOPMENT

Reaction rate expressions were derived for TDB and DDC on the basis of the mechanism in Figure 1 by invoking the pseudo-steady-state and long-chain approximations (12,13). These approximations allow formulation of the algebraic $\beta_i$ balance for compound A (TDB) as Equation 1,

$$r^A_{\beta_i} = 0 = k^A_{\mu_i}\mu^A_i - \sum_{j=1}^{3} k^{AA}_{ij}\beta^A_i R^A - \sum_{j=1}^{3} k^{AB}_{ij}\beta^A_i R^B \tag{1}$$

and this permits solution for $\mu^A_i$ as

$$\mu^A_i = y^A_i \beta^A_i \tag{2}$$

where

$$y^A_i = \frac{k^{AA}_i R^A + k^{AB}_i R^B}{k^A_{\mu_i}} \tag{3}$$

with $k^{AA}_i = \sum_{j=1}^{3} k^{AA}_{ij}$ and $k^{AB}_i = \sum_{j=1}^{3} k^{AB}_{ij}$.

Similarly, the $\beta^B_i$ balance leads to

$$\mu^B_i = y^B_i \beta^B_i \tag{4}$$

where the expression for $y^B_i$ can be obtained from Equation 3 by transposing the A and B superscripts.

The double subscript notation employed for the hydrogen abstraction rate constants identifies, respectively, the attacking radical and the resultant $\mu$ radical. The double superscript notation identifies, respectively, the substrate from which the attacking radical was derived and the substrate attacked. Primed and unprimed rate constants denote hydrogen abstraction from either of the substrates by $\mu$ and $\beta$ radicals, respectively.

The long-chain, steady-state $\mu^A_i$ balance is given as Equation 5.

$$r^A_{\mu_i} = 0 = \sum_{j=1}^{3} k^{AA}_{ji}\beta^A_j R^A - k^A_{\mu_i}\mu^A_i - \sum_{j=1\neq i}^{3} k'^{AA}_{ij}\mu^A_i R^A + \sum_{j=1\neq i}^{3} k'^{AA}_{ji}\mu^A_j R^A - \sum_{j=1}^{3} k'^{AB}_{ij}\mu^A_i R^B +$$

$$\sum_{j=1}^{3} k'^{BA}_{ji}\mu^B_j R^A + \sum_{j=1}^{3} k^{BA}_{ji}\beta^B_j R^A \tag{5}$$

The balance for $\mu_i^B$ is completely analogous and can be obtained by transposing the A and B superscripts in Equation 5.

Substituting Equations 2 and 4 for the concentrations of the $\mu_i^A$ and $\mu_i^B$ radicals, respectively, into Equation 5 leads, after considerable rearrangement, to Equation 6.

$$\sum_{j=1\neq i}^{3} Z_{ji}^{AA}\beta_j^A + \sum_{j=1}^{3} Z_{ji}^{BA}\beta_j^B = \beta_i^A\Big(\sum_{j=1\neq i}^{3} Z_{ij}^{AA} + \frac{R^B}{R^A}\big(\sum_{j=1}^{3} Z_{ij}^{AB}\big)\Big) \tag{6}$$

where

$$Z_{ij}^{AA} = k_{ij}^{AA} + y_i^A k_{ij}'^{AA} \tag{7}$$

$$Z_{ij}^{BA} = k_{ij}^{BA} + y_i^B k_{ij}'^{BA} \tag{8}$$

Expressions for $Z_{ij}^{BB}$ and $Z_{ij}^{AB}$ can be obtained from Equations 7 and 8, respectively, by transposing their superscripts.

Equation 6 and the analogous set of equations for substrate B provide five independent equations in the six unknowns $\beta_i^A$ and $\beta_i^B$. Thus a balance on the total radical population must be written to solve for the individual radical concentrations and ultimately the reaction rate. The free radical concentration changes only as a result of initiation and termination steps, thus applying the pseudo-steady-state approximation to the net rate of radical production results in equating the rates of initiation and termination.

Since both theory and experimental evidence suggest that rate constants for radical recombinations are typically $10^{9.0\pm0.5}$ l/mol-s (14,15), all termination rate constants were taken to be equal except for the statistical factor (16) that renders the rate constant for combination of two identical radicals, $\omega_T$, one-half that for two dissimilar species. This approximation combines with the initiation and termination steps depicted in Figure 1 to give Equation 9 as the steady-state radical balance.

$$\alpha_I^A R^A + \alpha_I^B R^B = \omega_T \left[\sum_{i=1}^{3}(\mu_i^A + \mu_i^B + \beta_i^A + \beta_i^B)\right]^2 \tag{9}$$

Eliminating $\mu_i^A$ and $\mu_i^B$ from Equation 9 via Equations 2 and 4, respectively, gives Equation 10.

$$\left[\frac{\alpha_I^A R^A + \alpha_I^B R^B}{\omega_T}\right]^{1/2} = \sum_{i=1}^{3}\left[\beta_i^A(1+y_i^A) + \beta_i^B(1+y_i^B)\right] \tag{10}$$

This equation, Equation 6, and analogous expressions for substrate B were solved numerically for the $\beta$ radical concentrations with estimated rate constants as parameters. Table II summarizes the Arrhenius parameter estimates used in the reaction model. These values are representative of literature estimates (1,2,14,15,17-22) for similar types of reactions.

The reaction rates were then determined from the long-chain rate expressions below.

$$-r_A = R^A \sum_{i=1}^{3}\left[\beta_i^A\left(k_i^{AA} - \frac{R^B}{R^A}k_i'^{AB}y_i^A\right) + \beta_i^B\left(k_i^{BA} + k_i'^{BA}y_i^B\right)\right] \tag{11}$$

$$-r_B = R^B \sum_{i=1}^{3}\left[\beta_i^B\left(k_i^{BB} - \frac{R^A}{R^B}k_i'^{BA}y_i^B\right) + \beta_i^A\left(k_i^{AB} + k_i'^{AB}y_i^A\right)\right] \tag{12}$$

Relative rates for DDC and TDB pyrolysis were calculated as the ratio of the rate at a given value of [TDB]/[DDC] (or [DDC]/[TDB]) to the rate calculated for the pyrolysis of the pure compound.

## RESULTS AND DISCUSSION

Figure 2 displays the relative rates calculated for DDC and TDB pyrolysis at 400°C as functions of the absolute concentration of substrate and the relative concentrations of the two components.

At a DDC concentration of 0.001M, the addition of small quantities of TDB accelerated DDC pyrolysis, and the relative rate reached a maximum value of 1.14. Further additions of TDB inhibited the rate, and it decreased to a minimum value of 1.06. Interestingly, upon continued addition, TDB again accelerated DDC pyrolysis. At [DDC] = 0.01M, TDB initially accelerated the rate, and a maximum value of 1.28 was attained. Additional quantities of TDB reduced the relative rate. A maximum relative rate was also observed at [DDC] = 0.10M. In this case the maximum value was 1.10 at a [TDB]/[DDC] ratio of 0.0158. When [DDC] = 1.00M, however, TDB acted only as an inhibitor.

The results for simulated TDB pyrolysis in the presence of added DDC at 400°C show that DDC had little effect on the relative rate until high ($> 10^{-1}$) [DDC]/[TDB] ratios were attained. At these high ratios, DDC accelerated TDB pyrolysis for [TDB] = 0.001 and 0.01M. The addition of DDC had little (< 0.3%) effect on TDB pyrolysis kinetics at the higher TDB concentrations.

These results clearly demonstrate that interactions occurring during the pyrolysis of a binary mixture of high-molecular-weight hydrocarbons can alter the apparent kinetics from those observed in pure component pyrolysis. They also show that inhibition and acceleration of reaction rates is a complex function of both the relative amounts of the two components as well as their absolute concentrations. For example, at a [TDB]/[DDC] ratio of 0.05, TDB can either inhibit, accelerate, or have no effect on the relative rate of DDC disappearance depending on the DDC concentration.

## ACKNOWLEDGEMENT

This work was supported in part by the University of Michigan Office of Energy Research.

## LITERATURE CITED

1. Gilbert, K. E., Gajewski, F. J. *J. Org. Chem.*, **1982**, 47, 4899.
2. Poutsma, M. L., Dyer, C. W. *J. Org. Chem.*, **1982**, 47, 4903.
3. Panvelker, S. V., Shah, Y. T., Cronauer, D. C., *Ind. Eng. Chem. Fundam.*, **1982**, 21, 236.
4. Benjamin, B. M., Raaen, V. F., Maupin, P. H., Brown, L. L., Collins, C. J., *Fuel*, **1978**, 57, 269.
5. Cronauer, D. C., Jewell, D. M., Shah, Y. T., Modi, R. J., *Ind. Eng. Chem. Fundam.*, **1979**, 18, 153.
6. Rebick, C. in Pyrolysis: Theory and Industrial Practice, L. F. Albright, B. L. Crynes, W. H. Corcoran, Eds. Academic press **1983**.
7. Zhou, P., Crynes, B. L., *Ind. Eng. Chem. Process Des. Dev.*, **1986**, 25, 898.
8. Allen, D. T., Gavalas, G. R. *Fuel*, **1984**, 63, 586.
9. Savage, P. E., Klein, M. T., *Ind. Eng. Chem. Research* **1987**, 26, 488.
10. Savage, P. E., Klein, M. T., *Ind. Eng. Chem. Research* submitted.
11. Savage, P. E., Klein, M. T., *Chem. Eng. Sci.* submitted.
12. Come, G., *J. Phys. Chem.*, **1977**, 81, 2560.
13. Gavalas, G. R., *Chem. Eng. Sci.*, **1966**, 21, 133.
14. Benson, S. W., Thermochemical Kinetics, John Wiley & Sons, New York **1976**.
15. Kochi, J. K., Free Radicals, John Wiley & Sons, New York **1973**.
16. Pryor, W. A., Free Radicals, McGraw-Hill **1966**.
17. Sundaram, K. W., Froment, G. F.,*Ind. Eng. Chem. Fundam.*, **1978**, 17, 174.
18. Kissin, Y. V., *Ind. Eng. Chem. Research*, **1987**, 26, 1633.
19. Ranzi, E., Dente, M., Pierucci, S., Biardi, G., *Ind. Eng. Chem. Fundam.*, **1983**, 22, 132.
20. Edelson, D., Allara, D. L., *Int. J. Chem. Kin.*, **1980**, 12, 605.
21. Ebert, K. H., H. J. Ederer, and P. S. Schmidt, in ACS Symposium Series No. 65, V. W. Weekman and D. Luss, Eds. **1978**, 313.
22. Miller, R. E., Stein, S. E., *J. Phys. Chem.*, **1981**, 85, 580.

## TABLE I: IDENTITY OF SPECIES IN FIGURE 1 FOR TDB-DDC COPYROLYSIS

| | | | | | | | |
|---|---|---|---|---|---|---|---|
| $\beta_1^A$ | Benzyl Rad | $\mu_1^A$ | $\gamma$-TDB Rad | $\beta_1^B$ | Cyclohexyl Rad | $\mu_1^B$ | $\beta$-DDC Rad |
| $\beta_2^A$ | Dodecyl Rad | $\mu_2^A$ | $\alpha$-TDB Rad | $\beta_2^B$ | Undecyl Rad | $\mu_2^B$ | 3°-DDC Rad |
| $\beta_3^A$ | Non-TDB Rad | $\mu_3^A$ | Other TDB Rad | $\beta_3^B$ | Non-DDC Rad | $\mu_3^B$ | Other DDC Rad |
| $\beta_1^A$H | Toluene | $Q_1^A$ | Tridecene | $\beta_1^B$H | Cyclohexane | $Q_1^B$ | Dodecene |
| $\beta_2^A$H | Dodecane | $Q_2^A$ | Styrene | $\beta_2^B$H | Undecane | $Q_2^B$ | Methylene Cyclohexane |
| $\beta_3^A$H | Minor Products | $Q_3^A$ | Minor Products | $\beta_3^B$H | Minor Products | $Q_3^B$ | Minor Products |

## TABLE II: RATE CONSTANT ESTIMATES FOR TDB-DDC COPYROLYSIS

| Type of Reaction | log A ($s^{-1}$ or $M^{-1}s^{-1}$) | $E_A$ (kcal/mol) | Rate Constants |
|---|---|---|---|
| <u>Initiation</u> | | | |
| TDB | 15.0 | 68.5 | $\alpha_I^A$ |
| DDC | 16.5 | 79.0 | $\alpha_I^B$ |
| <u>Termination</u> | 8.5 | 0 | $\omega_T$ |
| <u>$\beta$-scission*</u> | | | |
| B | 14.8 | 28.3 | $k_{\mu_1}^A$ |
| 2° | 13.0 | 28.5 | $k_{\mu_1}^B$ |
| 1° | 13.0 | 26.5 | $k_{\mu_2}^A$ $k_{\mu_3}^A$ $k_{\mu_2}^B$ $k_{\mu_3}^B$ |
| <u>Hydrogen Abstraction**</u> | | | |
| B + 2° H | 8.5 | 18.5 | $k_{21}'^{AB}$ $k_{11}^{AA}$ $k_{13}^{AA}$ $k_{21}'^{AA}$ $k_{23}'^{AA}$ $k_{23}'^{AB}$ $k_{11}^{AB}$ $k_{13}^{AB}$ |
| B + 3° H | 8.5 | 17.0 | $k_{22}'^{AB}$ $k_{12}^{AB}$ |
| B + B H | 8.5 | 14.0 | $k_{12}^{AA}$ |
| 3° + 2° H | 8.5 | 14.5 | $k_{21}'^{BB}$ $k_{23}'^{BB}$ $k_{21}'^{BA}$ $k_{23}'^{BA}$ |
| 3° + B H | 8.5 | 10.0 | $k_{22}'^{BA}$ |
| 2° + 2° H | 8.5 | 12.5 | $k_{13}'^{AA}$ $k_{31}'^{AA}$ $k_{11}^{BB}$ $k_{13}^{BB}$ $k_{13}'^{BB}$ $k_{31}'^{BB}$ $k_{11}'^{AB}$ $k_{13}'^{AB}$ $k_{31}'^{AB}$ $k_{33}'^{AB}$ $k_{31}'^{BA}$ $k_{33}'^{BA}$ $k_{11}^{BA}$ $k_{13}^{BA}$ $k_{11}'^{BA}$ $k_{13}'^{BA}$ |
| 2° + 3° H | 8.5 | 11.0 | $k_{12}^{BB}$ $k_{12}'^{BB}$ $k_{32}'^{BB}$ $k_{12}'^{AB}$ $k_{32}'^{AB}$ |
| 2° + B H | 8.5 | 8.0 | $k_{12}'^{AA}$ $k_{32}'^{AA}$ $k_{12}'^{BA}$ $k_{32}'^{BA}$ $k_{12}^{BA}$ |
| 1° + 2° H | 8.5 | 10.5 | $k_{21}^{AA}$ $k_{23}^{AA}$ $k_{31}^{AA}$ $k_{33}^{AA}$ $k_{21}^{BB}$ $k_{23}^{BB}$ $k_{31}^{BB}$ $k_{21}^{AB}$ $k_{23}^{AB}$ $k_{33}^{BB}$ $k_{31}^{AB}$ $k_{33}^{AB}$ $k_{21}^{BA}$ $k_{23}^{BA}$ $k_{31}^{BA}$ $k_{33}^{BA}$ |
| 1° + 3° H | 8.5 | 9.0 | $k_{22}^{BB}$ $k_{32}^{BB}$ $k_{22}^{AB}$ $k_{32}^{AB}$ |
| 1° + B H | 8.5 | 6.0 | $k_{22}^{AA}$ $k_{32}^{AA}$ $k_{22}^{BA}$ $k_{32}^{BA}$ |

* Reactions indicate type of radical produced (B - Benzylic, 2° - Secondary, 1° - Primary)

** Reactions indicate type of abstracting radical and type of hydrogen abstracted, respectively

**FIGURE 1: TDB-DDC PRIMARY COPYROLYSIS MECHANISM**

$R^A \longrightarrow 2\beta$ (Initiation)

$\beta_1^A + R^A \longrightarrow \beta_1^A H + \mu_1^A$
$\mu_1^A \longrightarrow \beta_1^A + Q_1^A$

$\beta_2^A + R^A \longrightarrow \beta_2^A H + \mu_2^A$
$\mu_2^A \longrightarrow \beta_2^A + Q_2^A$

$\beta_3^A + R^A \longrightarrow \beta_3^A H + \mu_3^A$
$\mu_3^A \longrightarrow \beta_3^A + Q_3^A$

<u>Chain Transfer</u>

$\beta_1^A + R^A \longrightarrow \beta_1^A H + \mu_2^A$
$\mu_1^A + R^A \longrightarrow R^A + \mu_2^A$

$\beta_2^A + R^A \longrightarrow \beta_2^A H + \mu_3^A$
$\mu_2^A + R^A \longrightarrow R^A + \mu_3^A$

$\beta_3^A + R^A \longrightarrow \beta_3^A H + \mu_1^A$
$\mu_3^A + R^A \longrightarrow R^A + \mu_1^A$

<u>Chain Transfer</u>

$\beta_2^A + R^A \longrightarrow \beta_2^A H + \mu_1^A$
$\mu_2^A + R^A \longrightarrow R^A + \mu_1^A$

$\beta_3^A + R^A \longrightarrow \beta_3^A H + \mu_2^A$
$\mu_3^A + R^A \longrightarrow R^A + \mu_2^A$

$\beta_1^A + R^A \longrightarrow \beta_1^A H + \mu_3^A$
$\mu_1^A + R^A \longrightarrow R^A + \mu_3^A$

<u>Termination</u>

$\beta_i^A + \beta_j^A \longrightarrow$
$\mu_i^A + \beta_j^A \longrightarrow$
$\mu_i^A + \mu_j^A \longrightarrow$

$R^B \longrightarrow 2\beta$ (Initiation)

$\beta_1^B + R^B \longrightarrow \beta_1^B H + \mu_1^B$
$\mu_1^B \longrightarrow \beta_1^B + Q_1^B$

$\beta_2^B + R^B \longrightarrow \beta_2^B H + \mu_2^B$
$\mu_2^B \longrightarrow \beta_2^B + Q_2^B$

$\beta_3^B + R^B \longrightarrow \beta_3^B H + \mu_3^B$
$\mu_3^B \longrightarrow \beta_3^B + Q_3^B$

$\beta_1^B + R^B \longrightarrow \beta_1^B H + \mu_2^B$
$\mu_1^B + R^B \longrightarrow R^B + \mu_2^B$

$\beta_2^B + R^B \longrightarrow \beta_2^B H + \mu_3^B$
$\mu_2^B + R^B \longrightarrow R^B + \mu_3^B$

$\beta_3^B + R^B \longrightarrow \beta_3^B H + \mu_1^B$
$\mu_3^B + R^B \longrightarrow R^B + \mu_1^B$

$\beta_2^B + R^B \longrightarrow \beta_2^B H + \mu_1^B$
$\mu_2^B + R^B \longrightarrow R^B + \mu_1^B$

$\beta_1^B + R^B \longrightarrow \beta_1^B H + \mu_3^B$
$\mu_1^B + R^B \longrightarrow R^B + \mu_3^B$

<u>Termination</u>

$\beta_i^B + \beta_j^B \longrightarrow$
$\mu_i^B + \beta_j^B \longrightarrow$
$\mu_i^B + \mu_j^B \longrightarrow$

Interactions

$\beta_1^A + R^B \longrightarrow \beta_1^A H + \mu_1^B$
$\beta_1^A + R^B \longrightarrow \beta_1^A H + \mu_2^B$
$\beta_1^A + R^B \longrightarrow \beta_1^A H + \mu_3^B$
$\mu_1^A + R^B \longrightarrow R^A + \mu_1^B$
$\mu_1^A + R^B \longrightarrow R^A + \mu_2^B$
$\mu_1^A + R^B \longrightarrow R^A + \mu_3^B$
$\beta_2^A + R^B \longrightarrow \beta_2^A H + \mu_1^B$
$\beta_2^A + R^B \longrightarrow \beta_2^A H + \mu_2^B$
$\beta_2^A + R^B \longrightarrow \beta_2^A H + \mu_3^B$
$\mu_2^A + R^B \longrightarrow R^A + \mu_1^B$
$\mu_2^A + R^B \longrightarrow R^A + \mu_2^B$
$\mu_2^A + R^B \longrightarrow R^A + \mu_3^B$

$\beta_3^A + R^B \longrightarrow \beta_3^A H + \mu_1^B$
$\beta_3^A + R^B \longrightarrow \beta_3^A H + \mu_2^B$
$\beta_3^A + R^B \longrightarrow \beta_3^A H + \mu_3^B$
$\mu_3^A + R^B \longrightarrow R^A + \mu_1^B$
$\mu_3^A + R^B \longrightarrow R^A + \mu_2^B$
$\mu_3^A + R^B \longrightarrow R^A + \mu_3^B$
$\beta_3^B + R^A \longrightarrow \beta_3^B H + \mu_1^A$
$\beta_3^B + R^A \longrightarrow \beta_3^B H + \mu_2^A$
$\beta_3^B + R^A \longrightarrow \beta_3^B H + \mu_3^A$
$\mu_3^B + R^A \longrightarrow R^B + \mu_1^A$
$\mu_3^B + R^A \longrightarrow R^B + \mu_2^A$
$\mu_3^B + R^A \longrightarrow R^B + \mu_3^A$

$\beta_1^B + R^A \longrightarrow \beta_1^B H + \mu_1^A$
$\beta_1^B + R^A \longrightarrow \beta_1^B H + \mu_2^A$
$\beta_1^B + R^A \longrightarrow \beta_1^B H + \mu_3^A$
$\mu_1^B + R^A \longrightarrow R^B + \mu_1^A$
$\mu_1^B + R^A \longrightarrow R^B + \mu_2^A$
$\mu_1^B + R^A \longrightarrow R^B + \mu_3^A$
$\beta_2^B + R^A \longrightarrow \beta_2^B H + \mu_1^A$
$\beta_2^B + R^A \longrightarrow \beta_2^B H + \mu_2^A$
$\beta_2^B + R^A \longrightarrow \beta_2^B H + \mu_3^A$
$\mu_2^B + R^A \longrightarrow R^B + \mu_1^A$
$\mu_2^B + R^A \longrightarrow R^B + \mu_2^A$
$\mu_2^B + R^A \longrightarrow R^B + \mu_3^A$

$\beta_i^A + \beta_j^B \longrightarrow$
$\mu_i^A + \beta_j^B \longrightarrow$
$\mu_i^A + \mu_j^B \longrightarrow$
$\mu_i^B + \beta_j^A \longrightarrow$

FIGURE 2: DDC–TDB COPYROLYSIS SIMULATION

RELATIVE RATE FOR DDC

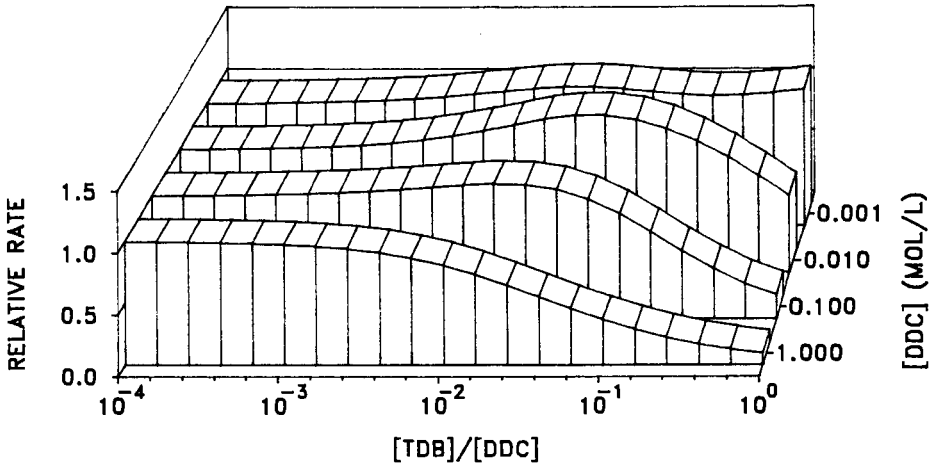


RELATIVE RATE FOR TDB

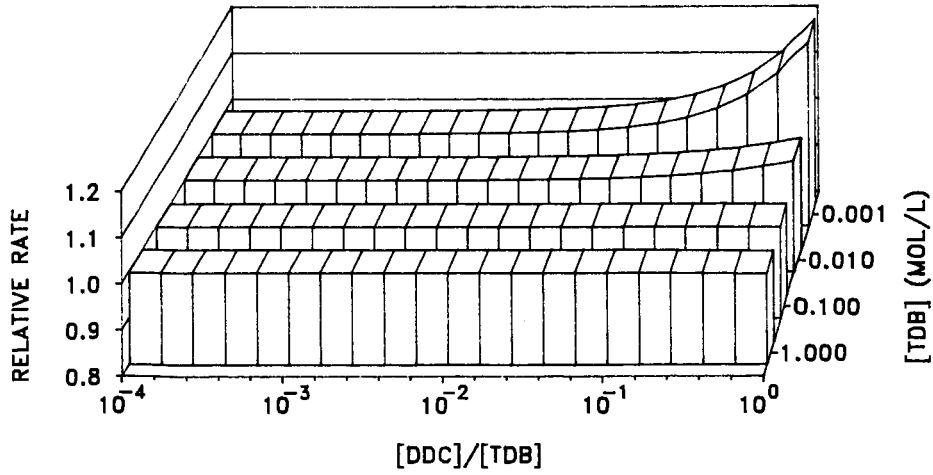

# PYROLYSIS OF COALS LOADED WITH POLYCYCLIC AROMATIC HYDROCARBONS

Ripudaman Malhotra, Gilbert St.John,
Doris S. Tse, and Donald F. McMillen

Chemical Kinetics Department, Chemical Physics Laboratory
SRI International, 333 Ravenswood Avenue, Menlo Park, CA 94025

## INTRODUCTION

The relative simplicity of pyrolysis offers significant advantages as a coal conversion approach. However, char yields are typically high and volatile products are generally distributed between low value light hydrocarbons and tars that can be very difficult to upgrade. Consequently, the pyrolysis of coals under conditions that would produce larger yields of condensible and readily upgradable hydrocarbons is clearly a desirable goal, and the literature contains many examples of approaches to augmenting pyrolysis yields. For this reason, it is desirable that additional efforts be conducted as much as possible in light what is known about the mechanism of volatiles production.

A fundamental aspect of the problem that is well recognized is the desirability of carrying out the process under reducing conditions in order to meet the stoichiometric requirements of bond rupture (replacement of C-C bonds with C-H bonds) and the ultimate desire (for fuel purposes) for substantially aliphatic products. This desirability has resulted in various hydropyrolysis approaches involving heating in the presence of medium- or high-pressure hydrogen. These approaches generally result in improved yields only when the reaction time is long, or when the temperature exceeds roughly 600°C (1112°F).(1,2) At short reaction times and temperatures below 600°C, the principal impact of $H_2$ pressure is to decrease volatile yields, apparently through the impeding of volatiles tranport out of the coal and from the pyrolysis region. The lack of any enhancement in volatiles yield is a result of the fact that below 600°C, $H_2$, although thermodynamically powerful, is kinetically an ineffective reducing agent owing to the high strength of the H-H bond and the resulting difficulty in thermally achieving significant concentrations of hydrogen atoms. Unfortunately, the 400 to 600°C region is precisely where coals become very reactive, and need effective reducing agents to prevent retrograde processes.

Recent mechanistic work indicates that bond scissions occuring during liquefaction (3) and pyrolysis (4) are not simply spontaneous thermal rupture of inherently weak bonds, but include to a substantial extent hydrogen-transfer-induced scission of strong bonds as well. One potentially effective way of engendering scission of strong bonds is by H-transfer from hydroaromatic (cyclohexadienyl) radicals. This suggestion finds support in the work of Huttinger and Sperling who have subjected several coals to rapid pyrolysis after loading with aromatics, hydroaromatics, or alkylaromatics and found increases in the tar yields and decreases in the char yields of 5 to 10 percentage points.(5) In contrast, Solomon and Serio have not observed any increase in the tar yields upon pyrolyzing coals in an atomosphere of aromatic hydrocarbons.(6) Earlier work by Mazumdar and coworkers with reduced coals shows significant enhancement in pyrolysis yields, but does not distinguish between the effect of hydroaromatic hydrogen introduction and bond cleavage that may have ocurred during reduction.(7,8)

Other work in this area appears to have focused on the impact of such additives on liquefaction yields, and on meso-phase formation during coke production. Mochida and co-workers have found some hydrogenated petroleum pitches to be effective liquefaction

agents.(9) These same researchers, as well as a number of other workers, have found additives rich in PCAH to markedly extend the range of fluidity in time and temperature and to promote the development of anisotropy during coke formation.

In order that the loading with aromatics be an effective pretreatment, the reaction conditions must allow for an opportunuity for the aromatics to react with the coal before they are simply devolatilized. Liquefaction and coking provide ample opportunity for reactions between the added aromatics and the coal while pyrolysis conditions generally do not favor such interactions. In this paper we report our efforts at determining the range of conditions under which loading of coals with PCAH may result in beneficial effects during pyrolysis.

## EXPERIMENTAL PROCEDURE

Coals and Coal Loading. Three coals were tested in this study: a Wyodak (WYO-1, courtesy Univ. of Wyoming), an Illinois No. 6 (PSOC 1098), and a Pittsburgh No. 8 (PSOC 1099). The coals were loaded either with a highly aromatic coal tar (Wt. Av. MW 310) or a vacuum residue derived from a hydroprocessed petroleum pitch (Wt. Av. MW 908).

A simple evapaorative loading technique has been used for all of the experiments reported here. The additive was dissolved in THF (stabilized) to produce a 10 wt% "solution," which was filtered through a 0.45 μm millipore filter. The filtrate was added to the ground coal, and then removed, with periodic stirring, using a stream of argon. In order to minimize removal of extractable materials by THF, and to maximize deposition of the additive within the pores of the coal, the solution was added only to the point of incipient wetness. Nevertheless, since it was anticipated that some extraction would inadvertantly occur and perhaps have a deleterious effect (10), "blank" coal samples were prepared by carrying out the loading procedure with pure THF. These THF-treated coals were used as the basis for judging the impact of the additives on loaded additive.

Pyrolysis. The TGA pyrolyses under argon were performed using a Dupont 1090 TGA system. The "rapid heating TGA" pyrolyses were performed using a specially constructed TGA consisting of a vertical tube furnace with a Cahn microbalance. The pyrolyses were performed with the maximum heating rate possible in this apparatus by raising the furnace, preheated to 1000°C, around a quartz vacuum envelope containing ~ 60 mg of coal suspended from the microbalance in a ~1-inch diameter quartz flask. This procedure provided a heating rate of about 600°C/min as measured by a thermocouple placed near the flask containing the coal sample. The PY-FIMS experiments were carried out in the programmed temperature inlet of a field ionization mass spectrometer (FIMS). This instrument provides molecular ion profiles and organic weight loss as a function of temperature up to 500°C, and has been extensively used for analysis of high boiling, complex mixtures.

## RESULTS

Following the rationale cited above, we have begun a series of experiments designed to test the effect on pyrolysis yields of loading coals with PCAH mixtures. We have thus far used three different pyrolysis techniqes with slow to moderate heating rates. These are: pyrolysis-FIMS at high vacuum, TGA in one atomosphere of argon, and rapid heating TGA in vacuum, at heating rates of 2.5°C/min, 20°C/min, and 600°C/min respectively. The results from these experiments are shown in Table 1. The yields have been adjusted for tar vaporization, assuming that the volatility of the tar is not changed by being loaded into the coal. This assumption is of course not strictly true;

the temperature profile of the coal tar components in the PY-FIMS experiments show that vaporization is retarded by about 50°C. However, because the total amount of tar used is only about 10% of the weight of the coal, the error in overestimating tar volatility leads to no more than a 2% underestimate of the coal devolatilization.

From the limited data given in Table 1, we note two significant results. First, with none of the three pyrolysis techniqes did the addition of 5 to 13 wt% of coal tar, hydrogenated coal tar, or vacuum resid from a hydrotreated petroleum resid, significantly increase the volatiles yield over THF-treated "blank" coals. Second, the THF treatment itself appears to have a deleterious effect on the release of volatiles from Wyodak coal, particularly above 500°C.

Effect of Changing Pyrolysis Conditions. It was anticipated that the impact of PCAH-loading would tend to increase with increasing heating rate and/or ability to retain the additive through the region of maximum tar formation reactivity. Specifically, since the results of Hüttinger and Sperling (5) were obtained at heating rates of 1000°C/s, we felt that increasing the heating rate from 20°C/min to 600°C/min would increase the chances of seeing substantial beneficial effect. Furthermore, rapid heating is known to increase the impact of coking additives on fluidity.(11) Although the data in Table 1 definitely show higher yields for the 600°C/min heating in vacuum as expected (12), there was no improvment in the response to tar treatment itself even at this higher heating rate.

Pre-Hydrogenation of the Tar. Although FIMS and nmr anaylses show the coal tar to have essentially no hydroaromatic character and only a small amount of alkylaromatic of the fluorene type), the known and projected benefits of large PCAH in shuttling indigenous coal hydrogen for use in conversion led us to use the tar as is for one series of experiments. However, because the added benefit of hydroaromatic hydrogen is well known, the tar was also subjected to mild hydrogenation and used for the coal treatment. The FI mass spectrum of the reduced tar showed 10 to 20 percent of the various PCAH were converted to the respective dihydroaromatics; nevetheless, treatment with this tar still showed no impact on pyrolysis yields.

Use of a Higher Boiling Additive. Since the coal tar itself was found to be 70% volatilized by 350°C (i.e., before the region of maximum chemical reactivity of the coal) under the atmopheric pressure TGA conditions and 88% under the PY-FIMS vacuum conditions, a slightly higher boiling additive was judged to be desirable under these slow heating conditions. Accordingly, we tested the use of the vacuum resid portion of a hydrogenated atomoshperic resid (72% volatile at 350 under PY-FIMS conditions), but found this switch to a higher boiling (but less aromatic) additive did not result in any benefit to the pyrolyses, under the conditions thus far used.

## DISCUSSION

Further efforts to define the extent of improvement in pyrolysis yields to be gained from PCAH additives as a function of coal type and reaction conditions will focus on the use of higher heating rates, higher boiling PCAH mixtures, and variations in the degree of sample confinement. It seems reasonable to assume any benefits to volatiles production will be maximized at high heating rate for the following three reasons.

- Volatiles yields tend to increase with increasing heating rates;(1,12)
- Coals of high fluidity tend to benefit most from this increase in heating rate;(3)
- PCAH additives increase fluidity under coking conditions.(11)

The probable impact of pressure is less clear. On the one hand, volatiles yields are often substantially larger under vacuum, owing to improved volatiles

transport.(1,12) On the other hand, higher pressures (up to 5 - 10 atm) have been reported to accentuate fluidity increases brought about by pitch additives.(11) Thus, it is not clear what trend will be observed with changing pressure. The experiments of Hüttinger and Sperling (5) were performed under nominal vacuum, but with the sample moderately confined in a Curie point pyrolyis capillary. This combination, along with the rapid heating, apparently resulted in enough of the various naphthalene derivatives remaining with the coal till temperatures of high coal reactivity were reached. Thus benficial effects were observed notwithstanding the low boiling point of the additives. It was for this reason that we originally thought that a higher boiling tar, with PCAH components known to be much better coal conversion agents (albiet liquefaction) than naphthalene derivatives, would likely show significant beneficial effects - even at the lower heating rates used in this study.

The apparent detrimental effect of THF in the treatment of Wyodak coal is potentially informative, since low rank coals are known to be particularly susceptible to retrograde reactions or other factors that can significantly decrease their convertibility. In the present case, comparison of the FI-mass spectra of the raw and THF-treated Wyodak samples reveals the the high mass envelope (which is never large in this coal) is significantly decreased by the THF treatment. Examination of the temperature profiles for the peaks in this range shows that these are evolved at substantially lower temperatures than the dominant peaks in the spectrum, the dihydroxybenzenes and the phenols. The devolatilization of the high mass materials is consistent with these materials being more aliphatic and pre-existing in the coal, whereas the low molecular weight phenols and dihydroxybenes are products of pyrolysis. With this difference in mind, it may be significant that substantial detrimental effect of the THF treatment was not observed until the temperature exceeded 500°C: aliphatics, though they have high hydrogen content and are potential sources of hydrogen for hydrocracking, cannot generally make this hydrogen readily available until the thermal hydropyrolysis temperature range (i.e., ~ 600°C). The extent and nature of this detrimental effect will be further explored.

Acknowledgement: Financial support for this work by the U.S. Department of Energy, METC, under contract No. DE-AC21-87MC23286 is gratefully acknowledged.

## REFERENCES

1. Howard, J. B., "Fundamentals of Coal Pyrolysis and Hyropyrolysis," in Chemistry of coal Utilization, Second Supplementary Volume, M. A. Elliott, Ed., John Wiley and Sons, New York, 1982, p. 665.

2. O'Brien, R. J.; Gibbins-Matham J. R.; Snape, C. E.; Kandiyoti, R, in Proceedings of the 1987 International Conference on Coal Science, J. A. Moulijn, K. A. Nater, and H.A.G. Chermin, Editors, Elsevier Science Publishers B. V., Amsterdam, 1987, p. 695.

3. McMillen, D. F.; Malhotra, R.; Chang, S.-J.; Hum, G. P., Energy & Fuels, 1987, 1, 193.

4. McMillen, D. F.; Malhotra, R.; Nigenda, S. E., "The Case for Induced Bond Scission During Coal Pyrolysis," Am. Chem. Soc., Div. Fuel Chem. Preprints, 1987, 32(3), 180.

5. Hüttinger, K. J.; Sperling; R. E.; "Flash Hydropyrolysis of Coals Doped with Aromatics," in Proceedings of the 1987 International Conference on Coal Science,

J. A. Moulijn, K. A. Nater, and H.A.G. Chermin, Editors, Elsevier Science Publishers B. V., Amsterdam, 1987, p. 699.

6. Solomon, P. S.; Serio; M. A., private communication.

7. Bhattacharyya, A. C.; Mazumdar, B. K.; Lahiri, A., Fuel, 1964, 43, 181.

8. S. Ganguly; Mazumdar, B. K., Fuel, 1964, 43, 281.

9. Mochida, I; Moriguchi; Y.; Korai; Y.; Fujitsu, H.; Takeshita, K., Fuel, 1981, 60, 746.

10. O'Brien, R. J.; Gibbins-Matham J. R.; Kandiyoti, R., Fuel Processing Technology, 1987, 15, 71.

11. Green, P. D.; Patrick, J. W.; Mark Thomas, K; Walker, A., Fuel, 1985, 64, 1431.

12. Gibbins-Matham, J. R.; Kandiyoti, R., "The Effect of Heating Rate and Hold Time on Primary Coal Pyrolysis Product Distribution," Am. Chem. Soc., Div. Fuel Chem. Preprints, 1987, 32(4), 318.

13. Reasoner, J. W.; Hower, J. C.; Yates, L. P.; Lloyd, W. G., Fuel, 1985, 64, 1269.

Table 1

WEIGHT LOSS FOR PYROLYSIS OF COALS AND TAR LOADED COALS

| Coal | % Wt. Loss* | | | | |
|---|---|---|---|---|---|
| | 2.5°C/min/vac | 20°C/min/Ar | | 600°C/min/vac | |
| Treatment | 500°C | 500°C | 900°C | 500°C | 900°C |
| Wyodak | | | | | |
| Raw | 30 | 27.9 | 63.1 | - | - |
| Blank (THF) | 32 | 22.0 | 43.8 | 41.8 | 61.7 |
| Coal-Tar | 34 | 22.0 | 44.8 | 36.6 | 54.5 |
| H-Coal-Tar | 32 | - | - | 40.4 | 53.4 |
| Ill. No. 6 | | | | | |
| Raw | - | 12.0 | 30.3 | - | - |
| Blank (THF) | 32 | 16.5 | 31.9 | - | - |
| Coal-Tar | 29 | 8.7 | 30.3 | - | - |
| H-Coal-Tar | - | - | - | - | - |
| H-Pet-Res | 28 | - | - | - | - |
| Pitts. No. 8 | | | | | |
| Raw | - | - | - | - | - |
| Blank (THF) | - | - | - | 30.0 | 46.8 |
| H-Coal Tar | - | - | - | 30.9 | 45.6 |
| H-Pet-Res | - | - | - | - | - |

* The %-volatility of the tars alone in vacuum and in Ar up to 500°C was 95 and 80% respectively. The volatilities shown above are for the whole coals. They are corrected for tar volatilities for the tar-loaded cases.

# Chemical Characteristics of Tars Produced in a Novel Low Severity, Entrained Flow Reactor

by
J.D. Freihaut, W.M. Proscia and D.J.Seery
United Technologies Research Center
East Hartford, Ct. 06108

## Introduction and Approach

The devolatilization of a high volatile bituminous coal follows the sequence indicated in Figure 1. The formation and evolution of heavy molecular weight hydrocarbons, tars, account for more than half the total mass loss of such coals (1,2,3,4). As observed in a wide range of heating conditions, the tars dominate the initial mass loss of bituminous particles. In addition, gas phase, "secondary" reactions of tars can account for major fractions of the light gas yields, depending on the heating conditions. The distribution of the light gases and chemical characteristics of the collected tars are dependent on the both the transient particle temperature and ambient gas temperature (5,6).

A number of investigators have reported that a range of coal types follows the same phenomenological sequence, although the tar yields vary significantly with coal rank characteristics (4,7,8). Moreover, chemical structural characteristics of "primary" tars are reported "similar" to those present in the parent coal, that is, the tar "monomers" reflect the coal "polymer" (3,9,10 ). "Primary" tars are those collected in conditions in which "secondary" reactions have been minimized. Some of these investigators have noted that, within the limits of experimental resolution, the chemical kinetic parameters that describe tar evolution from a wide range of coals do not vary with coal type (3,9 ). From this perspective, the phenomenological sequence, monomer-polymer relationship between tar and parent coal, and chemical kinetic parameters describing tar formation and evolution are all invariants in coal devolatilization.

On the other hand, some investigators note the phenomenological sequence of disperse phase devolatilization is the only commonality among coals of varying rank characteristics. Tar yields and chemical characteristics, relative to other coal tars as well as to the parent coal, vary signficantly with coal type. In addition, secondary reaction behavior varies according to chemical characteristics of the primary tars (7,11). Implicit in these structural observations with respect to primary tars is a questioning of the invariance of devolatilization/pyrolysis kinetics with coal type. Since all primary tars are not equally "similar" to the parent coal and the distribution of functional groups varies so extensively with coal type, it becomes difficult to understand the extent to which the same tar evolution and light gas formation chemical kinetic parameters could be used for a wide range of coal types.

Other investigators have noted the appreciable role transport parameters can exert in determining devolatilization phenomena. The formation of a glass-like "melt" as an intermediate phase during devolatilization of a

bituminous coal (12,13,14) and the observed changes in molecular weight characteristics of heavy hydrocarbons with ambient pressure (15,16), have led some investigators into a detailed examination of intraphase and interphase mass transport phenomena contributions in mass loss kinetics. Ignoring the details of product distributions and chemical characteristics of tars with changes in pyrolysis conditions, still other investigators have indicated that weight loss kinetics is determined primarily by heat transfer considerations (17,18).

As apparent from the diverse perspectives, a conceptual understanding of disperse phase coal devolatilization remains elusive and, consequently, comprehensive rate models remain difficult to extrapolate to a wide range of conditions. Among the considerable experimental difficulties are: rapidly quenching a heterogeneous process whose overall mass loss rate appears to adjust itself to heating conditions; isolating char particles, tar aerosols and light gas species that are coupled in product streams; minimizing gas phase reactions of thermally labile heavy molecular weight organic compounds; subsequent analysis of large, fragile organic species which have considerably different functional forms, depending on heating conditions and parent coal characteristics.

Batch reactors and single particle systems are often criticized for generating too small a tar sample in conditions unrepresentative of rapid heating. Continuous reactor systems, such as entrained flow reactors, provide acceptable heating conditions but due to residence time, the hot entrainment gases, and the large entrainment flow/sample mass, make it difficult to either time resolve weight loss kinetics or isolate primary tars for subsequent analyses.

This communication reports the utilization of a novel entrained flow reactor and product isolation system. In contrast to the operation of most entrained flow reactors, no attempt is made to match the entrainment gas and wall temperatures. Entrainment gas temperatures are purposely kept below wall temperatures to minimize extra-particle gas phase reactions of tars. To obtain char-free tar samples, an aerosol phase separation system is employed to isolate a significant fraction of entrained tar species from the char mass. Both the char particle and aerosol arms of the product separation system contain serially staged particulate separation systems followed by porous metal final filters that collect "pure" tar species.

## Experimental

### Reactor and Product Separation System

Figures 2 - 4 display the essential components of the entrained flow reactor, product separation and gas analysis systems. Figures 5 - 7 display the total power density, radiative power density and gas temperature profiles as a function of reactor position. The flux rate profiles are mesured by specially designed, calibrated probes. Incident, center-line radiative flux rates range from several watts/sq. cm. at wall temperatures of 750 C to approximately 25 watts/sq. cm. at wall temperatures of 1270 C. Gas temperature

profiles vary as shown. Gas temperature profiles were obtained by making a series of measurements with a set of decreasing thermocouple bead sizes with the asymptotic temperatures approached defined as the "true" local gas temperature. In general, the gas temperatures measured in this manner are consistent with those estimated from the magnitude of the convective heat transfer determined from the power density measurements.

The reactor creates a heat transfer field in which entrained particles are heated by radiation to the local, axial, entrained gas temperture within the reactor (Figures 8 , 9 ). The radiation flux induces an inverse diameter dependent heating rate on particles in an attempt to drive the particles to equilibrium with the radiating walls. The carrier gas imposes an inverse diameter squared component on the particle heating rate, which in effect insures small particle temperatures are not very different from the local gas temperature, assuming the devolatilization process is weakly endothermic or thermally neutral. Estimated particle heating rates are of the order of 5000 7000 C/sec in these conditions. Such heating rates are greater than that reproducibly obtainable in a heated grid apparatus operated in the same laboratory, but less than that expected in conventional entrained flow reactors wherein heating rates approaching 100,000 C/sec are indicated with estimated transient flux rates at the particle surface of nearly 100 watts/sq. cm. Operating an entrained flow reactor in this manner minimizes gas phase pyrolysis reactions of the intial tar species and allows collection of large quantities of tar species.

Normally, 60 - 75% of the total reactor flow is drawn through the aerosol separation (impactor train) system, that is F of Figures 3 and 4 is of the order 0.25. The temperature and path length of the cooled aerosol transfer line are varied according to the nature of the tars being collected, which, in turn, varies with the parent coal characteristics and reactor heating conditions. The aerosol phase separator is designed to "pull off" all particles or aerosols that are less than 2 microns. A qualitative check of the performance by scanning electron microscope examination of the deposits indicated that designed behavior is followed, provided proper flow rates are maintained throughout an experiment. Inertia carries larger particles into the char separation (cyclone train) system. Both separtation trains contain porous metal filters as final stages. Performance of the system is monitored by measuring the flow through the separation arms, pressure drop across the filter housings and determining the tar mass deposited on each of the filter systems. Tar mass ratios are expected to be of the ratio of the average mass flow ratio through the two separation systems during an experiment. This is observed to be the case.

## Sample Selection

The feed system utilized is capable of sustained delivery of optically thin streams of particles at constant mass delivery rate, provided the feeder is loaded with a narrow particle size range initially. Particle sizes as low as 10 microns and as large as 300 micron have been utilized. Since the feeder operates on aerodynamic principles, aerodynamically separated samples were employed (See acknowledgements). The location of the parent coal sample set on

a pseudo-coalification band plot is shown in Figure 10.

Sample Measurements

Mass loss is determined by ash tracer techniques. It is observed that experiment specific determinations of the parent coal ash need to be determined. This is accomplished by operating the system in cold flow conditions before and after a particular hot wall devolatilization test and determining the ash content of the particles collected in the first stage cyclone. This value becomes the initial ash value. It is observed that lower density particles are fed into the reactor initially despite the rather extensive efforts to match the aerodynamic characteristics of the feeder with those of the size separated samples provided. Consequently, sustained operation over a sequence of devolatilization conditions leads to significant variations in the average density, mineral content, of the feed, which, in turn, leads to inconsistent determinations in particle mass loss via ash tracer.

Elemental characterisitics of evolved tars and chars are determined by use of a Perkin-Elmer 240 instrument. IR absorbance characteristics are determined by an alkali-halide technique using a Fourier Transform - Infrared Spectrometer (FT-IR). The FT-IR is also used to determine the composition of the pyrolysis gases. The streams from the two separation systems are recombined and continuously passed through a multi-pass cell. The 43.5 meter path length is needed to measure the low levels of IR active light gases generated. Concentrations are low because the initial stages of devolatilization, the focus of this investigation, generate small amounts of such gases which are entrained in a relatively large volume of carrier gas.

Results

HVA Bituminous Coal

For the PSOC 1451D coal, an Appalachian high volatile bituminous coal, the ash tracer volatile yields for two particle sizes is shown in Figure 11 As indicated, despite the factor of three difference in paticles size, the reactor temperature sensitivity of the mass loss is very similar between the size cuts. Temperature calculations using the measured reactor characteristics as heat transfer conditions indicate this should indeed be the case (See above ). Figure 12 shows the relative gas yields, normalized with respect to maximum yields of each gas and plotted with respect to the peak reactor gas temperature, since gas phase reactions of tars are thought to account for substantial fractions of "coal" pyrolysis gases. It is noted that significant increases in acetylene and hydrogen cyanide gases are not observed until peak gas temperatures of 700 C are achieved. At lower gas temperatures, light gas yields are dominated by $CH_4$, $C_2H_4$, CO and $H_2O$, but these gases account for only 10 - 15% of the total 0.2 - 0.25 particle mass fraction loss observed for these reactor conditions. For this coal, tar yields dominate the mass loss at these and lower gas-particle temperatures. Appreciable tar yields, 0.10 - 0.15 mass fraction, are observed at gas temperatures of 350C (wall temperatures of 790C).

Examination of the elemental composition of the tars indicates that the tar evolution process resembles a distillation process from the point of view of hydrogen concentration versus characteristic temperature, gas or reactor wall (Table I ). As implied by the insensitivity of the total mass loss with particle size and as indicated by the temperature calculations, the elemental composition of the tars evolved from the two different particle sizes and for a particular stage of the reaction process should be similar. As indicated in Table I the elemental composition of the the 20 -30 micron tars and the 63 - 75 micron tars are quite similar in elemental composition. A distillation-like tar evolution process would also imply changing functionality and relative molecular weight characteristics of the samples with characteristic temperature. Figure 13 displays the relative -CH2- concentration of the tars for increasing reactor temperature and Table II indicates relative molecular weight moments as a function of reactor temperature.

In summary, the results indicate the hydrogen level, in particular the polymethylene concentration hydrogen level, of the collected tars systematically decreases with peak reactor temperature as the total tar yield increases. As the hydrogen level gradually decreases the relative molecular weight moments of the evolved tars increase to the point where the tar yield is believed to be maximized. Lower temperature tars contain less total oxygen and sulfur mass fractions than the total tar mass evolved to the point of maximum tar yield. Absolute tar yields are difficult to determine using an entrained flow reactor but investigation of the tar evolution process on a heated grid apparatus indicate total tar yields are 0.30 - 0.35 of the parent coal mass on an ash-free basis for this coal.

Coal Rank Effects

It is desirable to determine the change in the nature of the tars produced with changes in the chemical characteristics of the parent coal, while keeping the heating conditions constant. The heating conditions that maximized the tar yields for the high volatile bituminous coal (930C wall, 500 - 600 C gas temperture) while minimizing gas phase secondary reactions were selected, although it is recognized that each coal type may require a unique set of heating conditons to maximize its tar yield.j

Figures 14 and 15 compare the hydrogen and sulfur + oxygen levels of the tar species to those observed in the parent coals. As the rank characteristics of the parent coal increase the elemental composition of the tars become more like the parent coal. The similarity ratios asymptote toward unity. Conversely, the lower the rank of coal the more unlike in elemental composition are the primary tars. Figure 16 indicates the %H of the low rank coal tars can be as great as 9% in these conditions.

The most striking difference in the IR absorbance spectra of the low rank coal tars relative to the higher ranks resides in the polymethylene absorbance region (2920 cm-1). The low rank coal tars generally display much greater absorbance levels in this region per unit mass of sample than the high rank coal tars. Assuming the absorption coefficients of this band do not vary signficantly with coal rank, such behavior implies increasing concentrations of -CH2- levels with decreasing coal rank. The -CH2- absorbance band

correlates with the % H level in the tars (Figures 16,17,18).

The difference in structural characterisitics of the low temperature tars evolved from the lignite and subbituminous coals, relative to the bituminous coal tars, is again emphasized by comparing the molecular weight moments obtained by gel permeation chromatography. The data in Figure 19 indicates the tars evolved from the low rank coals at a particular temperature have greater molecular weight moments than the corresponding high rank coal tars. In the most elementary sense, the polystyrene calibrated gpc technique indicates only that aliphatic, hydrogen-rich low rank coal tars are structurally "larger" than the more aromatic bituminous coal tars with respect to a length to weight ratio parameter. These results likely reflect variation in conformational aspects of the tars as a function of rank rather than molecular weight or polarity differences. The long chain aliphatic tars characteristic of the low rank coals are not efficiently retained by the gel permeation column and, consequently, elute in the short retention times characterisitic of heavy polystyrene standards. The molecular "weight" moments appear to be more characteristic of relative molecular geometry than actual mass size when comparing tars from a range of coal ranks. The general observations with respect to the variations in low temperature coal tars with rank characteristics of the primary coal are indicated in Figure 20, the lower the rank of parent coal the more unlike the parent coal are the low temperature, primary tars. The dissimilarity appears primarily related to the aliphatic to aromatic hydrogen distribution and the oxygen-sulfur heteroatom content of the tars relative to the parent coal. Signficant polymethylene concentrations variations are observed with variation in coal type.

Although the nature of tars varies significantly with coal type, the particle devolatilization and gas phase reaction sequence did not. Table III displays the composition of tars from a subbituminous coal (PSOC 1520D) at various reactor temperatures. As in the high volatile bituminous coal, the hydrogen rich, more aliphatic, lighter molecular weight species vaporize before the heavier, more aromatic species during the evolution to the point of maximum tar yield. At gas temperatures of 700 C or above, gas phase reactions of pyrolysis of the polymethylene rich tars quickly leads to ring formation in the tar species. $C_2H_4$ and CO are major light gas products of these reactions and, at still higher temperatures, $C_2H_2$, CO and HCN. In short, the same light gas formation temprature pattern as indicated in Figure 12 for a HVA bituminous coal is followed by the lower rank coals. However, the absolute quantities vary signficantly with the nature of the low temperature tars.

## Summary and Conclusions

The entrained flow reactor investigation indicates that the phenomenology of coal devolatilization and pyrolysis is similar for a wide range of coal ranks. The phenomenology is summarized in Figure 1 . Heavy hydrocarbons are "formed" within (ATP = Attached Tar Precursors) the coal particle at relatively low temperatures (300 - 450 C). Further heating results in the extra-particle evolution of these heavy hydrocarbons (tars) and the onset of light gas production (450 - 700 C). The low temperature light gases consist mainly of $CH_4$ and higher alkanes, CO, $CO_2$, $H_2O$ and some $C_2H_4$. The absolute quantities of these species vary with coal type as do the absolute yields of

"primary" tars. Gas and particle temperatures greater than 700 C preferentially produce C2H2, HCN, CO and C2H4.

Although the sequence of tar evolution is phenomenologically similar, the structural characteristics of tars evolved from a range of coal types indicates quite different processes are occuring chemically. The lower the rank of coal, the more unlike the parent coal are the low temperature tars. Low temperature lignite tars appear to consist mainly of long chain aliphatic species with signficant levels of associated carboxylic and carbonyl groups. Low temperture tars from bituminous coals have structural characteristics more reflective of, but never identical to, the parent coal.

Gas phase reactions of low temperature, primary tars are rapid at gas temperatures of 700 C and above, common operating temperatures of conventional entrained flow reactors. Such reactions quickly lead to the ring formation reactions from polymethylene-rich low temperature tars conincidental with the evolution of the heavier tar species from the devolatilizing particle itself. Tars collected in these conditions, particularly tars collected in separation systems without extensive phase separation, will appear to be more like the parent coal than the primary tars originally evolved and collected in the above reactor system or other systems that minmize secondary tar reactions. The phenomenological sequence of heavy hydocarbon formation, tar evolution and gas phase reactions appear similar for a wide range of coals, but the relationship between the chemical structures of primary tars and parent coal varies widely with coal type.

The question of invariance in kinetic parameters among a range of coal types and whether chemical or transport phenomena dominate the evolution processes requires a multi-reactor approach in which the phases of tar formation and evolution can be deconvoluted. This will be the subject of future communications.

Acknowldegements

The authors are grateful to the Department of Energy, Pittsburgh Energy Technology Center, for coal samples provided in this investigation. In addition some of the results presented were obtained using funding provided by DE-AC22-84PC70768. The technical expertise of Gerald Wagner and Dave Santos are present throughout the work perfomred in this investigation. Brian Knight was responsible for the implementation and practical design of the phase separation system for this particular reactor.

## References


1. Suuberg, E.M., Peters, W.A. and Howard, J.B., Ind. Eng. Chem. Proc. Design and Dev., 17,37 (1978).
2. Arendt,P. and van Heek, K.H., Fuel, 60, 779 (1981).
3. Solomon, P.R. and Colket, M.B., Seventeenth Symposium (Internat.) on Combustion, 131, The Combustion Institute (1979).
4. Freihaut, J.D., Zabielski, M.F. and Seery, D.J., Nineteenth Symposium (Internat.) on Combustion, 1159, The Combustion Institute (1982).
5. Doolan, K.R., Mackie, J.C. and Tyler, R.J., Fuel, 66, 572 (1987).
6. Serio, M.A., Peters, W.A. and Howard, J.B., Ind. Eng. Chem. Res., 26, 1831 (1987).
7. Tyler, R.J., Fuel, 59, 218 (1980).
8. Teo, K. C. and Watkinson, A.P., Fuel, 65, 949 (1986).
9. Solomon, P.R.,et. al., Nineteenth Symposium (Internat.) on Combustion, 1139, The Combustion Institute (1982).
10. Squire, K.R., et.al., Fuel, 65, 833 (1986).
11. Calkins, W.H. and Tyler, R.J., Fuel, 63, 1119 (1984).
12. Klose, W. and Lent, M., Fuel, 64, 193 (1985).
13. Oh, M.S., Howard, J.B. and Peters, W.A., "Modeling Volatiles Transport in Softening Coal Pyrolysis", presented at AIChE National Meeting, San Francisco, November 1984.
14. Suuberg, E.M.,"Mass Transfer Effects in Coal Pyrolysis", in Chemistry of Coal Conversion, ed. by. R.H. Schlosberg, 67, Plenum Press (1985).
15. Oh, M.S., "Softening Coal Pyrolysis",Sc.D. Thesis, Department of Chemical Engineeering, MIT, Cambridge, Mass. (1985).
16. Unger, P.E. and Suuberg, E.M., Fuel, 63, 606 (1984).
17. Zielinski, E., Fuel, 46, 329 (1967).
18. Hertzberg, M. and Ng, Daniel,"A Microscopic and Kinetic Study of Coal Particle Devolatilization in a Laser Beam", in Fundamentals of the Physical-Chemistry of Pulverized Coal Combustion, ed. by J. Lahaye and G. Prado, NATO ASI Series, Series E, No. 137,104 (1987).

TABLE I

ELEMENTAL COMPOSITION OF TARS - TEMPERATURE EFFECTS
HVA BITUMINOUS COAL(PSOC 1451D)

| REACTOR WALL(C) | MAX. GAS(C) | %C | %H | %N | %(S+O) | H/C |
|---|---|---|---|---|---|---|
| | | ----------20 - 30 MICRONS---------- | | | | |
| 790 | 350 | 84.05 | 6.07 | 1.64 | 8.24 | 0.87 |
| 840 | 400 | 84.07 | 5.94 | 1.67 | 8.32 | 0.85 |
| 930 | 510 | 84.37 | 5.86 | 1.68 | 8.09 | 0.83 |
| | | 84.46 | 5.93 | 1.76 | 7.83 | 0.84 |
| 1020 | 665 | 84.62 | 5.55 | 1.69 | 8.14 | 0.78 |
| 1100 | 790 | 85.22 | 5.40 | 1.73 | 7.65 | 0.76 |
| 1190 | 890 | 85.55 | 5.27 | 1.74 | 7.44 | 0.74 |
| 1270 | 1000 | 86.00 | 5.08 | 1.73 | 7.19 | 0.71 |
| PARENT COAL..... | | 82.42 | 5.35 | 1.57 | 10.65 | 0.79 |
| | | 81.07 | 5.24 | 1.62 | 12.04 | 0.78 |
| | | ----------63 - 75 MICRONS---------- | | | | |
| 790 | 350 | 83.97 | 6.22 | 1.64 | 8.14 | 0.89 |
| 930 | 510 | 84.47 | 5.83 | 1.72 | 7.98 | 0.83 |
| | | 84.16 | 5.79 | 1.74 | 8.29 | 0.83 |
| 1270 | 1000 | 85.50 | 5.29 | 1.76 | 7.43 | 0.74 |
| PARENT COAL..... | | 82.55 | 5.53 | 1.59 | 10.32 | 0.80 |
| | | 81.86 | 5.43 | 1.66 | 11.02 | 0.80 |

TABLE II
Relative Molecular Weight of Charactertistic of Tars
Reactor Temperature Effects *
PSOC 1451D, 20-30 Microns

| Reactor Wall Temperature (C) | Position (cm) | Residence Time (msec) | Mn | Mw |
|---|---|---|---|---|
| 750 | 36 | 620 | 438 | 641 |
| 840 | 36 | 580 | 452 | 665 |
| 930 | 36 | 520 | 481 | 719 |
| 1020 | 36 | 470 | 491 | 743 |
| 1100 | 36 | 420 | 518 | 801 |
| 1190 | 36 | 385 | 509 | 803 |
| 1270 | 36 | 360 | 506 | 807 |

* Argon Carrier Gas

TABLE III
ELEMENTAL COMPOSITION OF TARS - TEMPERATURE EFFECTS
SUBBITUMINOUS COAL (PSOC 1520D)

| | | | | | | |
|---|---|---|---|---|---|---|
| 790 | 350 | 78.21 | 8.43 | 0.63 | 12.73 | 1.29 |
| 930 | 510 | 78.15 | 7.83 | 0.79 | 13.23 | 1.20 |
| | | 77.78 | 7.63 | 0.81 | 13.77 | 1.17 |
| 1270 | 1000 | 78.97 | 6.72 | 0.98 | 13.32 | 1.02 |
| PARENT COAL..... | | 63.77 | 4.54 | 0.83 | 30.84 | 0.86 |

* TARS = SPECIES COLLECTED ON FINAL FILTER OF IMPACTOR TRAIN

ARGON CARRIER GAS
PARTICLE RESIDENCE TIME: 600 msec

Fig. 1

# COAL DEVOLATILIZATION / PYROLYSIS

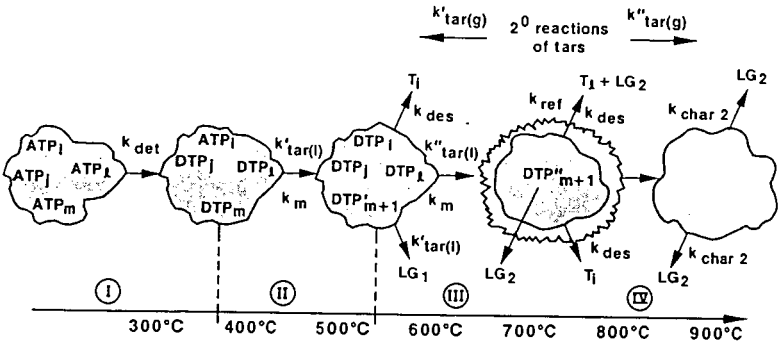


$k_{det} = k_{phy} + k_{chem}$ $k_{des} = k_{vap} + k_{conv} + k_{ned}$

RA2419TX.026

Fig. 2

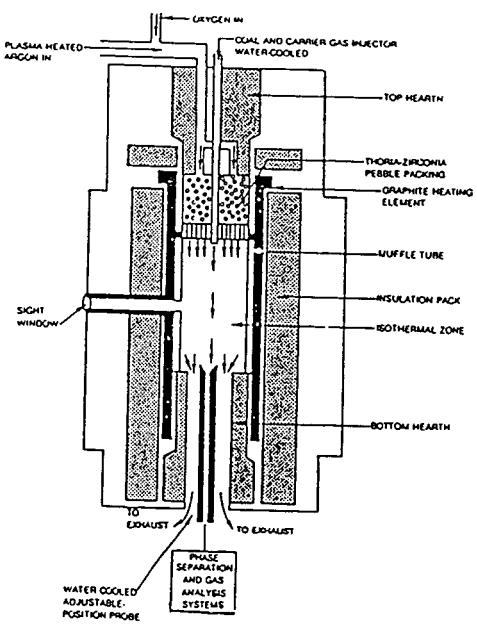

Fig. 3

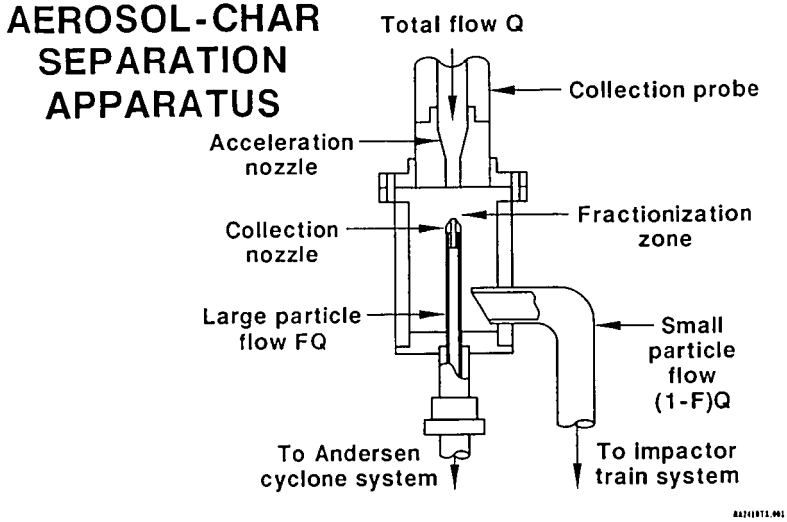
AEROSOL-CHAR SEPARATION APPARATUS
Total flow Q
Collection probe
Acceleration nozzle
Fractionization zone
Collection nozzle
Large particle flow FQ
Small particle flow (1-F)Q
To Andersen cyclone system
To impactor train system

Fig. 4

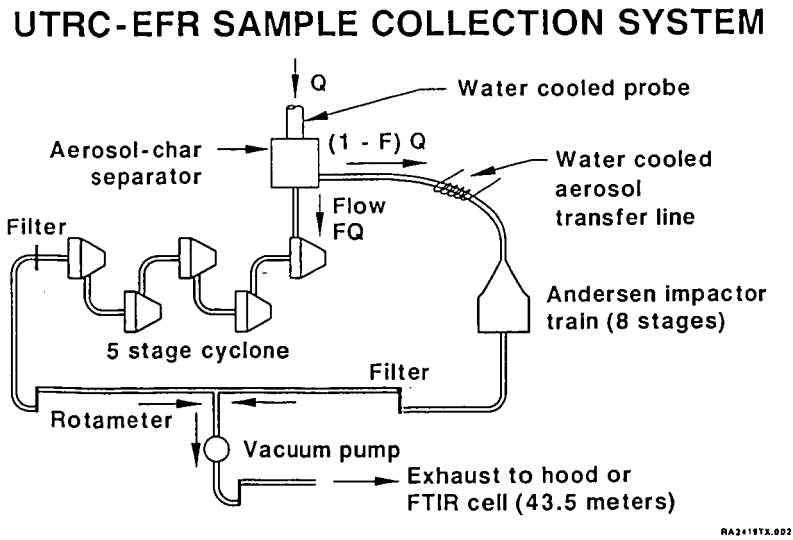
UTRC-EFR SAMPLE COLLECTION SYSTEM
Q
Water cooled probe
Aerosol-char separator
(1 - F) Q
Water cooled aerosol transfer line
Flow FQ
Filter
Andersen impactor train (8 stages)
5 stage cyclone
Filter
Rotameter
Vacuum pump
Exhaust to hood or FTIR cell (43.5 meters)

Fig. 5

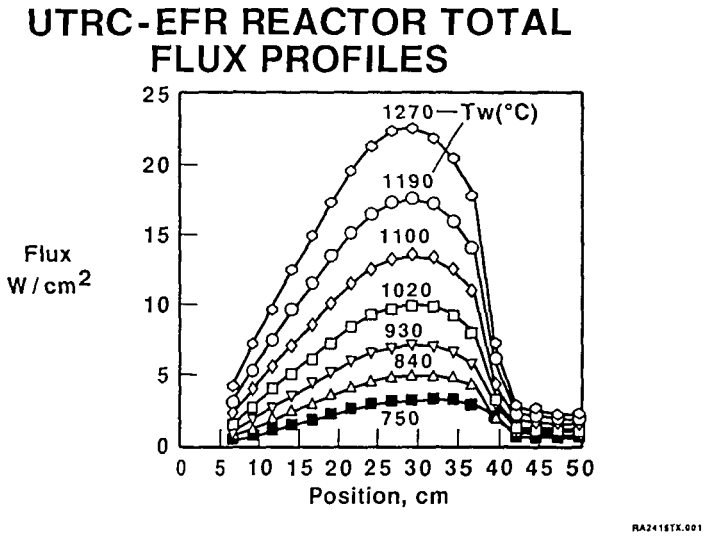
UTRC-EFR REACTOR TOTAL FLUX PROFILES
Flux W/cm2
25
20
15
10
5
0
1270—Tw(°C)
1190
1100
1020
930
840
750
0 5 10 15 20 25 30 35 40 45 50
Position, cm
RA2415TX.001

Fig. 6

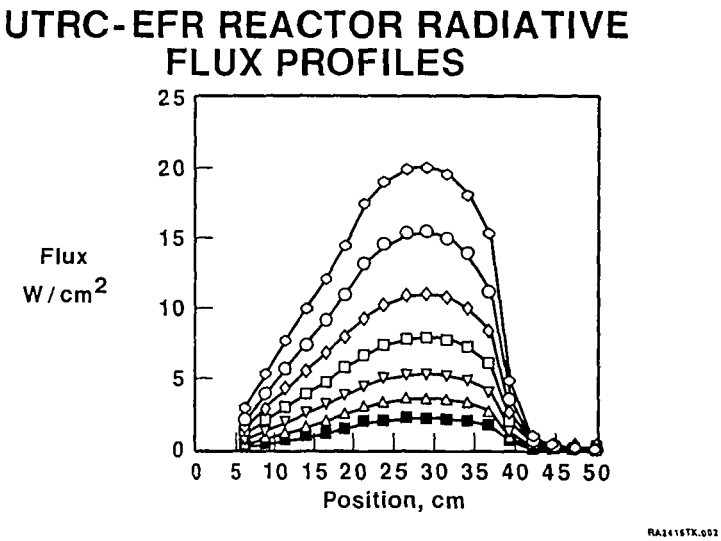
UTRC-EFR REACTOR RADIATIVE FLUX PROFILES
Flux W/cm2
25
20
15
10
5
0
0 5 10 15 20 25 30 35 40 45 50
Position, cm
RA2415TX.002

Fig. 7

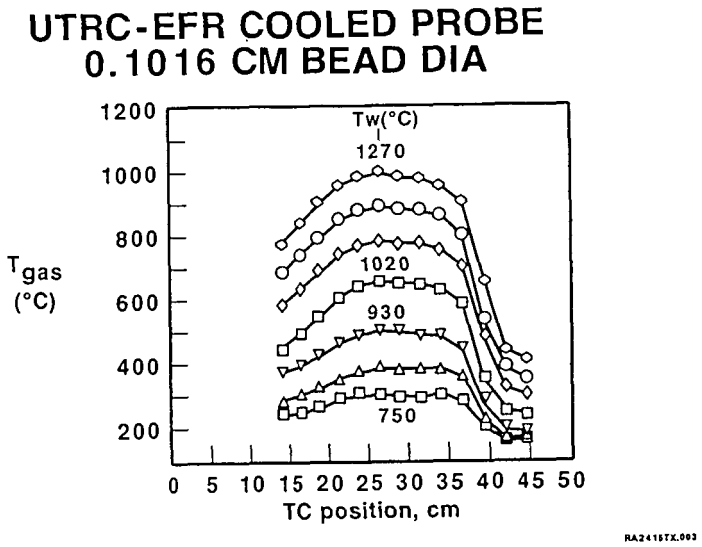
UTRC-EFR COOLED PROBE
0.1016 CM BEAD DIA
Tw(°C)
1270
1020
930
750
Tgas
(°C)
1200
1000
800
600
400
200
0 5 10 15 20 25 30 35 40 45 50
TC position, cm
RA2415TX.003

Fig. 8

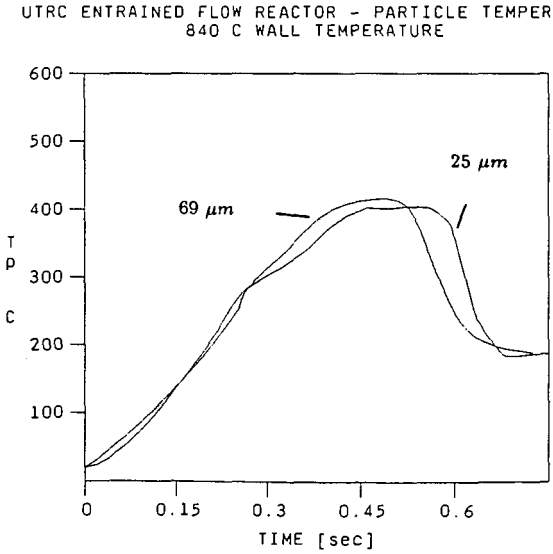
UTRC ENTRAINED FLOW REACTOR - PARTICLE TEMPERATURE
840 C WALL TEMPERATURE
25 μm
69 μm
T
P
C
600
500
400
300
200
100
0
0.15
0.3
0.45
0.6
TIME [sec]

Fig. 9

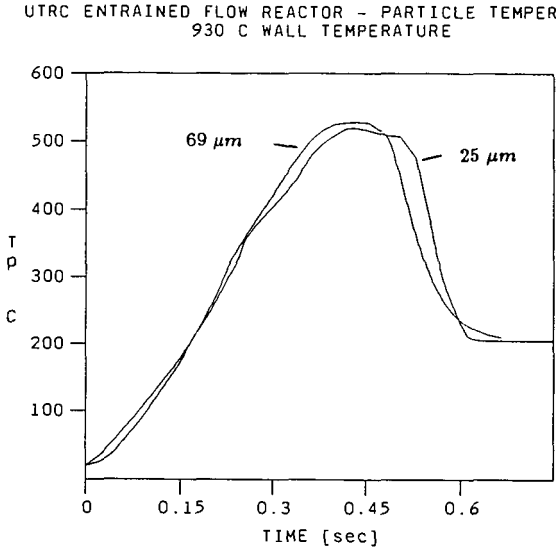
UTRC ENTRAINED FLOW REACTOR - PARTICLE TEMPERATURE
930 C WALL TEMPERATURE
600
500
400
300
200
100
T
p
C
69 μm
25 μm
0
0.15
0.3
0.45
0.6
TIME [sec]

Fig. 10

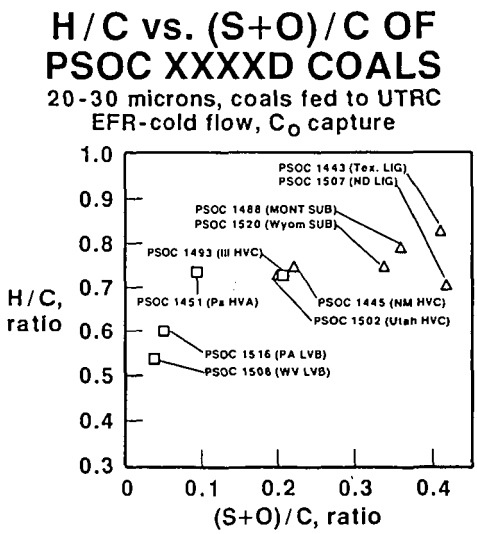
H/C vs. (S+O)/C OF
PSOC XXXXD COALS
20-30 microns, coals fed to UTRC
EFR-cold flow, $C_O$ capture
1.0
0.9
0.8
0.7
0.6
0.5
0.4
0.3
H/C, ratio
PSOC 1443 (Tex. LIG)
PSOC 1507 (ND LIG)
PSOC 1488 (MONT SUB)
PSOC 1520 (Wyom SUB)
PSOC 1493 (Ill HVC)
PSOC 1451 (Pa HVA)
PSOC 1445 (NM HVC)
PSOC 1502 (Utah HVC)
PSOC 1516 (PA LVB)
PSOC 1506 (WV LVB)
0
0.1
0.2
0.3
0.4
(S+O)/C, ratio

Fig. 11

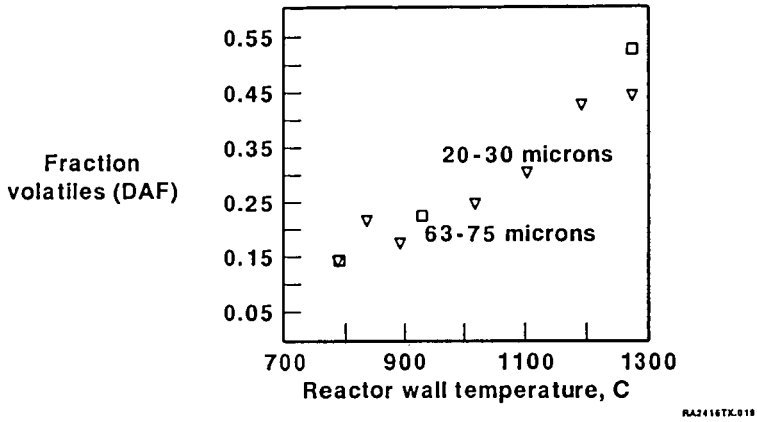
Fraction volatiles (DAF)
0.55
0.45
0.35
0.25
0.15
0.05
20-30 microns
63-75 microns
700
900
1100
1300
Reactor wall temperature, C
RA2416TX.018

Fig. 12

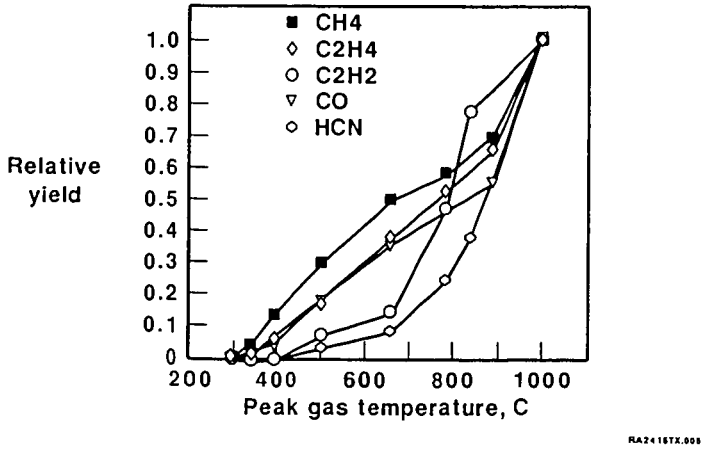
LIGHT GAS YIELDS vs. PEAK GAS TEMP. (C)
PSOC 1451D, 20-30 MICRONS, 600 MSEC
CH4
C2H4
C2H2
CO
HCN
Relative yield
1.0
0.9
0.8
0.7
0.6
0.5
0.4
0.3
0.2
0.1
0
200
400
600
800
1000
Peak gas temperature, C
RA2416TX.005

Fig. 13

# -CH2- STRETCH ABSORBANCE (2920 CM-1) vs. GAS TEMPERATURE

Triangle = PSOC 1451D, square = PSOC 1520D, 20-30 microns

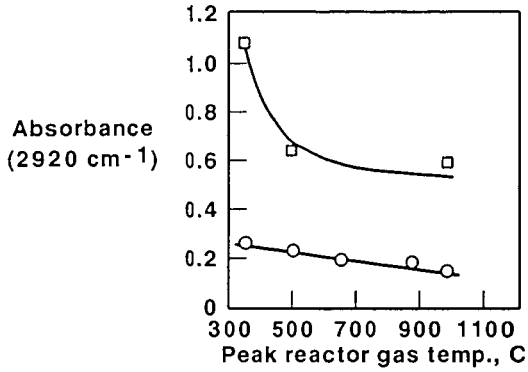


RA2415TX.009

Fig. 14

# %H(TAR) / %H(COAL) vs. COAL RANK

(PSOC XXXXD coals) 20-30 micron, particles, peak reactor gas temperature = 510C

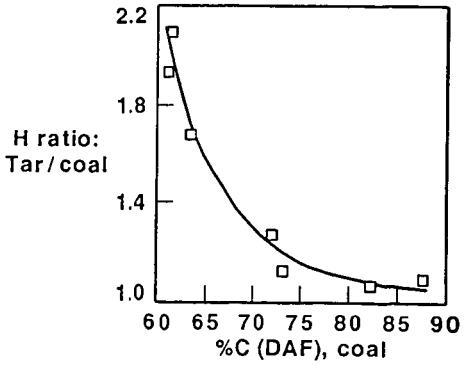


RA2415TX.013

Fig. 15

# % (S+0) - TAR / % (S+0) - COAL vs. COAL RANK

(PSOC XXXXD coals) 20-30 micron particles, reactor peak gas temperature = 510C

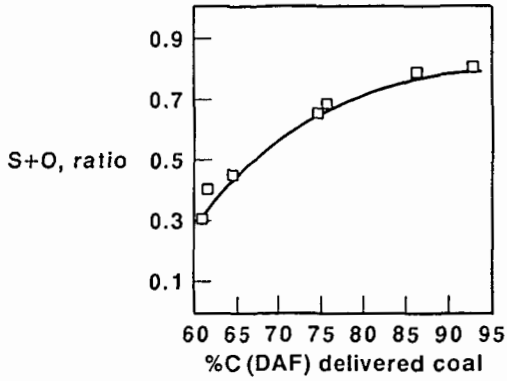


RA241STX.012

Fig. 16

# % HYDROGEN IN TARS vs. COAL RANK

(PSOC XXXXD coals) 20-30 micron, particles, peak gas temperature = 510C

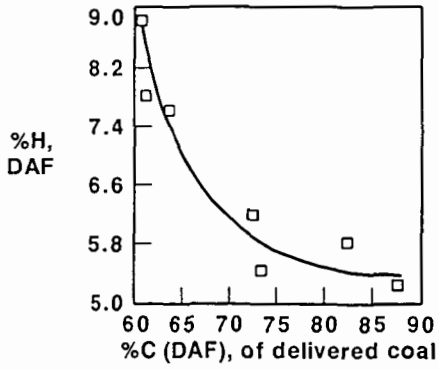

Fig. 17

## 2920 CM-1 ABSORBANCE OF TARS vs. COAL RANK

(PSOC XXXXD coals) 20-30 micron particles, peak gas temperature = 510C

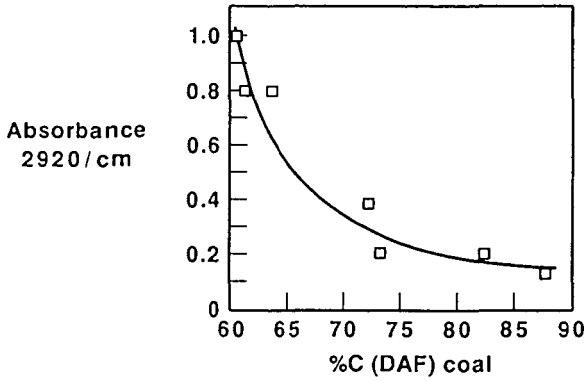


RA2415TX.015

Fig. 18

## ABSORBANCE (2920/CM) vs. % H (DAF) IN TARS

(PSOC XXXXD coals) 20-30 micron particles, peak gas temp. = 510C

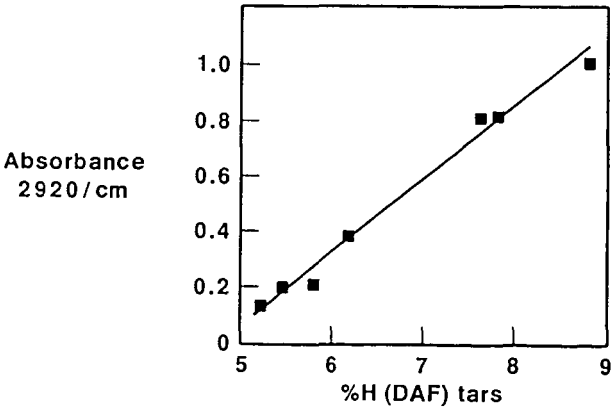


RA2416TX.016

Fig. 19

# RELATIVE NUMBER AND MASS AVERAGE MW OF TARS AND COAL TYPE

PSOC XXXX D coals, 20-30 microns, 510C peak gas temp.

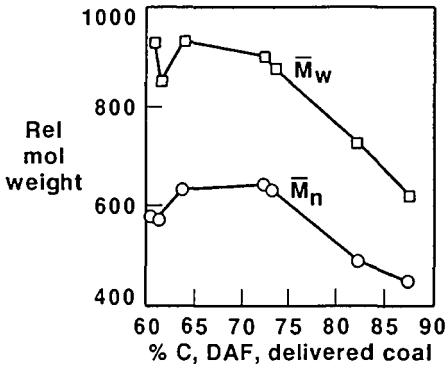


RA2415TX.008

Fig. 20

# PRIMARY TAR ⟷ PARENT COAL: STRUCTURAL COMPARISONS

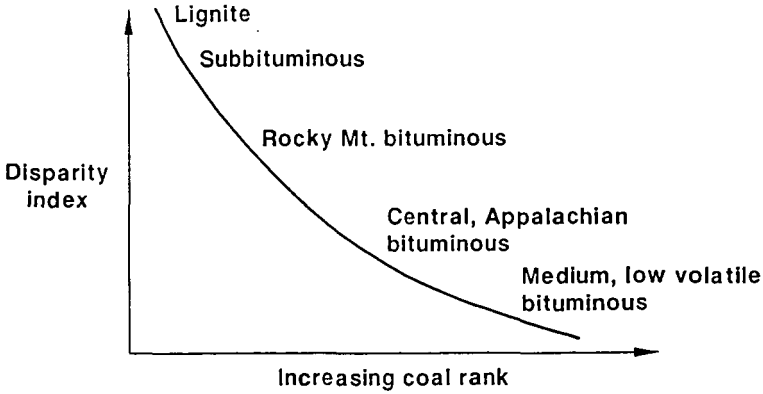


RA2415TX.011

# THERMAL AND KINETIC STUDY OF THE MILD PYROLYSIS OF SINGLE SUBBITUMINOUS COAL PARTICLES

Guangwei Huang, Francis J. Vastola and Alan W. Scaroni

The Pennsylvania State University
The Combustion Laboratory
404 Academic Activities Building
University Park, PA 16802

## INTRODUCTION

A detailed knowledge of coal pyrolysis is fundamental to the understanding of the early stages of many coal conversion processes. Pyrolysis studies have been conducted using a variety of techniques including the use of electric grids (1-3), thermogravimetric analyzers (4-6), entrained flow reactors (7-9), and fluidized beds (10,22). In order to eliminate the complexity introduced by particle interactions, some research has been directed towards the behavior of single coal particles (12-16). For example, Huang et al. (12) measured the transient temperature gradients in the gas surrounding a captive 1 mm diameter coal particle with a fast response thermocouple array (12) and found steep gradients up to 4 mm from the surface. Saito et al. (16) reported on differences between high temperature devolatilization in air and $N_2$ for 2-4 mm-sized particles, and conducted an isothermal kinetic analysis of the data. Hertzburg (17) analyzed experimental data from laser-heated coal pyrolysis experiments and concluded that the pyrolysis rate was controlled by the heat flux to the particle surface and by thermodynamic transport constraints within the particle. He proposed a "rate coefficient", which is the reciprocal of the overall enthalpy required for heating and devolatilization. The significance of heat transfer effects on coal pyrolysis were recently reviewed by Suuberg (18) and Gavalas (19), and it is clear that heat transfer plays an important role. Nevertheless, few references can be found in the literature on the instantaneous rate of heat transfer to pyrolyzing coal particles. Most measurements in this area have been made using Differential Scanning Calorimetry (DSC) which is limited to low heat fluxes during the heatup to pyrolysis temperature. The current work is an attempt to relate experimentally measured particle temperature and mild pyrolysis rates in order to determine meaningful kinetic parameters.

## EXPERIMENTAL

### Temperature Measurements

Pyrolysis experiments on 1 mm diameter coal particles were performed in a captive reactor, details of which have been provided elsewhere (12,13). It consists essentially of two enclosing horizontal tube furnaces which are heated electrically to preheat the incoming gas and maintain the reactor at a predetermined temperature. A subbituminous coal (volatile matter 50.5%, fixed carbon 36.0%, ash 13.5%) was used in this study. Prepurified nitrogen was used to purge air from the reactor but prior to the start of a run, the gas flow was stopped so that the experiments were essentially in a static system. For each run a 1 mm diameter coal particle was injected into a minicrucible inside the 873 K reactor. Temperature gradients in gas surrounding the reacting particle were measured by a thermocouple array (TCA) composed of four extra-fine thermocouples spaced 1.0 mm apart. The distance from the coal particle surface to the closest thermocouple was approximately 1 mm. A microcomputer collected the responses of the thermocouples at millisecond time intervals.

All experiments were conducted on dry coal particles, the coal being dried overnight at 383°K in a vacuum oven prior to use. A char particle was prepared by injecting a coal particle into the reactor in flowing nitrogen at 873 K for 5 minutes.

### Measurements of Weight Loss

Weight loss data for pyrolysis were obtained in a Dupont 951 Thermogravimetric Analyzer (TGA). To simulate the process of dropping a cold coal particle into a hot reactor, the TGA quartz tube was kept in the furnace during heatup in a 75 cc/min flow of prepurified nitrogen. The sample housing was then rapidly introduced into the hot quartz tube in the furnace after the furnace temperature had

stabilized (20,21). The same experimental conditions were used in the TCA and TGA experiments (temperature, particle size, etc.).

## RESULTS AND DISCUSSION

### Heat Transfer

The temperature histories measured by the TCA in the surrounding gas at different distances from the coal particle surface during pyrolysis are shown in Figure 1. Curves 1 to 4 express instantaneous temperatures at 1, 2, 3, and 4 mm from the particle surface, respectively. Because of thermal continuity in the gas surrounding the pyrolyzing coal particle, the measured data were extrapolated to the particle surface by a three order polynomial correlation in order to obtain the instantaneous particle surface temperature (Figure 2). The extrapolated surface temperature ($T_S$) is plotted as curve 0 in Figure 1. The temperature of the gas phase 5 mm from the particle was taken to be the furnace temperature ($T_f$) in the extrapolation. The validity of this assumption is based on solid evidence. Firstly, as heat was transferred to the vicinity of a cold coal particle , the temperature of the surrounding gas recovered to, but did not exceed, the furnace temperature (12). Secondly, the temperature perturbation decreased with distance from the particle surface. Figure 2 provides information on spatial temperature gradients, from which heat transfer boundary conditions were determined. Under the experimental conditions, the boundary was a spherical region with a radius of approximately 5 mm.

The three order polynomial used in the extrapolation is expressed as:

$$T = A_o + A_1X + A_2X^2 + A_3X^3 \qquad 1)$$

where $A_i(i = 0,1,2,3)$ is constant at a given time t, X is the dimensionless distance expressed by:

$$X = \frac{x}{x_b} \qquad 0 \le X \le 1 \qquad 2)$$

in which x is the distance from the particle surface and $x_b$ is the distance from the particle surface to the heat transfer boundary. From Equation (1) $T_S$ can be determined by:

$$T_s = T\Big|_{x=0} = A_o \qquad 3)$$

and bulk gas temperature can be expressed as:

$$T_f = T\Big|_{X=1} = \sum_{i=0}^{3} A_i \qquad 4)$$

Figure 3 shows temperature histories for char particles under the same experimental conditions as for the coal particles in Figure 1. The char particles were recovered from the preceding coal run . Since the coal used in this study is non-swelling (free swelling index = 0) the particle size and external surface areas of the coal and char particles were considered to be the same.

Particle surface temperatures for the coal and char are plotted in Figure 4. During the early stage of heatup to 700 K (up to ~ 2s) $T_S$ for the coal was about 80 K lower than $T_S$ for the char. This is due to the initial mass difference between the coal and char particles. At the onset of pyrolysis for the coal, there was an inflection in the $T_S$ curve. Endothermic pyrolysis reactions kept the coal particles at a lower temperature than the char which was undergoing a rapid heatup to the furnace temperature. The unambiguous surface temperature histories in Figure 4 indicate that there will be a gross error if the particle surface temperature is assumed to be the furnace temperature.

Heat flux by radiation from the furnace wall to the coal and char particles can be calculated from the following equation:

$$q_R' = \varepsilon\sigma(T_f^4 - T_s^4) \qquad 5)$$

To estimate maximum radiation, the emissivity $\varepsilon$ of coal and char is assumed to be unity. The rate of heat transfer by conduction from the hot surrounding gas can be expressed as:

$$q_c = K\bar{A}\frac{\Delta T}{\Delta x} = K\bar{A}\frac{(T_f - T_s)}{(d_b - d_s)} \qquad 6)$$

where

$$\bar{A} = \frac{A_b - A_s}{\ln\left(\frac{A_b}{A_s}\right)} = \frac{\pi\,(d_b^2 - d_s^2)}{2\ln\left(\frac{d_b}{d_s}\right)} \qquad 7)$$

Assuming the coal and char are surrounded by nitrogen, the thermal conductivity of nitrogen can be used in the calculation. The heat flux due to conduction to the coal and char particles can be estimated by:

$$q_c' = q_c/A_s \qquad 8)$$

The heat transfer coefficient for convection is determined from the Nusselt number (taken as two) (22) and the diameter of the particle, $d_s$, by:

$$h = Nu\,K/d_s \qquad 9)$$

where K is the thermal conductivity of the surrounding gas. The heat flux to the particle by convection can be determined by:

$$q_v' = h(T_f - T_s) \qquad 10)$$

The heat fluxes due to radiation, conduction, and convection as function of the time are shown in Figures 5 and 6 for coal and char particles, respectively. The instantaneous heat fluxes are a strong function of the residence time. The total heat fluxes varied from 27 w/cm$^2$ at the beginning to zero at the end of a run corresponding to a 9 s time interval. The dominant mode of heat transfer was conduction. Radiation contributed less than convection in the early heat up stage. However, after 2 s the same amount of heat was supplied by radiation as supplied by convection.

A comparison of the total heat flux to the coal and char particles is shown in Figure 7. The smooth decay in heat flux for both the char and coal in the early stage (< 2s) characterizes the heatup processes. An obvious inflection occurs in the heat flux curve for the coal, which implies the initiation of pyrolysis. More heat is received by the coal than the char to meet the needs of endothermic pyrolysis until the coal is converted into char. The total heat required to heat and pyrolyze the coal particles can be calculated by integrating the heat flux:

$$Q = \frac{A_s\int_0^\infty q_t'\,dt}{W_d} = \frac{A_s}{W_d}\left[\Sigma\,(q_c' + q_v' + q_R')\,\Delta t\right] \qquad 11)$$

where $W_d$ is the sample weight on a dry basis. The calculated heats required by the coal and char are shown in Figures 8 and 9, respectively. The figures show clearly that the heat transferred through the

surrounding gas by conduction and convection amounts to 80% of the total. Only 20% of the heat is contributed by radiation. This is not surprising since heat transfer by conduction and convection is proportional to the temperature difference, $\Delta T = T_f - T_s$, whereas the driving force for radiation is proportional to the difference between the fourth powers of the temperatures, $T_f^4 - T_s^4$, a much stronger function of the absolute furnace temperature. Therefore, at higher $T_f$, radiation plays a more important role. From Eq. (11) the total heat needed to heat the char to 873 K is 1917 J/g. The heat required to heat coal and pyrolyze it is 2219 J/g (dry basis). Assuming that the original coal, char and volatiles have the same specific heats, about 300 J/g is needed for the decomposition. This is less than 15% of the total heat required by the coal. Therefore, the heat capacity is the major term in the heat transfer calculation.

### Kinetics

Devolatilization results from the TGA experiments are presented in Figure 10. The data are expressed as the percentage weight loss of the coal (daf) versus residence time. The particle surface temperature for the same size coal particles at the same furnace temperature as for the TGA method is also plotted in Figure 10. The inflection point A on the $T_s$ curve is the pyrolysis initiation point, as discussed before, and the completion point B is defined as the time when $T_s$ equals $T_f$. The weight loss data are consistent with these temporal characteristics. Before the initiation point, only about 2% weight loss is observed, but up to the completion point more than 95% of the total weight loss is reached. The total weight loss is about 37% (daf) which is less than the ASTM proximate volatile matter (~ 50%). This is because the experiments were performed at a temperature of more than 300 K less than the ASTM test.

The fact that negligible weight loss was observed before point A proves that two distinct processes occur during pyrolysis, namely heatup and reaction. Badzioch and Hawksley (23) reported negligible weight loss until the coal particles reached about 673 K, before the pyrolysis reaction became significant. They expressed the total pyrolysis time as:

$$t_T = t_H + t_R \qquad 12)$$

where the subscripts T, H, and R represent the total, heatup, and reaction times, respectively. For millimeter-sized coal particles, the heatup stage is more significant. Under the conditions in this study, for 1 mm particles, it took 2 s to initiate the pyrolysis reaction.

As a first attempt to determine pyrolysis rates for the millimeter-sized single coal particles in the TGA, a simple first order model was used:

$$\frac{dV}{dt} = kV \qquad 13)$$

where

$$V = 1 - \frac{W}{W_\infty} \qquad 14)$$

and

$$k = k_o \exp(-E/RT_p) \qquad 15)$$

Because of the difficulty of measuring the particle temperature, $T_p$, most kinetic studies use Eq. (13) with the assumption that the coal particle is instantaneously heated to the furnace temperature. This may be allowable for smaller pulverized coal but is not acceptable for millimeter-sized, or larger particles, although it has still been used by others (16). In this study an attempt was made to reduce the error caused by the improper assumption of isothermality. The particle surface temperature, $T_s$, is substituted into Eq. (15) for $T_p$. This is based on the assumption that the thermal conductivity of the coal is infinite. This is not correct but is an improvement over use of the heat source temperature. Therefore, Eqs. (13) and (15) can be expressed as:

$$\frac{dV}{dt} = k_o \exp(-E/R\,T_s)\,V \qquad 16)$$

or:

$$\ln\left(\frac{1}{V}\cdot\frac{dV}{dt}\right) = \ln k_o - \frac{E}{R}\cdot\frac{1}{T_s} \qquad 17)$$

The logarithm term on the left hand side of Eq. (17) is plotted against the reciprocal of $T_s$ in Figure 11. The activation energy and pre-exponential factor were derived from the slope and the intercept of the straight line in Figure 11. The activation energy estimated from Eq. (17) is 34.0 kcal/mole and the pre-exponential factor is $4.8 \times 10^8\ s^{-1}$. The activation energy is more than four times that reported by Saito et al. (16) for pyrolysis of millimeter-sized subbituminous coal particles.

## CONCLUSIONS

A thermocouple array was used to measure temperature gradients in the gas phase around captive coal and char particles during heatup and pyrolysis in preheated nitrogen. Instantaneous particle surface temperatures were extrapolated from the measured gas temperatures at different distances from the particles. Based on basic heat transfer principles, heat fluxes of conduction, convection, and radiation were calculated. Heat fluxes to the particles were strongly dependent on residence time, varying from 27 $W/cm^2$ to 0 at the completion of pyrolysis. The total heat required for heatup and pyrolysis was determined by integration. The results indicated that 80% of the total heat was transferred through the gas phase by conduction and convection. Radiation at the low operating temperature made a minor contribution to the total heat transfer.

The temperature history of the 1 mm diameter coal particles indicated that pyrolysis did not occur isothermally. Two seconds elapsed prior to the onset of pyrolysis. Particle surface temperatures were substantially lower than the furnace temperature until pyrolysis was completed.

An attempt was made to use instantaneous particle temperatures in a kinetic analysis. Weight loss data were obtained using a modified TGA method which simulated the TCA conditions. An activation energy and pre-exponential factor were estimated from a first order rate expression the values being 34 kcal/mole and $4.8 \times 10^{-8}\ s^{-1}$, respectively.

## ACKNOWLEDGEMENTS

Financial support for this work was provided by the Penn State Cooperative Program in Coal Research. The coal was supplied by the Penn State/DOE Sample Bank and Data Base.

## NOMENCLATURE

| | |
|---|---|
| $\bar{A}$ | Logarithm average area, $cm^2$ |
| $A_b$ | Area of heat transfer boundary, $cm^2$ |
| $A_s$ | Area of particle surface, $cm^2$ |
| $d_b$ | Heat transfer boundary diameter, cm |
| $d_s$ | Particle diameter, cm |
| E | Activation energy, kcal/mole |
| h | Coefficient of convective heat transfer, $W/cm^2\ K$ |
| K | Thermoconductivity, W/cm K |
| k | Rate constant, $s^{-1}$ |
| $k_o$ | Pre-exponential factor, $s^{-1}$ |
| Nu | Nusselt number |
| Q | Total heat, J |
| $q_c$ | Heat transfer rate by conduction, W |
| $q_c'$ | Heat flux by conduction , $W/cm^2$ |
| $q_R'$ | Heat flux by radiation, $W/cm^2$ |
| $q_T'$ | Total heat flux, $W/cm^2$ |
| $q_V'$ | Heat flux of convection, $W/cm^2$ |
| R | Universal gas constant |
| $T_f$ | Furnace temperature, K |
| $T_p$ | Particle temperature, K |
| $T_s$ | Particle surface temperature, K |
| t | Time, s |
| $t_H$ | Heatup time, s |
| $t_R$ | Reaction time, s |
| $t_T$ | Total time, s |
| V | Fraction of remaining volatiles |
| W | Weight loss at time t |
| $W_d$ | Sample weight on dry basis, g |
| $W_\infty$ | Maximum weight loss, g |
| X | Dimensionless distance |
| x | Distance, cm |
| $x_b$ | Distance from particle surface to heat transfer boundary, cm |
| $\varepsilon$ | Emissivity |
| $\sigma$ | Stefan-Boltzmann Constant |

## REFERENCES


1) Anthony, D. B., Howard, J. B., Hottel, H. C. and Meissner, H. P. *15th Symp (Int.) on Combustion*, The Combustion Institute, 1974, p. 1303.
(2) Suuberg, E. M., Peters, W. A., and Howard, J. B. *17th Symp. (Int.) on Combustion*, The Combustion Institute, 1978, p. 117.
(3) Niksa, S., Russel, W. B., and Saville, D. A. *Fuel*, 1982, 61, 1207.
(4) Geng, L. and Guo, S. *Journal of Fuel Chemistry and Technology*, 1986, 11(3), 211.
(5) Vernekav, V.R.P., Rao, J. R.M., Rao, B.K.S. and Tiruhavayanan, M. A. *Fuel*, 1982, 61, 634.
(6) Smith, S. E., Neavel, R. C., Hippo, E. J. and Miller, R. N. *Fuel* , 1981, 60, 458.
(7) Tsai, C. Y. and Scaroni, A. W. *Energy & Fuels*, 1987, 1, 263.
(8) Maloney, D. and Jenkins, R. G. *20th Symp (Int.) on Combustion*, The Combustion Institute, 1984, 1435.
(9) Samuelson, G. S., Trolinger, J. D., Heap, M. P. and Seeker, W. R. *Combust. and Flame*, 1981, 40, 7.
(10) Desypris, J., Murdoch, P. and Williams, A. *Fuel*, 1982, 61, 807.
(11) Barooah, J. N. and Long, V. D. *Fuel*, 1976, 55, 116.
(12) Huang, G., Vastola, F. J. and Scaroni, A. W. *Prepr.-Amer. Chem. Soc., Div. Fuel Chem.*, 1987, 32(3), 1.
(13) Gomez, C. O. and Vastola, F. J. *Fuel*, 1985, 64, 558.
(14) Ragland, K. W. and Yang, J. T. *Combust. and Flame,* 1985, 60, 285.
(15) Zghoul, A.M. and Essenhigh, R. H. *Second Annual Pittsburgh Coal Conference Proceedings*, 1985, pp. 658-665.
(16) Saito, M., Sadakata, M., Sato, M. and Sakai, T. *Fuel*, 1987, 66, 717.
(17) Hertaberg, M., Zlochower, I. A., Conti, R. S. and Cashdollar, K. L. *Prepr.-Am. Chem. Soc., Div. Fuel Chem.*, 1987, 32 (3), 24.
(18) Suuberg, E. M. *Prepr.-Am. Chem. Soc., Div. Fuel Chem.*, 1987, 32(3), 51.
(19) Gavalas, G. R. *Coal Pyrolysis*, Elsevier, New York, 1982.
(20) Huang, Y. H. and Serageldin, M. A. *Thermochimica Acta*, 1987, 112, 161.
(21) Serageldin, M. A., and Wang, H. National Conference of Standards Laboratories, 1986 Workshop and Symposium Proceedings, 1986. 1, 8-1.
(22) Mitchell, R. E. and McLean, W. J. *19th Symp. (Int.) on Combustion*, The Combustion Institute, 1982, 1113.
(23) Badzioch, S., Hawksley, G. M. *Ind. Eng. Chem. Process Des. Dev.*, 1970, 9, 421.

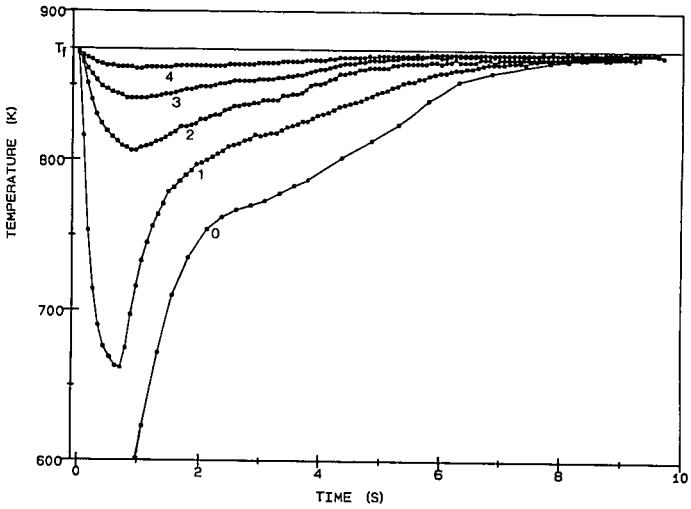


Figure 1. Gas Phase Temperature (0-4 mm From Particle Surface) During Pyrolysis of a 1 mm Diameter Coal Particle at 873 K

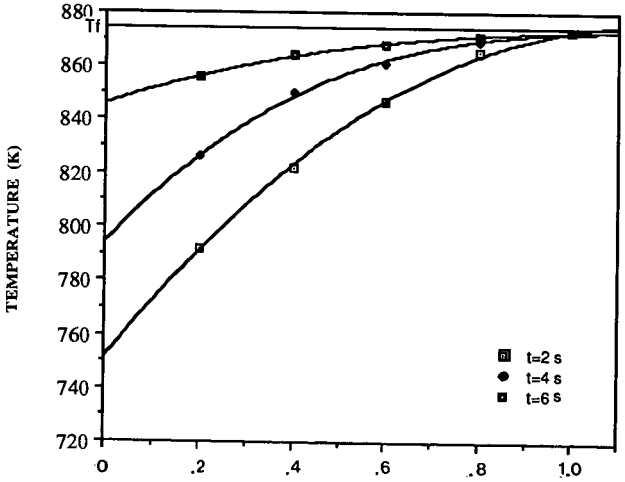


**Figure 2. Extrapolation of Data from Figure 1 to Predict Surface Temperature**

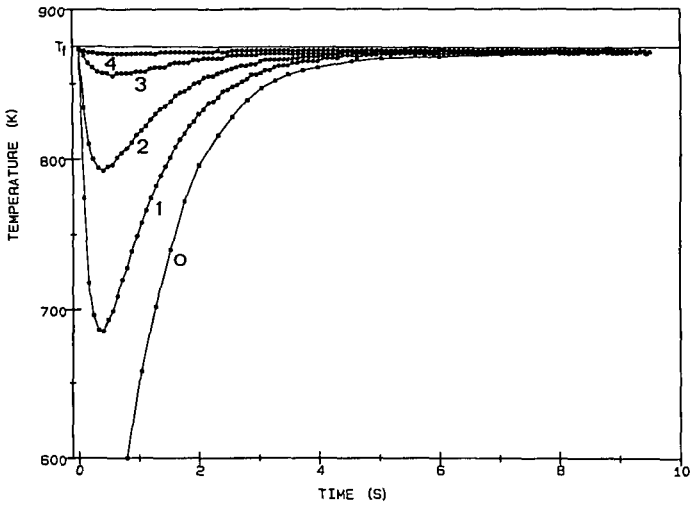


Figure 3. Gas Phase Temperature (0-4 mm From Particle Surface) During Heatup of a 1 mm Diameter Char Particle at 873 K

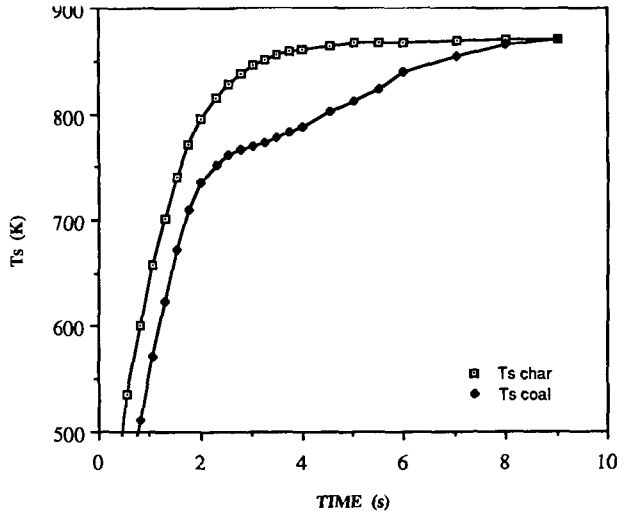


**Figure 4. A Comparision Between Coal And Char Surface Temperatures as a Function of Time During Heating in Nitrogen at a Furnace Temperature of 873 K**

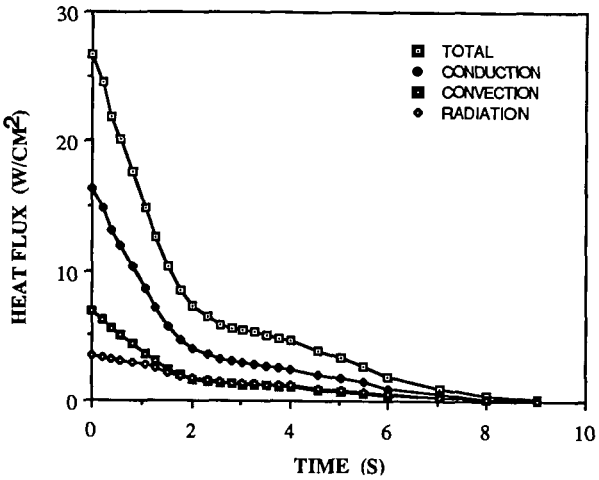


Figure 5. Time Dependency of the Contribution of Conductive, Convective and Radiative Heat Fluxes to the Total Heat Flux to a 1 mm Diameter Coal Particle Heated in Nitrogen at a Furnace Temperature of 873 K

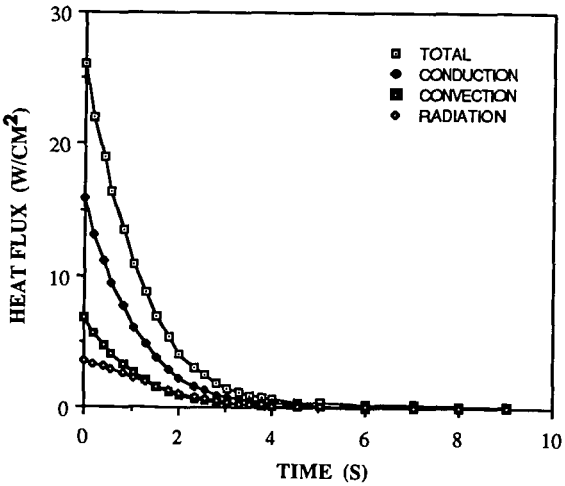


Figure 6. Time Dependency of the Contribution of Conductive, Convective and Radiative Heat Fluxes to the Total Heat Flux to a 1 mm Diameter Char Particle Heated in Nitrogen at a Furnace Temperature of 873 K

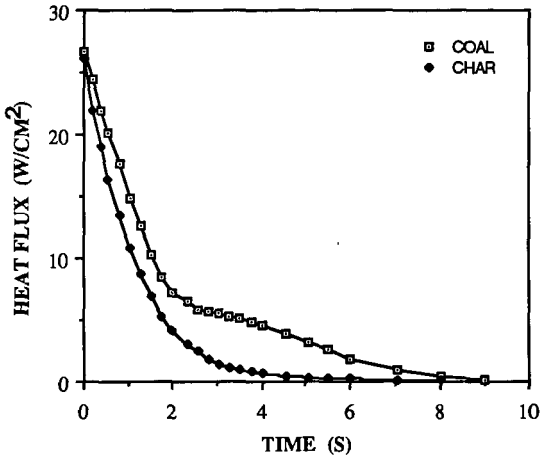


Figure 7. Comparison Between Total Heat Flux to 1 mm Diameter Coal and Char Particles Heated in Nitrogen as 873 K as a Function of Time

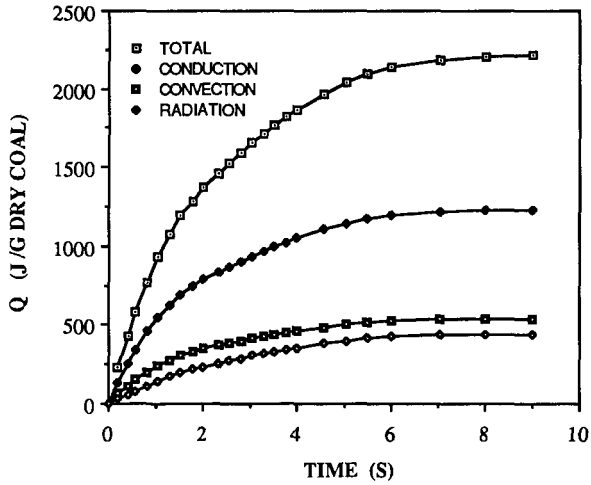


Figure 8. Heat Absorbed by a 1 mm Diameter Coal Particle Heated in Nitrogen at 873 K as a Function of Time

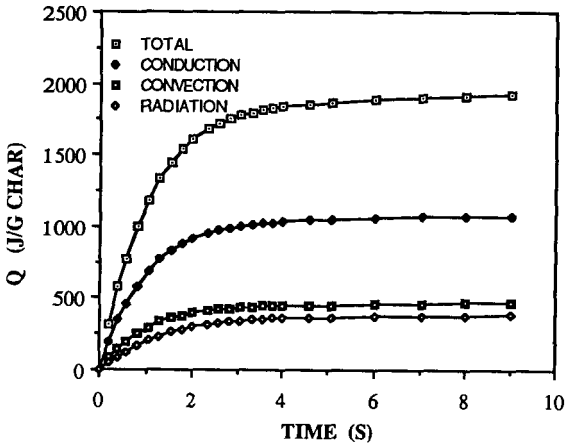


Figure 9. Heat Absorbed by 1 mm Diameter Char Particles Heated in Nitrogen at 873 K as a Function of Time

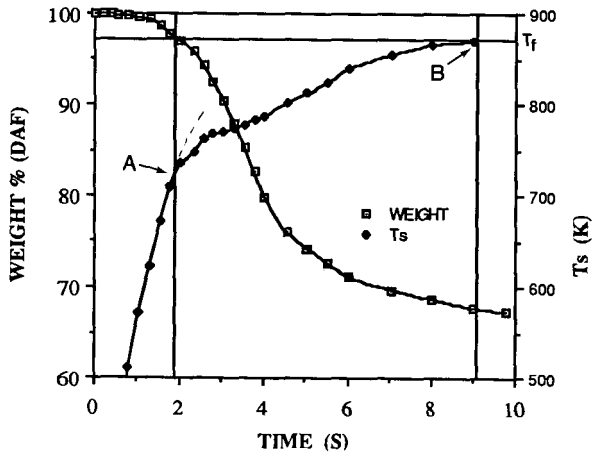


Figure 10. Weight Loss and Surface Temperature as a Function of Time for 1 mm Diameter Coal Particles Heated in Nitrogen at a Furnace Temperature of 873 K

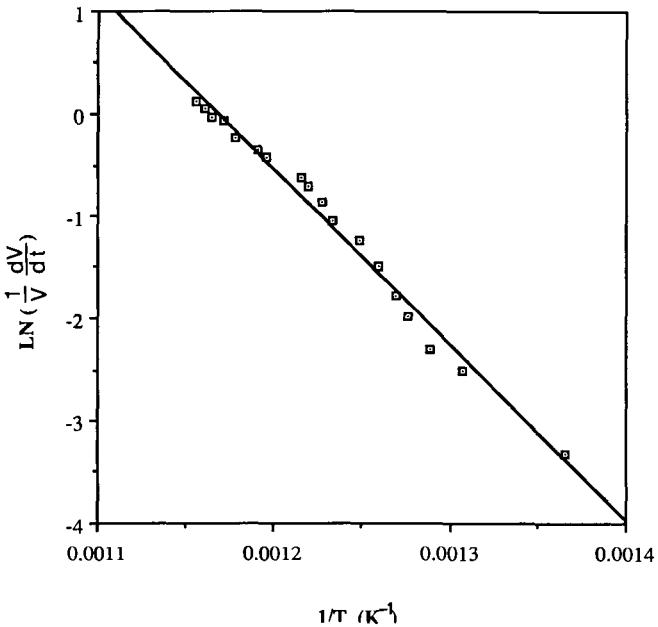


Figure 11. Arrhenius Plot for the Pyrolysis of 1 mm Diameter Coal Particles in $N_2$ at a Furnace Temperature of 873K

# PYROLYSIS OF THE ARGONNE PREMIUM COALS UNDER SLOW HEATING CONDITIONS

M.A. Serio, P.R. Solomon, and R.M. Carangelo

Advanced Fuel Research, Inc., 87 Church St., East Hartford, CT 06108 USA

## INTRODUCTION

The establishment of the Argonne Premium Sample Bank (1) will allow more meaningful comparisons to be made between pyrolysis studies from different laboratories. This sample bank also provides a good suite of coals for examining rank dependent phenomena, such as the kinetics of primary gas evolution. A recent "general" model of coal pyrolysis proposed by our research group (2-4) has as one of its assumptions that the kinetics of primary product evolution are rank-insensitive. This assumption was tested by a thorough examination of our data from experiments where only coal type was varied as well as data from similar experiments in the literature (5). The conclusion was that, with few exceptions, the kinetic rate constants for individual species evolved from coals pyrolyzed under the same conditions show little variation with rank. However, this conclusion remains controversial. The Argonne premium samples provide an opportunity to further test this assumption with a set of coals that was designed to cover a wide range of coal types. A slow, constant heating rate experiment was used, which is the most sensitive to rate variations.

A second controversial area is the importance of heating rate on the volatile product yield and distribution. Evidence has been presented which suggests no intrinsic effect of heating rate on pyrolysis yields (6) and other studies have indicated the converse to be true (7,8). However, often these studies have been done under sufficiently different experimental conditions that direct comparisons are difficult. Our own work has indicated a role for heating rate on tar yields for bituminous coals and on tar molecular weight distributions for lignites (3,9). We plan to extend this work to the Argonne coals in order to better establish these trends. The current paper is concerned primarily with pyrolysis of the Argonne coals under slow heating conditions in a unique TG-FTIR instrument developed in our laboratory. Results from slow heating rate pyrolysis into a FIMS apparatus are also presented. Experiments have also been done under rapid heating conditions. These will be the subject of another paper.

## EXPERIMENTAL

**Coal Properties** - Elemental data are given for the Argonne coals in Table I. This information was obtained from Ref. 1.

**TABLE 1 - ELEMENTAL ANALYSES OF ARGONNE PREMIUM COAL SAMPLES (1)**

| | %daf basis | | | | % dry basis |
|---|---|---|---|---|---|
| | C | H | O | S | Ash |
| 1. Pocahontas | 91 | 4.7 | 3 | 0.9 | 5 |
| 2. Upper Freeport | 87 | 5.5 | 4 | 2.8 | 13 |
| 3. Pittsburgh #8 | 83 | 5.8 | 8 | 1.6 | 9 |
| 4. Upper Kanawha | 81 | 5.5 | 11 | 0.6 | 20 |
| 5. Utah Blind Canyon | 79 | 6.0 | 13 | 0.5 | 5 |
| 6. Illinois No. 6 | 77 | 5.7 | 10 | 5.4 | 16 |
| 7. Wyodak | 74 | 5.1 | 19 | 0.5 | 8 |
| 8. Beulah-Zap | 73 | 5.3 | 21 | 0.8 | 6 |

**TG-FTIR** - The apparatus is the TG/PLUS offered by Bomem, Inc.. It consists of a sample suspended from a balance in a gas stream within a furnace. As the sample is heated, the evolving tars and gases are carried out of the furnace directly into a 5 cm diameter gas cell (heated to 150°C) for analysis by FT-IR. The TG/PLUS couples a Dupont 951 TGA with a Bomem Michelson 100 FT-IR spectrometer.

The apparatus is designed to carry evolved products from the furnace to the gas cell over a short path to minimize secondary reactions or condensation on cell walls. In addition, the furnace geometry, the sample size, the sweep gas and flow rate have been chosen to ensure that the condensable products form a submicron aerosol mist. This size aerosol has two advantages: 1) the particles follow the gas stream lines, thus minimizing condensation; and 2) the particles produce little scattering in the mid I.R., so the condensable products can be analyzed directly in the FT-IR cell.

The FT-IR can obtain spectra every 30 seconds to determine quantitatively the evolution rate and composition of most pyrolysis products. The system allows the sample to be heated in a gas flow of selected composition on a pre-programmed temperature profile at rates between 1°C $min^{-1}$ and 100°C $min^{-1}$ up to a temperature between 20 and 1000°C and held for a specified time. The system continuously monitors: 1) the time-dependent evolution of the gases (including specific identification of the individual species such as CO, $CO_2$, $H_2O$, $CH_4$, $C_2H_4$, $C_2H_2$, benzene, heavy paraffins, heavy olefins, HCN, HCl, $NH_3$, NO, $NO_2$, $SO_2$, $CS_2$, COS, $CH_3OH$, $CH_3CHO$ and $CH_3COCH_3$); 2) the tar evolution rate ind its infrared spectrum with identifiable bands from the functional groups; and 3) weight of the non-volatile material (char plus mineral components). An analysis of C, H, N and S in the residue at the end of the pyrolysis experiment can be obtained by introducing oxygen to burn the residue and analyzing the combustion products.

For the experiments reported here, approximately 35mg of each coal sample was heated at 30°C/min, first to 150°C for drying and then to 900°C for pyrolysis. Additional details on the TG-FTIR apparatus can be found in Refs. 10 and 11.

**FIMS** - Molecular weight distributions of the primary pyrolysis tars were determined at SRI, International using the Field Ionization Mass Spectrometry (FIMS) apparatus described by St. John et al. (12). The samples were heated at 0.05°C/sec in a vacuum chamber.

## RESULTS AND DISCUSSION

The quantitative gas evolution plots from all eight coals are presented in

Figs. 1-6 for tars plus aliphatics, $CH_4$, $CO_2$, CO, $SO_2$ and $H_2O$ respectively. The coals are arranged on each plot according to the rank order given in Table 1. The actual temperature-time profiles are given on the first plot in each figure.

The results show how the structure of the product gas evolution curves varies from simple in the case of hydrocarbons to complex in the case of oxygenated species. One reason is that the latter are likely to be influenced by mineral decomposition peaks. Of course this can be assessed to a large extent by running demineralized samples, which we are in the process of doing.

In order to determine how well pyrolysis of the Argonne coals agreed with the assumption of rank-insensitive kinetics, a compilation was made of the temperatures for maximum evolution rate for the evolution of the most consistently prominent peaks for each gaseous product. This was difficult in some cases because of the fact that numerous "subpeaks", shoulders and minor peaks were often present. However, it was the usual case that an identifiable peak appeared in the same temperature vicinity for each coal. The results of this analysis are tabulated in Table 2.

In general, the standard deviations are greatest for oxygenated gases ($CO_2$, CO, $SO_2$, $H_2O$) compared to hydrocarbon gases ($CH_4$, tar/aliphatics). This phenomena was also observed previously (5). If one assumes a 50 Kcal/mole activation energy, a range in the peak temperature of 40°C corresponds to a factor of 5 in the rate while a range in the peak temperature of 65°C corresponds to a factor of 10 (5). It appears that about one-half of the 10 products show a variation of x5 or less, while one-half show a variation of x10 or less.

An interesting feature of the tar evolution curves in Fig. 1 is a low temperature evolution peak which is probably due to unattached guest molecules in the coal. These are most apparent in the Pittsburgh and Upper Freeport evolution curves. A comparison of the infrared spectra obtained at the low and high temperature peaks is presented in Fig. 7. The spectrum taken at the early peak (Fig. 7b) has been scaled up to compare to the spectrum from the later peak (Fig. 7c). The earlier peak appears to have a slightly higher aliphatic to aromatic content compared to the later peak. This would be consistent with the concept of some guest polymethylene in the coal, perhaps mixed with small molecules more representative of the coal's average organic structure.

**FIMS Analysis**

Molecular weight distributions of coals were obtained at SRI International using the Field Ionization Mass Spectrometry (FIMS) apparatus described by St. John et al. (11). The coal samples were pyrolyzed directly in the FIMS apparatus. The FIMS technique produces little fragmentation of the evolved tars and so provides a good determination of the tar molecular weight distribution. Figures 8 and 9 present the weight loss of six of the eight Argonne coals heated in the FIMS apparatus at 0.05°C/sec.

The spectra show a distinct progression from low to high rank. The highest rank coals, Pocahontas (Fig. 8a) and Upper Freeport (Fig. 8b) both show low intensities at low molecular weights (100 - 200 amu). This suggests few one and two ring clusters. The intensity in the 200 - 600 amu range, however, suggests the presence of three, four and higher ring cluster sizes and dimers and trimers of these. The low yield for the Pocahontas is due to its higher bond energies (525°C tar peak in Fig. 1) and lower number of small ring clusters capable of being volatilized.

The intermediate rank coals, Pittsburgh (Fig. 9a), Utah (Fig. 9b) and Upper Knawha (Fig. 8c) all have similar molecular weight distributions showing substantial intensities in the 100 to 200 amu region indicative of one and two ring clusters as well as in the 200 to 600 amu range.

The low rank coal, Wyodak (Fig. 9c) shows high intensity between 100 and 200 amu, but substantially lower intensity above 200 amu. This is typical of the Zap lignite also, and has been explained by extensive cross linking related to carboxyl groups in low rank coals (4).

## CONCLUSIONS

1. For most species there is a trend of increasing evolution temperature with increasing rank. However, the variations are small enough that the assumption of rank-insensitive kinetics is a good first approximation for nearly all of the major volatile products.

2. There is a systematic variation in the tar molecular weight distribution with rank. Higher rank coals show greater intensity in the high molecular weight range (200-600 amu), while lower rank coals show greater intensity in the lower molecular weight range (100-200 amu).

## ACKNOWLEDGMENTS

This work was supported under DOE Contract DE-AC21086MC23075. Justin L. Beeson is the Project Manager.

## REFERENCES

1. Vorres, K.S., ACS Fuel Chem Div. Preprints, **32**(4), 221 (1987).

2. Solomon, P.S., Hamblen, D.G., Deshpande, G.V. and Serio, M.A., 1987 Int. Conf. on Coal Science, p. 601, Maastricht, The Netherlands, (Oct. 26-30, 1987).

3. Solomon, P.R., Hamblen, D.G., Carangelo, R.M., Serio, M.A. and Deshpande, G.V., ACS Fuel Div. Preprint, **32**(3), 83 (1987).

4. Solomon, P.R., Hamblen, D.G., Carangelo, R.M., Serio, M.A. and Deshpande, G.V., Combustion and Flame, **71**, 137 (1988).

5. Solomon, P.R. and Hamblen, D.G., Prog. Energy Combust. Sci., **9**, 323 (1983).

6. Howard, J.B., Chemistry of Coal Utilization, (M.A. Elliott, Ed.), John Wiley, NY, Chapter 12, p. 665 (1981).

7. Niksa, S., Heyd, L.E., Russel, W.B. and Saville, D.A., 20th Symp. (Int) on Combustion, The Combustion Institute, University of Michigan, Ann Arbor, MI, pp. 1445-1453 (August 12-17, 1984).

8. Gribbins-Matham, J. and Kandigoti, R., ACS Fuel Div. Preprints, **32**(4), 318 (1987).

9. Solomon, P.R., Hamblen, D.G., Carangelo, R.M., Serio, M.A. and Deshpande, G.V., "A General Model of Coal Devolatilization", submitted to Energy and Fuel (1987).
10. Carangelo, R.M., Solomon, P.R. and Gerson, D.J., Fuel, **66**, 960 (1987).

11. Whelan, J.K., Solomon, P.R., Deshpande, G.V., and Carangelo, R.M., Energy and Fuels, **2**, 65, (1988).

12. St. John, G.A., Butrill, Jr., S.E. and Anbar, M., ACS Symposium Series, **71**, 223 (1978).

TABLE 2

**Comparison of Temperatures for Maximum Evolution Rate for Volatile Products from Pyrolysis of the Argonne Premium Coals**

| SPECIES | PEAK # | POCAHONTAS | UPPER FREEPORT | PITTSBURGH | UPPER KNAWHA | UTAH | ILLINOIS | WYODAK | ZAP | AVERAGE |
|---|---|---|---|---|---|---|---|---|---|---|
| $SO_2$ | 1 | - | - | 375 | 375 | 375 | 360 | 360 | 330 | 363 ± 20 |
| $CO_2$ | 1 | - | 435 | 420 | 465 | 465 | 435 | 435 | 420 | 439 ± 19 |
| CO | 1 | 495 | 525 | - | 465 | 465 | 450 | 435 | 465 | 470 ± 30 |
| Tar/ Aliphatics | 1 | 525 | 510 | 485 | 485 | 485 | 470 | 465 | 465 | 485 ± 22 |
| $H_2O$ | 1 | 585 | 555 | 510 | 525 | 495 | 525 | 495 | 495 | 525 ± 32 |
| $CH_4$ | 1 | 570 | 555 | 555 | 555 | 555 | 555 | 555 | 570 | 560 ± 7 |
| $SO_2$ | 2 | 600 | 615 | 615 | 600 | 615 | 585 | 570 | 600 | 600 ± 16 |
| $CO_2$ | 2 | 705 | 750 | 705 | 660 | 735 | 735 | 690 | 615 | 700 ± 45 |
| CO | 2 | 780 | 795 | 795 | 765 | 705 | 780 | 795 | 765 | 773 ± 30 |
| $H_2O$ | 2 | 815 | 840 | 795 | 795 | 825 | 765 | - | - | 807 ± 28 |

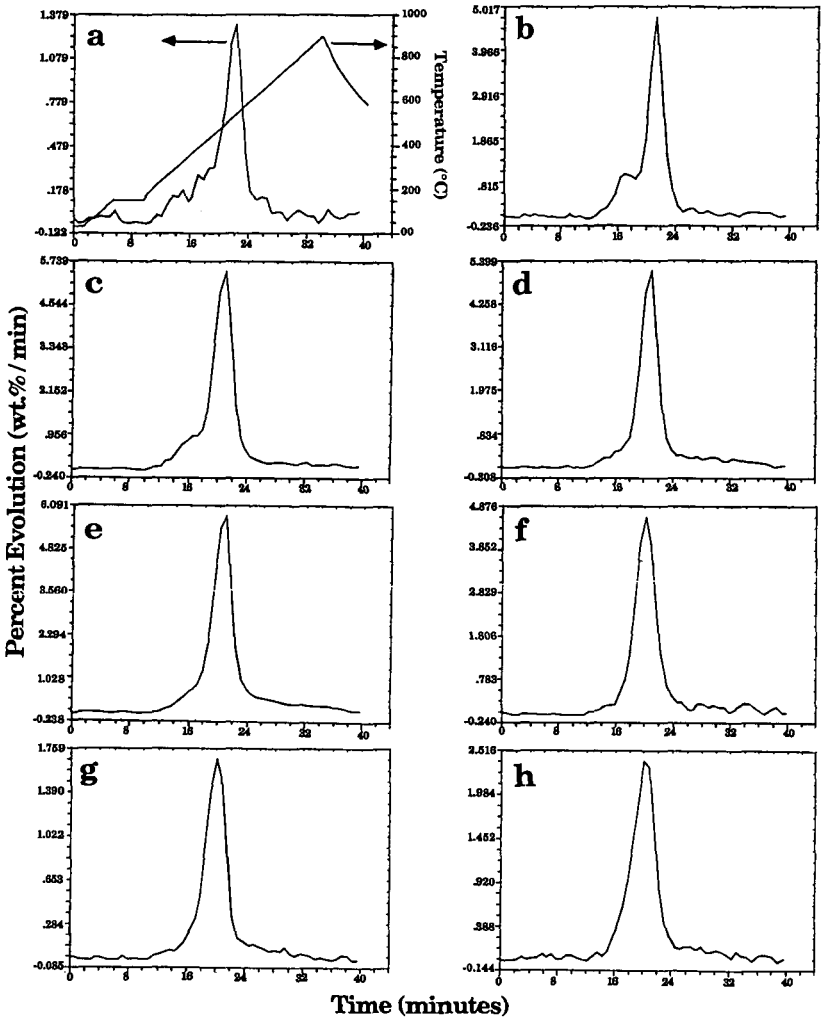


**Figure 1.** Evolution Rate for Tars/Aliphatic from the Eight Argonne Coals in a TG-FTIR at 0.5°C/s. a) Pocahontas; b) Upper Freeport; c) Pittsburgh; d) Upper Knawha; e) Utah Blind Canyon; f) Illinois No. 6; g) Wyodak; h) Zap.

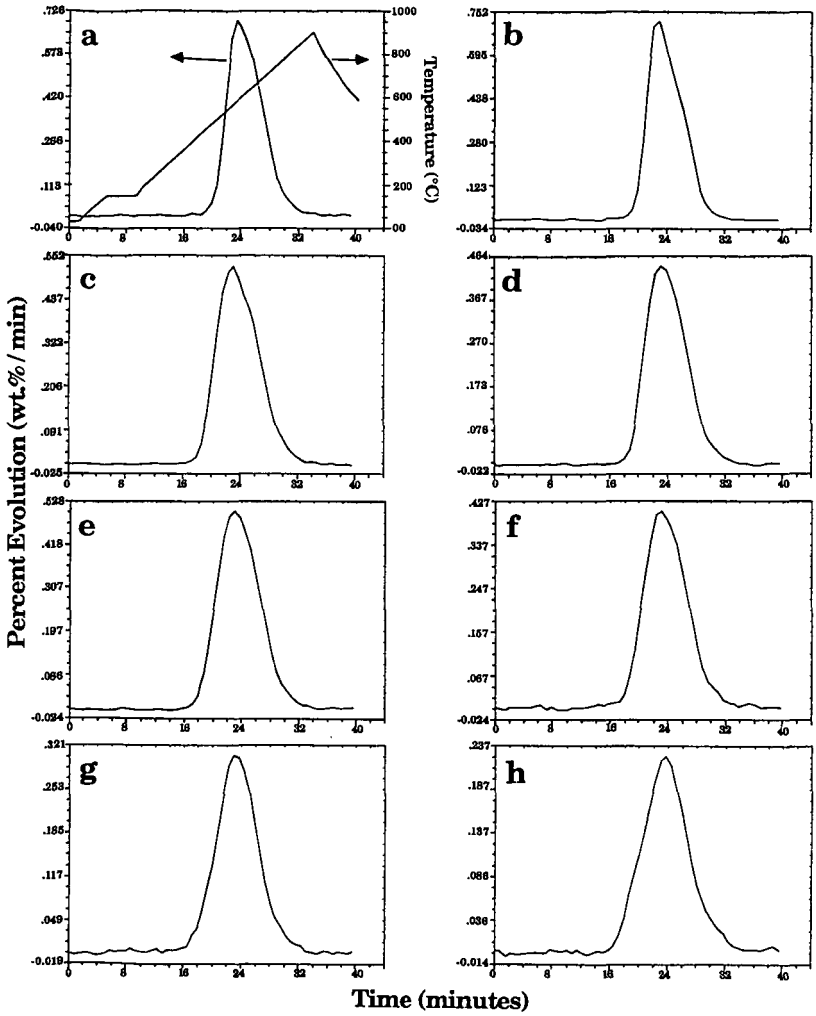


**Figure 2.** Evolution Rate for $CH_4$ from the Eight Argonne Coals in a TG-FTIR at 0.5°C/s. a) Pocahontas; b) Upper Freeport; c) Pittsburgh; d) Upper Knawha; e) Utah Blind Canyon; f) Illinois No. 6; g) Wyodak; h) Zap.

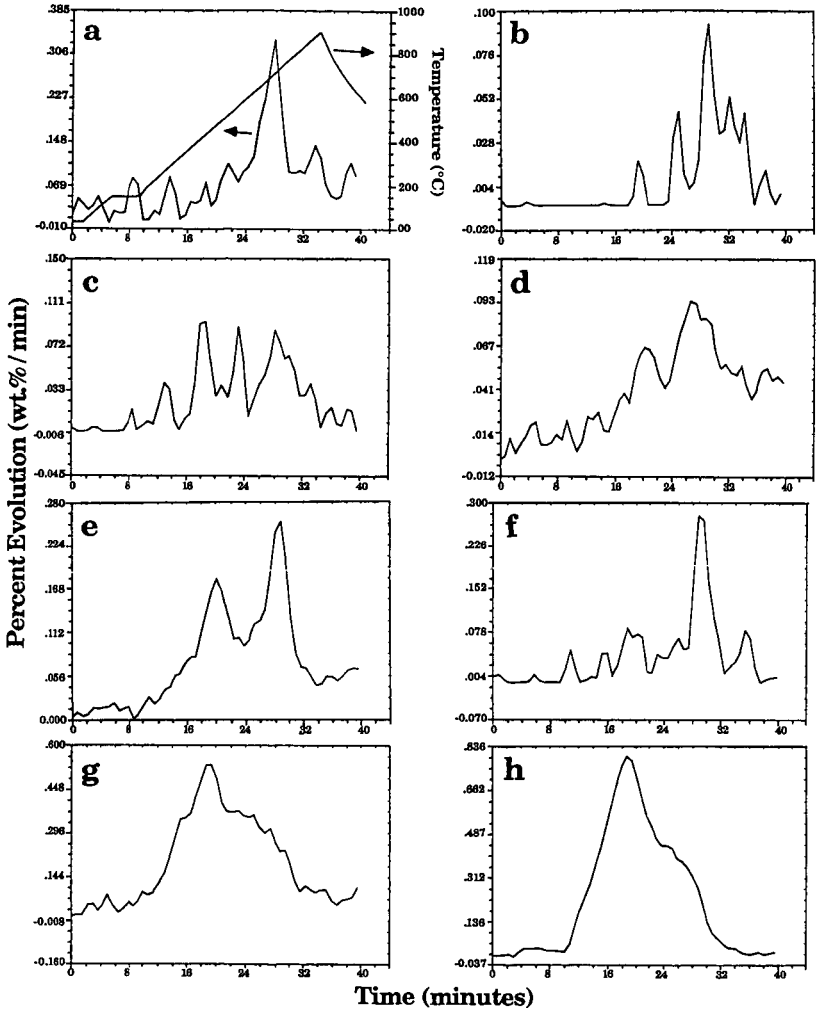


**Figure 3.** Evolution Rate for $CO_2$ from the Eight Argonne Coals in a TG-FTIR at 0.5°C/s. a) Pocahontas; b) Upper Freeport; c) Pittsburgh; d) Upper Knawha; e) Utah Blind Canyon; f) Illinois No. 6; g) Wyodak; h) Zap.

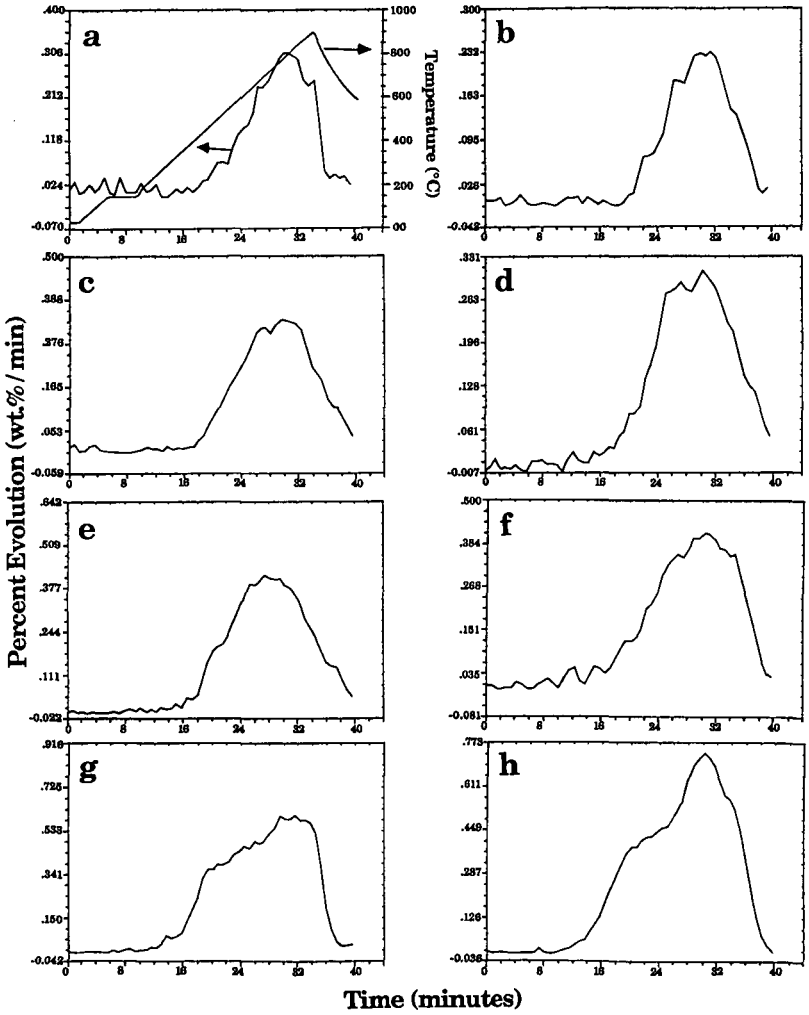


**Figure 4.** Evolution Rate for CO from the Eight Argonne Coals in a TG-FTIR at 0.5°C/s. a) Pocahontas; b) Upper Freeport; c) Pittsburgh; d) Upper Knawha; e) Utah Blind Canyon; f) Illinois No. 6; g) Wyodak; h) Zap.

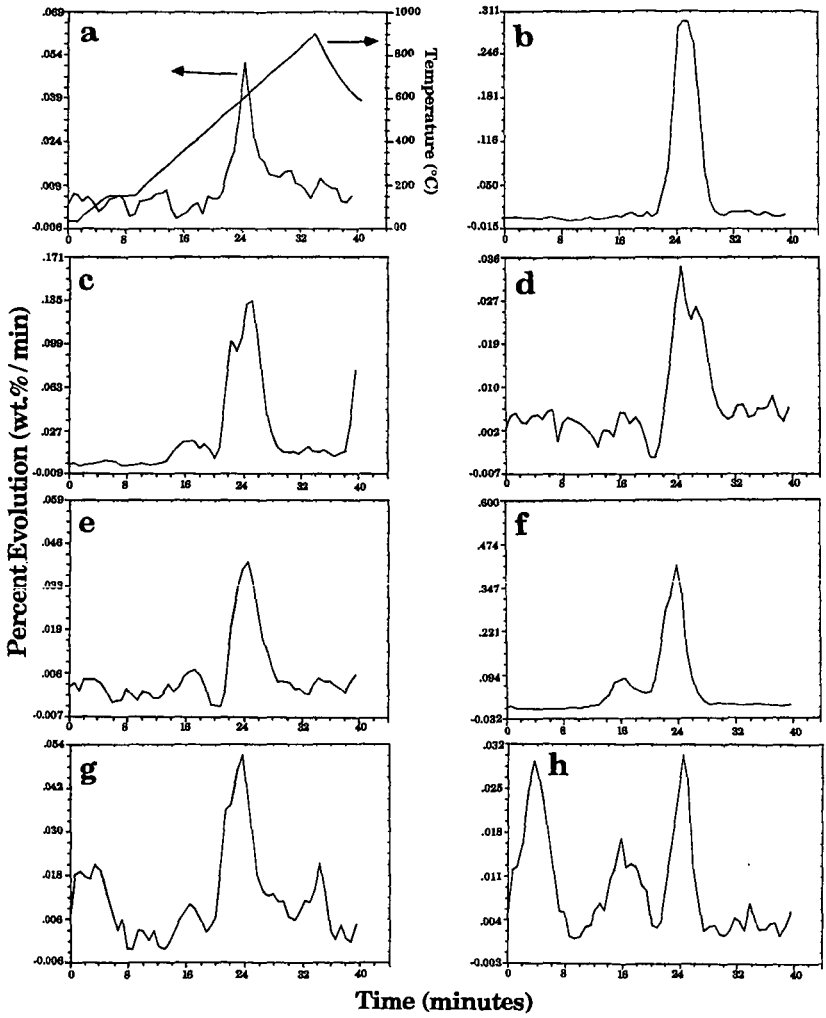


**Figure 5.** Evolution Rate for $SO_2$ from the Eight Argonne Coals in a TG-FTIR at 0.5°C/s. a) Pocahontas; b) Upper Freeport; c) Pittsburgh; d) Upper Knawha; e) Utah Blind Canyon; f) Illinois No. 6; g) Wyodak; h) Zap.

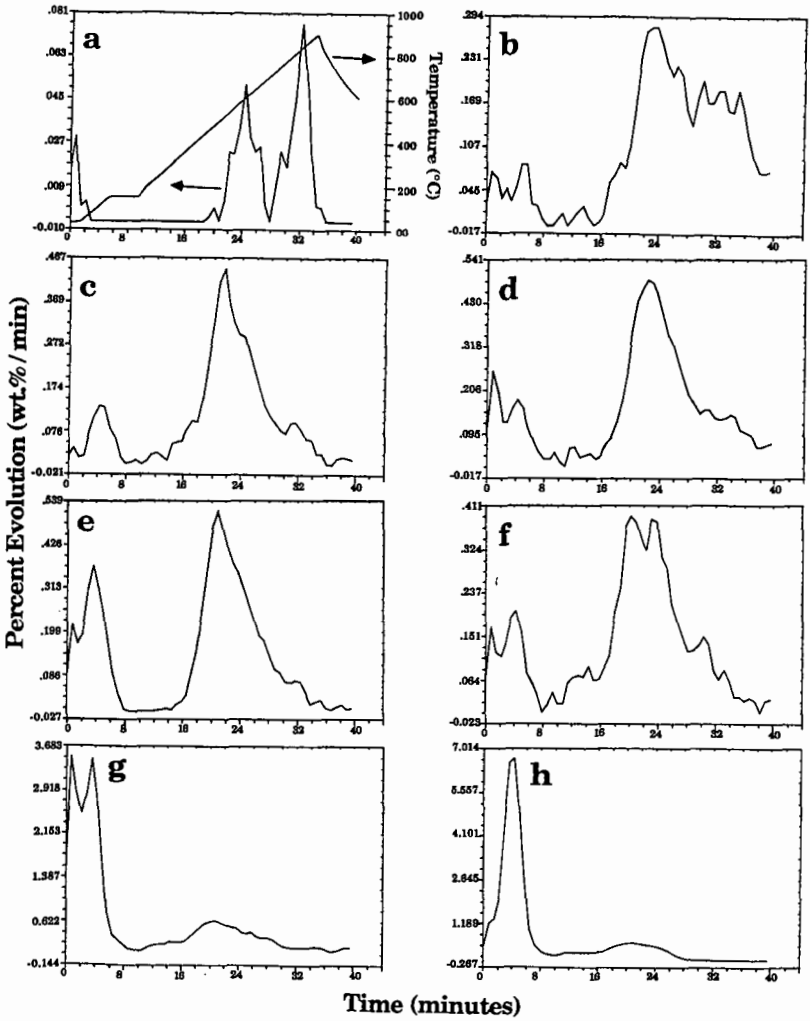


**Figure 6.** Evolution Rate for $H_2O$ from the Eight Argonne Coals in a TG-FTIR at 0.5°C/s. a) Pocahontas; b) Upper Freeport; c) Pittsburgh; d) Upper Knawha; e) Utah Blind Canyon; f) Illinois No. 6; g) Wyodak; h) Zap.

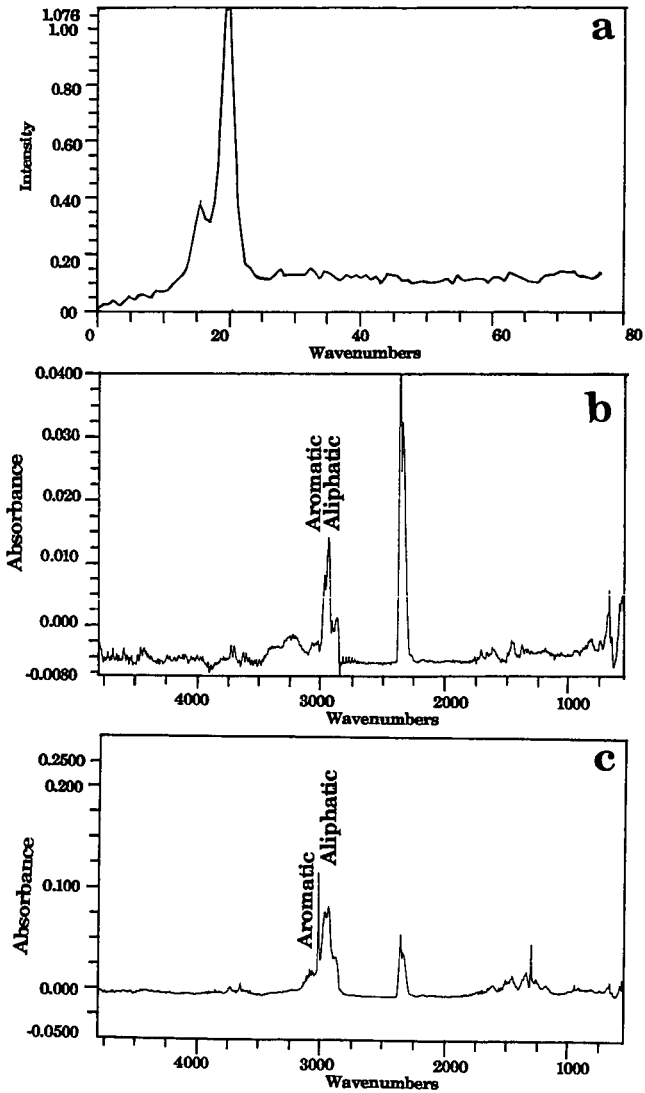


**Figure 7.** Spectrum of Products Evolved in Pyrolysis. a) Rate for Tar Evolution showing two Peaks, b) Spectrum at First Peak and c) Spectrum at Second Peak.

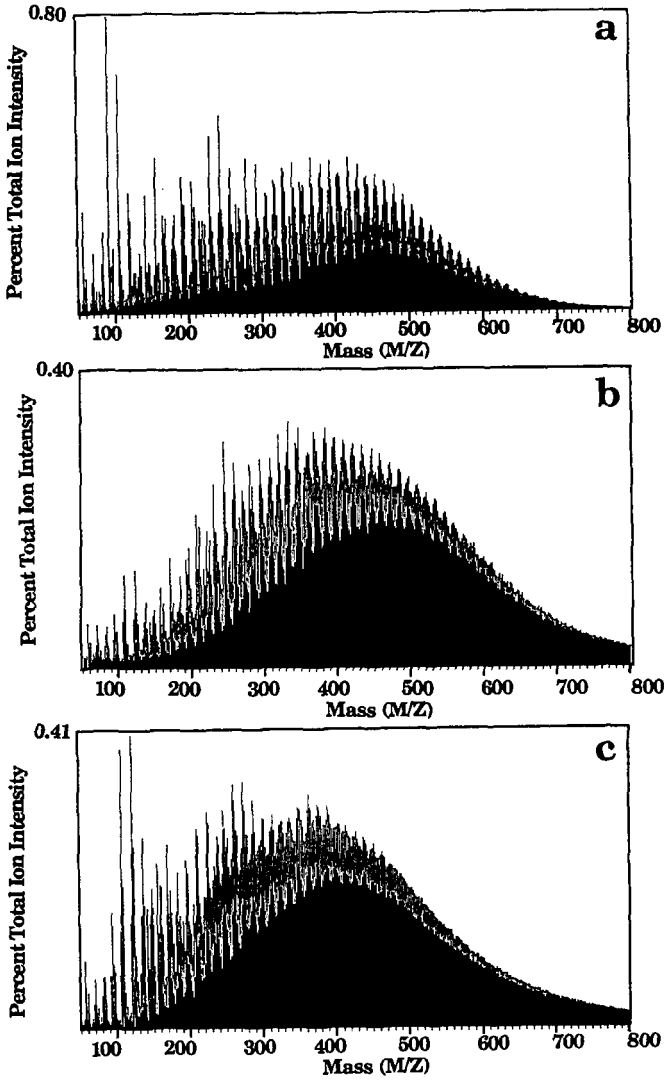


**Figure 8.** Tar Molecular Weight Distributions for Three Argonne Coals Pyrolyzed in the SRI FIMS Apparatus at 0.05°C/s. a) Pocahontas; b) Upper Freeport; c) Pittsburgh.

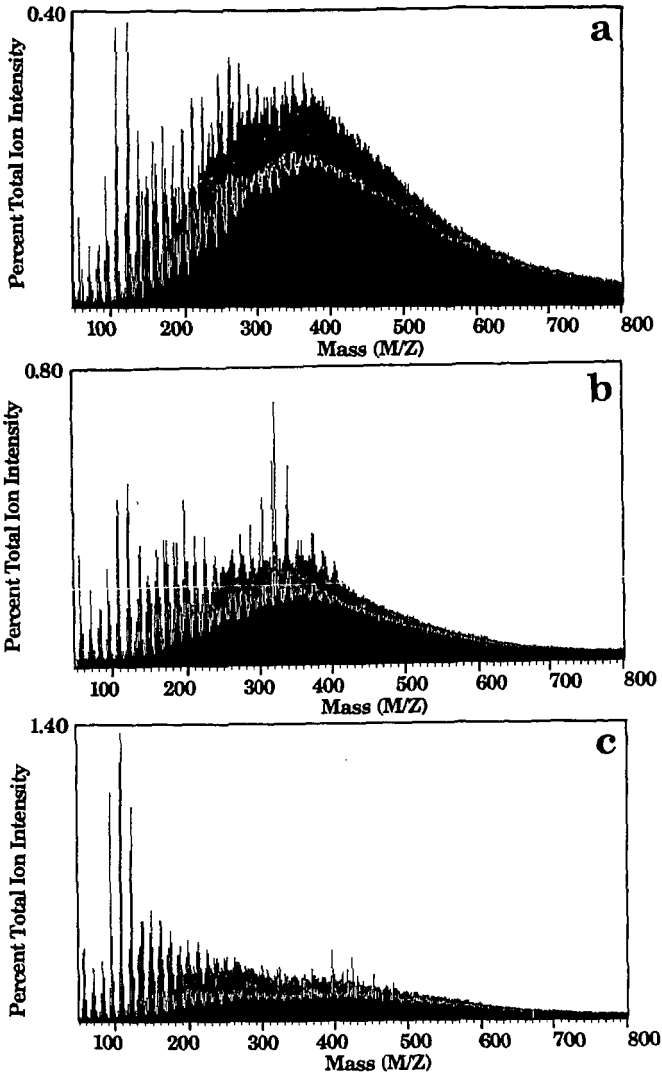


**Figure 9.** Tar Molecular Weight Distributions for Three Argonne Coals Pyrolyzed in the SRI FIMS Apparatus at 0.05°C/s. a) Upper Knawha; b) Utah Blind Canyon; c) Wyodak.

# CROSSLINKING REACTIONS IN COAL PYROLYSIS

G.V. Deshpande, P.R. Solomon, and M.A. Serio

Advanced Fuel Research, Inc., 87 Church Street, East Hartford, CT 06108

## INTRODUCTION

During coal pyrolysis, the break up of the coal macromolecular network is controlled by the relative rates of bond breaking, crosslinking and mass transport. Crosslinking reactions are important because the ultimate tar yield and tar molecular weight distribution are dependent on the extent of these reactions. Crosslinking, as measured by solvent swelling experiments, is observed to be rank dependent, with lignites crosslinking at lower temperatures than bituminous coals.

In a recent study of crosslinking, Suuberg et al. (1) observed that the crosslinking rate appeared to correlate with the evolution of $CO_2$. This correlation was confirmed by Solomon et al. (2,3). It appears that crosslinking may be related to the decomposition of carboxyl groups (whose concentration is rank dependent) to form $CO_2$. Recent research (4) has also demonstrated that substantial reductions in the crosslinking reactions can be achieved by ultra rapid heating. The high heating rate conditions for lignites produce melting and swelling of char, higher yields of soluble products, and product molecular weight distributions previously seen only for melting, easily soluble coals.

This paper describes a study of crosslinking behavior in which chars of a number of coals have been pyrolyzed under a variety of temperature histories and analyzed at intermediate extents of pyrolysis for solvent swelling behavior, functional group compositions and gas evolution. The behavior is consistent with the hypothesis that low temperature crosslinking is related to the decomposition of carboxyl groups to form $CO_2$.

## EXPERIMENTAL

### Coals Examined

Experiments were done with North Dakota (Zap), Big Brown Texas, and perdeutero-methylated Big Brown Texas lignites, Wellmore Kentucky #9, Pittsburgh Seam (high ash), Pittsburgh Seam (Argonne sample) bituminous coals and oxidized Pittsburgh Seam (high ash) bituminous coal. The ultimate analysis of each coal is given in Table I.

### Char Preparation

The experiments described here were carried out on chars formed from the coals given in Table I. The chars were formed by heating in an inert gas within an entrained flow reactor (EFR) and a heated tube reactor (HTR) for a variety of residence times and maximum temperatures, or by heating in a Thermogravimetric Analyzer (TGA) at 30°C/min to 900°C where the volatiles are analyzed on-line by Fourier Transform Infrared (FT-IR) spectroscopy (TG-FTIR). A more detailed description can be found in Ref. 5.

### Char Characterization

The chars were analyzed by quantitative FT-IR spectroscopy using the KBr pellet method (6,7). The chars were also analyzed using the solvent swelling techniques developed by J.W. Larsen and coworkers (8,9) to quantify and monitor the densities of covalent crosslinks inside the macromolecular framework of coal chars.

## RESULTS AND DISCUSSION

### Rank Dependence of Crosslinking Reactions

Measurements of the appearance of crosslinks during coal pyrolysis were recently reported by Suuberg et al. (1). Their results showed that lignites crosslink at temperatures (650 K) far below those where bituminous coals crosslink (800 K). This motivated the present study of systematically measuring the extent of crosslinking in coal pyrolysis.

Figure 1 shows the volumetric swelling ratio for Zap and Big Brown Texas lignites and Wellmore Kentucky #9, Pittsburgh Seam (Argonne sample) and Oxidized Pittsburgh Seam (high ash) bituminous coals measured as a function of temperature. The swelling ratio profiles are presented as (1-X) where X is the change in the solvent swelling ratio between the coal and char, normalized by the maximum change. The curves are quite different among the five samples. The lignites crosslink at much lower temperatures than the bituminous coals, while the oxidized bituminous coal is an intermediate case.

The extent of low temperature crosslinking correlates with the carbonyl concentration of the coal as measured by FT-IR. The carbonyl concentration is directly related to the concentration of carboxyl groups. The high rank coals have a very low concentration of carboxyl groups, as seen by a low intensity carbonyl band at 1700 wavenumbers, in Fig. 2. The oxidized Pittsburgh Seam coal and the low rank coals have much higher carbonyl peaks.

Big Brown Texas lignite shows a slightly slower rate of crosslinking than Zap lignite. Schobert et al. (10) compared the ESCA spectra of Big Brown Texas and Beulah Zap lignites and found that the carboxylic peak to be less pronounced in the Big Brown spectrum. Spackman (11) has also reported that Big Brown Texas lignite had a lower carboxylic content than the North Dakota Zap lignite. When both lignites are heated at 30°C/min to 600°C, Big Brown Texas lignite evolves less $CO_2$ (8%) than Zap lignite (11.3%). The area corresponding to the carbonyl peak in the FT-IR spectrum of Big Brown Texas lignite is also less (1.29) than for the Zap lignite (1.69). These observations are consistent with the hypothesis that early crosslinking reactions in lignites occur with loss of carboxyl groups and evolution of carbon dioxide and the extent of crosslinking is directly related to the amount of these labile carboxyl groups present in coal. Bituminous coals which do not have a large concentration of these groups do not undergo early crosslinking reactions. A major contribution of hydroxyl groups in early crosslinking reactions is not likely because bituminous coals have a larger concentration of hydroxyl groups than the carboxyl groups and do not crosslink at low temperatures.

### Heating Rate Dependence of Crosslinking Reactions

An important observation was made that crosslinking reactions could be minimized by carrying out the pyrolysis at a very high heating rate. In Fig. 3, the effect of heating rate on tar yield and volumetric swelling ratio in pyridine for North Dakota (Zap) lignite is compared for rapid pyrolysis (20,000°C/s) and slow pyrolysis (0.5°C/s). It can be clearly seen that the lignite starts to crosslink prior to the tar evolution in slow pyrolysis, whereas crosslinking occurs simultaneously with tar evolution in rapid pyrolysis. The tar yield obtained during rapid pyrolysis is higher than that obtained at low heating rate by more than a factor of two. Figure 4 compares scanning electron micrographs of lignite chars produced at 800°C with heating rates of 600°C/s and 20,000°C/s. The 600°C/s char shows little evidence of fluidity while the 20,000°C/s char shows fluidity, bubbling, and swelling. This is believed to be due to reduced crosslinking reactions.

## Chemical Modification of Crosslinking Reactions

In order to test the hypothesis of low temperature crosslinking in lignites due to carboxyl groups, slow pyrolysis (heating rate, 0.5 K/s) of Big Brown Texas and perdeutero-methylated Big Brown Texas lignites were carried out in the TG-FTIR. The sample of perdeutero-methylated Big Brown Texas lignite was provided for this study by Dr. Ron Liotta. The gas evolution rate profiles (in arbitrary units) for gas species CO, $CO_2$, paraffins, $CH_4$, and $H_2O$ are shown in Figs. 5a-5e, respectively, for Big Brown Texas and perdeutero-methylated Big Brown Texas lignites. The amount of gas species evolved is proportional to the area under the curve. It can be seen that during the pyrolysis stage (Time < 2000 s) the amount of $CO_2$, CO, and $H_2O$ evolved is less for the perdeutero-methylated coal while the amount of $CH_4$ evolved is slightly more.

The amount of paraffin evolved (which is related to the amount of tar evolved) is also higher for the perdeutero-methylated coal. The weight loss profile for these two coals is shown in Fig. 5f. The initial weight loss profile (Time < 800 s, T < 300°C) is different while the rest of the weight loss profile during the pyrolysis stage (800 < Time < 2000 s; 300 < T < 900°C) seems to be very similar. The increase in weight at 2040 sec is due to noise in the balance and is not a real effect. CO, $CO_2$, and $H_2O$ evolution is lower and $CH_4$ and paraffin (300 < T < 900°C) is higher for the perdeutero-methylated coal. Hence the difference in the weight loss profiles of the two lignites.

The effect of reduction in crosslinking reactions observed in pyrolysis of perdeutero-methylated coal is not only on the total amount of tar evolved but also on the molecular weight distribution of the tar. Figure 6 compares the FIMS spectra for raw and perdeutero-methylated Big Brown Texas lignites. The average molecular weight is substantially increased from that of the unmethylated coal and now resembles that of a bituminous coal.

## Effects of Minerals on Crosslinking Reactions

Several investigators (12-15) have studied the role of exchangeable cations in gasification and pyrolysis of low rank coals. The ion-exchange technique as outlined by Schafer (16,17) is used to exchange cations with ammonium ions or load the coal with a certain cation (e.g. calcium) in different amounts.

Tyler and Schafer (13) found that the removal of cations from Gelliondale coals increased the yields of both tar and total volatile matter. The converse was also observed in that the addition of $Ca^{2+}$ ions to an acid-form coal reduced the yields. The reversibility of the phenomena shows that the increase in yields on cation removal is not the result of any permanent chemical modification or degradation of the organic structure of the coal during the acid treatment (2N HCl at room temperature).

This motivated the study of effect of minerals on crosslinking reactions. As calcium has been the cation most extensively studied and low rank coals have a large amount of calcium cations attached to the carboxylate anions, Indian Head Zap lignite was used in this study. Two techniques were used to remove the calcium cations, the details of which can be found elsewhere (18,19). In the first technique, calcium ions were ion exchanged with 1N ammonium acetate for three 24 hour periods. The calcium content after ion exchange was reduced from 1.66 to 0.2%. In the second technique, demineralization with HCl and HF was used. The calcium content after demineralization decreased to 0.01%.

The swelling ratio profiles presented as (1-X) where X is the change in the solvent swelling ratio between the coal and char normalized by the maximum change

for ion exchanged Zap lignite, demineralized Zap lignite and Zap lignite are compared in Fig. 7. The crosslinking behavior for ion-exchanged Zap lignite is similar to raw lignite and shows early crosslinking. It should be noted here that the calcium has not totally been removed by the ion-exchange technique in this study.

The crosslinking behavior of demineralized Zap lignite is strikingly different from that of Zap lignite. It shows a shift to a higher temperature for the same loss in swelling due to crosslinking reactions. Both the raw and demineralized Zap lignites were pyrolyzed in the TG-FTIR apparatus. The tar evolved was higher (daf basis) and the CO and $CO_2$ evolutions were lower for the demineralized case. An increase in tar evolution is expected due to reduced crosslinking reactions. When pyrolysis of two lignites were carried out at high heating rate (5000 K/s) in the entrained flow reactor, the tar yield was increased from 14% (for raw lignite) to 22% due to demineralization. Similar increase in tar yield has been found for increase in heating rate during pyrolysis which has been discussed in the section entitled "Heating Rate Dependence of Crosslinking Reactions". This further supports the idea of reduced crosslinking due to demineralization.

It should be noted that the increase in tar yield due to the removal of calcium found by Tyler and Schafer (13) was for coals whose cations were removed by acid treatment. Both the lignite and the demineralized lignites were exhaustively extracted by pyridine in a soxhlet apparatus to determine whether any depolymerization of lignite had occurred. The amount of pyridine extractable material was 0% for the raw lignite and 2.6% for the demineralized lignite. The volumetric swelling ratio in pyridine was 2.4 for the raw lignite and 2.5 for the demineralized lignite. Both results show that a very small degree of depolymerization had occurred, if any, due to the demineralization procedure employed to remove the cations. Hence the increase in tar amount and shift of the crosslinking curve to a higher temperature for the same amount of loss in swelling due to crosslinking for demineralized Zap lignite appears to be due to the reduced mineral content.

**Effect of Oxidation on Crosslinking Reactions**

To further study the role of carboxyl groups in crosslinking, Pittsburgh Seam bituminous coal was oxidized in an oven in air to add carboxyl groups to the coal and see whether the oxidized coal behaved like a lignite in slow heating rate pyrolysis. After 239 hours of oxidation, a large increase in the absorption of IR due to carbonyl band at 1700 wavenumbers is observed which is shown in Fig. 2. There is a slight change in the OH band at 3300 wavenumbers, a large decrease in the aliphatic C-H at 2900 wavenumbers. This was consistent with the findings of other (20-22) investigators.

The chars of the oxidized coal formed at intermediate temperatures were swelled in pyridine to determine the crosslink densities. These results are shown in Fig. 1. The oxidized coal shows earlier crosslinking, as seen by the decrease in swelling ratio (decrease in value of (1-X)) at temperatures above 300°C. The decrease is not as large as that for the lignites because the concentration of carboxyl groups formed during oxidation is not as large as that found in the lignites. The height of the shoulder peak at 1700 wavenumbers corresponding to carbonyl band for oxidized coal is smaller than both the Zap lignite and the Big Brown Texas lignite.

The on-line FT-IR spectra of the gas evolution products from the raw coal and the oxidized coal were taken during pyrolysis and are shown for different temperatures during pyrolysis in Fig. 8. There is a larger amount of CO evolution at low temperatures for the oxidized coal than for the raw coal. This was also

found by Ignasiak et al. (21) in their study of pyrolysis of oxidized bituminous coals. The amount of $CO_2$ and CO evolved were higher for the oxidized bituminous coal. This is consistent with the larger carbonyl peak in the FT-IR spectrum of the oxidized coal. The amount of tar evolution (as seen from absorption of C-H band at 2900 wavenumbers) at temperatures between 400°C and 550°C is greater for the raw coal than the oxidized coal. This is consistent with the findings of Furimsky et al. (20). The tar, as it flows out of the pyrolysis chamber of the TG-FTIR into the FT-IR cell, forms an aerosol which causes scattering and results in increased absorption at high wavenumbers. The scattering is maximum at temperatures between 450 and 500°C and is also found to be greater for the raw coal than the oxidized coal.

## CONCLUSIONS

1. For the low rank coals, the amount of tar obtained in a pyrolysis process increases with the increase in the heating rate.

2. The initial crosslinking reactions in low rank coals appear to be due to the presence of carboxyl groups. High rank coals which do not have these groups in large concentration do not show this kind of behavior in pyrolysis.

3. Chemical modification of carboxyl groups in lignites by methylating results in increased tar yield and molecular weight distribution of tar looks like that of a bituminous coal.

4. Demineralization of the lignite results in decrease in the rate of crosslinking reaction and increase in tar yield and the increase is higher when pyrolysis is carried out at a higher heating rate. The amount of CO and $CO_2$ evolution is also decreased due to demineralization. These results are consistent with ion exchanged minerals playing an important role in the crosslinking reactions.

5. Oxidation of bituminous coal results in early crosslinking during pyrolysis due to the presence of carboxyl groups introduced during the oxidation process.

## ACKNOWLEDGEMENT

The authors wish to thank the Pittsburgh Energy Technology Center of the Department of Energy for the support of this work under Contract No. DE-FG22-85PC80910. The authors would also like to thank Dr. Ron Liotta for samples of perdeutero-methylated Big Brown Texas lignite.

## REFERENCES

1. Suuberg, E.M., Lee, D., and Larsen, J.W., Fuel, **64**, 1668, (1985).

2. Solomon, P.R., Hamblen, D.G., Carangelo, R.M., Serio, M.A., and Deshpande, G.V., Combustion and Flame, **71**, 137, (1988).

3. Solomon, P.R., Hamblen, D.G., Deshpande, G.V., and Serio, M.A., Coal Science and Technology II, (J.A. Moulijin, et al., Ed.) Elsevier Science Publishers, Amsterdam, p. 601, The Netherlands, (1987).

4. Solomon, P.R., Serio, M.A., Carangelo, R.M., and Markham, J.R., Fuel, **65**, 182, (1986).

5. Carangelo, R.M., Solomon, P.R., and Gerson, D.J., Fuel, **66**, 960, (1987).

6. Solomon, P.R. and Carangelo, R.M., Fuel, **61**, 663, (1982).

7. Solomon, P.R. and Carangelo, R.M., "FT-IR Analysis of Coal 2. Aliphatic and Aromatic Hydrogen Concentration", Accepted for publication, Fuel, (1988).

8. Green, T.K., Kovac, J., and Larsen, J.W., Fuel, **63**, 925, (1984).

9. Green, R.K., Kovac, J., and Larsen, J.W., in Coal Structure, (R.A. Meyers, Ed.) Academic Press, NY (1982).

10. Schobert, H.H., Montgomery, G.G., Mitchell, M.J., and Benson, S.A., "Characterization of the Organic Structure of U.S. Lignites by Electron Spectroscopy and Thermal Analysis", presented at the 1983 Int. Conf. on Coal Science, Pittsburgh, PA, pp. 350-353, (1983).

11. Spackman, W.A., et al., US DOE Report FE-2030-16, (1980).

12. Morgan, M.E. and Jenkins, R.G., ACS Div. of Fuel Chem. Preprints, **29**, (2), 141, (1984).

13. Tyler, R.J. and Schafer, H.N.S., Fuel, **59**, 487, (1983).

14. Jenkins, R.G. and Morgan, M.E., Fuel, **65**, 769, (1986).

15. Stournas, S., Papachristos, M., and Kyriakopoulos, G.B., ACS Div. of Fuel Chem. Preprints, **32**, (3), 227, (1987).

16. Schafer, H.N.S., Fuel, **49**, 197, (1970).

17. Schafer, H.N.S., Fuel, **51**, 4, (1972).

18. Solomon, P.R., Hamblen, D.G., Serio, M.A., Smoot, L.D., and Brewster, S., "Measurement and Modeling of Advanced Coal Conversion", First Annual Report, U.S. DOE/METC Contract No. DE-AC21-86MC23075, (1987).

19. Solomon, P.R., Serio, M.A., Hamblen, D.G., Markham, J.R., Bassilakis, R., and Best, P.E., "Chemical and Physical Development of Char Particles during Devolatilization", Seventh Quarterly Report, U.S. DOE/METC Contract No. De-AC21-85MC22050, (1987).

20. Furimsky, E., MacPhee, J.A., Vancea, L., Ciavaglia, L.A., and Nandi, B.N., Fuel, **62**, 395, (1983).

21. Ignasiak, B.S., Clugston, D.M., and Montgomery, D.S., Fuel, **51**, 76, (1976).

22. Ignasiak, B.S., Nandi, B.N., and Montgomery, D.S., Fuel, **49**, 214, (1970).

TABLE I

ULTIMATE ANALYSES OF COALS USED (%DAF)

| | C | H | N | S | O (diff) |
|---|---|---|---|---|---|
| Zap N. Dakota Lignite | 66.5 | 4.8 | 1.1 | 1.1 | 26.5 |
| Big Brown Texas Lignite | 72.4 | 5.5 | 1.4 | 1.2 | 19.5 |
| Wellmore Kentucky #9 Bituminous | 86.0 | 5.4 | 1.5 | 1.2 | 5.9 |
| Pittsburgh Seam #8 Bituminous | 82.1 | 5.6 | 1.7 | 2.4 | 8.2 |
| Pittsburgh Seam #8 (Argonne sample) Bituminous | 83.3 | 5.9 | 1.6 | 2.3 | 6.9 |

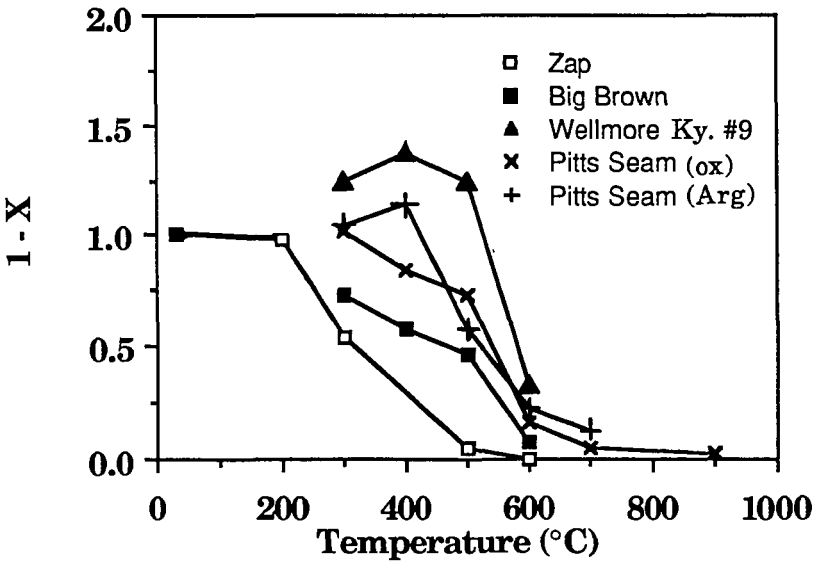


**Figure 1.** Comparison of Swelling Data of Zap Lignite, Big Brown Texas Lignite, Wellmore Bituminous Coal, Pittsburgh Seam Bituminous (high ash) Oxidized Coal and Pittsburgh Seam (Argonne sample) Bituminous Coal in a TG-FTIR at Various Final Temperatures (Heating Rate = 0.5 K/s).

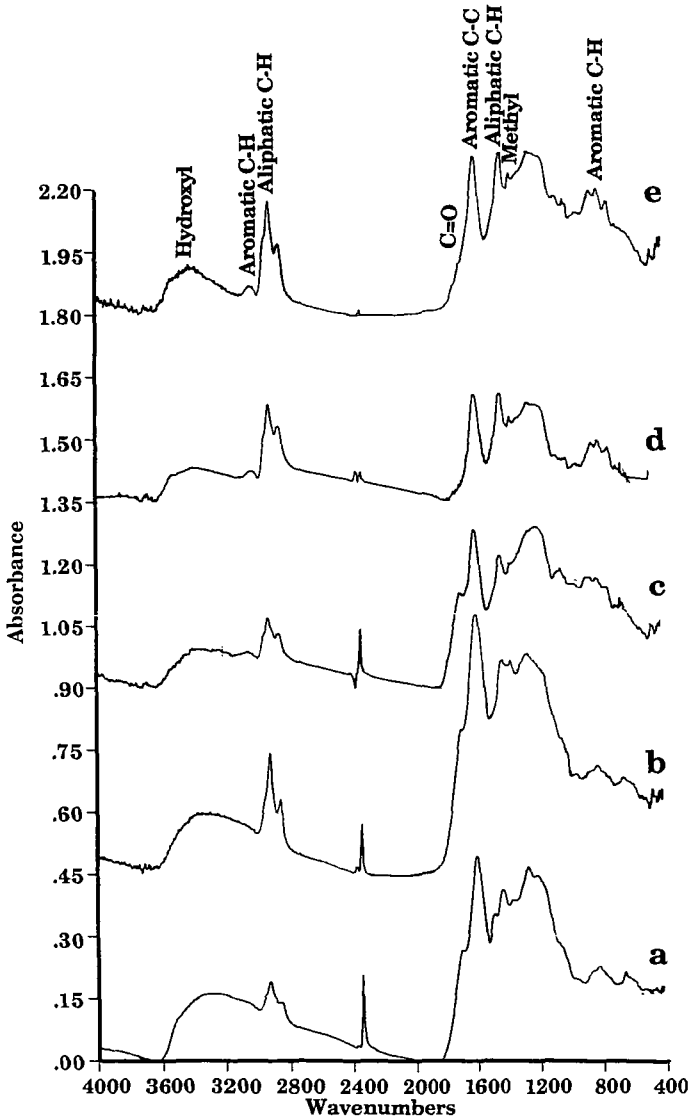


**Figure 2.** Comparison of the FT-IR Spectra of a) Zap Lignite, b) Big Brown Texas Lignite, c) Pittsburgh Seam Bituminous (high ash) Oxidized Coal, d) Pittsburgh Seam (Argonne) Bituminous, and e) Wellmore Coals Dry, Mineral Matter Corrected.

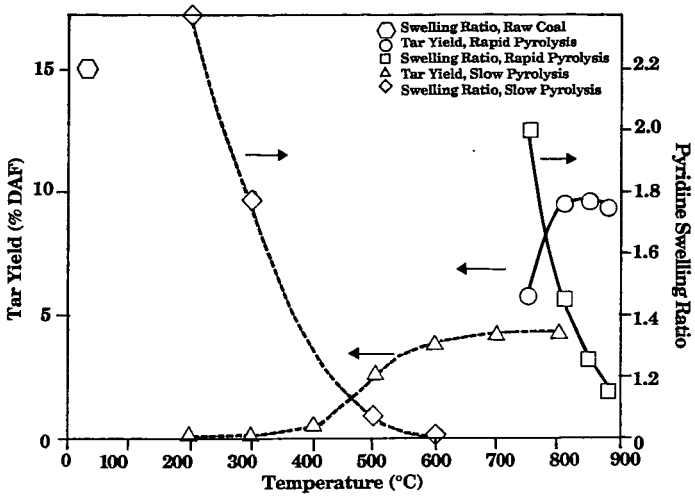


**Figure 3.** Effect of Temperature on Tar Yield and Pyridine Swelling Ratio of Char for Rapid Pyrolysis of Zap Lignite in Carbon Dioxide (solid line) and Slow Pyrolysis of Zap Lignite in Helium (dashed line).

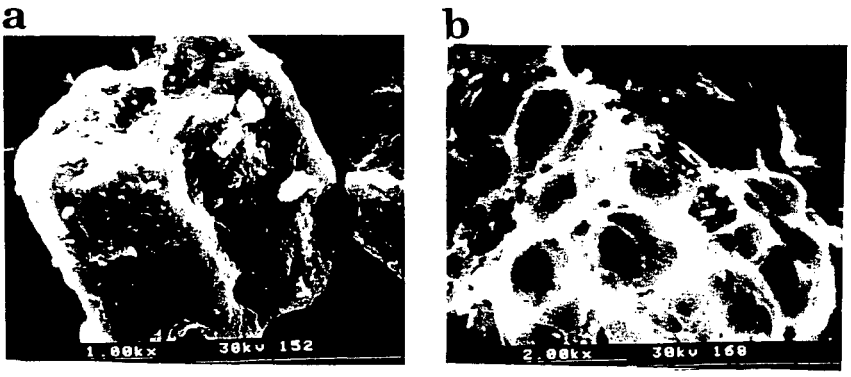


**Figure 4.** Scanning Electron Micrographs of North Dakota Lignite Chars. a) 600°C/sec Heating Rate and b) 20,000°C/sec Heating Rate.

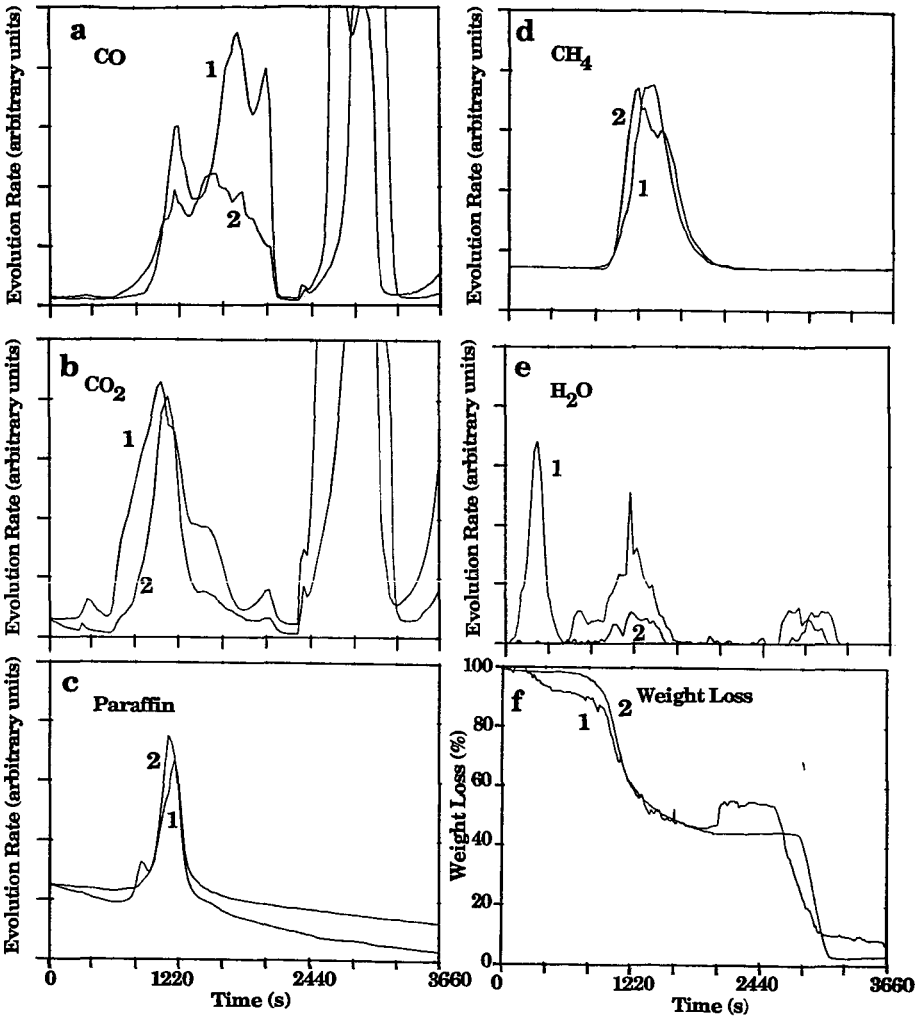


**Figure 5.** Thermogravimetric/Evolved Gas Analysis of Big Brown Texas and Perdeutero Methylated Big Brown Texas Lignites. a-e) Evolution Rate in Arbitrary Units for Individual Gas Species, and f) Measured Weight Loss. (Heating Rate = 0.5 K/s). 1 = Big Brown Texas Lignite and 2 = Perdeutero Methylated Big Brown Texas Lignite.

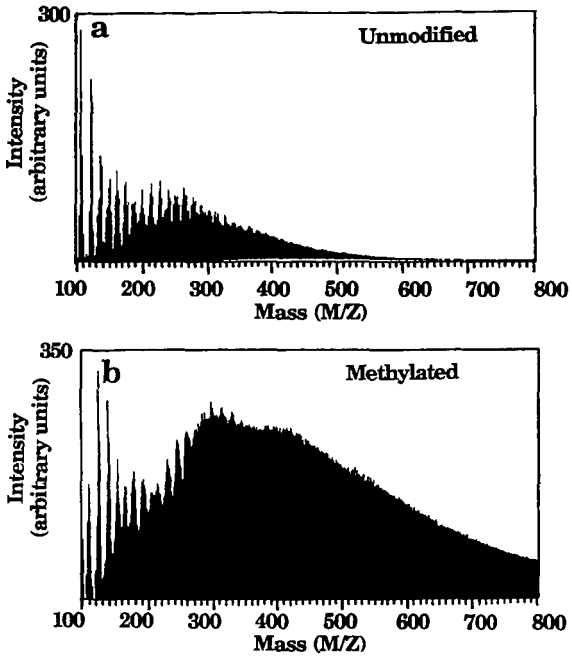


**Figure 6.** Comparison of FIMS Spectra for Raw and Perdeutero-methylated Big Brown Texas Lignite.

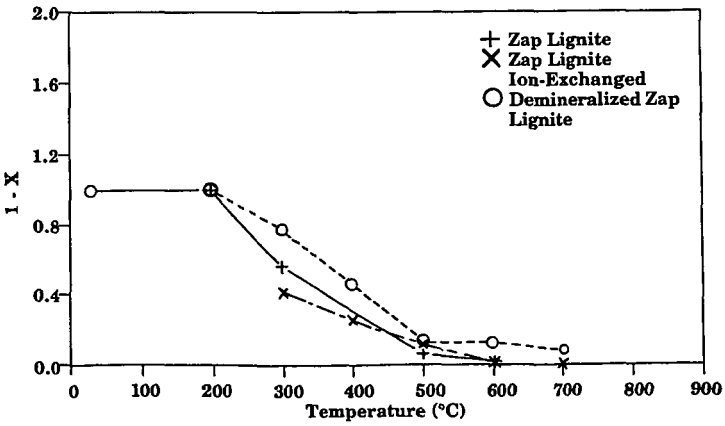


**Figure 7.** Effect of Removal of Ca by Ion Exchange or Demineralization on Crosslinking Behavior of Zap Lignite.

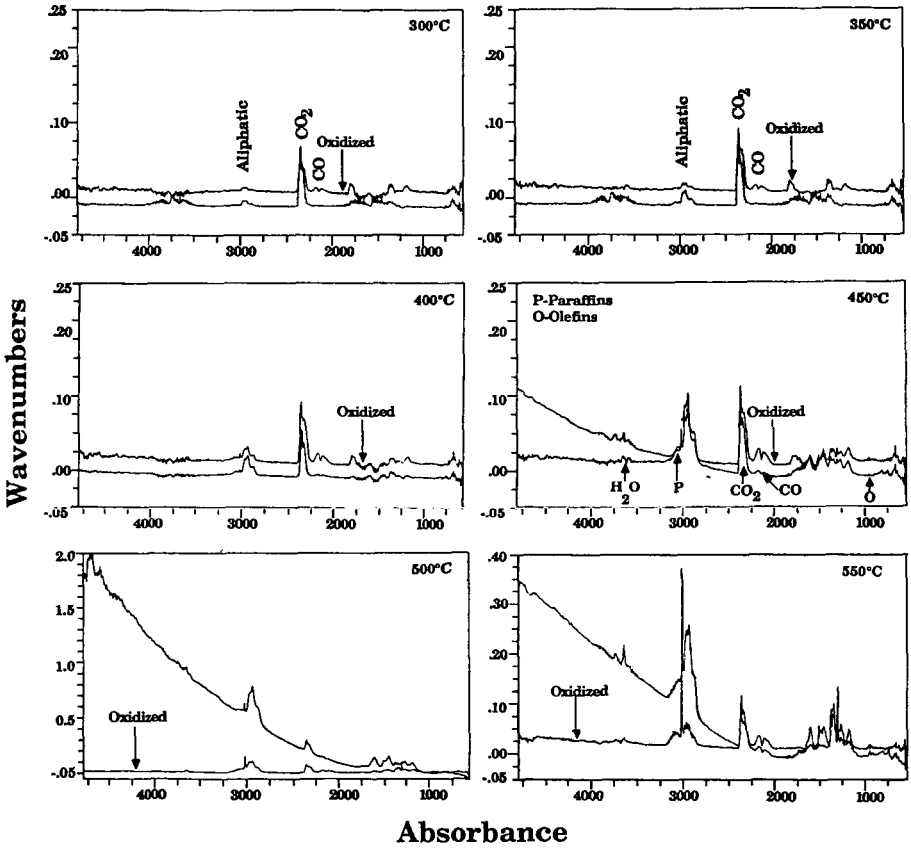


**Figure 8.** FT-IR Spectra of Evolved Products from Pyrolysis of Pittsburgh Seam Bituminous (high ash) Coal and Pittsburgh Seam Bituminous (high ash) Oxidized Coal.

# A CHEMICAL MODEL OF COAL DEVOLATILIZATION USING PERCOLATION LATTICE STATISTICS

D.M. Grant and R.J. Pugmire, University of Utah
Salt Lake City, UT 84112.
T.H. Fletcher and A.R. Kerstein, Sandia National Laboratories
Livermove, CA

## ABSTRACT

We have developed a model for coal devolatilization that incorporates the diversity of coal structure in such a way that the analytical data obtained from solid state NMR provides the initial input data. Using an experimentally determined kinetic rate parameters, it is possible to fit the gas, tar and char production of a lignite and high volatile bituminous coal. We have employed percolation theory to provide analytical expressions for the lattice statistics required in devolatilization modeling. The percolation theory allows one to avoid the more time consuming Monte Carlo technique with no loss of generality or important statistical features. Percolation theory analytically describes the size distribution of finite clusters of sites joined by intact bridges but isolated from all remaining sites by broken bridges. The theory specifies a critical bridge population, depending only on the site coordination number, above which infinite arrays will coexist with clusters of finite size. It is a simple matter to adapt the structural features of percolation theory to both the tar and gas obtained in coal pyrolysis. The infinite arrays of percolation theory are interpreted as the macroscopic lattice of unreacted coal and/or char while the relatively small tar molecules may be identified with the fine clusters of percolation theory. The details of the model will be discussed together with the results obtained in modeling devolatilization behavior of coals of various ranks.

## INTRODUCTION

A model for coal devolatilization, the chemical percolation devolatilization (CPD) model, has been developed[1] that incorporates the diversity of coal structure in such a way that the analytical data obtained from solid state NMR provides some of the initial input data. Using kinetic rate parameters reported by others[2], it is possible to fit the gas, tar, and char production of a lignite (Zap), and a high volatile bituminous coal (Illinois No. 6). Percolation theory is employed to provide analytical expressions for the lattice statistics required in the devolatilization modeling. Percolation theory allows one to avoid the time consuming Monte Carlo techniques with apparently no loss of generality or important statistical features. The straight forward computational technique is very efficient even on a small VAX computer as opposed to the more time consuming Monte Carlo methods which have shown that appropriate lattice statistics are important in coal devolatilization[3].

The CPD theory analytically describes the size distribution of finite clusters of sites joined by intact bridges but isolated from all remaining sites by broken bridges. In percolation statistics a critical bridge population exists which depends only on the site coordination number, $\sigma$, above which infinite arrays will coexist with clusters of finite size. It is a simple matter to adapt the structural features of percolation theory to both the tar and gas obtained in coal pyrolysis. The infinite arrays of

percolation theory are interpreted as the macroscopic lattice of unreacted coal and/or char while the relatively small tar molecules may be identified with the finite clusters of percolation theory.

## EXPERIMENTAL

The devolatilization data is that reported by Serio, et. al.[2], for a heated tube reactor of advanced Fuel Research. The raw kinetic data was kindly supplied by Serio and Solomon. The kinetic parameters used in the model are those obtained by Serio, et. al.[2], and are given in Table I. The NMR data for the coals are from Solum, et. al.[4]. The initial and final coal specific parameters are given in Table II.

## RESULTS AND DISCUSSIONS

The details of the Chemical Percolation Model have been described by Grant, et. al.[1], and the details of the model will not be repeated. The comparison of the theoretical simulations of the experimental data are given in Figures 1 and 2 for the Illinois No. 6 and ZAP coals. The yields of gas, tar and char/unreacted-coal are given as a function of reaction time along with the corresponding predicted dynamical variables required for the simulations. The success of the simulations is thought to be good considering the number of parameters which were constrained from other work. We are engaged in an assessment of the sensitivity of the simula-

tions upon the several parameters and eventually hope with more experimental data to employ multiregressional analysis of devolatilization data as a way to determine an optimal set of parameters. The correlation matrix between the several parameters is expected to enhance our understanding of the manner in which these parameters interact to influence the model.

Several of the features observed for these diverse coals are noteworthy and warrant comment in terms of the dynamical variables required in the simulations shown in Figures 1 and 2. The contrast in the material yields in both coals is quite apparent with the light gas exhibiting the typical exponential character, while the tar release exhibits a precipitous release or "flooding" because of the non-linear percolation statistics superimposed upon the multiexponential kinetic parameters which characterize the bridge-breaking processes. Even though the activation energy used for tar formation is lower than that for light gas release, considerable light gas is produced before any appreciable amount of tar is released. The "flood" of tar observed as the lattice begins to break down dramatizes the importance of lattice statistics in the tar release process. While the qualitative features are somewhat similar in both coals, significant quantitative differences may be observed in both material yields and the dynamical variables plotted for the two coals. The relative release with time of gas and tar have similar characteristics in both coals.

The model accurately predicts the modest but measurable loss of tar weight observed in the experimental data[2] after the initial "flooding" of tar. The maximum tar weight corresponds closely in time with the complete loss of labile bridges (see Figures 1 and 2). From this point on the decrease in tar weight arises from the release of light gases through continued cracking of the side chains as the material proceeds along the heated tube reactor. The rate of gas release slows with time as the more reactive bridge material is consumed in accordance with the distributed activation energy submodel. It is worth noting that this model predicts for both coals that a reasonably large side chain population will persist in both the tar and char throughout the whole process, and as a result light gases are released until the devolatilization is terminated at the end of the reactor tube. The gas release during the latter part of the process is not due to breaking of labile bonds with the accompanying release of bridge material, as the labile bridge population is zero during most of this latter period for the cases used in these simulations. Thus, the tar cluster size is not changing during this period of the reaction, but instead, the side chains are cracking to reduce the weight fraction of both the tar and the char.

For reaction conditions under 800°C, which obtain in the heated tube reactor experiments (Serio, et. al.[2]), the model predicts that a significant fraction of side chains persist throughout the whole reaction and

still exist even at the termination of the devolatilization process. Inspection of the plots of dynamical variables indicate that it is the $\delta$ variable (side chains) which exhibits the most interesting excursions with time rising and falling in concentration in the dynamical competition for bridge material. It is interesting to note that even when all of the labile bridges have been consumed and the number of char bridges have reached their final population, the reactive side chain population is still both appreciable and changing due to cracking of the side chain material. The amount of side chain material produced in the disappearance of the labile bonds is governed in part by the amount of transferable hydrogen. Thus, the rate constant of the side chain bond breaking would include explicitly the concentration of transferable hydrogen and a good test of the model would be its ability to simulated hydroliquifaction data obtained for various partial pressures of hydrogen.

The well known gas release occurring at early times is provided by low activation energies due to the distributed activation features incorporated in the model. The model also indicates a "tar" mass fraction of a few percent present at time zero in the unheated coals suggesting the presence of extractables in coals at ambient temperatures.

Future work will focus on model refinements to include a transport model. The molecular weight distribution of the tar is provided by the model and we will compare experimental molecular weight distribution data of Suuberg[5] with the theoretical predictions of the CPD model.

## ACKNOWLEDGEMENTS

This work was supported by the Advanced Combustion Engineering Research Center (ACERC) under grant no. CDR-8522618 from the National Science Foundation and by the U. S. Department of Energy. Two authors (DMG and RJP) express appreciation for support from the Associated Western Universities (AWU) to allow them to work for a period of time as guests at the Combustion Research Facility, Sandia National Laboratories. Helpful suggestions and assistance in computing by ACERC personnel (P.J. Smith, L.D. Smoot, L.L. Baxter, and J.D. Smith) are also acknowledged.

## REFERENCES


1. D.M. Grant, R.J. Pugmire, T.H. Fletcher, and A.R. Kerstein, submitted for publication, 1988.
2. M.A. Serio, D.G. Hamblen, J.R. Markham, and P.R. Solomon, Energy & Fuels, 1987, 1, 178.
3. P.R. Solomon, D.G. Hamblen, G.V. Desphande, and M.A. Serio, 1987. International Conference on Coal Science, J.A. Monlijn, K.A. Nater, H.A.G. Chermin (Eds., Elsevier, Amsterday, 1987, p. 601.
4. M.S. Solum, R.J. Pugmire, W.R. Woolfenden, and D.M. Grant, submitted for publication, 1988.
5. E.M. Suuberg, P.E. Unger, and J.W. Larsen, Energy & Fuels, 1987, 1, 305.

## Table I

**Kinetic Parameters for Coal Devolatilization**

| Parameter | Value | |
|---|---|---|
| | Fitting Parameters | Literature Derived Values |
| $E_b$ | | 55.4 Kcal/mole |
| $A_b$ | $4 \times 10^{15}$ $sec^{-1}$ | |
| $V_b$ | 2 Kcal/mole | |
| $E_g$ | | 69 Kcal/mole<br>(69, 66, 71 Kcal/mole)[a] |
| $A_g$ | | $3 \times 10^{15}$ $sec^{-1}$<br>($3.5, 2.9, 2.6 \times 10^{15}$ $sec^{-1}$)[a] |
| $V_g$ | 7 Kcal/mole | |
| $\rho$ | 0.89 $sec^{-1}$ [b] | |

a. Weighted average values for the Illinois #6 bituminous, Rosebud subbituminous, and Zap lignite coals, respectively.

b. As $E_\rho$ and $A_\rho$ can not be determined for the relatively small devolatilization temperature range affecting these data only a single effective rate parameter for $\rho$ may be used in this fitting.

## Table II

### Coal Specific Parameters

| Parameter | Zap Lignite | Rosebud Sub-Bit | Ill #6 High Vol. Bit. |
|---|---|---|---|
| Adjustable Fitting Parameter | | | |
| $\sigma + 1$ | 8.8 (>4.4)[a] | 8.8 (>4.1)[a] | |
| Parameters Set from NMR and Ultimate Gas Yield Data | | | |
| $\sigma + 1$ | | | 4.3 (4.3)[a] |
| $p_o$ (=$\pounds_o$)[b] | 0.44 | 0.45 | 0.73 |
| $f_{gas}(\infty)$ [c] | 0.55 | 0.46 | 0.41 |
| Calculated Parameters from Fitted and Set Parameters | | | |
| $1/\sigma$ | 0.13 | 0.13 | 0.30 |
| $(\sigma + 1) \cdot p_o$ [d] | 3.9 | 4.0 | 3.1 |
| $r = m_b/m_a$ [e] | 0.28 | 0.19 | 0.32 |

a. NMR estimates for $\sigma$ given in parentheses.

b. The simulation value for $\pounds_o$, which becomes $p_o$ under the assumption of $c_o$ = zero, are estimated reasonably reliably from NMR data on the number of methyls and of side chains attached to an aromatic cluster.

c. Solomon's ultimate light gas yields may be obtained by summing the $y_i$ from i = 1 to 17.

d. This quantity measures the number of intact bridges per cluster and is calculated from the above values of $p_o$ and $\sigma$.

e. Calculated from $\sigma$ and $f_{gas}(\infty)$.

f. The NMR estimates for r given in parentheses.

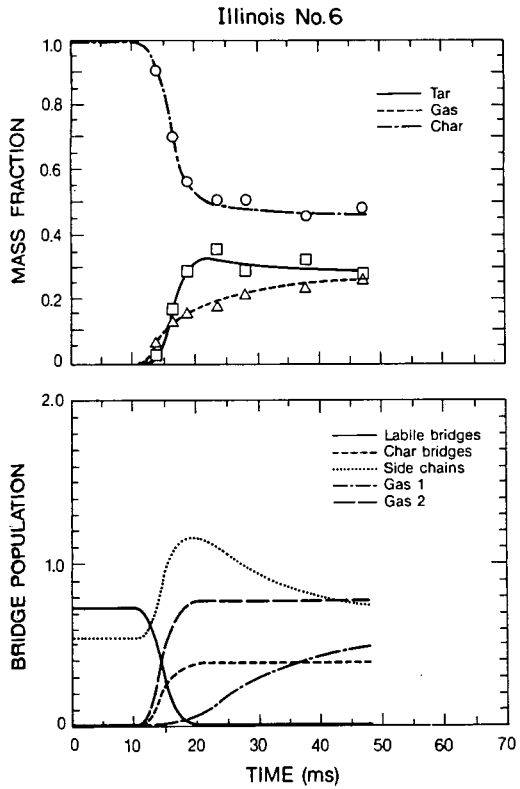


FIGURE 1. Simulation of devolatilization yields of char, tar, and light gases vs time for Illinois No. 6 high volatile bituminous coal are given in the upper plot. Experimental data are from Serio, et. al.[2]. Bridge dynamical variables are given as a function of time in the lower plot.

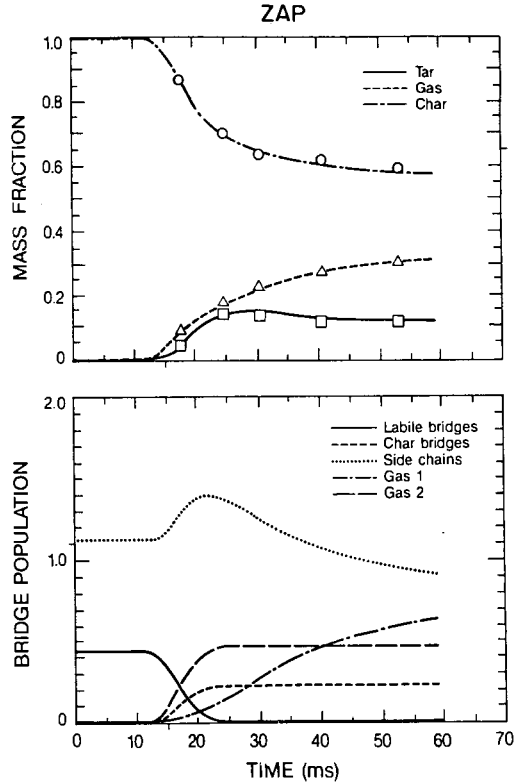


FIGURE 2. Simulations of devolatilization yields of char, tar, and light gases, vs. time for North Dakota lignite (ZAP) coal are given in the upper plot. Experimental data are from Serio, et. al.[2] Bridge dynamical variables are given as a function of time in the lower plot.

# KINETICS OF VACUUM DRYING AND REHYDRATION OF ILLINOIS #6 COAL SAMPLES. IMPLICATIONS FOR PORE STRUCTURE*

Karl S. Vorres**, Roger Kolman and Timothy Griswold
Chemistry Division, Building 211
Argonne National Laboratory
Argonne, Illinois 60439

*Work performed under the auspices of the Office of Basic Energy Sciences, Division of Chemical Sciences, U. S. Department of Energy, under contract number W-31-109-ENG-38.

**To whom correspondence should be addressed.

## ABSTRACT

The kinetics of vacuum dehydration and rehydration in nitrogen near room temperature have been studied with Argonne Premium Coal Samples. A block, -20 mesh and -100 mesh material were used. Three types of kinetic behavior were observed in dehydration and rehydration. These included a first order mass change, a combination of some or all of an initial linear, parabolic and final linear (LPL) segments, and a behavior which can be plotted to appear similar to an adsorption isotherm. The mechanisms involved in the linear-parabolic-linear sequence are tentatively assumed to be loss from macro pores, bulk diffusion, and loss of "bonded water" respectively. The rates are higher for dehydration in vacuum than for rehydration in nitrogen. The rates increase as the external surface increases from the block through the -20 mesh to the -100 mesh material.

## INTRODUCTION

Studies of oxidation of coal at ambient conditions by measurements of weight change are complicated by the mass changes due to loss of moisture. As an initial step in determining the rate of oxidation, the kinetics of moisture loss at room temperature were measured.

Drying is also one of the oldest chemical engineering unit operations. The process involves a complex interaction of heat and mass transfer (1). If the heat transfer effects are held constant in a series of experiments, then an understanding of the mass transfer effects may be gained. In the experiments to be described the experimental arrangement was maintained in order to focus on the mass transfer involved in the dehydration and rehydration.

Moisture is believed to reside in pores in the coal structure. These pores occur with a range of diameters. The diffusion from these pores would be expected to affect the drying behavior. Gan, Nandi and Walker (2) have studied coal samples with a range of ranks and observed variation in pore sizes and volumes. The rate of diffusion in and out of these pores could provide a more complete understanding of the pore and internal structure of coal, and later lead to better understanding of the kinetics of heterogeneous reactions for coal conversion.

## APPARATUS, MATERIAL AND PROCEDURE

The kinetic studies were made by placing the samples into a quartz pan, and suspending the pan inside of a quartz envelope under an Ainsworth thermobalance. The thermobalance provided electrical signals to a Bristol recorder which provided a continuous record of weight as a function of time (1" = 1 mg). The temperature was kept constant with a water bath which surrounded the sample. A weight switching mechanism provided a dynamic range of 400 mg weight change. Sample weights were in the range of 0.1 to 1 gram.

The coal samples were Illinois #6 material taken from the Argonne Premium Coal Sample Program -100 and -20 mesh material. The one-gram block was picked from a supply of material kept in chunk form, and collected at the same time and place that the Premium Sample was collected. This sample is a high volatile bituminous C rank coal with the following partial analysis:

| | | |
|---|---|---|
| moisture: | 7.97 % | |
| ash: | 15.48 % | (dry) |
| volatile matter: | 40.05 % | (dry) |
| carbon : | 77.67 % | (maf) |
| hydrogen: | 5.00 % | (maf) |

In a typical run the sample was quickly weighed, transferred to the thermobalance, and the quartz envelope placed around the sample. The recorder was started, and balance released to get an initial weight reading. The vacuum pump was used to reduce the pressure to about 200 microns inside of the envelope. A buoyancy effect was observed and correction was later made for it. The weight loss was recorded, and later reduced to a table of weight and time for computer analysis using Lotus 1-2-3 or a non-linear least squares program to provide for plots, and least squares fits for these plots. After a period of time the weight loss for the sample was extremely slow, and the dehydration was halted. Rehydration was done by stopping the vacuum pump, backfilling the envelope with dry nitrogen, removing the quartz envelope, and dropping an ice cube into it. After replacing the envelope, the apparatus was evacuated, and backfilled with nitrogen to avoid contact with oxygen. The ice cube was melted, and a water bath placed around the sample for the rehydration experiment. These experiments were also allowed to continue for up to several days. For experiments involving several cycles of dehydration and rehydration, the process was started again by removing the quartz envelope, pouring out the water, drying with acetone, blowing with dry nitrogen, and replacing the envelope as quickly as possible.

## RESULTS

The shape of the curve of mass loss or gain with time indicated a relatively rapid initial change which progressively became slower. Figures 1 and 2 indicate the weight change for the block on several cycles of dehydration and rehydration. The results of curve fitting efforts are also shown in the figures.

Similarly the changes and curve fitting for the -20 mesh material are indicated in Figures 3 and 4, while the results for the -100 mesh material are indicated in Figures 5 and 6.

## DISCUSSION

Three types of curves were observed when the mass was plotted as a function of time. Each of these involved a rapid initial loss which gradually slowed. While the overall shape of the curves was similar, the data from these experiments fit different equations, indicating differences in the rate determining steps.

The equilibrium Langmuir adsorption isotherm has a characteristic shape. The fraction of the available surface is plotted against a concentration variable such as partial pressure. This type of curve was also seen in these kinetic studies when the fraction of the moisture adsorbed was plotted against time. The amount of moisture adsorbed is proportional to the available sites. The effect of time may be seen if the time to adsorb one half of the total moisture is used as a unit. The shape of the adsorption isotherm would indicate that if the concentration of the adsorbed gas was doubled, then the amount adsorbed would increase from 1/2 to 2/3. If it were tripled then the amount adsorbed would be increased to 3/4 etc. In a similar way if the time for half sorption were doubled then the amount of sorbed gas would be increased to 2/3. The effect of doubling the time is similar to the effect of doubling the concentration. The label "adsorption" has been applied in the data analysis of data which fit this type of curve.

For a unimolecular reaction of a gaseous reactant on the surface of a solid, the rate is proportional to the fraction of the surface covered by the gas. At the beginning of the adsorption the water molecules are adsorbed on the bare surface and the rate is a maximum, governed by the vapor pressure of the water and the external surface accessible to the gas. However the equation applies over a time long enough to adsorb or desorb most of the water which implies a rapid transfer of moisture from the external surface to the interior. The rate is reduced and can be characterized by a time to reach a reduction by one half. The label "first order" has been applied to data which fit this type of curve.

The analysis of the data also indicated a behavior in which the mass change was resolved into three distinct regimes of weight loss. The initial one involved a linear weight loss with time. The second regime involved a parabolic weight loss with time, and the third regime was another linear loss with time, but with a much smaller slope than the first linear one. This was seen in the second dehydration of the -20 mesh material. The label "linear-parabolic-linear" or "LPL" has been applied to data which fit this type of curve. In some cases, such as rehydration of the block, the initial and final linear segments were very short or absent.

The <u>1.0 gram block</u> was obtained from a 5-gallon storage container kept under nitrogen. The conditions of collection and storage permitted some drying of the sample during the oxygen removal,

and transfer between containers. The initial dehydration was followed by a dehydration, and the cycle was repeated. The sample was then left under nitrogen in contact with saturated water vapor for three weeks. The subsequent (third) dehydration indicated that the sample had acquired a substantially larger amount of water than it possessed during either of the earlier experiments. A second cycle followed the dehydration. The arrows on Figure 1 indicate the relationship between the pairs of dehydration cycles.

The data analysis for the four cycles gave these results:

| Cycle | Dehydration | Rehydration |
|---|---|---|
| First: | Adsorption | Parabolic |
| Second: | Adsorption | Parabolic |
| Third: | Adsorption | Parabolic |
| Fourth: | Adsorption | Not Done |

The data analysis for the dehydration indicated that the fit was better for the adsorption type curve than either of the first order or a combination of the LPL curves. The initial portion of the adsorption curve frequently is linear on the chart paper, and is believed to involve transfer of moisture from the external surface or pores. The weight change required for a monolayer of moisture as typically determined by nitrogen adsorption is about one half milligram per gram of coal. The actual loss is larger than this by an order of magnitude, indicating that the surface moisture is replenished by large open pores. The further loss of moisture is assumed to involve a "bulk diffusion" mechanism. For a solid with a consistent set of pores or defects for diffusion a parabola is observed in a plot of weight change with time. The lack of a fit to a parabolic curve and more rapid decrease in rate than predicted from a parabolic fit is believed to be due to either to diffusion from progressively smaller pores with smaller diffusion constants or to blockage of pores. The data also indicate that the rate is dependent upon the amount of water which is available in the particle. This was especially noticeable after the extended rehydration between the second and third dehydration. The pores were not irreversibly collapsed but were able to accumulate a larger moisture content than was present at the beginning of the experiment. This amount exceeded the ASTM moisture determination.

The analysis for rehydration indicated a better fit for the parabolic equation. The rate for rehydration is significantly less than for dehydration. The minimal amount of linear contribution to the initial mass change indicates that the external surface was quickly covered and subsequent reaction was limited by diffusion through a growing interface layer. This layer may have been a set of blocked pores. The external surface is a minimum for a sample which is a single particle.

The <u>-20 mesh sample</u> was 0.100 grams of a supply kept in a plastic bottle filled from incompletely sealed ampoules. The material had been exposed to the drier atmosphere in the laboratory. The initial dehydration did not remove much moisture since much of it had already been lost. The rehydration restored a considerable amount of the moisture content, and led to a higher rate and a modified curve shape (LPL) for the second and third dehydrations.

The rehydration rates showed a very similar set of curve shapes, and a gradually diminishing rate due to progressive internal changes. Although the curve shapes for the rehydration were similar, the agreement with the adsorption type curve was clearly better than first order for the first two curves, and somewhat better for first order for the third curve.

The data analysis gave the following results:

| Cycle | Dehydration | Rehydration |
|---|---|---|
| First: | First order | Adsorption |
| Second: | Linear-Parabolic-Linear | Adsorption |
| Third: | Linear-Parabolic-Linear | First order |

The three regimes in the second and third dehydration indicate that three mechanisms of water loss were occurring during the dehydration. The initial linear loss is believed to be due to the loss of surface water from the external surfaces and macro pores. The parabolic weight loss is believed to be due to bulk diffusion from the coal of "dissolved" water. This water is believed to be caught in very small cavities or imperfections in the packing structure of the coal. These cavities can provide a temporary site for molecules as they diffuse from the bulk to some surface accessible to the external pores. The dynamic motion of the coal "molecules" may permit the opportunity for the water molecules to migrate from one site to another on the way to the external surface. The third regime, involving the second linear portion is believed to be due to the release of water from sites involving "bonded water". The low temperature provides relatively little thermal energy to permit release of the water, but enough to permit a measurement.

Assuming that the pores are filled with water, one can obtain a measure of the macro pore volume by calculating the moisture loss per gram of coal, and using the density of water. Similarly, one can obtain a measure of the "dissolved" water" by noting the weight of the water lost during the parabolic part of the total weight loss curve, and calculating the loss per gram of coal. Again, in a similar way, one could make the calculation for the "bonded water". This portion would represent the water tied to functional groups, or hydrogen bonded.

The first type of water should be "freezable" while the latter two should not have the properties to permit observation of freezing behavior. Freezing is a bulk property, and would require a number of molecules to demonstrate the existence of a solid crystalline material. Individual molecules, separated from other similar molecules would not be able to demonstrate this behavior.

The <u>-100 mesh material</u> was a 0.239 gram sample which had been equilibrated with water for at least 5 days at room temperature. The two dehydration runs fit the adsorption type curve. The two rehydration runs initially followed this type of curve, but later exhibited a more rapid rate and departure from the curve. This behavior is indicative of multilayer formation in the type IV adsorption isotherm, and may indicate a similar phenomenon here. The rates for the second dehydration or rehydration are lower than those for the first run in the cycles. The incremental

change in weight with time toward the end of the run is greater for the second run indicating a tendency to continue and possibly achieve a similar weight gain or loss over a very extended time. For these samples the initial dehydration proceeded with a higher rate than the second. The sample did not take up as much water during the rehydration as it lost during the initial dehydration.

The data analysis gave the following results:

| Cycle | Dehydration | Rehydration |
|---|---|---|
| First: | Adsorption | Adsorption + multilayer? |
| Second: | Adsorption | Adsorption + multilayer? |

## CONCLUSIONS

The rates of dehydration and rehydration near room temperature are complex. The specific form of the equation describing the rates varies depending on the particle size and history of the sample. Several rate equations can be used to provide a "best fit" to all of the data. Blocks of vacuum dried coal will continue to absorb significant amounts of water over a period of weeks at room temperature. The pores in the block were not irreversibly collapsed in a manner that prevented restoration of the moisture content.

The rate of dehydration in vacuum for a given sample is faster than the rate of rehydration in nitrogen. The presence of nitrogen apparently interferes with the rehydration.

The vacuum dehydration of the block of coal followed a first order curve. This is consistent with loss of moisture from the equivalent of a surface with all of the moisture initially upon it. The rehydration of the block follows a parabolic curve, which is consistent with a diffusion controlled process . This would be observed if the moisture diffused into the block through a layer which consisted of swollen pores, and the pores continued to swell as the moisture continued to diffuse. The behavior of the block is believed to represent the behavior of an independent particle. The -20 mesh vacuum dehydration followed a first order curve for most of the vacuum dehydration and one rehydration in nitrogen. The initial two rehydrations followed the adsorption type curve. This behavior is consistent with the limitation on moisture loss due to a transfer from a surface with all of the moisture initially on it, or surface sites equally accessible during rehydration. The appearance of the LPL sequence indicates that the rehydration put enough moisture back into the sample to allow some differentiation of the several mechanisms that were operative. Rehydration initially indicates adsorption to saturate the surface,and may be augmented by particle-particle interaction. The behavior of this sample is believed to reflect the behavior of a sample consisting of many small particles, and which has been exposed to some drying and atmospheric oxidation. The -100 mesh samples had been equilibrated with moisture, and showed an adsorption type of curve on both dehydration and rehydration. The initial steep part of the curve is attributed to the saturation of the surface with moisture. The moisture may be going to junctions between particles. The rehydration curves show evidence for multilayer adsorption as part of their shape.

The behavior of this sample is believed to reflect the behavior of a sample which consists of small particles, has been protected from oxidation and has been given an opportunity to adsorb moisture to achieve near equilibrium at the experimental temperature.

The use of several equations to give a fit to the data prevents a direct comparison of rates. However, one can rank the rates for the different particle sizes by establishing the time required to lose or gain half of the moisture over a reasonably long period of the experiments to be compared. If it is assumed that the -20 or -100 mesh particles would behave in the same manner whether 0.1 or 1 gram were used, then the rates are dependent on particle size, and increase from the block through -20 mesh to -100 mesh. This behavior indicates that the external surface area is important in the overall rates for both dehydration and rehydration.

## FUTURE WORK

It is intended to extend this work to the full set of the Argonne Premium Coals over a range of temperature to establish the similarity in behavior, effects of rank, and observe any special behavior that may be found for the low rank coals due to gel structure that may be present in them. In addition it is intended to observe the weight changes following vacuum drying upon introduction of other gases including those which are normally used to establish the surface area.

## ACKNOWLEDGMENTS

The authors gratefully acknowledge the support of the Office of Basic Energy Sciences, Chemical Sciences Division, and the Argonne National Laboratory Division of Educational Programs. The glassblowing by Joe Gregar is particularly appreciated. Useful discussions with Anthony Fraioli are also acknowledged.

## REFERENCES

1. Marshall, Jr., W. R. in Reaction Kinetics and Unit Operations, Chem. Engr. Progress Symp. Ser. 55, (1959), pp. 213, American Inst. of Chem. Engrs., N.Y.

2. Gan, H., Nandi, S. P., and Walker, Jr., P. L., Fuel, 51, 272(1972).

## FIGURE CAPTIONS

These are as indicated. Weight change in milligrams is plotted on the vertical axis, and time in minutes on the horizontal axis. Symbols indicate observed points. Lines indicate calculated values for the curves indicated in the text. The numbers adjacent to the curves indicate the cycle.

Figure 1.

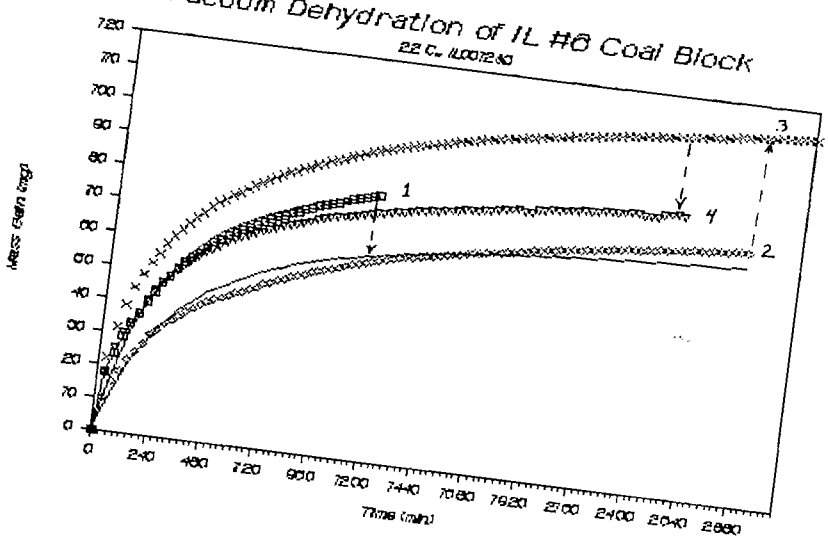


Figure 2.

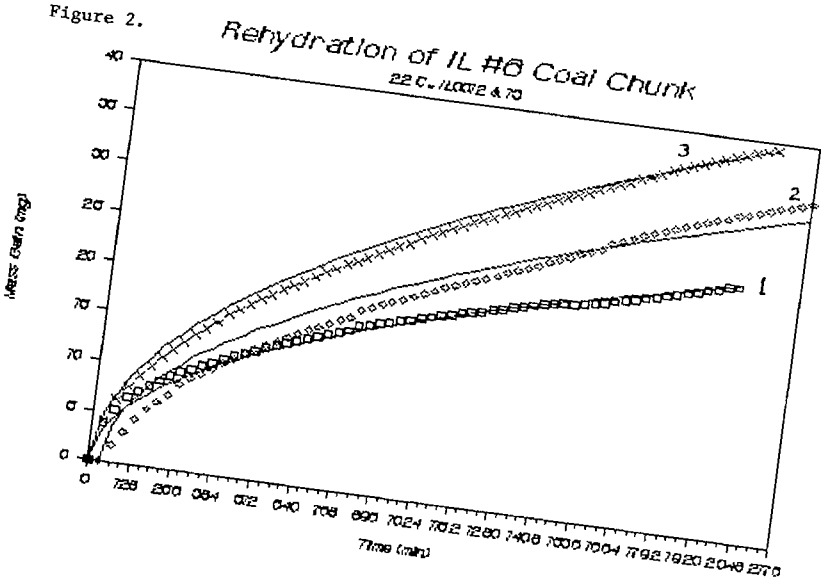

Figure 3. Vac. Dehydration IL#6, −20 Mesh

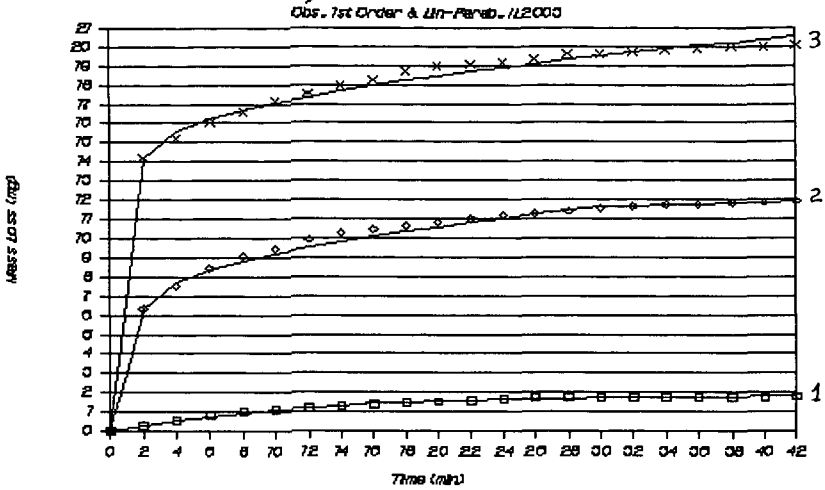


Figure 4. Rehydration of IL#6 in N2, −20 Mesh

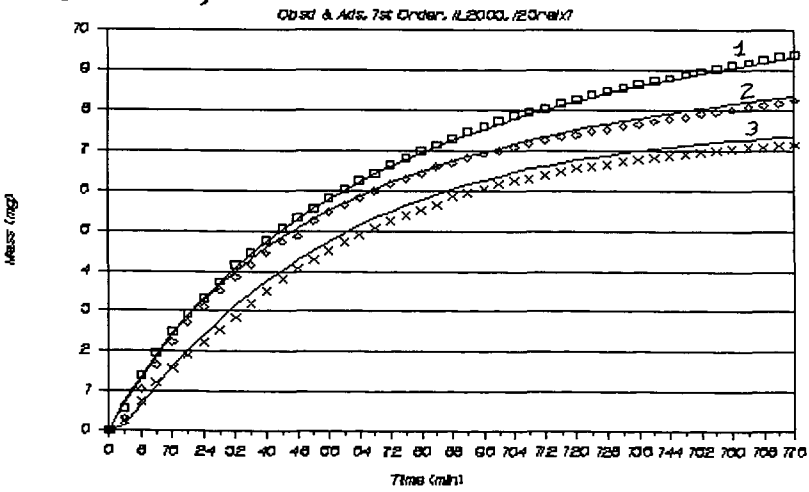

Figure 5. Vac Dehydration of IL #6 -100 Mesh

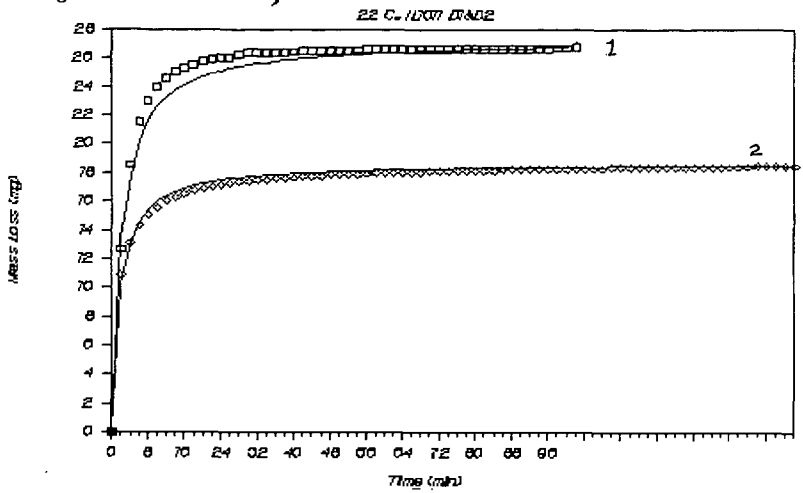


Figure 6. Rehydration of IL #6 -100 Mesh in N2

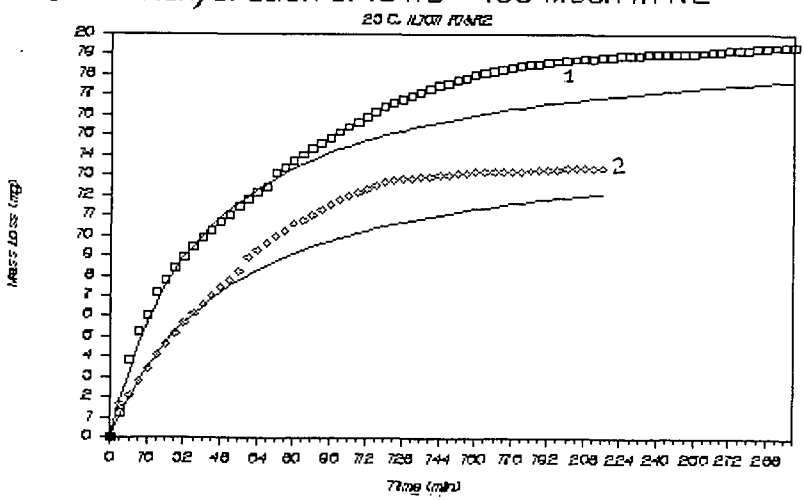

# Macromolecular and Chemical Changes Induced by Air-Oxidation of a Medium Volatile Bituminous Coal

Donald Schwartz[1], Peter J. Hall[2] and Harry Marsh,

Northern Carbon Research Laboratories,
School of Chemistry, Bedson Building,
University of Newcastle upon Tyne,
Newcastle upon Tyne, NE1 7RU, U.K.

[1]University of Colorado at Colorado Springs,
Department of Chemistry,
Colorado Springs, Colorado 80907, U.S.A.

[2]Division of Engineering,
Brown University,
Providence, Rhode Island, U.S.A.

## INTRODUCTION

The heterogeneity of coal, together with its complex macromolecular nature, has been responsible for much of the difficulties in elucidating its structure and chemical characterization. Most methods of investigation of the chemical structure and physical properties involve breaking macromolecules into smaller fragments by depolymerization, oxidation, reduction, dehydrogenation, acetylation, etc., which, for the most part, solubilizes a major fraction of the coal while trying to preserve as much of its original structure as possible. Depending upon the rank of coal and the solvent used, more than 80% of some coals have been solubilized.

Efforts have been made to study the macromolecular structure of coal as a complete entity with special emphasis on cross-linkages. Techniques are limited but swelling and Differential Mechanical Thermal Analysis (DMTA) have proved to be powerful tools in this important area. Although analyses of chemical fragments and macromolecular studies can give complementary information, neither approach alone can lead to final conclusions. No attempt is reported in the literature to simultaneously undertake both solubilization and macromolecular analyses. This paper reports the results of such an attempt. Air oxidation was chosen to modify the coal structure for several reasons.

Elliott (1) reviews the contributions made to the understanding of coal chemistry by researchers using destructive oxidation to reduce the macromolecular structure of coal to entities that can be explored with available instrumentation and known analytical procedures. Since air causes the natural oxidation of coal and because there is little chance that any atoms other than oxygen can be introduced into the coal molecule when it is used as the oxidant, only air was used for the oxidations in this study. The experiments were carried out at 200°C because no weight loss was observable upon heating in nitrogen at or below that temperature.

There have been many studies undertaken to determine the extent of cross-linking in the coal structure (2, 3). Most investigators believe that the more highly cross-linked the coal structure is, the less it will swell when contacted with an organic solvent. Liotta (4), using tetrahydrofuran on weathered coal, showed that swelling decreased as the time of weathering increased. However, if the nature of the cross-links are such that hydrogen bonds are responsible for much of the cross-linking, then work by Hall, et al., (2) suggests that attack by

a basic solvent may result in an increase in swelling.

The problem of understanding the structure of coal is a complex one. It must be remembered that different coals react differently to reagents. The results that are reported in this paper may be applicable to other coals of similar rank and even coals of different ranks, but no such assumption is made in this study.

It is the purpose of this paper to not only provide researchers with additional insight into the macromolecular structure of coal and its chemical characterization, but also to demonstrate that a concerted effort using a variety of techniques on coal and its oxidation products, can make an important contribution to coal science.

## EXPERIMENTAL

### Coal Characteristics

The coal sample used in this investigation was a Cortonwood coal from the Silkstone seam furnished by British Coal (NCB Coal Rank Code 501, ISO Classification 634) ground to µm size. Important characteristics of the coal are summarized in Table 1.

### Coal Oxidation

The coal was oxidized in air for one, two, four and six day periods at 200°C in a forced circulation oven.

### Humic Acid Preparations

Water-insoluble samples of the oxidized coal were extracted with 0.1 M NaOH and precipitated with 0.1 M HCl. Centrifugation at 3500 rpm was used along with filtration to speed the recovery of the humic acids. Considerable washing with distilled water removes any NaCl or HCl absorbed on the humic acids. The humic acids were dried at 105°C.

### Infrared Spectra of Coals

All spectra were recorded on a Nicolet 205 SXB FTIR spectrometer using KBr pellets. All samples submitted were dried at 105°C.

### Volumetric Swelling Technique

The technique perfected by Green, et al., (5) of the procedure developed by Liotta, et al., (4) for measuring swelling was used. In this technique, µm coal samples were centrifuged at 3500 rpm in 6 mm tubes to ensure tight packing. The height of the coal column was measured to ±0.01 mm using a cathetometer. Excess solvent was added. The ground glass stoppered tubes were shaken every 12 hours until equilibrium was reached. Constant height readings of the coal column indicated equilibrium. After equilibrium, the tubes were again centrifuged and the height of the coal column measured. The swelling ratio, Q, is equal to the height of the swollen coal divided by the height of the unswollen coal. Reproducibility was found to be ±0.05 which is in agreement with that of Green (5) and Hall (2). To examine the structure of the coal hydrogen bonding and how it changes on oxidation, swelling was carried out in a set of sterically similar substituted pyridines of differing basicity. Hall, et al., (2) have shown that the weaker bases swell coals by dissociating weak hydrogen bonds from the macromolecular network while the stronger bases swell coals by dissociating stronger

bonds from the structure. A plot of coal swelling (Q) against the pKb of the solvents gives an indication of the hydrogen bond energy distribution of the coal.

## Thermal Gravimetric Analyses

A Stanton Redcroft STA-780 Series Thermal Analyser was used for thermal gravimetric analyses. Sample masses of 12-26 mg was used, with heating rates of approximately 6°C to 20°C $min^{-1}$ in nitrogen at temperatures from room temperature to 1000°C.

## Petrographic Techniques

Reflectance was measured at 546 nm using oil immersion objectives (n=1.518 at 23°C) on a Leitz MPV3 Microscope Photometer. The photocathode was an EMI S-11. The samples were mounted in epoxy resins and were ground and polished according to the procedures prescribed by Stach, et al., (6). Twenty-five measurements were recorded for each sample in polarized light.

## Results and Discussional

### Humic Acid Formation

A series of experiments were carried out to determine the rate of oxidation in terms of humic acid formation as a function of time of oxidation. Table 2 and Figure 1 shows the yields of humic acid formation versus time of oxidation while Figure 2 shows a plot of the rate of humic acid production versus time of oxidation. From Figure 2, the maximum rate of humic acid formation should occur at 2.33 days. Of the four periods of oxidation used in these experiments, oxidation for two days showed the maximum yield.

The nature of the humic acids obtained from each of the samples oxidized for various lengths of time showed no functional group differences--as evidenced by infrared analyses. The spectra were characterized by the very broad bands covering C–H and O–H stretching frequencies at the 2500 $cm^{-1}$ to 3500 $cm^{-1}$ region; the $COO^-$ absorption at 1709 $cm^{-1}$; aromatic and/or hydrogen bonded carbonyls at 1604 and 1216 $cm^{-1}$; and the shoulder at 1376 $cm^{-1}$ usually assigned to phenolic O–H.

Upon petrographic examination, the humic acids appeared to be isotropic with a random orientation as evidenced when inserted in cross polars with a full wave length retarder plate. The colours were invariant purple during rotation of the stage. The reflectivity did not change on stage rotation using plane polarized light. No pyrite was visible in the humic acids. Large curved cracks from swelling and shrinking were evident. The surface was rather soft, probably due to the sample being polished with relief. The reflectivity was lower than the coal, in the 0.85 range. No visible fluorescence was noticed under ultra violet excitation. To the naked eye, the humic acids appeared to be a black, crystalline solid.

Because of the relative non-volatility of the coal as well as the humic acids, mass spectrometry did not provide useful data in this investigation. Instrument limitations prevented analyses beyond 300°C and thermal gravimetric analyses demonstrated that there was little or no weight loss of the coal below 400°C.

The oxidized coal residue, resulting after the humic acids were extracted, emitted a yellow-brown fluorescence under ultraviolet and blue wavelength excitation during observations made when using fluorescence microscopy indicating the presence of aliphatic hydrocarbons. A considerable amount of pyrite was visible when

viewed under polarized light in various states of preservation, ranging from pristine to a severely oxidized orange state. It appeared that 25-30% of the residue of the sample that was oxidized for six days was pyrite. Byers (7) presents an in-depth discussion of the problems caused by pyrites in coal during furnace operation. Although washing and float and sink methods have had some success in removing pyrites from many coals, small particles usually get into the furnace resulting in high sulphur emissions, slagging and furnace problems. Air oxidation at relatively low temperature followed by an alkaline wash may enhance pyrite removal from coal.

## Swelling as a Result of Oxidation

In the experiments carried out in this study, evidence is presented to indicate that basic organic solvents can effect cross-linkages caused by oxidation because of the formation and destruction of hydrogen bonds.

The effect of oxidation on the hydrogen bond structure can be interpreted from Figure 3. There is an initial increase in swelling from the fresh coal to the one day oxidized coal suggesting an initial increase in all strengths of hydrogen bonding. Oxidation from one to two days reduces swelling in the weaker bases (pKb<8) but increases swelling in the strongest base. This suggests that weak hydrogen bonds are being eliminated from the structure and hydrogen bonds are being formed that are not susceptible to attack by pyridine. Further oxidation does not change the density of weak hydrogen bonds to any great extent but swelling in the two strongest bases increases, which implies an increase in the density of strong hydrogen bonds in the structure.

When this data is coupled with the increase of humic acid yield on oxidation the implication is that initial oxidation (up to two days) attacks the alkane and cycloalkane groups, changing these into hydrogen bond crosslinks which are relatively weak and can be broken by the weaker bases. Further oxidation (after two days) is associated with significant production of humic acids. Humic acids have large concentrations of carboxylic acid groups and such groups may lead to strong hydrogen bonding in the coal matrix.

Infrared studies appear to support the data obtained from swelling studies. The oxidation of the coal to form humic acids appears to be due in part to the oxidation of aliphatic groups. The intensity of the alkyl group band at 2900 $cm^{-1}$ is diminished considerably after one day of oxidation. Under petrographic study, increases in the vitrinite reflectance along with increased reflectance of the exinite may be due to increased aromaticity as the coal is progressively oxidized for one and two days. After two days, further oxidation decreases the reflectance indicating the possible attack on aromatic structure. Table 3 shows the reflectance data for the unoxidized and oxidized coals and Figure 4 shows the plot of the data. Figure 5 shows the histograms. Thus it appears that initial oxidation attacks both the alkane and cycloalkane structure of the coal, some of which act as cross-linkages to aromatic clusters. The Cortonwood coal has a relatively high H/C ratio when compared to most medium volatile bituminous coals. The strong hydrogen bonds appear to be associated with the high density of carboxylic acids that are present in the humic acids. The infrared spectra of the unoxidized and oxidized coals show a strong band formed at 3418 $cm^{-1}$ and another strong band at approximately 1700 $cm^{-1}$ appearing after oxidation for one day indicating humic acid formation. The 3418 $cm^{-1}$ band is characteristic of strongly hydrogen bonded OH groups (8) and the 1700 $cm^{-1}$ peak is characteristic of $COO^-$ formation (9, 10, 11, 12). The intensity of the alkyl band at 2900 $cm^{-1}$ present in the spectra of the original coal is diminished considerably after one day of oxidation.

Using thermal gravimetric analyses, it can be demonstrated that the weight loss upon heating the unoxidized Cortonwood coal in nitrogen from 105°C to 200°C and maintaining the sample at 200°C for five minutes resulted in no weight loss. It is interesting to note that no appreciable weight loss occurred when pyrolysing the coal under nitrogen until over 400°C. Only about 32% of the coal is ever volatilized at temperatures up to 950°C. Figure 6 shows the results of the thermal gravimetric analyses of the unoxidized coal. The sample lost less then 1.9% moisture upon heating from room temperature to 105°C.

## SUMMARY

Air oxidation of a medium volatile bituminous coal at 200°C for six days yields 85% by weight humic acids. The rate of oxidation increases to a maximum at 2.33 days and decreases in a Gausian distribution. The humic acids are characterized by their infrared spectra showing a strong band at 1709 $cm^{-1}$ for the $COO^-$ group, the strong band at 1604 and 1216 $cm^{-1}$ indicative of aromatic and/or hydrogen bonded carbonyl, and a shoulder at 1376 $cm^{-1}$ usually assigned to phenolic OH. Oxidation of coal results in the formation and destruction of hydrogen bonds. Hydrogen bonds form as humic acids are produced from the oxidation of alkyl and alicyclic cross-linkages in the macromolecular structure. Weak hydrogen bonds, already existing in the coal and formed during the oxidation are attacked by pyridine and lead to swelling. Substituted pyridines having $pK_b$ values higher than pyridine are able to break stronger hydrogen bonds in the oxidized coals. Petrographic studies and thermal gravimetric analyses support the information generated by the data gathered from swelling experiments and infrared absorption investigation.

## ACKNOWLEDGEMENTS

The authors wish to thank Miss Nina Skorupska, Mr. Stephen Bend, Miss Lynda Jones and Mrs. Christine Morris for their assistance with the petrographic studies. Also, they wish to thank Mr. Oean Field for his assistance in the thermal gravimetric analyses.

## REFERENCES

1. Elliott, M.A., "Chemistry of Coal Utilization", John Wiley & Sons, 1981, p. 455-469.
2. Hall, P.J., Marsh, H. and Thomas, M.K., submitted to Fuel.
3. Korov, N.Y., O'Shea, J.M. and Sergeant, G.D., Fuel, 1967, 46, 415.
4. Liotta, R., Brown, G. and Isaacs, J., Fuel, 1984, 63, 935.
5. Green, T.K., Kovac, J. and Larson, J.W., Fuel, 1984, 63, 935.
6. Stack, E., Mackowsky, M-Th., Teichmuller, N., Taylor, G.H., Chandra, D., and Teichmuller, R., "Stack's Textbook of Coal Petrology", Gebruder Borutraeger, 1982, p. 295.
7. Byers, R.W., "The Physical and Chemical Characteristics of Pyrites and Their Influence on Fireside Problems in Steam Generators", ASME Paper No. 75-WA/CD-2, 1975.
8. Silverstein, R.M., Bossler, G.C., and Morrill, T.C., "Spectrometric Identification of Organic Compounds", 3rd Edition, John Wiley & Sons, 1974, p. 91.
9. Painter, P.C., Snyder, R.W., Pearson, D.E. and Kwong, J., Fuel, 1980, 59, 282.
10. Chang, K.K., Flagan, R.C., Gavalas, G.R. and Sharma, P.K., Fuel 1986, 65, 75.
11. Rhoads, C.A., Senftle, J.T., Coleman, M.M., Davis, A. and Painter, P.C., Fuel, 1983, 62, 1387.
12. Starsinic, M., Otake, Y., Walker, P.L. and Painter, P.C., Fuel, 1984, 63, 1003.

Table 1
Characteristics of Cortonwood Coal

| Proximate Analysis (as determined) | wt.% |
|---|---|
| Moisture | 1.0 |
| Ash | 2.2 |
| Volatile Matter | 34.7 |
| Fixed Carbon | 62.1 |
| **Ultimate Analysis (dry mineral matter free basis)** | |
| Carbon | 87.20 |
| Hydrogen | 5.60 |
| Oxygen (diff.) | 3.9 |
| Nitrogen | 1.70 |
| Sulphur | 0.70 |

Table 2
Yield of Humic Acids

| Time of Oxidation (days) | Yield of Humic Acids (%) |
|---|---|
| 1 | 3.4 |
| 2 | 18.8 |
| 4 | 78.7 |
| 6 | 85.8 |

Table 3
Reflectance of Unoxidized and Oxidized Cortonwood Coal

| Time of Oxidation (days) | Reflectance (% $R_{mean}$) | Standard of Deviation |
|---|---|---|
| 0 | 0.91 | 0.07 |
| 1 | 1.15 | 0.09 |
| 2 | 1.27 | 0.07 |
| 4 | 1.19 | 0.08 |
| 6 | 1.10 | 0.08 |

Figure 2. Rate of Humic Acid Production vs. Time

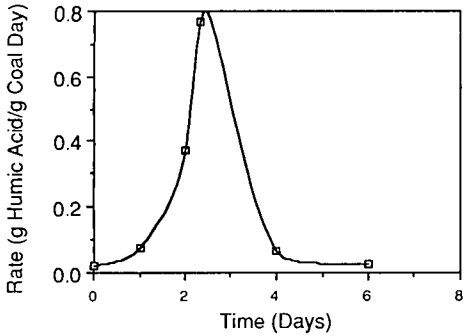


Figure 1. % Humic Acid Production vs. Time

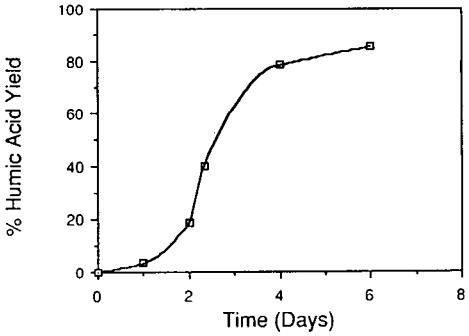

Figure 3. The Effect of Oxidation on Cortonwood Swelling

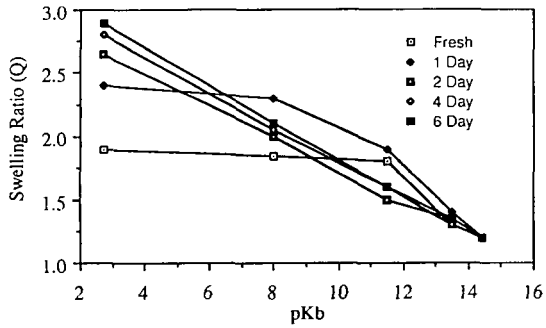


Figure 4. Reflectance vs. Time of Oxidation

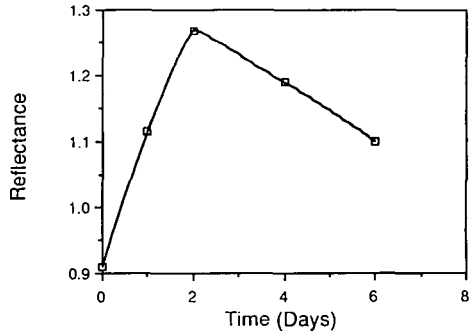

Figure 6. TGA of Cortonwood in Nitrogen

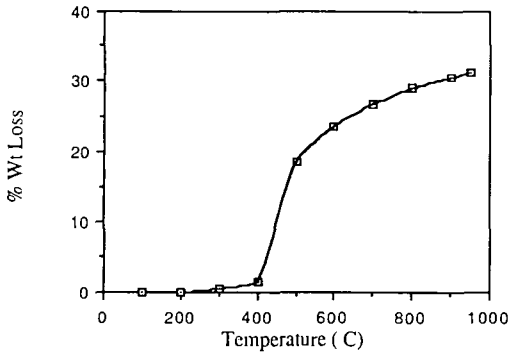


Figure 5. Reflectance Histogram of Unoxidized and Oxidized Cortonwood Coal

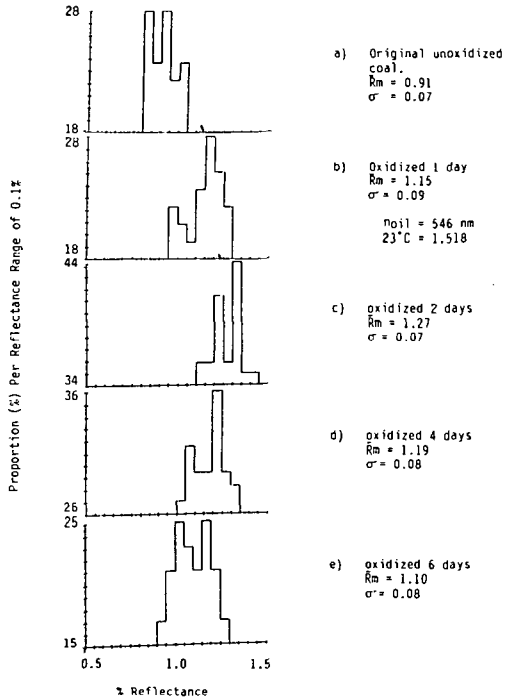

# BENEFICIATION OF A BITUMINOUS COAL AND A LIGNITE COAL BY AGGLOMERATION USING NOVEL BINDING OILS.

R.C. Timpe, C.L. Knudson, P. Mack,

University of North Dakota Energy and Mineral Research Center
P. O. Box 8213, University Station
Grand Forks, ND 58202

## ABSTRACT

Illinois #6 and both as received and hot water dried Zap (IndianHead) North Dakota lignite were agglomerated with Mandan refinery decant oil containing either p-xylene or deodorized rectisol naphtha from the Great Plains Gasification Plant. The effectiveness of each of the binding oils on agglomeration was determined from ash reduction and organic recovery as a function of mixing speed, mixing time, particle size, and oil-to-coal ratio. Results indicated that, although the ash reduction was significant in the Mandan decant/rectisol naphtha binder for both coals, greater reduction was achieved with the Mandan decant/p-xylene. Higher mixing speeds, longer mixing times, smaller particle size, and binder to coal ratio of 0.35 gave the greatest ash reductions. Agglomeration time was shortened substantially when either p-xylene or rectisol naphtha was added to the Mandan decant in place of using Mandan decant alone as binder.

## INTRODUCTION

With the recent effort to educate the world's population on the wise use of the dwindling petroleum reserves and the associated emphasis on coal utilization, the world's supply of high quality, easily mined, low ash coal has also begun to dwindle.(1) Finding new, more efficient methods of beneficiation of higher ash coals has become a priority in coal research. Among the most widely used methods of fine coal beneficiation at present is froth flotation. Although the technique works quite well with higher rank coals and fines with larger particle sizes and low ash, it does have some drawbacks, among them comparatively low yield and high moisture content of product when fines are <76 μm and have high ash content. In addition, the lower rank, more readily mined coals and oxidized coal surfaces are not amenable to beneficiation by flotation. A promising complementary and possibly alternative technique is oil agglomeration.(2)

Agglomeration studies of lignite and subbituminous (low-rank) coals have not met with a great deal of success primarily because the experiments have centered around the successful techniques used to agglomerate bituminous coal. Since agglomeration is a surface phenomenon, the binding oil selected to form the aggregates of fines must be compatible with the surface functional groups on the fines. Most oils used for this purpose are oleophilic and as a result are readily adsorbed to the surface of the coal particles provided they have minimal polar groups exposed. This is characteristic of the bituminous coals but not of the lower rank coals. The subbituminous and lignite coals contain large amounts of surface oxygen making their surfaces more oleophobic than the bituminous. Since the theory of agglomeration assumes mineral material is considerably more hydrophilic and oleophobic than the organic coal matrix, the mineral material will dissolve or form a suspension in an aqueous medium and the organic matter will form aggregates and separate from that phase. Again, this is true for the coals of higher rank but not for the lower rank coals with their more polar, hydrophilic surfaces. The focus of this study was to investigate the agglomeration of a well behaved bituminous coal and a lignite coal when light organic compounds and lower value streams from a petroleum refinery and coal gasification plant are used as

binding oils. The reduction in ash content in the coal was studied as a function of particle size, mixing conditions, and oil characteristics.

In a successful agglomeration, the mineral content of the coal will be reduced significantly as the coal forms aggregates of organic rich material and the minerals are suspended in the aqueous phase. The degree to which a coal can be beneficiated by agglomeration is limited by several factors. The first is the particle size. The finer the particle size the more liquid solid surface contact and, consequently, the better are the chances of the carbonaceous material liberating its associated minerals thus lowering the ash content (3). Although fine grind enhances inorganics removal, it creates problems in handling the cleaned product and provides more area for undesireable surface reactions with oxygen. Effective agglomeration following ash reduction helps to solve these problems.

The second factor to be considered is the composition of the oil used as a binder. Light agglomerating oils (density < 0.90 g/cc) have been shown to give ash reductions in bituminous coals within 10 to 20 percent of those obtained with the Stoddard solvent (4). These oils, however, do not wet the surface of low rank coals well, and are not useful as binding oils for these coals. If heavier oils such as coke oven tars, pitches, and petroleum crudes are used, low-rank coals can be agglomerated, but these oils are more difficult to recover for reuse (4).

pH is a third consideration when carrying out agglomeration. Removal of most mineral material can be done with pH adjustment. However, with elements such as pyritic sulfur which is best removed at a pH between 7-11 the coal becomes more hydrophilic and agglomeration is less effective, requiring multiple pH adjustments to get maximum ash removal and agglomerate size and to reduce agglomeration time (1). Table 1 shows the ash content of the coal used in this study.

TABLE 1.
Agglomeration Test Coals

| Sample | Mesh(70 wt %) | Ash mf(wt %) |
|---|---|---|
| Illinois #6 | 200 | 12.75 |
| Illinois #6 | 325 | 24.85 |
| Indian Head (AR) | 325 | 14.63 |

The size of the agglomerates produced is a function of such processing variables as mixing speed, mixing time, mixer design, and solvent to coal ratio. Physical impact forces result in reduced agglomerate sizes with increased mixing speed and mixing time and contact with surfaces of smaller surface areas such as blade edges.(5) To minimize these impacts a blunt stir bar providing maximum contact area between agglomerates and bar is recommended. Thorough agitation may increase the yield but not necessarily the size of the agglomerates. Increasing the ratio of binding oil to coal tends to increase agglomerate size, making binding oil recovery an economically important aspect of this method of beneficiation (6). Recovery of 40 to 50% of the binding oil by thermal treatment under reduced pressure maintains the calorific value of the product, decreases the moisture content, increases mechanical stability, and results in reduction of selfignition hazards.

## EXPERIMENTAL

Agglomeration tests were carried out on as-received Illinois #6 bituminous coal and an as-received and a hot water dried North Dakota lignite from the Indian Head mine. The coals were ground to 70 wt% 200 mesh (75 $\mu$m) and 325 mesh (45 $\mu$m).

The percent ash values on a moisture free basis are shown in Table 1.

Screening tests were carried on nine different liquids to determine the most suitable binding oil for agglomerating the test coals. The oils tested included Lummus Arabian and Lloydminster petroleum resids, North Slope ATB, Mandan Decant oil, Mayan crude, rectisol naphtha, JP4 aviation fuel, 1 octanol, and p-xylene. The Mandan crude exhibited better agglomerating results than the other oils for both the bituminous and the lignite coals. The binding oils selected for this study were Mandan Decant oil (MDO) from the Amoco refinery at Mandan,North Dakota, and mixtures of MDO with p-xylene (MDO/XY) or rectisol naphtha (MDO/RN) from the Great Plains Gasification Plant at Beulah, North Dakota. The solvent mixtures were 50 wt % Mandan Decant oil in either p-xylene or rectisol naphtha.

The laboratory experiments were carried out in both large and small scale mixers. The small scale experiments (called micro agglomeration) consisted of stirring 0.50 g coal, 0.15 to 0.35 g of oil, and 10 g H20 at 10,000 to 21,000 revolutions per minute (rpm) in a micro-agglomeration cell for measured time periods.

A variable speed blender with a fabricated bar propeller stirring rod was used to carry out the larger scale experiments. Five hundred ml of deionized water was poured into a stainless steel mixing cup. The weighed binding oil was poured into the cup and the oil and water mixture was stirred at 10,000-20,000 rpm for several minutes prior to introducing the weighed coal sample into the unstirred mixture. The water, oil, and coal was stirred at the above rate for from 1 to 6 minutes.

Following the stirring, the inherent pH of the slurry was measured using pH paper. (The effect of pH adjustment on the agglomeration was not included as part of the study reported here but instead is included in the work currently underway.) The slurry was then poured over a 100 mesh screen to collect the agglomerates. 500 ml of deionized water was used to rinse the agglomerates and then they were extracted with 100 ml tetrahydrofuran (THF), filtered under vacuum, and air dried over night. Moisture and ash content were then determined.

RESULTS AND DISCUSSION

The initial experiments were carried out with Mandan decant oil pxylene on the Illinois #6 bituminous coal since previous agglomeration work has been successful with this coal rank. Micro- and large-scale agglomeration experiments produced agglomerates which differed in size and texture with different solvent to coal ratios, mixing speeds and mixing times. A satisfactory solvent to coal ratio for agglomeration of the bituminous coal with Mandan decant oil was determined by first investigating the agglomerating properties of the oil itself and then by comparing those properties with those of dilutions of decant oil with p-xylene. Rectisol naphtha, a light oil stream obtained from the commercial coal gasification plant at Beulah, North Dakota, was substituted for the p-xylene in some of the later experiments. The ash content of the agglomerates formed in this solvent was determined and compared with that of agglomerates formed at the same conditions using the MDO p-xylene.

The characteristics of the agglomerates apparent to the eye are described in terms of size and texture. Micro-agglomerates or flocs are the smallest, discrete are "medium sized", and amalgams are the large coal-in-oil pastes. The texture is either firm or loose. Tables 2 and 3 show the characteristics of agglomeratesformed at a variety of conditions for both the bituminous and the lignite coal. The series of experiments carried out with Mandan Decant oil to determine its agglomerating ability gave the desired firm amalgam at a minimum solvent to coal ratio of 0.6 when allowed to stand overnight. Sun and McMorris

reported that high specific gravity oils do not disperse well enough in coal slurry to wet the coal (1). Since MDO has a specific gravity of 1.0202 (considered high), accounting for the slow formation of agglomerates, lower specific gravity organic liquids were added to reduce it to the medium range. A 50 wt % MDO in p-xylene gave a medium range specific gravity of 0.9400 and this binding oil agglomerated the 325 mesh bituminous coal sample within minutes at a solvent to coal ratio of 0.7 when stirred for 3 minutes at 10000 rpm. The larger 200 mesh particles formed firm agglomerates at a solvent to coal ratio of 0.5 under the same stirring conditions.

TABLE 2.

MICROAGGLOMERATION RESULTS FOR 325 MESH ILLINOIS #6 BITUMINOUS "COAL, AS RECEIVED

| Binding Oil | Solvent/Coal Ratio | Speed (rpm) | Mixing Time(min) Solvent | Mixing Time(min) Slurry | Agglomerates Type | Agglomerates Texture |
|---|---|---|---|---|---|---|
| Illinois #6 Bituminous | | | | | | |
| MDO | 0.4 | 10,000 | 1 | 3 | floc | loose |
| MDO | 0.5 | 10,000 | 1 | 3 | floc | loose |
| MDO | 0.6* | 10,000 | 1 | 3 | amal | firm |
| MDO | 0.7 | 10,000 | 1 | 3 | disc | loose |
| MDO/XY | 0.5 | 10,000 | 1 | 3 | disc. | firm |
| MDO/XY | 0.6 | 10,000 | 1 | 3 | disc. | firm |
| MDO/XY | 0.7 | 10,000 | 1 | 3 | amal. | firm |
| MDO/XY | 0.5 | 10,000 | 2 | 3 | amal. | firm |
| MDO/XY | 0.6 | 10,000 | 2 | 3 | amal. | firm |
| MDO/XY | 0.7 | 10,000 | 2 | 3 | amal. | firm |
| MDO/XY | 0.8 | 10,000 | 2 | 3 | none | -- |
| India Head Lignite | | | | | | |
| MDO/XY | 0.30 | 10,000 | 2 | 3 | floc | firm |
| MDO/XY | 0.40 | 10,000 | 2 | 3 | disc. | firm |
| MDO/XY | 0.50 | 10,000 | 2 | 3 | disc. | firm |
| MDO/XY | 0.60 | 10,000 | 2 | 3 | disc. | firm |
| MDO/XY | 0.70 | 10,000 | 2 | 3 | disc. | firm |
| Hot Water Dried Indian Head Lignite | | | | | | |
| MDO/XY | 0.30 | 10,000 | 2 | 3 | disc. | firm |
| MDO/XY | 0.40 | 10,000 | 2 | 3 | amal. | firm |
| MDO/XY | 0.50 | 10,000 | 2 | 3 | amal. | firm |
| MDO/XY | 0.30 | 20,000 | 2 | 3 | disc. | firm |
| MDO/XY | 0.40 | 20,000 | 2 | 3 | disc. | firm |
| MDO/XY | 0.50 | 20,000 | 2 | 3 | amal. | firm |

MDO/XY = 50 wt % MDO in XY
MDO = Mandan Decant Oil
XY = p-xylene
floc = micro-agglomerates
disc = discrete agglomerates

amal=amalgams
*agglomerates formed overnight

Table 4 shows the results in terms of product ash content of experiments carried out on the larger unit. Simple calculation from this table shows the ash reduction of the 325 mesh bituminous coal was greater than that of the 200 mesh samples. This is not unexpected in light of the fact that the smaller particles have more surface contact with the oil. Experiments with the 200 mesh bituminous

coal on the larger scale unit showed that firm amalgams could be formed at a ratio of as low as 0.3 when stirred for 6 minutes at 13,000 rpm resulting in an ash reduction of 8%. Although these particles are more easily handled physically, Table 4 shows that greater ash reduction is accomplished in forming the smaller particles.

TABLE 3.

MICROAGGLOMERATION RESULTS FOR 70 wt % 200 MESH IILLINOIS BITUMINOUS COAL, AS RECEIVED

| Binding Oil | Solvent/Coal Ratio | Speed (rpm) | Time(min) Solvent | Mixing Time(min) Slurry | Agglomerates Type | Texture |
|---|---|---|---|---|---|---|
| MDO/XY | 0.5 | 10,000 | 2 | 3 | amal. | firm |
| MDO/XY | 0.6 | 10,000 | 2 | 3 | amal. | firm |
| MDO/XY | 0.7 | 10,000 | 2 | 3 | amal. | firm |

The same solvent as in the experiments with the bituminous coal was used in the experiments with the Indian Head lignite. In the micro agglomeration tests with 325 mesh asreceived lignite at solvent to coal ratios of 0.250.70 and stirring rates of 10,000 rpm for 3 minutes no firm amalgams were formed. However, under identical conditions hot water dried lignite formed firm amalgams at solvent to coal ratios of 0.40, and at similar conditions but with a stirring rate of 20,000 rpm, amalgams formed in a solvent to coal ratio of 0.50. In large scale tests, the as received lignite formed only firm discrete agglomerates. With hot water dried lignite firm amalgams were formed in the MDO p-xylene when mixing at 10,000 rpm for 3 minutes in a solvent to coal ratio of 0.25 and resulted in a 21% reduction in ash content. Firm amalgams were also formed at ratios of 0.30, 0.35, and 0.40 at the same mixing speed and time conditions with nominally 8% reduction in ash. Increasing the mixing speed to 20,000 rpm resulted in firm amalgams at a ratio of 0.30 with a 14% reduction in ash. Substitution of the rectisol naphtha for the p-xylene in the solvent mixture was found to yield only firm discrete particles and the most satisfactory solvent to coal ratio was 0.40. The ash reduction was 13% as compared with a reduction of 17% with the MDO p-xylene at the same mixing conditions.

The pH was determined to be ~6 for the slurries included in this study. Current work getting underway includes a study of the effect of adjusting the pH to enhance agglomeration and ash reduction.

## CONCLUSIONS

The following conclusions are suggested by the data:

- Mandan Decant Oil, a high density oil, will agglomerate the studied coal types only after standing for extended periods of time, while a 50 wt % mixture of MDO in either p-xylene or rectisol naphtha, which forms a medium density oil, will agglomerate these coals within several minutes.

- Hot water drying of lignite enhances its agglomerating properties.

- Agglomerates which are flocculate or discrete in form generally gave higher ash reductions than amalgam agglomerates.

- Higher mixing speeds and longer mixing times although not giving large agglomerates, generally gave higher ash reductions with both coals studied.

- The MDO/XY binder caused greater reduction of the ash content of the 325 mesh as received lignite (17%) than the MDO/RN (13%).
- Agglomerate formation is dependent on the design of the stirrer.
- When using the MDO/XY solvent, the ash content of the 325 mesh bituminous coal was reduced more than that of the 200 mesh coal, showing reductions of 17% and 14% respectively. A 14% reduction in ash was realized for the 325 mesh hot water dried lignite as compared to 12% for the as received lignite.

TABLE 4.

AGGLOMERATION RESULTS FOR A 50 WT % MANDAN DECANT OIL IN P-XYLENE OR RECTISOL NAPHTHA.

| Solvent/Coal Ratio | Speed (rpm) | Time(min) Solvent | Time(min) Slurry | Agglomerates Type | Agglomerates Texture | Product % Ash * |
|---|---|---|---|---|---|---|
| 200 Mesh Illinois #6 Bituminous, as received | | | | | | |
| 0.30 | 13,000 | 2 | 3 | disc. | firm | 11.75 |
| 0.35 | 13,000 | 2 | 3 | disc. | firm | 10.91 |
| 0.40 | 13,000 | 2 | 3 | amal. | loose | 11.05 |
| 0.25 | 13,000 | 2 | 6 | disc. | firm | 11.97 |
| 0.30 | 13,000 | 2 | 6 | amal. | firm | 11.69 |
| 0.35 | 13,000 | 2 | 6 | amal. | firm | 11.37 |
| 0.25 | 16,000 | 2 | 6 | disc. | firm | 11.25 |
| 0.30 | 16,000 | 2 | 6 | disc. | firm | 11.07 |
| 0.35 | 16,000 | 2 | 6 | disc. | firm | 10.96 |
| 325 Mesh Illinois #6 Bituminous, as received | | | | | | |
| 0.25 | 16,000 | 2 | 6 | floc | firm | 21.83 |
| 0.30 | 16,000 | 2 | 6 | floc | firm | 20.99 |
| 0.35 | 16,000 | 2 | 6 | disc. | firm | 20.55 |
| 325 Mesh Indian Head Lignite, as received | | | | | | |
| 0.40 MDO/XY | 15,000 | 2 | 6 | disc. | firm | 12.09 |
| 0.40 MDO/RN | 15,000 | 2 | 6 | disc. | firm | 12.72 |
| 325 Mesh Hot Water Dried Indian Head Lignite | | | | | | |
| 0.25 | 10,000 | 2 | 3 | amal. | firm | 8.73 |
| 0.30 | 10,000 | 2 | 3 | amal. | firm | 10.29 |
| 0.35 | 10,000 | 2 | 3 | amal. | firm | 10.12 |
| 0.40 | 10,000 | 2 | 3 | amal. | firm | 10.27 |
| 0.30 | 20,000 | 2 | 3 | amal. | firm | 9.49 |
| 0.35 | 20,000 | 2 | 3 | disc. | firm | 9.44 |
| 0.40 | 20,000 | 2 | 3 | disc. | firm | 9.58 |

*Moisture free basis.
MDO/XY = 50 wt % Mandan Decant Oil in p-xylene
MDO/RN = 50 wt % Mandan Decant Oil in rectisol naphtha

REFERENCES


1. Sarkar, G.G., B.B.Konar, J. of Mines, Metals, and Fuels, 28, No. 5, 103, (1980).
2. Bandopadhyay, P., Urja, 15, No.5, 377, (1984).

3. Bhattacharyya, R.N., A.K. Muza, and G.G. Sarkar, "Role of Operating Variables in Oil Agglomeration of Coal", Agglomeration Seventy Seven, 2, 931938, (1977).

4. Liu, Y.A., Editor, Physical Cleaning of Coal, Chapter 6, Marcell Dekker, New York, (1982).

5. Hazra, S.K., T.C. Rao, G.G. Sarkar, "Effects of Process Variables on Size Distribution of Oil Agglomerates of Fine Coal", Coal Preparation, 3, 7787, (1986).

6. Masologites, G.P., "Process for Agglomerating Coal", Patent No. US 4355999, Atlantic Richfield Co., 1978.

ACKNOWLEDGEMENT

Financial support for this project was provided by the U.S.Department of Energy through the Pittsburgh Energy Technology Center under contract no. DEFC2186MC10637.

# THE COMPARISON OF A LIGNITE CHAR, SUBBITUMINOUS COAL CHAR, AND A BITUMINOUS COAL CHAR USED IN THE REACTION WITH STEAM TO PRODUCE HYDROGEN.

R.C. Timpe and R.E. Sears

University of North Dakota Energy and Minerals
Research Center, Grand Forks, North Dakota 58201

## ABSTRACT

The use of coal as a carbon source in the char-steam reaction to produce hydrogen gas over the temperature range 700°-800°C (973-1073 K) at atmospheric pressure has been studied in detail. Velva lignite has properties which give its char superior reactivity over those of the other coals tested. Catalysis with alkali carbonates enhanced the reactivity of Velva char substantially, whereas demineralization reduced the reactivity to a relatively constant value over the temperature range studied by removing inorganic material and altering the surface characteristics of the coal. Char produced from a Wyodak subbituminous coal and River King bituminous coal were much less reactive than Velva in the absence of catalyst but responded positively to the addition of alkali carbonates. Upon demineralization, these coals also showed reduced reactivity and altered surface features. This paper discusses the results of the experiments in terms of the reactivity data, SEM photos and elemental mapping, organic properties as determined from $^{13}C$ NMR and ESCA spectroscopy, and inorganic content of the substrates.

## INTRODUCTION

The bench-scale production of hydrogen at atmospheric pressure and moderate temperatures (700°-800°C) from the uncatalyzed and catalyzed reaction of low-rank coal char and steam has been studied extensively at the University of North Dakota Energy and Mineral Research Center (UNDEMRC). The gasification process focuses on utilizing the gasification and the water-gas shift reactions at these conditions to optimize hydrogen production. The limiting step in the process at these conditions is the char-steam reaction (1).

Although the low-rank coals that have been tested exhibit somewhat different reactivities from one another, they are generally more reactive than those of higher rank.(2) The reasons for the differences in reactivity within a rank remain controversial. However, surface area as it relates to turnover number, and the presence of specific catalytic inorganic materials, are certain to play a role in enhancing or retarding reaction rate. Similarly, the decrease in reactivity with increasing rank may be the result of one or both of these, along with the increasing aromatic nature of the coal. This study examined some of the similarities and differences in the chemical properties between representatives of the three ranks, that is, lignite, subbituminous and bituminous coals.

The selection of test coals for this study was based on previous gasification performance as determined from the char reactivity data base at UNDEMRC. One of the test coals that was known to gasify readily was a lignite from the Velva, North Dakota, coal mine. This coal has been extensively studied at UNDEMRC as a feedstock for the hydrogen production process. These studies indicate that this coal is an excellent candidate for use in the gasification process and is

currently being used as a basis for comparing other candidate coals. The subbituminous coal selectd was likewise a much-studied Wyodak coal from Wyoming. Although Wyodak reacts more slowly in the bench-scale tests than the Velva lignite, its reactivity is greatly enhanced when the reaction is catalyzed by an alkali catalyst. The bituminous coal was the unwashed high-ash Illinois #6 coal.

## EXPERIMENTAL

The reactions between the coal chars and steam were studied with two different Thermogravimetric Analysis (TGA) systems. The kinetic study of weight change of carbon with time for the char-steam reaction was carried out on a DuPont 951 Thermogravimetric Analyzer (TGA) interfaced with a DuPont 1090 Thermal Analyzer.

Approximately 30 mg samples of -100 x +140 mesh as-received or demineralized coal, or as-received coal containing $K_2CO_3$ catalyst, were devolatilized under argon flowing at 160 cc/min. The resulting char was then reacted with steam ($p_{(H2O)}$=0.1) for a period not exceeding 180 minutes. Weight, time, and temperature data were recorded for the duration of the experiment. Total gas (product gas plus carrier gas) samples were collected over the duration of the run and were analyzed by gas chromatography (GC).

Selected experiments were duplicated on an UNDEMRC-built large TGA (1) so that large gas samples could be collected, ensuring a more accurate gas analysis. Reactivity parameters, (k), were calculated at each of three temperatures (T) and Arrhenius plots of ln k vs 1/T were constructed for calculating energy of activation ($E_a$) and frequency factor, (A), as previously described.(3)
Char analyzed by spectroscopic techniques was prepared as in the char-steam reaction experiments, but was cooled to room temperature under argon. These samples were analyzed by Electron Spectroscopy for Chemical Analysis (ESCA) and 50 MHz solid $^{13}C$ Nuclear Magnetic Resonance Spectrometry (NMR). The NMR technique used on the samples was an adaptation of the Bloch Decay technique in which no cross-polarization with hydrogen and no proton decoupling was used (4). Instead, the $^{13}C$ spins were polarized directly rather than from rapidly relaxing hydrogen nucleii, thus removing the question of the quantitative nature of cross-polarization in hydrogen deficient species.(5) All spectra were obtained using the same pulsing parameters and TOSS was used to eliminate spinning sidebands. Samples of each char were examined by Scanning Electron Microscopy (SEM) to determine surface elemental distribution and to obtain photographs of the char surface. The field was scanned and representative particles were photographed and mapped to determine the elemental distribution.

## RESULTS AND DISCUSSION

There are several significant similarities and differences between the coals used in this study. Two of the basic differences in the coals used in this study were their rank and their geographical origins. The Velva lignite is a northern Great Plains lignite from a mine near Velva, North Dakota. The Wyodak subbituminous coal was from the Green River Basin in Wyoming. The Illinois #6 was a bituminous coal obtained from the River King mine in southern Illinois.

Proximate and ultimate analyses of the three coals are listed in

Table 1. The Velva lignite sample was higher in moisture and ash content than the Wyodak sample. The River King bituminous was lower in moisture but much higher in mineral matter than either of the other two. The three coals have equal quantities of MAF volatile matter and of fixed carbon by weight.

TABLE 1

PROXIMATE AND ULTIMATE ANALYSES

| Proximate Analyses | Velva | Wyodak | River King |
|---|---|---|---|
| Moisture % | 29.3 | 13.7 | 5.8 |
| Ash, wt % mf | 13.5 | 8.1 | 35.8 |
| Volatile Matter, wt % mf | 39.3 | 42.7 | 29.2 |
| Volatile Matter, wt % maf | 45.4 | 46.4 | 45.6 |
| Fixed Carbon, wt % mf | 47.2 | 49.3 | 35.0 |
| Fixed Carbon, wt % maf | 54.6 | 53.6 | 54.4 |
| Heating Value, Btu/lb AR | 7185 | 8057 | 9477 |
| Ultimate Analyses, mf, wt % | | | |
| Hydrogen | 3.84 | 4.76 | 2.61 |
| Carbon | 59.93 | 66.64 | 44.81 |
| Nitrogen | 0.94 | 0.91 | 0.40 |
| Sulfur | 0.53 | 0.51 | 5.16 |
| Oxygen (Diff) | 21.26 | 19.10 | 6.56 |

A third difference was in the reactivities of the coal chars in uncatalyzed char-steam reactions as illustrated by Figure 1. The Wyodak subbituminous coal char reacted more slowly than the lignite char but the slowest reaction was that involving the River King char. The reactions of all three chars were enhanced by the presence of alkali catalyst. The River King char reacted the slowest of the three, and therefore the uncatalyzed and catalyzed reaction of that char were only followed through < 25% carbon conversion.

The reactivities of the test coals, the coals containing $K_2CO_3$ catalyst, and the demineralized coals are shown in Table 2. Note that the bituminous coal char and the demineralized coal chars reacted with steam very slowly at all three temperatures resulting in the termination of each experiment before 50% conversion could be accomplished. The Velva lignite char had reactivities that were 1.5-2 times those of the other coals at each temperature. Catalysis of the reaction at the lower two temperatures increased the reactivity of the Wyodak to values exceeding those of the Velva coal char. However, at 800°C, the reactivity of the Velva was increased to ~2.5 times that of the Wyodak. The reactivity of the River King is greater over the first 0-15 wt % carbon conversion than over the remainder of the conversion as shown in Figure 1. This is attributed to the higher state of oxidation on the char surface particle compared to the subsurface layers, making the surface carbon functionalities more hydrophilic than those beneath the surface. The reactivity of the River King char is lower than that of the other two coal chars even when comparing its highest k value (15% carbon conversion) with 50% carbon conversion for each of the other two. In addition, of the forms tested for this River King, none was greatly responsive to changes in temperatures within the studied temperature range.

TABLE 2.

CHAR-STEAM REACTIVITIES FOR THREE COALS AT 700°, 750°, and 800°C.

| | Coal | | |
|---|---|---|---|
| | Velva | Wyodak | River King |
| Conversion, wt % C | 50 | 50* | 15 |
| | k | k | k |
| Temperature (°C) | | | |
| 700 | 1.35 | 0.84 | 1.10 |
| 750 | 2.10 | 0.94 | 1.23 |
| 800 | 3.56 | 2.23 | 1.52 |
| | | Coal w/ 10 wt % K2CO3 | |
| 700 | 4.06 | 9.87 | 5.00 |
| 750 | 8.17 | 11.13 | 5.81 |
| 800 | 34.81 | 13.07 | 8.41 |
| | | Demineralized Coal | |
| 700 | 1.06 | 1.51 | 1.49 |
| 750 | 1.40 | 3.25 | 3.06 |
| 800 | 1.15 | 8.33 | 3.13 |

* k calculated for 10% conversion of demineralized Wyodak char carbon.

The inherent inorganic contents of the ash for the three test coals are shown in Table 3. The aluminum, silicon, and iron concentration of the River King was much higher than in the other two coals. The potassium concentration was also higher in the bituminous coal than in the other two but apparently not in sufficient quantity to enhance the rate of reaction to a level near those of the lower rank coals. The sodium and calcium concentrations, two other elements known to be good catalysts, were much higher in the lower rank coals than in the River King. An effect related to a change in total inorganic content was noted. It was observed that on demineralizing the River King coal, the char reactivity was enhanced over that of the raw coal. Demineralization of the other two test coals left their chars less reactive than the those of the parent coal.

TABLE 3.

RESULTS OF ASH ANALYSES BY XRFA OF THREE COALS IN MOLES OF ELEMENT PER 10000 GRAMS OF COAL.

| ELEMENT | VELVA | WYODAK | RIVER KING |
|---|---|---|---|
| Aluminum | 3.02 | 2.38 | 10.81 |
| Silicon | 3.43 | 3.95 | 26.77 |
| Sodium | 1.06 | 0.27 | 0.00 |
| Potassium | 0.04 | 0.05 | 1.49 |
| Calcium | 8.32 | 3.38 | 2.34 |
| Magnesium | 2.87 | 1.20 | 1.16 |
| Iron | 0.94 | 0.70 | 9.43 |
| Titanium | 0.14 | 0.13 | 0.38 |
| Phosphorus | 0.10 | 0.14 | 0.04 |
| Sulfur | 1.41 | 1.02 | 1.64 |

The SEM photographs in Figure 2 show the surface effect that results from charring the test coals containing $K_2CO_3$ catalyst. The ragged, irregular surface and lack of apparent pores in the uncatalyzed char was in contrast to the rounded, nodular surface on the alkali catalyzed char. The degree to which the surface of the coal changed on charring with the addition of catalyst differed among the coals. The Velva char surface was remarkably porous and contained uniform, evenly spaced nodules of approximately 0.05 µm x 0.10 µm in size. The nodules on the surface of the catalyzed Wyodak and River King coal chars were rounded and numerous but not uniform in either size or distribution. The demineralized Wyodak and River King chars had a good deal of surface relief in the form of a few nodules and concavities whereas the surface of the demineralized Velva was relatively smooth. The differences in the surface relief appear to parallel the differences in reactivity and is probably due to changes in available active sites. SEM mapping of the surface for inorganic element distribution showed that the inorganic matter was not distributed uniformly over the surface of the chars except for the potassium. The uniform distribution of the potassium in even the low moisture coals imply a fluid dissemination of the catalyst.

Carbon-13 Nuclear Magnetic Resonance ($^{13}C$ NMR) spectra of chars prepared at temperatures of 750°C shown in Figure 3 indicated the loss of most of the aliphatic carbon on charring. Aromatic carbonyl groups were present in the demineralized Velva and Wyodak chars whereas they appeared to be absent in the other chars. Integration of the demineralized Velva char spectrum indicated the presence of more aliphatic carbon than in the raw Velva char. The opposite was observed for the Wyodak chars, in which the raw Wyodak char had more aliphatic carbon than its demineralized counterpart. The aliphatic content of the two River King chars did not differ significantly.

Table 4 shows the ratio of carbon to the other elements found by ESCA on the surface of the char particles. The carbon-to-oxygen ratio of the lignite was about the same on the surface of the raw char as it was on the demineralized char. However, the ratio increased by factors of 5 and 3 on the demineralized chars over the raw chars of Wyodak and River King, respectively. In the latter two cases, the demineralization appears to remove oxygen along with the mineral matter and/or remove C-O functionalities leaving less

TABLE 4.

SURFACE ATOMIC RATIOS AS DETERMINED BY ESCA, IN ATOMS C PER ATOM Y

| | VELVA | | | WYODAK | | RIVER KING | |
|---|---|---|---|---|---|---|---|
| Atomic Ratio | Raw | Dem | Dem* | Raw | Dem | Raw | Dem |
| C/O | 4.1 | 4.8 | 16.6 | 6.1 | 30.7 | 8.5 | 22.7 |
| C/N | 107 | 134 | 60.7 | 132 | 136 | 68.5 | ND |
| C/Na | 747 | 403 | 456 | 159 | ND | 411 | 466 |
| C/Si | 16.6 | 403 | 152 | 56.6 | 951 | 30.4 | ND |
| C/S | 372 | 806 | 456 | 397 | 476 | 117 | 93.1 |
| C/Ca | 374 | ND | ND | 33.0 | 951 | 822 | 466 |
| C/Al | 83.0 | 806 | 182 | 41.7 | 476 | 31.6 | 103 |
| C/Fe | ND | ND | ND | 793 | 951 | 822 | 466 |

* 90 minute sputter
ND = Not Detected

reactive carbon functionalities on the surface of the particles. The change in inherent catalyst materials, sodium (Na), calcium (Ca), and iron (Fe), between raw coal char and demineralized coal char from the same coal differed for each of the coals. No pattern that would indicate a particular catalytic effect was observed for any of the three. Likewise silicon (Si), nitrogen (N), and sulfur (S) changes showed little correlation to the effect of demineralization that would facilitate a conclusion.

## CONCLUSIONS.

All three coals responded to the addition of the $K_2CO_3$ catalyst in the char-steam reaction. Reactivity of the Velva char increased by factors of three to ten at a given temperature with the addition of the catalyst. However, the Wyodak char responded with greater increases in reactivity at the lower two temperatures upon catalyst addition, increasing reactivity six to ten times. The addition of catalyst to the River King char increased the reactivity by a factor of ~5 but the char reactivity was affected very little by temperature over the temperature range studied. Demineralization of the coals reduced the reactivity of the Velva char but increased the reactivity of the River King over that of their respective raw coal chars. Scanning electron microscopy showed that the char surface is affected by both demineralization and catalyst addition to the raw coal. Larger than expected aromatic carbonyl peaks were obtained in the $^{13}C$ NMR spectra of demineralized Velva and Wyodak chars:

## REFERENCES


1. Timpe, R.C., R.E. Sears, and G.G. Montgomery, ACS Div. Fuel Preprints, 32, No. 4, 1, (1987).
2. Takarada, T., Y. Tamai, and A. Tomita, Fuel, 64, 1438, (1985).
3. Timpe, R.C., S.A. Farnum, S.J. Galegher, J.G. Hendrikson, M.M. Fegley, ACS Div. Fuel Preprints, 30, No. 4, 481, (1985).
4. Axelson, D.E., Solid State Nuclear Magnetic Resonance of Fossil Fuels, Chapters 2-3, Multiscience Pub. Ltd., Canada, (1985).
5. Botto, R.E., R. Wilson, and R.E. Winans, Energy and Fuels, 1, 173-181, (1987).


## ACKNOWLEDGEMENTS


The authors would like to acknowledge Jan Lucht for assistance with the TGA experiments, George Montgomery for ESCA data, and Art Ruud for the $^{13}C$ NMR spectra. Gratitude is extended to Leland E. Paulson, Technical Project Officer, and Madhov Ghate, Chief, Combustion and Gasification Branch, Morgantown Energy Technology Center for their guidance and support. This work was carried out under DOE contract no. DE-FC21-86MC10637.

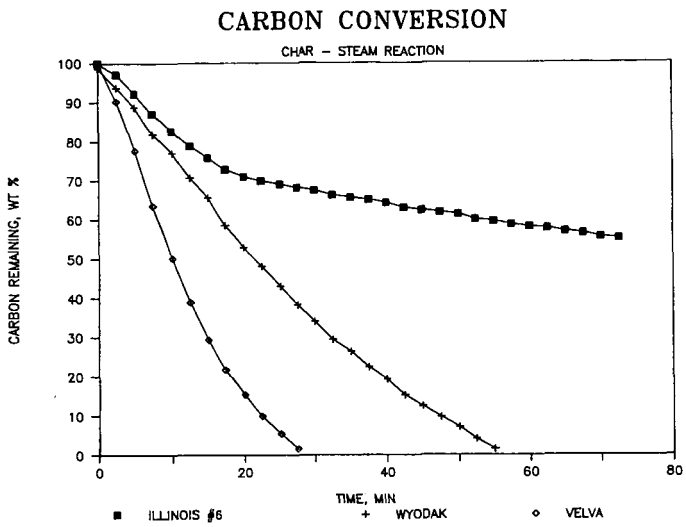


Figure 1. Conversion of Velva lignite, Wyodak subbituminous, and Illinois #6 char carbon on reacting with steam at 750°C.

(a) (b) (c)

Figure 2. SEM photos of chars of the raw (a, d, g) and demineralized (b, e, h) coals and chars of each coal with 10 wt % $K_2CO_3$ added (c, f, i). The photos shown are of chars of Velva lignite (a, b, c), Wyodak subbituminous (d, e, f), and Illinois #6 bituminous (g, h, i) coals.

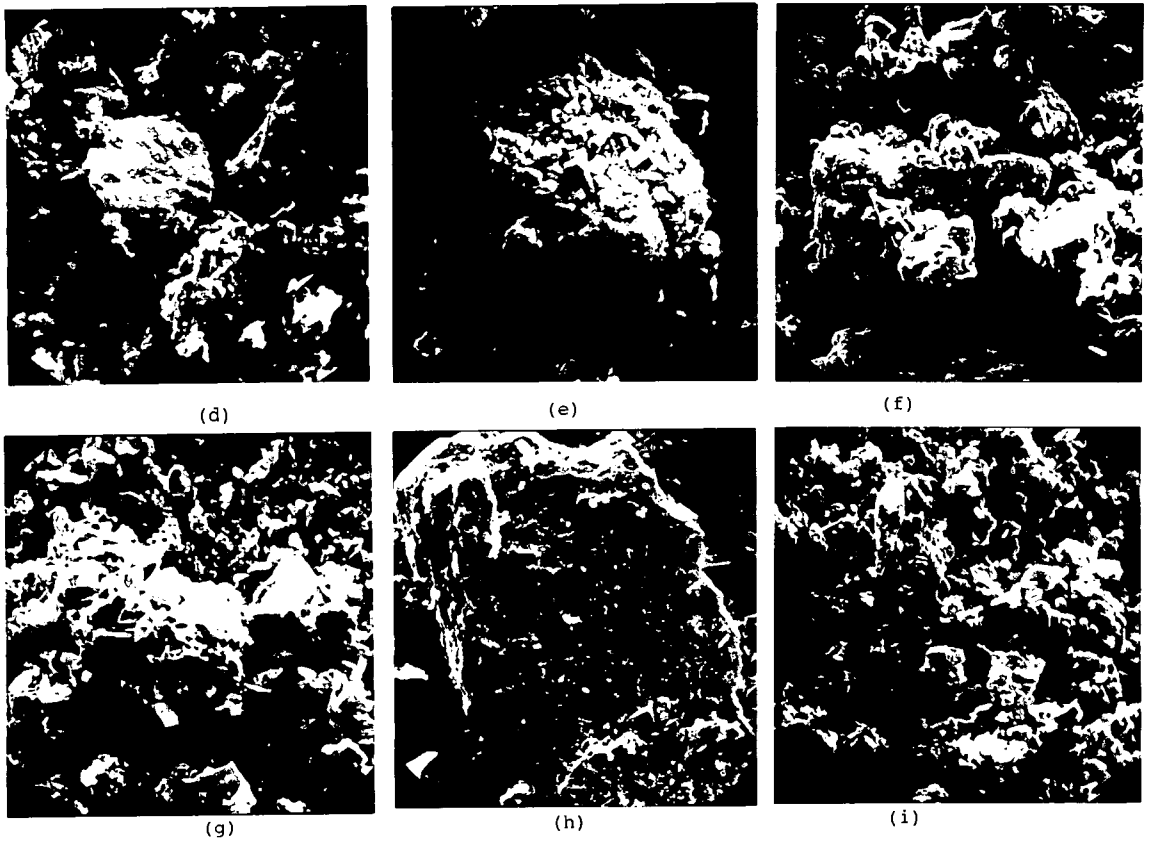


Figure 2 (continued).

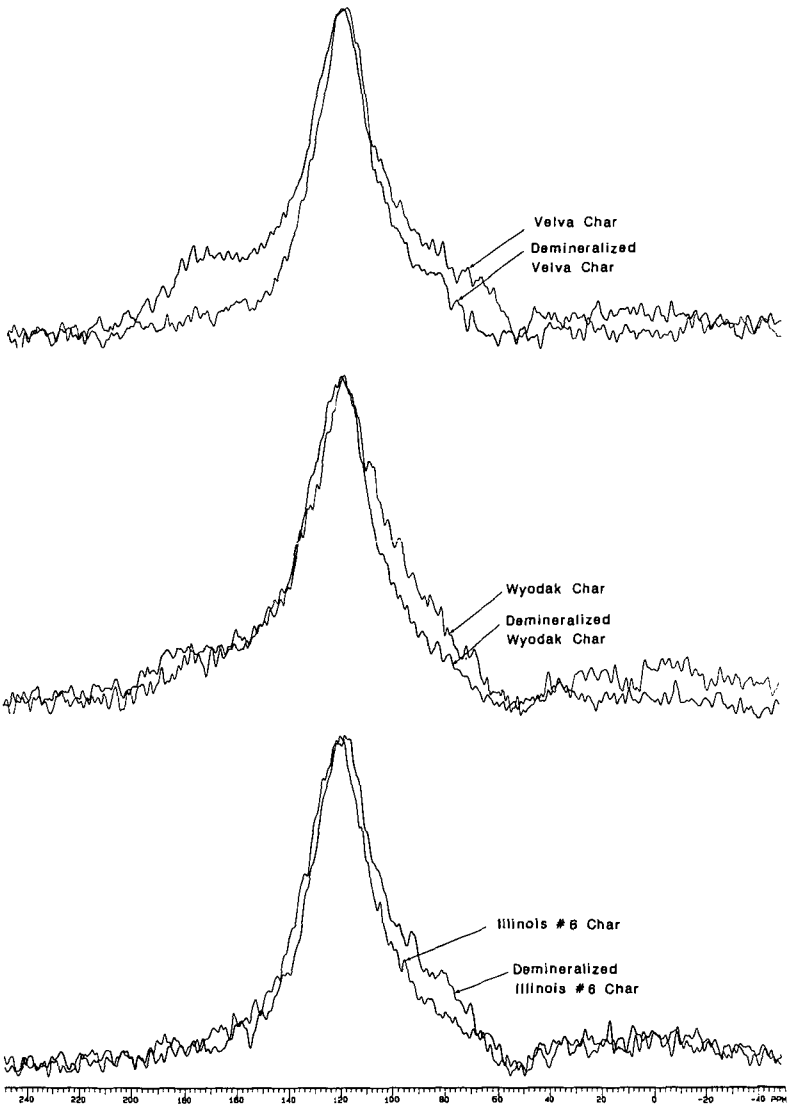


Figure 3. Solid $^{13}C$ NMR spectra of chars from raw and demineralized Velva lignite, Wyodak subbituminous, and Illinois #6 bituminous coals.

# COAL LIQUEFACTION USING DEUTERIUM-LABELED ANTHRACENE OIL SOLVENT

T.R. Aulich, C.L. Knudson, and S.B. Hawthorne

University of North Dakota
Energy and Minerals Research Center
Grand Forks, North Dakota 58202

## ABSTRACT

In order to better understand the reactions of heteroatom-containing organics which occur during liquefaction of subbituminous coal, it is necessary to distinguish between coal-derived and solvent-derived species. A coal-derived liquefaction solvent, A04, was deuterium-labeled by a method developed at the University of North Dakota Energy and Minerals Research Center and found to be stable under liquefaction conditions. The deuterium-labeled A04 was reacted in the presence of unconverted coal (tetrahydrofuran-insoluble material from a previous autoclave liquefaction test), water, carbon monoxide, and hydrogen sulfide at 350°C and 1000 psia for 30 minutes. No significant degradation in isotopic purity was observed in the mass spectra of the individual deuterated species comprising approximately 95 wt% of the deuterated solvent. Tests were also conducted with raw coal under similar liquefaction conditions to determine the amounts of coal-derived compounds evolved, and whether these compounds will undergo deuterium exchange with the deuterated solvent. Distillable products are being analyzed using GC/MS, and soluble and insoluble products are being analyzed using liquid proton and solid state C-13 NMR. The deuterium-labeling method has also been used to synthesize 16 model compounds including O-, S-, and N-containing aromatics to be used in future liquefaction tests. Analytical results including product component identification, coal conversion as determined by tetrahydrofuran solubility, and changes observed in NMR spectra will be presented.

## INTRODUCTION

The purpose of the described research is to study the reactivity of heteroatom-containing organics in Wyodak subbituminous coal under liquefaction conditions. The liquefaction solvent specified for use in the research is a coal-derived anthracene oil (A04). Several heteroatom-containing components of A04 (dibenzofuran, dibenzothiophene, and carbazole) are thought to be produced from coal during liquefaction. Other coal-derived liquefaction products such as phenol, cresols, and quinolines are also present in A04 as minor components. Clearly, a method is needed to distinguish between coal-derived and solvent-derived heteroatom-containing product species. By producing deuterium-labeled A04 and examining its behavior under liquefaction conditions, it should be possible to differentiate between coal-derived and solvent-contained species with gas chromatography/mass spectrometry (GC/MS) and nuclear magnetic resonance (NMR) techniques.

## SYNTHESIS OF DEUTERIUM-LABELED A04 LIQUEFACTION SOLVENT

Approximately 30 grams of deuterium-labeled A04 was synthesized

using a 1.0 liter autoclave constructed of "Hastelloy C", an alloy resistant to chloride ion corrosion. A six hour reaction at 300°C was carried out using 30 grams A04, and a 250 mL solution of 4% deuterium chloride in deuterium oxide with 10 mg/mL dissolved chromium metal. After cooling the autoclave overnight, the product was removed from the autoclave, dissolved in ether, washed, dried, and weighed to yield an approximate 97% recovery. Figure 1 shows a gas chromatogram of A04 before and after deuterium-labeling. The similarity in the two chromatograms demonstrates that essentially no degradation or loss due to volatilization of any major components occurred as a result of undergoing the deuteration reaction. Figure 2 shows representative mass spectra of several individual A04 components before deuteration (upper spectrum of each set) and after deuteration (lower spectrum). The spectra were obtained with a Hewlett Packard 5985 GC/MS using a 70 eV electron impact ionization potential. In general, isotopic purities of the individual aromatic components of the A04 were approximately 95%, as determined using GC/MS with low voltage (10 eV) electron impact ionization.

Proton NMR spectra obtained of the non-deuterated and deuterated solvents are presented in Figures 3a and 3b. Since deuterium is not detected with proton NMR, the area of the aromatic region (7-9 ppm) is greatly diminished relative to the aliphatic region (0.7-4.5 ppm) in the deuterated sample. This is because aromatic protons are more easily exchanged than aliphatic protons under the synthesis conditions utilized. Using data in Table 1, a calculation was made to estimate the extent of deuterium-for-hydrogen substitution required to produce the observed spectral difference between the deuterated and non-deuterated solvents. Assuming no exchange of deuterium for aliphatic protons, approximately 91% of the aromatic protons observed in the spectra of the original solvent would have to be replaced with deuterium to produce the observed spectra of the deuterated solvent. This value is in reasonable agreement with the 95% isotopic purity value calculated using GC/MS analysis.

## STABILITY TESTING OF DEUTERIUM-LABELED A04

Following the synthesis of deuterium-labeled A04 it was necessary to determine the stability of the individual deuterated species in the solvent under liquefaction conditions. To do this, a reaction system was needed that simulated as closely as possible conditions that exist during liquefaction, without using coal. The absence of coal is required to ensure that possible degradation in the isotopic purity of a solvent-derived deuterated compound is not masked by the formation of the same compound from coal. In order to provide the system with the catalytic activity normally derived from the mineral content of coal, it was decided that the reaction mixture should contain tetrahydrofuran-insolubles (THFI) produced from an actual liquefaction reaction. To generate the THFI, an autoclave liquefaction reaction was run at 350°C and 1000 psia for 30 minutes using 383 grams Clovis Point Wyodak coal, 500 grams non-labeled A04, 36 psi $H_2S$, and 964 psi CO. (Based on moisture- and ash-content tests run prior to the autoclave reaction, 383 grams raw coal would provide 250 grams moisture- and ash-free (MAF) coal.) The product slurry contained 15.3% THFI, 19.4% of which was ash. The stability of deuterated A04 was tested by performing duplicate tubing bomb reactions using deuterated A04 (2.5 grams),

water, and THFI from the autoclave run. Water and THFI were added in quantities that would be supplied by a MAF coal charge of 1.25 grams. The amount of water added (0.36 grams) was calculated based on a moisture content of 20.99 wt% raw coal, as determined immediately prior to the tubing bomb tests. The amount of THFI added (0.65 grams) was calculated based on the THF solubility of the product slurry resulting from the autoclave run. All other reaction conditions including $H_2S$ and CO pressures, and reaction time and temperature were identical to the conditions of the autoclave run.

The most important result of the stability tests on deuterated AO4 is the finding that the deuterated species comprising approximately 95 wt% of the solvent underwent no significant degradation in isotopic purity. Figure 4 displays mass spectra (70 eV) of 4 major components of deuterated AO4 before and after exposure to liquefaction conditions. The fact that the before and after spectra are essentially identical will enable distinction to be made between coal-derived and solvent-derived species found in future liquefaction product slurries resulting from reactions with deuterated AO4 and coal. For example, the assumption can be made that any non-labeled dibenzofuran resulting from the liquefaction of coal using deuterated AO4, must be derived from the coal, since all solvent-derived dibenzofuran should remain deuterium-labeled throughout the reaction.

Several minor component species displaying various degrees of degradation in isotopic purity based on mass spectral data include phenol, two cresol isomers, quinoline, and carbazole. These compounds, while displaying molecular ions of smaller mass after stability testing than before, are still distinguishable from non-labeled isotopes. Figure 5 displays the mass spectra of deuterium-labeled phenol as it appears in deuterated AO4 prior to stability testing (top spectra), deuterium-labeled phenol as it appears in deuterated AO4 following stability testing (middle spectra), and non-labeled phenol as it appears in non-labeled AO4 (bottom spectra). Coal-derived phenol (molecular ion at 94) produced during future liquefaction tests in which deuterated AO4 is used, should be easily distinguishable from solvent-derived phenol (molecular ion at 96).

Another result of the stability testing of deuterated AO4 is the conversion of approximately 24 wt% of the THFI (which by definition is unconverted coal and ash) from one liquefaction reaction, to THF-soluble products through a second liquefaction reaction under nearly identical conditions. A partial explanation of this conversion may be the fact that the residence time for the THFI was double that of the raw coal. The 24 wt% conversion value was calculated based on the ash-free weight of THF-insolubles reacted.

## LIQUEFACTION OF WYODAK COAL WITH DEUTERATED AO4

After demonstrating that deuterium-labeled AO4 is stable under the previously described liquefaction conditions, duplicate tubing bomb reactions were run using labeled AO4 with Wyodak (Clovis Point) coal. The feed slurry contained a 2/1 weight ratio of labeled AO4 to MAF coal. All reaction conditions were identical to those used in the previously described tubing bomb and autoclave reactions. Liquefaction conversion of the organic content of the coal was determined by THF solubility to be approximately 41 wt%.

The product slurries obtained were analyzed using GC/MS, and liquid proton NMR.

## ANALYSIS OF PRODUCTS FROM COAL LIQUEFACTION WITH DEUTERATED AO4

All GC/MS analyses were performed using methylene chloride as the solvent. Comparison of the mass spectra of deuterated AO4 in product slurries from liquefaction runs made with and without coal, has indicated that the composition and isotopic purity of the deuterated solvent recovered from both reactions are essentially identical. In an effort to demonstrate the formation of coal-derived compounds, 8 compounds were selected for comparative quantitative analysis. The compounds chosen for study (phenol, 3 cresol isomers, tetralin, naphthalene, phenanthrene, and dibenzofuran) were selected primarily because they were present in detectable quantities in both the stability test and coal liquefaction product slurries. Since any coal-derived compounds would be non-labeled, to determine whether any of the 8 compounds were formed from coal, a method was needed to compare the quantity of each non-deuterated compound to the quantity of its deuterated counterpart in both product slurries. A mass spectral technique was employed which enables the relative quantitation of the amount of material having a specified molecular ion weight, using "area counts" as units of quantitation. For example, phenol has a molecular ion at 94 mass units, while deuterated ($d_2$-) phenol has a molecular ion at 96. The relative quantities (in area counts) of phenol and $d_2$-phenol can be obtained by integrating the area under each molecular ion peak. A ratio can then be calculated relating area counts of phenol to area counts of $d_2$-phenol. If this ratio is calculated for the phenol quantities in the product slurries from both the stability test reaction and the reaction with coal, it is possible to ascertain whether phenol was in fact produced from coal, simply by comparing the two ratios. Table 2 is a list of area counts for the 8 non-labeled and labeled compounds present in the product slurries from both reactions. Ratios of area counts non-labeled to labeled compounds are given in column E for both reactions. The fact that the ratio of area counts of non-labeled to labeled phenol produced from the reaction with coal is approximately 4 times greater than the same ratio for the reaction with THFI, is evidence for the presence of 4 times the quantity of non-labeled phenol in the coal reaction product slurry. Since conditions during the two reactions were identical, it is logical that the extra phenol came from the coal. There is also strong evidence pointing to low-temperature (350°C) production of cresol from the coal. Since the area counts are low for tetralin (see explanation at bottom of table) evidence suggests only the possibility of tetralin formation from the coal. Based on the ratios in column E, it appears that naphthalene, phenanthrene, and dibenzofuran are present in greater quantities in the THFI reaction products than in the coal reaction products. There are two explanations, both of which may be partially responsible for this result. The first centers on the longer residence time spent under liquefaction conditions by the THFI. Since the THFI were reacted twice as long as the coal, it is possible that species which take longer to form may be more concentrated in the product slurry of the longer reaction. The second explanation deals with adduction of AO4 solvent (non-labeled) to the solid THFI during the autoclave

reaction. When the A04-containing THFI were then subjected to liquefaction conditions a second time, A04 could have been released from the THFI and rendered soluble. The preparation of the THFI from the autoclave reaction involved their separation from THF-solubles through a vacuum filtration and extraction with THF. The insoluble fraction was then dried in an oven overnight at 120°C. The coarse powder remaining constituted the THFI which were then reacted a second time. In order to determine the contribution of solvent adduction to the presence of certain species in the THFI reaction, it may be necessary to use THFI which have been "cleaned", possibly through an extended Soxhlet extraction.

The product slurries from the reactions of THFI with deuterated A04, and coal with deuterated A04 were also compared using proton NMR. Figure 6 is the NMR spectrum of the deuterated methylene chloride solubles obtained from the reaction of deuterated A04 and THFI. (Since deuterium is not detected with proton NMR, reaction products were extracted with deuterated methylene chloride.) Figure 7 is the NMR spectrum of the deuterated methylene chloride solubles obtained from the reaction of deuterated A04 and coal. These spectra can be compared to the deuterated A04 spectrum in Figure 3b. The main peaks that stand out as unique are those associated with protons on bridge carbons found in fluorene at 3.9 ppm and acenaphthene at 3.4 ppm. The acenaphthene bridge protons make up 3.3% of the area in the spectrum of deuterated A04, 3.0% of the area in the spectrum of the THFI reaction products, and 7.1% of the area in the spectrum of the coal reaction products (see Table 1). Fluorene bridge protons make up 3.9, 12.8, and 9.8% of the three spectra areas, respectively. Protons (and deuterium atoms) in these bridge positions are labile. Higher percentages of hydrogen on bridge carbons in reaction products than in the deuterated solvent, could be due to hydrogen replacing bridge position deuterium during the reactions with THFI or coal. Sources of hydrogen could be non-substituted hydrogen from the solvent, hydrogen from the coal, or hydrogen from the hydrogen sulfide used in the reaction. According to GC/FID area percent data, acenaphthene comprises 3.6% and fluorene 3.5% of the total A04. According to GC/MS data, during the reaction with coal, approximately 75% of the acenaphthene and 90% of the fluorene bridge position deuterium was replaced with hydrogen. During the reaction with THFI, approximately 25% of the acenaphthene and 90% of the fluorene bridge position deuterium was replaced with hydrogen. This indicates that in the presence of coal, acenaphthene exchanges slightly less bridge deuterium than fluorene, and exchanges significantly less in the presence of THFI. Fluorene gives up its bridge deuterium with equal ease in the presence of THFI or coal. Based on this evidence it is likely that fluorene would be a more efficient hydrogen shuttler than acenaphthene.

## THE FATE OF HETEROATOM-CONTAINING AROMATICS DURING LIQUEFACTION

Another aspect of this project involves monitoring the fate of heteroatom-containing species in coal under liquefaction conditions. A tubing bomb test was run with coal and non-labeled A04 which had been "spiked" with a set of 13 deuterated heteroatom-containing compounds and 3 deuterated aromatic hydrocarbons. All the heteroatom-containing organics used have been found in coal

liquefaction products, and many have also been identified as compounds emitted in substantial amounts during the pyrolysis of Wyodak coal (2). Analysis of the product slurry is currently in progress.

Deuterated compounds were synthesized using a reagent consisting of 4% deuterium chloride in deuterated water (deuterium oxide) with 10 mg/mL added chromium metal. The amount of reagent used in each reaction was calculated to give a reaction mixture containing a 20/1 molar ratio of deuterium to aromatic hydrogen. Syntheses were performed at 200 or 300°C for 2 or 15 hours as required to yield a product with both high isotopic and chemical purity (3,4). Table 3 is a list of the compounds along with their respective chemical and isotopic purities. Dihydrophenanthrene, dihydroanthracene, and hexahydropyrene are included in the table since these compounds served as hydrogen donors in another test involving the fate of hydrogen donors under liquefaction conditions. Most of the synthesized deuterated compounds had isotopic purities that approached 95% (as determined by 10 eV low-voltage EI mass spectrometry) which is the equilibrium value expected from using a reaction mixture containing a 20/1 molar ratio of deuterium to aromatic hydrogen. It is interesting to note that the hexahydropyrene showed 12 H/D exchanges even though only four aromatic hydrogens are present on the molecule. Proton NMR analysis of the deuterated product showed that the 8 aliphatic hydrogens bonded to the carbon atoms alpha to the aromatic rings were also replaced with deuterium during the synthesis. Aliphatic hydrogens were also replaced with deuterium during the synthesis of $d_6$-2-methylthiophene.

## CONCLUSIONS

It has been demonstrated that deuterium-labeled AO4 solvent undergoes no significant decrease in overall isotopic purity as a result of exposure to liquefaction conditions at 350°C and 1000 psia for 30 minutes. Although certain compounds such as phenol, cresols, acenaphthene, and fluorene undergo a reduction in isotopic purity under liquefaction conditions, the resulting mass spectra of the compounds are easily distinguishable from their non-deuterated counterparts. Despite a fairly low conversion, concrete evidence was found to substantiate the production of phenol and cresols during mild liquefaction of Wyodak coal. Production of tetralin was indicated but not substantiated by the data available. Analytical results from GC/MS and NMR were shown to correlate well.

## REFERENCES


1. Hawthorne, S.B., D.J. Miller, T.R. Aulich, and S.A. Farnum. "A Simple Method for the Synthesis of Perdeuterated Aromatic Hydrocarbons and Heterocyclic Compounds," ACS Fuel Division Preprints, 32, 471, (1987)

2. Miller, D.J. and S.B. Hawthorne. "Pyrolysis GC/MS Analysis of Low-Rank Coal," ACS Fuel Division Preprints, 32, 10, (1987)

3. Werstiuk, N.H. and Kadai, T. Can. J. Chem., 52, 2169, (1974)

4. Werstiuk, N.H. and Timmins, G. Can. J. Chem., 51, 1485, (1981)

TABLE 1

PROTON NMR SUMMARY

| Proton Type | ppm | Normalized Proton Distribution | | | |
|---|---|---|---|---|---|
| | | AO4 | D-AO4 | D-AO4 + IOM | D-AO4 + Wyodak |
| Aldehydic | 10.0-9.0 | 0.3 | 0.1 | 0.0 | 0.1 |
| Aromatic | 9.0-5.9 | 73.4 | 18.6 | 29.2 | 24.1 |
| Fluorenes | 4.4-3.5 | 4.0 | 3.9 | 12.8 | 9.8 |
| Acenaphthene Bridge H's | 3.5-3.3 | 4.6 | 3.3 | 3.0 | 7.1 |
| Alpha to Aromatic | 3.3-1.9 | 11.7 | 29.4 | 23.1 | 25.0 |
| Beta to Aromatic | 1.9-1.5 | 0.4 | 11.4 | 8.1 | 5.0 |
| Methylene | 1.5-1.0 | 4.1 | 22.6 | 15.1 | 19.2 |
| Methyl | 1.0-0.0 | 1.5 | 10.7 | 8.6 | 9.7 |

TABLE 2

MASS SPECTRAL AREA COUNT DATA

| A Compound | B Reaction | C Area Counts Non-labeled Compound | D Area Counts Labeled Compound | E Ratio C/D |
|---|---|---|---|---|
| Phenol | w/THFI | 726 | 3959 | 0.24 |
| Phenol | w/coal | 3624 | 3863 | 0.94 |
| m- & p-Cresol* | w/THFI | 398 | 907 | 0.44 |
| m- & p-Cresol* | w/coal | 1146 | 1058 | 1.08 |
| o-Cresol | w/THFI | 124 | 399 | 0.31 |
| o-Cresol | w/coal | 265 | 387 | 0.68 |
| Tetralin | w/THFI | 19 | 80 | 0.24 |
| Tetralin | w/coal | 124 | 32 | 3.88 |
| Naphthalene | w/THFI | 460 | 47066 | 0.0098 |
| Naphthalene | w/coal | 59 | 38410 | 0.0015 |
| Phenanthrene | w/THFI | 2802 | 169659 | 0.017 |
| Phenanthrene | w/coal | 351 | 149507 | 0.0024 |
| Dibenzofuran | w/THFI | 722 | 60837 | 0.012 |
| Dibenzofuran | w/coal | 32 | 48272 | 0.0007 |

* m- and p-cresol elute as one species under the chromatographic conditions used.

Ratios in column E are area counts non-labeled aromatics to area counts labeled aromatics, in product slurries from liquefaction reactions with coal, and in product slurries from liquefaction reactions with THFI.

Area counts less than 100 are subject to substantial error and

should not be used as conclusive quantitative data. Low area counts are listed in this table solely to provide a potential indication of some of the detectable product quantities resulting from the two reactions.

TABLE 3

ISOTOPIC AND CHEMICAL PURITIES OF DEUTERATED COMPOUNDS

| Compound | Isotopic Purity (%) | Chemical Purity (%) |
|---|---|---|
| d8-dihydrophenanthrene | 96.6 | 81.5 |
| d12-hexahydropyrene | 97.0 | 86.3 |
| $d_7$-dihydroanthracene | 97.2 | 89.0 |
| d10-phenanthrene | 95.3 | 101.0 |
| d10-pyrene | 95.0 | 98.8 |
| d10-biphenyl | 94.9 | 98.5 |
| d7-naphthol | 89.7 | 97.7 |
| d5-phenol | 96.0 | 95.9 |
| d4-o-cresol | 91.0 | 97.5 |
| d3-3-ethyl-5-methylphenol | 94.1 | 96.1 |
| d4-4n-propylphenol | 96.5 | 53.1 |
| d3-3-methylcatechol | 97.0 | 91.4 |
| d8-dibenzofuran | 95.4 | 100.0 |
| d9-phenanthridine | 79.5 | 100.0 |
| d7-quinoline | 64.7 | 102.0 |
| $d_5$-pyridine | 99.0 | 100.0 |
| d8-carbazole | 94.7 | 105.0 |
| d8-dibenzothiophene | 95.3 | 100.0 |
| d6-2-methylthiophene | 94.8 | 82.3 |

Chemical purity values are + or - 5%.

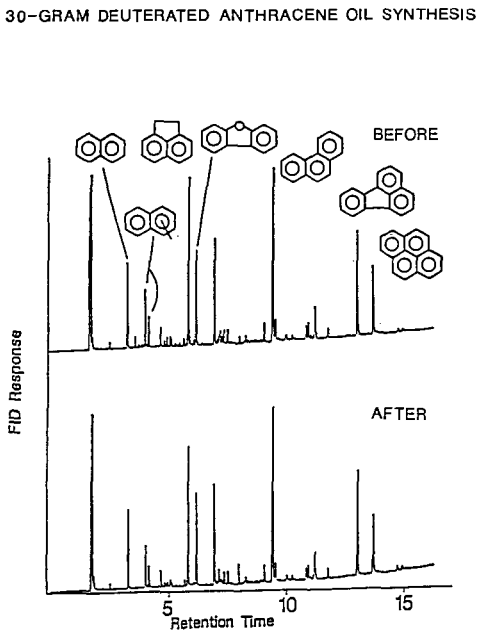


Figure 1. Gas chromatogram of AO4 before (top) and after (bottom) deuteration.

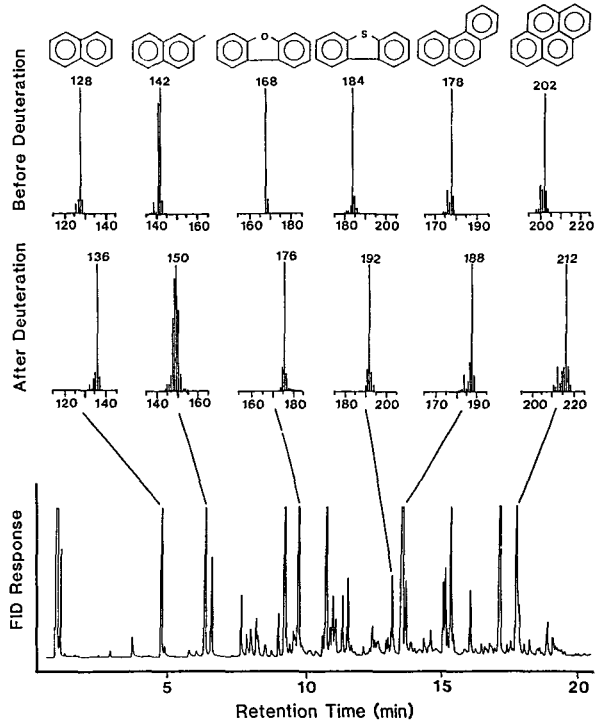


Figure 2. Mass spectra of components of AO4 before (top) and after (bottom) deuteration.

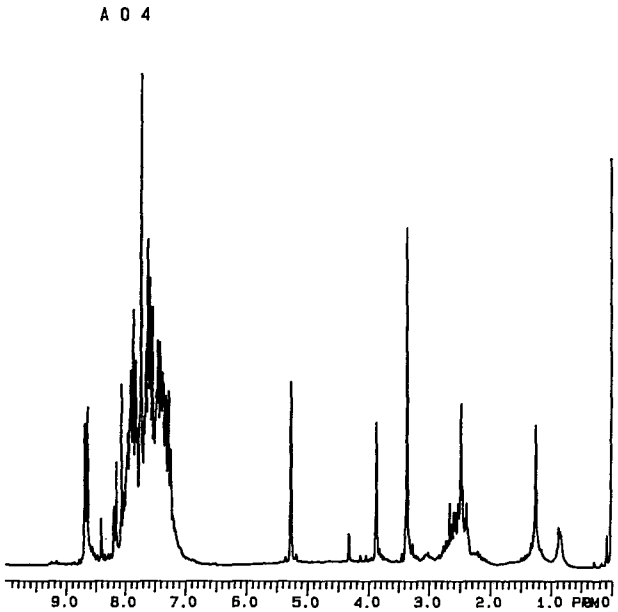


Figure 3a. Proton NMR spectrum of non-deuterated AO4.

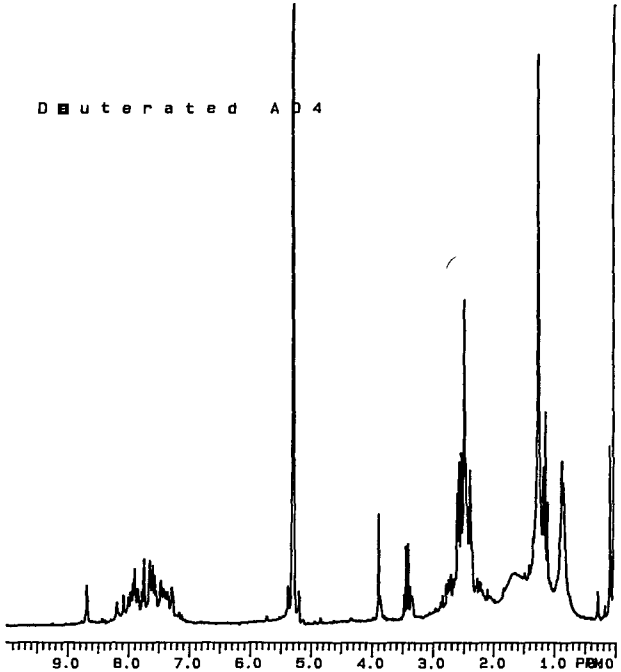


Figure 3b. Proton NMR spectrum of deuterated AO4.

Before (left) and after (right) liquefaction.

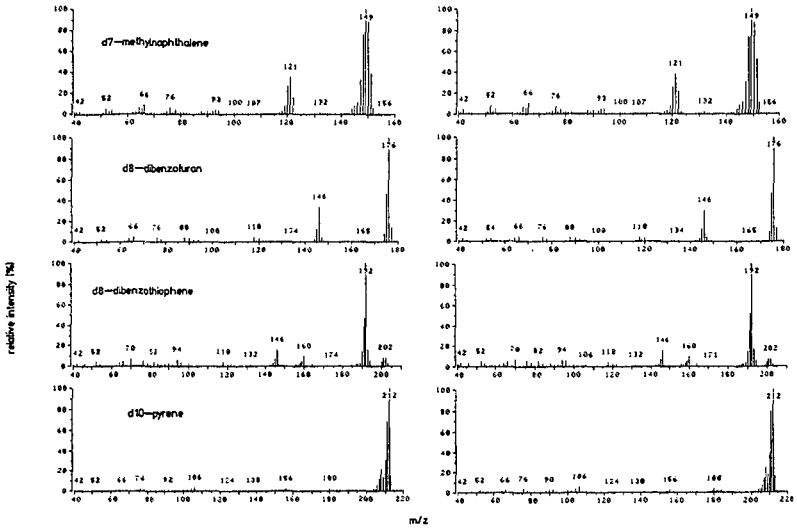


Figure 4. Mass spectra of 4 components of deuterated AO4 before (left) and after (right) exposure to liquefaction conditions with THFI, $H_2S$, CO, and water.

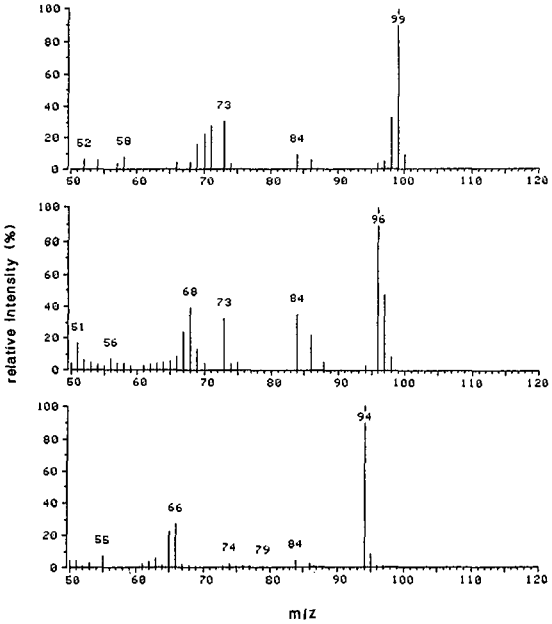


Figure 5. Mass spectra of $d_5$-phenol as it appears in deuterated AO4 prior to stability testing (top spectra), $d_2$-phenol as it appears following stability testing (middle spectra), and phenol as it appears in non-deuterated AO4 (bottom spectra).

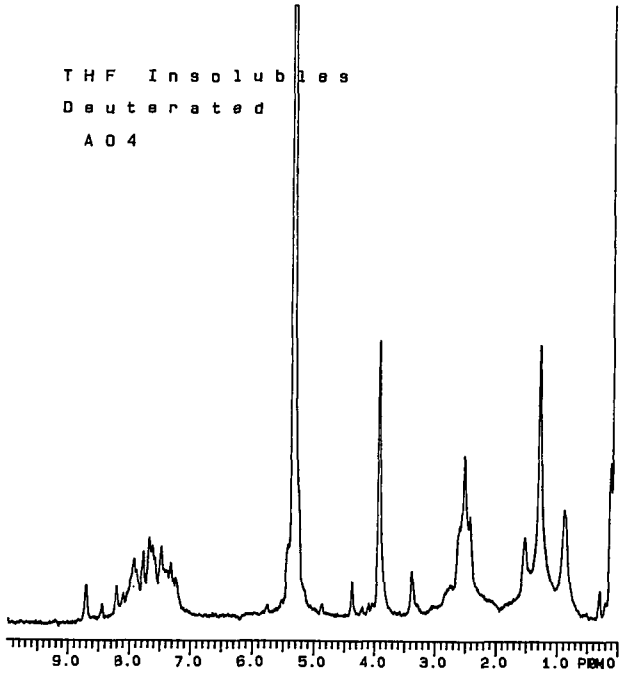


Figure 6. Proton NMR spectrum of methylene chloride solubles obtained from the reaction of deuterated AO4 and THF-insolubles.

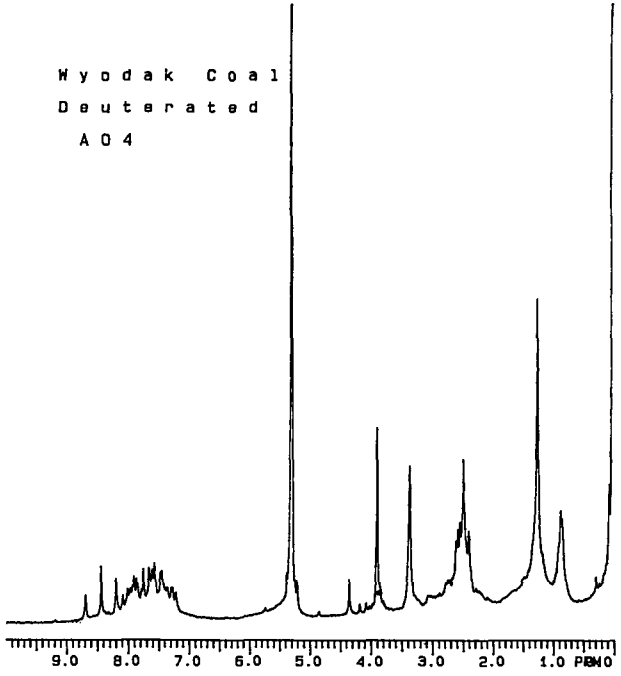


Figure 7. Proton NMR spectrum of methylene chloride solubles obtained from the reaction of deuterated AO4 and Wyodak coal.

# Nitrogen Bases and Carbon Deposits on Coal Liquefaction Catalysts

Diane R. Milburn, Bruce D. Adkins, and Burtron H. Davis

Kentucky Energy Cabinet Laboratory
P.O.Box 13015, Lexington, KY 40512-3015

## Introduction

The respective roles of coke and alkali as poisons of coal liquefaction catalyst activity have attracted the interest of numerous researchers in the past decade (1-17). It is believed that coke formation occurs on catalyst acid sites and that the basicity of coke precursors is an important factor in determining the propensity for coke formation. It is also well-known that alkali metals, especially sodium, can poison acid sites. The coal liquefaction catalyst environment often contains basic compounds (nitrogen bases) and alkali metals (in the coal ash).

Recently, we have correlated elemental analysis data obtained for catalyst samples from the Wilsonville, Alabama coal liquefaction pilot plant. We were surprised to find that a simple mechanistic model involving (a) nitrogen bases chemisorbed on acid sites, and (b) poisoning of acid sites by sodium, can explain virtually all of the interesting coke-formation trends seen in the Wilsonville process since the inception of the two-stage liquefaction (TSL) process mode. The purpose of this paper is to describe this model.

## Experimental

Catalyst samples used in this work were from the Wilsonville runs summarized in Table 1. Two catalysts are represented: Shell 324M NiMo/$Al_2O_3$ and Amocat 1C NiMo/$Al_2O_3$. Two coals are represented: Wyodak sub-bituminous and Illinois #6 bituminous. Four basic processing configurations are shown: Integrated Two-Stage Liquefaction (ITSL), Doubly Integrated Two-Stage Liquefaction (DITSL), Reconfigured Integrated Two-Stage Liquefaction (RITSL) and Close-Coupled Integrated Two-Stage Liquefaction (CCITSL). A more detailed description of these runs and process configurations can be found in reference (18) and in the Wilsonville run reports (19).

The important hydrotreater feedstream components in the model are represented by the three product streams from the critical solvent deashing unit, (CSD). The first, called the ash concentrate stream, contains coal ash and "resid" (defined as a vacuum non-distillate at 650 F and 0.1 mm Hg). The second, called the "thermal resid" (TR) stream, typically consists of resid and less than 10% distillate solvent; the third, called the "light thermal resid" (LTR) stream, typically consists of resid and 20-30% distillate solvent. Because of chemical and/or physical fractionation in the CSD unit, the resids in these streams are different: in terms of average molecular weight, one could expect "ash concentrate resid" > "TR resid" > "LTR resid". The streams also differ in resid concentration. For a given resid input to the CSD, the "TR resid" and "LTR resid" typically constitute about 40-50% each of the total, while the "ash concentrate resid" is usually less than 10% of the total. Thus the model does not

include a separate provision for "ash concentrate resid", but does provide for effects associated with the presence or absence of "TR resid", "LTR resid", and the coal ash in the ash concentrate stream.

Catalyst samples in process solvent were shipped from the Wilsonville pilot plant to our laboratory. THF-soluble material was removed from the catalysts using a Soxhlet extraction apparatus. Residual THF was desorbed in a vacuum oven overnight at ca. 120 C. Details of the elemental analyses can be found in reference (20). The total weight of deposited contaminants (C, H, N, Fe, Ti, Na and traces of Ca, V, K) was between 10 and 15% in all cases. Data are uncorrected for differences in weight basis.

## Results and Discussion

### Proposed Model

The following model, utilizing reactions involving basic nitrogen compounds, sodium, and acid sites, fits virtually all of the Wilsonville catalyst coking trends for runs 246 through 250:

$$CH + LTR \underset{k_{d,LTR}}{\overset{k_{a,LTR}}{\rightleftharpoons}} C^-(LTRH)^+ \qquad (1$$

$$CH + TR \underset{k_{d,TR}}{\overset{k_{a,TR}}{\rightleftharpoons}} C^-(TRH)^+ \qquad (2$$

$$CH + ANa \underset{k_{d,Na}}{\overset{k_{a,Na}}{\rightleftharpoons}} CNa + AH \qquad (3$$

$$BH + ANa \underset{k'_{d,Na}}{\overset{k'_{a,Na}}{\rightleftharpoons}} BNA + AH \qquad (4$$

where LTR represents nitrogen bases correlated with light thermal resid (or with distillate solvent), and TR represents nitrogen bases which correlate with thermal resid. CH represents an acid site that may react with either basic nitrogen or sodium, while BH represents a site that reacts with sodium alone. ANa represents sodium that is present in some ionic form in coal ash. $C^-(LTRH)^+$ and $C^-(TRH)^+$ represent the acid-base adducts, which are designated chemisorbed bases, and CNa and BNA represent the Na-exchanged acid sites, which are designated chemisorbed Na. Simplifying assumptions are that, on the average, base molecules contain only one nitrogen atom, and that saturation corresponds to one nitrogen atom per acid site. It is also assumed that CNa and BNA are not reactive towards nitrogen bases. In this model, the chemisorbed bases contain as much as 100% of the carbon on the catalyst at any time. The remainder of the carbon, if present, is assumed to be present as an essentially constant amount of non-nitrogen-containing process-derived coke.

The model, as written, is for Brönsted acid sites. However it can be written for combined Bronsted and Lewis acidity, or only Lewis acidity, with no loss of applicability. Of course, the

protonated nitrogen base must be held to the surface for Brönsted acidity to lead to carbon deposition by this model. Also, at this stage of development the model neglects condensation and/or hydrodenitrogenation (HDN) reactions of the chemisorbed nitrogen bases, since desorption of these bases is a key feature. The true coke formation mechanism is almost certainly more complicated than the model presented here.

## Catalyst Characterization

Wyodak Coal, Shell 324M Catalyst. Figure 1 shows the %C, %N and %Na determinations for Shell 324M catalyst in Wilsonville runs using a Wyodak sub-bituminous coal. The series shown (246-DITSL, 246-ITSL and 249-RITSL) is especially interesting because a single catalyst charge was used for all three runs. The entire catalyst lifetime is thus depicted from left to right in Figure 1.

DITSL operation (LTR, no TR or ash) is characterized by essentially constant C and N levels during the operating period, and no Na accumulation. This represents a rapid saturation of acid sites by LTR-bases; the N level at saturation for this catalyst is about 0.7%.

On switching to the ITSL mode (LTR and TR, no ash) C increases, N remains constant, and Na does not accumulate. In our model, this corresponds to a gradual exchange of LTR-bases with TR-bases. Assuming that a pseudo-saturated surface exists during the exchange period, this requires that TR bases have a higher average molecular weight than the LTR bases. This is certainly consistent with the resids contained in the LTR and TR streams. Stohl and Stephens (8) published C analyses for the last month of 246-ITSL which clearly show the establishment of a new saturation level at ca. 10% C. This level, sketched in Figure 1, is consistent with the carbon level at the start of the 249-RITSL run period.

Finally, in the RITSL period, C and N decrease while Na increases. In fact, N decreases to essentially zero while at the same time Na shows evidence of reaching a saturation level. In our model this is due to a gradual exchange of nitrogen poisoned acid sites with Na-poisoned sites. It is clear that coal ash is the source of Na deposited on the catalyst.

Illinois #6 Coal, Shell 324M Catalyst. Figure 2 shows the characterization data for Shell 324M catalysts when Illinois #6 bituminous coal was used. Runs 248-DITSL and 248-ITSL represent a single batch of catalyst subjected to first DITSL, then ITSL, processing, but Run 247-RITSL was conducted with a separate catalyst batch. In this respect the data obtained with Illinois #6 coal feed are different than the Wyodak data in Figure 1.

DITSL data for Illinois #6 coal are virtually identical to that for Wyodak coal with a saturation level of ca. 0.7% N and 8% C. On switching to the ITSL mode, the C level increases with no change in N or Na, again consistent with an exchange of LTR-base with TR-base at pseudosaturated conditions. It is, as before, not clear if the exchange with TR-base has gone to completion at the end of Run 248-ITSL. However, it is obvious that the TR-bases derived fron the Illinois #6 coal have a higher C/N ratio than TR-bases from the Wyodak coal because the C levels in 248-ITSL are higher than in 246-ITSL. Assuming an average of one N atom per base molecule, the average molecular weight of the Illinois #6 TR-

bases is 50% to 100% greater than that of the Wyodak TR-bases.

Run 247-RITSL data again show C and N decreasing as Na increases. In comparison to the Wyodak coal (Run 249-RITSL) data, more C is desorbed per desorbed N, again indicating Illinois #6 TR-bases have a higher average molecular weight than Wyodak TR-bases. Also, in comparison to Run 249, the N and Na levels at the end of Run 247 indicate that poisoning of acid sites had not reached completion when run 247 was terminated.

Since this RITSL catalyst was not previously subjected to the DITSL-ITSL exchange, the initial levels of C and N must correspond to a rapid saturation at startup; however, this saturation was not with LTR-bases, as occurs in DITSL mode. Instead, saturation occurs with the higher average molecular weight TR-bases. In contrast to organic base exchange, which is probably desorption-limited, adsorption on unsaturated sites should be rapid at process temperatures, and the rapid saturation with N indicates this to be the case. Stohl and Stephens (5) have shown that the presulfided Shell 324M catalyst will chemisorb N from a nitrogen-containing polycyclic aromatic coal liquid fraction rapidly enough to achieve saturation, reported by them to be 0.6% N, in two hours at 300 C. The initial C level in Run 247 shows reasonable agreement with the levels reached in 248-ITSL; this suggests the exchange of LTR and TR bases was near completion at the end of 248-ITSL.

Illinois #6 Coal, Amocat 1C Catalyst. The two periods of Run 250-CCITSL shown in Figure 3 used Illinois #6 coal and Amocat 1C $NiMo/Al_2O_3$ catalyst. These two periods are 250-CCITSL-NAR (no ash recycle) and 250-CCITSL-AR (ash recycle). They represent two separate batches of the Amocat 1C catalyst. Both batches indicate rapid initial saturation at ca. 12% C and 0.5% N, followed by a decrease in C and N levels and corresponding Na increase. The data taken in the ash-recycle period shows a more rapid increase in Na, and concurrent decrease in C, than the data for the no-ash-recycle period. This is most easily explained as a Na concentration effect, with the Na deposition rate increasing with sodium concentration in the reactor. The larger relative error in N determination makes the N trends less definite.

Elemental Correlations. Figure 4 shows plots of N versus C, normalized to moles per g catalyst, for all samples used in this study. Two distinct data clusters are immediately obvious: DITSL-ITSL data and RITSL-CCITSL data. All of the DITSL-ITSL data show essentially constant N content while for RITSL-CCITSL samples a direct relationship between C and N exists. The slope of the C-N data suggests stoichiometries for the desorbing bases. Trends show that the desorbing material is mainly coal-dependent: it has an average stoichiometry of about $C_{14}N$ for Wyodak sub-bituminous coal, and about $C_{24}N$ for Illinois #6 bituminous. These calculations are subject to the assumption that all of the net carbon loss is due to desorption of nitrogen bases. Also, the trends in the Amocat data are less well defined simply because the N-Na exchange is slower on this catalyst. Assuming that the initial coverage in all RITSL and CCITSL runs is essentially all TR base, then these average stoichiometries can be assigned to the TR bases.

Average stoichiometries for the bases chemisorbed on the catalyst when LTR and distillate derived from from the Wyodak or Illinois #6 coals can be calculated from 246-ITSL and 248-ITSL

data; in the model this represents exchanges from essentially 100% LTR coverage to 100% TR coverage. Assuming the LTR- and TR-saturation points indicated by the surrounding DITSL and RITSL data in Figures 1 and 2, and using the $C_{14}N$ and $C_{22}N$ stoichiometries calculated for the appropriate TR bases, we next calculate an average stoichiometry for LTR bases derived from both coals of about $C_8N$, with no strong dependence on coal type. This number is less certain than the TR-base calculations as both TR-base numbers and the absolute %C numbers were required. Nevertheless, the numbers summarized in Table 3 represent our best estimate of the average stoichiometries of the nitrogen bases required to fit the characterization data to our model.

Figure 5 shows N plotted against Na, both in moles per g catalyst, for the RITSL and CCITSL data (DITSL and ITSL data show no Na uptake). The correlation here is good: all of the Shell 324M data fall on one line, and all of the Amocat 1C data falls on another. This relationship should reflect characteristics of the acid site populations of the two catalysts. For Shell 324M catalyst, three Na atoms are chemisorbed for each N atom desorbed; for Amocat 1C, two Na atoms are chemisorbed for each N atom desorbed. Assuming one N atom (or one Na atom) per CH site, and one Na atom per BH site, and assuming that all CH sites can react with Na (strongly suggested by the desorption of essentially all N in Run 249, for Shell 324 catalyst, but not strongly indicated for Amocat 1C, for which complete desorption of N was not seen) then two BH sites exist for every CH site on the Shell 324M catalyst, and one BH site for every CH site on the Amocat catalyst.

## Laboratory Desorption of LTR-Bases

A key point in this model is the desorption of basic nitrogen compounds under coal liquefaction conditions. A laboratory experiment was performed recently in a 300 mL CSTR to duplicate the desorption of these bases indicated by the pilot plant data. A 100 g blend of various Wilsonville DITSL catalysts, still in the oil in which they were shipped, was placed in the reactor. THF was flowed over the catalyst bed at ca. 120 C until the oil was removed. This took approximately one week. Analysis of the catalyst at this point indicated about 0.45% N, which is somewhat lower than the saturation coverage of 0.7% N seen in the Wilsonville catalysts after THF Soxhlet extraction. As a separate check, a Wilsonville DITSL catalyst was Soxhlet extracted for almost 1000 hours and the %N level was found to remain constant. Temperature measurements indicated Soxhlet extraction occurs at about 65 C. It is possible that the CSTR extraction at 120 C causes bases to desorb that do not desorb in the Soxhlet apparatus.

After THF extraction in the CSTR, the feed was switched to tetralin at about 6 ml/hr and the temperature was increased to 350 C. $H_2$ was supplied only in makeup amounts, i.e. to enough to keep reactor pressure at about 2000 psi. The catalyst bed was gently stirred during the experiment. The reactor was cooled, and samples taken, twice weekly for the next month.

Results are shown in Figure 6. A significant loss of N, from 0.45% to a relatively stable 0.15% did occur during the run (figure 6b). The average stoichiometry calculated for the desorbing compounds (figure 6c), was $C_{30}N$, which is closer to TR-

base stoichiometry (estimated from process exchange) than the LTR-base stoichiometry. One possible explanation for the discrepancy could be the formation of non-nitrogen-containing coke on acid sites concurrent with nitrogen base exchange. Evidence for this was seen near the end of the CSTR experiment (figure 6a). Since only %C was used to estimate the LTR-base stoichiometry from the DITSL-ITSL exchanges, the $C_8N$ figure could be low for this reason. Also, accumulation and loss of bases may be complicated than a simple adsorption/desorption process. A kinetic analysis of the nitrogen content based on a first-order desorption mechanism is shown in Figure 6d. The rate constant for desorption of N in this experiment, $k_{d,TR}$, is 0.04 $day^{-1}$, which is within a factor of four of rate constants calculated from the data for the spent catalysts from the Wilsonville runs. Thus the CSTR experiment is in qualitative agreement with the kinetic analysis of the spent Wilsonville catalyst data. Most importantly, the lab experiment confirms the reversibility of the N contained in the organic residue on the catalyst.

## Conclusion

In this model, acid sites on the sulfided catalyst rapidly saturate with basic nitrogen compounds on start-up. These bases (called LTR-bases) are either in the LTR material, or in the distillate solvent. In turn these bases gradually exchange with nitrogen bases having a higher average molecular weight when the TR stream is introduced to the feed. This correlation does not necessarily imply any chemical difference in the two resids (LTR and TR), but may simply reflect an increase in the relative concentrations of distillate solvent and resid. On introduction of coal ash, the nitrogen-containing compounds desorb, and sodium is adsorbed on the catalyst. Coal dependence is seen in the TR-bases, with the Illinois #6 coal producing a higher average molecular weight deposit than the Wyodak coal; this is not seen for LTR-bases. Sodium adsorption demonstrates a catalyst dependence, indicating differences in acid site populations for the two Shell and Amocat catalysts.

Reversibility of the chemisorption of nitrogen bases has been demonstrated in our laboratory. Future experiments will concentrate on other key features of the model, such as base exchange and sodium poisoning.

## Acknowledgement

This work was performed at the Kentucky Energy Cabinet Laboratory (KECL). The KECL is operated by the University of Louisville for the Kentucky Energy Cabinet.

Table 1.

Summary of Wilsonville Runs Correlated in This Work

| Run | Coal | Configuration | Catalyst | Comments |
|---|---|---|---|---|
| 246A | Wyodak | DITSL | Shell 324M NiMo | |
| 246B | Wyodak | ITSL | Shell 324M NiMo | Started with catalyst from end of 246A |
| 247 | Illinois #6 | RITSL | Shell 324M NiMo | |
| 248A | Illinois #6 | DITSL | Shell 324M NiMo | |
| 248B | Illinois #6 | ITSL | Shell 324M NiMo | |
| 249 | Wyodak | RITSL | Shell 324M NiMo | Started with catalyst from end of 246B |
| 250-II | Illinois #6 | CCITSL | Amocat$^R$ 1C NiMo | No ash recycle |
| 250-III | Illinois #6 | CCITSL | Amocat$^R$ 1C NiMo | With ash recycle |

Table 2.

Hydrotreater Feed

| | TR Present? | LTR Present? | Coal Ash Present? |
|---|---|---|---|
| DITSL | No | Yes | No |
| ITSL | Yes | Yes | No |
| RITSL | Yes | Yes | Yes |
| CCITSL | Yes | Yes | Yes |

Table 3.

Best Estimate of Average Nitrogen Base Stoichiometry Required to Fit Our Model to Wilsonville Catalyst Data

| Coal | LTR-Bases | TR-Bases |
|---|---|---|
| Wyodak Sub-bituminous | $C_8N$ | $C_{14}N$ |
| Illinois #6 Bituminous | $C_8N$ | $C_{22}N$ |
| CSTR Laboratory Study | $C_{30}N$ | |

Figure Captions

Figure 1. Elemental analyses for Shell 324M catalyst and Wyodak sub-bituminous coal.

Figure 2. Elemental analyses for Shell 324M catalyst and Illinois bituminous coal.

Figure 3. Elemental analyses for Amocat 1C catalyst and Illinois bituminous coal.

Figure 4. C-N trends for all data.

Figure 5. N-Na correlations for all data.

Figure 6. Desorption of LTR-bases from Run 248 DITSL catalysts in CSTR at 350"c.

## References


1. P. Holloway, Sandia National Labs Report SAND78-0056 (1978).

2. A. Ocampo, J.T. Schrodt and S.M. Kovach, Ind. Eng. Chem. Prod. Res. Dev. 17 (1), 56 (1978).

3. T.L. Cable, F.E. Massoth and M.G. Thomas, Fuel Proc. Tech. 4, 265 (1981).

4. D.S. Thakur and M.G. Thomas, Ind. Eng. Prod. Res. Dev. 23, 349 (1984).

5. F.V. Stohl and H.P. Stephens, ACS Div. Fuel Chem. Prepr. 31, 251 (1986).

6. F.V. Stohl, ACS Div. Fuel Chem. Prepr. 33, 325 (1987).

7. F.V. Stohl, Q.A. Qader, F.E. Massoth and D.S. Thakur, Ind. Eng. Chem. Res. 26, 840 (1987).

8. F.V. Stohl and H.P. Stephens, Ind. Eng. Chem. Res. 26, 2466 (1987).

9. I. Mochida, K. Sakanishi, Y. Korai and H. Fujitsu, Fuel 65, 1090 (1986).

10. Y. Yoshimura, T. Sato, H. Shimada and A. Nishijima, Fuel Sci. Tech. Int'l. 4, 621 (1985).

11. Y. Yoshimura, H. Shimada, T. Sato, M. Kubota and A. Nishijima, Appl. Catal. 29, 125 (1987).

12. Y. Yoshimura, K. Hayamizu, T. Sato, H. Shimada and A. Nishijima, Fuel Proc. Techm 16, 55 (1987).

13. A. Nishijima, H. Shimada, Y. Yoshimura, T. Sato and N. Matsubayashi, Catalyst Deactivation 1987, B. Delmon and G. Froment, Eds., Amsterdam, p. 39 (1987).

14. E. Furimsky, Erdol und Kohle 35, 455 (1982).

15. S.M. Kovach, L.J. Castle, J.V. Bennett and J.T. Schrodt, Ind. Eng. Chem. Prod. Res. Dev. 17 (1), 62 (1978).

16. D. Garg and E.N. Givens, Fuel Proc. Tech. 9, 29 (1984).

17. J. R. Baker, R.L. McCormick and H.W. Haynes, Jr., Ind. Eng. Chem. Res. 26, 1895 (1987).

18. B.D. Adkins, S.R. Adkins, B.H. Davis and D.R. Milburn, in Catalyst Deactivation 1987, p. 469, B. Delmon and G. Froment, Eds., Elsevier, Amsterdam 1987.

19. Catalytic, Inc. "Run 250 with Illinois #6 Coal", Technical Progress Report DOE/PC/50041-81; "Run 249 with Wyodak Coal", Technical Progress Report DOE/PC/50041-75; "Run 248 with Illinois #6 Coal", Technical Report DOE/PC/50041-71; "Run 247 with Illinois #6 Coal", Technical Report DOE/PC/50041-67; "Run 246 with Wyodak Coal", Technical Report DOE/PC/50041-61.

20. B.D. Adkins, K. Cisler and B.H. Davis, Appl. Catal. 23, 111 (1986).

Shell 324M Catalyst, Wyodak Coal

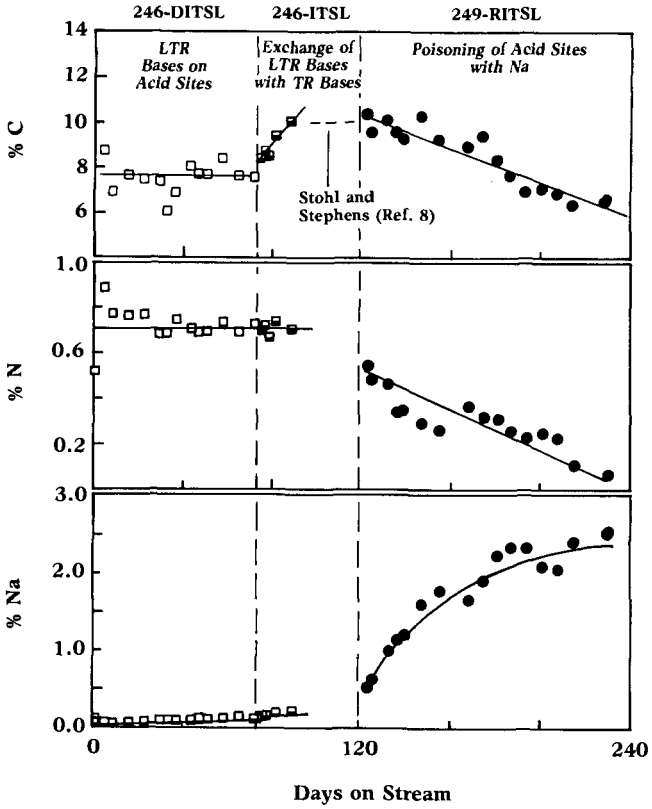

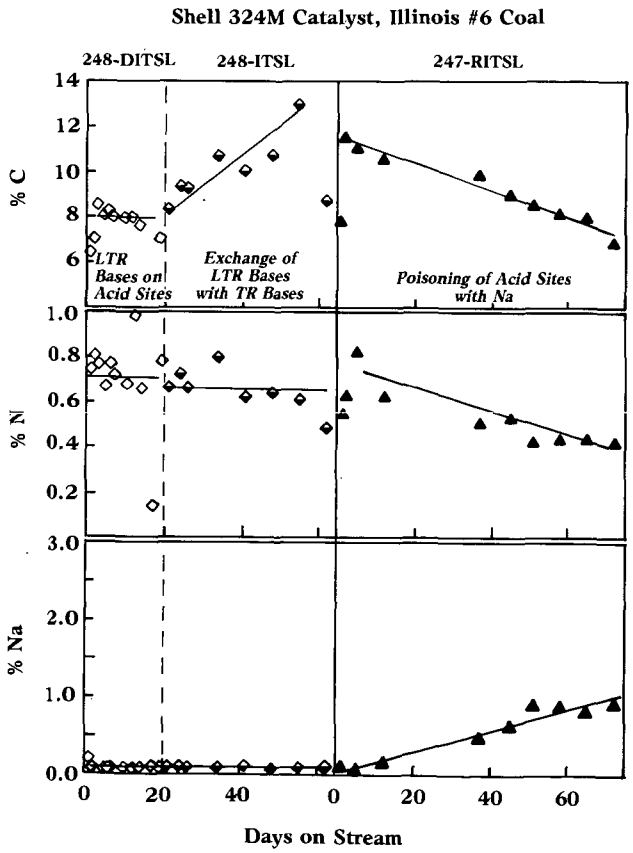
Shell 324M Catalyst, Illinois #6 Coal
248-DITSL
248-ITSL
247-RITSL
% C
% N
% Na
LTR Bases on Acid Sites
Exchange of LTR Bases with TR Bases
Poisoning of Acid Sites with Na
Days on Stream

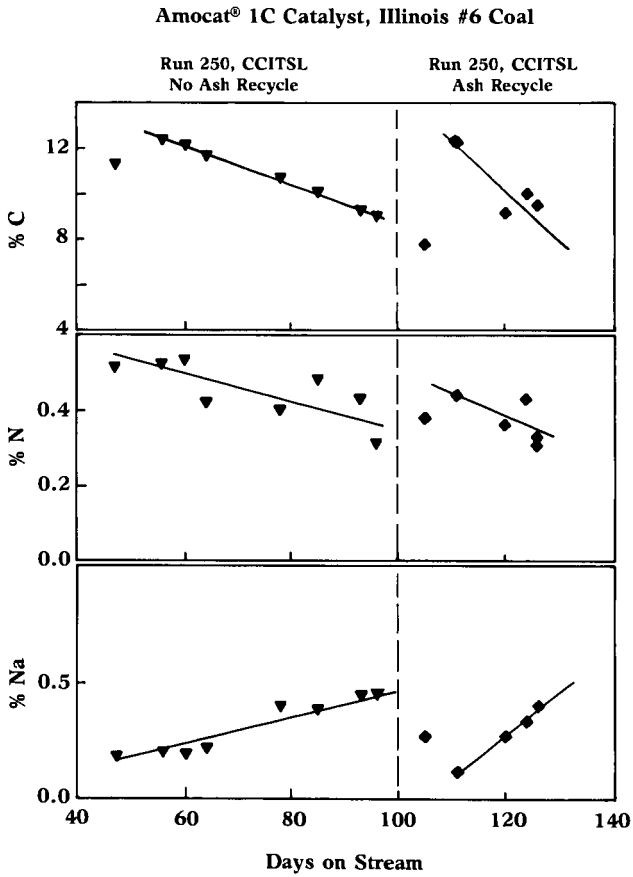
Amocat® 1C Catalyst, Illinois #6 Coal
Run 250, CCITSL
No Ash Recycle
Run 250, CCITSL
Ash Recycle
% C
12
8
4
% N
0.4
0.2
0.0
% Na
0.5
0.0
40
60
80
100
120
140
Days on Stream

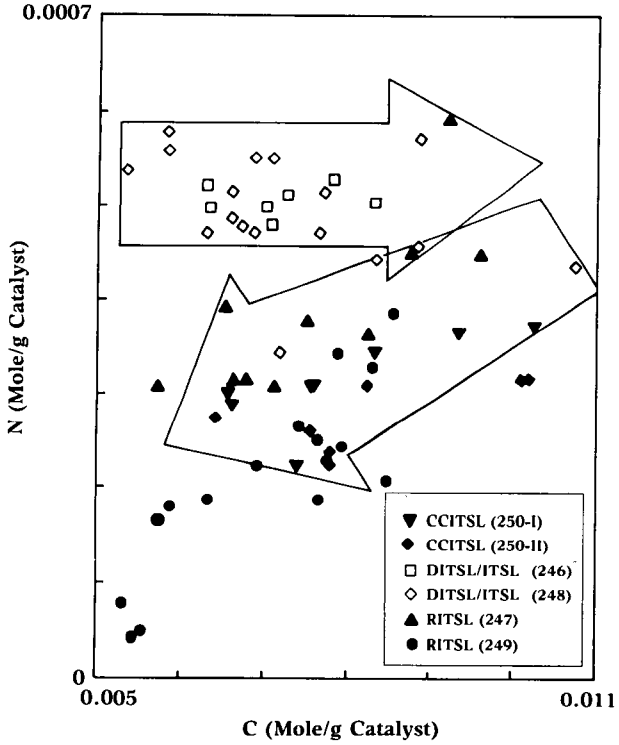
0.0007
0
0.005
0.011
N (Mole/g Catalyst)
C (Mole/g Catalyst)
CCITSL (250-I)
CCITSL (250-II)
DITSL/ITSL (246)
DITSL/ITSL (248)
RITSL (247)
RITSL (249)

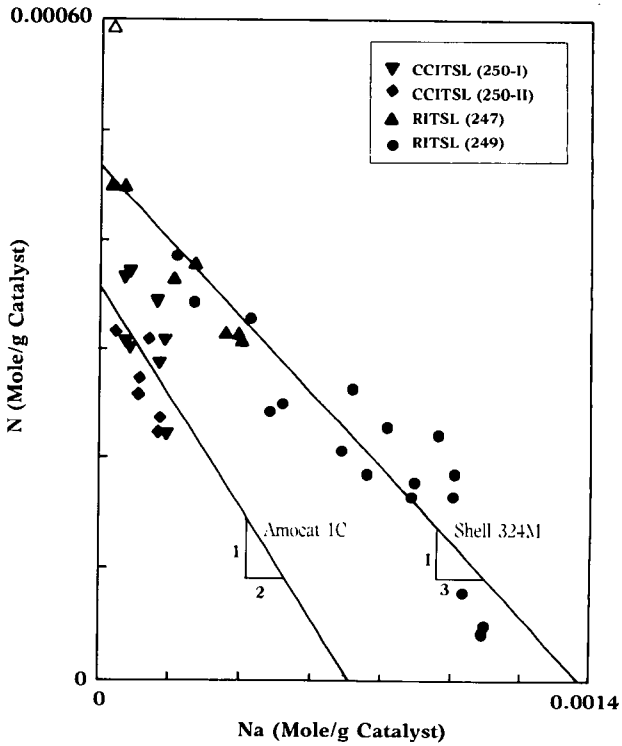
0.00060
0
0
0.0014
N (Mole/g Catalyst)
Na (Mole/g Catalyst)
CCITSL (250-I)
CCITSL (250-II)
RITSL (247)
RITSL (249)
Amocat 1C
1
2
Shell 324M
1
3

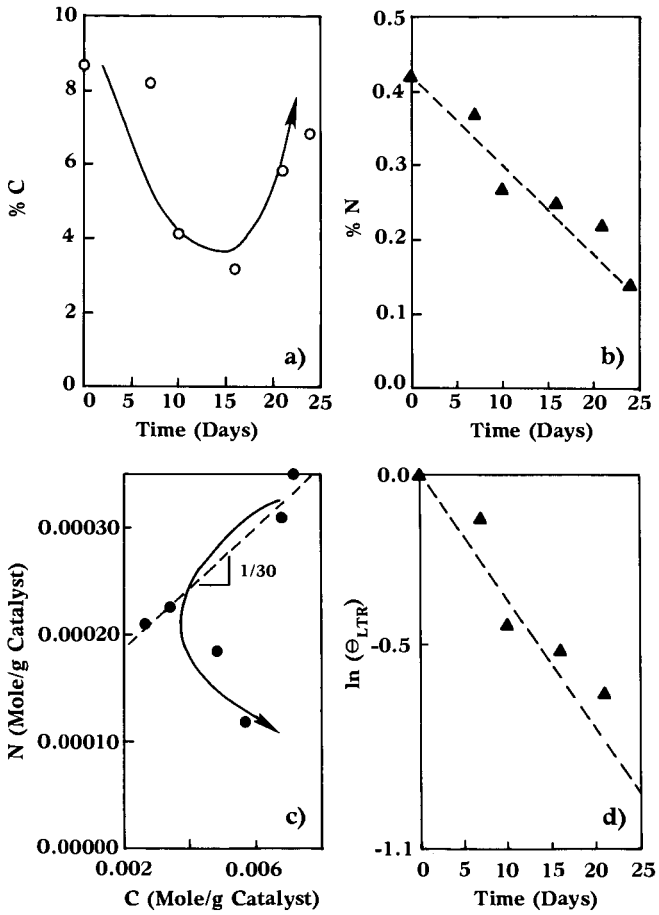
10
8
6
4
2
0
% C
a)
0 5 10 15 20 25
Time (Days)
0.5
0.4
0.3
0.2
0.1
0.0
% N
b)
0 5 10 15 20 25
Time (Days)
0.00030
0.00020
0.00010
0.00000
N (Mole/g Catalyst)
1/30
c)
0.002
0.006
C (Mole/g Catalyst)
0.0
-0.5
-1.1
ln (Θ_LTR)
d)
0 5 10 15 20 25
Time (Days)

# ANOMALOUSLY HIGH FLAMMABILITY OF LOW VOLATILITY FUELS DUE TO ANOMALOUSLY LOW IGNITION TEMPERATURES.

Joseph L. Walker, William W. Bannister,
CAPT Edward T. Morehouse, USAF, and Robert E. Tapscott

Fire Technology Branch, AFESC, Tyndall AFB, FL 32403

Fuel flammability is usually predicated on flash points, resulting from exposure of fuel to flame. Low molecular weight (high volatility) fuels have lower flash points and thus are judged more flammable than low volatility fuels. A startling reversed relationship has been shown to exist, however, for lower members of the alkane series, between molecular weight and ignition temperature (IT), occasioned by contact with hot surfaces: up to a point, less volatile higher molecular weight fuels have lower IT's and are more easily ignited when exposed to hot surfaces. For higher members of the alkane family this trend reverses, resulting in minimum IT's for the $C_5$ - $C_9$ alkanes. Branched chain alkanes, arenes and olefins also have anomalously high IT's. Free radical effects are unimportant among factors influencing ignition temperature; ionic effects may be important, as is the case for fires involving active metal, phosphorus, thermite and similar inorganic incendiary agents. This may be useful in fuel selection, if fires are anticipated to result from contact with hot metal surfaces, as in aircraft crashes, fuel spills on hot engine surfaces, or similar effects, instead of by contact with flame. Molecular modelling considerations will be discussed to explain the anomalous trends.

## I. Ignition Temperatures (IT).

Ignition temperature is a poorly understood fuel characteristic which has received little previous attention. This is despite the fact that ignition temperature may arguably be the single most important fuel characteristic in terms of catastrophic ignition by gunfire, aircraft crashes, fuel spills on hot engine surfaces, and other instances of obvious military (and commercial) aviation interest. From the standpoint of fire prevention, and in particular design of practical jet fuels capable of resisting ignition from such effects while fulfilling normal operational combustion performance requirements, it is suggested that IT's should be given an in depth examination.

Fuel ignition can be initiated by either of two effects: contact of the fuel with a flame, or with a hot surface. For ignition by flame contact, the important fuel characteristic is the flash point (FP); for ignition from a hot surface, ignition temperature is important.

Flash points are routinely measured by heating a sample of the liquid in either a closed or open cup assembly, with a small flame continually passed over the surface of the liquid. The flash point is the lowest temperature at which the fuel vapors ignite with propagation of the flame beyond the source of ignition. Since it is principally a measure of fuel volatility, flash point is most associated with the molecular weight of the fuel component within a given chemical family.

IT measurements are not as precise. Typically, fuel is directed onto a hot surface at a given temperature, and allowed to heat for up to ten minutes. (1) The IT is the lowest temperature at which a flame occurs (in some cases, exothermic decompositions not necessarily accompanied by a flame). Often the flammable liquid will decompose to other

materials during the heating period. Thus, ignition temperature may not really be a characteristic of the original material, but rather of its decomposition products. In addition to rate and duration of heating, other variables also affect IT measurements: shape and size of the test chamber, air concentration, nature of the heated surface (including catalytic effects), and temperature of the surface. Therefore, IT measurements are frequently only poorly reproducible: ignition temperature data for a compound, taken by different individuals, can have very greatly differing values. (2)

## II. Free Radical Fire Effects, and the Fire Tetrahedron. (3)

Until twenty years ago, there were three important requirements known for a fire -- fuel, oxygen, and heat. These were commonly considered as components of the "fire triangle", the removal of any one being sufficient to extinguish a fire, and the presence of all three required for fire initiation and propagation. As free radicals became more understood, the "fire triangle" was expanded to the "fire tetrahedron".

Free radicals are non-ionic high energy intermediates which form easily in high temperature reactions. Fire growth involves an avalanching oxidative propagation of free radicals in vaporized fuel-air mixtures: one free radical creates several others, and with descendent free radicals forming in profusion in a continuing and proliferating propagation throughout the fuel-air mixture.

Today, therefore, fires are characterized by the "fire tetrahedron" (fuel, heat, air, and the presence of propagating free radicals).

For ignition of fuels by contact with flame, in which flash points have most meaning, free radical events are entirely operational. In such fires, the flame ignition source actually is a free radical plasma, from which high energy free radicals are transferred to fuel vaporized by heat of the flame. Situations which promote free radical formation are conducive to ignition of the fuel under these conditions; and agents such as the Halons which quench free radical formation are thus optimum fire extinguishing agents for such fires.

## III. Ionic Fire Effects: A Return to the Fire Triangle?

This discussion will attempt to point out that not all fires should be characterized by the "fire tetrahedron". In fact, many fires of military and commercial importance may best be characterized by the "fire triangle", with free radicals being totally unimportant.

Thus, fires arising from ignition of magnesium, titanium, and other active metals would best be described as involving ionic (not free radical) effects in both initiation and growth of the fire.

e.g., $Mg^{o} + 1/2\ O_2 \text{ -----> } Mg^{++}\ O^{=}$ 1)

"Ionic fires" can perhaps best be differentiated from free radical fires in terms of the ionic pathways and products of the ionic reactions, with no role of free radical propagating intermediates. The "flame" of an ionic fire is a plasma of incandescent ions, lacking in free radical components.

Phosphorus, thermite and other inorganic or pyrotechnic fires also would appear to be ionic and not free radical in nature. For ignition

of other combustibles by active metal or other inorganic incendiaries, it is now suggested that the mode of such ignitions may be that of contact with a hot surface rather than by contact with a flame.

Along these lines, Halons which quench free radicals and thus prevent propagation of "free radical" types of fires are completely ineffective against active metal "ionic" types of fires.

## IV. Possible Ionic Effects in Ignition Temperature Correlations.

For fires resulting from ignition by contact of the fuel with hot surfaces, this discussion will attempt to demonstrate that while free radicals are certainly formed due to energy transfer and resulting bond breakages, the initiating events are not free radical in nature. In actuality, those fuels which would appear to be most susceptible to free radical formation often are among the most resistant to ignition by contact with hot surfaces! Thus, olefins and alkyl-substituted benzenes are far more susceptible to free radical substitution than are alkanes, due to resonance stabilization of the resulting free radical intermediates. (4) On the other hand, when comparing olefins and arenes with alkanes of similar volatility, the olefins and arenes frequently have higher ignition temperatures. Branched chain alkanes also undergo free radical reactions more readily than straight chain alkanes, but have higher IT's; and cyclopentanes are more reactive to free radicals than are cyclohexanes, but again the cyclopentanes have higher IT's (4,5) Representative data is shown in Table I.

Table I. Ignition Temperatures (IT) and Boiling Points (BP), in $^{o}$F, for Alkanes, Olefins and Arenes. (2,6,7)

| Alkane | BP | IT | Olefin | BP | IT | Arene | BP | IT |
|---|---|---|---|---|---|---|---|---|
| butane | 31 | 826 | 1-butene | 21 | 829 | | | |
| methyl-cyclohexane | 214 | 545 | | | | Toluene | 232 | 1026 |
| methyl-cyclopentane | 161 | 624 | | | | | | |
| octane | 257 | 428 | | | | | | |
| 2,2,4-trimethyl-pentane | 211 | 784 | | | | | | |

In Figure 1, moreover, there is an anomalous decrease in ignition temperature of alkanes with increasing molecular weight, for the range of alkanes from methane ($C_1$) through octane ($C_8$). Precise data is not prevalent for the higher alkanes. As shown in the lower projected track of the IT values for the various alkanes, one possibility certainly lies in an asymptotic sweep along a 400$^{o}$ IT isotherm, for alkanes beyond $C_8$. An inescapable suspicion lurks here, however,that a possible thermal cracking may occur at this temperature if the hydrocarbon is permitted to linger at the heated surface for up to ten minutes, in accordance with the ASTM operating procedures for this determination. (1) Thus, alkanes larger than nonane could conceivably have higher ignition temperatures; but by undergoing slow pyrolysis at 400$^{o}$ F, some alkanes in the minimum IT region characeristic of $C_5$ - $C_9$

would form, with these igniting at this spuriously low temperature.

There is indeed some evidence for a possible increase in IT's for the higher alkanes; i.e., a minimum zone of IT's may exist for alkanes in the region of pentane through nonane ($C_5$ - $C_9$). This is shown in Figure 1 as the upper projected track for the alkanes beyond $C_9$. It is obvious that either track could actually pertain, and that currently available data is insufficient and good values are probably poorly available with existing equipment and technique.

If this mimimum zone for ignition temperatures indeed exists, the hexane through decane range of alkane would appear to represent the most dangerous species in jet fuel formulations: these alkanes have unsuitably low flash points and ignition temperatures. In terms of ignition from hot surfaces, these would be highly prone to enflame due to the low ingition temperatures, and then would promote uncontrollable proliferation of the fire because of the low flash points.

Experimental evidence is too sparce to fully support an ionic event for typical hot surface ignitions. However, it has previously been demonstrated that the nature of the hot surface can have significant effects on ignition temperatures. Thus, benzene exhibits quite higher ignition temperatures in iron containers than in quartz, and even higher in zinc. (2) As will be discussed below, this may be most consistent with the relative emissivities of these materials. However, silica (quartz) can be acidic; and ferric oxide is significantly more acidic than zinc oxide. Thus, there may be cationic catalysis provided by an acidic surface, which can serve to greatly favor bond ruptures in alkanes. (4) Cationic and emissivity effects may be of importance with regard to incorporation of metals or coatings for aircraft parts which may be anticipated to be most likely to come into contact with fuel leaks in combat gunfire or in controlled crash situations.

## V. Surface Emissivity Effects.

Emissivity is the energy radiated from a unit area of a surface, in a unit of time. This is greatly dependent on the nature of the surface: for example, rough surfaces are more emissive than smooth surfaces. With regard to the decreasing ignition temperatures noted above, with zinc surfaces influencing a higher IT for benzene than iron, and quartz surfaces providing the coolest IT of all three, this is consistent with the relative trend of increasing emissivities: quartz is a more efficient heating surface than smooth unoxidized iron or zinc.

## VI. Molecular Effects Which May Influence Ignition Temperatures.

Fuel component characteristics have been identified as having possible impact on the ignition temperatures are described below. None of these appear in any way to be associated with free radical effects.

### 1. Molecular weight, and speed and inertia effects.

Since the anomalous decrease of ignition temperatures with increasing molecular weight is observed only from methane through nonane, other effects in the alkanes must offset any role of molecular weight in reducing ignition temperatures. Molecular weights are inversely proportional to molecular velocities, however, as shown in Figure 2. Since the heavier molecules have lower velocities, there is an increased residence time for these in the vicinity of a hot surface,

with increased time for energy transfer to the molecule. Heavier molecules also have greater inertia and thus less ability to move away from a hot surface than would a lighter molecule.

2. Molecular rigidity.

This appears to be a very important effect, not only in the straight chain alkane family, but even more so for branched chain alkanes, cycloalkanes, olefins and aromatics. As stated previously, these species are particularly susceptible to free radical reaction systems; but surprisingly, these are frequently very considerably more stable than are the alkane analogs, with regard to ignition by fuel contact with hot surfaces. Examinations of molecular models reveal that, compared to the straight chain alkanes, all these other species are very considerably more rigid, with very considerably reduced rotational degrees of freedom within the molecular structures. This would then impart a pronounced decrease in "floppiness" of the molecule in its impact with a hot surface, allowing the more rigid structure to rebound readily and rapidly, with correspondingly considerably reduced residence times in the vicinity of the hot surface, and considerably reduced energy transfer from the surface to the fuel molecule.

This effect may be of importance in design of new fuel compositions: olefinic, branched chain, cyclic (napthenic) and aromatic moeities would impart higher ignition temperature characteristics.

3. Specific molecular heat.

For the smaller molecules, apparently, factors of relative speed and relative rigidity are overpoweringly important. Within the lower range of the alkanes, each addition of a methylene unit imparts a significant increase in molecular weight and in internal degrees of rotational freedom. In going from ethane to propane, for example, there is a 17% decrease in speed at 1000° F; whereas decane is only 5% slower than nonane at this temperature. Internal rotational degrees of freedom are even more considerably enhanced for propane, which is very flexible compared with ethane, which is remarkably rigid; but decane and nonane have very little difference in "mushiness" due to this effect. Thus, decreased speed and rigidity effects arising from increased molecular weight are very much less important for the higher alkanes.

Moreover, higher alkanes begin to enjoy the benefit of increased "molecular specific heat". When lower alkanes such as ethane or propane are energized by radiational heat, all atoms of the small molecule are fairly equally irradiated. For significantly larger molecules, some atoms will be in the shadow of others. The hotter surface atoms can then transfer some of their increased energies to the cooler internal atoms. Thus, a higher ignition temperature will be required to attain decomposition energies for a molecule large enough to provide shadowing by some of its atoms to other neighboring atoms.

Thus, the anomalous high ignition temperatures for higher alkanes seen in Figure 1 may actually represent valid IT's; and the lower points constituting the asymptotic sweep at the 400° isotherm for these higher alkanes may prove to be unrealistically low.

## VII. Recommendations for an IT Differential Scanning Calorimeter.

If more realistic IT determinations had lower time requirements

(perhaps a second instead of ten minutes), IT values for fuel components would probably be considerably increased. Modification of a conventional differential scanning calorimeter (DSC) could provide a convenient and accurate determination. Minute samples of the fuel components could be periodically injected, at higher and higher temperatures, until a sudden exotherm signal is attained. The first derivative appearance of the IT point with this scheme may make for a more reproducible determination. Automatic injection devices, coupled with automatic temperature controlling, should provide rapid and easy injections with minimum attention requirements for the determination.)

## VIII. Fuel Design for Fire Prevention.

It may be possible to design fuels meeting operational combustion requirements, (i.e., burning satisfactorily when ignited with a flame), at the same time providing maximum resistance to ignition on contact with a hot surface (as in aircraft crashes, leakage of fuel onto hot engine surfaces, and similar situations). From the foregoing preliminary considerations, attention could be given to elimination of alkane content in the region $C_5$ - $C_{10}$), since these components may be in the minimum zone of IT's and also suffer from unduly low flash points. This cut could be catalytically dehydrogenated to olefinic or aromatic stocks, or catalytically rearranged to branched chain isomers or cyclolalkane analogs. It could also be alkylated with isobutylene to provide higher molecular weight and branched chain character. All of these should result in higher ignition temperatures, lower vapor pressure, increased density, and decreased viscosity effects, which should prove desirable from the standpoint of fuel characteristics.

## REFERENCES


1. "Autoignition Temperature of Liquid Chemicals", ASTM Designation E 659 - 78 (Reapproved 1984).

2. "Fire Hazard Properties of Flammable Liquids, Gases and Volatile Solids", National Fire Protection Association, Boston, MA (1960).

3. Hucknall, D. J. "Chemistry of Hydrocarbon Combustion", Chapman and Hall, New York (1985).

4. March, J. "Advanced Organic Chemistry: Reactions, Mechanisms and Structure", McGraw-Hill Book Co., New York (1968), pp. 153 - 155.

5. Brown, H.C.; Borkowski. J. Am. Chem. Soc. **1952**, 74, 1894; Brown, H.C.; Brewster, J. H.; Schechter, H. J. Am. Chem. Soc. **1954**, 76, 467.

6. Lange, N. A. "Handbook of Chemistry", 9th ed., Handbook Publishers, Inc., Sanduskey, OH (1956), 324.

7. Perry, J. "Chemical Engineering Handbook", 3rd ed., McGraw-Hill Book Co., New York (1950), pp. 1584-5.

8. Lange, N. A. "Handbook of Chemistry", 9th ed., Handbook Publishers, Inc., Sanduskey, OH (1956), 824.

9. "Handbook of Chemistry and Physics", 58th ed., CRC Press, Inc., Boca Raton, FL (1978, E-229-230.

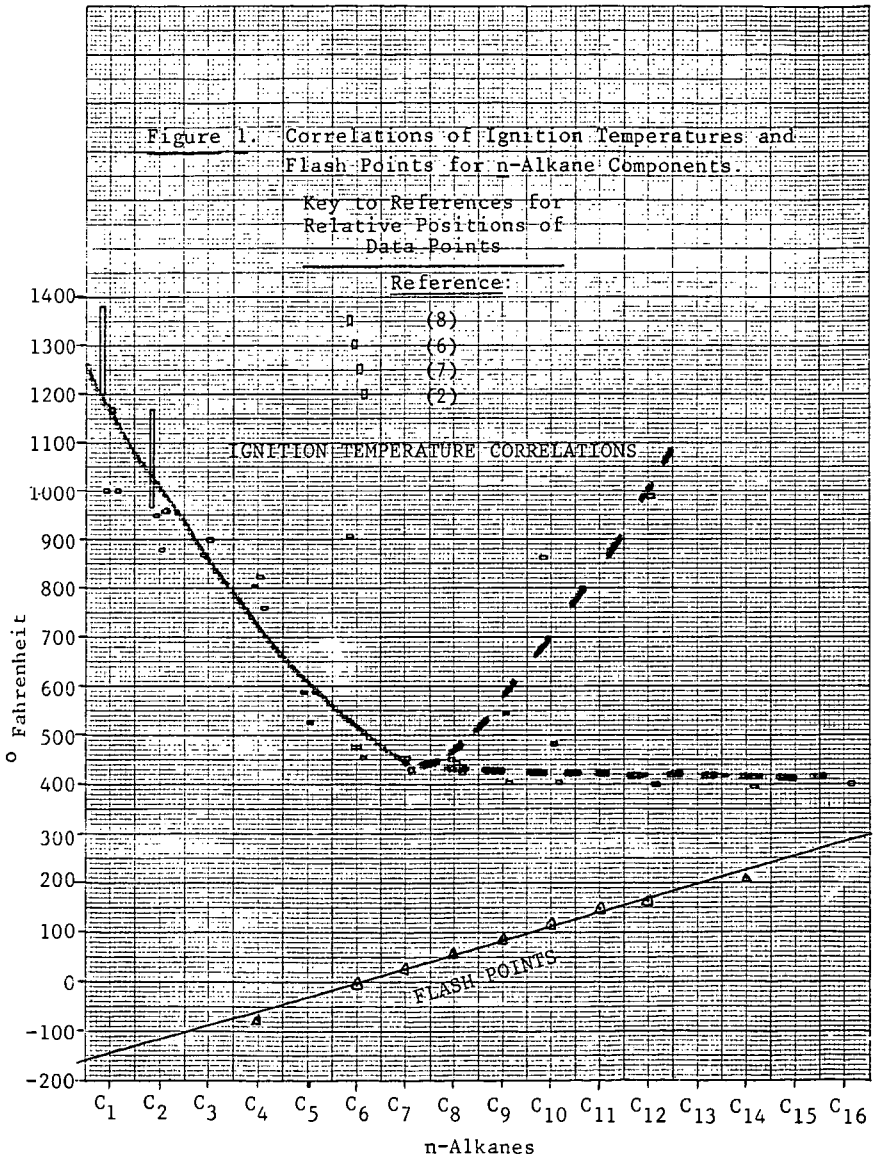


Figure 1. Correlations of Ignition Temperatures and Flash Points for n-Alkane Components.

Figure 2. Molecular Characteristics Affecting Ignition Temperatures.

Typical JP-8 component (A): dodecane

$CH_3-CH_2-CH_2-CH_2-CH_2-CH_2-CH_2-CH_2-CH_2-CH_2-CH_2-CH_3$

(slow movement of massive molecule)

Typical JP-4 component (B): heptane

$CH_3-CH_2-CH_2-CH_2-CH_2-CH_2-CH_3$

(smaller, rapid movement)

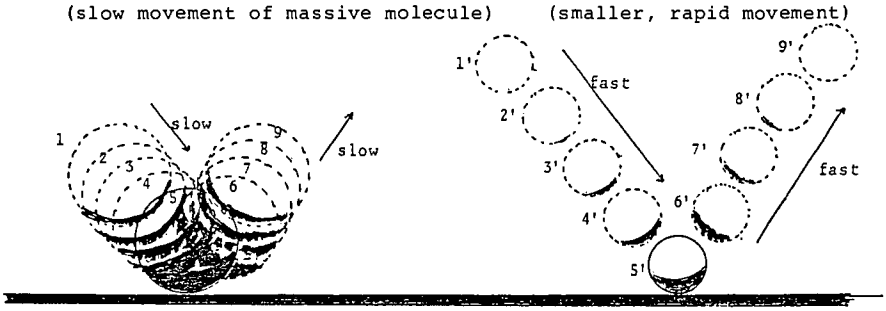


[(1), (2), (3) ... (8), (9) above indicate positions of molecules **A** and **B** at same time intervals, relative to hot surface area.]

Molecular velocity at temperature (T, $^{o}K$) is inversely proportional to the molecular weight (M); smaller molecules have greater speed.

$$\text{Average velocity} = 14{,}600(T/M)^{\frac{1}{2}} \text{ cm/sec}$$

The slow moving heavy molecule **A** (above) is therefore near the hot surface longer than the lighter and faster **B**, and **A** has more time available to absorb energy from the hot radiating surface.

The larger molecule **A** has more mobile C-C bonds and therefore more rotational degrees of freedom than the smaller **B**. Thus, A will tend to be "mushier" with less elastic recoil on impact with the hot surface than the smaller, more rigid **B** which can bounce away more readily. Again, molecule **A** will have more time to energize than B.

To offset this, and although the larger molecule has greater surface area enabling it to absorb more heat than the smaller molecule, the large molecule's volume is increased even more than is the surface area (by comparison with the smaller molecule). Absorbed heat is then dissipated more through the large molecule, which accordingly is cooler than the small molecule. This effect is more pronounced with increased molecular weights (and volumes). In this case **A** (dodecane) needs more heat (with a higher ignition temperature) to energize it to its decomposition point than does **B** (octane). For smaller molecules (e.g., comparing hexane [$C_6$] and propane [$C_3$]), this offsetting factor of increased molecular specific heats is not as important as the molecular speed and rigidity effects: in such cases the heavier molecule has the lower ignition temperature.

# X-RAY DIFFRACTION, MÖSSBAUER SPECTROSCOPIC AND ELECTRON MICROSCOPIC STUDY OF TIN "TITANATES" CATALYSTS USED FOR COPROCESSING MIXTURES OF COALS AND HEAVY OILS

Georges Dénès[a][1] and Jacques Monnier[b]

(a) Department of Chemistry and Laboratories for Inorganic Materials, Laboratory of Solid State Chemistry and Mössbauer Spectroscopy, CONCORDIA UNIVERSITY, 1455 West, de Maisonneuve Boulevard, Montréal, Québec, CANADA, H3G 1M8.

(b) Energy Research Laboratories, CANMET, Energy, Mines, and Resources Canada, 555, Booth Street, Ottawa, Ontario, CANADA, K1A 0G1.

## ABSTRACT

Tin "titanate" catalysts were prepared by ion exchange of sodium hydrous "titanate" $NaTi_2O_5H$ support in aqueous solutions of $SnCl_2 \cdot 2H_2O$, and tested as catalysts for coprocessing of subbituminous coals and heavy oils. The catalysts were characterized at each stage of preparation and use, i.e. before and after ionic exchange, after calcination and after use, using X-ray powder diffraction, $^{119}Sn$ Mössbauer spectroscopy and scanning electron microscopy. The samples are microcrystalline (30 - 300 Å particle diameter). Most of the tin is in the stannic form. The $SnO_2$ and $TiO_2$ polymorphs (rutile, anatase) present in the catalysts are stable during coprocessing. A $Ti_{1-x}Sn_xO_2$ rutile-type solid solution, found in some calcined catalysts, decomposes during coprocessing, with reduction of tin(IV) to tin(II) followed by sulfidation to SnS. This decomposition also leads to formation of $TiO_2$ anatase.

## INTRODUCTION

The large deposits of coal and heavy oil in Western Canada have prompted extensive research on coprocessing at CANMET (1-6). Hydrogenation of coal in the presence of bitumen or heavy oil of petroleum origin yields better conversions and higher quality liquids if catalysts are added to the liquid slurry (7). Recently, the Sandia National Laboratories of the US Department of Energy developed new catalyst supports for coal hydrogenation utilizing metal-exchanged hydrous titanates (8,9).

As interesting results have been obtained using tin catalysts for hydroliquefaction of coal (10-13), new tin catalysts on hydrous "titanate"[2] supports were prepared and tested at CANMET for coprocessing of heavy oil and coal (5). The present study reports the characterization of the catalysts by electron microscopy, X-ray powder diffraction and $^{119}Sn$ Mössbauer spectroscopy (15). The structure and texture of the catalysts are discussed as a function of the method of preparation, and their effect on the catalysts behavior is examined.

1 Author to whom all correspondence should be addressed.

2 Although no structural data suggest that discrete titanate ions are present in the catalysts, we use the name "titanates", as do Dosch, Stephens, and Stohl (8,9) The name "titanates" for these type of compounds is also used in well known inorganic chemistry textbooks (14).

## EXPERIMENTAL SECTION

### Preparation of the Catalysts

Metal-exchanged hydrous "titanates" (MEHT) were prepared according to Dosch, Stephens, and Stohl (8,9). Reaction of titanium(IV) 2-propoxide, $Ti[OCH(CH_3)_2]_4$ with a solution of sodium hydroxide in methanol produces a soluble intermediate, which yields sodium hydrous "titanate" precipitate, $NaTi_2O_5H$, upon addition of a mixture of 10 wt % water in acetone. The precipitate is washed with water and acetone, and then dried under vacuum, yielding hydrous titanate support, in the form of a white fluffy powder. Then, the support is loaded with tin in an aqueous solution of stannous chloride dihydrate, $SnCl_2 \cdot 2H_2O$, washed with water and acetone and dried under vacuum overnight. Before hydroprocessing tests, the titanate catalysts are calcined in air at 400 °C for 2 hours. Analytical results for the metals, obtained by neutron activation, are shown in TABLE I. The samples contain much more titanium than tin or sodium. The ratio of ionic exchange of Na by Sn is 70 % for MB-586 and 46 % for MB-599.

**TABLE I**
**Metal Content of the Catalysts**

| Catalyst[a] | | Weight % | | | Atomic Ratios | | |
|---|---|---|---|---|---|---|---|
| | | Ti | Sn | Na | Ti/Sn | Na/Sn | Na/Ti |
| MB-586 | nc | 41.88 | 11.44 | - | 9.10 | - | - |
| | c | 43.20 | 12.70 | 1.08 | 8.43 | 0.44 | 0.05 |
| | u | - | 1.56 | - | - | - | - |
| MB-599 | nc | - | - | - | - | - | - |
| | c | 36.50 | 16.80 | 3.86 | 5.38 | 1.19 | 0.22 |
| | u | - | 2.64 | - | - | - | - |

a: nc = non-calcined, c = calcined, u = used.

### Characterization Techniques

The texture of the catalysts and the particles shape and size were studied by scanning electron microscopy (SEM), which was performed using a Hitachi S-520 instrument with the filament energized at 15 kV. The samples were dried at 120 °C overnight to remove adsorbed water, stored in a dessicator and then gold coated.

X-ray powder diffraction (XRD), performed on a Picker X-ray diffractometer/X-ray fluorescence spectrometer dual instrument, using the Ni-filtered $K_\alpha$ radiation of Cu ( $\lambda K_\alpha Cu$ = 1.54178 A), provided information on the crystalline phases present in the catalyst, namely their identification and crystalline form, and the crystallite size.

Identification of the tin species and the degree of oxidation of tin in the catalysts were obtained by Mössbauer spectroscopy, using the 8.58 % natural abundance of the $^{119}Sn$ probe. The 23.875 keV Mössbauer $\gamma$-ray was obtained using a 15 mCi $Ca^{119m}SnO_3$ source purchased from Amersham. A 0.1 mm thick Pd foil was used to filter the 25.04 and 25.27 keV X-ray lines. The detector was a Harshaw Na(Tl)I scintillation counter operating at 900 V. Based on the analytical data of TABLE I, the appropriate amount of sample containing 10 mg $Sn.cm^{-2}$ were enclosed in a teflon holder with a thin window and tight fitting cap. Both source and absorber (sample) were maintained at ambient temperature for the measurements. The Doppler velocity was provided by an Elscint driving system, including a MVT-4 velocity

transducer, a MFG-N-5 function generator and a MDF-N-5 driver generator, located on a vibration-free table, and operating in the triangular mode in the velocity range -8.5 $mm.s^{-1}$ to +8.5 $mm.s^{-1}$. The signal was fed to a Tracor Northern 7200 multichannel analyzer operating in the multiscaling mode. After accumulation of 500,000 to 1,000,000 counts per channel, data acquisition was stopped and the data were stored on a diskette. The Doppler velocity was calibrated using $CaSnO_3$ and $\alpha$-$SnF_2$ standard absorbers. Computer fitting was performed on a CDC Cyber 835 main-frame computer using GMFP5 (16), a revised version of the General Mössbauer-Fitting Program (GMFP) of Ruebenbauer and Birchall (17). All chemical isomer shifts are referenced relative to $CaSnO_3$ at room temperature as zero shift.

## RESULTS AND DISCUSSION

### Scanning Electron Microscopy

FIGURE 1 shows SEM micrographs of the hydrous titanate support (FIGURE 1a), the MB-586 catalyst before (FIGURE 1b) and after calcination (FIGURE 1c), and of MB-599 before calcination (FIGURE 1d). The support is a fine powder, non-agglomerated with particle diameters up to 2 $\mu$m. Further magnification shows that the particles have no internal structure, and therefore are probably amorphous.

After ion-exchange (FIGURE 1b), a significant change has taken place as large blocks (10 - 50 $\mu$m edge) with no particular geometrical shape are observed, together with the powder. However, magnification of such a block to 8000X reveals that it is made of loosely bound powdered particles, which again have no internal structure. After calcination (FIGURE 1c), similar types of large blocks are observed, but these are still mixed with powder and show no smaller scale structure. The loosely bound powder inside these blocks are identical to those observed before calcination, and indicate that no sintering took place. FIGURE 1d reveals that the situation is the same for the MB-599 catalyst. Scanning electron microscopy shows that all catalysts have a low degree of ordering, at all steps of preparation, with little texture. This indicates that most likely they are amorphous or microcrystalline.

### X-Ray Powder Diffraction

The X-ray diffraction results for the two catalysts at various stages of preparation and use are given in FIGURES 2 and 3. FIGURE 2a shows the hydrous titanate support before ion exchange is totally amorphous. After ion-exchange (FIGURE 2b), a low degree of ordering is observed, in the MB-586 catalyst, in the form of weak, very broad bumps on the background, indicating the presence of microcrystallinity. Calcination results in significant crystallite growth, giving identifiable Bragg peaks for $TiO_2$ in the anatase and rutile forms and $SnO_2$ rutile. Little change is observed after the catalyst has been used in the coprocessing reaction, except that a few extra weak peaks indicate the formation of a small quantity of SnS and maybe some $\beta$-Sn.

For the MB-599 catalyst (FIGURE 3), the non-calcined catalyst after ionic exchange (FIGURE 3b) is also microcrystalline. Contrary to MB-586, the powder pattern of calcined MB-599 (FIGURE 3c) contains only a few very broad peaks; however, no $TiO_2$ anatase, $TiO_2$ rutile or $SnO_2$ rutile seem to be present. Instead, a broad peak is observed between the positions that would be occupied by any (hkl) peak of $TiO_2$ rutile and the same (hkl) peak of $SnO_2$ rutile. This is indicative of the formation of a rutile-type $Ti_{1-x}Sn_xO_2$ solid solution with unit-cell parameters intermediate between those of $TiO_2$ and $SnO_2$ (TABLE II).

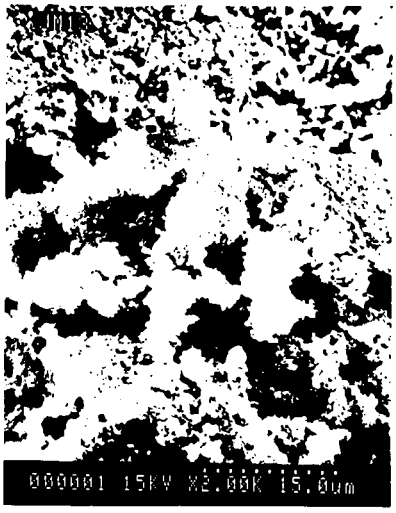


a: $NaTi_2O_5H$ support: SEM micrograph before cationic exchange, magnification= 5,000.

b: MB-586 catalyst before calcination: SEM micrograph at magnifications of 800 (top) and 8,000 (bottom).

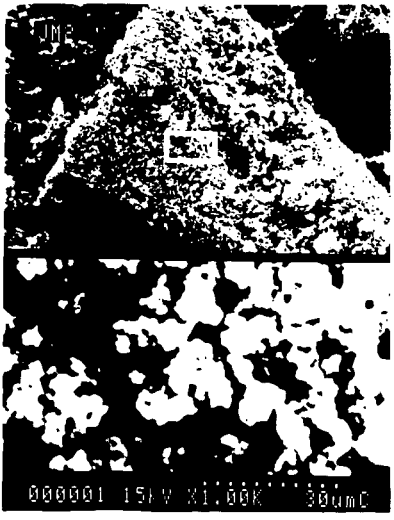

c: MB-586 catalyst after calcination: SEM micrograph at magnifications of 1,000 (top) and 10,000 (bottom).

d: MB-599 catalyst before calcination: SEM micrograph at magnifications of 800 (top) and 8,000 (bottom).

**Figure 1**

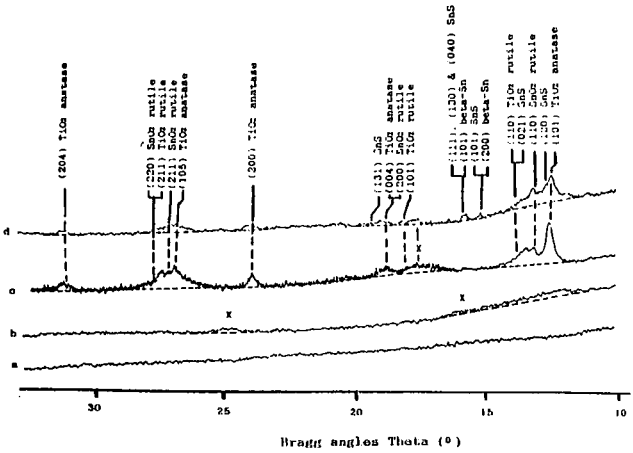


**Figure 2**: X-ray powder pattern (K Cu) of MB-586;
a: support
b: non-calcined ion-exchanged catalyst
c: calcined catalyst
d: used catalyst
X= unidentified peaks

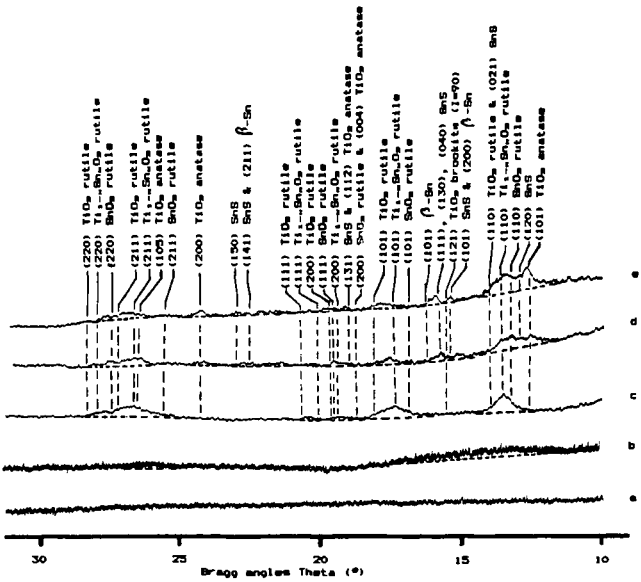


**Figure 3**: X-ray powder pattern (K Cu) of MB-599;
a: support
b: non-calcined ion-exchanged catalyst
c: calcined catalyst
d: used calcined catalyst
e: used non-calcined catalyst

**TABLE II**

**Unit-Cell Parameters of $TiO_2$, $Ti_{1-x}Sn_xO_2$, and $SnO_2$ Rutile-Type**

| Unit-cell parameters | $TiO_2$ | $Ti_{1-x}Sn_xO_2$ | $SnO_2$ |
|---|---|---|---|
| a (A) | 4.594 | 4.643 | 4.738 |
| c (A) | 2.958 | 3.100 | 3.188 |
| V ($A^3$) | 62.43 | 66.83 | 71.51 |

Contrary to MB-586, a drastic change takes place in MB-599 upon use (FIGURE 3d and 3e), as a mixture of $TiO_2$ anatase, $TiO_2$ rutile, $SnO_2$ rutile, SnS, and possibly β-Sn, is observed in addition to some unreacted $Ti_{1-x}Sn_xO_2$ solid solution. The details of the changes for the first group of peaks are given on FIGURE 4.

The MB-586 and MB-599 catalysts were prepared following the same procedure, except that, for MB-599, the sodium hydroxide solution was kept below 0 °C to minimize temperature rise during addition of titanium(IV) 2-propoxide, whereas for MB-586, this NaOH solution was not cooled before preparation of the soluble titanium intermediate. This difference in experimental procedure, not brought up in the literature, must be at the origin of the difference in the nature of the solid catalysts. It is most likely that additional intermediate species, precursors of $TiO_2$ anatase, are formed upon hydrolysis of titanium(IV)·2-propoxide at room temperature.

The catalyst are microcrystalline at all stages, even after calcination and use, as shown by the large linewidth of the Bragg peaks. Below 1000 A particle diameter, line broadening occurs, and below ca. 50 A, the peaks are so broad they cannot be distinguished from the background. The average particle size of each phase was estimated by using the Scherrer's formula (18), corrected for instrumental broadening with Warren's method (18). The results are given in TABLE III.

**TABLE III**

**Average Particle Size of Catalysts as Determined by Scherrer's Method from the Broadening of the Bragg Peaks**

| Catalysts[a] | $\theta(K_\alpha Cu)$(°) | $B_M$(°)[b] | $B_S$(°)[b] | B(°)[b] | t(A)[b] | Phase |
|---|---|---|---|---|---|---|
| Support | * | * | * | * | < 50 | microcrystalline |
| MB-586 nc | # | # | # | # | 50-100 | $TiO_2$ microcryst.<br>$SnO_2$ microcryst. |
| MB-586 c | 12.70 | 0.32 | 0.17 | 0.27 | 300 | $TiO_2$ anatase |
| MB-586 u | 12.70 | 0.52 | 0.18 | 0.49 | 170 | $TiO_2$ anatase |
| MB-599 nc | # | # | # | # | 50-100 | $TiO_2$ microcryst.<br>$SnO_2$ microcryst. |
| MB-599 c | 13.58<br>17.40 | 0.70<br>1.05 | 0.17<br>0.17 | 0.68<br>1.04 | 120<br>80 | $Ti_{1-x}Sn_xO_2$ rutile<br>$Ti_{1-x}Sn_xO_2$ rutile |
| MB-599 u-c | 17.60 | 0.80 | 0.17 | 0.78 | 107 | $Ti_{1-x}Sn_xO_2$ rutile |
| MB-599 u-nc | 12.64<br>17.60 | 0.30<br>0.50 | 0.17<br>0.17 | 0.25<br>0.47 | 330<br>177 | $TiO_2$ anatase<br>$Ti_{1-x}Sn_xO_2$ rutile |

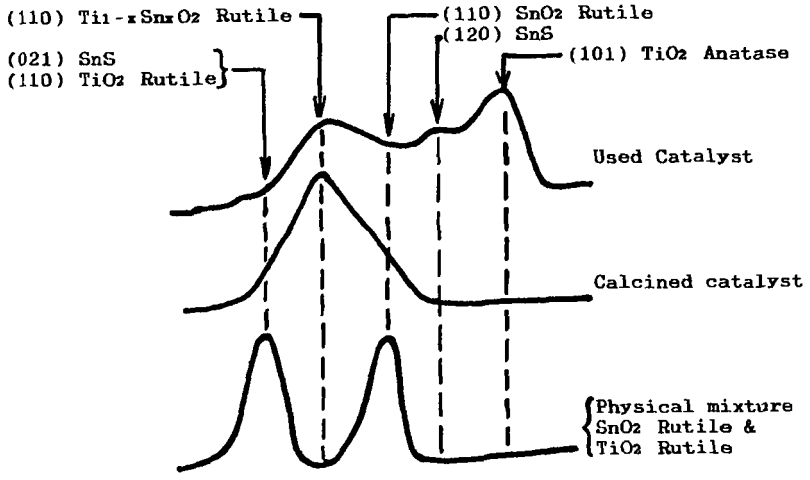


**Figure 4:** Comparison of the first Bragg peak of $Ti_{1-x}Sn_xO_2$ Rutile type solid solution in MB-599 calcined catalyst with a physical mixture of rutile type $SnO_2$ and $TiO_2$ and with the used catalyst.

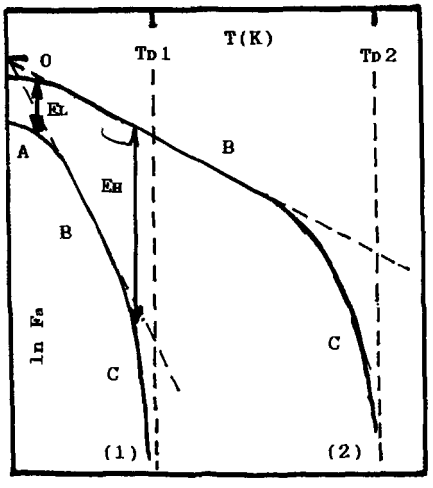


**Figure 5:** Evolution of the recoil-free fraction with temperature as a function of lattice strength

A= Zero point motion
B= Harmonic thermal vibrations
C= Anharmonic thermal vibrations
$E_L$ = Low temperature difference
$E_H$ = High temperature difference
$f_a$ = Absorber recoil-free fraction
$T_{D1}$, $T_{D2}$= Debye temperatures
(1)= Soft lattice
(2)= Hard lattice

a: nc = non-calcined, c = calcined, u = used, u-c = used calcined catalyst, u-nc = used non-calcined catalyst.
b: Scherrer's formula: $t = (0.9\lambda)/(B.\cos\theta)$ with t (A) = average particle size, B (°) = broadening at half-height due to small particles, $\lambda$ (A) = wavelength, $\theta$ (°) = Bragg angle.
* No Bragg peak observed.
# Very broad peak, cannot be measured.

X-ray diffraction results corroborate the information obtained from the SEM photographs, i.e. all samples are microcrystalline. It is not surprising that the particles of 1-2 $\mu$m diameter observed by SEM appear to have no internal structure. Indeed, each of them is made of about $10^{10}$ much smaller particles (diameter ca. 1000 times smaller) randomly distributed relative to one another. The support gives no Bragg peak at all, and therefore is amorphous or microcrystalline with particle diameter below 50 A. The non-calcined ion-exchanged catalysts shows very broad features barely distinguishable from the background, indicative of a particle size close to 50 A. The rutile-type $Ti_{1-x}Sn_xO_2$ solid solution has particle dimensions of about 100 A, while $TiO_2$ anatase has the largest crystallites (~ 300 A). Some crystallite growth occur upon calcination; however, all samples are still microcrystalline. No further crystal growth was observed during the tests.

Mössbauer Spectroscopy

$^{119}$Sn Mössbauer spectroscopy provides a direct probing of all tin sites, regardless of the degree of crystallinity or presence of other phases. This is very important for obtaining information on the oxidation state and the coordination of the active sites of these catalysts. Furthermore, of all metal-exchanged catalysts tested in (5), i.e. Mo, Co, Pd, Sn, and Ni, only tin has a Mössbauer isotope[3]. The Mössbauer results for MB-586 and MB-599 are summarized in TABLE IV.

The non-calcined ion-exchanged catalysts contain minor divalent tin and a major tetravalent tin species, both coordinated with oxygen. Sn(IV) is in pseudooctahedral coordination like in $SnO_2$, with various degrees of distortion relative to regular octahedral symmetry. The oxygenated ligands can be bridging oxygen, $OH^-$ or $H_2O$ molecules. The sample prepared at low temperature (MB-599) contains a larger proportion of Sn(II). Upon calcination in air, all tin(II) is oxidized to tin(IV) as expected. After coprocessing test, some stannous sulfide SnS is produced, in very small quantity (1 %) for MB-586, in much larger quantity (10 - 15 %) for MB-599. No ß-Sn was observed by Mössbauer spectroscopy; therefore, if it is indeed formed, it is in very small quantities.

Mechanism of formation of $TiO_2$ anatase and SnS during the coprocessing reaction

The X-ray diffraction results of FIGURES 2 to 4 and the Mössbauer data presented in TABLE IV show that, during coprocessing, a profound change takes place in the solid catalyst provided it was

---

3 Co catalysts can be studies by $^{57}$Fe Mössbauer spectroscopy; however, this requires preparing the catalyst using radioactive $^{57}$Co radioisotope, thus giving rise to additional experimental complications. In addition, electron-capture decay, and the following Auger cascade, often give extra Mössbauer lines and unexpected oxidation states of Fe, making the interpretation of the spectra more difficult (19).

**TABLE IV**

**Room Temperature $^{119}$Sn Mössbauer Parameters for MB-586 and MB-599 Tin Titanate Catalysts**

| Catalysts[a] | $\delta$(mm.s$^{-1}$)[b] | $\Delta$(mm.s$^{-1}$)[c] | Oxi[d] | Contr(%)[e] | Assignment[f] |
|---|---|---|---|---|---|
| MB-586 nc | - 0.09 | 0.15 | +4 | 95 | Sn/O octa sd |
| | 3.04 | 1.59 | +2 | 5 | Sn(II)/O |
| MB-586 c | - 0.03 | 0.30 | +4 | 100 | Sn/O octa di |
| MB-586 u | - 0.03 | 0.40 | +4 | 99 | Sn/O octa vd |
| | 3.16 | 0.98 | +2 | 1 | SnS |
| MB-599 nc | - 0.09 | 0.40 | +4 | 75 | Sn/O octa vd |
| | 3.13 | 1.78 | +2 | 25 | Sn(II)/O |
| MB-599 c | - 0.03 | 0.00 | +4 | 100 | Sn/O octa ud |
| MB-599 u-c | - 0.03 | 0.00 | +4 | 85 | Sn/O octa ud |
| | 3.22 | 0.86 | +2 | 15 | SnS |
| MB-599 u-nc | - 0.03 | 0.00 | +4 | 90 | Sn/O octa ud |
| | 3.28 | 0.86 | +2 | 10 | SnS |

a: nc = non-calcined, c = calcined, u = used, u-c = used calcined catalyst, u-nc = used non-calcined catalyst.
b: chemical isomer shift relative to $CaSnO_3$ at room temperature, error bar = 0.01 mm.s$^{-1}$.
c: quadrupole splitting, error bar = 0.01 mm.s$^{-1}$.
d: oxi = tin oxidation state.
e: contr = % contribution of each tin site to the total spectrum, error bar = 1 %.
f: Sn/O octa = tetravalent tin in octahedral or pseudo-octahedral coordination of oxygen, ud = undistorted, sd = slightly distorted, di = distorted, vd = very distorted, Sn(II)/O = divalent tin coordinated by oxygen.

formed of $Ti_{1-x}Sn_xO_2$ solid solution (MB-599). The amount of solid solution is reduced while a large amount of $TiO_2$ anatase is formed and ca. 15 % SnS. On the other hand, if the calcined catalyst contains $TiO_2$ anatase and rutile and $SnO_2$ rutile, and no $Ti_{1-x}Sn_xO_2$ (MB-586), no significant change is observed and little SnS is formed (1 %). Obviously, there is a correlation between the simultaneous disappearance of $Ti_{1-x}Sn_xO_2$ and the appearance of $TiO_2$ anatase and SnS. As the reaction with calcined MB-599 gives the highest yield in SnS, reduction of tin(IV) to tin(II) by hydrogen and/or coal first takes place, followed by sulfidation of the tin(II) formed (EQUATION 1), sulfur being provided by the oils (5 wt % S) and coals (0.5 wt % S).

$$\text{Sn(IV)} \xrightarrow{\text{C + H}_2\text{, 410 °C}} \text{Sn(II)} \xrightarrow{\text{oil, coal}} \text{SnS} \qquad 1)$$

As formation of SnS is observed only if $Ti_{1-x}Sn_xO_2$ is present, the reactions given in EQUATIONS 2 and 3 take place at 410 °C under 3.4 MPa pressure of hydrogen.

$$xS^{2-} + \underset{\text{rutile}}{Ti_{1-x}Sn_xO_2} + 2xH_2 \text{ ---> } \underset{\text{anatase}}{(1-x)TiO_2} + 2xH_2O + xSnS + 2xe^- \quad 2)$$

$$xS^{2-} + \underset{\text{anatase}}{Ti_{1-x}Sn_xO_2} + 2xC \text{ ---> } \underset{\text{anatase}}{(1-x)TiO_2} + 2xCO + xSnS + 2xe^- \quad 3)$$

Reactions 2 and 3 produce $TiO_2$ anatase and SnS and consume $Ti_{1-x}Sn_xO_2$, and therefore, account for the experimental observations. The reason the reaction works well with $Ti_{1-x}Sn_xO_2$ and not for $SnO_2$ rutile is probably that the $SnO_2$ lattice is much more stable. Indeed, the strain induced by the presence of two cations of significantly different size (Sn(IV) = 0.83 Å, Ti(IV) = 0.735 Å, in coordination number six) (20) in $Ti_{1-x}Sn_xO_2$ reduces the lattice energy and makes it more susceptible to the destabilizing power of chemical attacks.

The amount of SnS formed depends on the presence of the $Ti_{1-x}Sn_xO_2$ rutile-type solid solution, and is not favored by prior presence of tin(II) in the catalyst. The data of TABLE V show that the calcined MB-599 (0 % Sn(II)) yields 15 % SnS, while non-calcined MB-599 catalyst (25 % Sn(II)) gives 10 % SnS, i.e. less. Even in the case of the test with non-calcined MB-599, the used catalyst contains less divalent tin (10 %) than the catalyst before use (25 %), showing that direct sulfidation of tin(II) already present does not take place. To the contrary, presence of $Ti_{1-x}Sn_xO_2$ is required showing that its decomposition leads to SnS and $TiO_2$ anatase, according to equations 2 and/or 3.

**TABLE V**
**Amount of SnS versus Test Conditions**

| Catalyst | c/nc[a] | $T_S$[b] | $pH_2$ (psi)[c] | $T_R$ (°C)[d] | Time[e] | % SnS |
|---|---|---|---|---|---|---|
| MB-586 | c | RT | 500 | 410 | 3h45 | 1 |
| MB-599 | c | < 0 °C | 500 | 410 | 3h45 | 15 |
| MB-599 | nc | < 0 °C | 500 | 410 | 3h45 | 10 |

a: c = calcined, nc = non-calcined.
b: $T_S$ = temperature of preparation of support.
c: $pH_2$ = pressure of hydrogen (continuous flow) in the reactor during the test.
d: $T_R$ = temperature of reaction for the tests.
e: Time = time of the test reaction.

A surprising feature is the high amount of Sn(IV) in the catalysts before calcination, i.e. the large amount of divalent tin oxidized to tin(IV) during ion-exchange. TABLE V compares the relative amount of tin(II) as a function of the conditions of ion exchange.

**TABLE VI**
**Relative amount of divalent tin in ion-exchanged non-calcined catalysts as a function of preparative conditions**

| Catalyst | Water Degassing | pH | Stirring Time (min) | Sn(II)/total Sn (%) |
|---|---|---|---|---|
| MB-586 | No | 2.8 | 60 | 5 |
| MB-599 | Yes | 1.83 | 105 | 25 |
| MB-585 | Yes | 2.4 | 60 | 10 |

Although one could expect that prolonged exposure to dissolved atmospheric oxygen would increase the amount of tin(IV), the above data clearly indicate that the pH of the solution is the most important factor, followed by degassing. Most likely, at low pH less hydrolysis of tin(II) occurs, which is known to favor oxidation. However, a pH lower than 1.8 cannot be used because it dissolves the sodium titanate support. Oxidation to tin(IV) during calcination could be expected.

## CONCLUSION

Tin exchanged hydrous "titanates" have been prepared and characterized by some of the solid state techniques. The method of preparation, texture and structure of the catalysts, as well as the nature of the tin site, are important parameters for the understanding of their behavior during coprocessing reactions. The catalysts are microcrystalline in all stages of preparation, although significant crystallite growth of $TiO_2$ anatase occurs during calcination, from ca. 50 A to 300 A. The method of preparation of the support is critical as a room temperature reaction yields mostly $TiO_2$ anatase, while low temperature syntheses result in a rutile-type $Ti_{1-x}Sn_xO_2$ solid solution being formed, which easily decomposes upon reduction of tin(IV to tin(II), producing SnS and $TiO_2$ anatase at coprocessing conditions. X-ray diffraction and Mössbauer spectroscopy show that no Sn(IV) or Sn(II)/Sn(IV) mixed oxidation state sulfide is formed. In addition, no titanium sulfide or sodium-containing species was detected, despite the non-negligible sodium content (TABLE I). The coal/hydrogen reducing medium reduces Sn(IV) from $Ti_{1-x}Sn_xO_2$ and not from $SnO_2$, followed by sulfidation to SnS, using the natural sulfur content of coals and oils. $TiO_2$ anatase and rutile and $SnO_2$ rutile seem very stable.

The relative contribution of each tin species to the total Mössbauer spectrum, is not equal to the real amounts of these species in the samples if their recoil-free fractions are not the same, and the difference, which is a function of their Debye temperature, is temperature dependent, as shown on FIGURE 5. A variable temperature study is presently being undertaken in order to minimize the error due to recoil-free fraction difference. Calculations of equilibrium constants (21) for the reduction of oxides of Sn, Mo, Co, and Ni, at the temperature of the coprocessing reactions show that $SnO_2$ is more difficult to reduce in $H_2$ than NiO, CoO and $MoO_3$. If reduction of $SnO_2$ occured, NiO, CoO and $MoO_3$ would also be reduced in the reactions of (5). As no data are available on the equilibrium constant for $Ti_{1-x}Sn_xO_2$, reduction of NiO, CoO, and $MoO_3$ cannot be confirmed. The detailed study of the tin catalysts, which was possible because of the $^{119}Sn$ Mössbauer probe, provides a model for catalysts containing other metals, which have no Mössbauer nuclide.

## ACKNOWLEDGMENT

We wish to thank Prof. N. Kapoor, Ms. J. Fitzgerald, and Mrs. M. Dénès at Concordia University for technical assistance in electron microscopy and X-ray diffraction. Financial assistance from Concordia University for the purchase of the Mössbauer spectrometer and technical assistance from the Concordia University Science Technical Center are acknowledged. G.D. thanks the Natural Sciences and Engineering Research Council of Canada for a University Research Fellowship. This work was conducted under Supply and Services Canada Contract Serial Number OST85-00243.

## REFERENCES


1. J.F. Kelly, S.A. Fouda, P.M. Rahimi, and M. Ikura, Proceedings of the Coal Conversion Contractors' Review Meeting, J.F. Kelly Edit.; CANMET, Energy, Mines and Resources Canada, Ottawa, Ontario, Canada, 397 (1985).
2. J. Monnier and J.F. Kriz, Ind. Eng. Chem. Prod. Res. Dev. 25, 537 (1986).
3. S.A. Fouda and J.F. Kelly, Proceedings of the 1987 International Conference on Coal Science; J.A. Moulijn et al. Eds., Elsevier Science Publishers, 387 (1987).
4. P.M. Rahimi, S.A. Fouda, and J.F. Kelly, Proceedings of the 12th EPRI Annual Fuel Science and Conversion Conference, Palo Alto, California, USA (1987).
5. J. Monnier, G. Dénès, J. Potter, and J.F. Kriz, J. Energy & Fuels 1, 332 (1987).
6. J. Monnier, C.W. Fairbridge, J.R. Brown, and J.F. Kriz, Proceedings of the 9th International Congress on Catalysis 1, 182 (1988).
7. J. Monnier and J.F. Kriz, 10th Canadian Symposium on Catalysis, Preprints, 1 (1986).
8. R.G. Dosch, H.P. Stephens, and F.V. Stohl, US Patent 4 511 455 (1985).
9. H.P. Stephens, R.G. Dosch, and F.V. Stohl, Ind. Eng. Chem. Prod. Res. Dev. 24, 15 (1985).
10. S.W. Weller, in "Catalysis IV", P. Emmett Edit., Reinhold, New York, CHAPTER 7 (1956).
11. S.J. Cochran, M. Hatswell, W. Roy Jackson, and F.P. Larskins, Fuel 61, 831 (1982).
12. M. Mizumoto, H. Yamashita, and S. Matsuda, Ind. Eng. Chem. Prod. Res. Dev. 24, 394 (1985).
13. P.S Cook and J.D. Cashion, Fuel 65, 146 (1986).
14. F.A. Cotton and G. Wilkinson, "Advanced Inorganic Chemistry", 4th Ed., Wiley-Interscience, New York, USA, p. 695 (1980).
15. G. Dénès, "Characterization of Tin Catalysts by Mössbauer Spectroscopy", Final Report to CANMET under Supply and Services Canada Contract Serial Number OST85-00243; Department of Chemistry, Concordia University, Montréal, Québec, Canada (1987).
16. J. Monnier, G. Dénès, and R.B. Anderson, Can. J. Chem. Eng. 62, 419 (1984).
17. K. Ruebenbauer and T. Birchall, Hyperfine Interact. 7, 125 (1979).
18. B.D. Cullity, "Element of X-ray Diffraction", 2nd Ed., Addison-Wesley, Don Mills, Ontario, Canada, pp. 192, 284 (1978).
19. N.N. Greenwood and T.C. Gibb, "Mössbauer Spectroscopy", Chapman and Hall Limited, London, UK, p. 330 (1971).
20. R.D. Shannon, Acta Crystallogr. A32, 751 (1976).
21. I. Barin and O. Knacke, "Thermochemical Properties of Inorganic Substances", Springer-Verlag, West-Berlin, Germany, and New York, USA (1973).

# A NEW DETERMINATION OF EXCHANGEABLE OXYGEN IN COALS

Edwin S. Olson and John W. Diehl

University of North Dakota Energy and Mineral Research Center
Box 8213, University Station
Grand Forks, ND 58202

## Introduction

All facets of research on a coal sample require accurate knowledge of the moisture content, which obviously changes during any chemical or physical processing. The elemental analysis of coal significantly depends on the determination of the moisture content of the coal; and thus during the combustion (ultimate) analysis of a sample, the amount of water initially present in the coal sample must be accounted for in the water of combustion measured in the experiment, in order to determine the amount of hydrogen present in the coal sample. The amount of water present also must be known to determine the oxygen content. Although the weight loss drying method is standard practice for determining moisture, there are errors possible, especially in the low-rank coals, which may contain over 30 percent moisture. These errors could be due to incomplete drying or possibly oxidation during the determination.

Finseth has recently reported a new method for the determination of water in coals which utilizes isotope dilution (1). In this technique, a known amount of water which was enriched in $^{18}O$ was added to the weighed coal sample in a tube. Carbon dioxide was also added and the tube sealed and then heated to equilibrate the added labeled water with the natural abundance water present in the sample. The tube was then opened and the carbon dioxide analyzed by mass spectrometry to determine the isotopic ratio, from which the coal moisture could be calculated. The carbon dioxide acted as a probe molecule to facilitate the mass spectrometric analysis, since its oxygens exchange completely with those of the water. The results of Finseth's moisture determinations were compared with ASTM values for a number of Argonne premium coal samples and were in all cases somewhat larger than the ASTM values.

The mass spectrometers available in our laboratories are not adaptable to analysis of the $CO_2$, hence we sought an alternative for the analysis of the isotope ratio in the isotopically equilibrated water samples. The reaction of the water with several orthoesters to give the ester containing the water-derived oxygen (labeled oxygen) in the carbonyl group was investigated (see Equation 1). The orthoester selected for the analysis was trimethyl orthobenzoate, since it gave methyl benzoate which could be conveniently analyzed in our GC/FTIR/MS system.

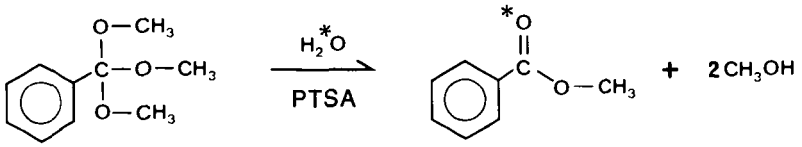


Equation 1. Reaction of trimethyl orthobenzoate with water.

## Results and Discussion

The reaction of water with the trimethyl orthobenzoate proceeded somewhat slowly; hence several catalysts for the reaction were investigated. Boron trifluoride etherate was unsuccessful since it appeared to catalyze the exchange of labeled oxygen of the water with the glass or possibly with the solvent. Methanesulfonic acid similarly gave poor results. A very dilute solution of p-toluenesulfonic acid in glyme was selected as the catalyst which gave the best reproducibility and calibration.

The isotope ratio of the natural and labeled methyl benzoate which results from the reaction of water with the trimethyl orthobenzoate was determined both from mass spectra and infrared spectra of the methyl benzoate peak eluting from the GC column. Adequate peak shape was obtained using a 60 m x 0.32 mm column with a 1.0 μ DB-5 film, so that reproducible integration of the peak for the quantitation could be obtained.

In the mass spectral measurement, the ratio of the integrated intensity of the $(M-31)^+$ ion corresponding to the labeled methyl benzoate (at m/e = 107) to that of the natural methyl benzoate (at m/e = 105) over the corresponding peaks was determined. A representative mass spectrum from the GC/MS determination of one of the known mixtures is shown in Figure 1 along with the reconstructed total ion chromatogram which shows the $^{18}O$-labeled and natural methyl benzoate peak and the unreacted trimethyl orthobenzoate peak.

A linear calibration plot (Fig. 2) was used for the mass spectral isotope ratios, since there were no overlapping peaks from the labeled compound (m/e = 107) and natural abundance analyte (m/e = 105). The small amount of m/e 105 peak in the spectrum of the labeled ester was due to the small amount of $^{16}O$ water (2 percent) in the $^{18}O$ water plus a small amount in the glyme solvent used in the reaction of the water with the orthoester. The glyme was purified and dried over lithium aluminum hydride and distilled onto molecular sieves. The m/e 105 peak in the standard will not affect the linearity but will change the intercept.

The absorbance reconstructed GC peaks of the natural methyl benzoate (over the range 1750 to 1742 $cm^{-1}$) and labeled methyl benzoate (over the range 1720 to 1712 $cm^{-1}$) were integrated to obtain the area ratios (A/S) of natural to labeled ester. A representative infrared spectrum from the GC/FTIR determination of one of the known mixtures is shown in Figure 3.

The calibration plot (Fig. 4) of the infrared data (amount ratio versus area ratio) was not linear since the absorption bands for the labeled and natural ester overlap slightly. The calibration data were fitted to a polynomial expression, which was then used for the determination of the unknown isotope ratios.

Three methods were investigated for the equilibration of the coal moisture with the added isotopically enriched standard. The equilibration was first carried out by adding a solution of the $^{18}O$ water in dried and purified glyme to the coal and heating in the sealed vial at 100°C overnight. Decent calibration curves were obtained by using volumetric aliquots of known concentrations of natural abundance and isotopically enriched water in glyme. The area ratios were reproducible, with deviations less than one percent for most points. Tests of the calibration with known concentrations of water in glyme showed that the method was accurate. However, tests with coal samples gave obviously poor results using this method. Exchange with the ether oxygen of the solvent appears to have occurred in the coal determinations, rendering the method useless. The same reaction in the absence of the coal but with an amount of natural abundance water corresponding to that expected in the coal gave no exchange with the solvent, even in the presence of acid catalyst. Acetonitrile was investigated as the solvent, but the methyl benzoate did not form.

The equilibration was then investigated using no solvent as Finseth has reported. To generate the calibration curves, the $^{18}O$ water and natural abundance

water were pipetted into a vial using micropipettes. Trimethyl orthobenzoate and catalyst were added and the vial was crimped. The methyl benzoate product was analyzed with GC/FTIR/MS as described above. The resulting calibration curves were somewhat erratic, and although points from the same solution were reproducible, tests of the calibration with new known mixtures gave large errors. The large errors and erratic calibration curves were attributed to errors in the volumetric measurements using the micropipettes, probably due to incomplete drainage.

Finally, the solutions for the calibration were made up by weighing milligram amounts of $^{18}O$ water and natural water. A linear calibration curve was obtained from the mass spectral data, and a smooth curve was obtained from the infrared data, from which a polynomial expression was derived. The infrared integrated absorbance ratios were reproducible within one percent, and the mass spectral intensity ratios were within one percent in the middle of the calibration curve and within four percent at each end. A test of the calibration using a new known solution gave errors of 1.8 percent using the infrared data and 4.5 percent using the mass spectral data.

The method was tested using a Beulah lignite sample by adding an analytically weighed amount of the $^{18}O$ water. The sample was sealed with a torch in such as manner as to leave a capillary at the sealed end. After equilibration in an oven overnight, the sample was then removed from the oven and placed in an oil bath so that the coal in the bottom of the tube was warmed and the moisture collected in the capillary tube. The tube was opened and the equilibrated water was obtained from the capillary and reacted with trimethyl orthobenzoate and p-toluenesulfonic acid catalyst. The analysis of the methyl benzoate with the GC/FTIR/MS system gave values for the exchangeable oxygen reservoir of 39.8 percent from the infrared data and 38.6 percent from the mass spectral data. The close agreement of these determinations was encouraging and demonstrated that the instrumental methodology was working extremely well. On the other hand, the large value obtained was not expected, since the ASTM drying weight loss method gave 33.6 percent moisture in this sample. The equilibration with the isotopically enriched water, of course, determines the size of the exchangeable oxygen reservoir. The problem is that we do not know if this includes portions of the organically bound oxygen, such as carboxylic acid groups. Finseth demonstrated that benzoic acid does not exchange under these conditions, however, we cannot be certain that the coal carboxylate and carboxylic acid groups do not exchange, considering that there may be catalysts for the exchange present in the coal.

The exchangeable oxygen determination was then performed on two of the Argonne premium coal samples and a sample of Big Brown lignite. Table 1 compares the values obtained using the isotope dilution GC/FTIR and GC/MS data with the fast drying ASTM method and the Finseth isotope dilution ($CO_2$) MS method. The values obtained for the Argonne premium sample of Illinois #6 bituminous coal and the Argonne premium Beulah-Zap lignite were very similar to those obtained by Finseth (1) and were somewhat higher than those found using the ASTM method. Further work with the Argonne premium samples will be undertaken to evaluate the infrared and mass spectral methods for water determination.

## Experimental

Coal samples were equilibrated with the weighed amount of $^{18}O$ water in sealed tubes at 100°C for 15 hours as reported by Finseth (1). The seal on the tubes was fashioned so that it formed a narrow capillary portion. After equilibration, the bottom of the tube was warmed so that moisture was trapped in the capillary portion of the tube. The capillary tube was then broken off, and the upper part containing the collected water was quickly transferred to a reaction vial, where it was crushed and the reagents added. For preparation of the derivative, 1 μ of a solution containing 1 mg/ml of p-toluene-sulfonic acid in dried glyme and 100 mg of trimethyl orthobenzoate were added to the vial, which was sealed with a crimped cap. The vial was heated for 1 hour at 100°C. Instrumentation for the GC/FTIR/MS determination was described earlier (2). All glassware was dried several hours at 110°.

## References

1. Finseth, D. ACS Div. of Fuel Chem. Preprints, (1987) 32(4), 260-5.
2. Olson, E.S. and Diehl, J.W., Anal. Chem. (1987) 59, 443.

## Acknowledgements

Financial support of this work was provided by the U.S. Department of Energy under Contract No. DOE-FE21MC10637.

TABLE 1. MOISTURE (EXCHANGEABLE OXYGEN) DETERMINATIONS

| COAL | ID/GC/FTIR | GC/MS | ID/MS($CO_2$)* | ASTM |
|---|---|---|---|---|
| AR. B-Z LIGNITE | 34.3% | 32.8% | 34.4% | 32.8% |
| AR. ILL #6 | 9.4% | 9.9% | 9.6% | 8.8% |
| UND B-Z LIGNITE | 39.8% | 38.6% | | 33.6% |
| UND BB LIGNITE | 28.9% | 29.4% | | 27.8% |

* Values from Finseth (Reference 1)

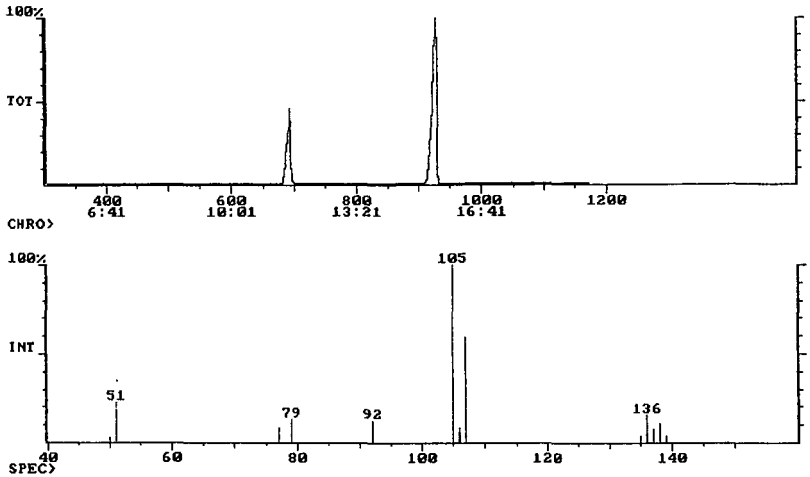


Figure 1. (a) Reconstructed total ion chromatogram of mixture of $^{18}O$- and $^{16}O$-labeled methyl benzoate, (b) Mass spectrum of above mixture.

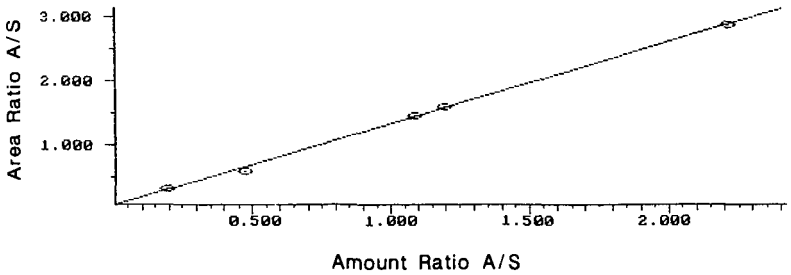


Figure 2. Mass spectra calibration curve for isotopic methyl benzoate ratios.

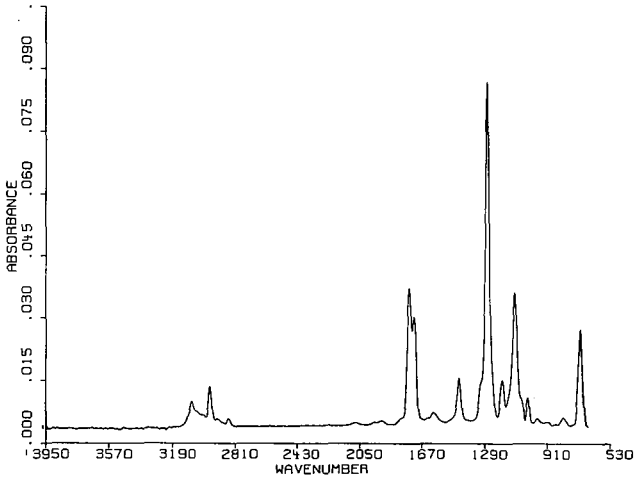


Figure 3. Infrared spectrum of mixture of $^{18}O$ and $^{16}O$-labeled methyl benzoate.

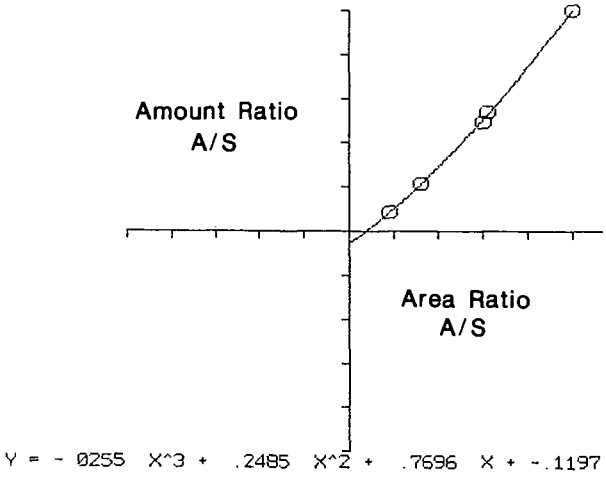


Figure 4. Infrared calibration curve for isotopic methyl benzoate ratios.

# ANALYSIS OF NONDISTILLABLES FROM COAL LIQUIDS BY SIZE EXCLUSION CHROMATOGRAPHY/FOURIER TRANSFORM INFRARED SPECTROMETRY (SEC/FT-IR)

C. V. Philip and R. G. Anthony

Kinetics, Catalysis and Reaction Engineering Laboratory
Department of Chemical Engineering, Texas A&M University
College Station, Texas 77843

## INTRODUCTION

Coal liquids may contain as much as 50% or more nondistillables. Most of the nondistillable materials are soluble in solvents such as tetrahydrofuran (THF) or pyridine. Currently, the nondistillables are characterized by elemental analysis, nuclear magnetic resonance (NMR), Fourier Transform infrared (FT-IR) spectrometry and heating values. The nondistillable and distillable fractions of a coal liquid can be separated and analyzed by size exclusion chromatography (SEC) (1-8). SEC separates molecules based on "linear molecular" size (3,4). The application of SEC is limited only by the solubility of the sample in a solvent. Although SEC has been used primarily for the separation and characterization of polymers based on molecular size or molecular weight, its use has been extended to the separation of smaller size molecules (10-13).

The separation of coal liquids by SEC is easily achieved with appropriate columns. Because coal-derived mixtures have several components of a similar size, the use of SEC alone is not adequate for the purpose of identification. Gas chromatography (GC) coupled with mass spectrometry (MS) has been used in conjunction with the SEC (14,15,16). The use of these three analytical techniques [SEC, GC, and MS] is a powerful analytical method for the analysis of the distillables of coal liquids, recycle solvents and anthracene oils (14, 15, 16).

Analysis of SEC fractions of nondistillables by FT-IR spectrometry is very useful in characterizing the coal liquids produced under different reaction conditions. Conventional FT-IR techniques are rather unreliable as well as time consuming, because the mass of coal liquid in a SEC fraction is very small. A new technique, which is more reliable and requires less time than the conventional techniques, is developed for the analysis of small samples. The residues from SEC fractions are spotted onto a potassium bromide (KBr) pellet. The spotted samples are then analyzed using a narrow focused beam in the Microbeam accessory of a Nicolet 60 SXR FT-IR spectrometer. The paper discusses the analytical technique as well as the FT-IR spectra of SEC fractions.

## EXPERIMENTAL

The low rank coal used in the liquefaction experiments (15) was Zap-2 Indian Head lignite from North Dakota. Minireactors (6.3 and 20 *ml*), which were made from Autoclave high pressure fittings (7) were used. The liquefaction solvents included anthracene oil and water under supercritical conditions. Hydrogen, carbon monoxide and hydrogen sulfide were the reactive gases. The experimental conditions are listed in Table 1, and the yields are listed in Table 2 (15).

Coal liquids from these experiments were separated by distillation at 230$^{o}$C and 1 Torr. The nondistillables were dissolved in THF and separated using a 60 cm long, 5 um, 10 nm PL gel column and THF as the mobile phase. The effluents were monitored by a Waters refractive index detector (Model 401). The SEC fractions were collected as one *ml* fractions. Most samples were separated into

10 fractions. The THF in these fractions was evaporated using a slow dry stream of nitrogen and occasionally warming the vials with warm air from a hot air blower. The residues were used for FT-IR analysis.

A Nicolet 60SXR FT-IR Spectrometer with Microbeam accessory and a MCT-A detector was used for the FT-IR analysis. The samples were dissolved in 2-5 *ml* and spotted on a 13 mm potassium bromide (KBr) pellet (100 mg) using a 5 *ml* syringe with a fused silica needle. The pellets were dried on a hot plate. Six 1-2 mm diameter sample spots were deposited on each KBr pellet. Each pellet was scanned using a motorized sample stage which is both manual and computer software controllable. The Microbeam accessory is used to focus the IR beam either manually or by the 60 SXR software. A narrow beam (0.1 mm dia.) was used for the analysis. The Microbeam accessory enables analysis of a sample as small as 0.1 mg with good absorption spectrum with about 2 absorbance unit for the largest peak. Absorptions due to water vapor and $CO_2$ were subtracted from all spectra. The spectra were subjected to baseline correction as well as the normalization of the largest peak to 2.00 absorbance units.

## RESULTS AND DISCUSSIONS

The coal liquids contained substantial amounts of nondistillables, which varied depending on the reaction conditions. Figure 1 shows the distribution of various chemical species in a coal liquid. A coal liquid from Wyodak subbituminous coal is used for the illustration.

One of the major results of SEC-GC-MS analysis of the distillables is the discovery of an orderly pattern (14,15,16), by which various isomers and homologues of similar chemical species exist in coal liquids. Direct coal liquefaction produces chemical species, which differ from each other by size and extent of isomerization but with an orderly continuous pattern. Alkanes ranging from $C_{12}H_{26}$ and $C_{44}H_{80}$ are detected in almost any coal liquid. Most of these are straight chain alkanes showing an orderly continuous pattern. Neither is a particular n-alkane almost absent nor is it present in a disproportionate amount. Exceptions exist for some branched alkanes such as pristine, phytane, and hopanes. These species are also called biomarkers and their concentration varies depending on the sample. The nondistillable fraction of coal liquids are expected to contain larger alkanes as a continuation of the alkane pattern. Since alkanes larger than $nC_{44}H_{80}$ are almost insoluble in THF, their presence in THF soluble nondistillables is limited and they may exist as nondistillables in the THF insoluble fractions.

Phenols are a major group of species present in coal liquids and have basically one or more aromatic ring structures with alkyl substituents. Methyl, ethyl and propyl are the most common alkyl substituents (14,15,16). The number of possible isomers increases as the possible number and size of alkyl substituents increases. It is expected that higher degrees of alkylation can produce larger molecules with a greater number of isomeric forms. Separation of these isomers is rather difficult even by high resolution GC methods. The larger phenols should be present in the nondistillables. If pattern observed for the distillables is continuous, the phenols are heavily alkylated and may contain other functional groups including additional hydroxy groups. SEC can separate these phenols based on "linear size" (length obtained from valence bond structures), and FT-IR gives an insight into the structural details. Interpretation of the FT-IR is difficult (17-20) and requires extensive use of the literature as well as conformation from other analytical methods.

The number of isomers of alkylated aromatics is enormous. Increased alkylation causes an increase in the number of isomers. In the case of both alkylated phenols and aromatics various isomers exist in a continuous pattern

(14,15,16). A low amount of alkylation gives a few well-resolved isomers. For aromatic species which have been extensively alkylated a large number of isomers are produced but in small concentrations. The two types of aromatics are expected in the nondistillables. Polycyclic aromatics such as pyrenes and corones are the first type which appear in SEC fraction 10. The second type is the alkylated aromatics which are heavy due to size and number of alkyl side chains. The trend in distillables indicates that the number of possible isomers is enormous. The use of FT-IR with SEC allows one to identify the functional groups for molecules with a known linear molecular size.

The THF soluble nonvolatiles shown in Figure 1 represent the nondistillables in a coal liquid. If we assume that the heavy alkanes are insignificant due to their limited THF solubilities, the nonvolatiles contain two major chemical species, i.e.alkylated phenolics and aromatics. Phenolic species will be found in the first few SEC fractions and the aromatics in the last few fractions.

Figures 2-4 illustrate the separation of three coal liquids by SEC. By using the Microbeam accessory on the FT-IR and the new technique, the small samples in the SEC fractions are readily analyzed. The Microbeam accessory is used to focus the IR beam to less than 0.5 mm diameter, and analyze small samples deposited as spots on a KBr pellet. This technique allows the analysis of up to six sample spots on a single 13 mm diameter pellet. Another advantage of this technique is that the area between the spots on the pellet is used for background subtraction to eliminate the absorptions from contaminants in the pellet such as absorbed water.

FT-IR has been used to characterize spectroscopic analysis of complex substances such as coal, oil shale, petroleum crude and various products derived from them (18-20). These fossil fuels as well as coal liquids are composed of various species with functional groups whose characteristic absorption bands may overlap and interfere with the interpretation of the spectra. We have shown (3,4) that SEC separates molecules on the basis of linear molecular size, and that the phenolics hydrogen bond with the THF. Thus SEC with THF solvent is capable of separating phenolics and aromatics. Therefore, SEC separation prior to FT-IR analysis is used to resolve some of the uncertainties associated with spectral interpretation.

Figure 5 shows the FT-IR spectra of 10 one ml SEC fractions of nondistillables from a liquefaction reaction in where water under supercritical conditions was used as the solvent along with reactive gases such as $H_2$, CO and $H_2S$ (See Table 1 & 2 for experimental conditions and product yields). Most reports on FT-IR analysis of coal points out the difficulties associate with the interpretation of the spectrum. A good discussion about the band assignments of functional groups found in coal and coal liquids is presented in a recent paper (19). Figure 6 shows the SEC/FT-IR analysis of anthracene oil distillate which was also used as solvent for liquefaction experiments. The effect of reaction time on the SEC/FT-IR data for the nondistillables produced when using anthracene oil distillate and water under supercritical conditions is illustrated in Figure 7.

Comparison of Figures 1,2,3 & 4 shows that any coal liquid sample can be separated over a 10 ml THF flow time. The first five fractions contain most of the nondistillables and the latter five fractions have most of the distillables.

The broad absorbing peak at 3400 $cm^{-1}$ in all spectra shown in Figures 5-7 indicate the species with phenolic or alcoholic hydroxy groups. The nondistillables from all four liquefactions experiments have species with hydroxyl group in the first six SEC fractions. SEC fractions 7 through 10

showed smaller amounts of phenols in two experiments(TEH 11 & 22) and very little in the other two experiments (THE 13 & 23). The product from the two short reaction time experiments (TEH - 13 and 22) have a larger broad peak at 3400 $cm^{-1}$ indicating more large molecular size phenols than the product produced in the two longer reaction time experiments (TEH 11 and 23). The absorption due to the phenolics reaches a maximum for SEC fraction 6 for two runs (TEH 22 & 23) where supercritical water was the solvent, and at SEC fraction 4 for one run (TEH-11) where anthracene oil and long reaction time were used. Short reaction time experiment (TEH-13) with anthracene oil followed an intermediate trend. The absorption at 2900 $cm^{-1}$ due to alkyl groups maximized in SEC fraction 5 for all coal liquid samples.

The broad absorption peak at 1700 $cm^{-1}$ is due mostly to various carbonyl groups. Short reaction time experiments (TEH-13 & 22) showed an increase in the amount of carbonyl groups in SEC fractions 2-5 as indicated by the single broad peak at 1700 $cm^{-1}$. Longer reaction time experiments (TEH 11 & 23) show smaller absorptions in SEC fractions 2-5 with a split broad peak. Longer reaction time experiment (TEH-11) showed an increase in the amount of carbonyl absorption in SEC fraction 6-10, compared to the shorter reaction time experiment (TEH -13). The absorption at 1600 $cm^{-1}$ appears to be due to aromatic species with substituents such as alkyl, carbonyl and hydroxy groups. These species did not show any trend in any of the SEC fractions, or with reaction conditions.

## CONCLUSION

The use of Microbeam accessory and the spotting of the sample on the KBr pellet enables the study of small samples of coal liquids by FT-IR combined with SEC. The analysis time is short and reproducible. The complex and unknown chemical composition of nondistillables in coal liquids makes the determination of the chemical significance of each IR absorption peak rather difficult. This is particularly the case with the limited number of experiments used in this report. But it appears that the nondistillables and distillables contain species with similar functional groups. The determination of the structure of nondistillables may be possible by use of the FT-IR data, and by extrapolation, using the known chemical nature of major species in distillables.

## ACKNOWLEDGEMENTS

The financial support of this project by the Center for Energy and Mineral Resources, a Texas A&M University agency is very much appreciated. Mr. Terry Helton conducted all the liquefaction experiments, and Ms. Joan Perry separated nondistillable samples into fractions by size exclusion chromatography. The authors acknowledge their professional help. The Energy Research Center at University of North Dakota furnished lignite samples and the anthracene oil for the study.

## REFERENCES

1. Philip, C. V., Anthony, R. G., *Fuel Processing Technology*, 1980, 3, p. 285.
2. Zingaro, R. A., Philip, C. V., Anthony, R. G., Vindiola, A., *Fuel Processing Technology*, 1981, 4, 169.
3. Philip, C. V., Zingaro, R. A., Anthony, R. G., Ed. Sullivan, R. F., *ACS Symposium Series No. 156*, 1981; p.239.
4. Philip, C. V., Anthony, R. G., *Fuel*, 1982, 61, 351.
5. Philip, C. V., Anthony, R. G., *Fuel*, 1982, 61, 357.
6. Philip, C. V. and Anthony R. G., "Size Exclusion Chromatography", Ed. Prouder, T., *ACS Symp. Series*, 1984, 245, 257.
7. Philip, C. V., Anthony, R. G. and Cui, Z. D., Chemistry of Low-Rank

Coals, Ed. Schobert, H. H., *ACS Symp. Series*, 1984, 264, 287.
8. Philip, C. V., Bullin, J. A. and Anthony, R. G., *Fuel Processing Technology*, 1984, *9*, 189.
9. Philip, C. V. and Anthony, R. G. *Chromatographic Science*, 1986, *24*, 438.
10. Hendrickson, J.G., *Anal. Chem.*, 1968, 40:49.
11. Majors, R.E.J., *Chromatog. Sci.*, 1980, 18, 488.
12. Caze, J. and D. R. Gaskill, *Sep. Sci.*, 1969 4, 15.
13. Krishen, A. and R. G. Tucker, *Anal. Chem.*, 1977 49, 898.
14. Philip, C. V., Moore, P. K., and Anthony, R. G. Advances in Size Exclusion Chromatography, *ACS Symposium Series*, 1987, 352, 183.
15. Anthony, R. G., Philip, C. V. and Moore, P.K., Final Technical Report for Low Rank Coal Liquefaction, March 15, 1983 - October 31, 1986, DOE/FC/1060-13.
16. Philip, C. V., and Anthony, R. G. *Am. Chem. Soc. Div. Fuel Chem. Preprints*, 1987, 32, 368.
17. Soloman, P. R., Carangelo, R. M. and Horn, E., *Fuel*, 1986, 65, 650.
18. Soloman, P. R., and King, H. H., *Fuel*, 1984, 63, 1302.
19. Cooke, N. E., Fuller, O. M. and Gaikwad, R. P., *Fuel*, 1986, 66, 1255.
20. Painter, P. C., Snyder, R. W., Starsinie, M., Colman, N. M., Kuehn, N. W., and Davis, A., *Applied Spectroscopy*, 1981, 35, 475.

Table 1. Liquefaction conditions

| Run No. | Temp. (K) | $H_2$ (%) | CO (%) | H2S (%) | Time (min.) | Max P (MPa) | Solvent |
|---|---|---|---|---|---|---|---|
| TEH-11 | 681 | 38.4 | 44.1 | 17.5 | 22.8 | 29.2 | A04 |
| TEH-13 | 690 | 38.4 | 44.1 | 17.5 | 4.4 | 23.2 | A04 |
| TEH-22 | 695 | 33.2 | 41.8 | 25.0 | 4.5 | 34.6 | $H_2O$ |
| TEH-23 | 695 | 33.2 | 41.8 | 25.0 | 19.8 | 34.6 | $H_2O$ |

Table 2. The Percentage yields based on dmmf lignite.

| Run No. | NDTHFS | Distillables |
|---|---|---|
| TEH-11 | 30.40 | 49.93 |
| TEH-13 | 50.76 | 6.79 |
| TEH-22 | 33.04 | 16.38 |
| TEH-23 | 47.22 | 18.58 |

THF = Tetrahydrofuran, NDTHFS = THF soluble nondistillables.

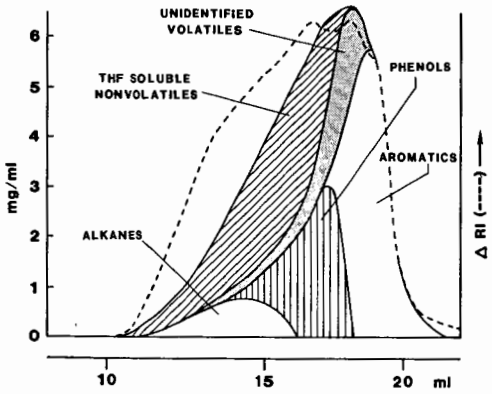


Fig. 1 SEC separation of Wyodak recycle solvent. The reconstructed chromatogram is shown to illustrate the size distribution various chemical species.

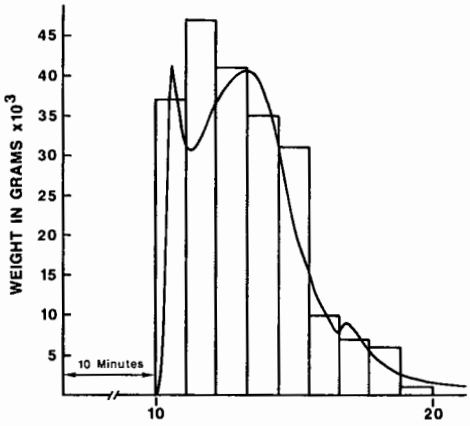


Fig. 3 SEC separation of THF soluble nondistillable from liquefaction experiment TEH-11. The solid curve shows the ΔRI responded.

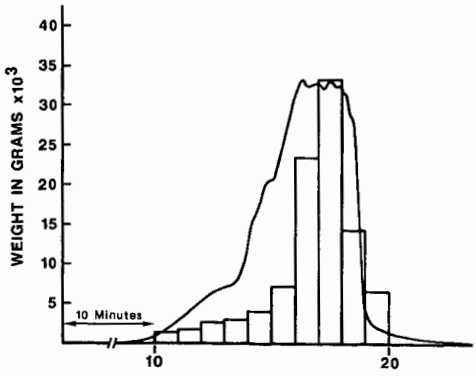


Fig. 2 SEC separation of Anthrazene oil which was used in liquefaction experiment TEH-11. The solid curve shows the ΔRI responded.

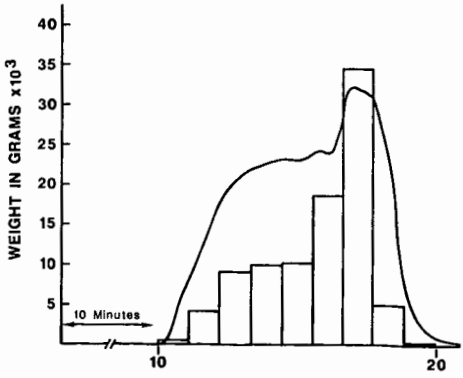


Fig. 4 SEC separation of THF soluble products from liquefaction experiment TEH-11. The solid curve shows the ΔRI responded.

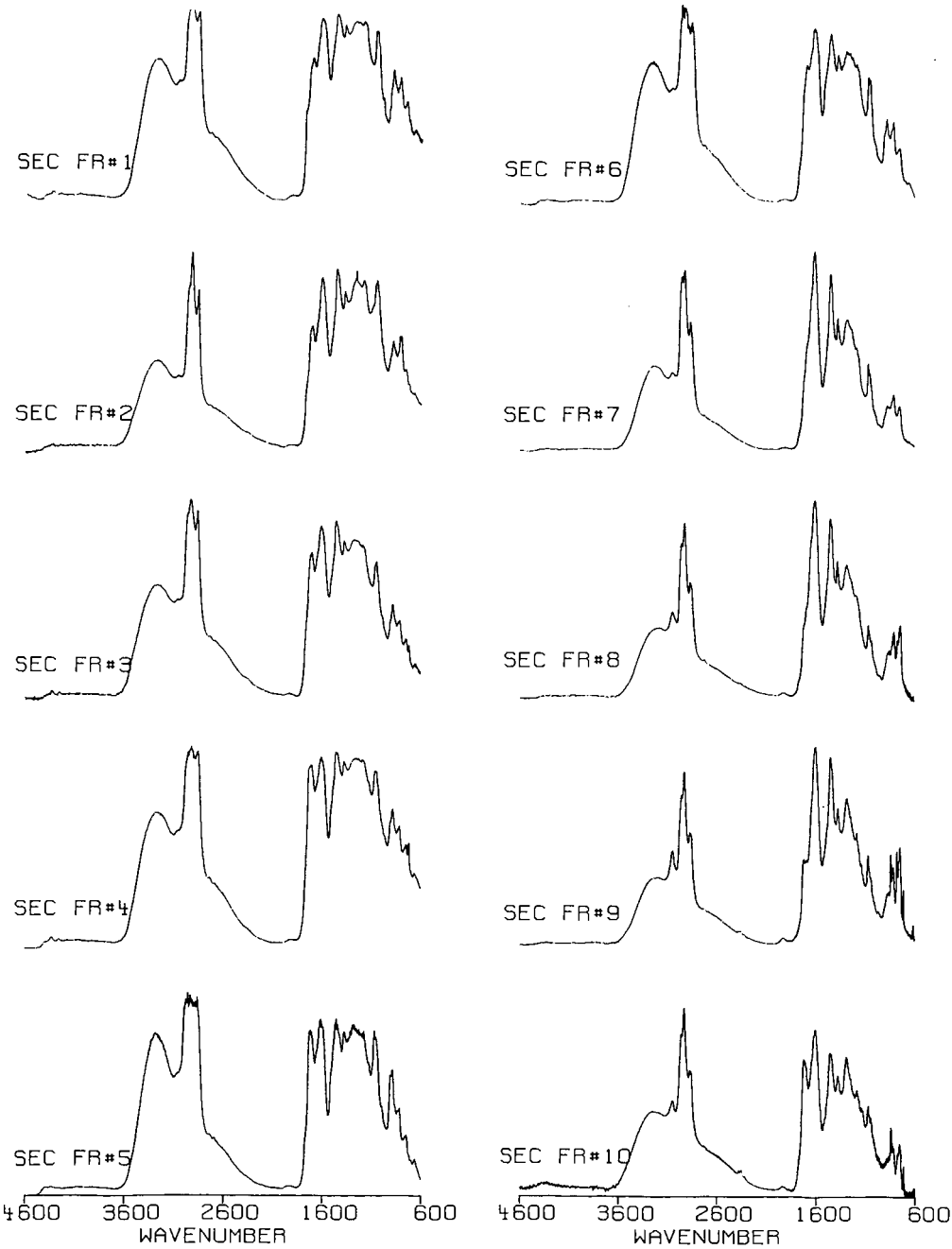


Fig 5. FT-IR spectra of SEC frs. of nonvolatiles from Zap-2 lignite liquefield using water under supercritical condition. See Table 1 & 2 for the reaction conditions & yield of TEH 22.

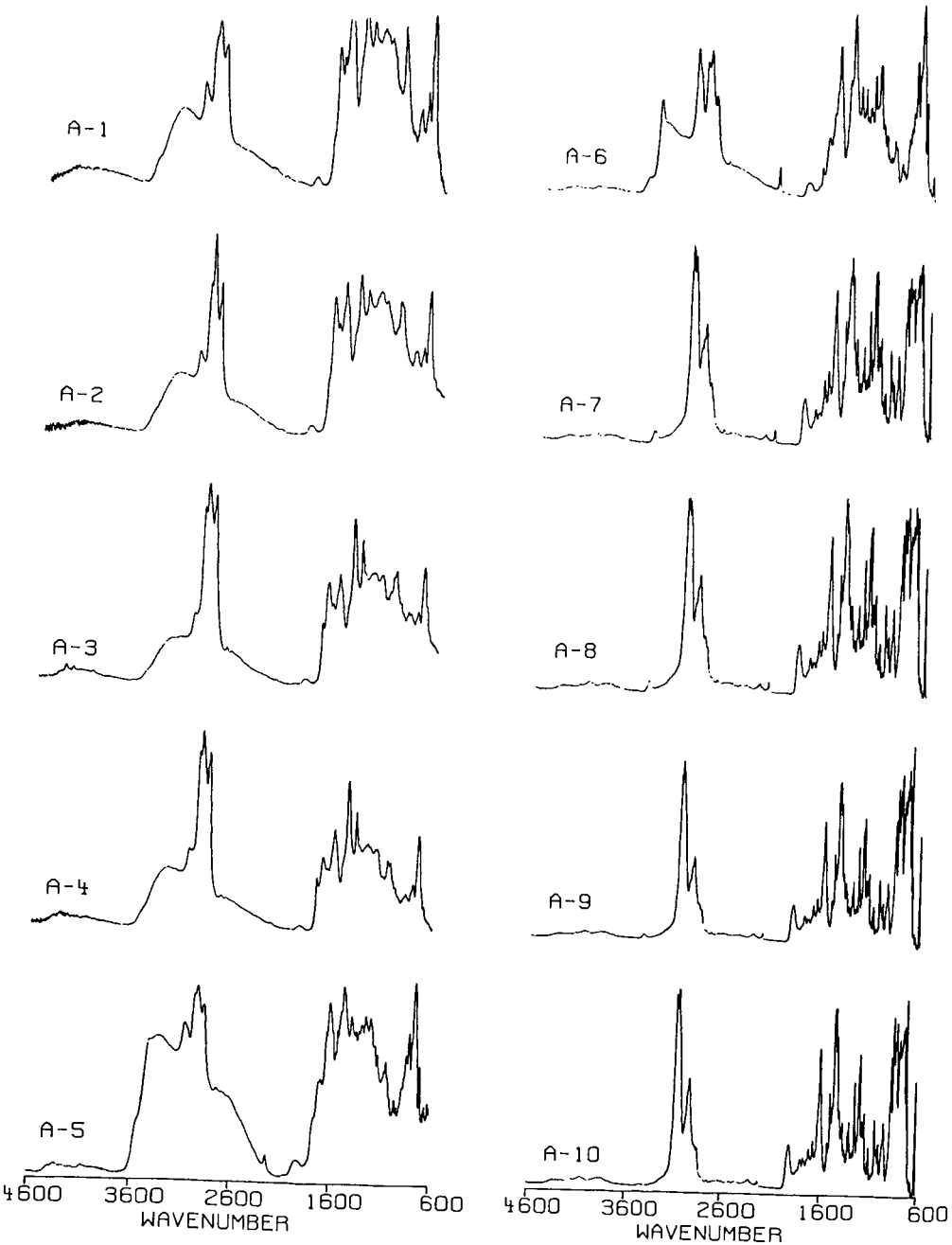


Fig 6. FT-IR spectra of SEC fractions of Figure 2 Anthracene oil distillate (A04). Figure 2 shows the SEC of A04.

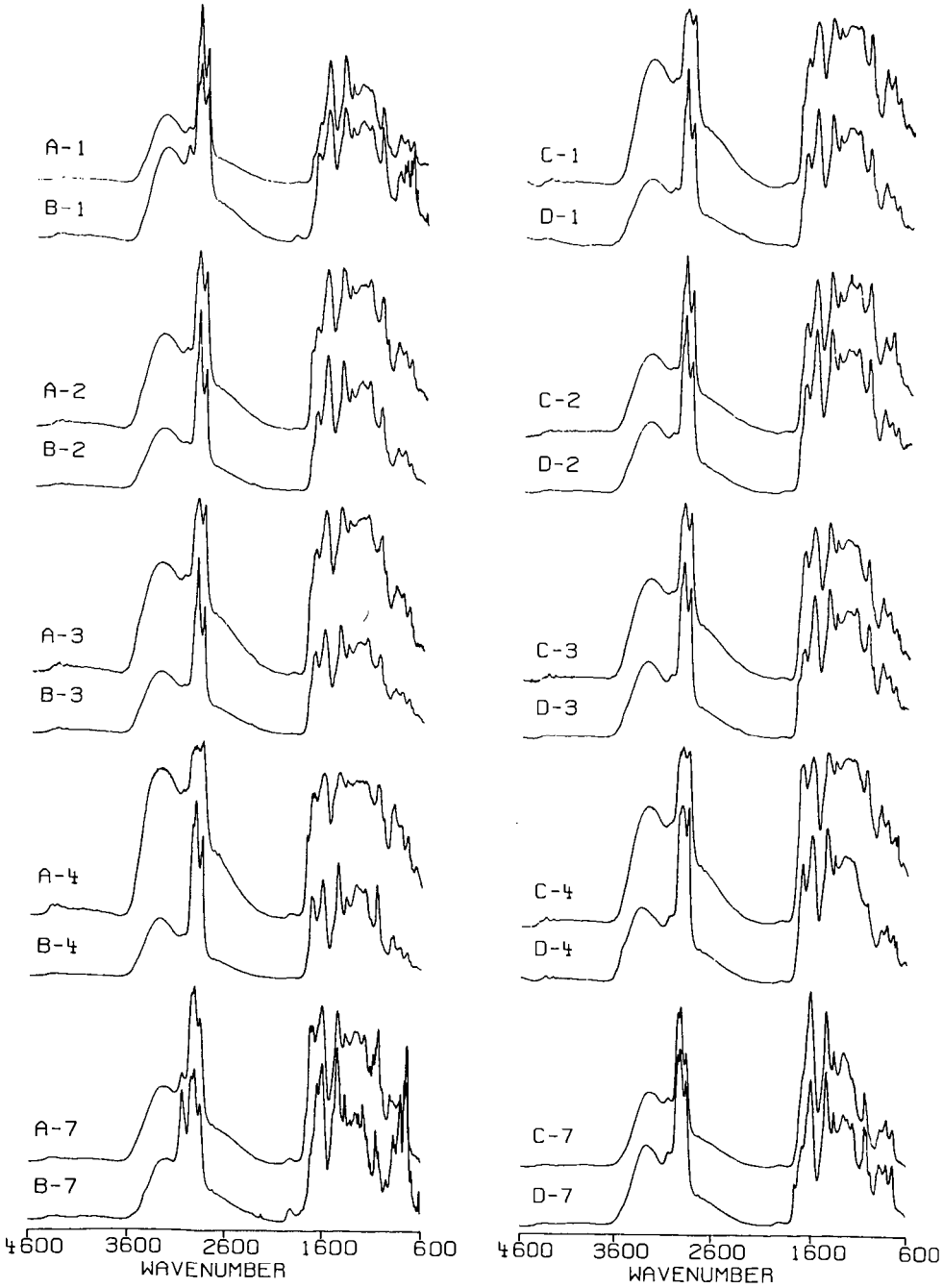


Fig 7. Comparison of FT-IR spectra of SEC fractions of non distillate obtained from four liquefaction experiments - A = TEH 13 and B= TEH 11 c= TEH 22 and D=TEH 23.

# Luminescence in Coal. The Effect of Mineral Matter, Air, and Swelling

Rita K. Hessley

Department of Chemistry, Western Kentucky University, Bowling Green, KY 42101

## Introduction

Based on the work of Coyne et al (1), who showed that simple dehydration of clay minerals results in measurable spontaneous emmission of light, we have undertaken the investigation of spontaneous light emmission in coals (2). Coal is frequently found in regions where clay minerals are abundant. Following Coyne, our initial study (2) monitored light emission from coal when an aqueous slurry of micronized coal was subjected to dehydration over $CaSO_4$. That work showed that luminescence did occur in a coal containing relatively little inorganic material (3% ash) as well as in a coal with a substantially higher (18%) content of mineral matter.

Several questions arose from that study. In particular, because the addition of as little as 1-2% (w/w) kaolinite to a coal sample exhibited a marked increase in luminescence, it was critical to determine, if possible, whether the photon release was caused only by the mineral matter content and not by the effect of dehydration on the coal structure itself. Thus, one goal of this phase of the investigation was to look for spontaneous luminescence in ash-free coal.

A second question was whether the phenomenon was related to, or dependent upon, excitation of the oxygen or nitrogen in air. Thus, the second goal of this work was to examine samples prepared with the exclusion of air.

Finally, Coyne et al (3) have also shown that kaolinites exhibit pronounced spontaneous luminescence as they swell in a slurry prepared with various amines. Because coal, also, generally swells readily in amine solvents, several measurements were carried out to determine whether coal luminescence could be detected as a function of solvent swelling.

## EXPERIMENTAL

### Preparation of Samples

The coal used for this study is a Western Kentucky hvA bituminous coal obtained from the Western Kentucky University Center for Coal Science. A summary of the analysis of the coal is given in Table I.

Table I

Analysis of Coal Bank Sample #86025

| | | | |
|---|---|---|---|
| Moisture(as det.) | 4.07 | Carbon | 66.74 |
| Ash | 15.50 | Hydrogen | 4.59 |
| VM | 35.3 | Nitrogen | 1.42 |
| fixed Carbon | 49.2 | Sulfur | 4.55 |
| BTU | 11,012 | Oxygen(diff) | 6.71 |

A portion of the 60-mesh coal was beneficiated in $ZnCl_2$ media of specific gravity 1.30. After cleaning, the recovered coal was micronized for 2 minutes in a Union Process Model 1-S stirred ball attritor mill. This effectively reduced the average particle size of the sample to 10 microns. Unbeneficiated 60-mesh coal was subjected to exhaustive solvent extraction with refluxing Dimethylformamide (DMF) under $N_2$. The

residue was then washed repeatedly with refluxing methanol under $N_2$ before being dried in a vacuum oven. The extracted material was recovered from the DMF and was also washed, and dried in vacuo.

The ash from the same coal was obtained according to ASTM D3173. The ash analysis is shown in Table II.

Table II

Major and Minor Metal Oxides in Ash from Coal Bank Sample #86025

| | Raw | Clean |
|---|---|---|
| % $SiO_2$ | 42.9 | 41.4 |
| % $Al_2O_3$ | 16.3 | 19.7 |
| % $Fe_2O_3$ | 33.3 | 21.2 |
| % CaO | 1.10 | .61 |
| % MgO | .51 | .33 |
| % $K_2O$ | 1.46 | 1.10 |
| % $MnO_2$ | .04 | .01 |

Measurement of Luminescence

Spontaneous luminescence was measured as a function of time. Single photon monitoring was carried out using the Packard Model 1500 "TriCarb" liquid scintillation counter. Data were recorded as counts per minute and were printed at one minute intervals for 99 minute maximum monitoring period.

A sample slurry was prepared by direct weighing and mixing of the solid and water. Typically, a coating of about 2.5 cm was applied to the inside of a standard scintillation vial above about 1 cm of indicating $CaSO_4$. For all trials, the slurry was applied manually and it was difficult to apply precisely the same amount of sample each time. Generally, 80-120 mg samples were used which consisted of at least a water:coal ratio of 2:1. For swelling experiments, the method described by Coyne (3) was used to prepare the samples. Pyridine and DMF were used as the swelling solvents. To prepare samples in an air-free environment, a stream of argon was used to purge the vial prior to and during application of the slurry.

RESULTS AND DISCUSSION

Figure 1 shows a portion of the photon output for the dehydration of the whole coal #86025 (15.5% ash). As in our previous study, the photon count was observed to decay monotonically until spontaneous luminescence occurred at some time after initiation of drying. Figure 2 shows data for the beneficiated sample (1.25% ash). These data confirm our earlier observations that even low ash coals exhibit luminescent behavior. Figure 3 shows that extraction residue, which retains most if not all of the inorganic matter in coal, also displays spontaneous luminescence during dehydration. The traces in these figures cannot be compared directly with regards to the time required for the on-set of photon emmission nor with regards to the intensity. Our earlier work showed that time and intensity differences between samples are dependent on the sample size (thickness) and total moisture content.

Figure 4 shows the trace of counts per minute with time for the material extracted from coal with refluxing DMF. This material is essentially ash-free, and shows no spontaneous luminescence during the period monitored. This is striking evidence that ash-free coal does not exhibit luminescent behavior. Of course, the extract from additional samples needs to be studied in order to confirm this observation conclusively. Measurement of photon emmission in recovered ash (Figure 5) was difficult to measure and was not nearly as impressive in its intensity as is

observed with kaolinite (1). The ash was very granular and difficult to grind sufficiently fine to prepare a smooth paste. It may also be important that the ash obtained from the coal used in this study was brick-red and contained 33.3 % (w/w) Iron oxide and, correspondingly, a smaller quantity of aluminum and silicon oxides. For comparison, the luminescence during dehydration for a coal ash containing much less iron oxide (based on its white coloration) was recorded and is shown in Figure 6. These data suggest that photon emmission from ash may be affected by its overall composition.

All attempts to induce measurable photon emmission in either whole coal or coal extract by solvent swelling have been unsuccessful. One explanation is that the small (mg) quantities of coal being used swell rapidly enough in the two amine solvents tested that luminescence accompanying swelling may be dissipated in the time required to grind and prepare the sample (3). These experiments are being continued using other, less vigorous, swelling solvents.

Using kaolinite, there is no change observed for spontaneous luminescence in samples prepared under argon. However, there remains some question whether the sample vials are air-tight throughout the counting period. Thus, our initial trials to determine the effect of air on the presence and intensity of spontaneous luminescence in coal are incomplete.

## CONCLUSIONS

It has been shown that spontaneous luminescence in coal during dehydration is dependent directly on the ash, or mineral matter content of the coal. In the absence of any ash, no photon emmission is observed. Coal extraction residue retains the property of luminescenc during dehydration; coal ash also exhibits luminescence, but appears to be affected strongly by the presence of iron oxide (or by the actual clay mineral content). Quantities of ash as small as a few percent by weight dispersed throughout the coal matrix are sufficient to cause the phenomenom to be observable. Work is continuing to explore the effects of air and solvent swelling.

## REFERENCES


1. Coyne, L. M., N. Lahav and J. G. Lawless, Nature, 292, 27 August, 819 (1981); Lahav, N., L. M. Coyne and J. G. Lawless, Clays Clay Miner., 30(1), 73 (1982).

2. Hessley, R. K. and L. M. Coyne, Preprints, Amer. Chem. Soc. Div. Fuel Chem., Denver, 32(1), 547 (1987).

3. Coyne, Lelia M., Glenn Pollack and Roger Kloepping, Clays Clay Miner., 32(1), 58 (1984).

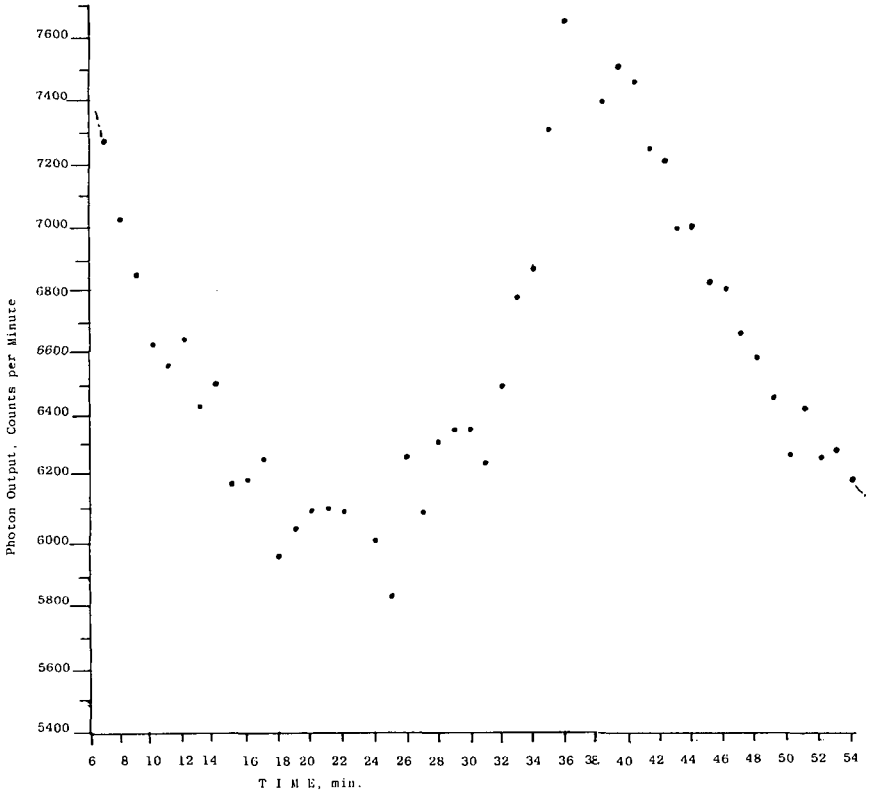


Figure 1. Photon output for Dehydration of whole coal (15.5% ash)

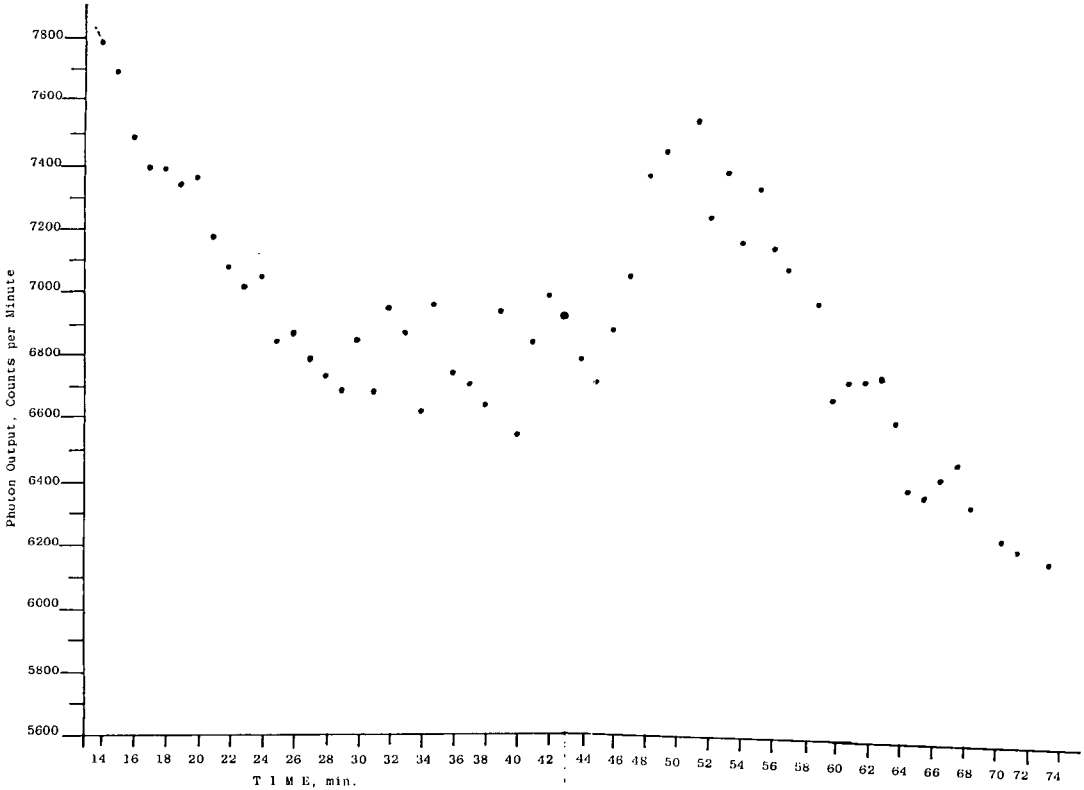


Figure 2. Photon Output for Beneficiated coal (1.25% ash).

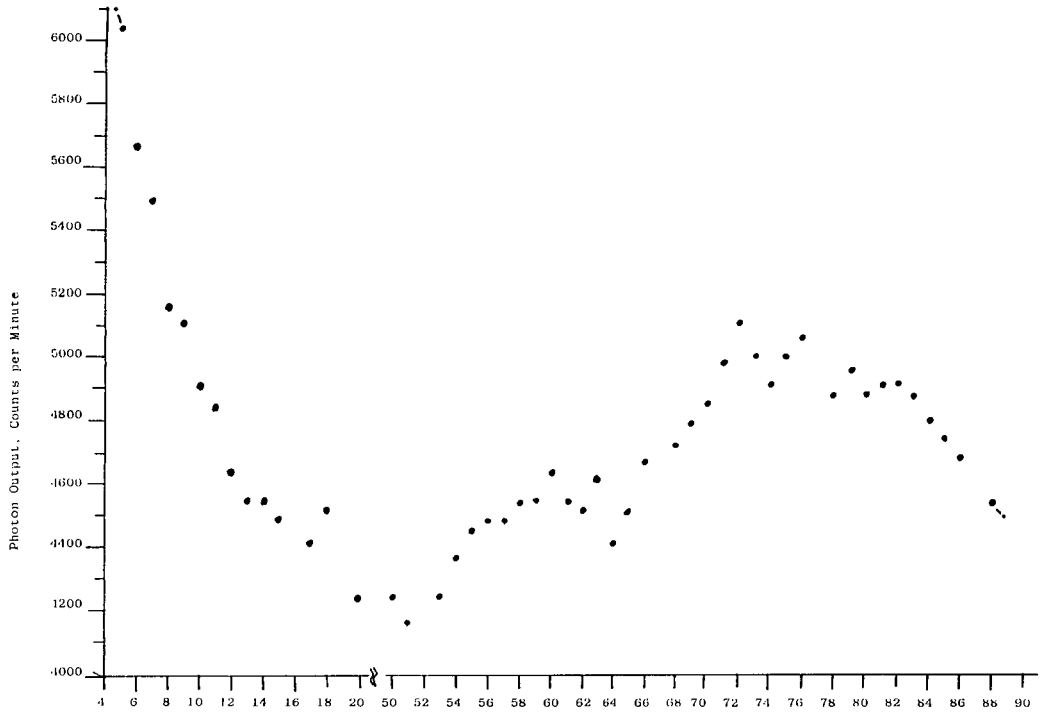


Figure 3. Photon Output on Dehydration for Coal Extraction Residue

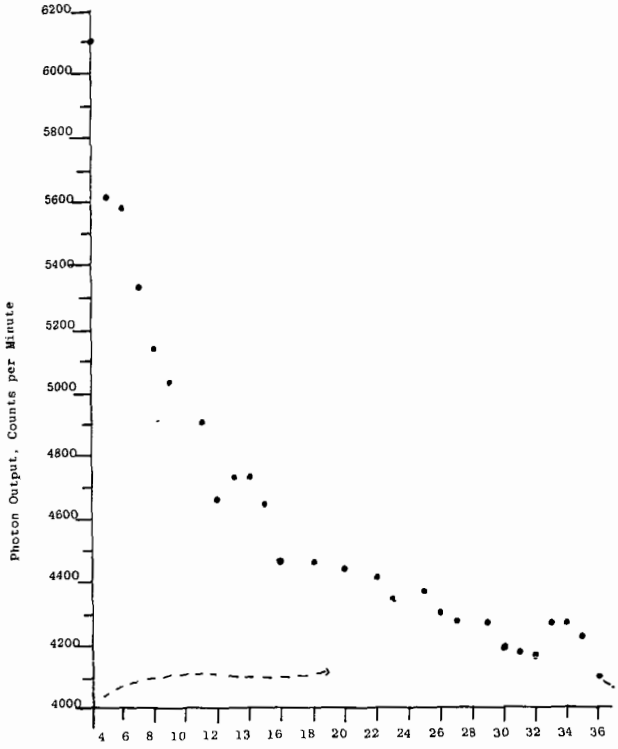


Figure 4. Photon Output for Dehydration of Whole Coal Extract

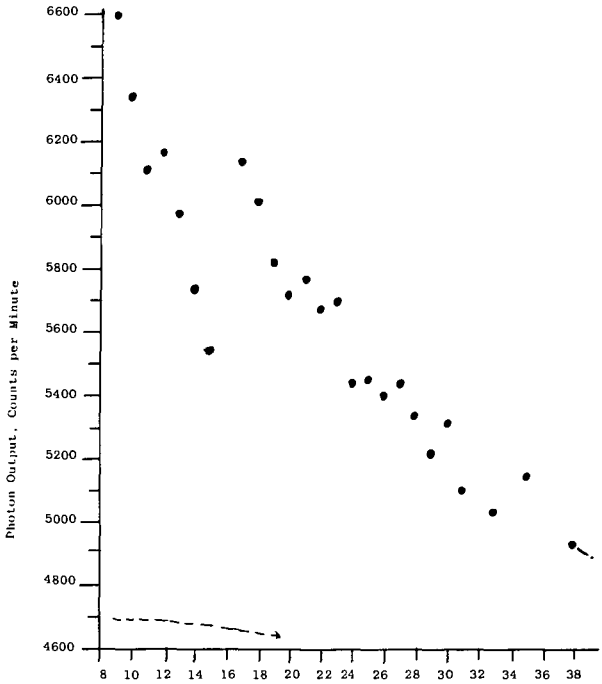


Figure 5. Photon Output for Dehydration of Recovered Coal Ash

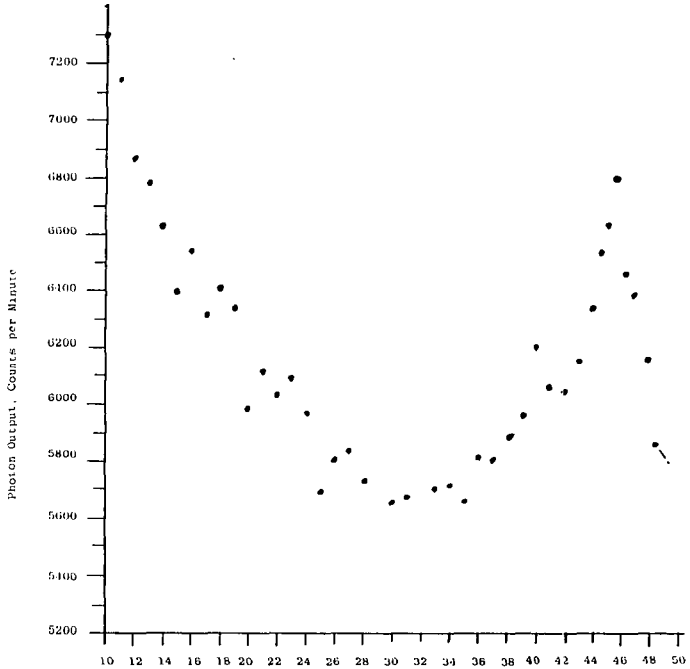


Figure 6. Photon Output for Dehydration of a Low-Iron Ash

# DETERMINATION OF COMPOUND CLASS COMPOSITION OF OIL FRACTIONS OF SOME COAL LIQUIDS BY ANALYTICAL LIQUID CHROMATOGRAPHY

B. Chawla and B. H. Davis

Kentucky Energy Cabinet Laboratory
P. O. Box 13015
Lexington, KY 40512

## ABSTRACT

A high-performance liquid chromatography method was developed to determine the amount of each of the compound classes (such as saturates, aromatics and polars) in the oil fraction (pentane soluble fraction) of coal liquids. The method utilizes bonded cyanosilane and aminocyanosilane columns and mixtures of benzene in n-hexane and tetrahydrofuran in methyl tert-butyl ether as mobile phases. A Tracor LC-rotating disc flame ionization detector was used to quantify the chromatographic peaks.

Oil fractions derived from different rank coals, liquefied at 385° and 445°C, were analyzed for their compound class compositions. The trends in the percentages of saturates, aromatics and polars varied with liquefaction temperature and coal rank.

## INTRODUCTION

The products from coal liquefaction processes are so complex that it is almost impossible to completely analyze them. Therefore, following a practical approach widely used with petroleum, the coal liquids are divided into solubility classes such as: (i) oils - pentane soluble, (ii) asphaltenes - benzene soluble, pentane insoluble, and (iii) preasphaltenes - pyridine or tetrahydrofuran (THF) soluble, benzene insoluble.

To obtain data suitable for mechanistic considerations, it is essential that fractions or classes of compounds obtained from coal liquefaction processes be quantitatively analyzed in more detail. Such efforts have been made recently, but there remains much to be learned about the compositions of these three solubility classes of coal products. A commonly used method for separation and/or analysis of the coal liquids is based on liquid chromatographic fractionation in terms of major components such as saturates, aromatics, more polar aromatics (non-basic N, O, S - heterocyclics), monophenols, basic nitrogen heterocyclics, polyphenols, and non-eluted unidentified materials.

One method was developed in 1976 by Farcasiu (1); it has also been used recently by Winans et al. (2) to characterize materials extracted, using benzene-methanol as a solvent, from several Argonne Premium Coal Samples. To understand the liquefaction behavior of a number of coals, separations of oil, asphaltene and preasphaltene fractions of coal liquids have also been reported (3-12). However, these chromatographic techniques are laborious and time consuming. To the best of our knowledge, the high-performance liquid chromatography (HPLC) coupled with the LC-Flame Ionization Detector (FID) have not been used for characterization and/or quantitation of coal liquids.

The purpose of our investigation was to adopt an analytical HPLC technique for separation and quantitation of oil fractions (pentane-soluble) of coal liquefaction products in terms of three compound classes such as saturates, aromatics, and polars. To learn if our HPLC procedure was suitable for oil fractions of supposedly different compositions, we have analyzed the oil fractions obtained from the liquefaction of coals of different rank at two reaction temperatures (385°C and 445°C).

## EXPERIMENTAL

The HPLC system consisted of two solvent delivery systems (Waters 6000A pumps), three Valco six-port valves, a Tracor 945 LC-FID and Nelson Analytical 3000 Chromatography System equipped with an ITT/XT computer and a Nelson Analytical Series 760 converter with a minimum detectable capability of 0.1 microvolt-second. Two analytical columns were used: a cyano column (Supelco 5 $\mu$m LC-CN, 25 cm x 4.6 mm i.d.) and an ammino-cyano column (Whatman 5 $\mu$m PAC, 25 cm x 4.6 i.d.). Mixtures of benzene in n-hexane and tetrahydrofuran (THF) in methyl tert-butyl ether (MTBE) were used as mobile phases. HPLC grade commercial solvents were used as received. However, the mobile phases were always degassed through a vacuum system just before their use. Of the several solvent flow rates that were tried, 1.0 to 1.5 ml/min was found to be the most suitable.

Following Pearson and Gharfeh's HPLC procedure (13) for the determination of hydrocarbon types in crude oil residues, we have used a rotating disc flame ionization detector (Tracor 945 LC-FID) developed by Tracor Inc. (14). The FID appears to be one of the few detectors among the various detectors used so far in HPLC procedures which tolerate a change from a nearly non-polar to a highly polar solvent system and can at the same time, be unaffected when the pressure drifts due to back and forth switching of the valves during a run.

In a typical run, the total column effluent is applied onto a fibrous quartz belt mounted on a rotating disc. As the disc rotates in the heated housing, the volatile solvent is vaporized and removed from the housing with the help of a vacuum pump. Non-volatile solutes remain on the fibrous belt and are carried into the flame where they are combusted and detected.

The operational logic of the HPLC system is shown in Figure I. During Step I, pump A (1.0 ml/min) with benzene solution in hexane was turned on. The switching valves were set in such a way that the mobile phase went first to the cyano column, then to an amino-cyano column and finally to the detector (see Figure I). This arrangement allowed the polar molecules to be retained by the cyano column and the aromatics to be retained by the amino-cyano column. About 3 to 4 minutes after the emergence of a saturates peak from the amino-cyano column, the system was switched to Step II. In Step II, the cyano column was isolated. Pump A was switched off and pump B with THF in methyl tert-butyl ether (MTBE), was operated at a flow rate of 1.0 ml/min. This arrangement allowed the retained aromatics to be backflushed from the amino-cyano column. Once the saturates and aromatics have been eluted, the system was switched to the final operation Step III where polars were backflushed from the cyano column using the THF/MTBE mobile phase. Upon completion of the separation, the system was brought back to its initial

conditions by reequilibriating the columns with benzene-hexane mixture. A typical chromatogram is shown in Figure II.

Liquefaction runs were made at two temperatures, 385° and 445°C, for 15 min. or 45 min. using tetralin as a solvent and a hydrogen atmosphere (800 psig, ambient). Typically 5g of dried coal and 7.5 g of tetralin were used for a run (see (15) for more experimental details). At the end of the experiment the reactor products were quantitatively removed and separated into three solubility classes through Soxhlet extractions. The oils were used for our HPLC analyses.

## RESULTS AND DISCUSSION

A number of coals were used in this study (Table 1). They were selected to cover the rank range, based upon %C(daf) or vitrinite reflectance, that is present in the western Kentucky coals. A Breckinridge sample, an unusual coal that approaches the properties of a cannel coal, was also included in the study.

It was pointed out earlier that the FID detector could tolerate the solvent changes and the pressure drifts employed in the study. However, it is necessary to determine a relative response factor (ions produced/unit mass) for the various compound classes of the oil. In order to accomplish this, it was important to have aliphatics, aromatics and polars with compositions that are similar in chemical compositions as those of these components in the investigated oil fractions. The oil fractions obtained from coal liquefaction runs contained about 90-95% tetralin, the solvent used in this reactions; the preparative liquid chromatography of these samples over silica gel was not fruitful. Therefore, the oil fraction of a sample (V-1064) from the first stage reactor of the Wilsonville, Alabama coal liquefaction plant was used to carry out a larger scale separation.

The LC separation was performed using freshly activated silica gel (400°C overnight) and hexane, benzene and THF as the mobile phases. Hexane was used to elute the aliphatics from the column and 15% benzene in hexane was used to elute the aromatics. Finally, the column was backflushed with THF to obtain a polar fraction. The aliphatic, aromatic and polar fractions were tested for completeness of separation with the analytical HPLC procedure described in this report and were found to be of acceptable purity ($>$98%). A GC of the aliphatic fraction showed that it contained $C_{15}$ - $C_{37}$ hydrocarbons; these were mostly normal alkanes. Alkanes with a carbon number greater than $C_{37}$ are present in very small amounts. Other components were not detected in any significant amount.

The absolute response factors for saturate, aromatic and polar fractions were obtained from the slopes of the linear plots (Figure III) of the peak areas versus their mass (over a range of concentration of 0-20 $\mu g/\mu l$). Their relative response factors, as area/mass, are in the ratio of 1:2.16:1.23 for saturates : aromatics : polars.

The precision and reproducibility of the data were established by making six repeated measurements on the separation of one of the oils used in this study. The maximum uncertainties in the weight percentages of saturates, aromatics and polars were determined to be within 2%, 2% and 4-5% respectively.

Finally, the oil fractions obtained from the liquefaction of eight coals at 385° and 445°C were analyzed. The results are presented in Table 2. The following observations may be made for the data in Tables 1 and 2:

(a) The relative aliphatic percentages decrease with an increase in reaction temperature for all the coals studied with the exception of Breckinridge coal sample which shows the opposite effect but this is what should be anticipated for this type of coal.

(b) The aromatic percentages remained almost constant with the increase in temperature for most of the coals including the Breckinridge sample.

(c) The polar percentages increased with an increase in temperature for all the coals except the Breckinridge sample.

(d) Aliphatic, aromatic and polar percentages do not show a systematic trend with the coal rank. However, the data at 445°C (see Table 2) show that aliphatics tend to decrease with decreasing coal rank.

(e) With the exception of the Breckinridge sample, the aliphatics, aromatics and polars are generally in the ratio of 1:2:5 (Table 2).

(f) Irrespective of the liquefaction temperature, the oil fractions from the Breckinridge coal contain extremely large amounts of aliphatics (45.8% and 55.4%) small amounts of aromatics (7.8% and 7.9%) and polars (46.4% and 36.7%) compared to those of other coals (aliphatics, 9-18%; aromatics, 19-28% and polars, 55-69%).

## ACKNOWLEDGEMENT

This work was supported by the Commonwealth of Kentucky, Kentucky Energy Cabinet and by DOE Contract No. DEFC 22-85PC80009 as part of the Consortium for Fossil Fuel Liquefaction Science (administered by the University of Kentucky). The Kentucky Energy Cabinet Laboratory is administered by the University of Louisville.

## REFERENCES

1. Farcasiu, M. Fuel 1977, 56, 9.

2. Xia, J. J.; Neill, P. H.; Winans, R. E. ACS Div. Fuel Preprints 1987, 32(4), 340.

3. Sternberg, H. W.; Raymond, R.; Schweighardt, F. K. Science 1975, 188, 49.

4. Given, P. H.; Cronauer, D. C.; Spackman, W.; Lovell, H. L.; Davis,A.; Biswas, B. Fuel 1975, 54, 34.

5. Given, P. H.; Cronauer, D. C.; Spackman, W.; Lovell, H. L.; Davis,A.; Viswas, B. Fuel 1975, 54, 40.

6. Liphard, K. G. Chromatographia 1980, 13(10), 603.

7. Sonnefeld, W. J.; Zoller, W. H.; May, W. E.; Wise, S. A. Anal. Chem. 1982, 54, 723.

8. Whitehurst, D. D.; Butrill, Jr. S. E.; Derbyshire, F. J.; Farcasiu, M.; Odoerfer, G. A.; Rudnick, L. R., Fuel 1982, 61, 994.

9. Lucke, R. B.; Later, D. W.; Wright, C. W.; Chess, E. K.; Weimmer, W. C. Anal. Chem. 1985, 57, 633.

10. Robbins, W. K.; McElroy, F. C. Liquid Fuel Technology 1984, 2(2), 113.

11. Allen, T. W.; Hurtubise, R. J.; Silver, H. F. Fuel 1987, 66, 1024 and references cited therein.

12. Kemp, W.; Steedman, W.; Scott, D. A.; Thomson, M. A. Fuel Process. Technol. 1987, 15, 341.

13. Pearson, D. C.; Gharfeh, S. G. Anal. Chem. 1986, 58, 307.

14. Dixon, J. B. Chimie 1984, 38, 82.

15. Chawla, B.; Keogh, R.; Davis, B. H. ACS Div. Fuel Preprints 1987, 32(3), 342.

**Table 1.** *Coal Analysis.*

| | W. Ky. #9 71154 | Breckinridge 71160 | W. Ky. #9 71148 | W. Ky. #9 71072 |
|---|---|---|---|---|
| 1. Ash (As-Received) | 30.03 | 6.36 | 14.87 | 9.04 |
| 2. Volatile Matter, daf | 47.83 | 74.28 | 46.10 | 42.90 |
| 3. Fixed Carbon, daf | 52.17 | 25.72 | 53.90 | 57.10 |
| 4. Sulfate S, daf | 0.00 | 0.01 | 0.17 | 0.14 |
| 5. Pyritic S, daf | 1.47 | 1.23 | 1.35 | 0.53 |
| 6. Organic Sulfur, daf | 2.27 | 0.55 | 1.70 | 1.91 |
| 7. Total Sulfur, daf | 3.74 | 1.81 | 3.22 | 2.57 |
| 8. Carbon, daf | 84.99 | 80.66 | 79.59 | 79.19 |
| 9. Hydrogen, daf | 6.16 | 8.51 | 5.62 | 5.44 |
| 10. Nitrogen, daf | 1.98 | 2.13 | 1.90 | 2.00 |
| 11. Oxygen, daf | 3.13 | 6.90 | 9.67 | 10.80 |

| | W. Ky. #11 71064 | W. Ky. #11 71081 | W. Ky. #11 71077 | W. Ky. #9 71095 |
|---|---|---|---|---|
| 1. Ash (As-Received) | 9.56 | 4.43 | 9.06 | 14.80 |
| 2. Volatile Matter, daf | 47.47 | 43.23 | 41.74 | 43.73 |
| 3. Fixed Carbon, daf | 52.53 | 56.77 | 58.26 | 56.27 |
| 4. Sulfate S, daf | 0.06 | 0.17 | 0.75 | 0.68 |
| 5. Pyritic S, daf | 1.06 | 0.64 | 2.09 | 4.48 |
| 6. Organic Sulfur, daf | 3.11 | 2.21 | 3.35 | 3.27 |
| 7. Total Sulfur, daf | 4.23 | 3.01 | 6.19 | 8.43 |
| 8. Carbon, daf | 78.80 | 78.28 | 76.96 | 76.63 |
| 9. Hydrogen, daf | 5.85 | 5.52 | 5.37 | 5.10 |
| 10. Nitrogen, daf | 1.70 | 1.70 | 1.63 | 1.70 |
| 11. Oxygen, daf | 9.42 | 11.49 | 9.85 | 8.14 |

Oxygen by difference.

**Table 2.** *HPLC Analysis of Oil Fractions at 385°C and 445°C.*

| | | Weight % | | | | | |
|---|---|---|---|---|---|---|---|
| | | 385°, 15 minutes | | | 445°C, 15 minutes | | |
| **Coal Number** | **C (daf)** | **Aliphatic** | **Aromatic** | **Polar.** | **Aliphatic** | **Aromatic** | **Polar.** |
| 71154 (W. Ky. #9) | 84.99 | 13.2 | 24.1 | 62.7 | 12.8 | 23.3 | 63.9 |
| Breckinridge | 80.66 | 45.8 | 7.8 | 46.4 | 55.4 | 7.9 | 36.7 |
| 71148 (W. Ky. #9) | 79.59 | 15.0 | 20.4 | 64.6 | 11.5 | 20.3 | 68.2 |
| 71072 (W. Ky. #9) | 79.19 | 18.4 | 21.6 | 60.0 | 12.1 | 19.7 | 68.2 |
| 71064 (W. Ky. #11) | 78.80 | 13.9 | 19.3 | 66.8 | 10.2 | 20.3 | 69.5 |
| 71081 (W. Ky. #11) | 78.28 | 11.0 | 24.3 | 64.7 | 9.7 | 20.5 | 69.8 |
| 71077 (W. Ky. #11) | 76.96 | 12.2 | 25.5 | 62.3 | 9.2 | 24.5 | 66.3 |
| 71095 (W. Ky. #9) | 76.63 | 16.6 | 28.2 | 55.2 | 8.8 | 22.0 | 69.2 |

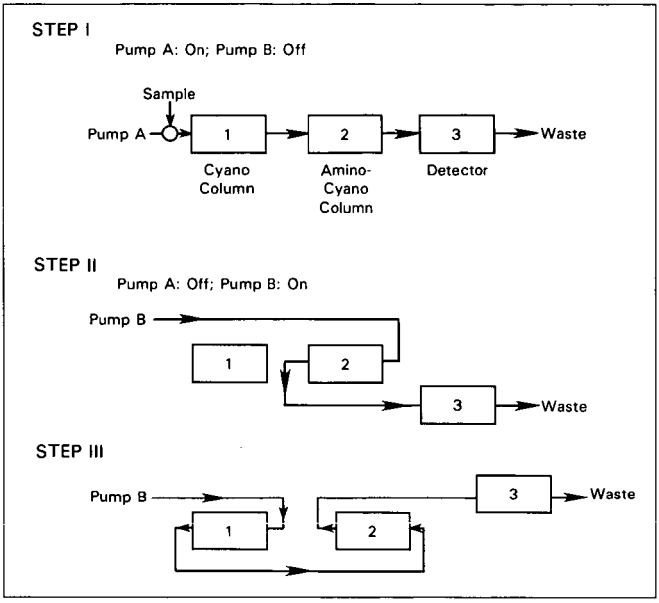


**Figure I.** *Operation of HPLC system.*

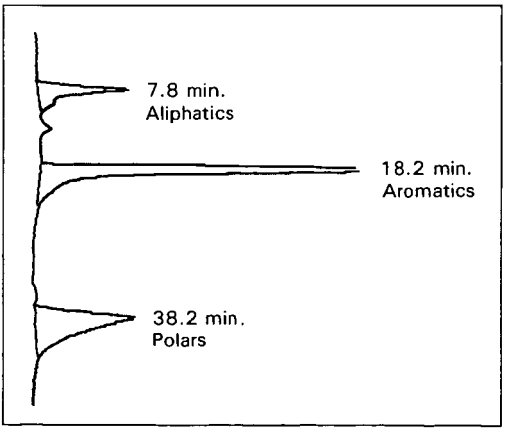


**Figure II.** *A typical chromatogram of an oil fraction separation.*

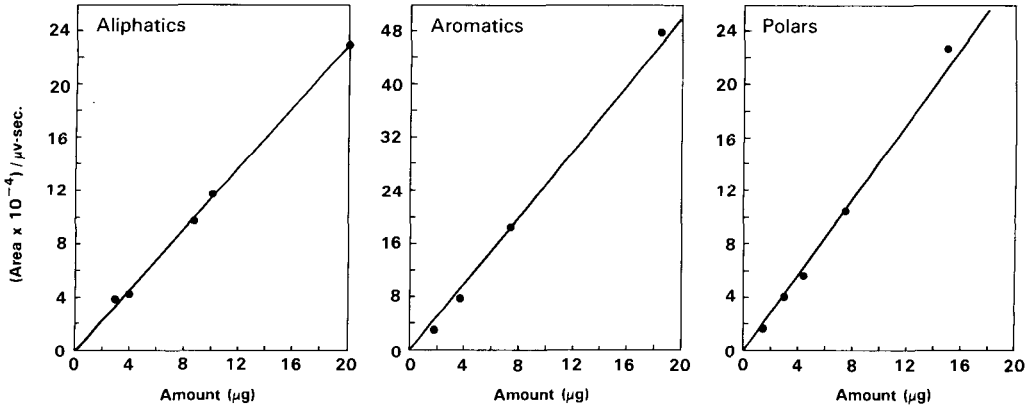


**Figure III.** *Calibration plots of aliphatics, aromatics, and polars.*

# THE ANALYSIS OF THE ORGANIC MATTER IN CHATTANOOGA SHALE BY OXIDATION WITH PERCHLORIC ACID

Bobby J. Stanton and Chris W. McGowan

Department of Chemistry
Tennessee Technological University
Cookeville, Tennessee 38505 (USA)

## ABSTRACT

A kerogen concentrate was prepared from a raw Chattanooga shale sample. The kerogen concentrate was oxidized in a stepwise fashion by varying the boiling point, and subsequent concentration and oxidizing strength of perchloric acid. The progress of the reaction was monitored with respect to the amount of undissolved material, the color of the aqueous phase, and the conversion of carbon to carbon dioxide. The dissolution of kerogen occurred between 150-180°C. The color intensity of the aqueous phase rose to a maximum, then faded to clear at 203°C. The maximum color corresponded to the dissolution of kerogen. The percentage of carbon converted to carbon dioxide was negligible when the boiling point of perchloric acid was below 150°C. Above 150°C, the carbon converted to carbon dioxide rose almost linearly. Polar unsaturated carboxylic acids were indicated as the major oxidation products.

## INTRODUCTION

For some time workers have attempted to characterize the kerogen present in oil shales. Kerogen is a high molecular weight, polymeric material which is said to be insoluble in common organic solvents. In order to characterize the kerogen in oil shale, it has been necessary to destroy the kerogen by oxidative degradation of the kerogen matrix with subsequent analysis of the oxidation products. Analysis of the soluble lower molecular weight oxidation products has yielded insight into the nature of the structure of kerogen in oil shale.

Leonard (1) used 3.5 percent ozone to oxidize Chattanooga shale. Similar ether and water soluble acids were extracted from the raw shale and a kerogen concentrate prepared from the raw shale sample. The ozonization products were primarily aliphatic hydroxy acids. Ozonolysis of the kerogen of Chattanooga oil shale by Kinney and Leonard (2) yielded highly oxygenated ether and water soluble acids. Kinney and Schwartz (3) oxidized Chattanooga shale with air at 200°C for 200 hours to produce the maximum amounts of humic acids. The acids were similar to those obtained from coal, and were quinoid in nature.

This paper describes the characterization of the kerogen of Chattanooga oil shale by oxidative degradation with perchloric acid of varying boiling point. Smith (4) demonstrated that the

apparent reduction potential of perchloric acid increases sharply as the boiling point rises above 150°C and the concentration increases. A stepwise oxidation of the kerogen can be effected by increasing the boiling point and subsequent oxidizing ability of perchloric acid. This study was analogous to the work completed by McGowan and Diehl (5,6,7) on Green River Shale.

## EXPERIMENTAL

A Gassaway member of the Chattanooga shale from the Eastern Highland Rim area of Tennessee was ground to -60 mesh. A kerogen concentrate was prepared from the raw shale sample by demineralization using a combination of hydrochloric and hydrofluoric acids. Samples of the kerogen concentrate were oxidized with boiling perchloric acid within a modified Bethge apparatus as described by McGowan and Diehl (5). Perchloric acid solution was added to the reaction flask of the Bethge apparatus, and the boiling point was adjusted to the desired temperature by positioning the teflon stopcock to remove reflux condensate, or by addition of water through the top of the water condenser. The boiling point was kept constant by returning the reflux condensate to the reaction vessel. The amount of perchloric acid added was varied such that approximately 50 ml of solution remained after the temperature adjustment was completed. After cooling to room temperature, three 1.00 ml aliquots were taken and titrated with 0.25 N sodium hydroxide. A 1-g sample of kerogen concentrate was added to the reaction vessel, and the system was purged for 30 minutes with nitrogen. A weighed Turner absorption bulb containing ascarite and anhydrous magnesium perchlorate was added to the reaction system. The reaction flask was heated for 1.5 hours. The stable reaction temperature was recorded. The system was repurged with nitrogen for 30 minutes at the termination of the reaction. The absorption bulb was reweighed and the percentage of carbon converted to carbon dioxide was calculated. The undissolved material was filtered and washed with 300 ml of distilled water. Upon dilution as a result of filtration, the perchloric acid solution became more aqueous, and a precipitate formed in the aqueous layer upon standing. The precipitate was filtered. The undissolved material, the aqueous layer, and the precipitate filtered from the aqueous layer were retained for the analysis of oxidation products.

The reaction time was reduced for samples KC-160 and KC-165 due to excessive foaming. Reaction KC-190 was violent. Flaming occurred on the surface of the reaction mixture. The reaction was contained in the reaction flask of the Bethge apparatus with no apparent damage to the reaction system. The sample size was reduced to 0.1 gram for KC-200 as a safety precaution. The reaction proceeded smoothly.

Each reaction was performed in a perchloric acid fume hood behind an explosion shield. The authors reccommend that extreme caution be exercised when perchloric acid alone is used to oxidize organic material.

The undissolved material was designated as KC-$^{o}$C-U, and the precipitate filtered from the aqueous layer was designated as KC-$^{o}$C-A. The undissolved material and the aqueous layer precipitate were washed free of perchloric acid with distilled water. The samples were dried and weighed.

Samples KC-110-U through KC-190-U of the undissolved material were washed with 0.25 N sodium hydroxide. The sodium hydroxide washings were acidified with 12 M hydrochloric acid. A brown precipitate formed and was filtered. The precipitate was washed with heptane into a weighed 50 ml flask. The heptane washings (KC-$^{o}$C-U1) were evaporated to dryness and weighed. The precipitate was then washed with benzene into a weighed 50 ml flask. The benzene washings (KC-$^{o}$C-U2) were evaporated to dryness and weighed. The undissolved material was washed with methanol into a weighed 50 ml flask. The methanol washings (KC-$^{o}$C-U3) were evaporated to dryness and weighed. The remaining precipitate (KC-$^{o}$C-U4) was sodium hydroxide soluble, and was retained for analysis.

Samples KC-150-A through KC-180-A of the precipitate filtered from the original aqueous layer were washed with heptane into weighed 50 ml flasks. The heptane washings (KC-$^{o}$C-A1) were evaporated to dryness and weighed. The precipitate was washed with benzene into a weighed 50 ml flask. The benzene washings (KC-$^{o}$C-A2) were evaporated to dryness and weighed. The precipitate was washed with methanol into a weighed 50 ml flask, the washings (KC-$^{o}$C-A3) were evaporated to dryness and weighed. Only a trace of precipitate remained after the washing of the precipitate with methanol which was sodium hydroxide soluble.

Ultraviolet spectra were recorded for all U3 and A3 samples. A portion of each sample was dissolved in methanol. A background spectrum of methanol was recorded. The spectra were recorded on a Perkin Elmer Lamda 4B UV/VIS spectrometer. Infrared spectra were obtained via a diffuse reflectance technique with a Nicolet 20 DXB FTIR spectrometer. All U3, U4, and A3 samples were esterified with methyl-8 methylating reagent. One milliliter of methyl-8 was added to 5-10 milligrams of sample. The mixture was heated for 20 minutes at 60$^{o}$C. The methyl esters produced from the acid oxidation products were to be analyzed by gas chromatography and gas chromatography/mass spectrometry, however, analysis was not completed at the time of the writing of this paper.

## RESULTS AND DISCUSSION

The kerogen concentrate produced from the raw Chattanooga shale sample was dark brown. The kerogen concentrate was 46.53 percent carbon, 4.34 percent hydrogen, 1.37 percent nitrogen, and 19.73 percent sulfur. The atomic hydrogen to carbon ratio was 1.1 to 1.0 indicating a high degree of unsaturation for the kerogen concentrate. Scanning Electron Microscope/X-Ray Diffraction analysis of the kerogen concentrate indicated the presence of iron, sulfur, and titanium. Iron constituted 18 percent of the mineral content present in the kerogen

concentrate, determined with a Perkin Elmer Inductively Coupled Plasma Spectrometer. The kerogen concentrate was approximately 34 percent ash. The mineral content was predominantly pyrite based on the analysis of the kerogen concentrate and the percentages of iron and sulfur present.

The extent of oxidation of the organic material in Chattanooga oil shale was determined by monitoring the percentage of undissolved material, noting color changes in the aqueous phase, and calculating the percentage of carbon converted to carbon dioxide. Results from the oxidation of the kerogen concentrate are presented in Table 1.

The results presented in Table 1 for the percentage of undissolved material indicated the kerogen dissolved between 150°C and 180°C. The percentage of undissolved material decreased approximately 27 percent between 140-155°C. This was probably due to the dissolution of pyrite, which was approximately 30 percent of the kerogen concentrate. The dissolution of pyrite in boiling perchloric at 140-155°C has been demonstrated (8). Aromatic material was suspected to have dissolved between 170-180°C. It has been demonstrated by $^{13}$C-NMR (9) that approximately half of the organic carbon present in Chattanooga shale is aromatic.

The color intensity of the aqueous phase rose to a maximum then faded to clear. The color changes ranged from colorless to pale yellow below 150°C, dark orange-brown between 150-180°C, dark yellow at 190°C, and clear at 203°C. The maximum color intensity corresponded to the dissolution of kerogen.

The data for the percentage of carbon converted to carbon dioxide presented in Table 1 for the kerogen concentrate indicated no significant amounts of carbon were converted to carbon dioxide when the boiling point of perchloric acid was below 150°C. The percentage of carbon converted to carbon dioxide rose in a linear fashion above 150°C. The results for the total carbon present in the kerogen concentrate at 203°C are not useful. It has been demonstrated that chlorine gas is produced by perchloric acid at 203°C (4). Thus, the calculated percentage of carbon converted to carbon dioxide at 203°C was elevated due to the absorption of chlorine onto ascarite.

The oxidation products were separated into fractions. The first type of oxidation product fractionated was the acidic fraction isolated from the undissolved material. The solid acids were separated into heptane, benzene, and methanol soluble fractions. There was no evidence that any material was extracted by heptane or benzene. Polar acids were extracted with methanol (KC-°C-U3). The remaining acids (KC-°C-U4) were sodium hydroxide soluble. The acid products KC-150-U3 through KC-170-U3 were brown in color and flaky in texture. Sample KC-180-U3 was brownish-yellow. Samples KC-150-U4 through KC-180-U4 were black. The second type of oxidation product was the precipitate which settled out of the aqueous layer. These acids were separated into heptane, benzene, and methanol soluble fractions. No acid

material was extracted with heptane or benzene. A trace of acid material remained after the methanol extraction was completed which was sodium hydroxide soluble (KC-$^{o}$C-A4). The methanol soluble acids (KC-$^{o}$C-A3) were identical in color and texture to the methanol soluble acids extracted from the undissolved material.

The infrared spectra recorded for selected U3, U4, and A3 samples were characteristic of unsaturated carboxylic acids. The spectra exhibited a broad band between 3500-3000 $cm^{-1}$ indicative of the hydroxyl stretch of a carboxylic acid. A band between 1750-1700 $cm^{-1}$ was typical for a carbonyl stretch of a carboxylic acid. The presence of aldehydes and ketones can not be ruled out. A peak from 1610 $cm^{-1}$ to 1590 $cm^{-1}$ was the typical region for carbon-carbon double bonds. The bands between 1200-1300 $cm^{-1}$ and 1400-1440 $cm^{-1}$ were typical for the C-O stretching and O-H bending of a carboxylic acid.

The ultraviolet spectra were recorded for all U3 and A3 samples. Each spectra contained one broad peak which was essentially identical for each sample. The maximum absorbance occurred between 206-211 nm. This was the characteristic region for unsaturated carboxylic acids which were also indicated by infrared analysis. Each peak exhibited a shoulder peak in the 230 nm to 255 nm region which was suspected to have arisen from the presence of aromatic material in the oxidation products.

## CONCLUSION

A stepwise oxidation of the kerogen of Chattanooga oil shale was effected by oxidative degradation with perchloric acid. The dissolution of the kerogen occurred between 150-180$^{o}$C. The atomic hydrogen to carbon ratio indicated a high degree of unsaturation. Highly polar unsaturated carboxylic acids were indicated as the primary oxidation products. Gas chromatography and gas chromatography/mass spectrometry analysis of the oxidation products were not completed at the time of the writing of this paper. No suitable technique has been developed to separate organic oxidation products from perchloric acid solution. Work will be continued in this area utilizing XAD resins. The GC/MS data and the data obtained from the oxidation of model compounds will be used to propose a model for the structure of the kerogen of Chattanooga oil shale.

## ACKNOWLEDGEMENTS

This work was funded through an American Chemical Society - Petroleum Research Fund grant-in-aid # 19461-B2, and a Faculty Research Grant from Tennessee Technological University. The authors would like to thank Dr. Wayne Leimer of the Geology Department at Tennessee Technological University, Glenn Norton from the Ames Laboratory at Iowa State University, and Karen R. Merkley from Fleetguard Inc. for technical assistance.

## REFERENCES


1. Leonard, J.T., Univ. Microfilms (Ann Harbor), L.C. Card No: Mic 59-2987: 1288, (1959).

2. Kinney, C.R. and Leonard, J.T., J. Chem. Eng. Data, 6: 474 (1961).

3. Kinney, C.R. and Schwartz, D., Ind. Eng. Chem., 49: 1125 (1957).

4. Smith, G.F., Analyst, 80: 16, (1955).

5. McGowan, C.W. and Diehl, H., Fuel Process. Technol., 10: 169, (1985).

6. McGowan, C.W. and Diehl, H., Fuel Process. Technol., 10: 181, (1985).

7. McGowan, C.W. and Diehl, H., Fuel Process. Technol., 10: 195, (1985).

8. McGowan, C.W. and Markuszewski, R., Fuel. Process. Technol., 17: 29, (1987).

9. Minkis, F.P. and Smith, J.W., Org. Geochem., 5: 193, (1984).


TABLE 1

Results obtained from the oxidation of the Kerogen Concentrate

| Sample | Normality $HClO_4$ | Boiling point $HClO_4$ ($^oC$) | Reaction temp ($^oC$) | Reaction time (hour) | Total Carbon (percent of sample) | Undissolved material (percent of sample) |
|---|---|---|---|---|---|---|
| KC-111 | 2.07 | 111 | 106 | 1.5 | 0.63 | 97.80 |
| KC-120 | 4.26 | 120 | 112 | 1.5 | 0.49 | 98.11 |
| KC-132 | 6.30 | 132 | 123-4 | 1.5 | 0.47 | 96.62 |
| KC-141 | 6.77 | 141 | 129-30 | 1.5 | 0.17 | 89.91 |
| KC-151 | 8.02 | 151 | 139-40 | 1.5 | 3.08 | 72.27 |
| KC-156 | 8.42 | 156 | 145-48 | 1.5 | 10.96 | 62.37 |
| KC-162 | 8.52 | 162 | 149-52 | 1.2 | 12.00 | 56.37 |
| KC-166 | 8.63 | 166 | 152-60 | 1.3 | 14.70 | 47.65 |
| KC-171 | 9.26 | 171 | 163-68 | 1.5 | 16.26 | 38.74 |
| KC-181 | 9.73 | 181 | 169-74 | 1.5 | 27.45 | 13.53 |
| KC-190 | 10.46 | 190 | 175-83 | 1.5 | 54.06 | 0.27 |
| KC-203 | 11.67 | 203 | 202 | 1.5 | 119.04 | 0.00 |

# RAPID EVALUATION OF REACTION CONDITIONS ON COAL PYROLYZATES USING COUPLED PYROLYSIS GC/MS

David J. Miller, Steven B. Hawthorne, and Ronald C. Timpe

University of North Dakota Energy and Minerals Research Center
Box 8213 University Station
Grand Forks, North Dakota 58202

## ABSTRACT

The optimization of processes using coal as a carbon source for reaction with steam to produce hydrogen requires an understanding of the composition of the volatile components released during the charring process. A coupled pyrolysis GC/MS method has been developed to rapidly evaluate the effect of reaction conditions, including catalysts used to accelerate the char-steam reaction on the composition of the coal pyrolyzate. Four samples (one uncatalyzed and three catalyzed with 10 wt% $CaCO_3$, $K_2CO_3$, and $Na_2CO_3$, respectively) of a North Dakota (Velva) lignite were pyrolyzed under helium at 700 °C for ten minutes. The volatile products (primarily benzene and alkylbenzenes, phenol and alkylphenols, dihydroxybenzenes, and methoxyphenols) were swept from the pyrolysis chamber directly into a capillary gas chromatographic column and cryogenically trapped prior to GC/MS analysis. While simulated distillation plots for the uncatalyzed Velva and three catalyzed samples were similar, dramatic reductions in the amounts of catechols and guaiacols were observed in the $K_2CO_3$ and $Na_2CO_3$ catalyzed samples.

## INTRODUCTION

Pyrolysis gas chromatography/mass spectrometry has become increasingly popular for the analysis of solid fuel and fuel related materials. In recent papers, pyrolysis-GC/MS has been applied to hydronaphthalenes to determine degradation pathways (1), asphaltenes (2), oil shale (3), kerogens (2), buried wood (4), coalified logs (4), and coal (5,6). Ekstrom and Callaghan have used pyrolysis coupled directly to the ion source of a mass spectrometer to study pyrolysis kinetics of oil shale (7). In general, pyrolysis probes utilizing 5 to 100 µg of samples are used for pyrolysis GC/MS. Our technique utilizes a larger sample size (2-4 mg) and split injection to obtain a more representative sample for GC/MS analysis. Pyrolysis products are introduced into a split injector and are cryogenically trapped at the head of a fused-silica capillary gas chromatographic column.

Timpe and co-workers have shown that the addition of alkali carbonates to low-rank coals prior to charring has increased the rate of hydrogen production from the char-steam reaction (8). We have used pyrolysis GC/MS to determine the effect of three alkaline carbonate catalysts, $CaCO_3$, $K_2CO_3$, and $Na_2CO_3$, on the composition of pyrolysis products produced at 700 °C.

## EXPERIMENTAL

### Samples

North Dakota (Velva) lignite was ground to -200 mesh and dried in a vacuum desiccator for 48 hours prior to pyrolysis. Three additional samples containing catalysts were prepared from the same North Dakota Lignite. Ten weight percent of dry $CaCO_3$, $K_2CO_3$, or $Na_2CO_3$ (Trona - a naturally occurring $Na_2CO_3$ mineral) was mixed with the North Dakota lignite and dried in the same manner as the uncatalyzed sample.

### Pyrolysis Gas Chromatography/Mass Spectrometry

GC/MS analysis of the pyrolysis products was performed with a Hewlett-Packard 5985B using a 60 m x 0.25 mm i.d. (0.25 µm film thickness) DB-5 fused silica capillary column (J & W Scientific, Folsum, CA). Electron impact (EI) mass spectra were generated at 70 eV with a scan range of 50-400 amu. Helium was used as the carrier gas at an approximate linear flow rate of 50 cm/sec.

Figure 1 shows a schematic diagram of the pyrolysis apparatus. Approximately 2-4 mg of coal was placed in a 30 cm x 4 mm i.d. quartz tube. The sample was positioned approximately 5 cm from the outlet of the quartz tube with a plug of quartz wool. 1-chloronaphthalene was added as an internal standard for each analysis by injecting 1 µl of a 1.47 µg/µl solution into the quartz plug and allowing the solvent to evaporate for 15 minutes prior to pyrolysis. The outlet of the tube was attached to a 1/4" x 1/16" stainless steel union fitted with a 2 in. x 0.20 mm i.d. needle. The upper end of the sample tube was then placed in a brass heater block (preheated to 700 °C) but the sample was maintained at ambient temperature. A helium purge line was attached to the upper end of the sample tube. During the pyrolysis step, the helium flow was diverted from the injection port to sweep the pyrolysis products out of the pyrolysis chamber and into the injection port, the needle was inserted into the split/splitless injection port, and the block heater was dropped down around the sample (this resulted in a temperature of 650 °C in 30 seconds and 700 °C in one minute). The pyrolyzates were swept into the split injection port and were cryogenically trapped on the head of a fused-silica capillary chromatographic column by holding the oven temperature a 0 °C during the 10 minute pyrolysis. Upon completion of the pyrolysis, the sample tube injection needle was removed from the injection port, the helium flow switched back to the injection port, the column oven was heated rapidly to 50 °C, followed by temperature programming at 8 °C/min to 320 °C.

## RESULTS AND DISCUSSION

Figures 2, 3, 4, and 5 show the total ion current chromatograms resulting from the pyrolysis of uncatalyzed Velva lignite, Velva with 10 wt% $CaCO_3$, Velva with 10 wt% $K_2CO_3$, and Velva with 10 wt% Trona. The numbered peaks in Figures 2, 3, 4, and 5 are identified in Table 1. Good chromatographic peak shapes were obtained with cryotrapping at 0 °C. The major species detected were benzene, toluene, and $C_2$-$C_4$ benzenes; phenol and $C_1$-$C_3$ phenols, catechol and $C_1$ catechols; and guaiacol and $C_1$ guaiacols. Also present were normal alkanes in the range from $C_6$ to $C_{26}$.

The boiling points of the normal alkanes found in the pyrolysis product of each sample were used to generate the simulated distillation plots shown in Figure 6. Cumulative integrated areas of the total ion current chromatograms (normalized to the internal standard) of the species eluting between the between n-alkanes (starting with $C_6$) were used to generate the plots shown in Figure 6. Each pyrolyzate showed similar simulated distillation plots with approximately one-half of the volatile species having boiling points of less than 250 °C. The slight variation in the plot for the Velva with 10 wt% $K_2CO_3$ as a catalyst may be due to the relatively small amount of catechol present and the absence of $C_1$ catechols in the pyrolyzate for this sample.

Figure 7 shows a plot of the molecular ion areas normalized to the area of the internal standard for several of the most abundant compound classes found in each of the pyrolyzates. Components 1 thru 4 are benzene and $C_1$-$C_3$ benzenes. All four samples contained similar amounts of these components with the $CaCO_3$ catalyzed sample having slightly lower amounts of benzene and toluene. Phenol, $C_1$ phenols, and $C_2$ phenols, (components 5, 6, and 7, respectively) generally decreased with added catalyst. An exception to this trend was the higher amount of phenol present in the Velva sample catalyzed with $K_2CO_3$.

Dramatic differences in the amounts of catechol, $C_1$ catechols, guaiacol, and $C_1$ guaiacols (components 8, 9, 10, and 11) were observed. Both the $K_2CO_3$ and the Trona catalyzed samples showed a large reduction in catechol (>90%) and $C_1$ catechols (>80%) compared to the uncatalyzed sample while pyrolysis with $CaCO_3$ showed little reduction. Catalysis with $K_2CO_3$ showed a larger reduction in guaiacol and $C_1$ guaiacols than the other catalysts. The mechanism for this process is not known and will require additional investigation using model compounds.

## CONCLUSIONS

Coupled pyrolysis gas chromatography/mass spectrometry with split injection can be a valuable tool for studying the effect of catalysts on the composition of pyrolyzates. The use of an internal standard allows direct comparison of pyrolyzates and can be used to estimate liquid yields and liquid quality. The addition of catalysts to the Velva lignite had minor effects on pyrolyzate yield. However, catalysis with $K_2CO_3$ and Trona showed large reductions in catechols and guaiacols.

## CREDIT

The authors would like to thank the U.S. Department of Energy for support for this work under contract number DE-FG22-86PC90911.

## REFERENCES

1. Bredael, P., and Vinh, T. H., Fuel, 58, 211-214 (1979).

2. Solli, H., and Leplat, P., Org. Geochem., 10, 313-329 (1986).

3. Suuberg, E., Sherman, J., Lilly, W. D., Preprints, Div. of Petroleum Chem., ACS, 32(1), 138-142 (1987).

4. Hatcher, P. G., Lerch, H. E., Kotra, R. K., and Verheyen, T. V., Preprints, Div. of Fuel Chem., ACS, 32(1), 85-93 (1987).

5. Siskin, M. and Aczel, T., Fuel, 62, 1321-1326 (1983).

6. Miller, D. J., and Hawthorne, S. B., Preprints, Div. of Fuel Chem., ACS, 32(4), 10-17 (1987).

7. Ekstrom, A., and Callaghan, G., Fuel, 66, 331-337 (1987).

8. Timpe, R. C., Sears, R. E., and Montgomery, G. G., Div. of Fuel Chem., ACS, 32(4), 1-9 (1987).

TABLE I. Identification of Numbered Peaks from Figures 2, 3, 4, and 5.

| Peak Number | Species |
|---|---|
| 1 | 1-hexene |
| 2 | hexane |
| 3,5 | $C_6H_8$ isomer |
| 4,6 | $C_6H_{10}$ isomer |
| 7 | benzene |
| 8 | thiophene |
| 9,11,12 | $C_7H_{14}$ isomer |
| 10 | $C_7H_{16}$ isomer |
| 13 | toluene |
| 14 | $C_7H_{10}$ isomer |
| 15 | $C_8H_{16}$ isomer |
| 16 | $C_8H_{18}$ isomer |
| 17,18 | $C_2$ benzene |
| 19 | $C_9H_{18}$ isomer |
| 20 | cyclooctatetraene |
| 21 | $C_2$ benzene |
| 22 | $C_9H_{20}$ isomer |
| 23,24,25 | $C_3$ benzene |
| 26 | phenol |
| 27 | $C_{10}H_{22}$ isomer |
| 28,29 | $C_3$ benzene |
| 30 | $C_4$ benzene |
| 31,32 | $C_1$ phenol |
| 33 | guaiacol |
| 34 | $C_{11}H_{24}$ isomer |
| 35,36,37,38 | $C_2$ phenol |
| 39 | catechol |
| 40 | $C_2$ benzofuran |
| 41 | $C_3$ phenol |
| 42,43 | $C_1$ catechol |
| 44 | $C_1$ naphthalene |
| 45,46 | $C_1$ guaiacol |
| 47 | 1-chloronaphthalene (IS) |
| 48 | $C_2$ naphthalene |
| 49 | $C_{15}H_{32}$ isomer |
| 50,51,52 | M=206 sesquiterpene isomer |
| 53 | $C_{16}H_{34}$ isomer |
| 54 | $C_3$ naphthalene |
| 55 | $C_{17}H_{36}$ isomer |
| 56 | M=266 biological marker |
| 57 | $C_{18}H_{38}$ isomer |
| 58 | $C_{19}H_{40}$ isomer |
| 59 | $C_{20}H_{42}$ isomer |
| 60 | $C_{21}H_{44}$ isomer |
| 61 | $C_{22}H_{46}$ isomer |
| 62 | $C_{23}H_{48}$ isomer |
| 63 | $C_{24}H_{50}$ isomer |
| 64 | $C_{25}H_{52}$ isomer |
| 65 | $C_{26}H_{54}$ isomer |

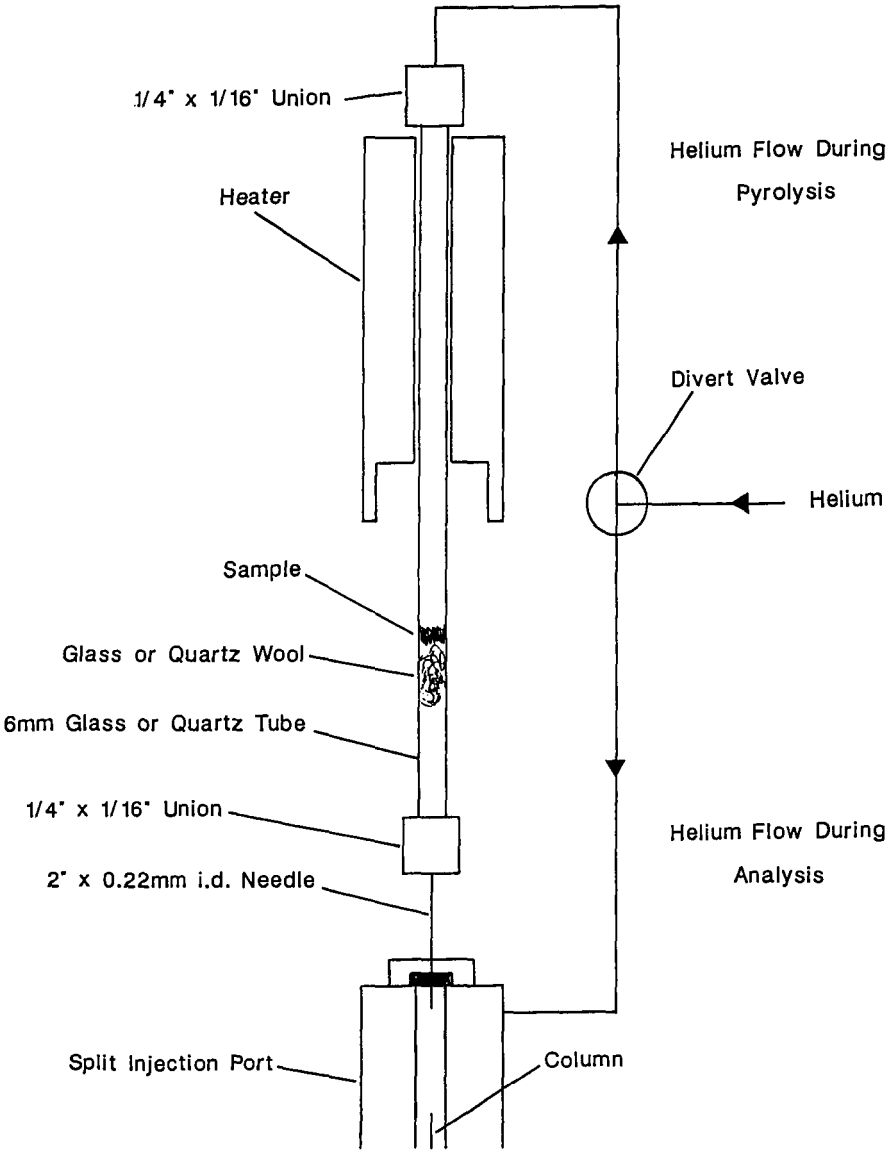


Figure 1. Pyrolysis Apparatus.

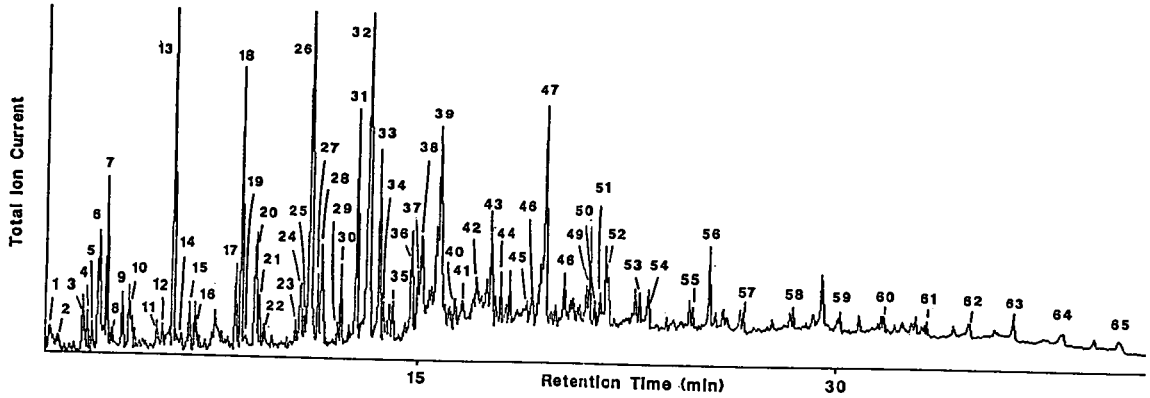


Figure 2. Pyrolysis TIC trace from uncatalyzed Velva lignite.

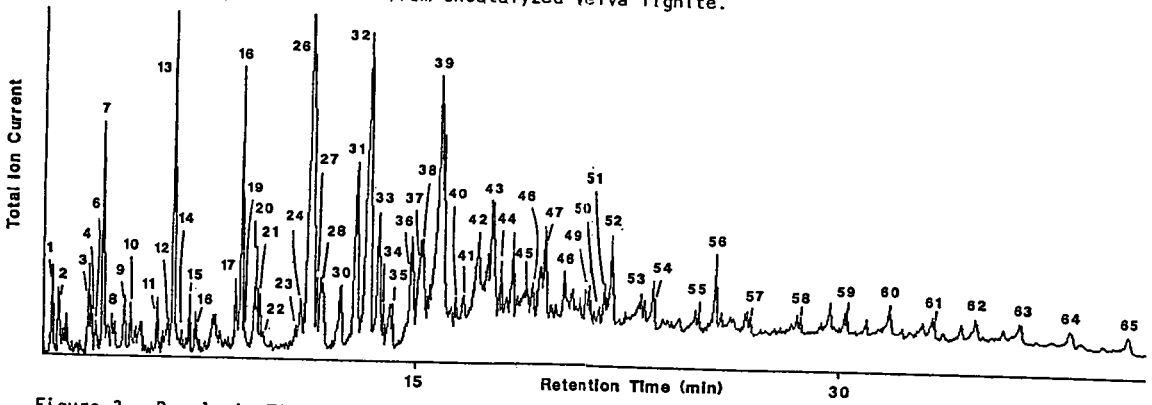


Figure 3. Pyrolysis TIC trace from $CaCO_3$ catalyzed Velva lignite.

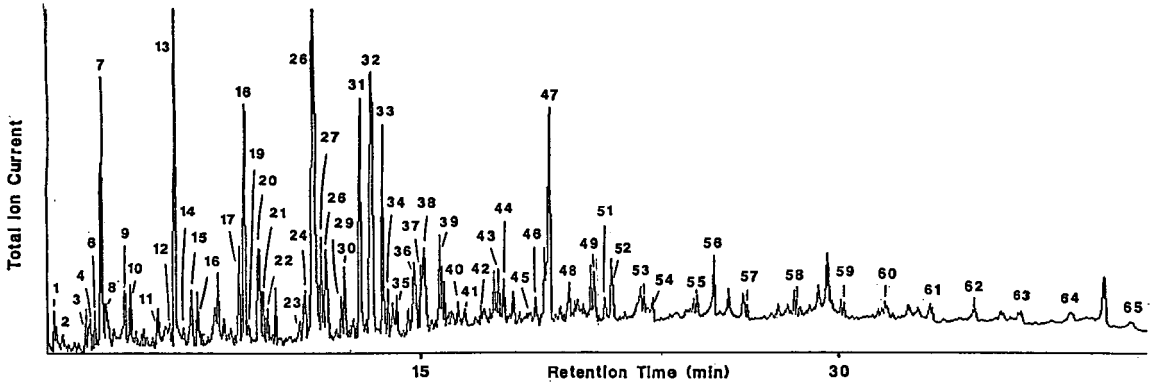


Figure 4. Pyrolysis TIC trace from $K_2CO_3$ catalyzed Velva lignite.

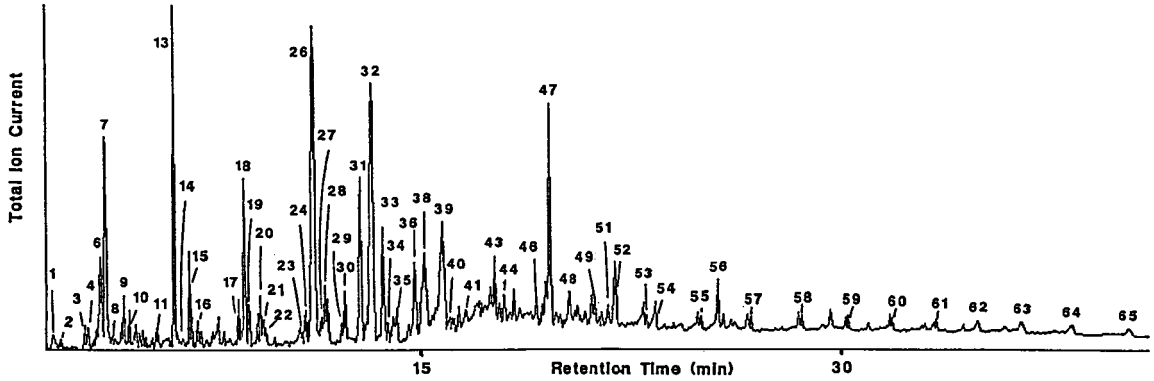


Figure 5. Pyrolysis TIC trace from $Na_2CO_3$ catalyzed Velva lignite.

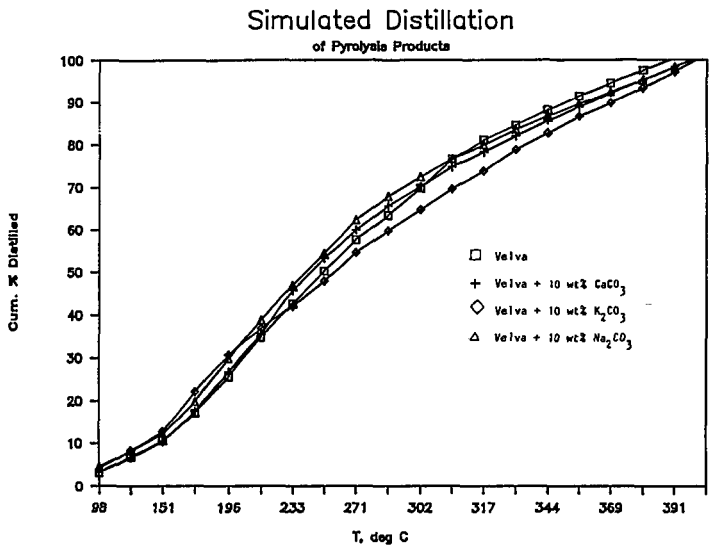


Figure 6. Simulated distillation plots for Velva lignite with and without catalyst.

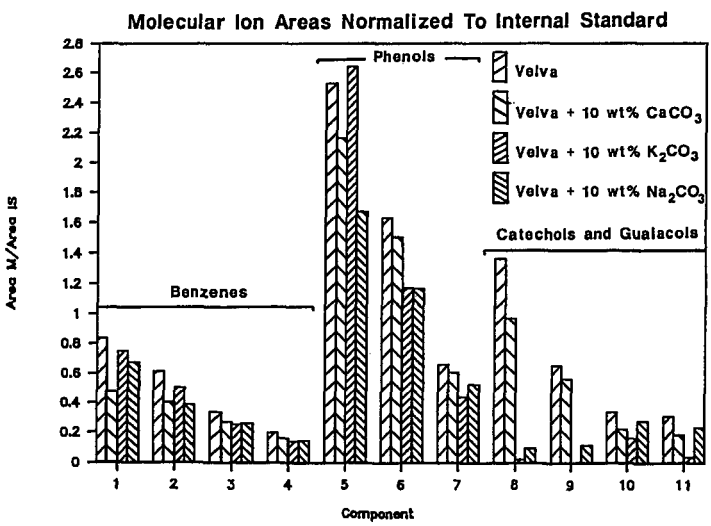


Figure 7. Comparison of the most abundant compound classes in the pyrolysis products of Velva lignite with and without catalyst. Components: 1-benzene, 2-toluene, 3-$C_2$ benzenes, 4-$C_3$ benzenes, 5-phenol, 6-$C_1$ phenols, 7-$C_2$ phenols, 8-catechol, 9-$C_1$ catechols, 10-guaiacol, 11-$C_1$ guaiacols.